ORC AND ENTREPENEURSHIP IN 2015

Gilles David

Enertime SAS

ABSTRACT

The creation from scratch and development of an industrial company in the 21st century is a challenging but rewarding experience. The ORC technology is a perfect choice for would-be industrial entrepreneurs. Gilles David will speak about the genesis of Enertime, an ORC manufacturer he created in 2008. He will explain the technical choices made, the experience gained in creating and establishing a company that design and build large ORC for the international market and his view of the ORC market drivers.

THERMAL STABILITY OF HEXAMETHYLDISILOXANE (MM) FOR HIGH TEMPERATURE APPLICATIONS

Markus Preißinger*, Dieter Brüggemann

University of Bayreuth, Center of Energy Technology (ZET),
Institute of Engineering Thermodynamics and Transport Processes (LTTT),
Universitätsstraße 30, 95447 Bayreuth, Germany
e-mail: zet@uni-bayreuth.de
Web page: http://www.zet.uni-bayreuth.de

* Corresponding Author

ABSTRACT

The design of efficient ORC units for the usage of industrial waste heat at high temperatures requires direct evaporating systems without an intermediate thermal oil circuit. Therefore, the thermal stability of high temperature working fluids gains importance. In this study, the thermal degradation of hexamethyldisiloxane (MM) is investigated in an electrically heated tube. The results include qualitative remarks on degradation products as well as the annual degradation rate as quantitative parameter. It is shown that MM is stable up to a temperature of 300 °C with annual degradation rates of less than 3.5 %. Furthermore, the break of a silicon-carbon bond can be a main chemical reaction that influences the thermal degradation. Finally, the impact of the results on the future design of ORC units is discussed.

1. INTRODUCTION

Linear siloxanes like hexamethyldisiloxane (MM) are promising working fluids for high temperature applications like biomass fired power plants (Obernberger, 1998; Obernberger et al., 2002). In such systems, a thermal oil circuit based on synthetic oils with degradation temperatures of more than 300 °C (Mang and Dresel, 2007) is used to avoid thermal stress of the ORC working fluid. However, for industrial waste heat recovery a trend is noticed to direct evaporating systems without thermal oil circuit. The advantages are higher efficiencies, lower investment costs and a much simpler system design. Although evaporation temperatures of MM are limited to a value below 240 °C for typical working pressures of about 17 bar, the film temperature at the heat exchanger surface, hot-spots within the heat exchanger and the failure mode (e.g. standstill of the ORC pump but no shutdown of the heat source) have to be kept in mind.

Therefore, if we want to use MM in a wide range of heat source temperatures, reliable data for its thermal stability are essential. Colonna et al. (2006) report a limit of 400 °C, however, the duration of the experiments, the heating rate and the pressure remain unclear. For cyclic siloxanes, Angelino (1993) gives a similar value of 400 °C. Dvornic (2000, 2008) investigates extensively thermal properties of polysiloxanes, however, without giving quantitative results for the degradation temperature of MM.

To attain such results, different methodologies concerning design of the test rig and evaluation method are found in literature. Ginosar et al. (2011) report a method to separate catalytic from thermal effects within a glass tube. The standard test procedure for the thermal stability of refrigerants is carried out almost similar (ANSI/ASHRAE, 2007). For the same chemical class, the method of adiabatic compression is used to avoid the thermal degradation at hot surfaces (Buravtsev et al., 1994). Thermogravimetric analyses within vacuum (Grassie and Macfarlane, 1978; Grassie et al., 1979; Deshpande and Rezac, 2002) as well as the analysis of different catalysts (Kuramochi et al.,

1993) are also widespread. A test rig designed especially for measurements of ORC working fluids, and in particular of methylbenzenes, is reported by Angelino et al. (1991). Calderazzi and Colonna (1997) use a similar test rig for different refrigerants. In both cases, the sample is located in a metallic cylinder and heated in an oven. Based on isothermal long-time experiments, the degradation rate is calculated.

In the present study, we redesign the test rig by using an electrical heated tube which allows for high heating rates which can be accurately controlled. The main objective is to gain more knowledge on the influence of the working fluid temperature as well as the duration of the experiment. Furthermore, knowledge about the chemical composition of the degradation products is of main interest for a secure operation of direct evaporating ORC systems.

2. METHODOLOGY

2.1 Test rig and procedure

A stainless steel tube with a length of 220 mm and an outer diameter of 18 mm is electrically heated according to Figure 1. The volume of the reactor accounts for 70.2 ml. The power of the heating wire is 850 W on a length of 5 m allowing a continuous and uniform heating of up to 450 °C. Compared to the heating in an oven, faster heating rates are achieved and the heating rate can be chosen constant for all tests. Within a second tube with an outer diameter of 3 mm the temperature within the reactor is measured with a thermocouple and used as pre-set temperature for the isothermal test procedure. To ensure constant test conditions, the reactor volume is flushed with nitrogen and evacuated two times before each test. The vacuum pump has a pressure limit of 1.0E-6 bar. Therefore, the remaining mass of nitrogen in the reactor is negligible. A sample mass of about 7 g is fed into the reactor through the filling valve at the bottom of the tube. Afterwards the reactor is sealed through blind plugs, heated until the preset temperature with a constant heating rate of 0.3 K/s and the time measurement starts. After the test period, the electrical heating is switched off and the reactor is cooled down to ambient temperature through natural convection. Subsequently, the analysis of the time-dependent temperature and pressure curve as well as the analysis of vapour and liquid phase by means of gas chromatography, mass spectroscopy and Karl-Fischer-titration is carried out. The raw material is MM with a purity of 97 % from the company Wacker Chemie in Burghausen, Germany (Wacker® AK 0.65).
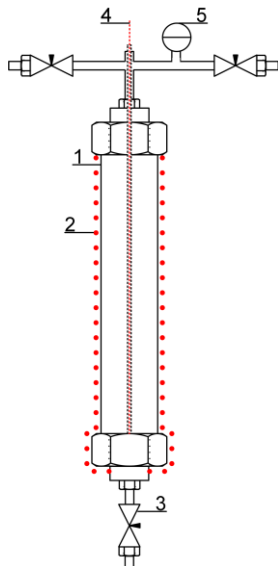

Figure 1: Stainless steel tube (1), electrical heating wire (2), needle valve (3), thermocouple (4) and pressure sensor (5)

Figure 2: Reactor in the lab

2.2 Evaluation method

To describe the evaluation method, an experiment with a temperature of 420 °C and duration of 72 h is selected exemplarily.

First of all, the heating period is analysed. Figure 3 shows the pressure within the tube depending on temperature. The characteristic progression of the bubble line is obtained until a pressure of about 10 bar. However, due to the fact that the heating is much faster than the mixing of the fluid within the reactor, the vapour pressure at a specific temperature is lower than it is expected. Afterwards the slope of the curve drops as the specific volume of MM within the reactor is higher than the critical specific volume (Stephan et al., 2009). Due to the subsequent full mixing within the reactor, the pressure increases marginally at a constant temperature of 420 °C. The slightly right bended part between 120 °C and 160 °C is caused by contaminants within the raw material.

Secondly, the pressure profile during the isothermal test period in Figure 4 shows a value of 15.2 bar with a fluctuation range of 0.05 bar. The pressure changes indicate the formation of molecules with lower or higher molecular mass. The noise signal of the pressure sensor (±5 mbar) does not affect the result. As the pressure changes are not clearly pronounced, further evaluation methods are needed.
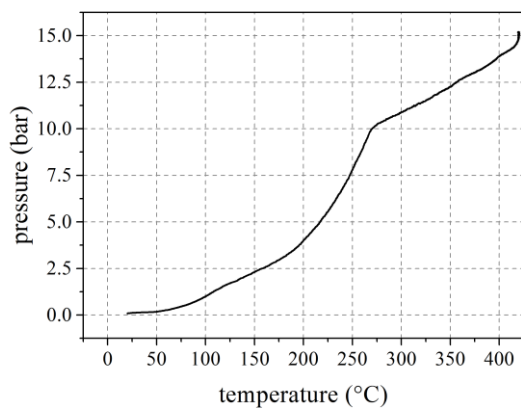

Figure 3: Pressure depending on temperature during heating period ($T = 420$ °C, $t = 72$ h)
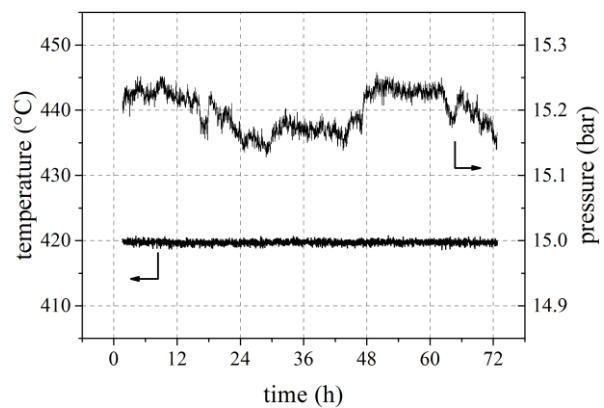

Figure 4: Temperature and pressure depending on time ($T = 420$ °C, $t = 72$ h)

The comparison of the pressure in the reactor before and after the experiment (Figure 5 and Figure 6) confirms the formation of molecules with lower molecular mass than MM. At a constant temperature and a fixed volume of the reactor, the pressure after the experiment is much higher as before which is caused by high vapour pressure of the degradation products.
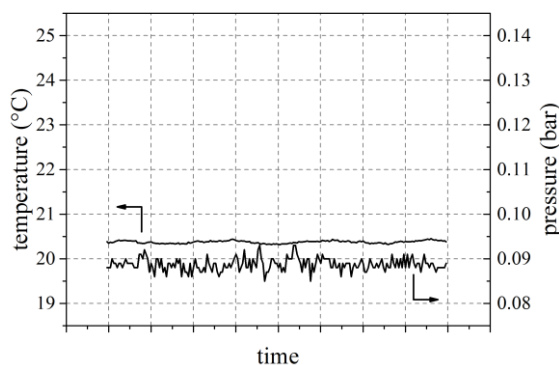

Figure 5: Temperature and pressure before experiment ($T = 420$ °C, $t = 72$ h)
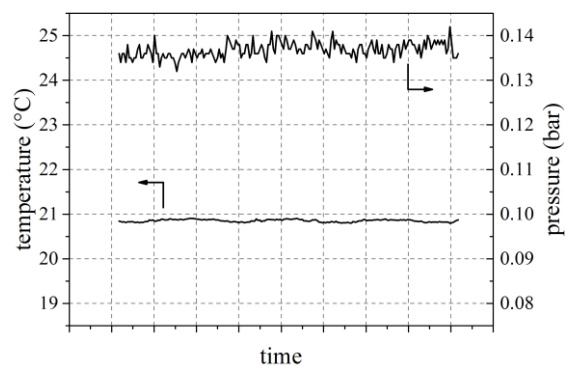
Figure 6: Temperature and pressure after experiment ($T = 420$ °C, $t = 72$ h)

The chemical analysis of the products and the raw material by means of gas chromatography proves the assumption of low molecular substances. The mean relative error caused by the gas chromatograph is lower that 2 %. All components with a mass fraction higher than 0.4 % in the vapour phase are displayed in Figure 7. The mass fraction of MM drops to 58 %. The main

degradation products are low molecular hydrocarbons. This confirms the results from laser impulse experiments of Manders and Bellama (Manders and Bellama, 1985). Within the liquid phase traces of high molecular siloxanes are measured which fits the theory of Dvornic (Dvornic, 2000, 2008). However, the mass fraction of MM within the liquid phase still exceeds 99 % and indicates that the degradation products are mainly found in the vapour phase. As water catalyses the thermal degradation of many organic compounds, the water content of the raw material is measured by means of Karl-Fischer titration which gives a marginal value of 140 ppm. Furthermore, the nitrogen-flushing of the reactor and the subsequent evacuation ensures that no free water or contaminants remain within the tube which would influence the experiments.
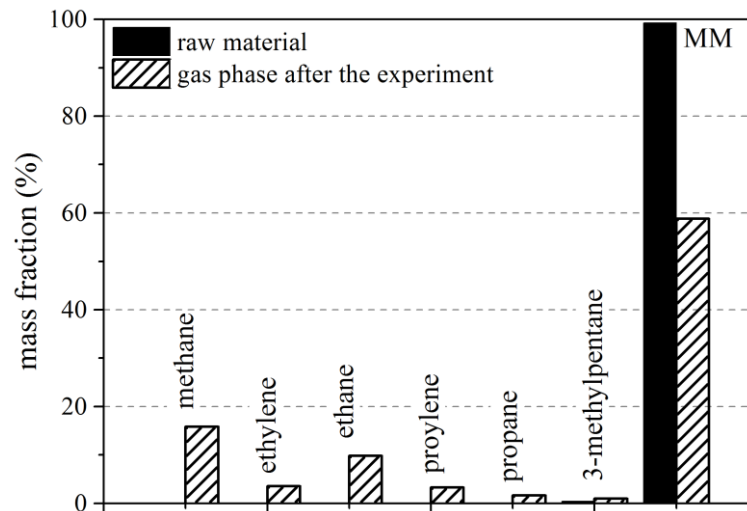

Figure 7: Mass fraction of vapour phase after the experiment and of raw material
($T = 420\ °C$, $t = 72$ h, relative error caused by gas chromatograph < 2 %)

3. RESULTS

3.1 Influence of temperature on thermal degradation

The influence of temperature on the thermal degradation is evaluated in Figure 8. The mass fraction of MM drops with increasing temperature. Below a temperature of 300 °C, methane is the dominant degradation product and higher molecular hydrocarbons are hardly detected. At 360 °C, higher amounts of ethane and ethylene are detected for the first time. The mass fraction of propane and propylene remains below 1.5 %. This value increases up to 7.3 % at 420 °C. In general, the variation margin of the mass fraction increases with increasing temperature.

3.2 Influence of time on thermal degradation

In general, the retention time within an ORC evaporator is far less than 72 h. However, due to impropriate mixing and dead volume, high residence times may occur in reality as well. Furthermore, short retention times could give knowledge about the chemical reactions involved in the degradation process. Therefore, the influence of time on the degradation is evaluated. A temperature of 420 °C is chosen to attain high degradation rates which are essential for meaningful results on the influence of time. The mass fraction of MM in Figure 9 drops and the ones of the degradation products increase with increasing time. The slope is almost linear within the first 24 h, for longer times the curves flatten.
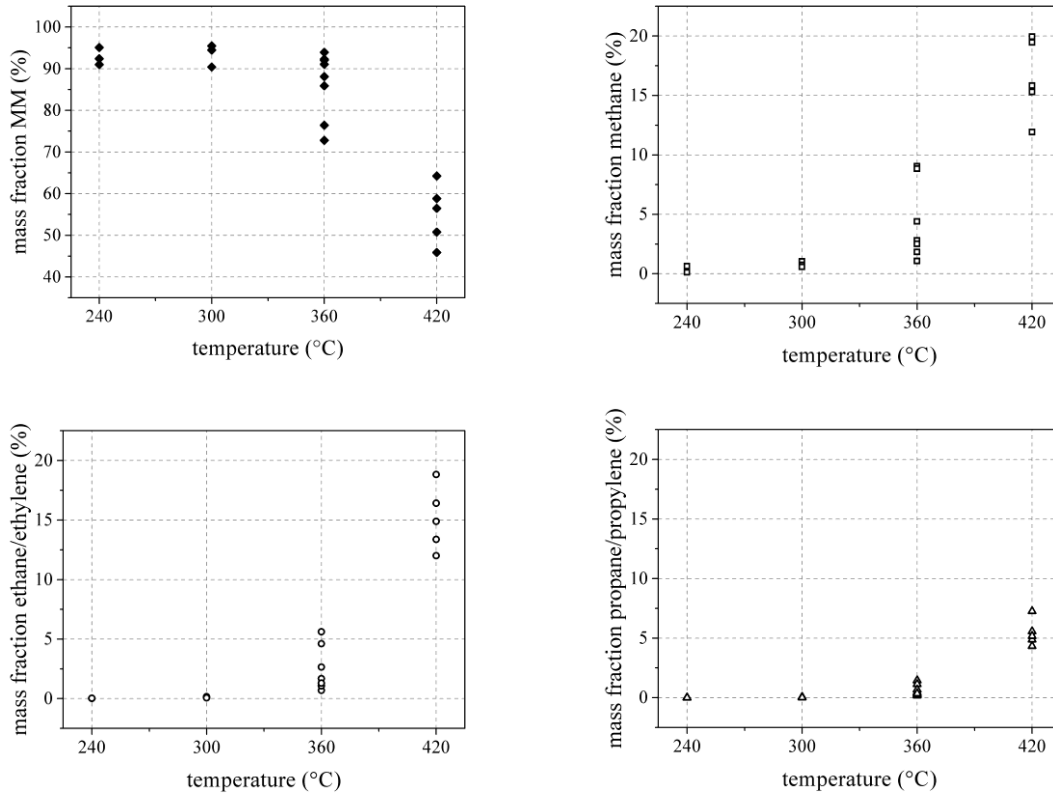
Figure 8: Mass fraction of MM, methane, ethane/ethylene and propane/propylene in the vapour phase after the experiment depending on temperature ($t = 72$ h)
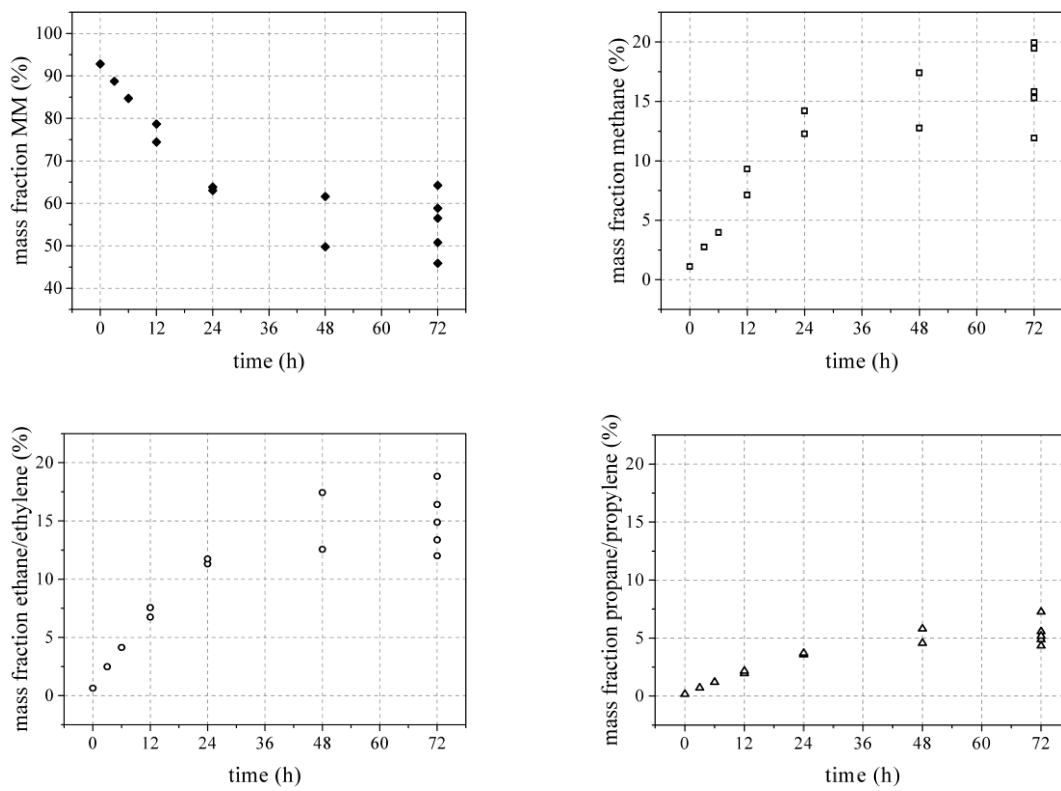

Figure 9: Mass fraction of MM, methane, ethane/ethylene and propane/propylene in the vapour phase after the experiment depending on time ($T = 420$ °C)

4. DISCUSSION

4.1 Qualitative evaluation of degradation products

The formation of C1-/C2- and C3-hydrocarbons suggests that the break of a Si-C-bond and the subsequent formation of methyl radicals can be seen as the start reaction of thermal degradation. The increased variation margin above a temperature of 360 °C in Figure 8 suggests complex recombination effects which differ especially for longer times of the experiment and are strongly influenced by number and kind of available radicals. The theory of free radicals is also supported by the results in Figure 9. The lower the duration of the experiment, the fewer radicals are available and the straighter forward is their influence on the mass fraction especially of MM, methane and ethane/ethylene. This leads to the characteristic linear slope for times lower than 24 h. The number and types of radicals and, therefore, the variation margin increases for longer times of the experiments.

4.2 Quantitative evaluation of degradation

The mass of gaseous MM before and after the experiment is calculated from the composition of the vapour phase. In combination with the overall mass of MM in the reactor, the annual degradation rate is deduced (Figure 10).
The typical exponential progression according to Arrhenius' law is observed. The absolute value for temperatures below 300 °C is mainly lower than the typical leakage rates of 3 %/a (Heberle et al., 2012) that are assumed for geothermal applications. The degradation rate increases considerably for temperatures higher than 300 °C.
Figure 10 also gives the error-containing values for the degradation rate if we assume the following typical errors for the input data of the calculation:

volume of the reactor and mass of MM in the reactor	± 2.0 %
mass fraction of MM in liquid and vapour phase	± 2.0 %
density of MM in liquid and vapour phase	± 1.0 %
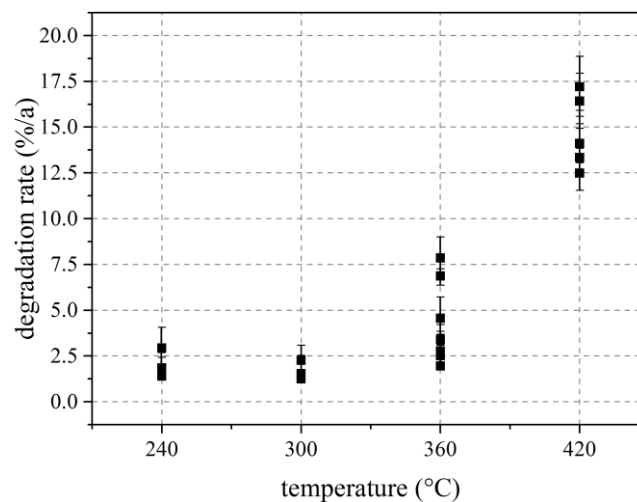
Figure 10: Degradation rate depending on temperature (t = 72 h)

The dependency of the annual degradation rate on the duration of the experiments in Figure 11 shows a steep decrease for times lower than 12 h, subsequently the curve flattens. Note that error-containing minimum and maximum values are given again. It is obvious that the relative failure increases for lower durations of the experiment as the values are extrapolated to gain the annual degradation rate. Furthermore, according to Figure 11 the annual degradation rates which were calculated from the experiments for duration of 72 h (Figure 10) are probably higher in real ORC units, in which the retention time of the working fluid in the evaporator is far less. To account for this, a test series is carried out in which MM is just heated up to the pre-set temperature and instantly cooled down

afterwards. Therefore, it is possible to "simulate" the heating in the evaporator and instant cooling in the turbine and condenser in an ORC unit. It is shown that the amount of low molecular hydrocarbons is low until a temperature of 300 °C (Figure 12). At 360 °C, the mass fraction of methane increases. Subsequently, the mass fraction of ethane/ethylene and propane/propylene increases at 420 °C. This again proves the assumption that the break of a Si-C-bondage and the set free methyl radicals influence the thermal degradation of MM.
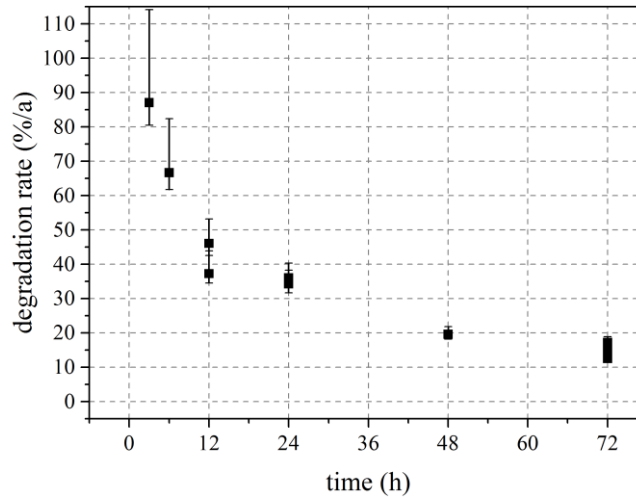
Figure 11: Degradation rate depending on time ($T = 420$ °C)
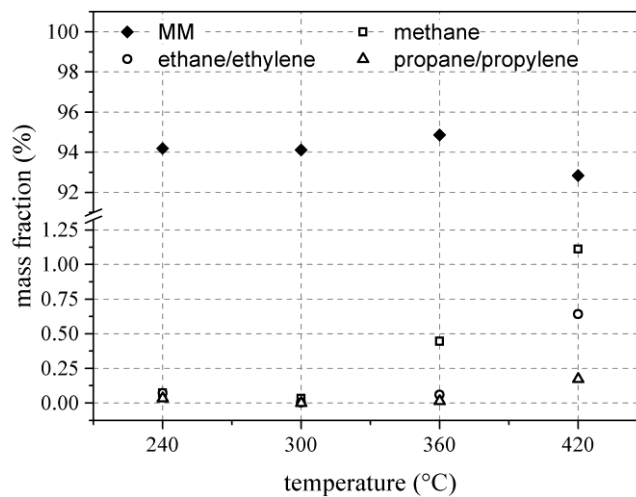
Figure 12: Mass fraction of MM, methane, ethane/ethylene and propane/propylene in the vapour phase after the experiment depending on temperature (test series: heating and instant cooling)

4.3 Impact on the set-up of ORC power units

From the gained results, it can be concluded that the use of MM in ORC units without intermediate thermal oil circuit is possible as long as the fluid temperature does not exceed 300 °C. As the thermodynamic suitable evaporation temperatures are around 240 °C, these conditions can be achieved if special care on evaporator design, particularly concerning film temperature and hotspots, is taken. Furthermore, Figure 12 shows that the formation of methane is an indicator for the thermal degradation. Therefore, in future ORC units a methane sensor could be placed at the top of the evaporator to give evidence on the degradation of MM (for example in case of unforeseen hotspots or in failure mode). In combination with a bleeder valve, the degradation products could be released before influencing the whole ORC system.

5. CONCLUSIONS

The thermal degradation of MM depending on temperature and time was analysed qualitatively and quantitatively and the impact on the set-up of ORC power units was pointed out. The main results can be summarized as follows:

- The main degradation products of MM are low molecular hydrocarbons like methane, ethane/ethylene and propane/propylene.
- The degradation rate is strongly influenced not only by the temperature but also by the retention time.
- MM is stable up to a temperature of 300 °C with annual degradation rates of less than 3.5 %.
- Methane can be used as indicator for ongoing thermal degradation of MM.
- The design of direct evaporating systems based on MM requires special care concerning film temperature and avoiding hot spots in the evaporator.

Ongoing and future work will include the evaluation of free water on the thermal degradation of MM and the comparison with other linear siloxanes (MDM, MD_2M). Furthermore, a dynamic test rig including pump, preheater, evaporator, superheater, throttle valve and condenser is planned to account for mechanical stress of the working fluid due to the cycle as well.

NOMENCLATURE

C	carbon	
MDM	octamethyltrisiloxane	
MD_2M	decamethyltetrasiloxane	
MM	hexamethyldisiloxane	
ORC	Organic Rankine Cycle	
Si	silicon	
t	time	(h)
T	temperature	(°C)

REFERENCES

ANSI/ASHRAE Standard 97-2007, 2007, Sealed glass tube method to test the chemical stability of materials for use within refrigerant systems.

Angelino, G., 1993, Cyclic Methylsiloxanes as Working Fluids for Space Power Cycles, *Transactions of the ASME - N - Journal of Solar Energy Engineering*, vol. 115, no. 3: p. 130–137.

Angelino, Gianfranco (Ed.), 1991, Modern research topics in aerospace propulsion, New York, Springer.

Buravtsev, N., Grigor'ev, A., Kolbanovskii, Y., Ovsyannikov, A., 1994, Thermal and thermooxidative stability of ozone-safe freons, *Russian Journal of Organic Chemistry*, vol. 30, no. 12: p. 1880–1890.

Calderazzi, L., Colonna, P., 1997, Thermal stability of R-134a, R-141b, R-13I1, R-7146, R-125 associated with stainless steel as a containing material, *International Journal of Refrigeration*, vol. 20, no. 6: p. 381–389.

Colonna, P., Nannan, N., Guardone, A., Lemmon, E., 2006, Multiparameter equations of state for selected siloxanes, *Fluid Phase Equilibria*, vol. 244, no. 2: p. 193–211.

Deshpande, G., Rezac, M. E., 2002, Kinetic aspects of the thermal degradation of poly(dimethyl siloxane) and poly(dimethyl diphenyl siloxane), *Polymer Degradation and Stability*, vol. 76, no. 1: p. 17–24.

Dvornic, P. R., 2000, Thermal properties of polysiloxanes. In: Richard G. Jones (Ed.): Silicon containing polymers: The science and technology of their synthesis and applications, Dordrecht, Kluwer Acad. Publ, p. 185–212.

Dvornic, P. R., 2008, High temperature stability of cyclosiloxanes. In: Gelest Inc. (Ed.): Silicon Compounds: Silanes and Silicones. A survey of properties and chemistry, 2nd Edition: p. 441–454.

Ginosar, D. M., Petkovic, L. M.,Guillen, D. P., 2011, Thermal Stability of Cyclopentane as an Organic Rankine Cycle Working Fluid, *Energy Fuels*, vol. 25, no. 9: p. 4138–4144.

Grassie, N., Macfarlane, I., 1978, The thermal degradation of polysiloxanes-I. Poly(dimethylsiloxane), *European Polymer Journal*, vol. 14, no. 11: p. 875–884.

Grassie, N., Macfarlane, I.,Francey, K., 1979, The thermal degradation of polysiloxanes-II. Poly(methylphenylsiloxane), *European Polymer Journal*, vol. 15, no. 5: p. 415–422.

Heberle, F., Brüggemann, D., Obermeier, A., 2012, Mögliche Emissionen bei der Strom- und Wärmeerzeugung aus Geothermie durch den Einsatz von F-Gasen im Energiewandlungsprozess mittels ORC, (in German), Umweltbundesamt (Ed.), Dessau-Roßlau (Climate Change, 16/2012), available online: http://www.uba.de/uba-info-medien/4323.html

Kuramochi, H., Imai, F., Kondoh, H., Kunimori, K., Uchijima, T., Nozoye, H., 1993, Decomposition of cyclopentane on Ni(755): peculiar decomposition behavior of cyclopentane, *Surface Science*, vol. 287–288, part 1: p. 217–221.

Manders, W. F., Bellama, J. M., 1985, Multiphoton infrared laser-induced degradation of polydimethylsiloxane and hexamethyldisiloxane, *J. Polym. Sci. Polym. Chem. Ed.*, vol. 23, no. 2: p. 351–357.

Mang, T., Dresel, W., 2007, Lubricants and lubrication. 2nd edition, Weinheim, Wiley-VCH.

Obernberger, I., 1998, Decentralized biomass combustion: state of the art and future development, Paper to the keynote lecture of the session "Processes for decentralized heat and power production based on cumbustion" at the 9th European Bioenergy Conference, June 1996, Copenhagen, Denmark, *Biomass and Bioenergy*, vol. 14, no. 1: p. 33–56.

Obernberger, I., Thornhofer, P., Reisenhofer, E., 2002, Description and evaluation of the new 1000 kWel organic Rankine cycle process integrated in the biomass CHP plant in Lienz, Austria, *Euroheat & Power*, vol. 10: p. 18–25.

Stephan, P., Schaber, K., Stephan, K., Mayinger, F., 2009, Thermodynamik – Grundlagen und Technische Anwendungen, Band 1: Einstoffsysteme, 18th edition, Berlin, Springer, p. 243.

ACKNOWLEDGEMENT

MULTI-OBJECTIVE OPTIMIZATION OF ORGANIC RANKINE CYCLE POWER PLANTS USING PURE AND MIXED WORKING FLUIDS

Jesper G. Andreasen [1*], Martin R. Kærn[1], Leonardo Pierobon [1], Ulrik Larsen [2], Fredrik Haglind [1]

[1] Technical University of Denmark, Building 403, Nils Koppels Allé, DK-2800 Kgs. Lyngby, Denmark. jgan@mek.dtu.dk*, pmak@mek.dtu.dk, lpier@mek.dtu.dk, frh@mek.dtu.dk

[2] Department of Shipping and Marine Technology, Chalmers University of Technology, SE-412 96 Gothenburg, Sweden. ulrik.larsen@chalmers.se

* Corresponding Author

ABSTRACT

For zeotropic mixtures, the temperature varies during phase change, which is opposed to the isothermal phase change of pure fluids. The use of such mixtures as working fluids in organic Rankine cycle power plants enables a minimization of the mean temperature difference of the heat exchangers when the minimum pinch point temperature difference is kept fixed. A low mean temperature difference means low heat transfer irreversibilities, which is beneficial for cycle performance, but it also results in larger heat transfer surface areas. Moreover, the two-phase heat transfer coefficients for zeotropic mixtures are usually degraded compared to an ideal mixture heat transfer coefficient linearly interpolated between the pure fluid values. This entails a need for larger and more expensive heat exchangers. Previous studies primarily focus on the thermodynamic benefits of zeotropic mixtures by employing first and second law analyses. In order to assess the feasibility of using zeotropic mixtures, it is, however, important to consider the additional costs of the heat exchangers. In this study, we aim at evaluating the economic feasibility of zeotropic mixtures compared to pure fluids. We carry out a multi-objective optimization of the net power output and the component costs for organic Rankine cycle power plants using low-temperature heat at 90 °C to produce electrical power at around 500 kW. The primary outcomes of the study are Pareto fronts, illustrating the power/cost relations for R32, R134a and R32/R134a (0.65/0.35$_{\text{mole}}$). The results indicate that R32/134a is the best of these fluids, with 3.4 % higher net power than R32 at the same total cost of 1200 k$.

1. INTRODUCTION

The organic Rankine cycle (ORC) power plant is a technology that enables the utilization of low-temperature heat for electricity production. The working fluid selection for the ORC power plant is a critical design decision which affects the thermodynamic performance and the economic feasibility of the plant. The use of zeotropic mixtures as working fluids has been proposed as a way to improve the performance of the cycle (Angelino and Colonna, 1998). Zeotropic mixtures change phase with varying temperature, which is opposed to the isothermal phase change of pure fluids. As the temperature of the heat source and heat sink change during heat exchange, zeotropic working fluids enable a closer match of the temperature profiles in the condenser and the boiler, compared to pure fluids. This results in a decrease in heat transfer irreversibilities and an increase in cycle performance. The condenser has been identified as the component where the irreversibilities decrease the most when using mixed working fluids (Heberle et al., 2012; Lecompte et al., 2014), and the increment in cycle performance when using zeotropic mixtures instead of pure fluids is largest when the heat source temperature is low (Chys et al., 2012).

Heberle et al. (2012) optimized the performance of ORC systems using zeotropic working fluids for utilization of geothermal heat at 120 °C. Compared to pure isobutane, a mixture of isobutane/isopentane $(0.9/0.1_{mole})$ achieved an increase in the second law efficiency of 8 %. They also compared the *UA*-values (the product of the overall heat transfer coefficient and the heat transfer area) of the heat exchangers in the cycle, and found that the mixture compositions resulting in the highest cycle performance also required the highest *UA*-values. This suggests that the cost of heat exchangers is larger when the mixture is used. Le et al. (2014) performed maximizations of the exergy efficiency and minimizations of the levelized cost of electricity for ORC systems using mixtures of R245fa and pentane as working fluids. Pure pentane was identified as the best fluid, in both optimizations. In the minimization of the levelized cost of electricity, the minimum value for pentane was found to be 0.0863 \$/kWh. The mixtures pentane/R245fa $(0.05/0.95_{mass})$ and pentane/R245fa $(0.1/0.9_{mass})$ obtained similar values at 0.0872 and 0.0873 \$/kWh, respectively.

In the present study, we carry out a multi-objective optimization of net power output and component cost for an ORC power plant utilizing a low-temperature water stream at 90 °C. The objective of the study is to investigate and compare the relationship between cost and performance for ORC power plants using pure fluids and zeotropic mixtures as working fluids. The fluids considered are R32, R134a and R32/R134a $(0.65/0.35_{mole})$. These fluids are selected, since they achieved high thermodynamic performance at subcritical turbine inlet pressure in a previous study (Andreasen et al., 2014).

Previous studies (e.g. (Heberle et al., 2012; Trapp and Colonna, 2013; Andreasen et al., 2014)) which compare pure fluids and zeotropic mixtures focus mainly on the evaluation of the thermodynamic performance of the fluids. These studies indicated that the thermodynamic performance can be increased by using zeotropic mixtures as working fluids, while the size and thereby the cost of the heat exchangers increase. In order to evaluate the feasibility of zeotropic mixtures, it is, therefore, necessary also to assess the cost of equipment such that the working fluids are compared based on the same investment costs. Le et al. (2014) included a single-objective optimization of the levelized cost of electricity. However, they did not consider the simultaneous optimization of thermodynamic performance and cost as is done in the present study. It is advantageous to implement the multi-objective optimization since it enables a comparison of fluid performance based on the same equipment costs.

The paper begins with a description of the methodology in Section 2. The results are presented and discussed in Section 3 and conclusions are given in Section 4.

2. METHODS

The multi-objective optimization method is developed in Matlab version 2014b (Mathworks, 2014) based on the framework described by Pierobon et al. (2014). The steady state ORC system model, capable of handling both pure fluids and mixtures through REFPROP® version 9.1 (Lemmon et al., 2013), is adapted from a previous study (Andreasen et al., 2014) and integrated within the simulation tool. A sketch of the ORC power plant is depicted in Figure 1.

The heat source is a low-temperature water stream as investigated in Andreasen et al. (2014). Table 1 shows the hot fluid parameters along with the fixed input parameters assumed for the cycle. The hot fluid and cooling water pumps are denoted as auxiliary pumps.

The optimization variables include cycle and heat exchanger design parameters; see Table 2. The lower boundary for the turbine inlet pressure is defined as the bubble point pressure at a temperature 30 °C higher than the cooling water inlet temperature $(T_{cool,i})$, and the upper boundary is 90 % of the critical pressure (P_c). The superheating degree is defined as the temperature difference between the dew point temperature and the turbine inlet temperature, and the bounds for the baffle spacing are set relative to the shell diameter (d_s). The lower bounds for the pinch points in the condenser and the boiler are set to 0.1 °C. Such low pinch points are not feasible in practice, but they are allowed in this study in order to
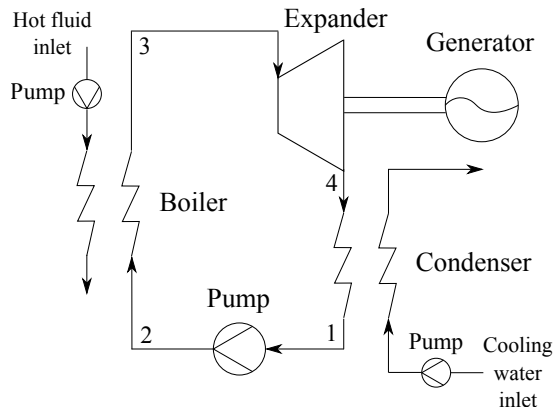
Figure 1: Organic Rankine cycle power system

Table 1: ORC system modelling conditions

Parameter description	Value	Unit
Hot fluid (water)		
Hot fluid inlet temperature	90	°C
Hot fluid mass flow	50	kg/s
Hot fluid pressure	4	bar
Condenser		
Cooling water inlet temperature	15	°C
Outlet vapour quality	0	-
Cooling water pressure	4	bar
Working fluid pump		
Isentropic efficiency	0.8	-
Auxiliary pumps		
Isentropic efficiency	0.7	-
Turbine		
Isentropic efficiency	0.8	-
Minimum outlet vapour quality	1	-

compare the fluids based on a wide range of equipment costs.

The objective functions for the optimization are the net power output and the total cost of the components. The net power is calculated as

$$\dot{W}_{NET} = \dot{m}_{wf}(h_3 - h_4 - (h_2 - h_1)) - \dot{W}_{aux.,pumps} \tag{1}$$

where $\dot{m}_{wf}$ is the working fluid mass flow, h is the mass specific enthalpy and $\dot{W}_{aux.,pumps}$ is the power consumption of the hot fluid and cooling water pumps. The total cost (C_{tot}) of the components is found by adding the cost of the turbine (C_{turb}), working fluid pump ($C_{wf,pump}$), condenser (C_{cond}), boiler (C_{boil}), generator (C_{gen}) and the two auxiliary pumps ($C_{aux.,pumps}$)

$$C_{tot} = C_{turb} + C_{wf,pump} + C_{cond} + C_{boil} + C_{gen} + C_{aux.,pumps} \tag{2}$$

The total cost considered in this paper is the equipment cost, thus further expenses are expected for the construction of the ORC power plants, e.g. installation costs.

Table 2: Optimization variables

Parameter description	Lower bound	Upper bound	Unit
Cycle parameters			
Turbine inlet pressure	$P_{bub}(T_{cool,i} + 30)$	$0.9 \cdot P_c$	bar
Superheating degree	0	40	°C
Condensing temperature	$T_{cool,i} + 5$	$T_{cool,i} + 20$	°C
Boiler pinch point temperature	0.1	20	°C
Condenser pinch point temperature	0.1	20	°C
Condenser design			
Inner tube diameter	16	26	mm
Number of tubes	10	200	-
Baffle spacing	$0.5 \cdot d_s$	$3 \cdot d_s$	mm
Boiler design			
Inner tube diameter	16	26	mm
Number of tubes	10	200	-
Baffle spacing	$0.5 \cdot d_s$	$3 \cdot d_s$	mm

The optimization framework comprises the following steps (Pierobon et al., 2014):

- Calculation of the process states by use of the cycle model (without pressure losses)

- Layout of the geometry of the condenser and the boiler and calculation of the heat transfer area and the pressure losses

- Calculation of the net power output by use of the cycle model (with pressure losses)

- Calculation of the total component cost

2.1 Heat Exchanger Modelling

The heat exchanger models are developed based on the shell-and-tube model used in Kærn et al. (2015). In order to avoid leakage of working fluid, which for zeotropic mixtures can result in undesirable composition shifts, both the boiler and the condenser are designed with the working fluid flowing inside the tubes (Cavallini et al., 2003). The heat exchangers are designed as TEMA E type shell-and-tube heat exchangers with one shell pass and one tube pass. A 60° triangular tube layout is used; see Figure 2.

Table 3 lists the modelling conditions used for the shell-and-tube heat exchangers including the geometric parameters and the ranges for the flow velocities. The velocities must be high enough to avoid excessive fouling, but not so high that the heat exchanger material is eroded. The boundaries for the flow velocities are selected based on recommendations from Nag (2008), Shah and Sekulić (2003) and Coulson et al. (1999). The shell side velocity is only checked at the inlet, since the density variations of the hot fluid and the cooling water are small. The tube side outlet velocity for the condenser is allowed to be lower than the minimum value of 0.9 m/s for liquid in-tube flow found in Shah and Sekulić (2003). Full liquid flow is only present at the end of the condenser tube as all vapour is condensed. It is, therefore, assumed that the liquid velocity can reach 0.5 m/s at the condenser outlet without the risk of excessive fouling formation.
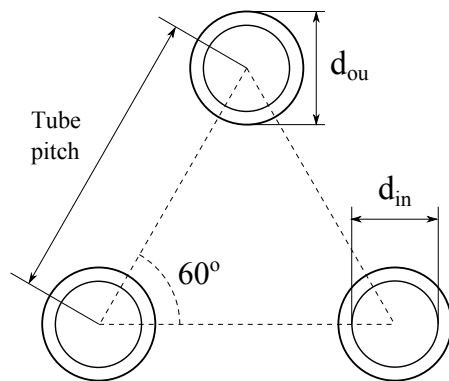

Figure 2: Tube layout

Table 3: Heat exchanger modelling conditions

Parameter description	Value/range	Unit
Tube configuration	Rotated square 45°	-
Tube thickness	3	mm
Tube pitch	$1.5 \cdot d_{ou}$	mm
Baffle cut	$0.25 \cdot d_s$	mm
Tube wall conductivity	16	W/mK
Number of control volumes	30	-
Condenser velocities		
Tube side inlet	$5 - 22$	m/s
Tube side outlet	$0.5 - 4$	m/s
Shell side inlet	$0.3 - 1.5$	m/s
Boiler velocities		
Tube side inlet	$0.9 - 4$	m/s
Tube side outlet	$5 - 22$	m/s
Shell side inlet	$0.3 - 1.5$	m/s

The heat transfer and pressure drop characteristics on the shell side are estimated based on the Bell-Delaware method (Shah and Sekulić, 2003). The method is implemented for tubes without fins and for a shell design without tubes in the window section. The effects of larger baffle spacings at the inlet and outlet ducts compared to the central baffle spacing are neglected.

For single-phase flow, the heat transfer coefficient is calculated using the correlation provided by Gnielinski (1976). The two-phase heat transfer coefficient of boiling is estimated based on the correlation provided by Gungor and Winterton (1987) and Thome (1996)

$$\alpha_{2p,boil} = \alpha_L \left[1 + 3000(BoF_c)^{0.86} + 1.12 \left(\frac{x}{1-x} \right)^{0.75} \left(\frac{\rho_L}{\rho_V} \right)^{0.41} \right] \tag{3}$$

where *Bo* is the boiling number, x is the vapour quality, ρ_L is the density of saturated liquid, ρ_V is the density of saturated vapour and α_L is the liquid only heat transfer coefficient which is calculated using the Dittus-Boelter correlation (Dittus and Boelter, 1930). The ratio of the nucleate boiling heat transfer coefficient to the ideal nucleate boiling heat transfer coefficient, $F_c = \alpha_{nb} / \alpha_{nb,id}$, is calculated by

$$F_c = \left[1 + \left(\frac{\alpha_{nb,id}}{q_{nb}} \right) (T_{dew} - T_{bub}) \left[1 - \exp \left(\frac{-Bq_{nb}}{\rho_L h_{LV} \beta_L} \right) \right] \right]^{-1} \tag{4}$$

where q_{nb} is the nucleate boiling heat flux, T_{dew} is the dew point temperature, T_{bub} is the bubble point temperature, B is a scaling factor, h_{LV} is the enthalpy of vaporization, and β_L is the liquid phase mass transfer coefficient. The values of B and β_L are set to $B = 1$ and $\beta_L = 0.0003$ m/s according to Thome (1996). The ideal nucleate boiling heat transfer coefficient, $\alpha_{nb,id}$ is calculated using the correlation by Stephan and Abdelsalam (1980).

For in-tube condensation, the heat transfer coefficient is estimated using the following correlation (Shah, 2009):

$$\alpha_{2p,cond} = \begin{cases} \alpha_I & J_g \geq 0.98(Z + 0.263)^{-0.62} \\ \alpha_I + \alpha_{Nu} & J_g < 0.98(Z + 0.263)^{-0.62} \end{cases} \tag{5}$$

where Z is Shah's correlating parameter and J_g is the dimensionless vapour velocity.

The heat transfer coefficients α_I and α_{Nu} are calculated as

$$\alpha_I = \alpha_{LT} \left(\frac{\mu_L}{14 \mu_V} \right)^{0.0058 + 0.557 P_r} \left[(1 - x)^{0.8} + \frac{3.8 x^{0.76} (1 - x)^{0.04}}{P_r^{0.38}} \right] \tag{6}$$

$$\alpha_{Nu} = 1.32 Re_L^{-1/3} \left[\frac{\rho_L (\rho_L - \rho_V) g \lambda_L^3}{\mu_L^2} \right]^{1/3} \tag{7}$$

where α_{LT} is the heat transfer coefficient assuming all mass to be flowing as liquid and Re_L is the Reynolds number for the liquid phase only. The variable α_{LT} is calculated using the Dittus-Boelter equation (Dittus and Boelter, 1930). For mixtures the heat transfer coefficient obtained from equation (5) is corrected using the method proposed by Bell and Ghaly (1973). For in-tube flow, the single-phase pressure drops are calculated based on the Blasius equation (Blasius, 1913) and the two-phase pressure drops are calculated using the correlation by Müller-Steinhagen and Heck (1986).

2.2 Cost Correlations

The cost (in US\$) of the components in the cycle are estimated based on correlations found in the literature. The turbine is assumed to be axial, since axial turbines are commonly used by manufacturers in the range of power (approximately 50-600 kW) considered in the present paper (Quoilin et al., 2013). The cost (in €) of the turbine is estimated based on the correlation provided by Astolfi et al. (2014)

$$C_{turb} = 1.230 \cdot 10^6 \left(\frac{1}{2} \right)^{0.5} \left(\frac{\sqrt{\dot{V}_4} / (\Delta h_{is})^{0.25}}{0.18} \right)^{1.1} \tag{8}$$

where $\dot{V}_4$ is the volume flow at the turbine outlet and Δh_{is} is the isentropic enthalpy drop across the turbine. An euro-to-dollar conversion factor of 1.2 is used to convert the turbine cost to US\$.

The costs of the pumps, the heat exchangers and the generator are estimated by

$$C_E = C_B \left(\frac{Q}{Q_B} \right)^M f_M f_P f_T \tag{9}$$

where C_E is the equipment cost for equipment with capacity Q, C_B is the base cost for equipment with capacity Q_B, M is a constant exponent, and f_M, f_P are f_T correction factors accounting for materials of construction, design pressure and design temperature.

The economic parameters needed in the cost correlation are listed in Table 4. For the heat exchangers, the pressure correction factor is obtained by linear interpolation between the values reported in Smith (2005). The component costs are corrected for inflation by using the Chemical Engineering Plant Cost Index.

Table 4: Economic parameters

Component	C_B	Q_B	M	f_M	f_P	f_T	Reference
Heat exchangers	32.8 k\$	80 m^2	0.68	1.7	(Smith, 2005)	1	(Smith, 2005)
Pumps	9.48 k\$	4 kW	0.55	1	1	1	(Smith, 2005)
Generator	3.7 k\$	1000 kW	0.95	1	1	1	(Boehm, 1987)

3. RESULTS AND DISCUSSION

Figure 3 shows the Pareto fronts for multi-objective optimizations of net power output and cost for R32, R134a and R32/R134a (0.65/0.35). The results indicate that R32/R134a is the best of the three fluids, since it enables the highest net power output at the lowest component cost. R32 is the second best fluid while R134a is performing worst.

When the fluids are compared based on a single-objective optimization of net power output, R32/134a (0.65/0.35) reaches 13.8 % higher net power output than R32 and 14.6 % higher than R134a (Andreasen et al., 2014). However, this approach does not account for the equipment cost, and it was therefore not ensured that the fluids were compared based on similar cost. The multi-objective optimization, on the other hand, does enable a fluid comparison based on fixed equipment cost. For a total cost of 1200 k\$, R32/R134a reaches a 3.4 % higher net power than R32 and 10.9 % higher than R134a. At $C_{tot} = 800$ k\$, the mixture obtains 2.1 % higher net power than R32 and 12.6 % higher than R134a. It should be noted that in the single-objective optimization, which was presented in Andreasen et al. (2014), the mixture composition was optimized, but in the multi-objective optimization, carried out in the present paper, it is not. It is, therefore, possible that higher performance can be achieved with the mixture if the composition is optimized in the multi-objective optimization.
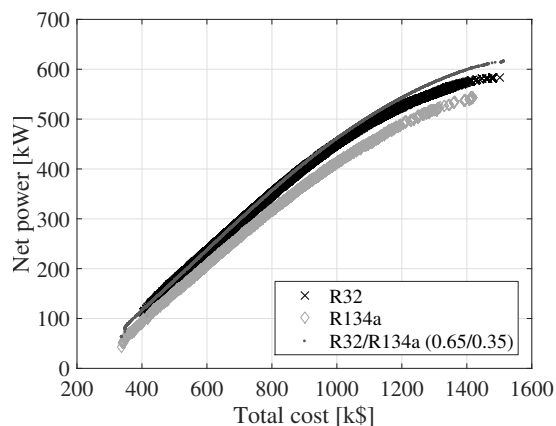

Figure 3: Pareto fronts
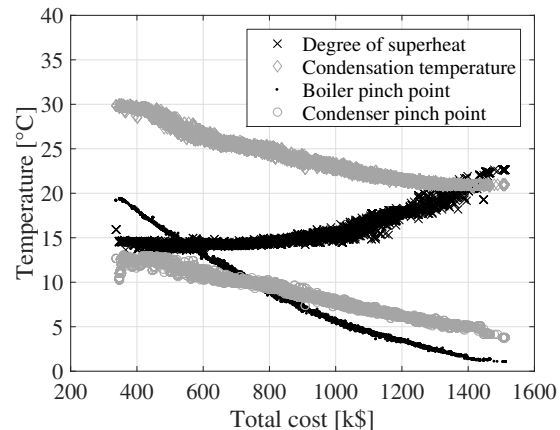
Figure 4: Temperatures, R32/R134a

In Figure 4, the optimal degree of superheating, condensing temperature, boiler pinch point and condenser pinch point are plotted as a function of the total cost for R32/R134a. The degree of superheating increases from about 13 to 23 °C as the total component cost increases. The condensing temperature, boiler pinch point and condenser pinch point all continuously decrease as the total component cost increases. The decrease in boiler pinch point results in an increase in the heat input to the cycle. This trend positively affects the net power output while increasing the investment cost for the boiler. The decrease in the condensing temperature has a positive effect on net power output, but requires larger heat

transfer areas since the temperature difference between the cooling water and the condensing working fluid decreases. The larger heat transfer areas result in higher investment costs for the condenser. For fixed cycle conditions (condensing temperature, mass flow, etc.), the condenser pinch point only affects the net power output of the cycle through the power consumption of the cooling water pump. The pinch point temperature of the condenser thereby primarily affects the cost of the condenser. Therefore, the condenser pinch point tends to be as large as possible, while respecting the following constraints: 1) the cooling water outlet temperature must be larger than the inlet temperature and 2) the flow velocity in the condenser shell should not be higher than 1.5 m/s. A high condenser pinch point results in a low cooling water temperature increase and thereby a high cooling water mass flow and a high shell flow velocity. For R32/R134a, the temperature glide of condensation is 5.3 °C, while the cooling water temperature increase ranges from 5.7 to 14.5 °C. In thermodynamic analyses of zeotropic mixtures, optimum conditions are typically obtained when the temperature glide of the mixture and the temperature increase of the cooling water are matched (Heberle et al., 2012; Chys et al., 2012; Lecompte et al., 2014; Andreasen et al., 2014). The present study does on the other hand indicate that optimum conditions are reached when the temperature increase of the cooling water is larger than the temperature glide of condensation.

For total costs of 1300 k$, the boiler pinch point drops below 2.5 °C. It is unusual that solutions with pinch points below 2.5 °C represent economically feasible solutions. In Figure 3 at a total cost of 1300 k$, the curves are levelling off, meaning that an increase in investment cost results in a low increase in net power output compared to when the total cost is lower. It is therefore likely that the more economically feasible solutions are found at total costs below 1300 k$. It should be noted that the Pareto fronts do not provide information which directly can be used to make an investment decision, since they do not include information about the possible income related to the power delivered by the ORC power plant. Such information is necessary in order to estimate, e.g., net present value or payback periods which are useful figures for making investment decisions. The Pareto fronts should rather be used for assessing the feasibility of working fluids based on equal component costs, thereby ensuring a fair basis for comparison.
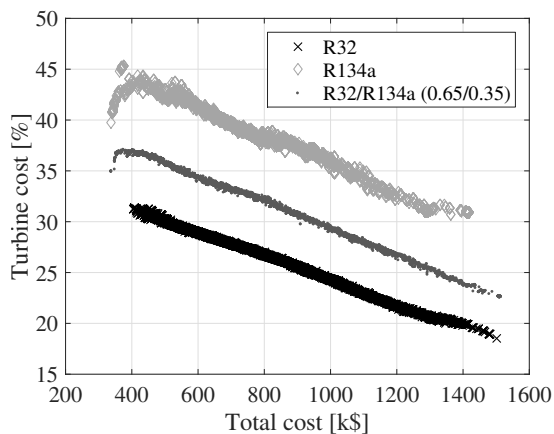

Figure 5: Relative turbine costs   **Figure 6: Relative condenser costs**
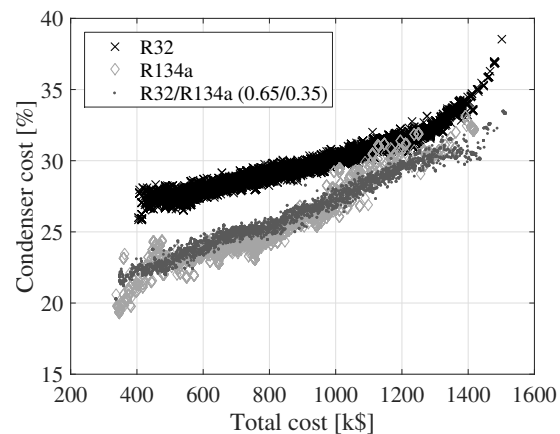
Figures 5, 6 and 7 depict the variation of the cost of the turbine, condenser and boiler as a function of the total cost for the three fluids. The cost values displayed on the y-axes are relative to the total cost. The relative size of the turbine cost decreases, while the relative costs of the condenser and boiler increase. The relative turbine costs decreases since the turbine cost is a function of the turbine outlet volume flow rate and the isentropic enthalpy drop across the turbine. An increase in the outlet volume flow rate or a decrease in the isentropic enthalpy drop results in an increase in the turbine cost. These two parameters can be varied by changing e.g. the boiler pressure or the turbine inlet temperature. By modifying the boiler pressure or the turbine inlet temperature it is, however, not certain that the net power output increases. The cost of the condenser and the boiler can be increased by decreasing the

pinch point temperatures of the heat exchangers or the condensing temperature. This has a positive effect on the net power output. Thus, the cost of the heat exchangers are not as tightly connected to the cycle as the turbine is.
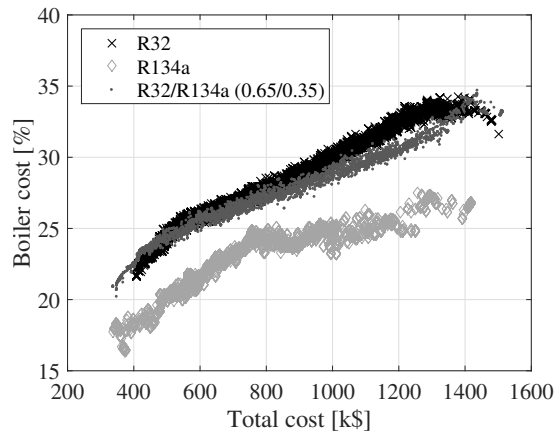
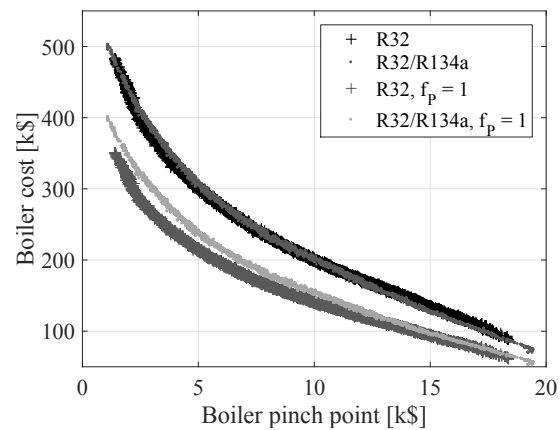

Figure 7: Relative boiler costs

Figure 8: Boiler cost comparison

The boiler pressures range from 39-45 bar for R32, 28-35 bar for R32/R134a and 16-22 bar for R134a. Correspondingly the critical pressures are 57.8 bar, 51.8 bar and 40.6 bar for R32, R32/R134a and R134a, respectively, thus indicating that higher critical pressures are related to higher optimum boiling pressures. Figure 8 displays a comparison of the boiler costs for R32 and R32/R134a with and without the pressure correction factor (f_P). The boiler pinch point is plotted on the x-axis. It is, thereby, possible to compare the boiler costs for a given pinch point temperature difference. When the pressure correction factor is unity, the boiler costs are higher for the mixture compared to R32. When the pressure correction factor is employed as a function of the boiler pressure, the boiler costs are similar for the two fluids. This indicates that the boiler pressure reduction, achieved when using the mixture, can compensate for the increase in boiler cost caused by the degradation of the heat transfer coefficient and the lower temperature difference of heat transfer.

For R32/R134a, the shell length to diameter ratio of the shell-and-tube heat exchanger designs are in a range of 37-110 for the condenser and 76-180 for the boiler. Shah and Sekulić (2003) advise a desirable range of 3-15 for this ratio, meaning that the condensers and the boilers should consist of numerous shorter shell-and-tube heat exchangers in series, in order not to violate this practical limit. The shells designed in this paper are long since the number of tubes must be relatively low in order to ensure reasonable flow velocities in the tubes. Selecting a heat exchanger layout with multiple tube passes is a viable solution for increasing the number of tubes while maintaining high flow velocities in the tubes. Another option is to place the working fluid in the shell rather than in the tubes. This would increase the risk of working fluid leakage, which is problematic in the case of zeotropic mixtures.

4. CONCLUSION

This paper present the results from a multi-objective optimization of net power output and component cost for ORC power plants using R32, R134 and R32/R134a ($0.65/0.35_{mole}$). For a low-temperature heat source, the results indicate that R32/134a (0.65/0.35) is the best fluid and that R134a performs worst. For a total cost of 1200 k$, the mixture reaches 3.4 % higher net power than R32 and 10.9 % higher than R134a. The relative increase in net power output for the mixture compared to R32 is significantly lower than the 13.8 %, which was estimated in a single-objective optimization of net power, i.e., not considering the cost of the cycle components. This exemplifies the importance of accounting for economic criteria in ORC system optimizations and fluid comparisons. This is especially important when pure fluids and mixtures are compared due to the generally lower temperature difference of heat transfer

and the degradation of heat transfer coefficients for zeotropic mixtures. Moreover, the differences in operating pressures can have a significant effect on the cost of the ORC power plant. It is thus possible to reduce the cost of the boiler by using R32/R134a as the working fluid compared to R32, since the optimum pressure is lower for the mixture.

Future work on this topic will include performance comparisons for a larger group of pure fluids and mixtures and an extension of the economic analysis enabling the estimation of payback periods and net present values, such that the more cost efficient working fluids can be identified. An uncertainty analysis, assessing the influence of the uncertainties related to heat transfer and equipment cost correlations, is also a topic for further investigation, especially in the light of the relatively small performance differences observed for R32 and R32/R134a.

NOMENCLATURE

Symbol			**Subscript**	
A	heat transfer area	(m^2)	1p	one-phase
B	scaling factor	()	2p	two-phase
Bo	boiling number	()	B	base
C	cost	(US\$)	boil	boiler
d	diameter	(mm)	bub	bubble point
f	correction factor	()	c	critical
F_c	$\alpha_{nb}/\alpha_{nb,id}$	()	cond	condenser
g	gravitational acceleration	(m/s^2)	cool	cooling water
G	mass flux	$(kg/(s\ m^2))$	dew	dew point
h	specific enthalpy	(kJ/kg)	E	equipment
J_g	dimensionless vapour velocity	()	gen	generator
M	Exponent in cost correlation	()	HEX	heat exchanger
$\dot{m}$	mass flow rate	(kg/s)	i	inlet
P	pressure	(bar)	id	ideal
Q	equipment capacity	(m^2), (kW)	in	inner
q	heat flux	(kW/m^2)	is	isentropic
Re	Reynolds number	()	L	saturated liquid
T	temperature	(°C)	LT	all mass as liquid
$\dot{V}$	volume flow	(m^3/s)	LV	vaporization
$\dot{W}$	work	(kW)	nb	nucleate boiling
x	vapour quality	()	NET	net
Z	Shah's correlating parameter	()	ou	outer
α	heat transfer coefficient	$(W/(m^2\ K))$	pump	pump
β	mass transfer coefficient	(m/s)	r	reduced
Δ	difference	()	s	shell
λ	thermal conductivity	$(W/(m\ K))$	tot	total
μ	viscosity	(kg/(s m))	turb	turbine
ρ	density	(kg/m^3)	V	saturated vapour
			wf	working fluid

REFERENCES

Andreasen, J. G., Larsen, U., Knudsen, T., Pierobon, L., and Haglind, F. (2014). Selection and optimization of pure and mixed working fluids for low grade heat utilization using organic Rankine cycles. *Energy*, 73:204–213.

Angelino, G. and Colonna, P. (1998). Multicomponent working fluids for organic Rankine cycles (ORCs). *Energy*, 23(6):449–463.

Astolfi, M., Romano, M. C., Bombarda, P., and Macchi, E. (2014). Binary ORC (Organic Rankine Cycles) power plants for the exploitation of medium-low temperature geothermal sources - Part B: Techno-economic optimization. *Energy*, 66:435–446.

Bell, K. and Ghaly, M. (1973). An approximate generalized design method for multicomponent/partial condenser. *AIChE Symp. Ser*, 69:72–79.

Blasius, H. (1913). Das Ähnlichkeitsgesetz bei Reibungsvorgängen in Flüssigkeiten. In *Mitteilungen über Forschungsarbeiten auf dem Gebiete des Ingenieurwesens 131*, pages 1–41. Springer, Berlin, Germany.

Boehm, R. F. (1987). *Design analysis of thermal systems*. John Wiley & Sons, Inc., New York, United States of America.

Cavallini, A., Censi, G., Del Col, D., Doretti, L., Longo, G., Rossetto, L., and Zilio, C. (2003). Condensation inside and outside smooth and enhanced tubes — a review of recent research. *Int. J. Refrig.*, 26(4):373–392.

Chys, M., van den Broek, M., Vanslambrouck, B., and De Paepe, M. (2012). Potential of zeotropic mixtures as working fluids in organic Rankine cycles. *Energy*, 44(1):623–632.

Coulson, J., Richardson, J., and Backhurst, J. (1999). *Coulson and Richardson's Chemical Engineering*. Butterworth-Heinemann, Oxford, Great Britain.

Dittus, W. and Boelter, L. M. K. (1930). Heat transfer in automobile radiators of the tubular type. *Univ. Calif. – Publ. Eng.*, 2(13):443 – 461.

Gnielinski, V. (1976). New Equation for Heat and Mass Transfer in Turbulent Pipe and Channel Flow. *Int. Chem. Eng.*, 16:359–368.

Gungor, K. E. and Winterton, R. H. S. (1987). Simplified general correlation for saturated flow boiling and comparisons of correlations with data. *Chem. Eng. Res. Des.*, 65(2):148–156.

Heberle, F., Preißinger, M., and Brüggemann, D. (2012). Zeotropic mixtures as working fluids in Organic Rankine Cycles for low-enthalpy geothermal resources. *Renew. Energy*, 37(1):364–370.

Kærn, M. R., Modi, A., Jensen, J. K., and Haglind, F. (2015). An Assessment of Transport Property Estimation Methods for Ammonia–Water Mixtures and Their Influence on Heat Exchanger Size. *Int. J. Thermophys.*

Le, V. L., Kheiri, A., Feidt, M., and Pelloux-Prayer, S. (2014). Thermodynamic and economic optimizations of a waste heat to power plant driven by a subcritical ORC (Organic Rankine Cycle) using pure or zeotropic working fluid. *Energy*, 78:622–638.

Lecompte, S., Ameel, B., Ziviani, D., van den Broek, M., and De Paepe, M. (2014). Exergy analysis of zeotropic mixtures as working fluids in Organic Rankine Cycles. *Energy Convers. Manag.*, 85:727–739.

Lemmon, E. W., Huber, M., and McLinden, M. (2013). NIST Standard Reference Database 23: Reference Fluid Thermodynamic and Transport Properties-REFPROP, Version 9.1, National Institute of Standards and Technology, Standard Reference Data Program, Gaithersburg.

Mathworks (2014). Matlab 2014b documentation. Technical report, Massachusetts, The United States of America.

Müller-Steinhagen, H. and Heck, K. (1986). A simple friction pressure drop correlation for two-phase flow in pipes. *Chem. Eng. Process. Process Intensif.*, 20(6):297–308.

Nag, P. K. (2008). *Power Plant Engineering*. Tata McGraw Hill Education Private Limited, New Delhi, India, 3 edition.

Pierobon, L., Benato, A., Scolari, E., Haglind, F., and Stoppato, A. (2014). Waste heat recovery technologies for offshore platforms. *Appl. Energy*, 136:228–241.

Quoilin, S., van den Broek, M., Declaye, S., Dewallef, P., and Lemort, V. (2013). Techno-economic survey of Organic Rankine Cycle (ORC) systems. *Renew. Sustain. Energy Rev.*, 22:168–186.

Shah, M. M. (2009). An Improved and Extended General Correlation for Heat Transfer During Condensation in Plain Tubes. *HVAC&R Res.*, 15(5):889–913.

Shah, R. K. and Sekulić, D. P. (2003). *Fundamentals of Heat Exchanger Design*. John Wiley & Sons, Inc., New Jersey, United States of America.

Smith, R. (2005). *Chemical process: design and integration*. John Wiley & Sons, Inc., West Sussex, England.

Stephan, K. and Abdelsalam, M. (1980). Heat-transfer correlations for natural convection boiling. *Int. J. Heat Mass Transf.*, 23(1):73–87.

Thome, J. R. (1996). Boiling of new refrigerants: a state-of-the-art review. *Int. J. Refrig.*, 19(7):435–457.

Trapp, C. and Colonna, P. (2013). Efficiency Improvement in Precombustion CO 2 Removal Units With a Waste–Heat Recovery ORC Power Plant. *J. Eng. Gas Turbines Power*, 135(4):042311.

ACKNOWLEDGEMENT

EFFECT OF WORKING-FLUID MIXTURES ON ORGANIC RANKINE CYCLE SYSTEMS: HEAT TRANSFER AND COST ANALYSIS

Oyeniyi A. Oyewunmi and Christos N. Markides[*]

Clean Energy Processes (CEP) Laboratory, Department of Chemical Engineering,
Imperial College London, London SW7 2AZ, United Kingdom
*E-mail: c.markides@imperial.ac.uk
Web-page: www.imperial.ac.uk/cep

ABSTRACT

The present paper considers the employment of working-fluid mixtures in organic Rankine cycle (ORC) systems with respect to heat transfer performance, component sizing and costs, using two sets of fluid mixtures: *n*-pentane + *n*-hexane and R-245fa + R-227ea. Due to their non-isothermal phase-change behaviour, these zeotropic working-fluid mixtures promise reduced exergy losses, and thus improved cycle efficiencies and power outputs over their respective pure-fluid components. Although the fluid-mixture cycles do indeed show a thermodynamic improvement over the pure-fluid cycles, the heat transfer and cost analyses reveal that they require larger evaporators, condensers and expanders; thus, the resulting ORC systems are also associated with higher costs, leading to possible compromises. In particular, 70 mol% *n*-pentane + 30 mol% *n*-hexane and equimolar R-245fa + R-227ea mixtures lead to the thermodynamically optimal cycles, whereas pure *n*-pentane and pure R-227ea have lower costs amounting to 14% and 5% per unit power output over the thermodynamically optimal mixtures, respectively.

1. INTRODUCTION

Recently, the selection of working fluids for organic Rankine cycle (ORC) systems has received close attention, including a particular interest in multi-component fluid mixtures, due to the opportunities they offer in improving thermodynamic performance. Various authors have carried out investigations to demonstrate and quantify these benefits, which have shown that working-fluid mixtures can exhibit an improved thermal match with the heat source compared to the isothermal profile of (isobaric) evaporation of pure-component fluids, therefore reducing exergy losses due to heat transfer, and increasing thermal and exergy efficiencies (Angelino and di Paliano, 1998; Garg et al., 2013; Wang et al., 2010).

Investigators have carried out both experimental and theoretical studies across a range of heat-source temperatures into the benefits of employing refrigerant (Sami, 2010; Chen et al., 2011; Aghahosseini and Dincer, 2013), hydrocarbon (Heberle et al., 2012; Shu et al., 2014), and siloxane (Dong et al., 2014), working-fluid mixtures. Compared to pure fluids, binary mixtures showed increased power outputs by up to 30% and thermal efficiencies by over 15% in some cases. Excellent second law analyses have also shown significant potential benefits (Lecompte et al., 2014). (Some exceptions to these general trends have also been reported (Li et al., 2014).) Additionally, fluid mixtures can be used to adjust the environmental and safety-related properties of ORC working fluids or to improve design parameters of system components. At the same time, some investigators have begun to develop and apply advanced computer-aided molecular design (CAMD) methodologies (Papadopoulos et al., 2010; Lampe et al., 2014) with a view towards identifying or designing optimal fluids for ORC systems.

While these efforts have demonstrated the potential advantages of working-fluid mixtures, notably in terms of power output and efficiency, many of the associated conclusions have been derived strictly based on thermodynamic cycle analyses that do not fully consider the expected heat transfer performance between the heat source/sink and working-fluid streams in the heat exchangers of ORC engines. In particular, the heat transfer and cost implications of using working-fluid mixtures have not been properly addressed. Refrigerant mixtures are known to exhibit reduced heat-transfer coefficients (HTCs) compared to their pure counterparts (Jung et al., 1989). Specifically, HTCs for refrigerants mixtures are

usually lower than the 'ideal' values, linearly interpolated between the mixture components. This, coupled with the reduced temperature difference between the heat source/sink and the working-fluid mixture, will invariably lead to larger and more expensive heat exchangers in an ORC system. Therefore, although working-fluid mixtures may allow a thermodynamic advantage over single-component working fluids, they may also lead to higher system costs owing to a deterioration in their thermal performance.

By presenting a method for evaluating the HTCs of working-fluid mixtures, this work aims to explore the effects of using such mixtures on the heat transfer processes in ORC engines, which are important in understanding the role that these fluids play on the overall system performance and cost. A simple ORC engine model is presented that incorporates a suitable heat transfer description of the heat exchangers used for the heat addition and heat rejection processes. The heat exchangers are discretized along their lengths into segments (accounting for phase-change and single-phase regions), with suitable estimates of the HTCs in the different segments. Overall HTCs and heat-transfer areas (HTAs) are then evaluated, and simple cost models are used to estimate the relative costs of the components, and by extension of the entire engine. Using a selection of alkane and refrigerant working-fluid mixtures, the heat transfer characteristics and ORC-system equipment/component costs are thus investigated.

2. THERMODYNAMIC OPTIMIZATION

We begin with a simple thermodynamic optimization of an ORC system in a specified geothermal application with two sets of working-fluid mixtures: the *n*-hexane + *n*-pentane alkane system; and the R-245fa + R-227ea refrigerant system. Earlier studies have shown that these mixtures can provide significant thermodynamic benefits in ORC systems (Lecompte et al., 2014; Chys et al., 2012; Braimakis et al., 2014). Further, pentane and the selected refrigerants are presently being used in actual installations, especially in geothermal ORC setups, such as the one considered here.

2.1 ORC Model
We consider a sub-critical, non-regenerative ORC, consisting of four basic processes (pumping, heat addition, expansion and heat rejection), carried out by an organic working fluid (wf). Briefly, for completeness, the power required to pump the working fluid from State 1 (saturated liquid) to State 2 is:

$$\dot{W}_{\text{pump}} = \dot{m}_{\text{wf}} \left(h_2 - h_1 \right) = \dot{m}_{\text{wf}} \left(h_{2\text{s}} - h_1 \right)/\eta_{\text{is,pump}} \,. \tag{1}$$

The heat extracted from the heat source is transferred to the working fluid assuming no heat losses and no pressure losses (*i.e.*, an isobaric process). In our engine, the working fluid exits this process as a saturated vapour (State 3), since superheating has been shown to be detrimental to ORC performance (Oyewunmi et al., 2014). Thus, the rate of heat input from the heat source (hs) is given by:

$$\dot{Q}_{\text{in}} = \dot{m}_{\text{hs}} \, c_{p,\text{hs}} \left(T_{\text{hs,in}} - T_{\text{hs,out}} \right) ; \text{ and, } \dot{Q}_{\text{in}} = \dot{m}_{\text{wf}} \left(h_3 - h_2 \right). \tag{2}$$

The power generated as the working fluid is expanded to State 4 is:

$$\dot{W}_{\text{exp}} = \dot{m}_{\text{wf}} \left(h_3 - h_4 \right) = \eta_{\text{is,exp}} \, \dot{m}_{\text{wf}} \left(h_3 - h_{4\text{s}} \right). \tag{3}$$

During heat rejection, the working fluid transfers heat to a cooling stream (cs) at a rate given by:

$$\dot{Q}_{\text{out}} = \dot{m}_{\text{wf}} \left(h_4 - h_1 \right) ; \text{ and, } \dot{Q}_{\text{out}} = \dot{m}_{\text{cs}} \, c_{p,\text{cs}} \left(T_{\text{cs,out}} - T_{\text{cs,in}} \right). \tag{4}$$

The pump and expander isentropic efficiencies ($\eta_{\text{is,pump}}$ and $\eta_{\text{is,exp}}$) are taken as 75%, while all necessary fluid properties are calculated with REFPROP 9.1 (Kunz and Wagner, 2012; Lemmon et al., 2013).

2.2 Application
A wide variety of fluid streams can be used as ORC-system heat sources, including thermal oil (*e.g.*, in solar applications), process streams (*e.g.*, in industrial applications), geothermal water/steam, exhaust/flue

gases, *etc*. For the purpose of this work, it is more appropriate to consider liquid-phase source and sink streams; gaseous streams would dominate the thermal resistances on the source and sink sides of the heat exchangers, thereby overshadowing the thermal resistances on the working-fluid vapour and liquid streams, and limiting the information we hope to derive by employing different working-fluid mixtures. Thus, the heat source selected in the present work is a hot-water stream from the 80 kW$_e$ Birdsville geothermal ORC power-plant in Australia (Beardsmore et al., 2015), with an inlet temperature ($T_{hs,in}$) of 98 °C and a flow rate of 27 kg.s^{-1} (inlet enthalpy flow of 8.8 MW$_{th}$). This is typical of what is obtainable from other (low-pressure) geothermal reservoirs and also (low-grade) waste-heat streams in industrial processes. The heat sink is a water stream at ambient conditions (in at 20 °C; out at 30 °C).

An optimization problem is set up to maximize the expansion power-output ($\dot{W}_{exp}$) and, concurrently, the cycle thermal and exergy efficiencies (η_{th} and η_{ex}) for the specified heat-source enthalpy flow, while specifying that all of the working-fluid cycles are subject to the same (theoretical) total heat input from the source ($\dot{Q}_{in}$ = 1 MW$_{th}$; $T_{hs,out}$ = 89.2 °C). While this latter constraint does not represent the actual working condition in the Birdsville plant, it is imposed in order to ensure the same overall heat-exchange duty across the working-fluid mixtures, thus enabling a uniform basis for comparison. The objective function definition assumes that the pumping-power requirement is at least an order of magnitude smaller than the expansion power-output, $\dot{W}_{pump} \ll \dot{W}_{exp}$. The decision variables are the evaporation and condensation pressures, while an additional constraint concerns the heat exchangers' pinch conditions ($\geq$ 10 °C).

2.3 Optimal Cycles with Working-Fluid Mixtures

The ORC is optimized for maximum $\dot{W}_{exp}$, using the Interior Point algorithm (Byrd et al., 1999). The optimal power outputs and associated operating pressures are presented in Figure 1, and the expander performance parameters are presented in Figure 2. All other cycle parameters are given in Table 1.

Table 1: ORC optimization results

$x_{C_6H_{14}}$	η_{th} %	η_{ex} %	w_{exp} kJ/kg	$\dot{W}_{pump}$ kW	$\dot{m}_{wf}$ kg/s	$\dot{m}_{cs}$ kg/s	$\dot{Q}_{Ph}$ kW	$\dot{Q}_{Ev}$ kW	$\dot{Q}_{Dsh}$ kW	$\dot{Q}_{Cn}$ kW	x_{227ea}	η_{th} %	η_{ex} %	w_{exp} kJ/kg	$\dot{W}_{pump}$ kW	$\dot{m}_{wf}$ kg/s	$\dot{m}_{cs}$ kg/s	$\dot{Q}_{Ph}$ kW	$\dot{Q}_{Ev}$ kW	$\dot{Q}_{Dsh}$ kW	$\dot{Q}_{Cn}$ kW
0.0	7.79	39.5	33.5	1.41	2.37	21.4	251	749	81.0	841	0.0	7.65	39.5	16.7	2.84	4.74	21.4	284	715	62.0	861
0.1	8.24	41.6	36.5	1.33	2.29	21.3	260	740	84.1	833	0.1	8.00	41.5	17.5	3.48	4.78	21.3	318	682	68.5	851
0.2	8.53	43.1	38.5	1.24	2.25	21.2	266	734	86.9	828	0.2	8.12	42.4	17.3	4.05	4.92	21.3	339	661	72.4	846
0.3	8.71	43.9	39.9	1.15	2.21	21.2	270	730	89.3	824	0.3	8.12	42.7	16.7	4.64	5.13	21.3	356	644	75.4	843
0.4	8.70	43.8	40.1	1.04	2.20	21.2	267	732	89.9	823	0.4	8.07	42.8	15.9	5.31	5.40	21.3	373	627	77.8	841
0.5	8.67	43.6	40.0	0.94	2.19	21.2	266	733	90.8	822	0.5	8.03	43.0	15.1	6.12	5.72	21.3	393	607	80.5	839
0.6	8.64	43.4	39.8	0.87	2.19	21.2	265	735	91.9	822	0.6	7.87	42.6	14.0	6.97	6.11	21.4	410	589	82.5	839
0.7	8.56	43.0	39.2	0.79	2.21	21.2	263	737	92.7	822	0.7	7.60	41.7	12.8	7.83	6.57	21.4	426	575	84.3	840
0.8	8.43	42.3	38.1	0.72	2.23	21.2	259	740	92.7	822	0.8	7.32	40.8	11.6	8.77	7.09	21.5	442	559	86.0	842
0.9	8.19	41.1	36.3	0.64	2.27	21.3	252	748	91.4	826	0.9	7.04	39.9	10.5	9.79	7.64	21.6	460	540	86.9	843
1.0	7.85	39.3	33.8	0.55	2.34	21.4	240	760	88.5	833	1.0	6.74	38.9	9.51	10.8	8.23	21.6	478	522	86.4	846

Of the 1 MW$_{th}$ heat inflow to the cycle, roughly ~75% is used to evaporate the alkane working fluids (50% − 70% for the refrigerants), while the rest is used for pre-heating the fluids to their bubble points. On average, about 0.85 MW is rejected during the condensation process. A working-fluid mixture with $x_{C_6H_{14}}$ = 0.3 results in the cycle with the highest power output and efficiency. The (pure) *n*-hexane cycle has the lowest power output (Figure 1a), followed closely by the *n*-pentane cycle; their power outputs are 10.5% and 10.1% lower than that of the optimal mixture, respectively. For the R-245fa + R-227ea system, the equimolar mixture ($x_{R-227ea}$ = 0.5) is the optimal working fluid (Figure 1b).

The working-fluid mixtures with *n*-hexane fractions between 30 mol% and 60 mol% have the highest power outputs and also the lowest working-fluid flow-rates (from Table 1). This results in cycles with the highest specific work-outputs (defined as $w_{exp} = \dot{W}_{exp}/\dot{m}_{wf}$), with $x_{C_6H_{14}}$ = 0.4 having the highest. The pure fluids have the highest mass flow-rates and this, coupled with their lower work-outputs, results in cycles with the lowest work densities, which are about ~16% lower than that of the optimal fluid-mixture. For the R-245fa + R-227ea system, the optimal working-fluid flow-rate increases monotonically from pure R-245fa to pure R-227ea, and R-227ea has the cycle with the lowest specific work.
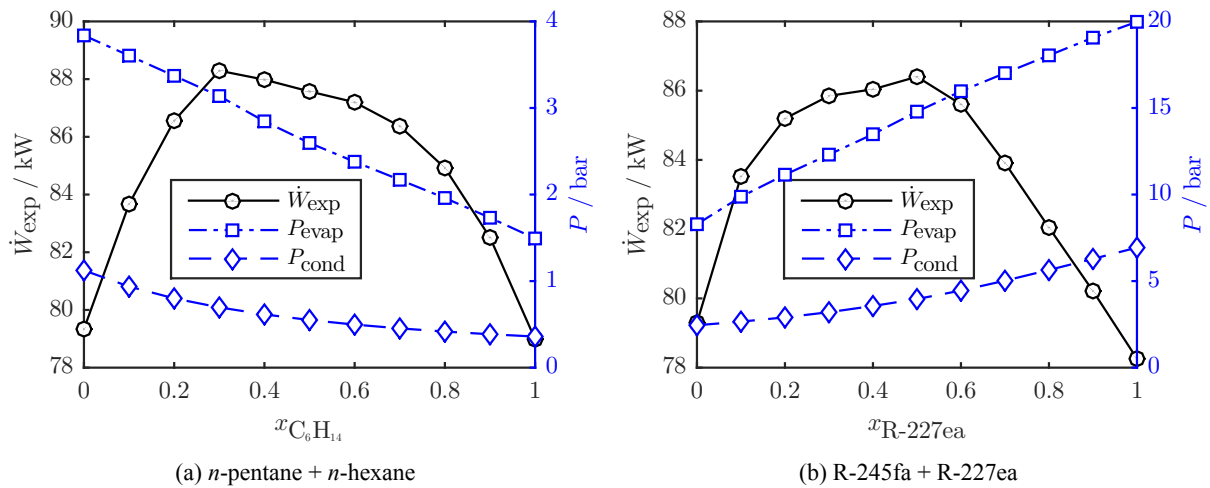
(a) *n*-pentane + *n*-hexane

(b) R-245fa + R-227ea

Figure 1: Optimal expander power-output and corresponding operating phase-change pressure

(a) *n*-pentane + *n*-hexane
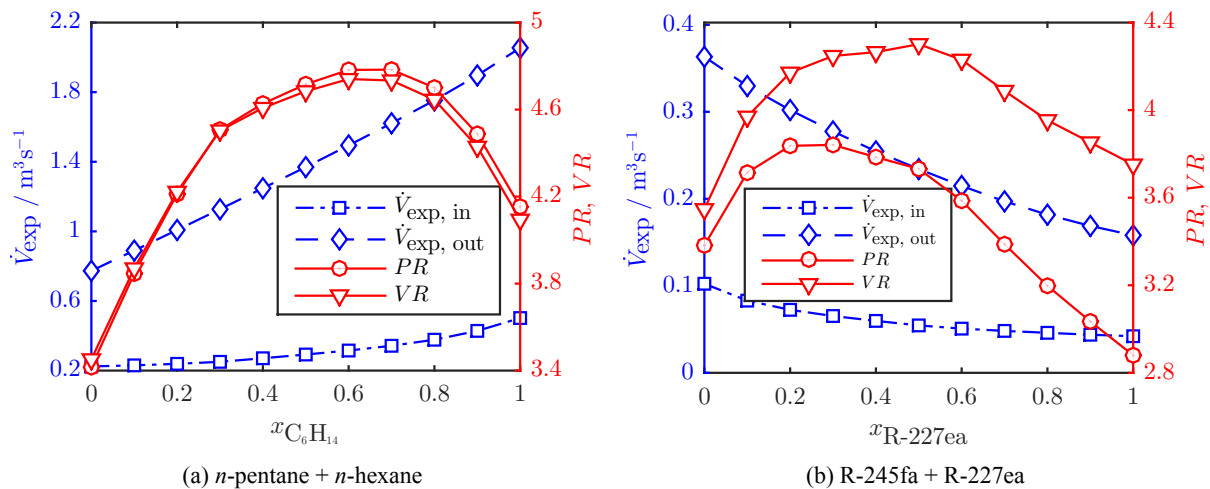
(b) R-245fa + R-227ea

Figure 2: Expander volumetric flow-rate, volume and pressure ratio at optimal power output

The temperature glides (not shown) are smaller in the evaporator than in the condenser. In both heat exchangers these follow a parabolic variation with *x*, reaching a maximum of 6 – 8 K at the equimolar mixture (*n*-pentane + *n*-hexane) and 6 – 9 K at $x_{R\text{-}227ea} = 0.3$ (R-245fa + R-227ea). These do not directly correspond to the optimal mixtures, but are close. In fact, the temperature glide is a reasonably good predictor of the maximum power-output in our study, since high power-output mixtures have relatively high temperature glides, which are also closer to the external heat source and sink temperature changes (8 and 10 K). Although this holds true for closely related binary mixtures, it has been suggested that mixtures of highly dissimilar fluids may not follow this trend (Li et al., 2014; Oyewunmi et al., 2014).

The optimal evaporation and condensation pressures (Figure 1a and 1b, RHS axes) reduce linearly from *n*-pentane (R-227ea) to *n*-hexane (R-245fa). This is because the saturation pressures of *n*-pentane (R-227ea) are higher than those of *n*-hexane (R-245fa) at the same temperature, since the critical temperature of *n*-pentane (R-227ea) is lower than that of *n*-hexane (R-245fa). In the R-245fa + R-227ea system, the entire condensation process occurs at above atmospheric pressures, whereas in the *n*-pentane + *n*-hexane system, only *n*-pentane condenses at above atmospheric conditions (the other working fluids condense at sub-atmospheric pressures). The pumping power (while being negligible compared to the expander output) mirrors the behaviour of the optimal evaporation pressure in both working-fluid systems.

The volumetric flow-rates through the expander, $\dot{V}_{exp}$ (Figure 2a and 2b, LHS axes) are linear, increasing steadily from *n*-pentane (R-227ea) to *n*-hexane (R-245fa) due to the reduction in the saturation pressures during evaporation and condensation at higher concentrations of *n*-hexane (R-245fa). The pressure ra-

tio, *PR*, and expansion ratio, *VR*, (Figure 2a and 2b, RHS axes) follow similar trends, with a minimum observed for one of the pure-fluid components (*n*-pentane and R-227ea, respectively), and a maximum observed for a fluid mixture. The low expansion-ratios and volumetric flow-rates for the pure components suggest they would require smaller expanders than the mixtures, potentially leading to cost savings. Also, they would require fewer expansion stages, further increasing the potential cost savings.

3. HEAT TRANSFER ANALYSIS OF OPTIMAL CYCLES

In the previous section we demonstrated the thermodynamic benefits of employing working-fluid mixtures in ORCs, especially for cases when the heat source and sink profiles are constrained. As expected, there are working-fluid mixtures that realize higher power outputs and efficiencies than both pure fluids as a result of the temperature glides during the phase change processes. The associated expansion and pressure ratios of such working-fluid mixtures are comparable to those of the pure working-fluids.

However, these results were derived purely from a thermodynamic perspective; the effects of such mixtures on the heat transfer processes in the heat exchangers, and especially the evaporator and the condenser, have not yet been considered. Experimental investigations have shown that working-fluid mixtures are likely to experience lower HTCs than pure fluids under similar conditions. Thus, it is imperative to examine the consequences of selecting fluid mixtures on the heat transfer processes in an ORC system, with a view towards determining the sizes and costs of the main system components, and therefore their contributions to overall system cost. The pump and expander costs depend on their power ratings and volume/pressure ratios, which were derived from the thermodynamic optimization and thus need no further treatment. The costs of the heat exchangers on the other hand depend on their sizes, which cannot be obtained from thermodynamic calculations alone, and require appropriate heat transfer models.

3.1 Heat Exchanger Sizing

The heat addition process is carried out in two heat exchangers: (1) the Preheater (Ph), used to pre-heat the working fluid to saturated liquid; and (2) the Evaporator (Ev), used to evaporate the working fluid to the saturated vapour state. Similarly, the heat rejection process is carried out in the Desuperheater (Dsh) and the Condenser (Cn). All heat exchangers are modelled as counter-current, shell-and-tube exchangers (shell and tube diameters: 70 mm and 25 mm; tube thickness: $dx = 5$ mm) constructed from carbon-steel (thermal conductivity: $k = 51$ W.m^{-1}.K^{-1}), and are discretized into 100 (variable-sized) segments, i (= 1 − 100), each segment having an equal heat transfer/duty, *i.e.*, $\dot{Q}_{in}/100$ or $\dot{Q}_{out}/100$. In all heat exchangers, the working fluid flows through the tube-side (tb), while the heat source and sink streams are the shell-side (sh) fluids. Thus, the total rates at which heat is transferred to/from the working fluid in relation to Equations (2) and (4), respectively, are given by:

$$\dot{Q}_{in} = \dot{Q}_{Ph} + \dot{Q}_{Ev} = \sum_{i=1}^{100} \dot{Q}_i + \sum_{i=1}^{100} \dot{Q}_i \; ; \text{ and, } \dot{Q}_{out} = \dot{Q}_{Dsh} + \dot{Q}_{Cn} = \sum_{i=1}^{100} \dot{Q}_i + \sum_{i=1}^{100} \dot{Q}_i \; . \tag{5}$$

Furthermore, for each segment an overall heat-transfer coefficient, U_i, can be defined such that:

$$\dot{Q}_i = U_i \, A_i \, \Delta T_{lm,i} \; ; \text{ where:} \tag{6}$$

$$\Delta T_{lm,i} = \frac{(T_{sh,i+1} - T_{tb,i}) - (T_{sh,i} - T_{tb,i-1})}{\ln\left[(T_{sh,i+1} - T_{tb,i})/(T_{sh,i} - T_{tb,i-1})\right]} \; ; \text{ and, } U_i^{-1} = h_{sh,i}^{-1} + dx/k + h_{tb,i}^{-1} \; . \tag{7}$$

Single-phase local HTCs (h_{sh}, h_{tb}) can be calculated by using the Dittus-Boelter Nusselt number ($Nu_{i,sp}$) correlation, whereas two-phase HTCs can be calculated by suitably modifying $Nu_{i,sp}$ with empirical functions of the Martinelli parameter, X_{tt} (Jung et al., 1989; Shin et al., 1996). In the present work, this modification was fitted specifically to results from experiments involving horizontal turbulent-flow boiling of refrigerant mixtures, as:

$$Nu_{i,tp} = F(X_{tt}) \, Nu_{i,sp} \; ; \text{ where: } F(X_{tt}) = 1 + 1.8 X_{tt}^{-0.82} \; , \text{ and } X_{tt} = \left(\frac{1-q}{q}\right)^{0.9} \left(\frac{\rho_v}{\rho_l}\right)^{0.5} \left(\frac{\mu_l}{\mu_v}\right)^{0.1} \; . \tag{8}$$

Equation (8) can be applied directly for pure fluids using the overall mixture composition for the liquid and vapour-phase properties. For the fluid mixtures, X_{tt} is calculated using the equilibrium liquid and vapour-phase compositions (not the overall composition) at the saturation temperature and corresponding vapour quality, q on mass basis (Jung et al., 1989). The HTAs of all segments are then calculated from Equation (6) and summed to give the total HTA (A_{HX}) for the heat exchanger of interest.

3.2 Heat Exchanger Sizing for Optimal Cycles

First, we verify the overall HTCs calculated using Equations (7) – (8), especially for the heat exchangers involving phase change (Evaporator and Condenser). The overall HTCs at the 20th, 50th and 80th segments of these heat exchangers, and for the single-phase heat exchangers, are presented in Figure 3 for the R-245fa + R-227ea system. The calculated values are in good general alignment with the experimental data obtainable for flow boiling of refrigerant mixtures found in Jung et al. (1989) and Shin et al. (1996). Also in agreement with experimental observations, the HTCs for the working-fluid mixtures at each of the segments appear lower than the linearly interpolated values between the two pure-fluid components that make up the mixture. While various explanations have been proposed for this phenomenon, most authors contend that it is due to mass-transfer effects caused by the composition differences between the vapour and liquid phases during the phase-change process.

In the single-phase heat exchangers (Preheater and Desuperheater), the overall HTCs for the mixtures are also lower than the linearly interpolated values, although this deviation is less pronounced for the R-245fa + R-227ea mixtures. Overall, the HTCs are highest in the Evaporator, followed by the Condenser, and lowest in the Desuperheater. Higher HTCs are achieved in the Condenser and Evaporator due to change of phase. The working-fluid vapour results in the low HTC values in the Desuperheater.

Based on the knowledge of the HTCs and the associated heat-transfer rates, the HTAs for all segments of the heat exchangers can be calculated from Equation (6). The HTAs of the segments in the Evaporator and the Condenser (for R-245fa + R-227ea) are presented in Figure 4; similar observations can be made by considering n-pentane + n-hexane. As the mole fraction of R-227ea is increased in the mixture, the HTA is seen to increase and then decrease such that the pure fluids (R-245fa and R-227ea) have heat exchangers with the lowest HTAs. This is the case across all of the segments and in both the Evaporator and the Condenser as a direct result of the lower HTCs of the working-fluid mixtures, with the only exception being that of the Evaporator for R-245fa + R-227ea where some mixtures (*e.g.*, $x_{R\text{-}227ea} = 0.8$) have lower HTAs than pure R-245fa; pure R-227ea still has the lowest areas across all of the sections.

The HTA variations are less pronounced in the Evaporator than in the Condenser where large differences exist between the pure fluids and the mixtures. The pure fluids have the smallest areas primarily due to their higher HTC values. For example, even though the Evaporator for the case of pure n-hexane has the highest heat-transfer rate (see Table 1), it has the smallest areas because n-hexane has the highest overall HTC amongst all the working fluids. In a similar manner, although the condenser for pure R-245fa has the highest duty, its high HTC enables it to have a lower HTA than those of the mixtures.
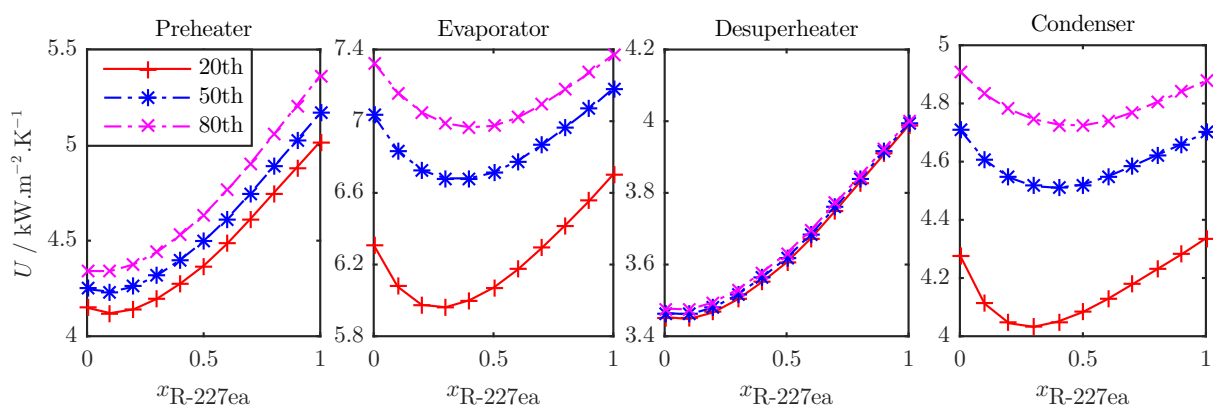

Figure 3: Overall HTCs at segments along the heat exchangers for R-245fa + R-227ea system
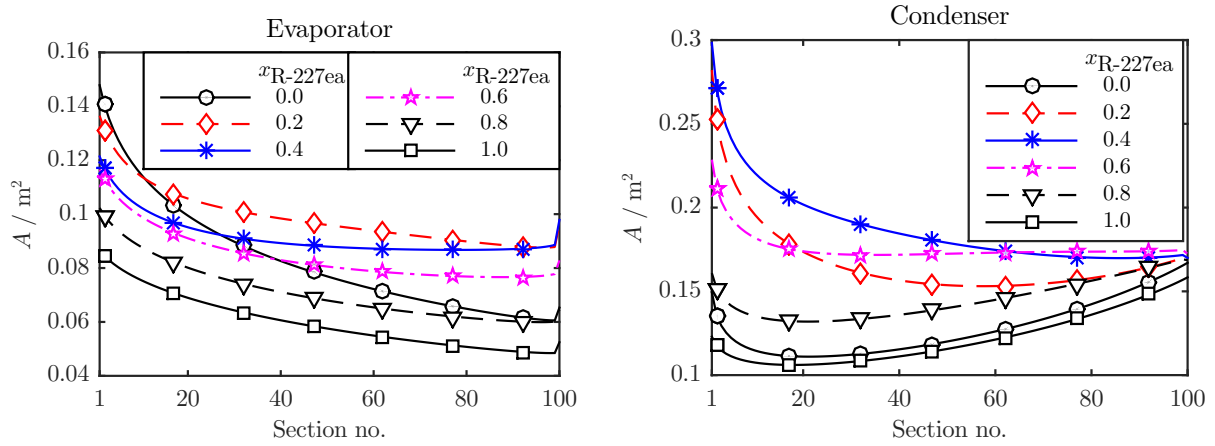
Figure 4: Heat-transfer areas along the Evaporator and Condenser for R-245fa + R-227ea system

The total HTAs for each of the heat exchangers with the different working-fluid mixtures are presented in Figure 5. As expected by consideration of their thermal duties (see Table 1), the Evaporators are generally three times as large as the Preheaters, while the Condensers are $8 - 13$ times larger than the Desuperheaters. Although the Condenser thermal-duties are only about 15% higher than those of the Evaporators, the Condensers are twice as large as the Evaporators in most instances. This is due to the lower overall HTCs and the lower temperature differences across the Condensers.

As the concentration of R-227ea in the refrigerant-mixture system is increased, the Ph and Dsh heat duties increase, and so do the total HTAs of both heat exchangers. The Dsh area reaches a maximum at 90 mol% R-227ea and then decreases slightly for pure R-227ea. The Dsh and Ph areas for the *n*-pentane + *n*-hexane systems are also directly governed by their heat duties. It should however be noted that these variations in HTA with working-fluid mixtures (range of 0.13 m^2 and 0.10 m^2; 1.12 m^2 and 0.31 m^2) are much smaller than those associated with the two-phase heat exchangers. This is important, in that it suggests that working-fluid mixtures have a more profound effect on the Evaporator and Condenser sizes than they do on the single-phase heat-exchangers, at least in the present study.

From Figure 5, it is clear that the pure working-fluids have smaller Evaporator HTAs compared to the mixtures. The only exception is found in the R-245fa + R-227ea system, where fluid mixtures with $x_{\text{R-227ea}} \geq 0.6$ have lower Ev areas than pure R-245fa. Furthermore, due to the deterioration of HTCs during condensation, the Condensers for the working-fluid mixtures are much larger than those for the pure fluids. In the case of the R-245fa + R-227ea system, the HTAs range from 12.2 m^2 ($x_{\text{R-227ea}} = 1$) to 18.8 m^2 ($x_{\text{R-227ea}} = 0.4$), representing a difference of 54%. Such large differences in HTAs between working-fluid mixtures and pure fluids can lead to considerable differences in plant size and cost.
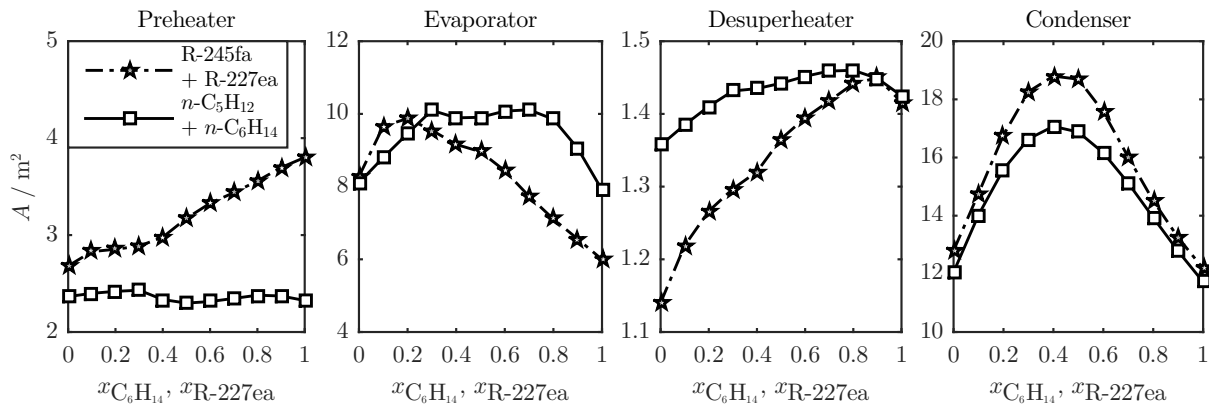

Figure 5: Total heat-transfer areas for heat exchangers with the different working-fluid mixtures

4. COST ANALYSIS OF OPTIMAL CYCLES

We conclude this paper with a brief investigation of the cost implications of employing working-fluid mixtures in ORC systems. The key components affected by the choice of working fluid are those illustrated previously – the working-fluid pump, the expander and the heat exchangers. The costs of these components are added to give an estimate of the plant cost. Although this sum does not give the total installation cost, it is through this amount that the effects of working-fluid choice on plant costs are manifested directly. Other factors that contribute to the plant installation costs would be similar for the various working fluids considered. Component-base costs (C_B, indexed in year 2006; £1 ≡ €1.47, $1.84) are calculated using logarithmic correlations of component size factors (S) according to Seider et al. (2009) and are presented in Table 2. Also in Table 2 are the cost coefficients (converted to SI units). The calculated component-base costs of the optimal cycles are presented in Figure 6 (LHS axes).

Table 2: Component cost coefficients used in $C_B = (F)\exp\{C_0 + C_1[\ln S] + C_2[\ln S]^2\}$

Component	S	F	C_0	C_1	C_2
Pump	$\dot{V}\sqrt{H}$ (m^3.s^{-1}.m$^{1/2}$)	2.7	9.0073	0.4636	0.0519
Expander	$\dot{W}_{exp}$ (kW)	1.0	6.5106	0.8100	0.0000
Expander*	$\dot{W}_{exp}$ (kW)	1.0	7.3194	0.8100	0.0000
Heaters/Coolers	A (m^2)	1.0	10.1060	-0.4429	0.0901
Evaporator/Condenser	A (m^2)	1.0	9.5638	0.5320	-0.0002

* Sub-atmospheric pressure discharge expander (applicable to $x_{C_6H_{14}} \geq 0.1$)

The pumps cost around £5,200, with the cost reducing monotonically from pure *n*-pentane (R-227ea) to *n*-hexane (R-245fa) as a direct result of the lower evaporation pressures as the concentration of *n*-hexane (R-245fa) in the working fluid is increased (in line with Figure 1). Similarly, the costs of the single-phase heat exchangers (Ph and Dsh) are low (£5,000 – £6,000). However, the evaporator and condenser costs are well in excess of £25,000. The expander costs fall into two classes: (i) sub-atmospheric pressure discharge expanders that cost about £35,000; and (ii) standard expanders with a considerably lower cost of about £15,000. From these results, it is clear that the expander and the phase-change heat exchangers present the dominant costs of the ORC system considered here.

The pure fluids (pure *n*-pentane and *n*-hexane; R-245fa and R-227ea) generally have the lowest-cost evaporators and condensers, while the mixtures ($x_{C_6H_{14}} = 0.7$ and $x_{C_6H_{14}} = 0.4$; $x_{R\text{-}227ea} = 0.2$ and $x_{R\text{-}227ea} = 0.4$ respectively) have the highest costs. The condenser size and cost is smallest for *n*-pentane despite it having a larger heat duty and working-fluid flow-rate (see Table 1) than those for the mixtures.

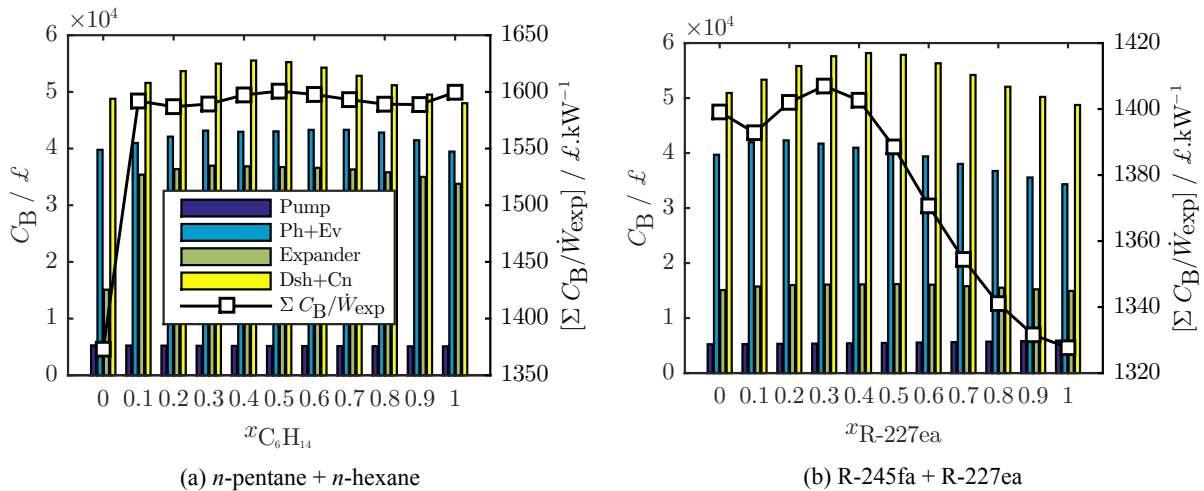(a) *n*-pentane + *n*-hexane   (b) R-245fa + R-227ea

Figure 6: Optimal cycles' component costs (bars; LHS axes) and cost per kW (line; RHS axes)

From Figure 6a and 6b, it is clear that the expander costs mirror the trend exhibited by the optimal power output in Figure 1a and 1b especially as they are correlated with the power output. However, for the n-pentane + n-hexane system, the expander cost for pure n-pentane ($x_{C_6H_{14}} = 0$) is over 50% lower than those of the other working fluids. After expansion, the n-pentane vapour exits the expander at above atmospheric pressure while all the other fluids exit at sub-atmospheric pressures and had their expander costs calculated with the low-pressure discharge expander correlation in Table 2. This in turn makes the cost of the n-pentane expander much lower than the rest.

We complete the analysis by considering the 'rated costs' for the optimal cycles, *i.e.*, cost per kilowatt of power generated ($\Sigma C_B/\dot{W}_{exp}$). This is done such that high power output fluids (especially the fluid mixtures) are not unnecessarily penalized. The rated costs of the optimal cycles are plotted in Figures 6a and 6b (RHS axes). As expected, the ORC system with n-pentane as the working fluid has the lowest rated cost (£1,370/kW) due to its very low expander cost compared to the other working fluids while the cycle with $x_{C_6H_{14}} = 0.5$ has the highest rated cost at £1,600/kW. For the R-245fa + R-227ea system, the ORC system with pure R-227ea has the lowest rated cost (£1,330/kW) while that with $x_{R\text{-}227ea} = 0.3$ has the highest rated cost. The previously identified, thermodynamically optimal fluid mixtures ($x_{C_6H_{14}} = 0.3$ and $x_{R\text{-}227ea} = 0.5$; see Figure 1) have cycle rated costs of £1,600/kW and £1,400/kW respectively. On the other hand, the cost optimal working fluids are n-pentane and R-227ea, which give rated cost reductions of 14% and 5% respectively over the thermodynamically optimal working fluids.

5. CONCLUSIONS

The first aim of this study was to investigate the thermodynamic benefits of employing working-fluid mixtures in organic Rankine cycle (ORC) systems, and a second aim was to examine the effects of selecting such mixtures on the sizes and costs of the resulting ORC engines. Two sets of fluid mixtures, namely n-pentane + n-hexane and R-245fa + R-227ea, were used for this investigation due to their common use in ORC installations. A low-temperature geothermal hot-water heat-source stream was considered. The thermodynamic optimization (maximum expansion power output) resulted in optimal working-fluid mixtures in both cases; the performance indices of these mixtures along with corresponding costs are summarized and compared with those of their constituent pure components in Table 3 below.

Table 3: Performance indices and costs of pure fluids and thermodynamically optimal mixtures

$x_{C_6H_{14}}$	$\dot{W}_{exp}$ kW	PR -	VR -	A_{Ev} m^2	A_{Cn} m^2	$\Sigma C_B/\dot{W}_{exp}$ £/kW	x_{227ea}	$\dot{W}_{exp}$ kW	PR -	VR -	A_{Ev} m^2	A_{Cn} m^2	$\Sigma C_B/\dot{W}_{exp}$ £/kW
0.0	79.3	3.42	3.45	8.11	12.1	1370	0.0	79.3	3.38	3.55	8.28	12.8	1400
0.3	88.3	4.51	4.50	10.1	16.6	1590	0.5	86.4	3.73	4.30	8.96	18.7	1390
1.0	79.0	4.15	4.09	7.91	11.7	1600	1.0	78.3	2.88	3.75	6.00	12.2	1330

The analyses revealed that the temperature glides of the working-fluid mixtures during evaporation and condensation resulted in higher power output and thermal/exergy efficiencies for fluid mixtures. Mixtures containing 30 mol% of n-hexane 50 mol% R-227ea had the highest output, more than either set of pure fluids. The pure fluids did however result in smaller expanders due to their low volumetric flow-rates and expansion ratios. Fluid mixtures appeared to have the largest evaporators and condensers, requiring more expensive heat exchangers than the pure fluids. Moreover, due to sub-atmospheric expansion, the expander costs in the case of the n-pentane + n-hexane working-fluid mixtures (and n-hexane) were much higher than those for pure n-pentane. Generally, equipment sizes and costs were larger for both set of mixtures than for the constituent pure fluids. Thus, the working-fluid mixtures would require larger plant layout areas, contributing significantly to their overall installation costs.

Although the mixtures were found to have the highest power output, they also had the highest rated cost (equipment cost per kilowatt power generated). On the other hand, ORC systems with pure n-pentane working had the lowest rated cost followed by those with n-hexane. For the case of R-245fa + R-227ea

working fluids, pure R-227ea had the lowest rated costs. These observations imply that the thermo-dynamic benefits derived from using the working-fluid mixtures may be outweighed by the increased costs incurred. The fact that these insights were only possible from a direct consideration of thermal and cost factors as exemplified here, underlines the importance of employing a combined thermodynamic, thermal and cost approach in the selection of optimal working-fluid (mixtures) for ORC systems.

REFERENCES

Aghahosseini, S. and Dincer, I. (2013). Comparative performance analysis of low-temperature organic Rankine cycle (ORC) using pure and zeotropic working fluids. *Applied Thermal Engineering*, 54(1):35–42.

Angelino, G. and di Paliano, P. C. (1998). Multicomponent working fluids for ORCs. *Energy*, 23(6):449–463.

Beardsmore, G., Budd, A., Huddlestone-Holmes, C., and Davidson, C. (2015). Country update—Australia. In *Proceedings World Geothermal Congress 2015*, pages 19–24.

Braimakis, K., Leontaritis, A.-D., Preißinger, M., Karellas, S., Brüggeman, D., and Panopoulos, K. (2014). Waste heat recovery with innovative low-temperature ORC based on natural refrigerants. In *27st International Conference on Efficiency, Cost, Optimization, Simulation and Environmental Impact of Energy Systems*.

Byrd, R., Hribar, M., and Nocedal, J. (1999). An interior point algorithm for large-scale nonlinear programming. *SIAM Journal on Optimization*, 9(4):877–900. doi: 10.1137/S1052623497325107; 26.

Chen, H., Goswami, D. Y., Rahman, M. M., and Stefanakos, E. K. (2011). A supercritical Rankine cycle using zeotropic mixture working fluids for the conversion of low-grade heat into power. *Energy*, 36(1):549–555.

Chys, M., van den Broek, M., Vanslambrouck, B., and Paepe, M. D. (2012). Potential of zeotropic mixtures as working fluids in organic Rankine cycles. *Energy*, 44(1):623–632.

Dong, B., Xu, G., Cai, Y., and Li, H. (2014). Analysis of zeotropic mixtures used in high-temperature organic Rankine cycle. *Energy Conversion and Management*, 84(0):253–260.

Garg, P., Kumar, P., Srinivasan, K., and Dutta, P. (2013). Evaluation of isopentane, R-245fa and their mixtures as working fluids for organic Rankine cycles. *Applied Thermal Engineering*, 51(1–2):292–300.

Heberle, F., Preißinger, M., and Brüggemann, D. (2012). Zeotropic mixtures as working fluids in organic Rankine cycles for low-enthalpy geothermal resources. *Renewable Energy*, 37(1):364–370.

Jung, D. S., McLinden, M., Radermacher, R., and Didion, D. (1989). Horizontal flow boiling heat transfer experiments with a mixture of R22/R114. *International Journal of Heat and Mass Transfer*, 32(1):131–145.

Kunz, O. and Wagner, W. (2012). The GERG-2008 wide-range equation of state for natural gases and other mixtures: An expansion of GERG-2004. *Journal of Chemical & Engineering Data*, 57(11):3032–3091.

Lampe, M., Kirmse, C., Sauer, E., Stavrou, M., Gross, J., and Bardow, A. (2014). Computer-aided molecular design of ORC working fluids using PC-SAFT. *Computer Aided Chemical Engineering*, 34(0):357–362.

Lecompte, S., Ameel, B., Ziviani, D., van den Broek, M., and Paepe, M. D. (2014). Exergy analysis of zeotropic mixtures as working fluids in organic Rankine cycles. *Energy Conversion and Management*, 85:727–739.

Lemmon, E. W., Huber, M. L., and McLinden, M. O. (2013). NIST standard reference database 23: Reference fluid thermodynamic and transport properties-REFPROP.

Li, Y.-R., Du, M.-T., Wu, C.-M., Wu, S.-Y., and Liu, C. (2014). Potential of organic Rankine cycle using zeotropic mixtures as working fluids for waste heat recovery. *Energy*, 77(0):509–519.

Oyewunmi, O. A., Taleb, A. I., Haslam, A. J., and Markides, C. N. (2014). An assessment of working-fluid mixtures using SAFT-VR Mie for use in organic Rankine cycle systems for waste-heat recovery. *Computational Thermal Sciences: An International Journal*, 6(4):301–316.

Papadopoulos, A. I., Stijepovic, M., and Linke, P. (2010). On the systematic design and selection of optimal working fluids for organic Rankine cycles. *Applied Thermal Engineering*, 30(6–7):760–769.

Sami, S. M. (2010). Energy and exergy analysis of new refrigerant mixtures in an organic Rankine cycle for low temperature power generation. *International Journal of Ambient Energy*, 31(1):23–32.

Seider, W. D., Seader, J. D., and Lewin, D. R. (2009). *Product & Process Design Principles: Synthesis, Analysis And Evaluation*. John Wiley & Sons.

Shin, J. Y., Kim, M. S., and Ro, S. T. (1996). Correlation of evaporative heat transfer coefficients for refrigerant mixtures. In *International Refrigeration and Air Conditioning Conference*, page 316.

Shu, G., Gao, Y., Tian, H., Wei, H., and Liang, X. (2014). Study of mixtures based on hydrocarbons used in ORC (organic Rankine cycle) for engine waste heat recovery. *Energy*, 74(0):428–438.

Wang, J. L., Zhao, L., and Wang, X. D. (2010). A comparative study of pure and zeotropic mixtures in low-temperature solar Rankine cycle. *Applied Energy*, 87(11):3366–3373.

INTEGRATED DESIGN OF WORKING FLUID MIXTURES AND ORGANIC RANKINE CYCLES (ORC) IN THE CONTINUOUS-MOLECULAR TARGETING (COMT) FRAMEWORK

Matthias Lampe[1], Peter Edel[1], Johannes Schilling[1], Joachim Gross[2], André Bardow[1*]

[1] Chair of Technical Thermodynamics, RWTH Aachen University,
Schinkelstraße 8, 52062 Aachen, Germany
E-mail: andre.bardow@ltt.rwth-aachen.de

[2] Institute of Thermodynamics and Thermal Process Engineering, Stuttgart University,
Pfaffenwaldring 9, 70569 Stuttgart, Germany

* Corresponding Author

ABSTRACT

Organic Rankine Cycles (ORCs) provide power by exploiting low-temperature heat of renewable sources or waste heat. To enhance the efficiency of ORCs, binary mixtures have been proposed as working fluids. Using a working fluid mixture leads to a temperature glide during evaporation and condensation and thus to a better match between the temperature profile of the heat source and the working fluid. We present a method for the integrated optimization the working fluid mixture, i.e., its components and its composition, and the ORC process parameters. Mixture properties are calculated by the PC-SAFT equation of state. In our design framework, the so-called continuous-molecular targeting (CoMT), the pure component parameters are relaxed in the optimization to allow for a simultaneous optimization of the working fluid mixture and the process. However, the resulting optimal mixture components do in general not coincide with any real fluid. Real fluids are identified in the second step of the CoMT framework, the structure-mapping. In this paper, only the CoMT optimization is employed to quantify the potential benefit of working fluid mixtures. The results show that mixtures are not always thermodynamically beneficial and that their benefit depends on the conditions under which the ORC system is finally installed.

1. INTRODUCTION

Organic Rankine Cycles (ORCs) convert low-temperature heat to power. Typically, the exergy content of such sources is low. Thus, efficiency of the cycle is crucial. To enhance the power output, mixtures have been proposed as working fluids (Angelino and Colonna, 1998). Mixtures have a temperature glide, i.e., the temperature is not constant during the phase-change. Due to the temperature glide, a better match of the temperature profile of working fluid and (sensible) heat source is achieved (see figure 1). Better matching of heat source and working fluids is equivalent to less exergy destruction and thus thermodynamically favorable (Heberle et al., 2012). Therefore, zeotropic mixtures can enhance the efficiency of an ORC system (Angelino and Colonna, 1998; Wang and Zhao, 2009; Heberle et al., 2012). Also economically, mixtures were found to be outperforming pure components. Oyewunmi et al. (2014) state lower investment cost by 20 - 30 % when comparing a mixture to a pure component. However, the comparison of the performance of mixtures and pure working fluids might still be biased by the selection of reference pure working fluids and selection of mixtures for assessment. Only the comparison of optimal working fluid mixture to an optimal pure component enables an unbiased analysis.

The selection of an optimal pure component working fluid is already non-trivial (Quoilin et al., 2013; Bao and Zhao, 2013). The selection of an optimal working fluid *mixture* introduces further complexity. Approaches based on trial and error are prohibitive as the combinatorial nature of the problem cannot
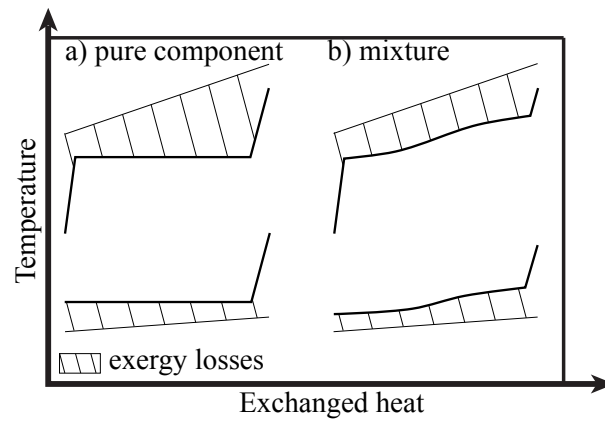
Figure 1: Comparison of the exergy loss during the heat exchange between heat source/sink (thin lines) and the working fluid (thick line), which is a) a pure fluid and b) a mixture. The inlet and outlet temperatures as well as the minimal approach temperature is kept constant. The hatched areas between heat source/sink and working fluid profile reflect the exergy loss due to heat transfer.

be tackled efficiently. Thus, systematic methods for the design of working fluid mixtures are needed (Molina-Thierry and Flores-Tlacuahuac, 2015). Based on their pioneering work for pure fluids (Papadopoulos et al., 2010), Papadopoulos et al. (2013) identify high-performance working fluid mixtures by computer-aided molecular design (CAMD). In their approach, the constituting equations enforcing the feasibility of the component are skipped for one component and an optimal second component is identified. The result is used to limit the search space for the second component and the problem is solved to identify a mixture. Mavrou et al. (2015) compared the resulting mixtures to other proposed mixtures and confirm that the designed mixtures perform better. Furthermore, methods have been developed to select a mixture from a database of components by genetic algorithms (Andreasen et al., 2014).

The continuous-molecular targeting computer-aided molecular design (CoMT-CAMD) framework developed by the authors enables the selection of an optimal working fluid by simultaneously optimizing working fluid and process parameters (Lampe et al., 2014b). Due to the discrete nature of working fluid selection, the simultaneous optimization would lead to a mixed-integer nonlinear program (MINLP) of prohibitive size and complexity. In CoMT-CAMD, the simultaneous optimization is still achieved by exploiting the PC-SAFT equation of state (Gross and Sadowski, 2001, 2002). In PC-SAFT, each working fluid is represented by a set of pure component parameters. These pure component parameters are relaxed to continuous values during the optimization. The relaxation allows for optimization of working fluid and process in a single nonlinear program (NLP). The optimization in the relaxed search-space is the first step of CoMT-CAMD, the continuous-molecular targeting (CoMT). The resulting set of optimal pure component parameters does in general not coincide with the pure component parameters of any real working fluid. Real working fluids are identified in a second step, the so-called structure-mapping. The structure-mapping can be based on a database of existing fluids (Lampe et al., 2014b) or novel working fluids can be generated using CAMD (Lampe et al., 2014a). The CoMT-CAMD framework has also been applied successfully to solvent selection (Bardow et al., 2010; Stavrou et al., 2014).

In this paper, the CoMT-step of the framework is extended for the optimization of binary working fluid mixtures. The extension of the framework allows for the design of an optimal working fluid mixture simultaneously with the optimization of the process itself. The mixture components, the composition and the key process parameters are the degrees of freedom for the optimization. In section 2, the formulation of the integrated mixture and process design is introduced. The continuous-molecular targeting framework is used to identify the optimal working fluid mixture. The resulting optimal hypothetical mixture is compared to the result of the same optimization for a pure component in a case-study (sec. 3). The optimal hypothetical mixture and the hypothetical pure component fluid provide an upper bound on the possible performance for real fluids. Thus, the comparison of an optimal working fluid mixture

to an optimal pure working fluid allows to quantify the potential benefit of employing a working fluid mixture. The results show that mixtures are not always beneficial and that their benefit depends on the conditions under which the ORC system is finally installed.

2. GENERAL PROBLEM FOR WORKING FLUID MIXTURE OPTIMIZATION

In the continuous-molecular targeting, the working fluid mixture and the process are optimized simultaneously. For the formulation of the optimization problem, a generic model of the process is employed.

$$
\begin{aligned}
\min_{x, z_1, z_2, x_{\mathrm{wf}}} \quad & f(x, \theta) & & \text{objective function} \\
\text{s.t.} \quad & g_1(x, \theta) \leq 0 & & \text{process model inequalities} \\
& g_2(x, \theta) = 0 & & \text{process model equalities} \\
& \theta = h(x, z_1, z_2, x_{\mathrm{wf}}) & & \text{PC-SAFT} \\
& A\, z_1 \leq b & & \text{convex hull (fluid 1)} \\
& A\, z_2 \leq b & & \text{convex hull (fluid 2)} \\
& x_{\min} \leq x \leq x_{\max} \in \mathbb{R}^n & & \text{process variables} \\
& 0 \leq x_{\mathrm{wf}} \leq 1 \in \mathbb{R} & & \text{mixture composition} \\
& z_{\min} \leq z_1, z_2 \leq z_{\max} \in \mathbb{R}^m & & \text{mixture components.}
\end{aligned}
\tag{1}
$$

The process model comprises an objective $f(x, \theta)$ (e.g. net power output, efficiency, or second law efficiency) as well as inequality and equality constraints $g_1(x, \theta)$ and $g_2(x, \theta)$, respectively. The process model depends on two vectors of variables: the optimized process parameters x (e.g., mass flow rate, or pressure level) and thermo-physical properties of the working fluid θ (e.g., enthalpies, or entropies of each state point). The thermo-physical properties θ are calculated by PC-SAFT ($\theta = h(x, z_1, z_2, x_{\mathrm{wf}})$). In PC-SAFT, binary mixtures are defined by their composition x_{wf} and two sets of pure component parameters z_1 and z_2. For the optimized process parameters, bounds can be derived based on the application of the ORC system (e.g., upper and lower pressure level). To limit the search space of the pure component parameters z_i, we construct a convex hull around a database of known pure components. The convex hull yields a set of linear constraints $A\, z_i \leq b$ for both of the mixture components. Thus, the complete search space of working fluids is feasible for each component.

The simultaneous optimization of mixture and process in eq. (1) identifies the optimal process parameters x^* as well as an optimal working fluid mixture represented by the components z_i^* and the composition x_{wf}^*. The optimization is performed as one single nonlinear program and no discrete degrees of freedom are introduced. However, the resulting optimal mixture components z_i^* do in general not coincide with any real fluid. Real fluids are identified in the second step of the CoMT-CAMD framework, the structure-mapping. In this paper, only the first step of the method is employed. This CoMT step does not identify real components, but yields an upper bound for the performance of any working fluid mixture, as the relaxed problem contains all discrete solutions.

Optimization problem (1) is a nonconvex NLP. In nonconvex problems, multiple local minima can occur. In fact, the search space is symmetric in the compounds of the mixture and thus there at least are two globally optimal solutions, which both represent the same mixture: For any combination of two components z_1 and z_2, and their composition x_{wf}, an identical symmetric solution can be obtained by exchanging the fluids (i.e., $\bar{z}_1 = z_2$ and $\bar{z}_2 = z_1$) and adapting the composition (i.e., $\bar{x}_{\mathrm{wf}} = 1 - x_{\mathrm{wf}}$). The symmetry of the search space can be prevented by a symmetry breaking constraint, e.g., bounding the mixture composition to $x_{\mathrm{wf}} \leq 0.5$. Symmetry breaking constraints should be employed when global optimization is used to speed up the optimization (Liberti and Ostrowski, 2014). For local search algorithms, symmetry breaking constraints are not always beneficial (Prestwich and Roli, 2005), as additional local minima can be introduced to the problem. In this work, optimization is performed using sequential quadratic programming (SQP) implemented in Matlab (2012) based on (Han, 1977; Powell, 1978, 1979)

Table 1: Specification of the heat source for the generic example.

Parameter	Symbol	Value
heat source mass flow rate	$\dot{m}_{\mathrm{HS}}$	$50 \frac{\mathrm{kg}}{\mathrm{s}}$
heat source specific heat capacity	$c_{p,\mathrm{HS}}$	$4.185 \frac{\mathrm{kJ}}{\mathrm{kg\,K}}$
heat source inlet temperature	$T_{\mathrm{in,HS}}$	$270\,^{\circ}\mathrm{C}$

on a standard desktop PC (Core i5 CPU, 1.7 GHz with 4 GB RAM) using the default settings. To prevent the solver from converging to a local optimum, different starting values have been used.

3. ILLUSTRATIVE EXAMPLE

The comparison of mixtures of existing working fluids to existing pure components in the literature shows advantages for the mixtures compared to pure components. However, this comparison can be misleading when a good mixture is compared to a bad pure component. Eq. (1) yields an optimal hypothetical mixture and the corresponding process parameters. The same optimization can be performed for a pure working fluid by enforcing a composition of $x_{\mathrm{wf}} = 0$. This allows for the identification of an optimal hypothetical pure working fluid. The results of both optimizations can be used for a unbiased assessment of the potential benefit of mixtures.

To assess the potential of mixtures, a generic example of an ORC system is used. Changing the model for the cooling of the cycle allows to identify how the cold side effects the optimal mixture. A recuperated ORC is considered. The minimal temperature difference to heat source and heat sink are $\Delta T_{\mathrm{min}} = 0$ K. The heat source is defined by a mass flow rate of hot water (see table 1). The degrees of freedom x for the process are the pressure levels for evaporization p_{evap} and condensation p_{cond} as well as the mass flow rate of working fluid $\dot{m}_{\mathrm{wf}}$. The system is optimized for an optimal net power output

$$P_{\mathrm{net}} = \dot{m}\left[(h_4 - h_5) - (h_2 - h_4)\right] \ ,$$

where the enthalpies are calculated assuming boiling liquid after the condenser (state 1) and saturated steam after the evaporator (state 4). To calculate the enthalpy after the turbine (state 5) and after the pump (state 2), constant isentropic efficiencies of turbine and condenser are assumed ($\eta_{\mathrm{T}} = \eta_{\mathrm{P}} = 0.85$). For the recuperator, a minimal approach temperature of $\Delta T_{\mathrm{min}}^{\mathrm{regen}} = 30\,^{\circ}\mathrm{C}$ is assumed.

For the cooling of the system, different options and model formulations are employed in the following to demonstrate their effect on the optimal working fluid mixture.

3.1 Constant Cooling Temperature
The most simple model of a cooling system assumes a constant lower temperature limit. The lower limit is selected according to a considered cooling system. For this example, a lower temperature limit of $70\,^{\circ}\mathrm{C}$ is considered. Eq. (1) is used to optimize two sets of pure component parameters z_1 and z_2 as well as the optimal mixture composition x_{wf}.

For a constant cooling temperature, the resulting optimal mixture is basically a pure component ($x_{\mathrm{wf}}^* = 0.005$). The illustration of the cycle in a T,h-diagram in figure 2 allows to identify the properties of the working fluid leading to optimality: The working fluid is fitted optimally between the temperature profiles of the heat source and heat sink. As the lower temperature level is constrained by a constant temperature, the temperature glide of a mixture cannot be exploited for the condensation (states 5'-1). For the heating of the system, working fluid and mass flow rate are selected to allow for a minimal temperature difference in the preheating (states 2'-3). This combination of the practically pure working fluid and process is not the most efficient cycle, regarding thermal efficiency. The deficit in efficiency is overcome by matching preheating and heat source such that the heat source is cooled down as far as possible. Thus, the cycle is optimal with respect to the net power output.
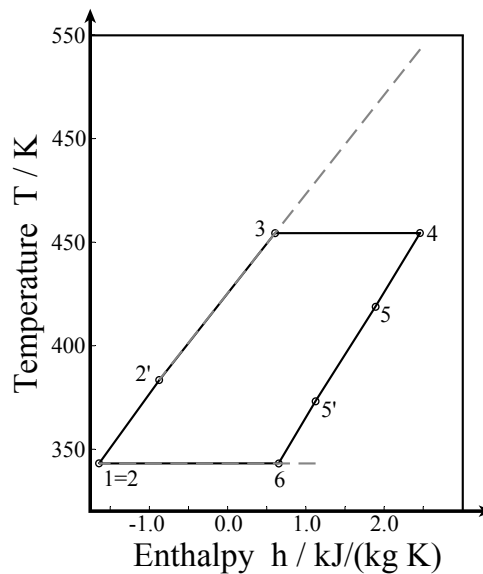
Figure 2: Resulting ORC from the CoMT-optimization for a constant lower temperature limit.
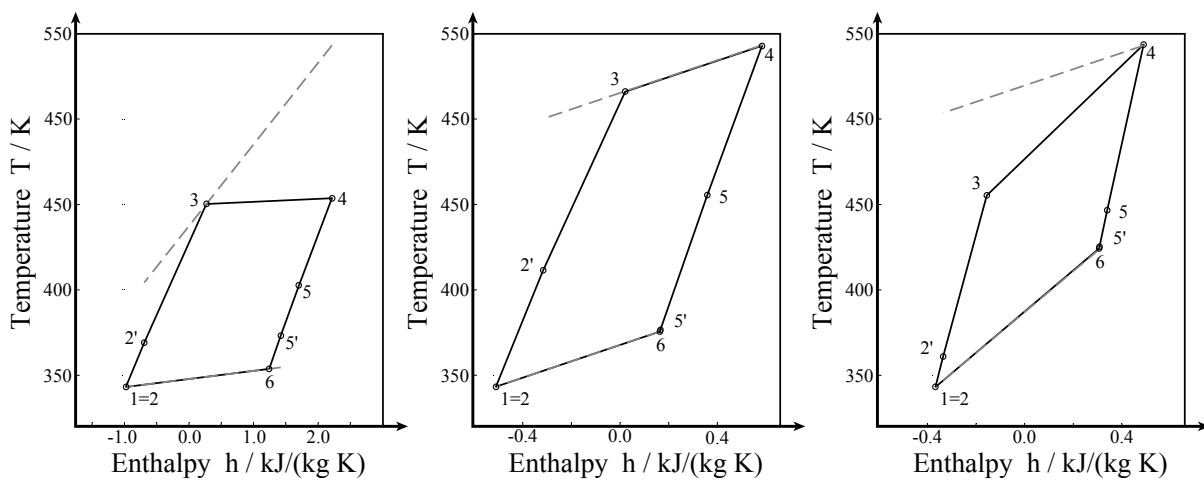

Figure 3: Resulting ORC from the CoMT-optimization for a cooling source with constant mass flow rate of a) $500 \frac{\mathrm{kg}}{\mathrm{s}}$**, b)** $50 \frac{\mathrm{kg}}{\mathrm{s}}$ **and c)** $20 \frac{\mathrm{kg}}{\mathrm{s}}$**.**

The assumption of a constant lower temperature limit leads to the identification of a pure working fluid: due to the constant lower temperature of the cooling system, a pure working fluid already enables an optimal match for a constant lower temperature limit. The effect of a sensible heat carrier in the cooling system is considered in the following.

3.2 Fixed Mass Flow Rate of Cooling Agent

In this section, the cooling system is modeled in the same way as the heat source; i.e., a mass flow rate of cooling agent is supplied with a specified temperature. Three different mass flow rates are assessed to show the effect of a variation of the value of this parameter ($500 \frac{\mathrm{kg}}{\mathrm{s}}$, $50 \frac{\mathrm{kg}}{\mathrm{s}}$, and $20 \frac{\mathrm{kg}}{\mathrm{s}}$). The value of $50 \frac{\mathrm{kg}}{\mathrm{s}}$ corresponds to the same heat capacity flow rate $(\dot{m}\,c_p)_{\mathrm{HS}}$ as for the heat source.

In figure 3a, the result of the optimization is shown for a flow rate of $\dot{m}_{\mathrm{CS}} = 500 \frac{\mathrm{kg}}{\mathrm{s}}$. The result is a mixture with a composition of $x_{\mathrm{wf}} = 0.29$ (see table 2). The temperature glide follows the cooling agent exactly. To enable the perfect match of cooling agent and working fluid the condensation pressure p_{cond} and the mass flow rate $\dot{m}_{\mathrm{wf}}$ are selected to the according values. The evaporation pressure p_{evap} is chosen to exploit the minimal allowed temperature difference to the heat source.

Table 2: Resulting mixtures from the CoMT-optimization for different mass flow rates of cooling agent

Parameter	Unit	Values		
$\dot{m}_{\mathrm{CS}}$	$\frac{\mathrm{kg}}{\mathrm{s}}$	500	50	20
x_{wf}	—	0.29	0.1	0.16
m_1	—	1.84	1.91	1.85
σ_1	Å	3.41	4.32	4.15
$\left(\frac{\epsilon}{k}\right)_1$	K	503	489	543
m_2	—	2.04	1.84	1.84
σ_2	Å	4.36	3.91	3.32
$\left(\frac{\epsilon}{k}\right)_2$	K	392	400	392
p_{evap}	bar	1.26	8.68	5.13
p_{cond}	bar	0.05	0.13	0.25
$\dot{m}_{\mathrm{wf}}$	$\frac{\mathrm{kg}}{\mathrm{s}}$	57.0	15.2	12.5

The results for the varied mass flow of cooling source are similar to this result (figures 3b and 3c). The cooling agent is dominating the value for the temperature glide, regardless of the heat source properties. The optimal match of cooling agent and working fluid leads to a thermodynamically optimal cycle. However, only a comparison based on an economic objective function would give a final answer to the question, if mixtures can outperform pure components: the optimal cycles in this and the previous section exploit a perfect match of working fluid and cooling agent in the condenser. This leads to low temperature differences for the heat transfer and accordingly to large required heat exchange area. The larger heat exchange area might lead to prohibitive investment cost to employ the cycle in a ORC system.

3.3 Modeling of an Air-Cooled System

The comparison based on a constant mass flow rate of cooling agent in section 3.2 might lead to the conclusion that mixtures are performing better for real ORC systems. However, the assumption of a constant mass flow rate of the cooling agent might still be misleading. Besides the negative effect on the heat exchange area, the assumption of a constant mass flow rate of cooling agent is not valid for many applications: When an air-cooled system is employed, the amount of air for cooling the system is not limited by any constraint, in general. The amount of air that is fed to the system results from a tradeoff between cost for the compression of the air and the effectiveness of the cooling-system.

To reflect this tradeoff, a model for the compressor of an air-cooled system is employed. The model is based on a constant isentropic efficiency of the compressor $\eta_{\mathrm{comp}} = 0.75$. The mass flow rate of cooling agent is assumed to be the minimal mass flow rate allowing for the cooling of the cycle. Thus, effort for cooling at lower temperatures is considered in the optimization. The air is entering the compressor at $T_{\mathrm{air,in}} = 15\,°\mathrm{C}$ and fed to an heat exchanger. The pressure drop to be overcome by the compressor is $\Delta p = 0.01\,\mathrm{bar}$.

Under these conditions, the CoMT optimization results in a mixture (figure 4a and table 3). The optimal process has a lower temperature than the previous cases. The lower temperature is feasible, as the constraint on the lower temperature is less restrictive. A moderate temperature glide is employed (see figure 4a). The net power output optimal mixture with the optimal process is $P_{\mathrm{net}} = 2.76\,\mathrm{MW}$.

For an assessment of the effect of mixtures on the performance of the cycle, the optimization is performed for pure component working fluids. The optimal mixture and an optimal pure component are compared. Thus, the comparison is unbiased by the selection of a specific mixture and a set of pure components.

The result of the CoMT-optimization for the pure component is similar to the result of the mixture optimization (see figure 4b). The optimal pure component has pure component parameters close to com-
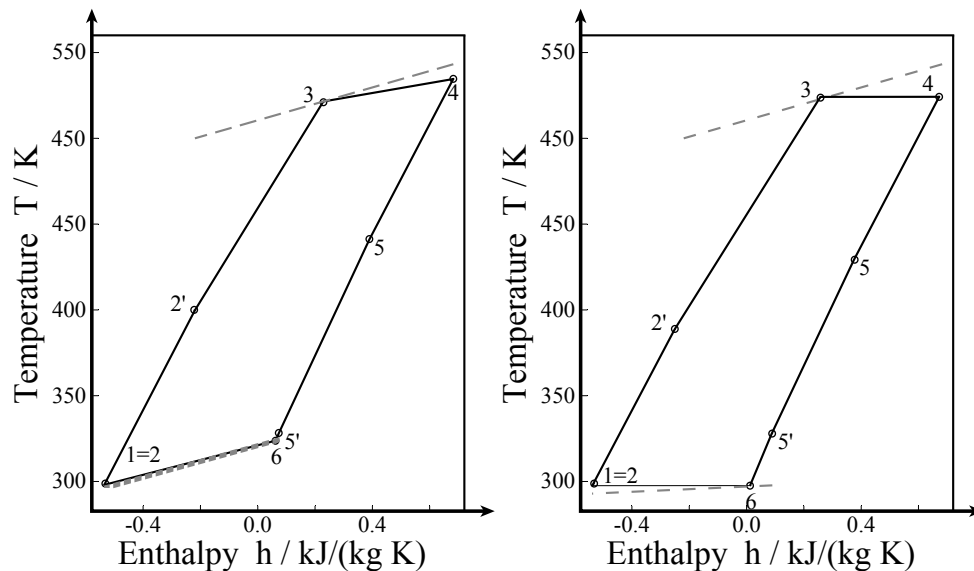
Figure 4: a) Result of the CoMT-optimization employing a model of and air-cooling system. b) Result of the CoMT-optimization for a pure component employing a model of and air-cooling system.

ponent 1 from the optimal mixture (table 3). The net power output of the pure component cycle is $P_{\text{net}} = 2.69$ MW. Thus, the net power output is only 3 % lower than the value for the optimal mixture.

4. SUMMARY

The CoMT method for the integrated optimization of working fluid and process is extended to the design of working fluid mixtures. The optimization was applied successfully to the identification of optimal mixtures under different specifications for the application.

The hypothetical optimal mixture results in a optimal match of the heat transfer profile of the working fluid and the cooling agent in all examples. For a constant temperature of the cooling agent, the optimal working fluid is a pure component. When the mass flow rate of the cooling agent is constant, mixtures are preferable due to their ability to adapt to the temperature profile of the cooling agents.

Overall, the results show that pure component working fluids are competitive with mixtures and indeed optimal in some cases. By employing a model of the cooling system, the trade-off between the efficiency of the cycle and power consumption of the cooling system is reflected. For this case, a mixture is the

Table 3: Results of the CoMT-optimization using an air-cooled system.

Parameter	Unit	Pure component	mixture
x_{wf}	—	-	0.1
m_1	—	1.84	1.84
σ_1	Å	5.21	5.18
$\left(\frac{\epsilon}{k}\right)_1$	K	519	543
m_2	—	—	1.89
σ_2	Å	—	4.35
$\left(\frac{\epsilon}{k}\right)_2$	K	—	400
p_{evap}	bar	6.79	6.43
p_{cond}	bar	0.01	0.01
$\dot{m}_{\text{wf}}$	$\frac{\text{kg}}{\text{s}}$	14.5	14.6

optimal solution. However, the difference to the optimal pure component working fluid is below 3 %. For the construction of a real ORC system, the small difference might favor the selection of a pure component for simplicity of the system design.

The comparison of mixtures to pure working fluids indicates that there are pure components that can compete with mixtures in terms of thermodynamical performance. Still, economic criteria will decide in practice about the use of working fluid mixtures. Thus, economic criteria should be included in the analysis in future work.

REFERENCES

Andreasen, J. G., Larsen, U., Knudsen, T., Pierobon, L., and Haglind, F. (2014). "Selection and optimization of pure and mixed working fluids for low grade heat utilization using organic Rankine cycles". *Energy*, 73:204–213.

Angelino, G. and Colonna, P. d. P. (1998). "Multicomponent Working Fluids For Organic Rankine Cycles (ORCs)". *Energy*, 23(6):449–463.

Bao, J. and Zhao, L. (2013). "A review of working fluid and expander selections for organic Rankine cycle". *Renewable and Sustainable Energy Reviews*, 24:325–342.

Bardow, A., Steur, K., and Gross, J. (2010). "Continuous-Molecular Targeting for Integrated Solvent and Process Design". *Industrial & Engineering Chemistry Research*, 49(6):2834–2840.

Gross, J. and Sadowski, G. (2001). "Perturbed-Chain SAFT: An Equation of State Based on a Perturbation Theory for Chain Molecules". *Industrial & Engineering Chemistry Research*, 40(4):1244–1260.

Gross, J. and Sadowski, G. (2002). "Application of the Perturbed-Chain SAFT Equation of State to Associating Systems". *Industrial & Engineering Chemistry Research*, 41(22):5510–5515.

Han, S. P. (1977). "A globally convergent method for nonlinear programming". *Journal of Optimization Theory and Applications*, 22(3):297–309.

Heberle, F., Preißinger, M., and Brüggemann, D. (2012). "Zeotropic mixtures as working fluids in Organic Rankine Cycles for low-enthalpy geothermal resources". *Renewable Energy*, 37(1):364–370.

Lampe, M., Kirmse, C., Sauer, E., Stavrou, M., Gross, J., and Bardow, A. (2014a). "Computer-aided Molecular Design of ORC Working Fluids using PC-SAFT". In Eden, M. R., Siirola, J. D., and Towler, G., editors, *Proceedings of the 8th International Conference on Foundations of Computer-Aided Process Design*, volume 34 of *Computer Aided Chemical Engineering*, pages 357–362. Elsevier Science, Burlington.

Lampe, M., Stavrou, M., Bücker, H. M., Gross, J., and Bardow, A. (2014b). "Simultaneous Optimization of Working Fluid and Process for Organic Rankine Cycles Using PC-SAFT". *Industrial & Engineering Chemistry Research*, 53(21):8821–8830.

Liberti, L. and Ostrowski, J. (2014). "Stabilizer-based symmetry breaking constraints for mathematical programs". *Journal of Global Optimization*, 60(2):183–194.

Matlab (2012). *The MathWorks Inc., R2012b (8.0.0.783), 32-bit*.

Mavrou, P., Papadopoulos, A. I., Stijepovic, M. Z., Seferlis, P., Linke, P., and Voutetakis, S. (2015). "Novel and conventional working fluid mixtures for solar Rankine cycles: Performance assessment and multi-criteria selection". *Applied Thermal Engineering*, 75:384–396.

Molina-Thierry, D. P. and Flores-Tlacuahuac, A. (2015). "Simultaneous Optimal Design of Organic Mixtures and Rankine Cycles for Low-Temperature Energy Recovery". *Industrial & Engineering Chemistry Research*, 54(13):3367–3383.

Oyewunmi, O. A., Taleb, A. I., Haslam, A. J., and Markides, C. N. (2014). "An Assessment of Working-Fluid Mixtures Using SAFT-VR MIE for Use in Organic Rankine Cycle Systems for Wastte-Heat Recovery". *Computational Thermal Sciences: An International Journal*, 6(4):301–316.

Papadopoulos, A. I., Stijepovic, M. Z., and Linke, P. (2010). "On the systematic design and selection of optimal working fluids for Organic Rankine Cycles". *Applied Thermal Engineering*, 30(6-7):760–769.

Papadopoulos, A. I., Stijepovic, M. Z., Linke, P., Seferlis, P., and Voutetakis, S. (2013). "Toward Optimum Working Fluid Mixtures for Organic Rankine Cycles using Molecular Design and Sensitivity Analysis". *Industrial & Engineering Chemistry Research*, 52(34):12116–12133.

Powell, M. J. D. (1978). "A fast algorithm for nonlinearly constrained optimization calculations". In Watson, G., editor, *Numerical Analysis*, volume 630 of *Lecture Notes in Mathematics*, pages 144–157. Springer Berlin Heidelberg.

Powell, M. J. D. (1979). "Variable metric methods for constrained optimization". In Glowinski, R., Lions, J., and Laboria, I., editors, *Computing Methods in Applied Sciences and Engineering, 1977, I*, volume 704 of *Lecture Notes in Mathematics*, pages 62–72. Springer Berlin Heidelberg.

Prestwich, S. and Roli, A. (2005). "Symmetry Breaking and Local Search Spaces". In Barták, R. and Milano, M., editors, *Integration of AI and OR Techniques in Constraint Programming for Combinatorial Optimization Problems*, volume 3524 of *Lecture Notes in Computer Science*, pages 273–287. Springer Berlin Heidelberg.

Quoilin, S., Broek, Martijn Van Den, Declaye, S., Dewallef, P., and Lemort, V. (2013). "Techno-economic survey of Organic Rankine Cycle (ORC) systems". *Renewable and Sustainable Energy Reviews*, 22:168–186.

Stavrou, M., Lampe, M., Bardow, A., and Gross, J. (2014). "Continuous Molecular Targeting–Computer-Aided Molecular Design (CoMT–CAMD) for Simultaneous Process and Solvent Design for CO 2 Capture". *Industrial & Engineering Chemistry Research*, 53(46):18029–18041.

Wang, X. D. and Zhao, L. (2009). "Analysis of zeotropic mixtures used in low-temperature solar Rankine cycles for power generation". *Solar Energy*, 83(5):605–613.

A REVIEW OF POTENTIAL WORKING FLUIDS FOR LOW TEMPERATURE ORGANIC RANKINE CYCLES IN WASTE HEAT RECOVERY

Jason R. Juhasz, Luke D. Simoni, PhD

The Chemours Company, LLC.
Wilmington, Delaware, USA
jason.r.juhasz@chemours.com
luke.d.simoni@chemours.com

presented by Claus-Peter Keller, Chemours Deutschland GmbH, claus-peter.keller@chemours.com

ABSTRACT

The focus of this paper will be specific to working fluids for use in various technologies for waste heat recovery (WHR) of exhaust heat including internal combustion engines (ICE) and in the use of Organic Rankine Cycles (ORC). Several novel fluids have been developed (DR-2 or HFO-1336mzz(Z) and DR-12) which have a good potential fit for these low temperature heat recovery applications (up to 250°C) and they have been characterized as having desirable working fluid properties such as good safety classification and environmental footprint. Additional properties from an ORC system, where mechanical systems are incorporated, are good thermal stability, chemical compatibility, material compatibility and thermodynamic performance. These systems must be reliable and therefore the interactions with the working fluids are paramount as design basis becomes an important attribute in the development of ORC components. The aforementioned HFO fluids will be assessed on the criteria mentioned to help identify their candidacy in using them in heat recovery technology platform, where interest is specifically ORC based. These novel HFO fluids provide a good alternative to existing working fluids currently under consideration with an added advantage of meeting low GWP regulations.

1. INTRODUCTION

The need to improve energy efficiency and fuel utilization efficiency has been a topic of discussion for the last couple of decades, the direction of integrating heat recovery systems in truck, marine, geothermal, biomass and waste heat from other various heat sources are progressively being adopted to help address this concern. In all of these applications, there are an array of potential different classes of working fluids, CFCs, HCFCs, PFCs, siloxanes, alcohols, hydrocarbons, ethers, amines, fluids mixtures, HCFOs and HFOs, which can be considered for use in ORCs and should be evaluated on a broad basis in order to identify the ideal working fluid for the desired system.

In recent years, an increased scrutiny has been placed on the environmental aspect of these fluids and regulatory pressures are driving global awareness of their impact on the environment. The ozone depletion potential (ODP) and greenhouse gas emissions (GHG) are of particular interest here and emphasis has been placed on choosing a working fluid which demonstrates an ability to meet these climate protection initiatives. When reviewing the various classes of working fluids listed above, certain characteristics will become unviable and as a result, CFCs and PFCs will not be evaluated due to their ODP and high GWP concerns, respectively. The ethers present another concern around

reactivity and stability; the amines have been shown to have major toxicological effects, therefore these components were deemed to be outside the scope of good working fluids.

Within these classes of potential viable working fluids, a select few are provided to show their basic characteristics so a further discussion on relevant use in applications can be made more constructive. Additionally, the novel hydrofluoro-olefin (HFO) based fluids (DR-2 and DR-12) will be discussed as they have been developed specifically to address these concerns as well as having of other favorable characteristics such as being non-flammable and low toxicity concerns.

2. FLUID CHARACTERIZATION FOR LOW TEMPERATURE ORC

2.1 Simple Organic Rankine Cycles

The primary aim in identifying feasibility of working fluids for ORC system rests on conducting a thermodynamic analysis where the cycle configuration is an important variable. Determining the cycle performance is dependent on having precise evaporating and condensing temperatures combined with fluid properties (latent heat of vaporization, temperature, pressure, entropy, enthalpy and liquid and gas densities) and using these variables to determine expander output, required pumping power, net cycle efficiencies, mass flow rates and turbine size parameters for the fluids of interest. Without knowing exact system configurations, it is difficult to assess one fluid's benefits over another so temperature-entropy diagram and vapor pressure versus temperature curve will be provided for selected fluids as a general guideline. The properties shown in *Figures 1 through 3* were calculated by REFROP and CoolProp software, where each fluid and their respective EOS used are referenced in *Table 1*.

Table 1. EOS reference for Working Fluids using REFPROP and CoolProp

|	program/ method	EOS reference:
HCFC-123 (R-123)	REFPROP	Younglove, B.A. and McLinden, M.O., "An International Standard Equation of State for the Thermodynamic Properties of Refrigerant 123 (2,2-Dichloro-1,1,1-trifluoroethane)," J. Phys. Chem. Ref. Data, 23:731-779, 1994.
HFC-134a (R-134a)	REFPROP	Tillner-Roth, R. and Baehr, H.D., "An international standard formulation of the thermodynamic properties of 1,1,1,2-tetrafluoroethane (HFC-134a) for temperatures from 170 K to 455 K at pressures up to 70 MPa," J. Phys. Chem. Ref. Data, 23:657-729, 1994.
HFC-245fa (R-245fa)	REFPROP	"Short Fundamental Equations of State for 20 Industrial Fluids," J. Chem. Eng. Data, 51:785-850, 2006.
DR-12	REFPROP	Peng-Robinson by Pavan Naicker
DR-2	REFPROP	Created at DuPont Based on Experimental Fit of PR-EOS - P. Naicker
SES36	CoolProp	Unpublished report: Monika Thol, Eric W. Lemmon, Roland Span, \"Equation of State for a Refrigerant Mixture of R365mfc (1,1,1,3,3-Pentafluorobutane) and Galden® HT 55 (Perfluoropolyether)\" https://github.com/ibell/coolprop/blob/master/CoolProp/pseudopurefluids/SES36.cpp
HCFO-1233zdE	REFPROP	"Thermodynamic Properties of Trans-1-chloro-3,3-trifluoropropene (R1233zd(E)): Vapor Pressure, p-rho-T Data, Speed of Sound Measurements
HMDSO	REFPROP	Multiparameter Equations of State for Selected Siloxanes, Fluid Phase Equilibria, 244:193-211, 2006.
Ethanol	REFPROP	A New Fundamental Equation for Ethanol, Master's Thesis, University of Idaho, 2011.
Toluene	REFPROP	Lemmon, E.W. and Span, R.,"Short Fundamental Equations of State for 20 Industrial Fluids,"J. Chem. Eng. Data, 51:785-850, 2006.
n-Pentane	REFPROP	Span, R. and Wagner, W."Equations of State for Technical Applications. II. Results for Nonpolar Fluids,"Int. J. Thermophys., 24(1):41-109, 2003.
	REFPROP:	Lemmon, E.W., Huber, M.L., McLinden, M.O. NIST Standard Reference Database 23: Reference Fluid Thermodynamic and Transport Properties-REFPROP, Version 9.1, National Institute of Standards and Technology, Standard Reference Data Program, Gaithersburg, 2013.
	CoolProp:	http://www.coolprop.org/citation.html
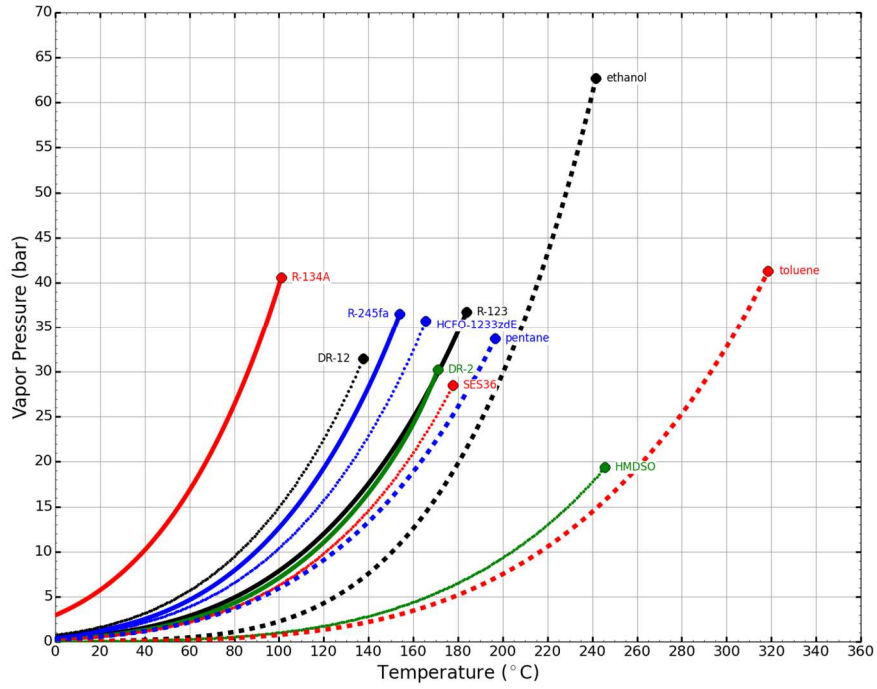
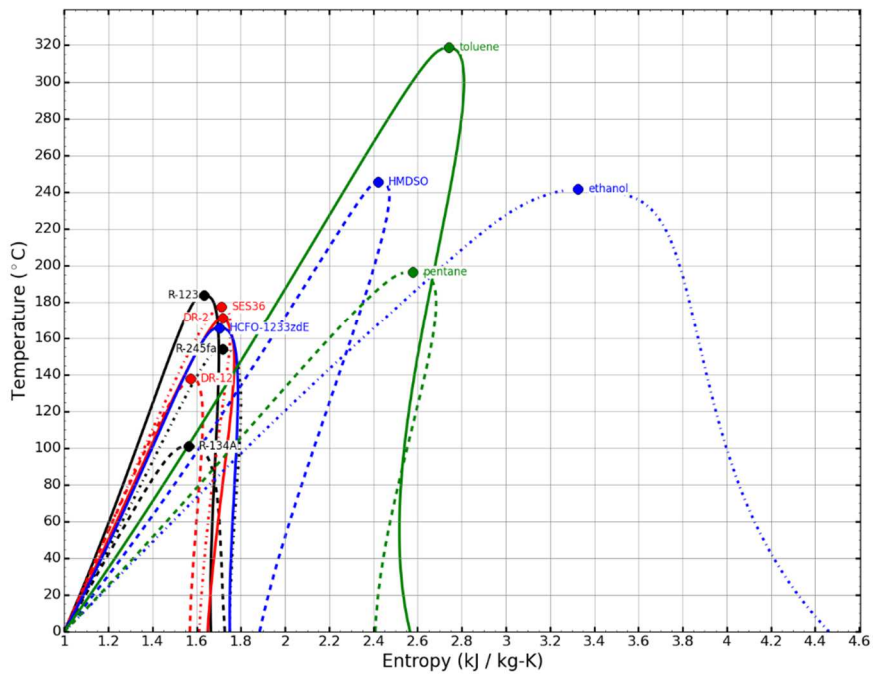**Figure 1**. Vapor Pressure of Selected Working Fluids for Comparison

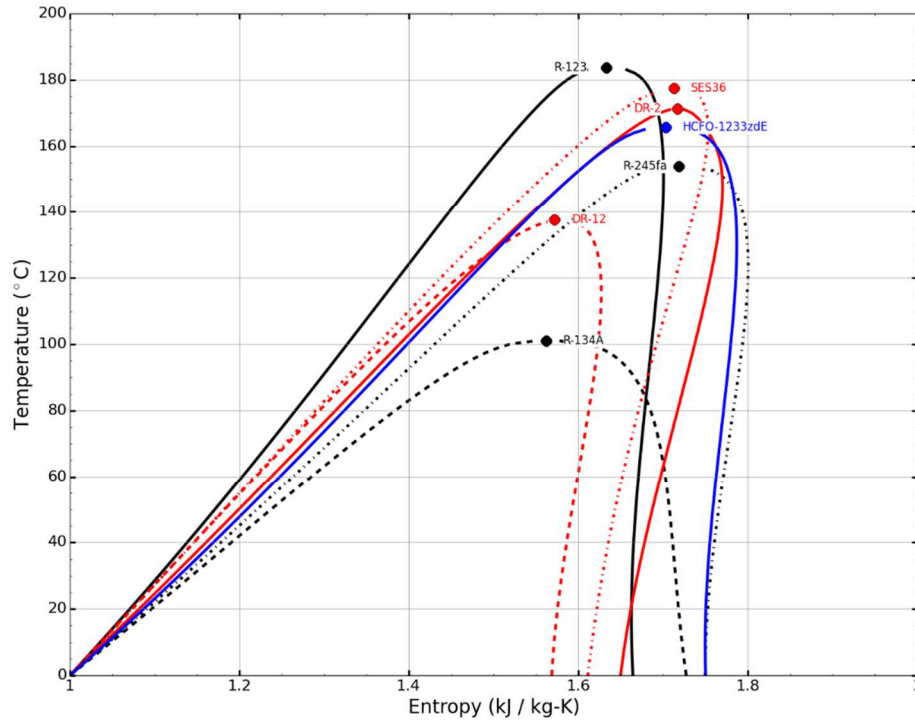**Figure 2**. Temperature-Entropy Diagram for Selected Working Fluids for Comparison

Figure 3. Enlarged Region of Temperature-Entropy diagram for Selected Working Fluids

Examples for Simple Organic Rankine Cycles systems are shown below and *Figure 5* illustrates heat being captured from the exhaust of internal combustion engine (Dupachy *et al*., 2009).
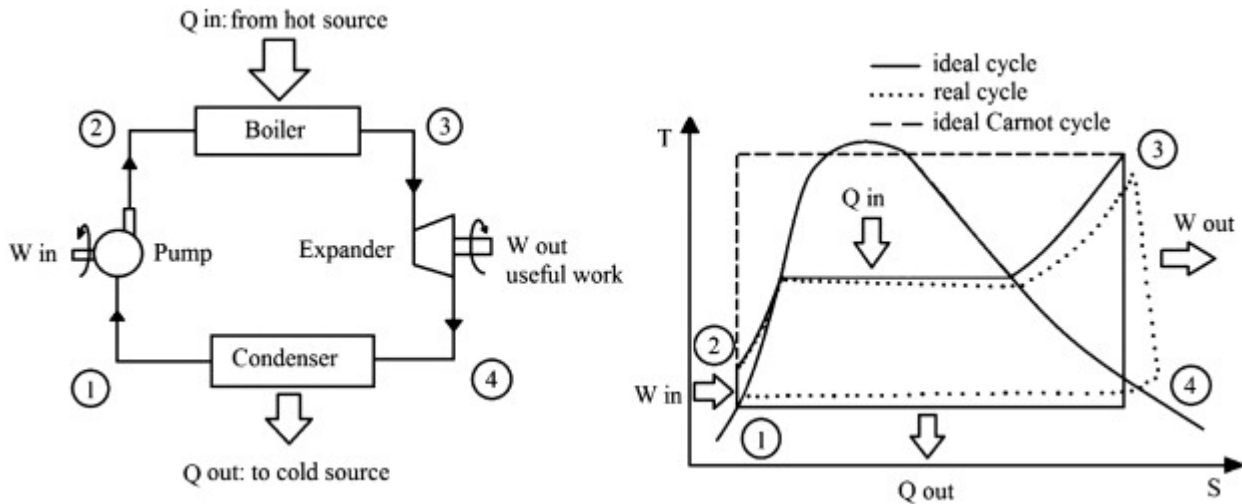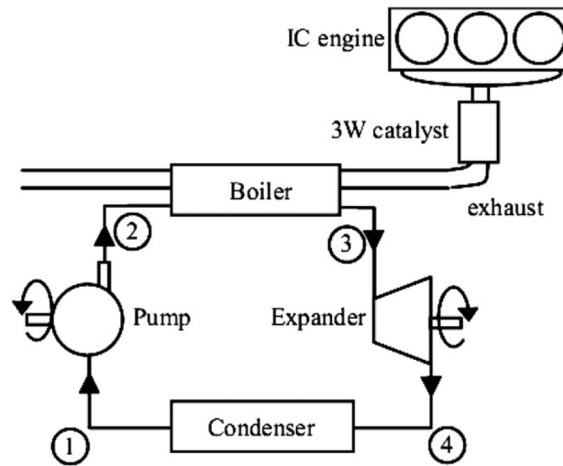

Figure 4. Rankine Cycle System

Figure 5. Layout of the waste heat recovery Rankine bottom cycle

Basic component selection for the expanders, pumps and heat exchangers is based on understanding the thermodynamics properties of the working fluids; however, there are other properties which can be overlooked which could be just as critical when selecting a fluid (safety, thermal stability, chemical and material compatibility, viscosity, etc.). These properties could influence reliability, the material construction – plastics, elastomers and metals as well as the robustness of the system where higher operating pressures and/or corrosion potential exists. From the refrigeration industry, many guidelines have been developed to address the safety management piece around the safe handling, storing and personnel exposure. Additional agencies such as NFPA, DOT, CFR, OSHA and TDG have placed many restrictions pertaining to the safe practice of toxic and flammable fluids and thus impose limitation which can affect a distribution and service facilities in terms of cost for electrical classification, breathing apparatuses and/or other infrastructure needs.

2.2 Working Fluids
An effective way to screen out potential working fluid candidates can be an arduous task where emphasis of thermodynamic performance may be deemed as the most important element. Even though this is true, aspects such as flammability and toxicity affect the ability to safely work with the fluids in a given environment. Additionally, ODP and GWP are becoming a growing concerns as environmental restrictions and regulations may be imposed and ultimately negate the use of certain compounds (potential working fluids) as more friendly alternative fluids come into existence. In *Table 2* below, an overview of working fluids are provide to differentiate each based on physical properties, toxicity, flammability, GWP and ODP. Toxicity and flammability characterization for refrigerant fluids is provided in the last row, ratings specifically for HMDSO, ethanol and toluene are conducted by ASHRAE (2000, 2007, 2013) as they use represents a serious safety concern. *Table 3* highlights the general safety classification that is used to characterize working fluids. The category of A and B are used to distinguish the toxicity. The increasing number following the letter distinguishes the increasing flammability aspect of the fluid.

Table 2. Working fluid comparison of key thermodynamic, safety, health and environmental characteristics.

Properties	HCFC-123	HFC-134a	HFC-245fa	DR-12	DR-2	HCFO-1233zd(E)	SES36	n-Pentane	HMDSO[1]	Ethanol[2]	Toluene[3]
Normal Boiling Point, °C	27.8	-26.1	15.1	7.5	33.4	18.3	36.7	36.1	101	78.4	110.6
Critical Temperatures, °C	185	101.1	154	137.7	171.3	165.6	177.6	196.5	245.5	240.8	318.6
Critical Pressure, Mpa	3.67	4.06	3.65	3	2.9	3.57	2.85	3.36	1.94	6.15	4.13
Latent Heat @ 25 °C (KJ/Kg)	171.37	177.79	190.32	144.96	168.12	191.76	162.75	366.29	229.96	920.66	412.85
Specific Heat @ 0.1 Mpa 25°C (KJ/Kg-K)	1.02	1.43	1.32	1.09	1.19	1.24	1.08	2.32	1.91	2.44	1.7
Toxicity Class	See ASHRAE safety group rating								slightly	NA[7]	moderate toxic
Flammability Class[4]									serious flammable	severe flammability	serious flammability
Ozone Depletion Potential	0.02	0	0	0	0	0.0003		0		0	0
Global Warming Potential[5]	79	1300	858	32[6]	2	1	3710	5	ND[8]	1	3
safety group (ASHRAE)	B1	A1	B1	A1[6]	A1	A1	A1	A3	ND[8]	ND[8]	ND[8]

(1) Fisher Scientific, Hexamethildisiloxane, Material Safety Data Sheet, February 29,2008.
(2) NCP Alcohols, Ethanol, Material Safety Data Sheet, May 3, 2012.
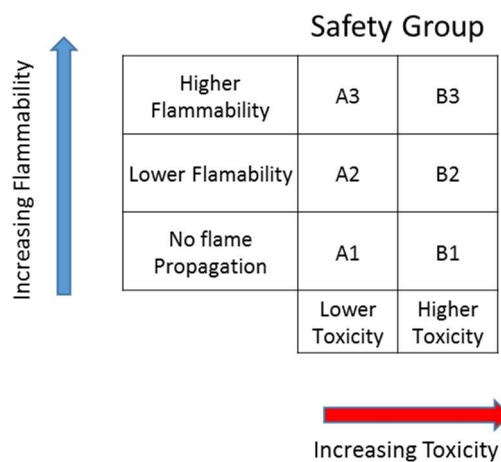(3) Honeywell, Toluene, Material Safety Data Sheet, December 21, 2005.
(4) ASTM (2004)
(5) Myhre et al. (2013)
(6) Expected value
(7) Not associated
(8) Not determined

Table 3. General Safety Group Classification

2.3 Thermal Stability

From *Table 2* above, an analysis can be made that the working fluids on the right side present concerns of flammability and of which, two have toxicity issues. A smaller subset of these fluids were screened for thermal stability in sealed tube tests to assess their suitability for higher temperature systems. Four of the fluids investigated, HFCF-123, HFC-245fa, DR-2, DR-12 and HCFO-1233zd(E), and subjected to 250°C for 1 and 7 days with metal coupons. An IC analysis for the anions F$^-$ and Cl$^-$ were conducted after the exposure conditions on the remaining fluids. Additional stability test of 14 days was carried out on HCFO-1233zd(E) and DR-2; results form HCFO-1233zd(E) were less favorable at 250°C, therefore a lower temperature study was performed at 200°C. As seen in the data in *Table 4*, results for HCFO-1233zd(E) at 200°C reflect significant degradation of the molecule as a function of time. DR-2

and DR-12 showed extremely favorable results. Interesting results were discovered regarding DR-12, where the fluoride ion was below detectable limits. The purity of DR-12 was only 98.1% and has no chlorines in its molecular structure; however, some trace chlorine containing species were present and very evident in the IC analysis as the Cl⁻ ions are seen at these elevated temperatures. These HFO fluids have an unsaturated (double bond) molecule and yet they do not demonstrate poorer thermal stability than saturated compounds. The notion that unsaturated compounds have less stability in a closed system at elevated temperatures is not necessarily correct a correct assumption. In a closed system, with all materials specified, only chemical and material compatibility tests with the exact system (including HFOs) can determine stability. Data presented in *Table 4* below incorporates some results previously presented by Kontomaris *et al*. (2013).

Table 4. Thermal Stability with IC Analysis Results

Fluid	Temperature (°C)	Duration	Coupon	IC Anion Results (PPM)	
				F-	Cl-
HCFO-1233zd-E	200	1 day	steel	8.23	61.5
HCFO-1233zd-E	200	7 days	steel	9.48	143.97
HCFO-1233zd-E	200	14 days	steel	34.28	554.18
HCFC-123	250	1 day	steel	328.43	496.44
HCFO-1233zd-E	250	1 day	steel	11.66	170.45
HFC-245fa	250	1 day	steel	3.6	< MDL
DR-12	250	1 day	steel	< MDL	18.28
DR-2	250	1 day	steel	0.6	11.3
HCFC-123	250	7 days	steel	2460.3	218.96
HCFO-1233zd-E	250	7 days	steel	1400.18	3854.26
HFC-245fa	250	7 days	steel	20	< MDL
DR-12	250	7 days	steel	< MDL	35.23
DR-2	250	7 days	steel	1.55	3.39
HCFO-1233zd-E	250	14 days	steel	2668.5	3194.7
DR-2	250	14 days	steel	1.83	2.02

2.4 Material Compatibility

An investigation was conducted on material compatibility for DR-2 where the study looked at 15 common materials in the presence of POE lubricant oil with DR-2 (Kontomaris, 2014); they were elevated to a temperature of 100°C for 14 days and their weight and hardness changes were measured at the conclusion of the experiment. Results display only a mild interaction between these plastics and elastomers and DR-2; they suggest that DR-2 would be suitable for use. It is recommend that further evaluations be conducted for material and chemical compatibility not only plastics and elastomers, but also covering various metals and lubricating typically found in a heat recovery system. This study is only a subset of current experiments from the lab. Future studies will be available where a selection of lubricant and recommendations will be incorporated as a function of temperature for DR-2 and DR-12.

Table 5. Weight Changes of Various Elastomers and Plastics with DR-2

DR-2 Compatibility with Plastics & Elastomers: (I)

Weight changes of polymeric specimens after exposure to
HFO-1336mzz-Z/POE Lubricant blends for 14 days at 100 °C

Material	Immediately after Exposure %	Twenty Four Hours after Exposure %
Neoprene	-0.55	-0.98
EPDM	2.39	0.84
Polyester Resin	10.04	4.94
Nylon Resin	-0.74	-0.79
Epoxy	0.66	0.56
Polyester PET	3.73	3.54
Polyester PBT	1.15	1.13
Polycarbonate	0.74	0.75
Polyimide	0.79	0.79
Teflon PTFE	3.05	2.72
Teflon FEP	3.29	3.09
Tefzel ETFE	6.25	5.61
Phenolic	-0.18	-0.31
PVC	0.68	0.70
PEEK	-0.06	0.01

**Mild Interactions between HFO-1336mzz-Z and
Many Plastics and Elastomers**

Table 6. Hardness Changes of Various Elastomers and Plastics with DR-2

DR-2 Compatibility with Plastics & Elastomers: (II)

Hardness changes of polymeric specimens after exposure to
HFO-1336mzz-Z/POE Lubricant blends for 14 days at 100 °C

Material	Immediately after Exposure %	Twenty Four Hours after Exposure %
Neoprene	7.10	2.58
EPDM	2.56	0.64
Polyester Resin	-1.01	-0.51
Nylon Resin	-1.00	-2.00
Epoxy	-1.01	-3.54
Polyester PET	0.00	0.00
Polyester PBT	-1.00	-1.00
Polycarbonate	-1.00	0.00
Polyimide	0.00	0.00
Teflon PTFE	-0.50	0.00
Teflon FEP	0.00	-0.51
Tefzel ETFE	0.00	0.00
Phenolic	0.00	0.00
PVC	0.00	0.00
PEEK	0.00	0.00

**Mild Interactions between HFO-1336mzz-Z and
Many Plastics and Elastomers**

3. CONCLUSION

The basis of this work was not to provide a deep analysis of ORC systems, but to focus on the viability and the selection process that comes with identifying good working fluid properties. The criteria to develop working fluids which perform under the high temperatures of heat recovery systems is essential as well as the need to have safe and environmental friendly alternatives to choose from. The ultimate goal from this study is to provide insight to existing entities like ASHRAE that review working fluids for the refrigerant industry, where all potential candidates are reviewed by a body of engineers and chemists for safety in use. It is conceivable that different environments may dictate that some safety concerns would represent less of an issue and they should be investigated based on their own merit. In general use, both flammability and toxicity are highlighted to pose significant risks and additional precautions are necessary to address their suitability for use. GWP and ODP represent two additional criteria which will influence working fluid selections in the future as regulations strive to find better alternatives as they affect the environment. Even though these influencers limit the choices of potential candidates, it does not mean that a significant loss of performance must be sacrificed to adhere to these values. The new HFO fluids offer comparable thermodynamic performance similar to fluids in their class and provide thermal stability as well. The DR-2 molecule with its low GWP and no ODP, has shown extremely good thermal stability at temperature up to 250ºC. These new class compounds, HFOs, have been shown to exhibit good overall characteristics for use in low and possible medium temperature ORC applications.

NOMENCLATURE

WHR	*waste heat recovery*
ORC	*organic Rankine cycle*
GHG	*greenhouse gases*
ICE	*internal combustion engine*
ODP	*ozone depletion potential*
GWP	*global warming potential*
EOS	*equation of state*
CFC	*chlorofluorocarbon*
HCFC	*hydrochlorofluorocarbon*
HFO	*hydrofluoro-olefins*
PFC	*perfluorocarbons*
HMDSO	*Hexamethyldisiloxane*
NFPA	*National Fire Protection Association*
DOT	*Department of Transportation*
CFR	*Code of Federal Regulations*
TDG	*Transportation of Dangerous Goods*
OSHA	*Occupational Safety and Health Administration*
ASHRAE	*American Society of Heating, Refrigeration and Air Conditioning Engineers*

REFERENCES

Myhre, G., Shindell D., Breon F., Collins W., Fuglestvedt J.,Huang J., KochD., Lamarque J., Lee, D., Mendoza B., Nakajima T., Robock A., Stephens G., Takemura T., Zang H., 2013, Anthropogenic and Natural Radiative Forcing, In: Climate Change: The Physical Science Basis, Contribution of Working Group I to the Fifth Assessment Report of the Intergovernmental Panel on Climate Change, Cambridge University Press, Cambridge, United Kingdom and New York, NY, USA.

Kontomaris, K., Minor B., Hydutsky B., 2013, Low Global Warming Potential Working Fluids for Organic Rankine: DR-2; Chemical Stability at High Temperatures, *2nd International Seminar on Organic Rankine Cycle Power Systems, ASME ORC 2013*, Rotterdam, The Netherlands (October 7-8).

Kontomaris, K., 2014, Zero-ODP, Low-GWP, Nonflammable Working Fluids for High Temperature Heat Pumps, *ASHRAE 2014 Annual Conference*, Seattle, Washington, USA (June 28- July 2).

Duparchy A., Leduc P., Bourhis G., Ternel C., 2009, Heat Recovery for the Next Generation of Hybrid Vehicles: Simulations and Design of a Rankine Cycle System, *World Electric Vehicle*, vol. 3, P. 3-6.

ASTM, 2004, ASTM E681-04, Standard Test Method for concentration Limits of Flammability of Chemicals (Vapors and Gases), American Society for Testing and Materials, Philadelphia, USA.

ASHRAE, 2000, Addenda to ANSI/ASHRAE Standard-1999, Addenda to Designation and Safety Classifications of Refrigerants, ASHRAE, Atlanta, USA.

ASHRAE, 2007, ASHRAE Standard 97-2007, Sealed Glass Tube Method to Test the Chemical Stability for Materials for Use within Refrigeration Systems, ASHRAE, Atlanta, USA.

ASHRAE, 2013, ANSI/ASHRAE Standard 34-2013, Designation and Safety Classification of Refrigerants, ASHRAE, Atlanta, USA.

APPLICATION OF REFRIGERANT WORKING FLUIDS FOR MOBILE ORGANIC RANKINE CYCLES

Christopher R. Nelson*

Cummins Inc, Research & Technology
Columbus, IN, USA
oo647@cummins.com

* Corresponding Author

ABSTRACT

Cummins Inc. has been a leading developer of Organic Rankine Cycle (ORC) systems for application to heavy-duty, on-highway trucks in the United States for several years. Cummins has passed through several generations of ORC system architecture and has fielded several on-highway vehicles equipped with ORC systems as a part of research conducted in partnership with the United States Department of Energy. Throughout this development, Cummins has carefully evaluated potential working fluids for ORC application and has remained committed to using safe and environmentally friendly refrigerants such as R245fa and its recently introduced ultra-low GWP replacements for on-highway use.

Integration of Organic Rankine Cycle (ORC) systems into heavy duty, on-highway vehicles requires consideration of a significant number of factors, not the least of which is the choice of working fluid. The selection of fluid is primarily driven by safety, environmental and health effects of the fluid, potential performance considering the application at hand, availability, serviceability, etc. Given the working fluid, selection/sizing of various system components and optimization of the system architecture may be made.

This paper will briefly review Cummins' ORC history and discuss the background leading to Cummins' selection of refrigerant working fluids for on highway application. Details of technology that allow a refrigerant's safe and effective use in this application will also be discussed. An architecture comparison between systems using a refrigerant such as R245fa and ethanol will be made and a performance comparison between R1233zd(e), an ultra-low GWP replacement for R245fa, and ethanol will be presented.

1. INTRODUCTION

Since approximately 2003, Cummins Inc. has investigated the potential practicality and benefit of applying Organic Rankine Cycles (ORC) to its heavy duty diesel engines applied to on-highway, linehaul vehicles. Cummins settled upon non-flammable refrigerants, such as R245fa, as viable ORC working fluids. Refrigerants were already applied in the ORC industry and had a proven record of effective performance. Cummins evaluated many different working fluids but considerations of safety, environmental responsibility, feasibility, performance, etc., led the researchers to make R245fa their initial prime-path fluid of choice.

Cummins early ORC systems (see Figure 1, below) were designed before the introduction of Selective Catalytic Reduction (SCR) aftertreatment. These ORC systems took advantage of a high flowrate of Recirculated Exhaust Gas (EGR) and were expected to achieve nearly an 8% fuel economy benefit.
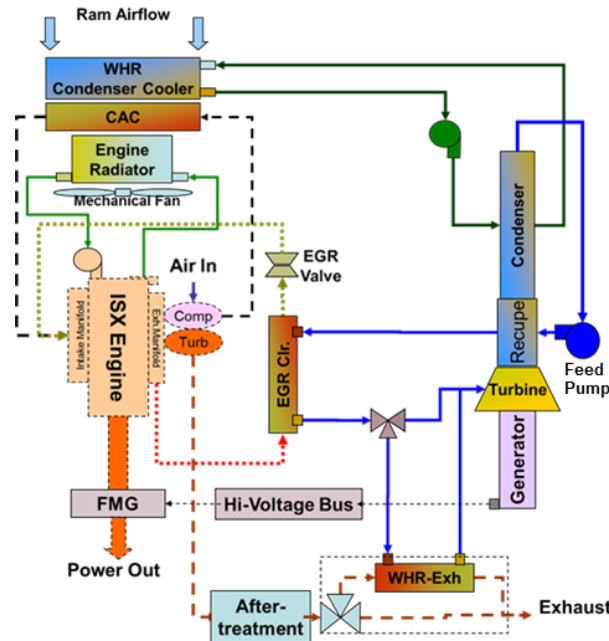

Figure 1: Early Cummins ORC system

At the time, conversion of recovered power to electricity was preferred as integration of the ORC with potential hybrid drive systems was anticipated. Compatibility of electronic systems, cost and complexity of electrical components, and the then expected drive cycle benefit of hybrid systems in linehaul applications drove the ORC architecture away from electrical integration. The concept of mechanically linking recovered power directly to the engine was developed into an architecture as presented in Figure 2, below.
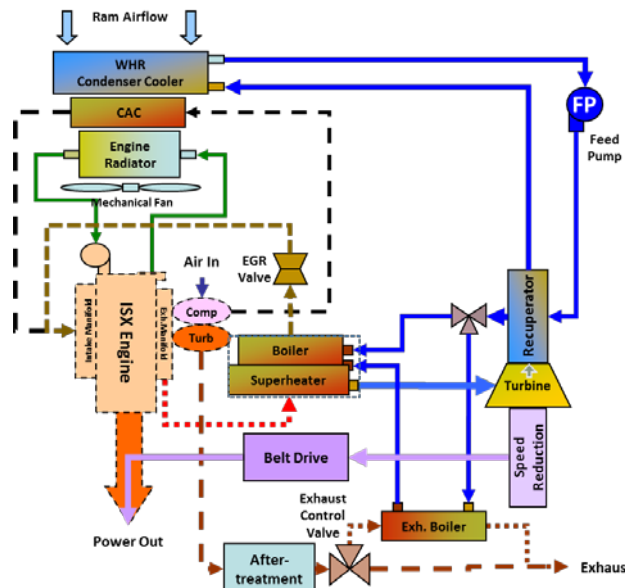
Figure 2: Mechanically-coupled ORC system architecture

Direct-to-air condensing was adopted to avoid an unnecessary pump parasitic. A speed-reducing gearbox and effective, self-contained lubrication system were designed using typical refrigeration-

based technologies. Recovery of charge air heat was not pursued as it did not appear to offer a cost-effective benefit. System performance was reduced to approximately 5% fuel economy benefit at this point due to a significant reduction in EGR flow as a result of adopting SCR aftertreatment. The system architecture settled upon in Figure 2 was successfully demonstrated in-vehicle under the United States Department of Energy's Supertruck Program. Cummins applied R245fa as a working fluid throughout these developments but became aware of refrigeration industry plans to introduce ultra-low Global Warming Potential (GWP) 'drop-in' replacements.

2. Safe and Effective Application

Use of halogenated fluid to cool pre-combustion gases (such as EGR or air) necessarily requires a robust and durable method to prevent leakage of the fluid into the combustion airstream. In response to this challenge, Cummins investigated and embraced a heat exchanger architecture which provides a 'leak to atmosphere' feature. This architecture is described in SAE Paper 2006-01-2163 (David B. Sarraf, Heat Pipe Heat Exchanger with Two Levels of Isolation for Environmental Control of Manned Spacecraft Crew Compartment) and is presented in Figure 4 below. Initially, an isolation method of this nature was considered untenable as it would significantly deteriorate the heat transfer effectiveness of any EGR heat exchanger. However, analysis and hardware evaluation showed that any decrease in effectiveness was negligible. Extensive hardware reliability testing has since shown that a robust EGR heat exchanger design can be successfully executed in this manner. Solutions of this nature are available from several manufacturers.
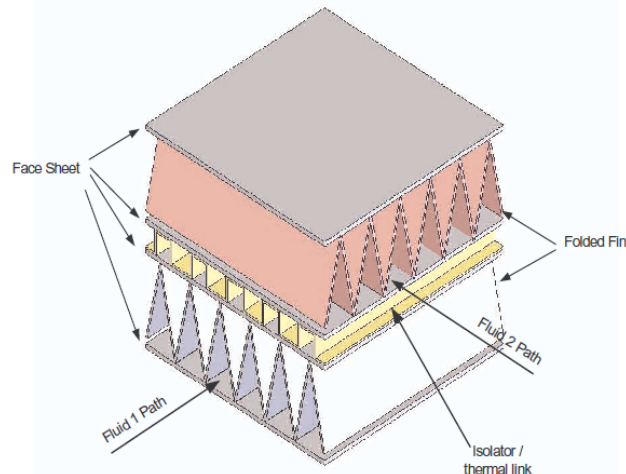

Figure 3: Schematic of a folded fin heat exchanger element with an isolation layer (Ref: SAE 2006-01-2163)

In addition to leakage through heat exchangers into the combustion airstream, leakage of refrigerant working fluid into air within and around the engine compartment was another potential opportunity for generation of harmful emissions. Cummins extensively studied leakage, and the potential for engine ingestion in this regard as well. Recognized standards such as SAE J2773 (Standard for Refrigerant Risk Analysis for Mobile Air Conditioning Systems) and SAE J639 (Safety Standards for Motor Vehicle Refrigerant Vapor Compression Systems) among others were applied to evaluate potential risk. It was concluded that the risk of applying refrigerant as an ORC working fluid posed no significantly greater risk than that which already existed from MAC systems. Impingement of refrigerant leaking upon hot engine surfaces (and tailpipe components) were also studied. It was determined that leaking refrigerant liquid or vapor would not significantly deteriorate but would simply tend to cool those areas of impingement.

3. R245fa Alternatives

Awareness of regulatory restrictions imposed upon Mobile Air Conditioning (MAC) systems in the European Union (EU) led Cummins to investigate alternatives to R245fa. R245fa, with a GWP of

~1000, though with no Ozone Depletion Potential (ODP), applied as a working fluid in a vehicle ORC system would achieve a significant reduction in the emission of carbon dioxide over the life of the vehicle. However, similarity of ORC systems to MAC systems suggested that similar legislated regulations may be applied to ORC systems using refrigerants. Contact with major manufacturers such as Honeywell, DuPont, etc., of R245fa and similar halocarbons revealed intentions to develop and release ultra-low GWP equivalents in the 2015 timeframe. These fluids, such as R1233zd(E), are now available in the market and offer an effective alternative to R245fa. Cummins performed comparative hardware performance testing with several of these alternative fluids (see Figure 4, below) with excellent results. Operating points such as A100, B75, etc. reflect engine operation at Environmental Protection Agency, Federal Test Procedure conditions.
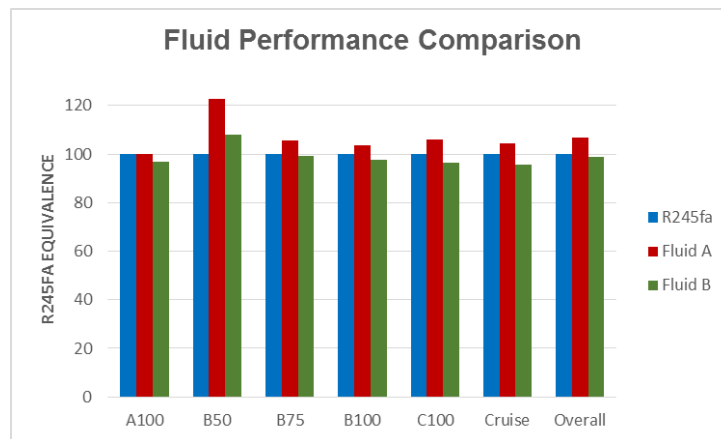
Figure 4: Performance comparison of R245fa against low-GWP equivalents

It was clear from the results that not only were there 'drop-in', ultra-low GWP replacements for R245fa readily available, but a slight increase in performance was potentially possible. As a result, Cummins decided upon a low-GWP alternative to R245fa as the concept moves towards a production configuration.

4. Comparisons with Ethanol

4.1 Performance

Ethanol has been taken up as a potential ORC working fluid by many system developers. Ethanol operates very well in this role. At first glance, it is an effective and low-cost choice. Ethanol is generally regarded as non-toxic and environmentally friendly. Typical ethanol ORC system architectures assume rejection of condensation heat into a coolant stream common with the engine (engine and ORC condenser plumbed in parallel, receiving the same radiator return temperature coolant). Many comparisons of performance between R245fa and ethanol simply adopt this cooling system arrangement to evaluate both fluids. However, in doing so, performance potential of R245fa (or R1233zd(e)) is obscured.

A model-based comparison of ethanol and R1233zd(e) at equivalent maximum (225°C) and minimum (80°C) temperatures, maximum operating pressures (2400 kPa) and equally arranged and capable ORC systems (same component efficiencies and effectiveness) shows a stark difference in performance (Figure 5, below).
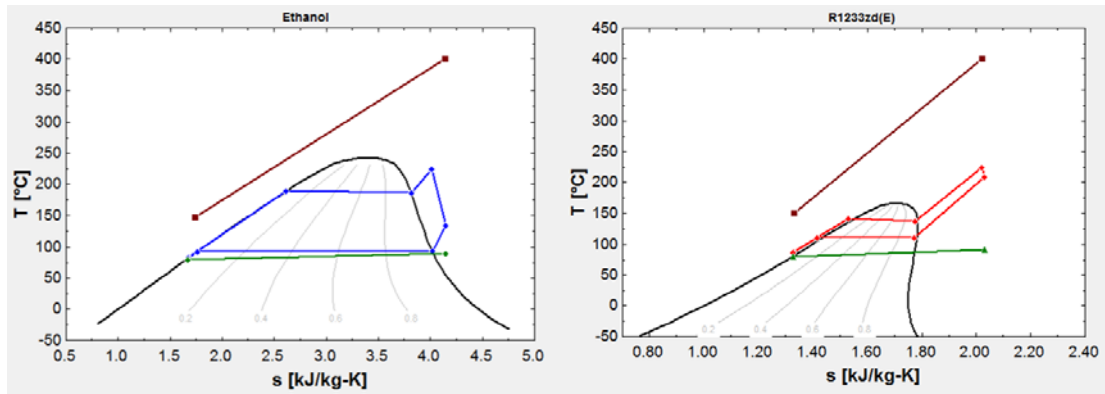
Figure 5: Performance comparison between ethanol and R1233zd(e) in equivalent systems with equal maximum temperatures/pressures and equal condensing temperatures.

For reference, net power from the ethanol system was 18.8 kW, net power from R1233zd(e) was 4.6 kW. Condenser heat rejection was 146 kW for ethanol and 158 for R1233zd(e). Input heat energy to both systems was diesel exhaust at 400°C flowing at 0.6 kg/s. Condensing temperature for ethanol is 93°C, R1233zd(e) is 111°C.

For system application, consideration is necessarily given to the availability of cooling. As presented above, Cummins settled upon a 'direct to air' condensing arrangement early in its development. The availability of near ambient air temperature cooling lent further reason to remain with refrigerant working fluids like R1233zd(e).

Ambient air temperature is, on average in the lower contiguous 48 United States approximately 12°C (http://www.ncdc.noaa.gov/). Average EU temperature is only slightly higher. In this case, the results are significantly different as presented in Figure 6, below.
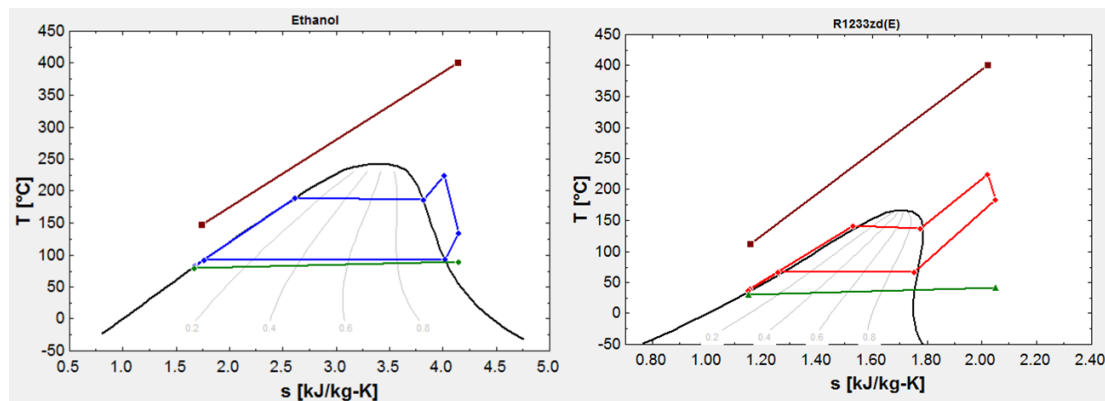

Figure 6: Comparison of ethanol and R1233zd(e) with equivalent systems but with condensing temperature appropriate for an in-vehicle R1233zd(e) system.

For reference in this case, net power from the ethanol system remained at 18.4 kW. Net power from the 1233zd(e) system increased to 14.3 kW. Condenser heat rejection remained 146 kW for ethanol but now increased to 174 kW for R1233zd(e). Input heat energy to both systems as above. Condensing temperature for ethanol remains at 93°C, R1233zd(e) is now 67°C.

An obvious feature of above the R1233zd(e) Temperature-Entropy (T-s) diagram is the opportunity to apply recuperation to the cycle. No such opportunity exists for ethanol due to its 'wet' nature. The amount of superheating remaining in the ethanol flow upon leaving the expander is too little to usefully recover. While the addition of a recuperator to an R1233zd(e) system necessarily adds cost to its

arrangement, it provides a significant benefit in power and a reduction in heat rejection. Figure 7 below presents the cycles once again but now the R1233zd(e) cycle has a reasonably effective recuperator (effectiveness of 70%, 50 kPa 'cold side' restriction, 10 kPa 'hot side' restriction).
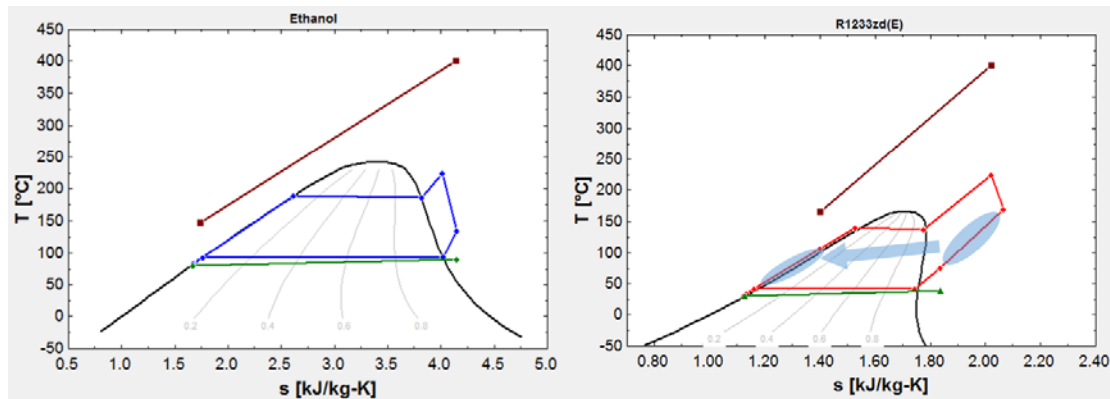

Figure 7: Comparison of ethanol and a recuperated R1233zd(e) cycle.

For reference, net power from the ethanol system remained at 18.4 kW, net power from the R1233zd(e) system increased to 22.7 kW. Condenser heat rejection remained 146 kW for ethanol and but now decreased to 131 kW for R1233zd(e). Input heat energy to both systems as above. Ethanol's condensing temperature remains at 93°C, R1233zd(e) is now 41°C.

While the results above are only model-based, they represent a fair comparison of the two working fluids considering their potential arrangement in-vehicle. The key take-away is that comparisons between refrigerant and ethanol systems should be made using systems optimized for each fluid. Modeling was performed using Engineering Equation Solver (EES) software with fluid properties currently available through NIST REFPROP. R245fa and R1233zd(e) modeled performance was validated from hardware test experience.

4.2 System Hardware Arrangements

The Cummins R245fa-based ORC system demonstrated during the Supertruck project is illustrated in Figure 8, below.
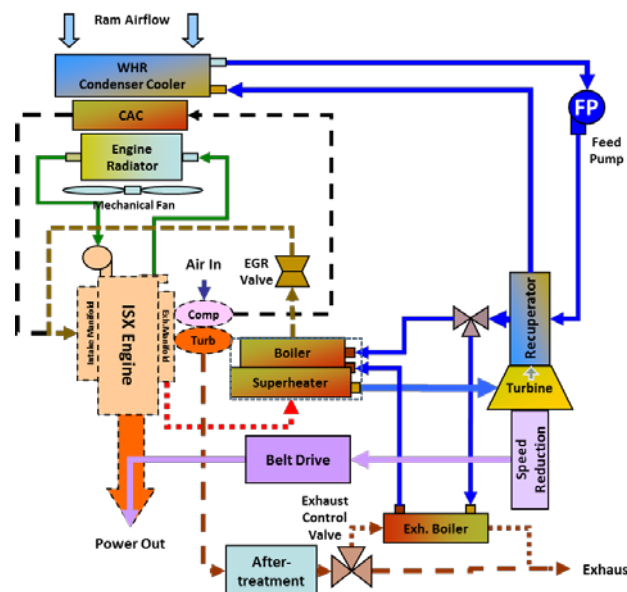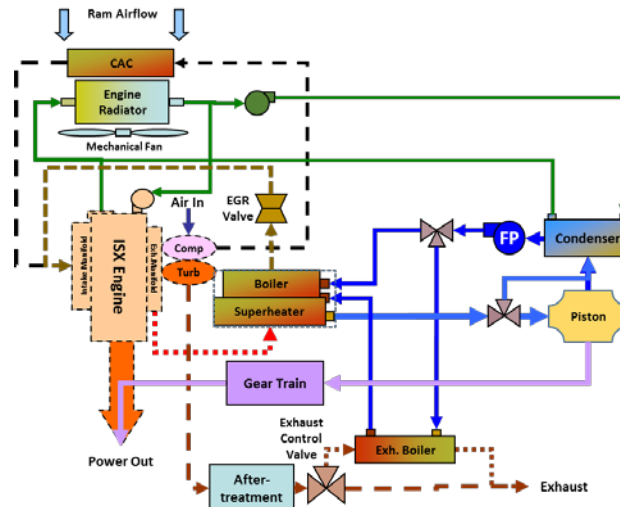
Figure 8: Cummins Supertruck ORC Arrangement

A potential ethanol-based ORC is presented in Figure 9.

Figure 9: Potential ethanol ORC system arrangement

In this arrangement, the ethanol system has one fewer heat exchanger than the R245fa system since it doesn't call for a recuperator. In this arrangement, ethanol would be cooled with radiator return temperature coolant. If lower temperature condenser coolant is desired, an additional heat exchanger would be necessary, making the systems equivalent in their number of heat exchangers. It should also be noted that the ethanol condenser, plumbing, etc. must be manufactured from material robust against ethanol corrosion. Typically, stainless steels are applied when dealing with ethanol. In comparison, R1233zd(e) is compatible with aluminum and other lightweight, low-cost materials already commonly deployed in MAC systems.

The ethanol system requires either a shared main engine water pump or a separate water pump, likely electrically driven to provide coolant to that system's condenser. The refrigerant system, being directly cooled to air, does not require this.

An ethanol system, using a low-speed, piston-type expander may directly mechanically couple its power to the engine's geartrain. However, an additional bypass valve around any positive-displacement expander will be necessary to guard against possible liquid ingestion/hydraulic lock and potential damage to the expander and the engine's geartrain. In comparison, refrigerant-based systems using a high-speed turbine expander, will need speed-matching equipment to provide mechanical power coupling to the engine. ORC systems using isentropic or dry working fluids and turbine machines will not need to apply a bypass valve given adequate control of liquid superheating. Turbines are robust to low flowrates of low pressure wet or liquid working fluid. Additionally even a high flow of 'wet' vapor may enter the turbine as, on expansion/acceleration through entry nozzles, the fluid rapidly becomes superheated vapor, leaving little risk of expander blade erosion.

4.3 Other Considerations

Application of either ethanol or refrigerant must consider the arrangement of sealing against the intrusion of outside air. This is not typically an issue during operation as both systems should operate with a 'low-side' (condensing) pressure greater than atmospheric pressure. However, during cold operation or during cold storage, the fluid's saturation pressure can be significantly important. Figure 10, below, presents a comparison of the saturation curves for R1233zd(e) and ethanol.
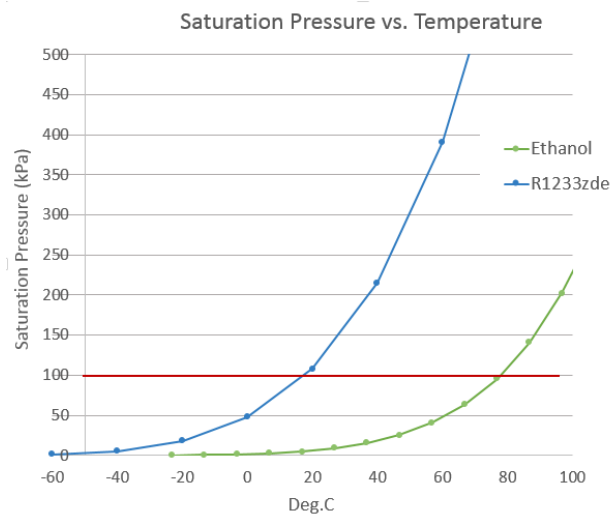
Figure 10: Comparison of saturation pressures

As shown in Figure 10, the saturation pressure of ethanol falls below atmospheric pressure at temperatures less than ~80°C. At room temperature, it's only about 8 kPa absolute. This means that during shutdown, especially in cold ambient temperatures, there will be a significant risk of air ingress to the ethanol system. Blending ethanol with water further suppresses the saturation pressure. R1233zd(e)'s saturation pressure falls below atmospheric pressure as well at approximately 18°C but it does not reach a significantly hard vacuum until nearly -40°C and degrades at a substantially slower rate. Air ingress will cause unnecessarily high expander back-pressure and decreased system performance. Either system, if executed with mechanical power coupling thus requiring an output shaft seal, would need a seal robust both to pressure during operation as well as vacuum when stored.

Additionally, in regard to low saturation pressures, feedpump cavitation may be expected to occur more frequently in systems using ethanol. Extremely low feedpump Net Pump Suction Head Required (NPSHR) will be a necessary requirement, or an additional 'boost' pump will become necessary. This problem is not only related to cold temperatures. Some ethanol systems have been shown to have vented their condensers to atmosphere in an attempt to increase feedpump inlet available suction head (NPSHA). While this may allow better operation close to sea level, higher altitude operation (and thus lower atmospheric pressure) may lead to feedpump cavitation and a loss of performance if condensing temperatures are below 80°C.

5. Further Development

Application of ORC systems to mobile internal combustion engines is not a new idea but it is certainly not a field whose opportunities have been fully explored. It is hard to imagine the potential performance mobile ORC might provide today had it undergone the same intensity and duration of research and development as the internal combustion engine. Though, as a bottoming cycle, it may never reach the thermal efficiency of the engines to which it is applied, it can certainly grow in its ability and benefit. In doing so it will meet and exceed the economic challenges which have typically kept it from production implementation.

It's quite easy to recovery heat. The real challenge is how to reject it. Thermodynamically, any recovered energy cycled through a heat engine loses some of its energy potential making it more difficult to reject. Given the finite cooling capacity available in current and future heavy duty vehicles, a thorough understanding of cooling system function and its duty-cycle based load will determine how much potential benefit any bottoming cycle can provide. Unused cooling capacity during engine operation below worst case conditions is potential ORC benefit. The optimized sharing of cooling

capacity between the engine and ORC is an area of research 'outside the cylinder' which should be developed as vigorously as are combustion, air handling, and aftertreatment.

The engines to which ORC systems are being applied today will certainly change as the emphasis for increased efficiency and reduced emissions continues. Further development of ever more capable NOx reducing aftertreatment may very well result in the removal of EGR. Increased emphasis upon exhaust energy recovery will occur but it will also focus attention to potential recovery of other engine waste heat streams. Charge air and engine coolant may become viable opportunities for cost-effective recovery. An ORC system architecture which can usefully approach these waste heat streams will certainly be the most viable long-term solution. Today's typical engine coolants offer a bulk temperature considered to be too low for effective use. However, the potential for hotter coolant (and thus more thermally efficient diesel engines) is a real possibility. In this case, an additional 'necessary' heat stream (as is EGR today) of recoverable energy will become available for the ORC to convert to useful power.

ORC system components are just beginning to attract the attention of manufacturers. As typical system arrangements coalesce across the industry, availability of more capable and more cost effective components will increase. Development of ORC components is just beginning and will certainly offer performance and efficiency benefits as it grows.

As mobile ORC is a new and relatively undeveloped field which will affect a significant portion of the engine system, there will necessarily be a great deal of work to establish standards, methods, and procedures around its safe and effective application. The handling of its fluids, the ratings of its components, the controls interaction between ORC and other engine systems will all require careful review and consideration by the industry's governing bodies and professional organizations.

6. Conclusions

This paper covers the use and application of R245f or R1233zd(e) and potentially other halocarbons as working fluids in mobile ORC systems. A brief review of the ORC project at Cummins and system architectures from the project's early phases through its most recent demonstrations have been shared and discussed. Reasons for Cummins' choice and adherence to low GWP refrigerant as its on-highway ORC working fluid have been provided. System considerations and features that allow the safe and effective application of these fluids in mobile ORC systems have been shared. Mention and comparison of ultra-low GWP working fluid alternatives to R245fa has been made. A model-based comparison of R1233zd(e) and ethanol has been provided to show that performance between the two working fluids is not quite as different as may be gathered from other work. Application considerations between the two fluids have also been discussed to offer developers some insight as to why R1233zd(e) is an appealing and viable working fluid for application in mobile ORC systems. Considerations for future development have been provided and briefly discussed.

ORC application to on-highway engines was once considered to be a 'tried and failed' technology. The emphasis on efficiency and emissions has resurrected it once again. The potential benefit it offers is the most significant efficiency increase available in quite some time and perhaps, for some time to come. New materials, controls, components, and ideas will help it leap the economic hurdle to reach mainstream, production implementation.

ACKNOWLEDGEMENT

IMPROVING TRAIN ENERGY EFFICIENCY BY ORGANIC RANKINE CYCLE (ORC) FOR RECOVERING WASTE HEAT FROM EXHAUST GAS

D. Serrano[1]*, P. Smague[1], P. Tona[1], P. Leduc[1], A.C. Mintsa[2], A. Leroux[2] and P. Chevalier[3]

[1]IFP Energies nouvelles (IFPEN), Institut Carnot IFPEN Transports Energie,
1 & 4, avenue de Bois-Préau, 92852 Rueil-Malmaison Cedex, France
E-mail: david.serrano@ifpen.fr

[2]ENOGIA SAS,
51 rue le Châtelier, 13015 Marseille, France
E-mail: andre-charles.mintsa@enogia.com

[3]ALSTOM TRANSPORT,
48 Rue Albert Dhalenne - 93482 SAINT OUEN Cedex, France
E-mail: philippe.chevalier@transport.alstom.com

* Corresponding Author

ABSTRACT

In a context of energy cost increase, reducing engine fuel consumption has become a key issue for transportation industry. Many paths exist to achieve substantial fuel savings: downsizing, hybridization, energy recovery… IFPEN has carried out an analysis of heat losses showing that recovering exhaust heat energy is a promising solution for improving fuel economy. Thus, IFPEN and ENOGIA have co-developed an Organic Rankine Cycle (ORC) system for direct recovering energy from exhaust heat. This system has been designed in order to be implemented on a Diesel-electric regional train manufactured by ALSTOM TRANSPORT. The train has several Diesel engines that produce mechanical torque needed for generators used for train electric propulsion. The ORC recovers energy from the exhaust heat of the different Diesel engines.

The project funded by the French national agency for research (ANR) started with 0D simulations in order to identify the optimal ORC architecture as well as some promising working fluids. More than 100 fluids were evaluated and finally two fluids were retained for this application thanks to their safety features, eco-friendliness and thermodynamic potential. A pre-design study defined the main components (boiler, condenser, pump…) that answer to the major constraints: cost, compactness, efficiency. ENOGIA developed the "heart" of the ORC, a dedicated turbine coupled with a high-speed generator on the same axle. The objective is that the electricity produced by the turbo-generator is re-injected for the train electrical propulsion. An ORC prototype has been assembled with a special care for avoiding any organic fluid leaks. The prototype has then been tested in an engine bench with the same Diesel engine as in the regional train. At the engine bench, the electricity produced by the ORC is re-injected in the French grid by means of inverters and transformers.

Based on previous experiences, IFPEN has developed an advanced control system for this application, which allows transient control of ORC operation by regulating vapor superheating at evaporator outlet. The machine has been largely instrumented for monitoring Rankine cycle operation. At the time of paper writing, around 10kW of ORC electricity output power has been reached in stable conditions.

1. INTRODUCTION

In Europe, more than 50% of the railway network is not electrified. Thus, Diesel electric trains are widely used for regional passenger transportation. In these trains, the Diesel engines are linked to

high-voltage generators to provide direct current (DC) to the electric train traction. Each regional train has several engines consuming each around 50l/100km of fuel. In a context of energy saving and global warming awareness, train manufacturers have been focusing their research and innovation efforts on the fuel consumption reduction of their engines. But despite all these improvements, engine efficiency is reaching an asymptote around 40-45%. At least 60% of the energy content of the fuel is lost in exhaust gas heat (~30%) and engine coolant (~30%). Many paths exist to achieve substantial fuel savings. Among these, hybrid concepts show significant efficiency improvements but with high cost. That's why some scientists are focusing their interest on how recovering energy from engine losses. Heat conversion to mechanical or electrical work can't only be reduced to energy consideration, then the concept of exergy derived from the second law of thermodynamics has to be introduced. It represents the part of the energy that can be really extracted for a thermodynamic closed system reversibly from its initial state to equilibrium. Exergy (Ex) variation between states 1 and 2 of a system in contact with its environment is defined as:

$$\Delta Ex_{12} = (H_2 - H_1) - T_0 \cdot (S_2 - S_1) \tag{1}$$

El Habchi (2010) shown that recovering energy from the exhaust presents higher potential than coolant energy recovery. As an example, over a specific mission profile (Artemis Motorway, for passenger car) for a 2L gasoline engine, exhaust gas exergy represents 26% of fuel lower heating value whereas coolant exergy is only 3%. Several technologies exist to convert exhaust heat into useful work such as turbo-compound, thermoelectric generator or thermo-acoustic engine and finally thermodynamic systems (Rankine, Stirling, Ericsson cycles). However, the complexity or the cost of some technologies is disproportionally high in comparison to the heat recovery potential: considering this, Rankine cycle seems to be the most promising approach. Heat recovery technology is already widely exploited in stationary equipment or for heavy ships. The implementation on mobile applications is challenging due to the transient behavior of the heat source. No serial production Rankine system exists yet for heavy-duty or train application.

Considering this context, IFPEN and ENOGIA have co-developed an Organic Rankine Cycle (ORC) system for recovering energy from exhaust heat from a Diesel-electric regional train made by ALSTOM TRANSPORT. The train has several Diesel engines developing more than 300kW max. power each. They have a two-stage turbocharging which limits even more exhaust gas temperature compared to a biogas spark-ignited stationary engine for example. The Rankine system produces work by the mean of a working fluid that exchanges heat between a hot source and a cold sink as described in figure 1. The working fluid is circulated and pressurized thanks to a volumetric pump. The fluid is then vaporized inside a boiler by exchanging heat with a hot source, exhaust gas in this case. This vapor at high pressure is then expanded in a turbine generator which produces electricity that is used for electric train propulsion. The working fluid is liquefied in a condenser by exchanging heat with a cold source before it is pumped again. The ORC works in a medium range of temperatures (100 to 200°C) compared to steam Rankine systems that operate at higher temperatures.
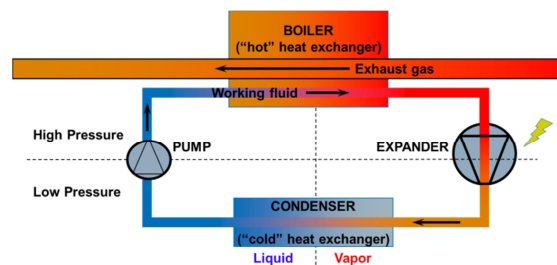

Figure 1: Rankine cycle principle

The project has followed different steps from blank sheet to a prototype: a ORC pre-sizing stage including selection of the ORC architecture and the working fluid, the ORC prototype conception and manufacturing, the testing in realistic conditions at engine bench.

2. SIZING THE ORC

2.1 Heat recovery potential on the train

The first step of this work is to evaluate the heat recovery potential of the train application depending on the hot source and cold sink. To achieve this study, a 0D dynamic low-frequency model of the train system propulsion has been made using the tool LMS Imagine Lab Amesim with IFPEN-Drive engine dedicated library. The IC engine, the generator and electrical load have been simulated using two real mission profiles given by the train manufacturer:

- Profile A: interurban route between two cities at high speed (average speed 120km/h) shown in figure 2.
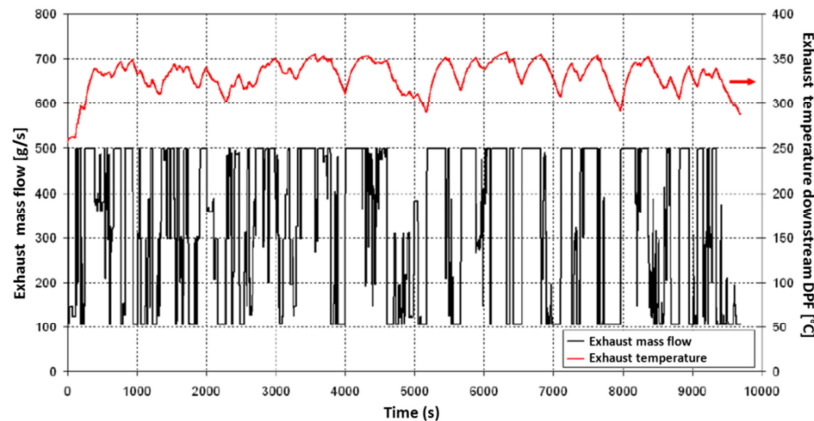- Profile B: one suburban route with a lot of stop & go (average speed 77km/h).

Figure 2: Exhaust mass flow and temperature evolution over mission profile A

The simulator evaluates the recoverable exergy along the chosen mission profiles by using input data of exhaust temperature and exhaust mass flow given by train manufacturer and the heat flow estimation evaluated thanks to REFPROP thermodynamic database of the NIST. Different ORC configurations have been simulated by varying 3 parameters in realistic conditions:

- The cold sink temperature: the ambient temperature impacts the cold sink temperature and thus the exergy recovery potential can be limited.
- The maximum working fluid temperature (for simulating thermo mechanical turbine constraint or limit before chemical degradation of the working fluid).
- The recovery system location: boiler position downstream the Diesel Particulate Filter (DPF).

Table 1: Heat recovery potential simulation results

ORC Configuration	1.	2.	4.	3.	5.
Cold sink T [°C]	50°C	50°C	25°C	50°C	50°C
Max. fluid T [°C]	No limitation	No limitation	200°C	200°C	150°C
Boiler position	Just after DPF	1m downstream DPF	Just after DPF	Just after DPF	Just after DPF
Exergy on profile A [% mech. energy]	48kW (14%)	24kW (7%)	42kW (13%)	39kW (12%)	36kW (12%)
Exergy on profile B [% mech. energy]	49kW (14%)	24kW (7%)	41kW (13%)	38kW (11%)	36kW (10%)

The assumption is that exhaust heat is recovered in both Exhaust Gas Recirculation (EGR) and exhaust line downstream DPF, that's why the levels of exergy are quite high (up to 14%). As EGR heat recovery is deeply intrusive in existent engine architecture and calibration, it has been abandoned at this stage of the project and energy will be recovered only on exhaust line. The main influence factor on recoverable exergy is the recovery system location: the results show that the boiler should be placed as closed as possible downstream DPF to maximize thermal exhaust energy. Then the maximum fluid temperature has a strong influence too: if the max. working fluid temperature is reduced by 50°C, the exergy potential is reduced by ~10%. Finally, the cold sink temperature has a

medium influence on recoverable exergy especially when max. fluid temperature is already limited. Moreover, the 2 different mission profiles have minor impact on exergy potential. These results have to be moderated as the fuel consumption reduction will be different between the 2 mission profiles. Indeed, the ORC turbine has a variable efficiency depending on the operating conditions, especially at part load and during transient conditions, which is hard to be fully taken into account in the simulation.

2.2 Screening the working fluid

The working fluid plays a key role in a Rankine cycle. It is repeatedly vaporized, expanded and re-condensed. The work output for a given temperature gradient differs significantly for different fluids. That's why a screening of different working fluids is carried out to choose the most suitable fluid for this application according to specific criteria:

- Thermodynamic performance: high expansion work output. The pressure in the boiler should be as high as possible to increase the turbine expansion rate. Finally, the pressure downstream the condenser should be as closed as possible to atmospheric pressure also to increase the turbine expansion rate.
- Mollier's diagram shape (temperature versus entropy): the dry working fluids are more suitable as they don't liquefy during their expansion in the turbine. The need for superheating is then reduced and the risk of droplet generation during expansion (leading to turbine blade erosion) is avoided. For a mobile application with high space constraints, the fluid needs to have a high specific heat capacity and latent heat of vaporization to minimize flow rates and by the way the size of components especially the boiler and the required pumping power.
- Safety: inflammability (explosion protection due to critical flashpoint) and toxicity.
- Chemical stability: molecule decomposition under ageing or thermal effects.
- Environment aspects: GWP, ODP.
- Material compatibility: corrosiveness, lubricant properties of the turbine.
- Equilibrium pressure when ORC is stopped: if ORC is under atmospheric pressure when stopped, air can enter inside the circuit if leaks are present and thus degrading Rankine cycle efficiency.
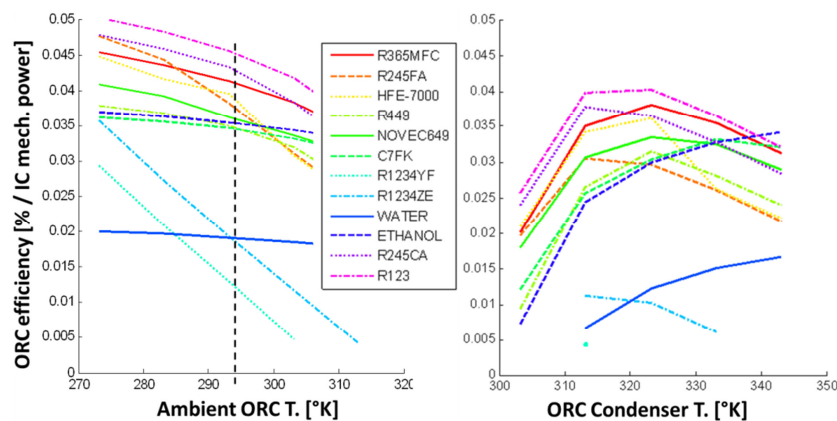- Low freezing point: compliance with train parking with cold conditions (-30°C).

Figure 3: Global ORC efficiency simulated for different fluids for ambient and condenser T. variations

The fluid screening has been carried out with an ORC 0D steady-state model using Matlab platform. Different types of working fluids have been tested including water, ammonia, SO_2, hydrocarbons, alcohols and hydrofluorocarbons: more than 100 different fluids have been analyzed. The thermodynamic data of the fluids have been estimated thanks to the REFPROP V9.1 software of the NIST. The ORC efficiency is calculated for the engine point producing the maximum power (>300kW) taking into account realistic train conditions. Thus, every ORC component has been described by assumed realistic values of efficiencies for the turbine generator and the pump and using water as cold sink. This water circuit is cooled by an electric cooling fan. The fluid is superheated, its minimal pressure is above 1 bar, its maximum pressure is below 25bar and its maximum temperature

is below 200°C. The Rankine circuit is also optionally composed of a regenerator that exchanges heat between vapor phase from downstream turbine and liquid phase from downstream pump.

Finally, about 500 000 simulations have been carried out in this project. In figure 3, the results show the maximum global ORC efficiency defined as the ratio between the electric output net power of the ORC over the mechanical engine power. This efficiency is between 3 to 5% depending on the conditions (ambient or condenser temperatures…). This global ORC efficiency decreases at low condensing temperatures as more energy is spent to cool the water (cold sink) than the gain in ORC thermal efficiency (Carnot theorem). Because of safety issues, hydrocarbons, alcohols and ammonia are disqualified for train application. Water is also not adapted as efficiencies are really low. Finally, HFC presents good trade-off with a 4% ORC efficiency potential combined with acceptable toxicity and environmental characteristics. Finally, the project has chosen two fluids for experimental testing :
- R245fa: high efficiency and long partner experience with this fluid but high GWP.
- Fluid B: high efficiency, not sensible to condenser water temperature variation, low GWP but high cost.

Table 2: Working fluid specifications

Fluid characteristic	Formula	Max. continuous T	Critical P/T	Inflammability NFPA / HMIS	Toxicity NFPA / HMIS	ODP GWP	Supplier Cost
R245fa	C3H3F5	154°C	154°C 36,5bar	1 / 1 Non flammable	2 / 2	0 950-1030	Honeywell Medium
Fluid B	Confidential	<300°C	<200°C <20bar	0 / 0 Non flammable	Low	0 <50	Confidential High

2.3 Expected performances

Finally, simulations allow to obtain the expected performances for the selected ORC architecture with the two different working fluids. The ORC efficiency expected is around 6 to 7% with both fluids meaning that 6 to 7% of the heat power received by the fluid in the boiler will be re-injected for the electric train traction.

Table 3: Predicted performances at steady-state max. power engine operating point

Fluid	R245fa	Fluid B
Heat power received by the fluid in the boiler	134 kW	122 kW
Heat power lost by the fluid in the condenser	117 kW	107 kW
Electrical power generated by the turbine	16 kW	14 kW
Electrical pump power consumption	1,8 kW	1,6 kW
Cooling power consumption	5,8 kW	3,6 kW
ORC efficiency (compared to heat on fluid)	6,3 %	7,2 %
Fluid mass flow	2150 kg/h	3600 kg/h
P / T in HP branch	25 bar / 167 °C	15 bar / 200 °C
P / T in LP branch	3,6 bar / 41°C	1,5 bar / 50 °C

3. ORC PROTOTYPE AND IMPLEMENTATION AT ENGINE BENCH

3.1 ORC architecture

After the first stage of pre-sizing, IFPEN and ENOGIA co-designed an ORC layout taking into account the previous recommendations in order to be tested at engine bench. The layout is displayed in figure 4. The heat is recovered in the exhaust line downstream the DPF in order to avoid the boiler clogging. The exhaust line has been modified by the implementation of two exhaust throttles allowing the exhaust gas going through the boiler or bypassing it, depending on exhaust thermal energy available. The expansion machine is a turbine that is coupled to a generator for electricity production. Among the conventional components of an ORC cycle, one can notice the presence of a regenerator to improve the cycle efficiency with an intermediate heat exchange in order to pre-heat the pressurized liquid with the vapor after expansion on the turbine. The ORC is instrumented with thermocouples, pressure sensors and flow meters in order to allow real-time monitoring of the ORC energy balance.

3.2 Component description

To pressurize the working fluid, an industrial volumetric pump self-lubricated has been chosen with a variable capacity between 80 to 1000L/min. It is driven by an electrical motor of 3 kW max power with a chain transmission. The boiler has been chosen with specific criteria for maximizing heat exchange with exhaust gas with the minimum pressure drop in exhaust gas (for no impact on engine fuel consumption) and with a reasonable cost. The chosen technology consists in a cross flow stainless steel exchanger mixing tubes (for fluid) and plates (for exhaust gas). Total surface plates (>50m²) is much greater than surfaces of tubes (>3m²) to compensate lower heat transfer coefficient of the gas compared to the liquid. The boiler has been sized to reach the expected performance shown in table 3. ENOGIA has designed and manufactured the expansion machine. It is an axial turbine coupled with a generator on the same axle. The shape of the turbine blades have been adapted to the 2 different fluids based on the experience and know-how of ENOGIA. The robust design of the turbine allows to operate the ORC in flexible operating conditions without any risk of damaging turbine blades and the smart design permits to reduce significantly maintenance intervals of the expander. The condenser and the regenerator are off-the-shelf plate exchangers for cost and planning reasons, taking into account weight and compactness for a further train integration.
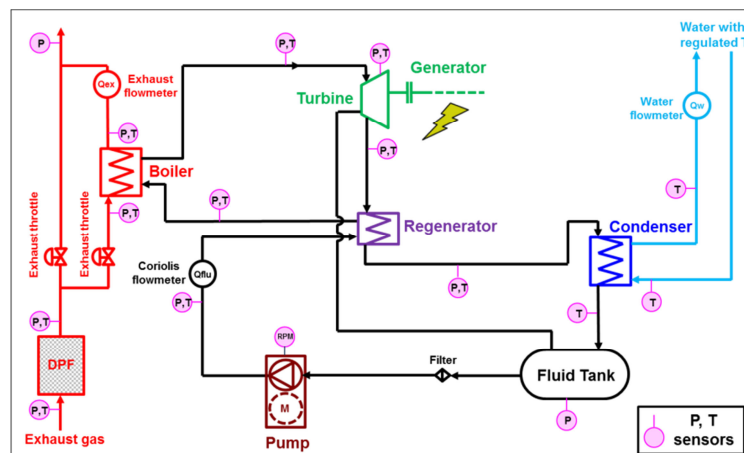

Figure 4: ORC prototype system layout with its measurement equipment for engine bench

3.3 Implementation at engine test bench

The design has taken into account a first level of constraints in terms of train integration. Train integration study has not been fully completed but has highlighted some general guidelines in order that the ORC prototype implemented at engine bench should become compatible with real train integration in the near future. A volume has been defined by the train manufacturer to implement the ORC on the train: it is represented in figure 5 by the tubular frame in blue. This constraint imposed to make a chain transmission between the electrical motor and the fluid pump. Moreover, the condenser and the regenerator had to be inclined to fit in the available room.
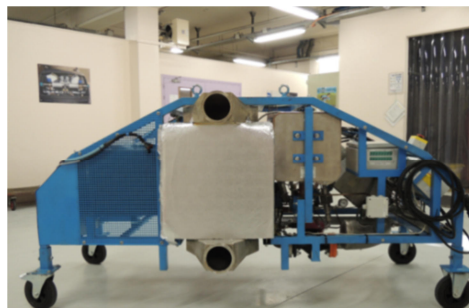

Figure 5: ORC prototype before entering in the test cell

The ORC has been manufactured with the dedicated pressure and temperature sensors. The prototype has been implemented at engine test cell and coupled up with the one Diesel engine identical to the

ones used on the train as presented in figure 6. The exhaust throttles have been mounted: the chosen technology is a flap with an electrohydraulic actuator with position feedback. The electricity generated by the ORC is injected in the test facility grid by means of a smart inverter and a transformer. The smart inverter used in this application, provided by MAVEL, allows a turbine speed regulation and real-time monitoring of the electrical power produced. For each point of the ORC circuit, based on the measurements of pressure and temperature, the fluid and exhaust gas specific enthalpies are tabulated thanks to the thermodynamic data given by the NIST software: REFPROP V9.1. The fluid and exhaust gas heat power are obtained by introducing the measurement fluid mass flow and the enthalpy of a reference state for 20°C. The heat transfer efficiencies of each exchanger are evaluated: boiler, condenser and regenerator ; the turbine efficiency is estimated by making the difference between the isentropic expansion work and the real work measured.
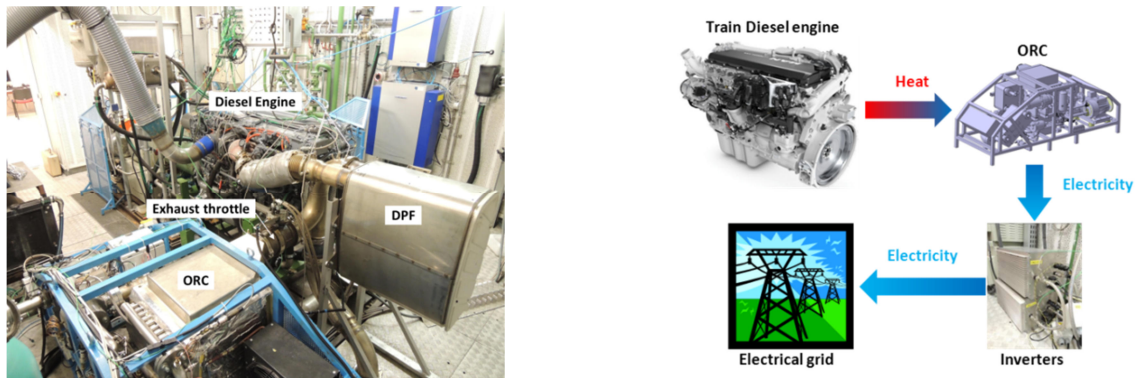

Figure 6: ORC prototype implementation at the engine bench

4. ORC CONTROL SYSTEM

One challenge of this project is to control dynamically the ORC which is a complex system evolving in transient conditions. The principle of the ORC control consists in dynamically adjusting the corner points of the thermodynamic cycle on the Mollier diagram (pressure vs. enthalpy) to ensure safe and efficient operation, with respect to changing external conditions. Ideally, one should be able to adapt both the high pressure (HP) point at evaporator outlet and the low pressure (LP) point at condenser outlet. However, this means being able to control four different thermodynamic variables (two for each point), which is in general unachievable due to the reduced number of available actuators and their lack of control authority. In practice, depending on the ORC configuration, only a few variables can be tightly controlled, and sometimes just one. All the different configurations tested during the project fall into the generic ORC layout shown in figure 7 with the inputs/outputs for control.
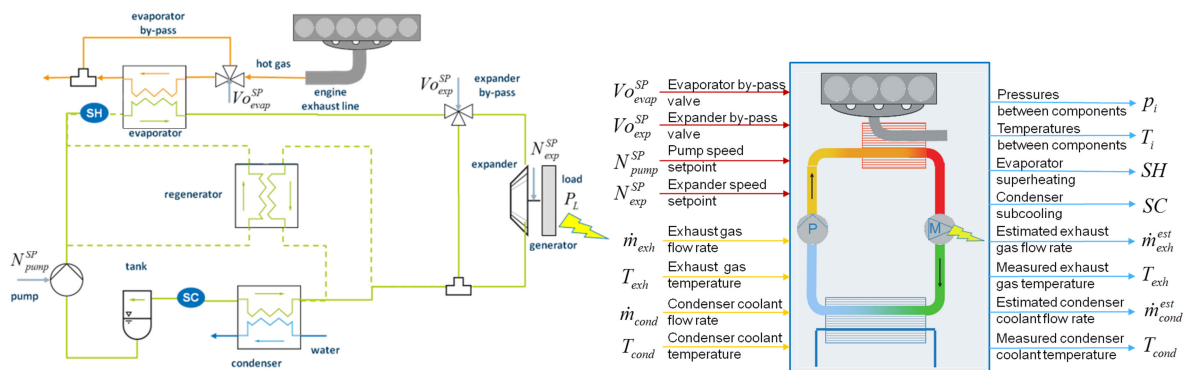

Figure 7: ORC control layout with I/O
(red: manipulated ; yellow: disturbance ; blue: measured/estimated variables)

No actuator is available for control purposes on the condenser side, which means that cooling conditions are entirely seen as an external disturbance. The turbine speed setpoint N_{exp}^{SP} sent to the inverter has little effect in the project conditions and can only be used to optimize turbine efficiency.

The turbine bypass Vo_{exp}^{SP}, which has been integrated in some configurations for safety reasons, cannot be used during nominal (power production) operation. The pump speed setpoint N_{pump}^{SP} is the only actuator with large enough control authority and can be used to control, for instance, the superheating SH at evaporator outlet, a variable which is meaningful both in terms of performance and safety. Thus, a main control loop acting on pump speed to regulate evaporator superheating can be designed, as described in Peralez et al., 2014, for a long-haul truck application. There is one last actuator available, the evaporator bypass Vo_{evap}^{SP}, which has a safety purpose too, but could in principle be used for slow regulation of another variable (HP pressure, for instance), as suggested in Peralez et al., 2014. However, contrary to long-haul truck applications, where ORC systems are most often designed for operation at roughly one third of engine full load (corresponding to flat highway conditions), see for instance Espinosa et al., 2010, the ORC system under investigation is optimized for use at engine full load. Thus, the usefulness of a control loop acting on the proportional evaporator bypass valve to regulate pressure at evaporator (fluid) outlet is very limited in this context.
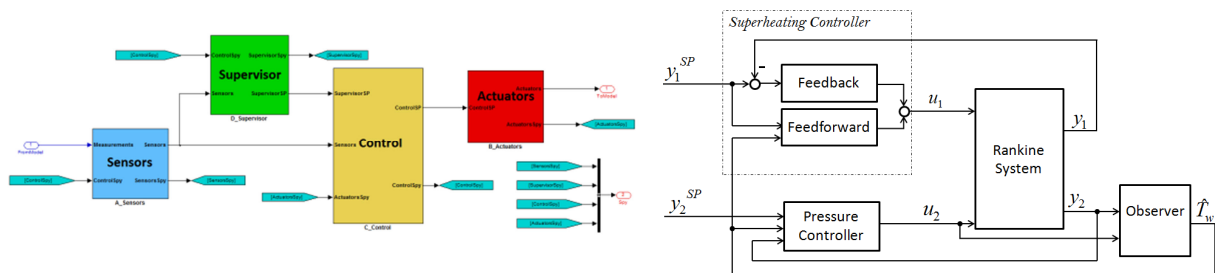

Figure 8: Global supervision and control system in Simulink (left) and decentralized control loops layout (right)

Based on these considerations, in the global supervision and control system in Simulink (figure 8), only the first decentralized control loop (the superheat controller of figure 8, where $u_1 = N_{pump}^{SP}$ and $y_1 = SH$) has been implemented so far. The superheat controller is made of two parts. The feedback part is a gain scheduled PI controller where for the feedforward part two solutions are available: a static feedforward, heuristically calibrated, and the model-based feedforward, presented in Peralez et al., 2013. A first calibration of the gain scheduled PI controller can be directly obtained using a dynamic ORC simulator, based on moving-boundary modeling of heat exchangers coded in Modelica/Dymola, coupled to the control system coded in Simulink. However, a thorough system identification campaign on several operating points is required to obtain an accurate representation of ORC dynamic behavior and finalize controller calibration.

5. EXPERIMENTAL RESULTS

5.1 Relevant results in steady-state conditions

Figure 9 presents the best results on the maximum power engine point (>300kW) for each ORC configuration tested. For confidentiality reasons, the heat power recovered from exhaust gases and the electric power produced at the output of the ORC turbine generator are normalized in reference to the first configuration using R245fa fluid without regenerator. The different bars of the graphs correspond to the different steps of the ORC improvements by the means of the fluid, extra exchanger, mass fluid and boiler optimizations.

The first level of optimization consisted in changing the working fluid from R245fa to fluid B and adding the regenerator. The turbine blades were changed and optimized for the use of fluid B. The chart shows a significant improvement (+22%) on the heat power recovered from the exhaust gases. Thanks to a special shape in its Mollier diagram, fluid B is specially adapted to run with an intermediate exchanger (regenerator) upstream the boiler. Indeed, this exchanger allows pre-heating the pressurized working fluid in liquid state upstream the boiler (the HP branch) with the hot working fluid in vapor state downstream the turbine (the LP branch). The drawbacks of using such exchanger are the extra mass of working fluid (cost issue) and the rising complexity of ORC control. In this project, we estimate the increase of the mass working fluid around 18% leading to an 15% extra cost

of the total ORC fluid cost. This 15% increase cost has to be compared to the 40% ORC electricity production enhancement allowed by this intermediate exchanger and the use of this new fluid B.
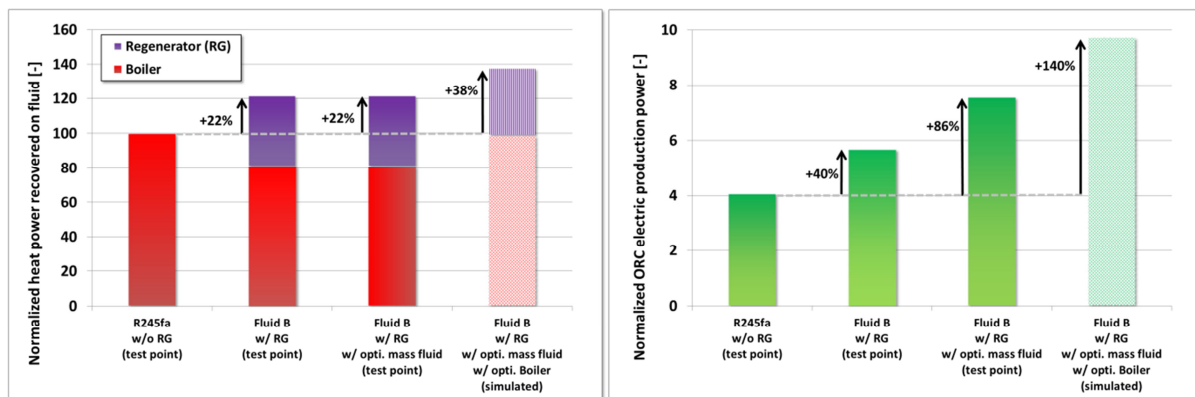

Figure 9: Tests results at max. power engine for different ORC configurations in terms of normalized heat power recovered on the fluid and ORC electric production power

The second step was to optimize the mass of working fluid inside the ORC. This operation is needed to avoid pump cavitation in case of fluid lacking or to avoid non optimized fluid liquefaction in the condenser in case of fluid overload. Furthermore, this optimized working mass fluid allows to maximize the thermodynamic efficiency of the cycle by establishing the optimized pressures in the LP and HP branches. The last step is still ongoing and the tests have not yet been done. Calculations have predicted that with an optimized boiler with higher exchange surface, exhaust gas heat recovering can be improved by 38% compared to the first configuration and ORC electric power output increased by 140%. The tests are still on-going and at the time of paper writing, more than 150hours of ORC operation have been carried out and 600 operating points (steady-state or transient) have been recorded. As a significant achievement, around 10kW of electricity power produced by the ORC turbine generator have been measured continuously in the last tests.

5.2 Boiler hunting

In this project, among all the technical challenges that have been taken up, the boiler has shown sometimes an unstable behavior in steady-state thermal conditions. Indeed, with stabilized constant exhaust gas and working fluid mass flows, temperature periodic oscillations can appear downstream the boiler. This phenomenon is well-known in refrigerating applications like described by Mithraratne et al., 2002, with diphasic exchangers and it has been called "boiler hunting". More recently, Yuh-Ren et al., 2014, faced the same problem with an ORC using R245fa. In this project, we observed the boiler hunting for both working fluids R245fa and fluid B (see figure 10) with the same boiler but with different signal properties. The signal period were respectively 40s and 17s whereas peak amplitude were respectively 8°C and 6°C for R245fa and fluid B. As a remark, temperature sensors accuracy is around ±0,5°C. Until now, no consistent scientific explanation exists justifying such behavior. Some scientists assume that the phenomenon depends on the working fluid characteristics and on the boiler internal geometry. This abnormal behavior must be avoided to ensure a robust and consistent ORC control in transient conditions.
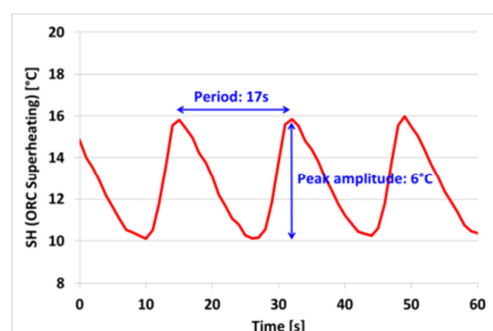

Figure 10: ORC superheating oscillations in steady-state conditions (T, P) after the boiler for fluid B

6. CONCLUSIONS

This pre-industrial project has succeeded in building an operational ORC prototype for a train application by merging the skills of IFPEN and ENOGIA. A pre-sizing study allowed to identify the exergy potential on a realistic train mission profile and the optimal recovery system location provided by ALSTOM TRANSPORT. Then, the screening fluid allowed to choose 2 suitable working fluids for this application considering all the safety, thermodynamic and cost constraints. The expected results were evaluated by simulation. The ORC prototype was built by ENOGIA by selecting the optimal components and respecting a limited volume for further train integration. The prototype has then been implemented at the test bench at IFPEN. An ORC control has been deployed using the know-how of IFPEN previous experiences on Rankine systems. These tools work with the help of exhaustive measures of temperature, pressure and mass flows allowing to evaluate in real-time conditions the energy balance of the whole ORC system. Experimental results showed the high increase of waste heat recovery and electric produced power after each improvement step along the project duration. The change of fluid and the addition of the regenerator increased the electric production by 86% compared to the first configuration. At the time of paper writing, around 10kW of ORC electricity output power has been reached in stable conditions and more than 150h of testing have been carried out. Further improvements should be attainable.

NOMENCLATURE

DPF	Diesel Particulate Filter
GWP / ODP	Greenhouse Warming Potential / Ozone Depleting Potential
IFPEN	IFP Energies nouvelles
NIST	US National Institute of Standards and Technology
ORC	Organic Rankine Cycle
SH/SC	SuperHeating/SubCooling
WHR	Waste Heat Recovery

REFERENCES

El Habchi, A., Ternel, C., Leduc, P., Hetet, J.F., 2010, Potential of waste heat recovery for automotive engines using detailed simulation, *ASME Conference on Thermal and Environmental Issues in Energy Sytems*.

Espinosa, N., L. Tilman, V. Lemort, S. Quoilin, B. Lombard, 2010, Rankine cycle for waste heat recovery on commercial trucks: approach, constraints and modeling, in Proceedings of the Diesel International Conference and Exhibition, SIA.

Mithraratne, P., Wijeysundera, N.E., 2002, An experimental and numerical study of hunting in thermostatic-expansion-valve-controlled evaporators, *International Journal of Refrigeration*, Volume 25, Issue 7, p. 992-998, ISSN 0140-7007.

Peralez, J., Nadri, M., Dufour, P., Tona, P. ; Sciarretta, A., 2014, Control design for an automotive turbine Rankine Cycle system based on nonlinear state estimation, *2014 Conference on Decision and Control (CDC)*, IEEE, p. 3316 - 3321.

Ringler, J., Seifert, M., Guyotot, V., Hübner, W., 2009, Rankine cycle for waste heat recovery of IC engines, *SAE Int. J. engines*, Vol. 2, Issue 1, p. 67-76.

Yuh-Ren, L., Chi-Ron, K., Chih-His, L., Ben-Ran, F., Jui-Ching, H., Chi-Chuan, W., 2014, Dynamic Response of a 50 kW Organic Rankine Cycle System in Association with Evaporators, *Energies 7*, no. 4: 2436-2448.

ACKNOWLEDGEMENT

PERFORMANCE ANALYSIS OF WASTE HEAT RECOVERY WITH A DUAL LOOP ORGANIC RANKINE CYCLE SYSTEM FOR DIESEL ENGINE

Hongjin Wang[1,2]*, Hongguang Zhang[1,2]

[1]College of Environmental and Energy Engineering，Beijing University of Technology，
Pingleyuan No.100, 100124 Beijing, China
[2]Collaborative Innovation Center of Electric Vehicles in Beijing, Pingleyuan No.100, 100124
Beijing, China
e-mail:bjgywanghongjin@163.com

* Corresponding Author

ABSTRACT

To take full advantage of the waste heat from a diesel engine, a set of dual loop organic Rankine cycle system (ORCs) was designed to recover exhaust energy, waste heat from the coolant system, and released heat from turbocharged air in the intercooler of a six-cylinder diesel engine. Aspen plus software was used to model the dual loop ORCs. According to the simulation model, the operating performance of the dual loop ORCs and the fuel economy of the diesel engine were investigated. The results show that the thermodynamic performance and economy performance of the diesel engine can be effectively improved by using the dual loop ORCs. At the engine rated condition, the overall net power output of the dual loop ORCs is up to 43.65 kW. The brake specific fuel consumption (BSFC) and the thermal efficiency of the diesel engine-dual loop ORCs are 191.24 g·(kW·h)$^{-1}$ and 37.57%, respectively. Compared with the diesel engine, the thermal efficiency of the combined system can be increased by 13.69% and the BSFC can be reduced by 15.86%.

1. INTRODUCTION

A large amount of petroleum resources has been consumed by automobiles. Meanwhile, given the low utilization rate for internal combustion engine, the thermal efficiency is only 30%-45% for diesel engine and 20%-30% for gasoline engine. And then the remaining heat is released into the atmosphere (Dolz *et al.*, 2012, Roy *et al.*, 2010). Therefore, discovering a more effective way to recover internal combustion engine waste heat so as to increase engine thermal efficiency and decrease fuel consumption has become a hot focus of recent research work.

ORCs has been widely used to recover and utilize the low-grade waste heat and recently numerous scholars have investigated the use of ORCs to recover engine exhaust waste heat energy (Fang *et al.*,2010, Liu *et al.*, 2012). Shu *et al.* (2014) designed a set of dual loop ORCs to recover exhaust waste heat energy and coolant system waste heat. Results showed that using the dual loop ORCs can effectively improve the thermodynamic performance of the engine. Gao *et al* (2013) proposed ORCs to recover the exhaust waste heat of a turbocharged diesel engine. The results showed that the net power output of the diesel engine can improve 12%. Meinel *et al* (2014) compared a two-stage ORC with internal heat recovery with a simple standard ORCs and an ORC with a recuperator based on Aspen Plus software. The thermodynamic efficiencies of the two-stage cycle exceed the corresponding values of reference ORCs by up to 2.25%.

Although many scholars have analyzed the performance of different kinds of ORCs, most research takes only internal combustion engine exhaust energy into account. Few of them have considered recovering the waste heat from the coolant system, and the released heat from turbocharged air in the intercooler of internal combustion engine. In this paper, a set of dual loop ORCs is designed to recover exhaust waste heat energy, waste heat from the coolant system, and released heat from turbocharged air in the intercooler of a diesel engine. Aspen plus software is used to model the dual

loop ORCs, and then the operation performance is analyzed based on the sensitivity analysis under the different high temperature cycle evaporation pressure and the working fluid mass flow rate.

2. MODEL OF DUAL LOOP ORC SYSTEM

2.1 Model of Dual Loop ORCs Based on Aspen Plus
The exhaust temperature of diesel engine is generally high. However, the temperatures of the coolant and the turbocharged air are relatively low. To take full advantage of the waste heat energy from the diesel engine, a set of dual loop ORCs is designed. As shown in Figure 1, the dual loop ORCs contains a high temperature (HT) loop ORCs (the lower part) and a (low temperature) LT loop ORCs (the upper part). The HT loop ORCs is used to recover the high-temperature exhaust energy, while the LT loop ORCs is used to recover the waste heat from the coolant system, the released heat from turbocharged air in the intercooler and the residual heat of low-temperature exhaust energy. Figure 2 and Figure 3 are the *T-s* diagram of the HT loop and LT loop in the dual loop ORCs, respectively.

The dual loop ORCs system operates according to the following process. In the HT loop ORCs (corresponding to Processes 1-7), the working fluid is pressurized into the saturated liquid state working fluid using Pump 1. Then it is preheated in the Recuperator. Subsequently, the working fluid turns into a saturated vapor state in the Evaporator 1. Then, the saturated vapor enters Expander 1 to produce useful work. Finally, the superheated vapor exported from Expander 1 turns into a saturated liquid state after the heat transfer process in the Recuperator and Condenser1. With this change, the HT loop ORCs completes one working cycle. Meanwhile, in the LT loop ORCs (corresponding to Processes 10-16), Pump 2 pressurizes the saturated liquid state working fluid and sends it into the Intercooler to exchange heat with the turbocharged intake air. Then, the working fluid flows into the Preheater and is heated up into the two-phase state by the engine coolant. Later, the two-phase working fluid is heated up into a saturated vapor state by the residual heat of the low-temperature exhaust energy in the Evaporator 2. The saturated vapor enters Expander 2 to make it do work. Finally, the superheated vapor exported from Expander 2 condenses into a saturated liquid state in the Condenser 2. The whole process is then completed.
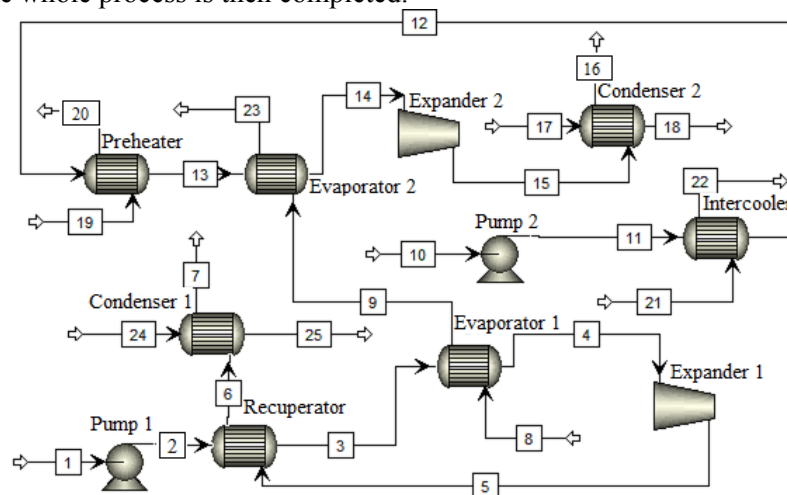

Figure 1: Model of the dual loop ORCs

2.2 Boundary Conditions
(1) The thermodynamic properties of fluid are calculated based on the Peng-Robinson state equation. R123 is selected as the working fluid, water is selected as the coolant. The diesel engine air fuel ratio is set to 19.7, mass fraction of the exhaust components CO_2、H_2O、N_2 and O_2 is 15.1%、5.5%、71.6% and 7.8%, respectively. (Shu *et al*., 2014).
(2) The isentropic efficiencies of expander 1 and expander 2 are both set to 0.7. The isentropic efficiencies of Pump 1 and Pump 2 are both set to 0.65.
(3) The ambient temperature is set to 291.15 K.
(4) The working fluid temperature at the evaporator 1 outlet is set to 456K. When the exhaust

temperature drops below the dew point, the exhaust pipes and evaporator surfaces can erode, so the exhaust temperature at the evaporator 2 outlet is set to 380K. (Bahadori, 2011).

(5) The mass flow rate of the HT loop ORCs is set to 0.4-0.8 kg/s; The evaporation pressure of HT loop ORCs is set to 1.0-2.5MPa.

(6) The cooling water inlet temperature and mass flow rate of Condenser1 are set to 285K and 2kg/s (corresponding to Processes 24-25 in Figure 1); The same as the Condenser2 are set to 285K and 3kg/s (corresponding to Processes 17-18 in Figure 1).

(7) The outlet temperature of engine coolant is set to 340K (corresponding to Processes 21-22 in Figure 1)

(8) The outlet temperature of turbocharged intake air is set to 350K (corresponding to Processes 19-20 in Figure 1)

(9) The test parameters of the diesel engine at rated conditions are listed in Table 1.
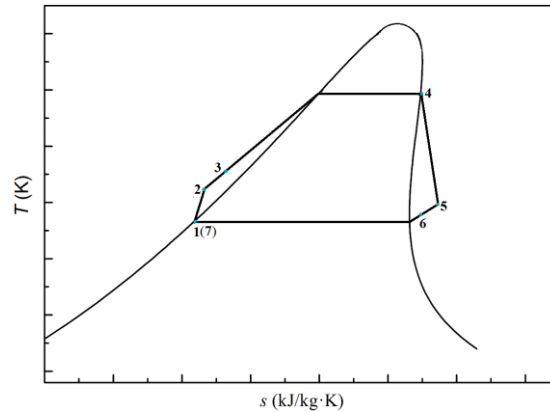
Figure 2: *T-s* diagram of the HT loop ORCs
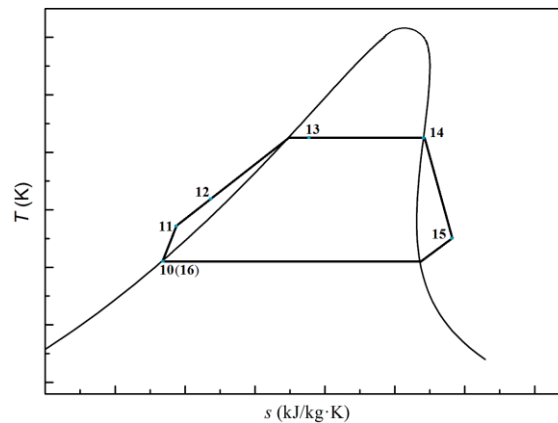
Figure 3: *T-s* diagram of the LT loop ORCs

Table 1: Test parameters of the diesel engine

Items	value
Rated speed/ r·min^{-1}	2000
Rated power / kW	275
Exhaust temperature/ K	783
Air intake mass flow rate/ kg·s^{-1}	0.43
Fuel consumption/ kg·h^{-1}	60.97
Intake air temperature/ K	407
Engine coolant mass flow rate/ kg·s^{-1}	1.30
Engine coolant temperature/K	370

2.3 Thermodynamic Model of the Dual Loop ORCs

To evaluate the performance of the dual loop ORCs, the following parameters are selected in the study.

The net power output of HT loop ORCs is given in Equation (1):

$$\dot{W}_{H} = \dot{W}_{exp1} - \dot{W}_{p1} \tag{1}$$

The net power output of LT loop ORCs is given in Equation (2):

$$\dot{W}_{L} = \dot{W}_{exp2} - \dot{W}_{p2} \tag{2}$$

Where $\dot{W}_{p1}$ and $\dot{W}_{p2}$ are the power consumed by pump 1 and pump 2, respectively. $\dot{W}_{exp1}$ and $\dot{W}_{exp2}$ are the power output of the expander 1 and expander 2, respectively.

The overall net power output of the dual loop ORCs is given in Equation (3):

$$\dot{W}_{oa} = \dot{W}_{H} + \dot{W}_{L} \tag{3}$$

The thermal efficiency of the dual loop ORCs is given in Equation (4):

$$\eta_{oa} = \frac{\dot{W}_{oa}}{\dot{Q}_{oa}} \times 100\% \tag{4}$$

Where $\dot{Q}_{oa}$ is the overall heat transfer rate of the dual loop ORCs：

$$\dot{Q}_{oa} = \dot{Q}_{e1} + \dot{Q}_{e2} + \dot{Q}_{int} + \dot{Q}_{pre} \tag{5}$$

Where $\dot{Q}_{e1}$, $\dot{Q}_{e2}$, $\dot{Q}_{int}$ and $\dot{Q}_{pre}$ are the heat transfer rate of evaporator 1, evaporator 2, intercooler and preheater, respectively.

To assess the economy performance of the diesel engine-dual loop ORC combined system, the brake specific fuel consumption (BSFC) of the combined system is defined as:

$$bsfc_{cs} = \frac{\dot{F}}{\dot{W}_{eng} + \dot{W}_{oa}} \times 1000 \tag{6}$$

Where $\dot{F}$ represents the fuel consumption of the diesel engine；$\dot{W}_{eng}$ represents the power of diesel engine.

The BSFC of the diesel engine is defined as:

$$bsfc_{eng} = \frac{\dot{F}}{\dot{W}_{eng}} \times 1000 \tag{7}$$

The improvement ratio of BSFC of the combined system is defined as：

$$\eta_{cs} = \frac{bsfc_{eng} - bsfc_{cs}}{bsfc_{eng}} \times 100\% \tag{8}$$

The thermal efficiency of the diesel engine is given in Equation (9):

$$\eta_{eng} = \frac{\dot{W}_{eng}}{\dot{Q}_{cs}} \times 100\% \tag{9}$$

Where $\dot{Q}_{cs}$ represents the overall energy generated by fuel combustion of the diesel engine.

The thermal efficiency of the combined system is defined as:

$$\eta_{cst} = \frac{\dot{W}_{oa} + \dot{W}_{eng}}{\dot{Q}_{cs}} \times 100\% \tag{10}$$

The increasing ratio of thermal efficiency in the combined system is defined as:

$$\eta_{tei} = \frac{\eta_{cst} - \eta_{eng}}{\eta_{eng}} \times 100\% \tag{11}$$

The exergy destruction rate of the each components are given in Equations (12)-(22):

$$\dot{I}_{p1} = T_0 \dot{m}_H (s_2 - s_1) \tag{12}$$

$$\dot{I}_{p2} = T_0 \dot{m}_L (s_{11} - s_{10}) \tag{13}$$

$$\dot{I}_{r} = T_0 \dot{m}_H [(s_6 - s_5) + (s_3 - s_2)] \tag{14}$$

$$\dot{I}_{e1} = T_0 \dot{m}_H [(s_4 - s_3) - \frac{h_4 - h_3}{T_{H,H}}] \tag{15}$$

Where $T_{H,H}$ is the temperature of the high temperature heat source in the HT loop ORCs, and is assumed to be equal to $T_{H,H} = T_4 + 5$.

$$\dot{I}_{e2} = T_0 \dot{m}_L [(s_{14} - s_{13}) - \frac{h_{14} - h_{13}}{T_{L,H}}] \tag{16}$$

Where $T_{L,H}$ is the temperature of the high temperature heat source in the LT loop ORCs, and is assumed to be equal to $T_{L,H} = T_{14} + 5$.

$$\dot{I}_{exp1} = T_0 \dot{m}_H (s_5 - s_4) \tag{17}$$

$$\dot{I}_{exp2} = T_0 \dot{m}_L (s_{15} - s_{14}) \tag{18}$$

$$\dot{I}_{int} = T_0 \dot{m}_L [(s_{12} - s_{11}) - \frac{h_{12} - h_{11}}{T_{int,H}}] \tag{19}$$

Where $T_{int,H}$ is the temperature of the heat source in the intercooler, and is assumed to be equal to $T_{int,H} = T_{12} + 5$.

$$\dot{I}_{pre} = T_0 \dot{m}_L [(s_{13} - s_{12}) - \frac{h_{13} - h_{12}}{T_{pre,H}}] \tag{20}$$

Where $T_{pre,H}$ is the temperature of the heat source in the intercooler, and is assumed to be equal to $T_{pre,H} = T_{13} + 5$.

$$\dot{I}_{con1} = T_0 \dot{m}_L [(s_7 - s_6) - \frac{h_7 - h_6}{T_{H,L}}] \tag{21}$$

Where $T_{H,L}$ is the temperature of the low temperature heat source in the HT loop ORCs, and is assumed to be equal to $T_{H,L} = T_7 - 5$.

$$\dot{I}_{con2} = T_0 \dot{m}_L [(s_{16} - s_{15}) - \frac{h_{16} - h_{15}}{T_{L,L}}] \tag{22}$$

Where $T_{L,L}$ is the temperature of the low temperature heat source in the LT loop ORCs, and is assumed to be equal to $T_{L,L} = T_{16} - 5$.

Note that Eq. (15),(19),(21)and (22) are derived from Ref. (Yang *et al.*, 2014)

3. RESULTS AND DISCUSSION

The variation of the net power output in LT loop ORCs with the evaporation pressure and mass flow rate of the HT loop ORCs is shown in Figure 4. The graph shows that at a certain evaporation pressure of HT loop ORCs, the net power output of the LT loop ORCs decreases gradually with the increase of the mass flow rate of HT loop ORCs. This primarily because that, the heat transfer rate of evaporator 1 increases with the increase of mass flow rate at the HT loop ORCs. Therefore, the heat transfer rate of evaporator 2 decrease. At a certain mass flow rate of HT loop ORCs, the net power output of the LT loop ORCs increases gradually with the increase of the evaporation pressure of HT loop ORCs. When the evaporation pressure and mass flow rate of HT loop ORCs are 2.5 MPa and 0.4 kg·s^{-1}, the net power output of the LT loop ORCs reaches the upper limit and is 24.63 kW.

The variation of the net power output in HT loop ORCs with the evaporation pressure and mass flow rate of the HT loop ORCs is shown in Figure 5. The graph shows that at a certain evaporation pressure of HT loop ORCs, the net power output of the HT loop ORCs increases gradually with the increase of the mass flow rate of HT loop ORCs. At a certain mass flow rate of HT loop ORCs, the net power output of the HT loop ORCs increases gradually with the increase of the evaporation pressure of HT loop ORCs. When the evaporation pressure and mass flow rate of HT loop ORCs are 2.5 MPa and 0.8 kg·s^{-1}, the net power output of the HT loop ORCs reaches the upper limit and is 24.99 kW.
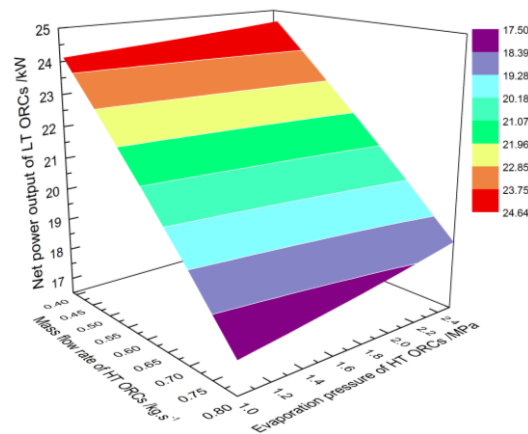
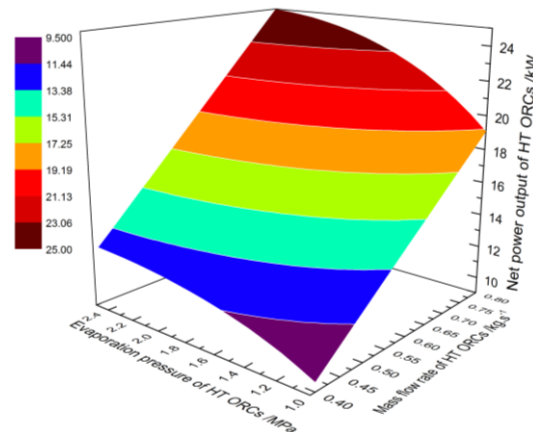**Figure 4:** Net power output of the LT loop ORCs

Figure 5: Net power output of the HT loop ORCs

Through the comparison between Figure 4 and Figure 5, it can be concluded that the net power output of the LT loop ORCs and the HT loop ORCs are affected more by mass flow rate of the HT loop ORCs. And the net power output of the LT loop ORC system is greater than that of the HT loop ORC system under the same evaporation pressure of HT ORCs.

The variation of the overall net power output in dual loop ORCs with the evaporation pressure and mass flow rate of the HT loop ORCs is shown in Figure 6. The graph shows that at a certain evaporation pressure of HT loop ORCs, the overall net power output of the dual loop ORCs increases gradually with the increase of the mass flow rate of HT loop ORCs. This primarily because that, with the increase of the mass flow rate of HT loop ORCs, the variation of net power output of HT loop ORCs is relatively higher than that of LT loop ORCs. At a certain mass flow rate of HT loop ORCs, the net power output of the dual loop ORCs increases gradually with the increase of the evaporation pressure of HT loop ORCs. When the evaporation pressure and mass flow rate of HT loop ORCs are 2.5 MPa and 0.8 kg·s^{-1}, the overall net power output of the dual loop ORCs reaches the upper limit and is 43.65 kW.

The variation of the thermal efficiency in dual loop ORCs with the evaporation pressure and mass flow rate of the HT loop ORCs is shown in Figure 7. Moreover, the thermal efficiency has the same variation tendency with the overall net power output of the dual loop ORCs. The reason can be explained as follows. According to Eq. (4), the thermal efficiency of dual loop ORCs is related to the overall heat transfer rate and the overall net power output of the dual loop ORCs. The overall heat transfer rate is constant due to the constant operating condition of diesel engine, while the overall net power out of dual loop ORCs increases with evaporation pressure and mass flow rate of HT loop ORCs, as shown in Figure 6. When the evaporation pressure and mass flow rate of HT loop ORCs are

2.5 MPa and 0.8 kg·s^{-1}, the thermal efficiency of the dual loop ORCs reaches the upper limit and is 10.52%.
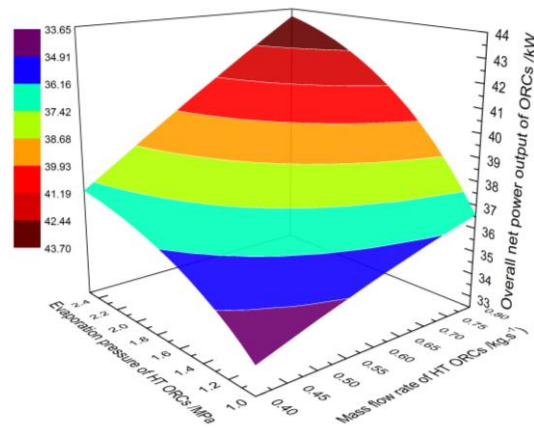
Figure 6: Overall net power output of the dual loop ORCs
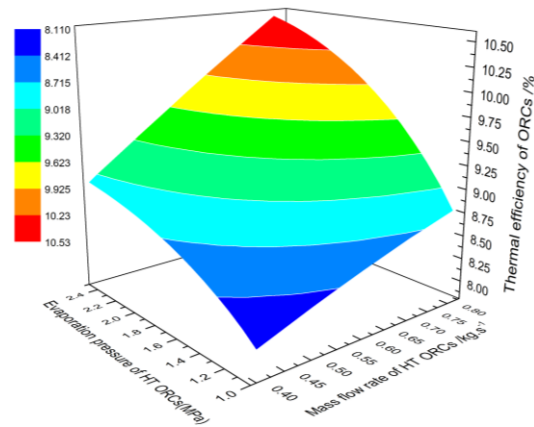
Figure 7: Thermal efficiency of the dual loop ORCs
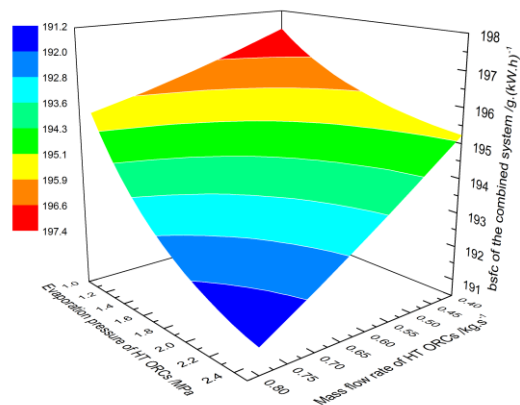
Figure 8: BSFC of the combined system

The variation of the BSFC in diesel engine-dual loop organic Rankine cycle (ORC) combined system with the evaporation pressure and mass flow rate of the HT loop ORCs is shown in Figure 8. The graph shows that at a certain evaporation pressure of HT loop ORCs, the BSFC of the combined system decreases gradually with the increase of the mass flow rate of HT loop ORCs. At a certain mass flow rate of HT loop ORCs, the BSFC of the combined system decreases gradually with the

increase of the evaporation pressure of HT loop ORCs. The reason can be explained as follows. According to Eq. (6), the BSFC of combine system is related to the fuel consumption, the power of diesel engine and the overall net power output of the dual loop ORCs. The fuel consumption and the power of diesel engine is constant due to the constant operating condition of diesel engine, while the overall net power out of dual loop ORCs increases with evaporation pressure and mass flow rate of HT loop ORCs, as shown in Figure 4. When the evaporation pressure and mass flow rate of HT loop ORCs are 2.5 MPa and 0.8 kg·s^{-1}, the BSFC of the diesel engine-dual loop ORC combined system reaches the minimum and is 191.24 g·(kW·h)$^{-1}$.

The variation of the improvement ratio of BSFC in diesel engine-dual loop ORC combined system with the evaporation pressure and mass flow rate of the HT loop ORCs is shown in Figure 9. The graph shows the improvement ratio of BSFC in the combined system gradually increases with evaporation pressure and mass flow rate of HT loop ORCs. Moreover, the minimum improvement ratio of BSFC is 10.9%. When the evaporation pressure and mass flow rate of HT loop ORCs are 2.5 MPa and 0.8 kg·s^{-1}, the improvement ratio of BSFC in the diesel engine-dual loop ORC combined system reaches the upper limit and is 13.69%.
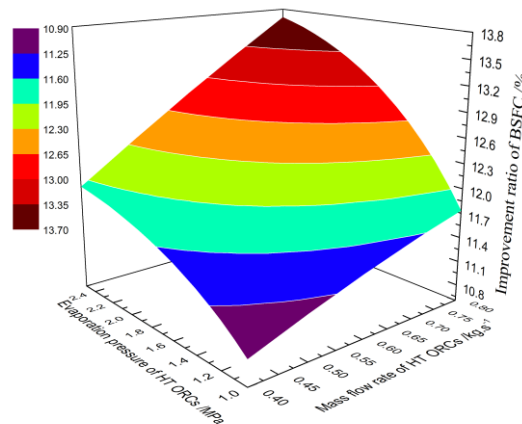
Figure 9: Improvement ratio of BSFC in the combined system
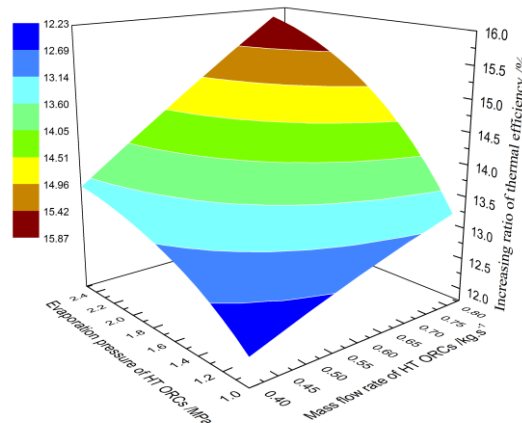
Figure 10: Increasing ratio of thermal efficiency in the combine system

The variation of the thermal efficiency improvement in diesel engine-dual loop ORC combined system with the evaporation pressure and mass flow rate of the HT loop ORCs is shown in Figure 10. Compare with Figure 6, the increasing ratio of thermal efficiency in the combine system has the same variation tendency with the overall net power output of the dual loop ORCs. Moreover, the minimum thermal efficiency improvement is 12.23%. When the evaporation pressure and mass flow rate of HT loop ORCs are 2.5 MPa and 0.8 kg·s^{-1}, the increasing ratio of thermal efficiency in the diesel engine-dual loop ORC combined system reaches the upper limit and is 15.86%.

Figure 11 shows the variations of the exergy destruction rate in dual loop ORCs under the condition of the overall net power output reaches the upper limit. The graph shows that, the exergy destruction rate of the condenser 2 is bigger than that of other components and is 15.64kW, followed by condenser 1 and evaporator 1. They are 14.70 kW and 13.33 kW, respectively. The exergy destruction of condenser 1 and condenser 2 are all bigger due to the higher temperature difference between the working fluid and cooling water at the condenser. Whereas, the exergy destruction of evaporator 1 is bigger because of the higher temperature difference between the working fluid and exhaust gas at the evaporator 1. The exergy destruction rate of the dual loop ORCs and LT ORCs are 40.78 kW and 29.75 kW, respectively.
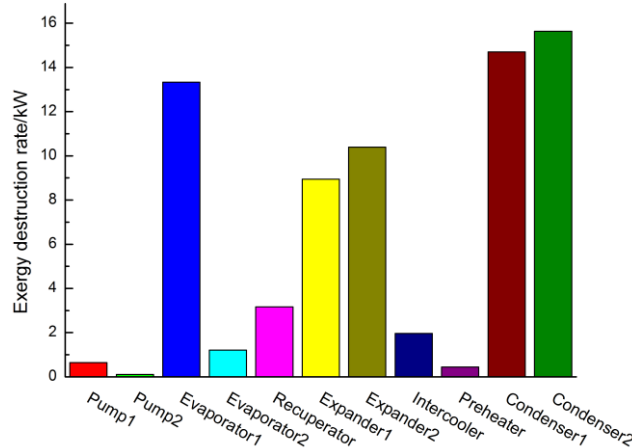
Figure 11: Exergy destruction rate of the dual loop ORCs

4. CONCLUSIONS

- By employing the dual loop ORC system, the waste heat of exhaust energy, coolant system, and released heat from turbocharged air in the intercooler can be effectively recovered and utilized. The overall net power output and thermal efficiency of the dual loop ORCs can reach 43.65kW and 10.52%, respectively.
- The fuel economy of the diesel engine can be notably improved, by employing the dual loop ORCs. When the evaporation pressure and mass flow rate of HT loop ORCs are 2.5 MPa and 0.8 kg·s^{-1}, the BSFC of the diesel engine-dual loop ORC combined system is 191.24 g·(kW·h)$^{-1}$, which reduced by 13.69% compared with the diesel engine itself.
- The net power output of LT loop ORCs is greater than that of HT loop ORCs. At the maximum overall net power output condition, the exergy destruction rate of the LT loop ORC system is higher than that of the HT loop ORC system and the difference can reach 11.03kW.

NOMENCLATURE

m	mass flow rate	(kg·s^{-1})
h	enthalpy	(kJ·kg^{-1})
Q	heat transfer rate	(kJ)
S	entropy	(kJ/kg·K)
T	temperature	(K)
W	work	(kJ)
η	efficiency	(%)
F	fuel consumption	(kg·h^{-1})
I	exergy destruction	(kW)

Subscript

1,2, 3…   state point in cycle
H   HT loop ORCs/high temperature heat source
L   LT loop ORCs/low temperature heat source
p   pump
e   evaporator
r   recuperator
exp   expander
int   intercooler
pre   preheater
con   condenser
eng   diesel engine
cs   combined system
oa   overall of dual loop ORCs
cst   thermal efficiency of the combined system
tei   thermal efficiency improvement

REFERENCES

Dolz, V., Novella R., García, A., et al. 2012, HD Diesel engine equipped with a bottoming Rankine cycle as a waste heat recovery system. Part 1: study and analysis of the waste heat energy. *Appl Therm Eng*, vol. 36: p. 269-278.

Roy, J.P., Mishra, M.K., Misra, A., 2010, Parametric optimization and performance analysis of a waste heat recovery system using Organic Rankine Cycle. *Energy*, vol. 35: p. 5049-5062.

Fang, J.L., Wei, M.S., Wang, J.R., et al, 2010, Simulation of Waste Heat Recovery from a Heavy-Duty Diesel Engine with a Medium Temperature ORCs. *Transactions of CSICE*, vol. 4, no. 28: p. 362-367.

Liu, B., Rivière, P., Coquelet, C., et al, 2012, Investigation of a two stage Rankine cycle for electric power plants. *Appl Energ*, vol. 100: p. 285-294.

Tian, H., Liu, L.N., Shu, G.Q., et al, 2014, Theoretical research on working fluid selection for a high-temperature regenerative transcritical dual-loop engine organic Rankine cycle. *Energ Convers Manage*, vol. 86: p. 764-773.

Shu, G.Q., Liu, L.N., Tian.H., et al, 2014, Parametric and working fluid analysis of a dual-loop organic Rankine (DORC) used in engine waste heat recovery. *Appl Energ*, vol. 113: p. 1188-1198.

Gao, W.Z., Zhai, J.M., Li, G.H., et al, 2013, Performance evaluation and experiment system for waste heat recovery of diesel engine. *Energy*, vol.15, no. 55: p. 226-235.

Meinel, D., Wieland, C., Spliethoff, H, 2014, Effect and comparison of different working fluids on a two-stage organic rankine cycle (ORC) concept. *Appl Therm Eng*, vol. 63: p. 246-253.

Yu, G.P., Shu, G.Q., Tian, H. et al. 2013, Simulation and thermodynamic analysis of a bottoming Organic Rankine Cycle. *Energy*, vol. 51: p. 281-290.

Bahadori, A., 2011, Estimation of combustion flue gas acid dew point during heat recovery and efficiency gain. *Appl Therm Eng*, vol. 31: p. 1457-1462.

Yang, F.B., Dong, X.R., Zhang, H.G. et al, 2014, Performance analysis of waste heat recovery with a dual loop organic Rankine cycle (ORC) system for diesel engine under various operating conditions. *Energ Convers Manage*, vol. 80: p. 243-255.

ACKNOWLEDGEMENT

POTENTIAL OF SMALL-SCALE TURBOMACHINERY FOR WASTE HEAT RECOVERY ON AUTOMOTIVE INTERNAL COMBUSTION ENGINGES

Kévin ROSSET[1*], Violette MOUNIER[1], Eliott GUENAT[1], Olivier PAJOT[2], Jürg SCHIFFMANN[1]

[1]Ecole Polytechnique Fédérale de Lausanne, Laboratory for Applied Mechanical Design, Neuchâtel, Switzerland
kevin.rosset@epfl.ch, violette.mounier@epfl.ch, eliott.guenat@epfl.ch, jurg.schiffmann@epfl.ch

[2]PSA Peugeot Citroën, Research, Innovation & Advanced Technologies Division, Lausanne, Switzerland
olivier.pajot@mpsa.com

* Corresponding Author

ABSTRACT

This paper investigates the waste heat recovery potential of internal combustion engines, using organic Rankine cycles running on small-scale radial turbomachinery. ORC are promising candidates for low-grade thermal sources and the use of dynamic expanders yields very compact systems, which is advantageous for automotive applications. As engine coolant and exhaust gases are the major available heat sources, different cycle configurations and working fluids have been investigated to capture them, in both urban and highway car operation. Pareto fronts showing the compromise between net power output and total heat exchange area have been identified for a set of cycle's variables including turbine inlet conditions and heat exchanger pinches. A preliminary optimization, including only R-1234yf working fluid, shows that a single-source regenerative cycle harvesting the high temperature exhaust gas stream performs averagely better than coolant-driven and dual-source cycles. A more in-depth optimization including eight working fluids as well as aerodynamic and conceptual limitations related to radial turbomachinery and automotive design constraints, finally shows that an ICE exhaust heat recovery ORC could improve the first law efficiency of the driving system by up to 10% when implemented with fluid R-1233zd.

1. INTRODUCTION

Nowadays, concerns about fossil fuel shortage and global warming advocate for a more rational use of primary energy. Transportation, which represents about 28% of the world energy consumption (IEA, 2014), is a sector where efficiency improvements are particularly awaited. Indeed, according to Legros (2014) passenger cars are barely using one third of the available fuel power to drive the wheels. The remaining two thirds are rejected to the environment as waste heat, mainly through coolant and exhaust gas streams. Recovering part of this energy would not only save fuel but also decrease pollutants emissions. The conversion of heat into useful electrical or mechanical energy may be performed by technologies like thermoelectric, thermoacoustic and thermophotovoltaic generators or by various thermodynamic cycles such as Stirling, Brayton and Rankine cycles, according to Legros (2014). Although they are compact, thermoelectric devices require expensive materials and have rather low efficiency, as shown by LeBlanc (2014). As it can be seen in Wu *et al.* (2014) ongoing research on thermoacoustic generators shows good efficiency but prototypes are still bulky. Thermophotovoltaic systems are getting mature but prototypes show limited efficiency and mostly, they require a high temperature source, involving combustion, to efficiently convert heat into thermal radiations (Ferrari *et al.* 2014). Although free-piston Stirling engines are an efficient and mature

technology, they are best suited to slow changing of power output and require long warm-up period (Kongtragool and Wongwises 2003). While open Brayton cycles are adequately exploited in gas turbines and turbojet engines, their efficiency seriously drops when trying to operate them in closed loop with a low temperature heat source. To compensate for this, Wright *et al.* (2006) proposed a design with multiple inter-stage heating/cooling between the expansion/compression stages. The resulting complexity and associated cost make this cycle unsuitable for vehicle integration. Rankine cycles are an attractive candidate, especially when running with organic working fluids, where low- to medium-grade heat sources can be harvested, as shown in the review by Sprouse and Depcik (2013). In such systems, the expansion technology is the most important element since it is responsible for the extraction of the fluid power. For small-scale power generation, volumetric expanders are usually selected since they can handle low fluid flowrates. However, friction between the moving parts causes wear and eventually failure if no lubricant is mixed with the working fluid. In addition to reducing expander and evaporator performance, auxiliary oil circuits add complexity and cost to the system. For these reasons, dynamic expanders would be the preferred solution. In the turbomachinery domain, radial inflow turbines are promising since they can achieve much higher stage pressure ratios than axial machines. Yet, in order to process low flowrates, radial rotors need to be downsized, which is advantageous for vehicle packaging, but however implies high rotor speeds. Improvements in dynamic gas bearing technology make this possible, as shown by Schiffmann and Favrat (2009) and Demierre *et al*. (2015), who successfully operated small-scale radial turbo-compressors and turbo-expanders at speeds up to 210 krpm. The objective of this article is to evaluate the potential of Rankine cycles combined with small-scale turbomachines for waste heat recovery on automotive internal combustion engines. Several cycle topologies and working fluids are included in the investigation to identify the most promising configuration for maximizing waste heat recovery while reducing the required heat exchange area.

2. SYSTEM DESCRIPTION

2.1 Engine characterization

The considered commercial vehicle is equipped with a 96 kW gasoline engine. Test data have been analyzed to extract waste heat flows and temperatures associated with urban (50 km/h) and highway (120 km/h) operations. As shown in Table 1, exhaust gas and coolant streams were identified as valuable heat sources with respect to the engine power. From an exergetic point of view though, coolant yields significantly less recoverable power than exhaust gases, due to its lower temperature.

Table 1: Vehicle power streams characterized in terms of temperature, power and exergy

Vehicle operating point	Engine	Exhaust gases			Coolant			
	$\dot{W}_{mec}$	T	$\dot{Q}$	$\dot{E}$	T_{in}	T_{out}	$\dot{Q}$	$\dot{E}$
	kW	°C	kW	kW	°C	°C	kW	kW
Urban	3.80	425	2.64	0.97	105	104	2.17	0.46
Highway	22.9	706	19.2	9.21	105	101	12.6	2.61

2.2 Cycle configurations

In order to extract useful power from engine waste heat, a basic Rankine cycle (Figure 1a) is first considered. In this cycle, a selected working fluid is successively compressed through a pump where little power is consumed (1-2), evaporated through a heat exchanger in contact with a heat source (2-3), expanded through a turbine where useful power is extracted (3-4), and finally condensed through a heat exchanger in contact with a heat sink (4-1) considered to be ambient air in the studied system. To further increase the cycle efficiency, an internal heat exchanger (IHX) can be added as shown in Figure 1b, so that the working fluid is preheated (resp. precooled) before being evaporated (resp. condensed). Yet, in these two configurations, only one single source can be harvested. Since the goal is to maximize heat recovery, two additional configurations are proposed, where both the exhaust gas

and the coolant heat sources are exploited. The first one uses two heat exchangers in series (Figure 1c), with the coolant stream preheating the working fluid and the exhaust gas stream evaporating it. The second one integrates two pumping and expansion stages with heat exchangers in parallel (Figure 1d). In this configuration, the coolant and exhaust gas streams are respectively associated with the intermediate and high pressure evaporators. Although other configurations could have been studied, it was decided, in view of the targeted automotive application where compact packaging is a key aspect, to limit the number of heat exchangers in the evaluated systems to a maximum of three. In order to reduce exergetic losses, all evaporators are considered counter-flow and all condensers cross-flow. The first type is well suited to transfer heat from the engine waste heat streams to the working fluid while the second one is better adapted to reject heat from the working fluid to the ambient air.
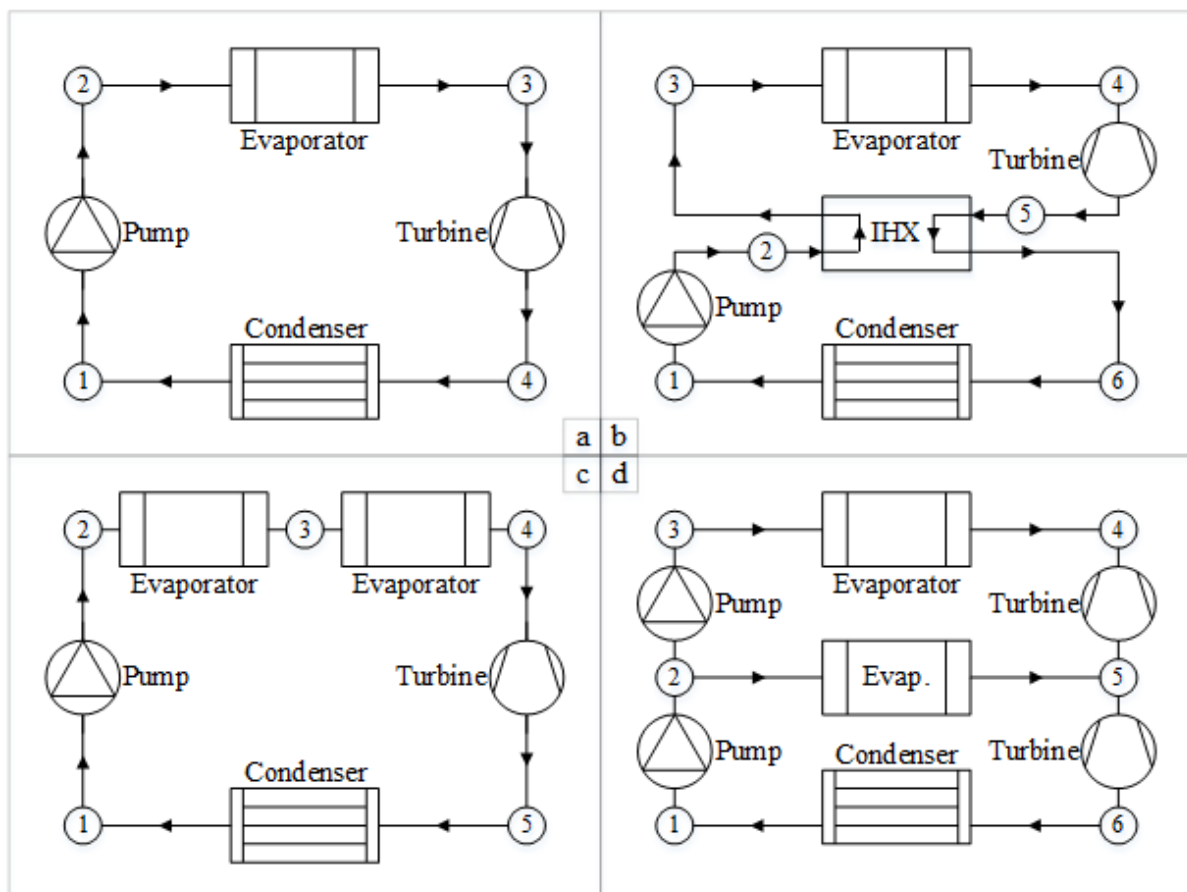
Figure 1: Evaluated Rankine cycle configurations: Basic single-source (a), Regenerative single-source (b), Series dual-source (c), Parallel dual-source (d)

2.3 Fluid candidates

Several working fluids may be appropriate candidates for Rankine cycles. Beyond the critical point, indicating the maximum pressure and temperature levels at which a fluid can experience a two-phase state, environmental indicators are also essential selection criteria. As such, working fluids should show null Ozone Depletion Potential (ODP), low Global Warming Potential (GWP) and low toxicity and flammability (ASHRAE standard 34). Refrigerants R-134a, R-152a and R-245fa were consequently identified as good candidates. Because of their high GWP however, R-134a and R-245fa are likely to be phased out and replaced by their respective counterparts R-1234yf/R-1234ze and R-1233zd, which are therefore included in the evaluation. Other considered fluids are ethanol and water. Table 2 summarizes the selected fluids, also highlighting their expansion behavior from a saturated vapor state at the turbine inlet.

Rankine cycles generally operate close to the saturation lines. Therefore ideal or perfect gas assumptions to retrieve the fluid's thermodynamic properties are not valid. This article uses REFPROP® based thermodynamic data to perform cycle calculations.

Table 2: Working fluid candidates

Working fluid	P_{cr} [bar]	T_{cr} [°C]	ODP	GWP	ASHRAE 34	Expansion
R-134a	40.6	101	0	1430	A1	Wet
R-1234yf	33.8	95	0	4	A2L	Dry
R-1234ze	36.3	109	0	6	A2L	Dry
R-152a	45.2	113	0	124	A2	Wet
R-245fa	36.5	154	0	1030	B1	Dry
R-1233zd	35.7	166	0	7	A1	Dry
Ethanol	62.7	242	0	0	-	Wet
Water	220.6	374	0	0	A1	Wet

2.4 Heat sink

In addition to the available heat sources, proposed cycle configurations, and working fluids, a heat sink also has to be characterized. As ambient temperatures ranging from 20 to 25°C were observed in the vehicle test data, the reference cold source temperature is set to 25°C. Assuming a 10°C temperature increase in the cross-flow condensers, an average air exchange temperature of 30°C is then considered.

3. SIMULATION MODELS

In order to assess the performance of a Rankine cycle on the two vehicle operating points, steady-state models have been implemented for each cycle configuration. Typical model inputs are the heat source and sink mass flowrates and temperatures, working fluid subcooling/superheating at the pump/turbine inlets, turbomachines efficiency and heat exchangers temperature pinch. Calculated outputs are the system efficiency, net power output, turbomachinery pre-design (rotor speed and diameter) and heat exchangers area. Model resolution is based on mass and energy conservation laws with the following general assumptions:
- Fluid flow is one-dimensional.
- Fluid kinetic and potential energy variations are neglected.
- Heating and cooling transformations are isobaric.
- Heat exchangers are perfectly insulated.

3.1 Turbomachinery modeling

The net power output of a cycle is calculated from the difference of the generated turbine powers $\dot{W}_t$ and consumed pump powers $\dot{W}_p$. Each of them is predicted from the product of the working fluid mass flowrate ($\dot{m}_t$, $\dot{m}_p$) with the isentropic specific enthalpy difference through the device ($\Delta h_{t,s}$, $\Delta h_{p,s}$), corrected to account for entropy and electromechanical losses:

$$\dot{W}_{net} = \sum_t \dot{W}_t - \sum_p \dot{W}_p = \sum_t \left(\dot{m}_t \Delta h_{t,s} \cdot \eta_{t,s} \eta_{t,em} \right) - \sum_p \left(\dot{m}_p \Delta h_{p,s} / \eta_{p,s} \eta_{p,em} \right) \quad (1)$$

While electromechanical efficiencies $\eta_{t/p,em}$ are considered fixed for simplicity, isentropic efficiencies $\eta_{t/p,s}$ are extracted from Balje's diagrams (Balje, 1981), that plot iso-efficiency lines as a function of specific speed n_s and specific diameter d_s, defined as:

$$n_s = \frac{\omega \, \dot{V}^{0.5}}{|\Delta h_s|^{0.75}} \qquad (2)$$

$$d_s = \frac{d \, |\Delta h_s|^{0.25}}{\dot{V}^{0.5}} \qquad (3)$$

Determining these two dimensionless parameters from the optimal efficiency on the radial pump / turbine diagram and knowing the fluid flowrate $\dot{V}$ at the pump inlet / turbine outlet as well as the absolute fluid isentropic enthalpy difference $|\Delta h_s|$, both the rotor angular velocity ω and tip diameter d can be estimated. Also, to avoid restricting the feasible design, radial pumps and turbines are not considered coupled on the same shaft.

3.2 Heat exchangers modeling

Predicting the volume of a heat exchanger is a difficult task. It depends not only on the flow conditions, but also on the detailed heat exchanger geometry and materials. Since heat exchangers design is beyond the scope of this work, it was decided to evaluate their size in terms of heat exchange surface. For this purpose, the Logarithmic Mean Temperature Difference (LMTD) method (Incropera *et al.*, 2006) was used. It states that the power $\dot{Q}$ exchanged between two streams is equal to:

$$\dot{Q} = UA\Delta T_{lm} \qquad (4)$$

where U is the overall heat transfer coefficient, A the heat exchange area and ΔT_{lm} the logarithmic mean temperature difference. By assuming that fluids are separated by an infinitely thin wall, the heat exchange area becomes identical on each side and the overall heat transfer coefficient derives from an inverted sum of the hot and cold fluid convective heat transfer coefficients U_h and U_c; which used values are presented in Table 3, depending on the fluid type:

$$\frac{1}{U} = \frac{1}{U_h} + \frac{1}{U_c} \qquad (5)$$

Table 3: Typical convective heat transfer coefficients (Marechal, 2012)

	Gas	Liquid	Condensing fluid	Evaporating fluid
U_{conv} [W/m^2K]	60	560	1600	3600

The LMTD is given by:

$$\Delta T_{lm} = \frac{\Delta T_2 - \Delta T_1}{\log(\Delta T_2/\Delta T_1)} \qquad (6)$$

where ΔT_1 and ΔT_2 are the fluid temperature differences between the two streams on each side of the heat exchanger.

4. OPTIMIZATION RESULTS AND DISCUSSION

The implemented models being highly non-linear, non-differentiable and with numerous inputs, a genetic algorithm has been used to perform the optimizations. The goal is to identify the most promising cycle configuration and working fluid and to determine the possible trade-offs between system performance and size, in accordance with vehicle expectations. Two objective functions were defined: net power output maximization and total heat exchange area minimization. As observed by

Molyneaux (2002) and Leyland (2002), genetic algorithms are well indicated to come up with Pareto frontiers when dealing with complex energy systems.
The optimization was performed in two stages: a first run comparing the four cycles presented in Figure 1 and a second run confronting the eight fluids listed in Table 2.

4.1 Optimization stage I
The first optimization stage aimed at comparing the cycle configurations exposed in Figure 1. It has been performed using refrigerant R-1234yf, which is the standard working fluid replacing R-134a in vehicle cabin air conditioning, with a pump inlet subcooling of 2°C, a pinch of 10°C in all heat exchangers, and no electromechanical losses. Three decision variables were accounted for, as shown in Table 4.

Table 4: Decision variables for optimization stage I

#	Decision variable	Range
1	Working fluid evaporating pressure	2 – 40 bar
2	Working fluid temperature at turbine inlet	60 – 250 °C
3	Exhaust gas temperature at evaporator outlet	80 – 200 °C

Figure 2 presents the Pareto fronts resulting from the first-stage optimization. At first glance, it can be seen that cycles recovering the coolant waste heat only are the least profitable ones and that an internal heat exchanger (IHX) does not increase the extracted power. On the contrary, single-source waste heat recovery using the exhaust gases is much more valuable and, in this case, regeneration through an IHX significantly increases the conversion to useful power. With equal powers for lower areas, the dual-source series configuration always shows better performance than the parallel configuration. This is due to the engine coolant temperature (about 100°C), which imposes the cycle intermediate pressure level (about 30 bar for R-1234yf at 90°C) and therefore limits the topping cycle pressure ratio (1.33 for a maximum pressure of 40 bar) in the parallel configuration.

In urban vehicle operation, the overall Pareto front is shared by the exhaust-gas-driven basic cycle up to 0.13 kW (36% of available power range), the exhaust-gas-driven regenerative cycle from 0.13 to 0.28 kW (42%) and finally the dual-source series cycle from 0.28 to 0.36 kW (22%). In highway vehicle operation however, only exhaust-gas-driven cycles take part in the overall Pareto front, with the basic configuration being optimal up to 1.4 kW (50% of available power range) and the regenerative configuration being optimal from 1.4 to 2.8 kW (50%). Consequently, recovering the engine exhaust gases waste heat using a Rankine cycle that includes an internal heat exchanger, gives the best vehicle efficiency improvement perspectives.
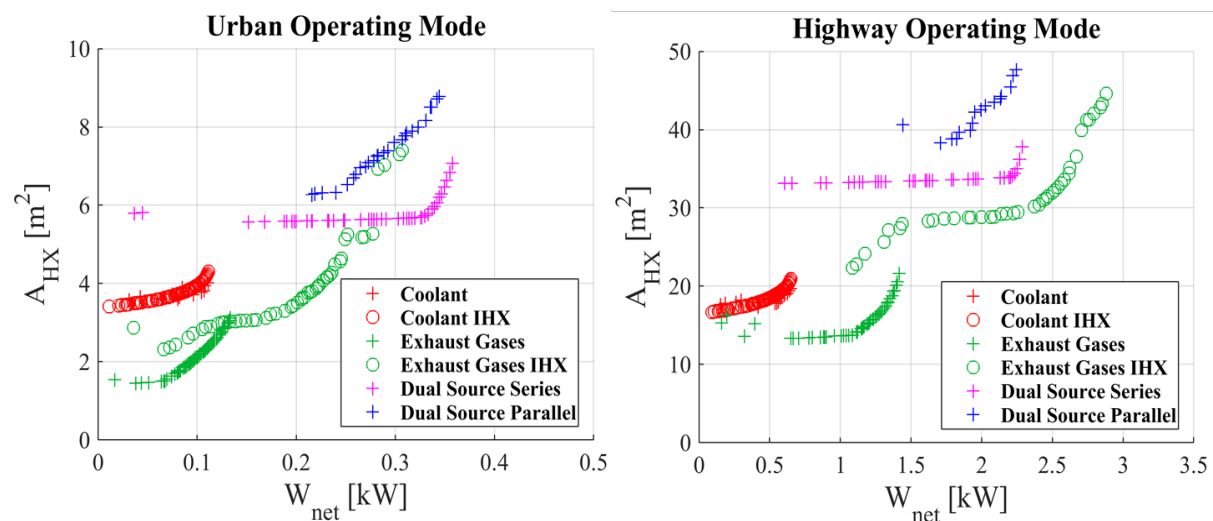

Figure 2 : Heat recovery system Pareto fronts from different cycle configurations

4.2 Optimization stage II

The second optimization stage aimed at comparing the fluid candidates exposed in Table 2. It has been performed using a regenerative exhaust-gas-driven cycle, which is the optimal configuration from the first-stage optimization, with a pump inlet subcooling of 5°C to prevent cavitation, turbomachine electromechanical efficiencies of 85% to account for bearing and generator losses, a minimum working fluid pressure of 1 bar to avoid subatmospheric processes and possible contamination by air, a maximum working fluid pressure of 30 bar to make piping and evaporator costs accessible to automotive industry, a minimum exhaust gas outlet temperature of 150°C to avoid acid condensation in the last section of the exhaust pipe, and a minimum turbine tip diameter of 10 mm for manufacturability. Furthermore, Balje's (1981) predictions for radial pump isentropic efficiencies being overestimated (up to 92%), the pump isentropic efficiency has been fixed to a more realistic value of 60%. Four decision variables were accounted for, as shown in Table 5.

Table 5: Decision variables for optimization stage II

#	Decision variable	Range
1	Working fluid superheating at turbine inlet	0 – 200 °C
2	Condenser pinch	5 – 25 °C
3	Evaporator pinch	5 – 25 °C
4	IHX pinch	5 – 25 °C

In addition to the above constraints, cycle pressure ratio limitations have been considered, so that the expansion is feasible across a single-stage turbine. The advantage is that it significantly decreases the complexity and consequently the manufacturing cost of the turbo-generator unit. Yet, as dynamic machine stage pressure ratio is strongly dependent on rotor design and fluid density differentials, a one-dimensional aerodynamic analysis has been performed on an existing small-scale radial turbine design presented by Demierre *et al.* (2015), which goal was to determine for each working fluid, the maximum stage pressure ratio as a function of the turbine inlet superheating. In this analysis, sonic limitations at the nozzle and rotor throats were accounted for, as well as a maximum rotor peripheral speed of 400 m/s, for mechanical strength reasons.

Results from the second-stage optimization (Figure 3) suggest that whether the vehicle is operated in urban or highway mode, ethanol as well as refrigerants R-245fa and its substitute clearly show the best objectives combinations, with R-1233zd being optimal in terms of net power output. Nonetheless, if the main criterion is to minimize the heat exchange area, ethanol then takes the first place in the ranking. For further comparison, Table 6 presents for each working fluid, some of the main system characteristics at maximum net power output; that is turbine diameter d_t and rotational speed N_t, cycle pressure ratio π, evaporating pressure P_{ev} and efficiency η_C, and system overall efficiency η_S. The first-law efficiencies are defined below, as a function of evaporator load $\dot{Q}_{ev}$ and heat source available power $\dot{Q}_{source}$.

$$\eta_C = \frac{\dot{W}_{net}}{\dot{Q}_{ev}} \tag{7}$$

$$\eta_S = \frac{\dot{W}_{net}}{\dot{Q}_{source}} \tag{8}$$

It should here be mentioned that the cycle condensing pressures were determined from the average heat sink temperature and accounting for the condenser pinch, subcooling at the pump inlet and minimum pressure constraint. Then, the evaporating pressure was calculated from the optimal pressure ratio at corresponding turbine inlet superheating and accounting for the maximum pressure constraint. As shown in Table 6, this last constraint mainly explains why refrigerants R-152a, R-134a and substitutes exhibit lower performance. On the contrary, with a condensing pressure of 1 bar,

natural working fluids do not suffer from the maximum pressure constraint. While water-based systems performance is limited by the zero-droplet tolerance and by the limitation of the rotor peripheral speed, ethanol-based systems show promising results with the best Pareto frontier from 0.15 to 0.2 kW in urban operating mode and from 1.5 to 1.8 kW in highway operating mode. Nonetheless, these two fluids present relatively high and therefore challenging rotational speeds (300 to 600 krpm), which associated with 20 to 10 mm rotors, lead to much higher peripheral speeds compared to refrigerant-based systems.
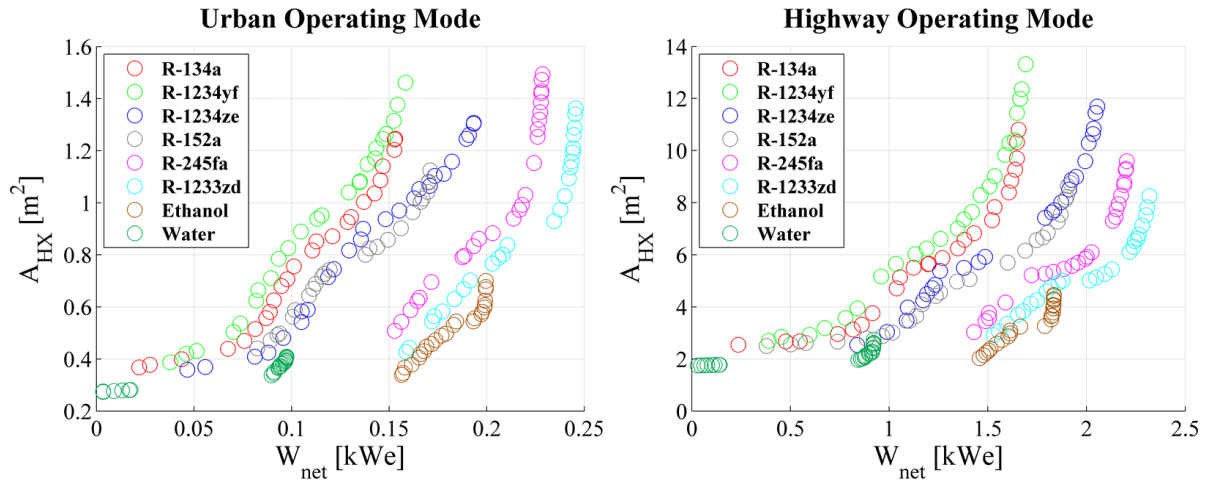

Figure 3: Heat recovery system Pareto fronts from different working fluid candidates

No matter the working fluid, turbine design is always characterized by the smallest accepted design diameter and a high rotational speed when optimizing the heat recovery system for an urban vehicle operation. This is disadvantageous for production and performance since manufacturing tolerances (linked with efficiency) and rotor balancing (linked with stability) become stricter, as observed by Schiffmann and Favrat (2010) and Schiffmann (2013). In addition, efficiencies are lower compared to the highway operation systems. Hence, from this refined optimization and considering both cycle net power outputs and turbine design characteristics, it can be concluded that the waste heat recovery system should be designed for the highway vehicle operation, using refrigerant R-1233zd as cycle working fluid. The expected gain ranges from 1.5 to 2.3 kW of electrical power that is a 6.5 to 10% increase in the first-law efficiency of the vehicle drivetrain.

Table 6: System characteristics at maximum net power outputs

Working fluid	Urban						Highway					
	η_S %	η_C %	P_{ev} bar	π -	N_t krpm	d_t mm	η_S %	η_C %	P_{ev} bar	π -	N_t krpm	d_t mm
R-134a	5.8	8.4	30.0	2.93	261	10.0	8.6	10.5	30.0	2.90	244	12.0
R-1234yf	6.0	8.7	30.0	2.94	250	10.0	8.8	10.8	30.0	2.93	214	12.9
R-1234ze	7.3	10.6	30.0	3.89	293	10.0	10.7	13.1	30.0	3.89	250	13.0
R-152a	6.5	9.4	30.0	3.20	340	10.0	10.0	12.2	30.0	3.27	368	10.9
R-245fa	8.7	12.6	18.2	5.15	309	10.0	11.4	14.0	23.6	5.18	227	15.2
R-1233zd	9.3	13.5	17.4	5.28	329	10.0	12.0	14.7	20.3	5.31	218	16.4
Ethanol	7.6	11.0	5.95	5.95	606	10.0	9.5	11.7	5.94	5.94	335	19.3
Water	3.7	5.4	2.49	2.49	600	10.4	4.8	5.9	2.49	2.49	395	17.9

5. CONCLUSIONS

In view of reducing vehicle fuel consumption and carbon dioxide emissions, Rankine cycle systems have been studied to recover the waste heat from engine coolant and exhaust gas streams. Two representative vehicle operating points were analyzed with four possible cycle configurations and a set of eight working fluids. Targeting both maximum performance and minimum size criteria, multi-objective optimizations were performed, accounting for automotive and turbomachinery design constraints. From the resulting Pareto fronts, it has been found that the optimal recovery system should be designed for the highway vehicle operation, using a regenerative exhaust-gas-driven cycle and refrigerant R-1233zd. The expected benefit is an additional 2.3 kW of electrical power that is a 10% increase in the vehicle efficiency. For achieving this performance, the optimal expander is a 16.5 mm tip diameter radial inflow turbine rotating at about 220 krpm. In order to validate the complete system design, its behavior should now be evaluated for other vehicle operating points, including off-design performance evaluation and engine dynamics.

NOMENCLATURE

Symbols

A	Area	m^2
d	Tip diameter	mm
d_s	Specific diameter	–
$\dot{E}$	Exergy	W
h	Specific enthalpy	J/kg
$\dot{m}$	Mass flowrate	kg/s
N	Rotational speed	rpm
n_s	Specific speed	–
P	Pressure	bar
$\dot{Q}$	Heat	W
T	Temperature	$°C$
U	Heat transfer coefficient	W/m^2K
$\dot{V}$	Volumetric flowrate	m^3/s
$\dot{W}$	Electrical power	We
$\dot{W}$	Mechanical power	W
Δh	Specific enthalpy diff.	J/kg
ΔT	Temperature difference	$°C$
η	Efficiency	–
π	Pressure ratio	–
ω	Angular velocity	rad/s

Subscripts

C	Cycle

c	Cold
$conv$	Convective
cr	Critical state
em	Electromechanical
ev	Evaporation
HX	Heat exchange
h	Hot
in	Inlet
lm	Logarithmic mean
mec	Mechanical
net	Net
out	Outlet
p	Pump
ref	Reference (Ambient)
S	System
s	Isentropic
t	Turbine

Acronyms

GWP	Global Warming Potential
ICE	Internal Combustion Engine
IHX	Internal Heat Exchanger
ODP	Ozone Depletion Potential
ORC	Organic Rankine Cycle

REFERENCES

Balje, O. E., 1981, *Turbomachines: A Guide to Design, Selection, and Theory*, John Wiley & Sons Inc., New York, 513 p.

Demierre, J., Rubino, A., Schiffmann, J., 2015, Modeling and Experimental Investigation of an Oil-Free Microcompressor-Turbine Unit for an Organic Rankine Cycle Driven Heat Pump, *Journal of Engineering for Gas Turbines and Power (ASME)*, vol. 137, no. 3: p. 032602.

Ferrari, C., Melino, F., Pinelli, M., Spina, P. R., 2014, Thermophotovoltaic energy conversion: Analytical aspects, prototypes and experiences, *Appl. Energy*, vol. 113: p. 1717-1730.

IEA, 2014, 2014 Key World Energy STATISTICS, *International Energy Agency*.

Incropera, F. P., DeWitt, D. P., Bergman, T. L., Lavine, A. S., 2007, *Fundamentals of Heat and Mass Transfer*, John Wiley & Sons Inc., New York, 997 p.

Kongtragool, B., Wongwises, S., 2003, A review of solar-powered Stirling engines and low temperature differential Stirling engines, *Renew. Sustain. Energy Rev.*, vol. 7: p. 131-154.

LeBlanc, S., 2014, Thermoelectric generators: Linking material properties and systems engineering for waste heat recovery applications, *Sustainable Materials and Technologies*, vol. 1-2: p. 26-35.

Legros, A., Guillaume, L., Diny, M., Zaïdi, H., Lemort, V., 2014, Comparison and Impact of Waste Heat Recovery Technologies on Passenger Car Fuel Consumption in a Normalized Driving Cycle, *Energies*, vol. 7: p. 5273-5290.

Leyland, G. B., 2002, Multi-Objective Optimization Applied to Industrial Energy Problems, *Ecole Polytechnique Fédérale de Lausanne*, PhD Thesis no. 2572.

Marechal, F., 2012, *Process integration techniques for improving the energy efficiency of industrial processes*, EPFL Advanced Energetics coursebook.

Molyneaux, A., 2002, A Pratical Evolutionary Method for The Multi-Objective Optimisation of Complex Integrated Energy Systems Including Vehicle Drivetrains, *Ecole Polytechnique Fédérale de Lausanne*, PhD Thesis no. 2636.

Schiffmann, J., Favrat, D., 2009, Experimental investigation of a direct driven radial compressor for domestic heat pumps, *Int. J. Refrig.*, vol. 32, no. 8: p. 1918-1928.

Schiffmann, J., Favrat, D., 2010 Integrated Design and Optimization of Gas Bearing Supported Rotors, *Journal of Mechanical Design*, vol. 132

Schiffmann, J., 2013 Enhanced Groove Geometry for Herringbone Grooved Journal Bearings, *Journal Of Engineering For Gas Turbines And Power (ASME)*, vol. 135, no. 10, p. 102501.

Sprouse III, C., Depcik, C., 2013, Review of organic Rankine cycles for internal combustion engine exhaust waste heat recovery, *Appl. Therm. Eng.*, vol. 51, no. 1-2: p. 711-722.

Wright, S. A., Vernon, M. E., Pickard, P. S., 2006, Concept Design for a High Temperature Helium Brayton Cycle with Interstage Heating and Cooling, *Sandia National Laboratories*.

Wu, Z., Zhang, L., Dai, W., Luo, E., 2014, Investigation on a 1kW traveling-wave thermoacoustic electrical generator, *Appl. Energy*, vol. 124: p. 140-147.

PARAMETRIC OPTIMIZATION AND PERFORMANCE ANALYSIS OF ORGANIC RANKINE CYCLE (ORC) FOR ENGINE WASTE HEAT RECOVERY

Fubin Yang[1,2]*, Hongguang Zhang[1,2]

[1]Beijing University of Technology, College of Environmental and Energy Engineering,
Beijing, China
E-mail: yangfubinnuc@163.com

[2]Collaborative Innovation Center of Electric Vehicles in Beijing,
Beijing, China
E-mail: yangfubinnuc@163.com

* Corresponding Author

ABSTRACT

This study examines the parametric optimization and performance analysis of ORC system using genetic algorithm (GA) for engine waste heat recovery. The effects of three key parameters, including evaporation pressure, superheat degree, and condensation temperature on the net power output per unit heat transfer area and exergy destruction rate under engine various operating conditions are analyzed. Subsequently, the performances of a finned-tube evaporator used in this ORC system are evaluated. The results indicate that the optimal evaporation pressures are mainly influenced by the engine operating conditions. Moreover, superheat degree and condensation temperature presents slight variation over the whole operating range. At rated condition, the ORC system achieves maximum net power output per unit heat transfer area of $0.74kW/m^2$. Furthermore, the ratio of maximum effective heat transfer area to the actual area of the evaporator is 69%, which has great influence on the performance of the ORC system.

1. INTRODUCTION

Over the past few years, the energy consumption has kept increasing with the development of industrialization process in China. Thereinto, internal combustion engines (ICEs) have consumed about 60% of overall oil consumption. Due to the low thermal efficiency of the ICEs, only about one-third of total fuel combustion energy becomes power output. The exhaust waste heat recovery of ICEs presents a potential for converting waste heat into electrical energy to improve the engine thermal efficiency and reduce emissions.

As a solution to the low grade waste heat recovery, Organic Rankine cycle (ORC) has been applied widely because of its high efficiency, low cost and simple structure. Zhai *et al*. (2014) showed that the ORC system is one of the most effective methods for recovering energy from low grade heat sources. Walraven *et al*. (2015) observed that the discount rate, electricity price, brine inlet temperature and annual electricity price evolution have a strong influence on the configuration and efficiency of the ORC and on the economics of the project. Heberle *et al*. (2012) showed that the use of mixtures as working fluids leads to an efficiency increase compared to pure fluids. Li *et al*. (2014) showed that there exists a possible relationship between the critical temperature of working fluids and the economical performance of the system.

Currently, much attention has also been paid to waste heat recovery for the ICEs based on ORC system. Wang *et al*. (2014) indicated that the exhaust energy recovery system serve more applicable on the heavy-duty diesel engine. Teng *et al*. (2006) demonstrated that with the hybrid power system of the

diesel engine and the Rankine engine operated with waste heat, substantial enhancement in engine power and improvement in fuel economy can be achieved. Vaja *et al*. (2010) showed that a 12% increase in the overall efficiency can be achieved compared with the engine with no bottoming.

Based on the aforementioned analysis, the ORC system has already been extensively applied and investigated in low grade heat sources, especially in ICEs waste heat recovery. In this paper, the thermodynamic model of the ORC system is established based on the first and second laws of thermodynamics. The optimal operating parameters of the ORC system are investigated under diesel engine various operating conditions with evaporation pressure, superheat degree, and condensation temperature of the working fluid as optimization parameters for the maximum net power output per unit heat transfer area (POPA) and the minimum exergy destruction rate (EDR) using genetic algorithm (GA).

2. SYSTEM DESCRIPTION

The schematic and *T-s* diagram of the ORC system for recovering engine exhaust waste heat are shown in Figures 1 and 2. The liquid working fluid is pressurized to the evaporator by the pump. Then the subcooled liquid working fluid absorbs heat from the exhaust gas in the evaporator and turns into saturated or superheated vapor. After that, the vapor flows into the expander to do work and drives the generator to produce electricity. Finally, the superheated vapor exported from the expander condenses into saturated liquid state in the condenser. Subsequently, the liquid working fluid is pressurized by the pump to begin the new cycle again.
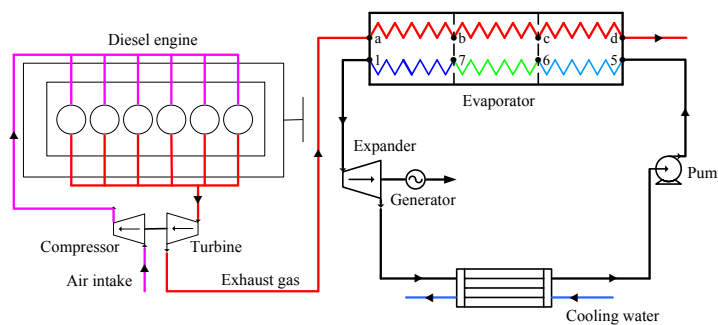

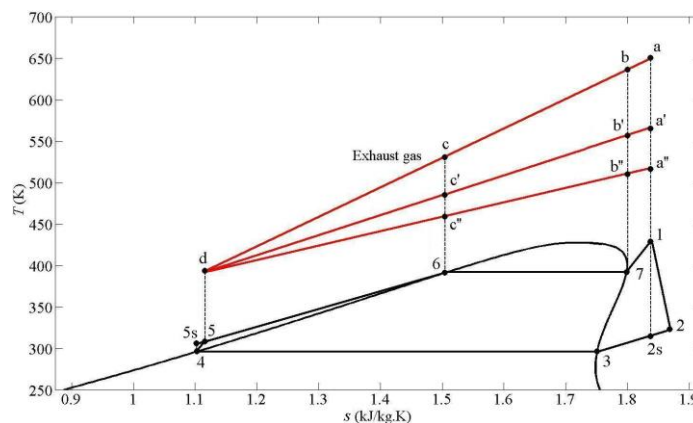**Figure 1:** Schematic diagram of the ORC system

Figure 2: *T-s* diagram of the ORC system

The optimal working fluid should not only ensure higher waste heat recovery efficiency for the ORC system, but also meet the requirement of environmental protection, safety, and economy. Wang *et al*. (2011) compared nine different pure organic working fluids based on their thermodynamic performances. R245fa is the most suitable working fluid for engine waste heat recovery application.

Therefore, R245fa is selected as the working fluid in this study.

3. MATHEMATICAL MODEL

3.1 Thermodynamic model

Process 1-2 (Expander):

The power output and the exergy destruction rate of the expander are given by:

$$\dot{W}_{\mathrm{exp}} = \dot{m}_{\mathrm{wf}}(h_1 - h_2) \tag{1}$$

$$\dot{I}_{\mathrm{exp}} = T_0 \dot{m}_{\mathrm{wf}}(s_2 - s_1) \tag{2}$$

The isentropic efficiency of expander is given by:

$$\eta_{\mathrm{exp}} = \frac{h_1 - h_2}{h_1 - h_{2\mathrm{s}}} \tag{3}$$

Process 2-4 (Condenser):

The heat transfer rate and the exergy destruction rate of the condenser can be expressed as:

$$\dot{Q}_{\mathrm{con}} = \dot{m}_{\mathrm{wf}}(h_2 - h_4) \tag{4}$$

$$\dot{I}_{\mathrm{con}} = \dot{m}_{\mathrm{wf}}[(h_2 - h_4) + T_0(s_2 - s_4)] \tag{5}$$

Process 4-5 (Pump):

The power consumed and the exergy destruction rate of the pump can be determined as:

$$\dot{W}_{\mathrm{p}} = \dot{m}_{\mathrm{wf}}(h_5 - h_4) \tag{6}$$

$$\dot{I}_{\mathrm{p}} = T_0 \dot{m}_{\mathrm{wf}}(s_5 - s_4) \tag{7}$$

The isentropic efficiency of the pump is given by:

$$\eta_{\mathrm{p}} = \frac{h_{5\mathrm{s}} - h_4}{h_5 - h_4} \tag{8}$$

Process 5-1 (Evaporator):

The heat transfer rate and the exergy destruction rate of the evaporator can be expressed as:

$$\dot{Q}_{\mathrm{eva}} = \dot{m}_{\mathrm{exh}}(h_{\mathrm{a}} - h_{\mathrm{d}}) = \dot{m}_{\mathrm{wf}}(h_1 - h_5) \tag{9}$$

$$\dot{I}_{\mathrm{eva}} = \dot{m}_{\mathrm{exh}}[(h_{\mathrm{a}} - h_{\mathrm{d}}) + T_0(s_{\mathrm{a}} - s_{\mathrm{d}})] - \dot{m}_{\mathrm{wf}}[(h_1 - h_5) + T_0(s_1 - s_5)] \tag{10}$$

For each heat transfer area in the evaporator, the heat transfer rate between the exhaust and the working fluid can be calculated using the following equations:

$$\dot{Q}_{71} = \dot{m}_{\mathrm{exh}}(h_{\mathrm{a}} - h_{\mathrm{b}}) = \dot{m}_{\mathrm{wf}}(h_1 - h_7) \tag{11}$$

$$\dot{Q}_{67} = \dot{m}_{\mathrm{exh}}(h_{\mathrm{b}} - h_{\mathrm{c}}) = \dot{m}_{\mathrm{wf}}(h_7 - h_6) \tag{12}$$

$$\dot{Q}_{56} = \dot{m}_{\mathrm{exh}}(h_{\mathrm{c}} - h_{\mathrm{d}}) = \dot{m}_{\mathrm{wf}}(h_6 - h_5) \tag{13}$$

To investigate the heat transfer performance of the evaporator, the ratio of effective heat transfer area to actual area is defined as:

$$\eta_{\mathrm{ht}} = \frac{A_{\mathrm{eff}}}{A_{\mathrm{act}}} \tag{14}$$

The aim of this paper is to conduct the parametric optimization and evaluate the performance of a finned-tube evaporator used in the ORC system. Therefore, the isentropic efficiencies of the pump and the expander are set to constant values. Therein, several assumptions for the thermodynamic model

are listed as follows:
(1) The ORC system operates under steady state conditions.
(2) There are no pressure drops in the pipes and the components.
(3) The heat losses in each component are also neglected.
(4) The isentropic efficiencies of the pump and the expander are set to 0.65 and 0.7 respectively.
(5) The ambient temperature is set to 291.15 K.

3.2 Evaporator model
In this study, we select a fin-and-tube evaporator used in our lab for thermodynamic analysis. The schematic and the geometric dimensions of the fin-and-tube evaporator are shown in Figure 3 and Table 1, respectively. The engine exhaust gas flows outside the tube, and the working fluid flows inside the tube. The evaporator model refers to Zhang *et al*. (2013).
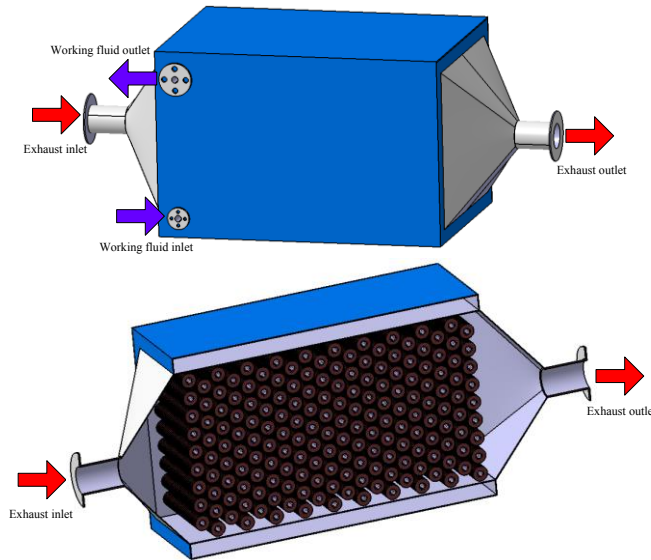

Figure 3: Schematic of the fin-and-tube evaporator

Table 1: Geometric dimensions of the fin-and-tube evaporator

Items	Parameters	Units
Number of tubes in each row	9	-
Number of tube rows	20	-
Tube outer diameter	25	mm
Tube inner diameter	20	mm
Tube pitch	60	mm
Row pitch	100	mm
Fin height	12	mm
Fin width	1	mm
Rib effect coefficient	3	-
Tube row alignment	Staggered type	-
Tube material	Stainless steel316L	-
Fin material	Stainless steel316L	-
Inner heat transfer area	9	m^2
Tube length	8.8	m

4. OPTIMIZATION METHODOLOGY

4.1 Description of genetic algorithm
The diesel engine operates under various operating conditions for the practical applications. Therefore,

the coordinated variation of each operating parameters in the ORC system is indispensable to achieve the optimal performance. Genetic algorithm which was invented by professor Holland (1975) is adaptive heuristic search algorithm based on the evolutionary ideas of natural selection and genetics.

In the present study, the POPA and the EDR are evaluated as objective functions with evaporation pressure, superheat degree and condensation temperature of the working fluid as optimization variables. Therefore the optimization of the ORC system is performed by using GA in MATLAB. The multi-objective optimization function can be described as:

$$\max(\text{POPA}) = f(P_7, T_1, T_4) \tag{15}$$

$$\min(\text{EDR}) = f(P_7, T_1, T_4) \tag{16}$$

The lower and upper bounds of decision variables and parameter setting of GA are listed in Tables 2 and 3.

Table 2: Lower and upper bounds of decision variables

Decision variables	Lower bound	Upper bound
Evaporation pressure (MPa)	0.8	3
Superheat degree (K)	0	20
Condensation temperature (K)	298.15	353.15

Table 3: Parameter setting of genetic algorithm

Parameters	Value
Population size	150
Selection process	Tournament
Crossover fraction	0.8
Mutation function	Adaptive feasible
Stop generations	600

5. ENGINE WASTE HEAT EVALUATION

The engine used as the topping cycle in this study is a six-cylinder in-line diesel engine. The main technical performance parameters of the diesel engine are listed in Table 4.

Table 4: The main technical parameters of the diesel engine

Items	Parameters	Units
Rated power	247	kW
Maximum torque	1600	N.m
Displacement	11.596	L
Cylinder number	6	
Air intake type	Turbocharged and Intercooled	
Fuel injection system	High pressure common rail	
Speed at maximum torque	1400	r/min
Stroke and cylinder bore	155×126	mm
Compression ratio	17.1	

Figure 4 shows the performance maps of the diesel engine over the whole operating range. The variation of BSFC (brake specific fuel consumption) is illustrated in Figure 4(a), which indicates that the BSFC is mainly influenced by engine torque. When the diesel engine is operating under the high load conditions, it has the lower BSFC within the range of 196 g/(kW.h) to 205 g/(kW.h). Moreover, at the engine rated condition, the power output of the engine reaches a maximum value of 247 kW. Figure 4(b) shows the variation of the exhaust temperature with the engine speed and load. It can be seen that the exhaust temperature varies slightly with engine speed, but increases rapidly with engine

load. When diesel engine is operating under the medium-low speed and medium-high load conditions, the exhaust temperature is relative high and can reach its maximum value of 667 K. The exhaust mass flow rate of the diesel engine, which is the sum of fuel consumption and intake air mass flow rate per unit time, is shown in Figure 4(c). It is obvious that the exhaust mass flow rate increases with engine speed and engine load. At rated condition, the exhaust mass flow rate reaches a maximum of 0.36 kg/s. Figure 4(d) shows the available exhaust energy of the diesel engine over the whole operating range. Note that the available exhaust energy is mainly affected by exhaust mass flow rate and exhaust temperature. Therefore, the available exhaust energy shows the same variation tendency compared with Figures 4(b) and 4(c). Under the medium-high speed and medium-high load conditions, the available exhaust energy ranges from 47 kW to 103 kW. At rated condition, the maximum available exhaust energy of the diesel engine is 103 kW.
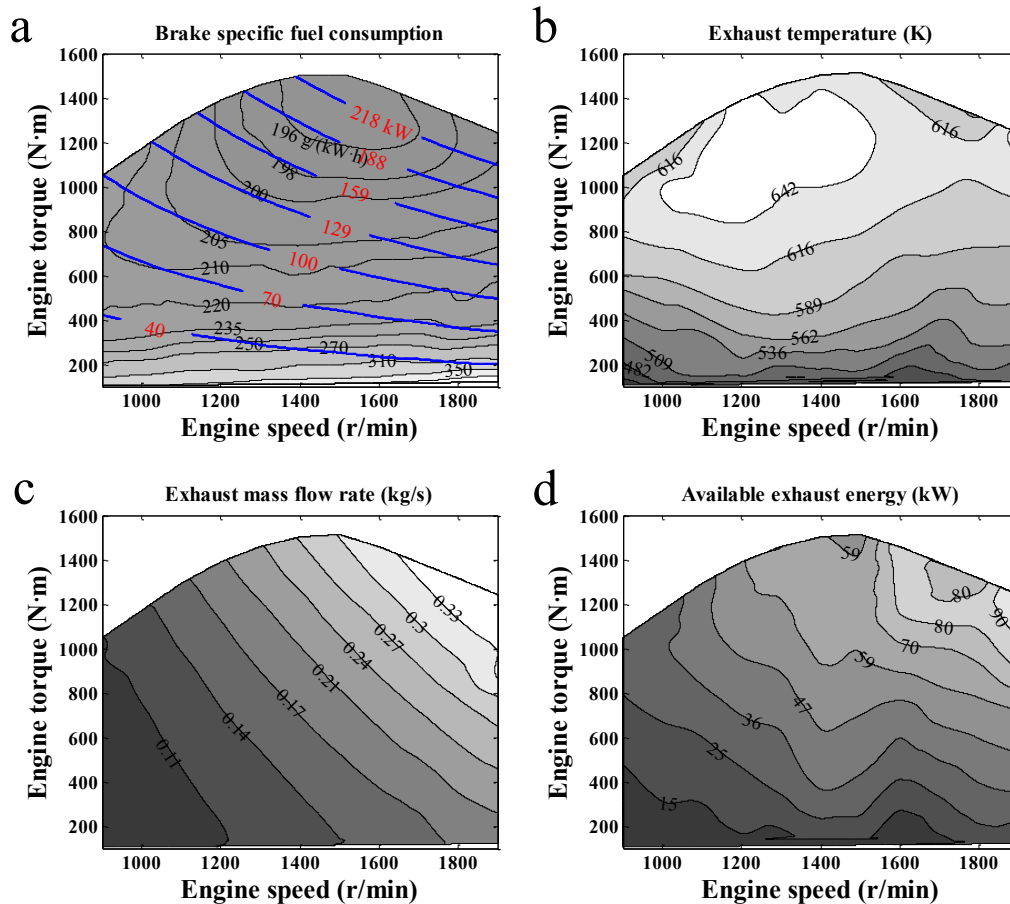

Figure 4: Performance maps of the diesel engine

6. RESULTS AND DISCUSSION

Based on the thermodynamic model established of the ORC system, the optimization using GA for the exhaust waste heat recovery is performed over the whole operating range of the diesel engine. The aim of the optimization process is to achieve the maximum POPA and the minimum EDR.

Figure 5 shows the optimization results of the two objective functions over the whole operating range of the diesel engine. The maximum POPA of the ORC system is presented in Figure 5(a). It can be observed that the maximum POPA is influenced by engine operating conditions significantly, namely available exhaust energy. From Figures 4(d) and 5(a), the maximum POPA increase with the available exhaust energy. This can be explained since the more exhaust energy will lead to an increase in the quantity of evaporated working fluid, which resulted in the increase of the net power output. Over the

whole operating range, the maximum POPA of the ORC system ranges from 0.06 kW/m^2 to 0.74 kW/m^2. At rated condition, the maximum POPA of the ORC system is 0.74 kW/m^2. Figure 5(b) shows the variation of the minimum EDR with the engine speed and load. Similarly to the POPA, engine's operating conditions have a great impact on the EDR. When the diesel engine operates under the medium-low speed and medium-low load conditions, the ORC system can provide lower EDR, whose values range from 0.61 kW to 10.75 kW. It also can be seen that when the diesel engine operates under high speed and high load conditions, the ORC system has the higher EDR. This is due to the exhaust temperature increases with the engine speed and load, which resulted in higher temperature difference between the exhaust gas and the working fluid.
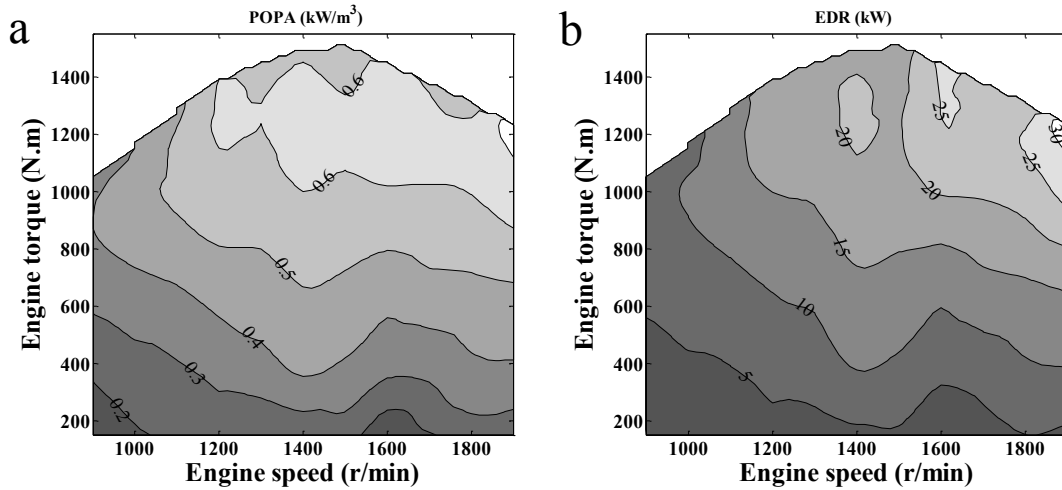

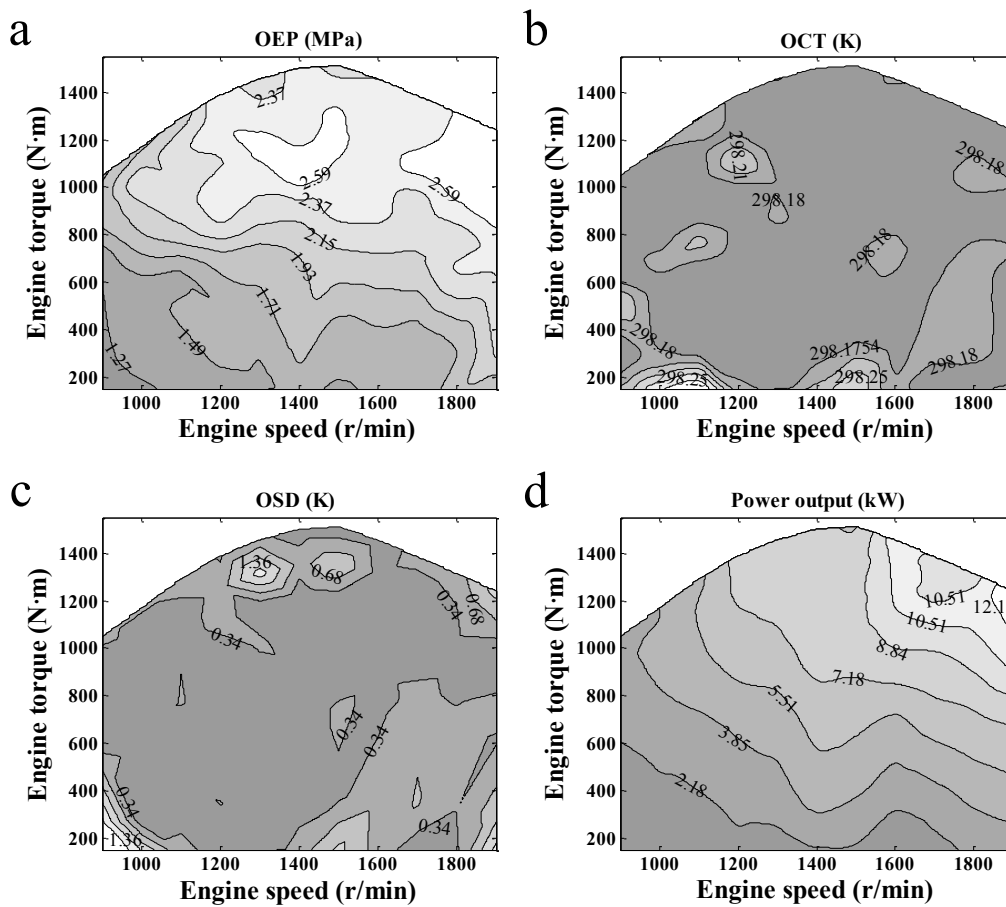**Figure 5:** Optimization results of the two objective functions

Figure 6: Optimization results of operating parameters and power output for the ORC system

Figure 6 shows the optimization results of operating parameters for the ORC system, including OEP (optimal evaporation pressure), OCT (optimal condensation temperature), and OSD (optimal superheat degree). In addition, the variation of the ORC system power output with the engine's operating conditions is presented in Figure 6(d). Figure 6(a) demonstrates that the overall trend about the OEP increases with the increment of engine speed and engine torque. Over the whole operating range, the OEP for the working fluid is in the range of 1.09 MPa to 2.81 MPa. Therefore, it is necessary to select the OEP for each operating condition of the diesel engine. As can be seen in Figure 6(b), the OCT has a small variation in its range, which is nearly kept constant at 298.15 K. As we all known, higher evaporation pressure and lower condensation temperature will lead to an increase in the thermal efficiency of the ORC system. Therefore, the optimization results of the OEP and the OCT are consistent with the analysis based on the first and second laws of thermodynamics. Figure 6(c) shows the variation of OSD over the engine whole operating range. It can be seen that the OSD is in the range of 0 K to 2.13 K. Under the most operating conditions of the diesel engine, the OSD values are in the range between 0 K to 1 K. That is to say, the working fluid does not need to be superheated, which has the similar results for dry organic fluids with Mago *et al.* (2008). In the practical applications of the ORC system, such small OSD cannot be met perfectly due to the limitation of technology problems. From Figure 6(d), it can be concluded that the net power output exhibits the same variation tendency with available exhaust energy presented in Figure 4(d). The net power output increases with increasing available exhaust energy. Over the whole operating range of the diesel engine, the net power output of the ORC system is in the range of 0.32 kW to 13.84 kW. At the engine rated condition, the net power output is 13.84 kW.

Figure 7(a) shows the thermal efficiency of the ORC system over the whole operating range of the diesel engine. It can be observed that the thermal efficiency of the ORC system is mainly affected by the engine torque. When the diesel engine operates at the high load regions, the ORC system presents higher thermal efficiency. This is due to the increase in the net power output obviously at these regions. At engine rated condition, the thermal efficiency of the ORC system reaches the maximum of 13.33%. The POIR (power output increasing rate) is the ratio of the net power output of the ORC system to the engine power output, which is used to evaluate the performance improvement of the diesel engine. The variation of the POIR over the engine whole operating range is shown in Figure 7 (b). It can be observed that the ORC system generates higher POIR at the low torque regions of the diesel engine. That is to say, when the diesel engine operates at the low torque regions, the ORC system can improve the power performance of the diesel engine notably. At the low torque regions of the diesel engine, the POIR is in the range of 3.23% to 9.41%. When the diesel engine operates at the medium-high torque regions, the POIR changes gently.
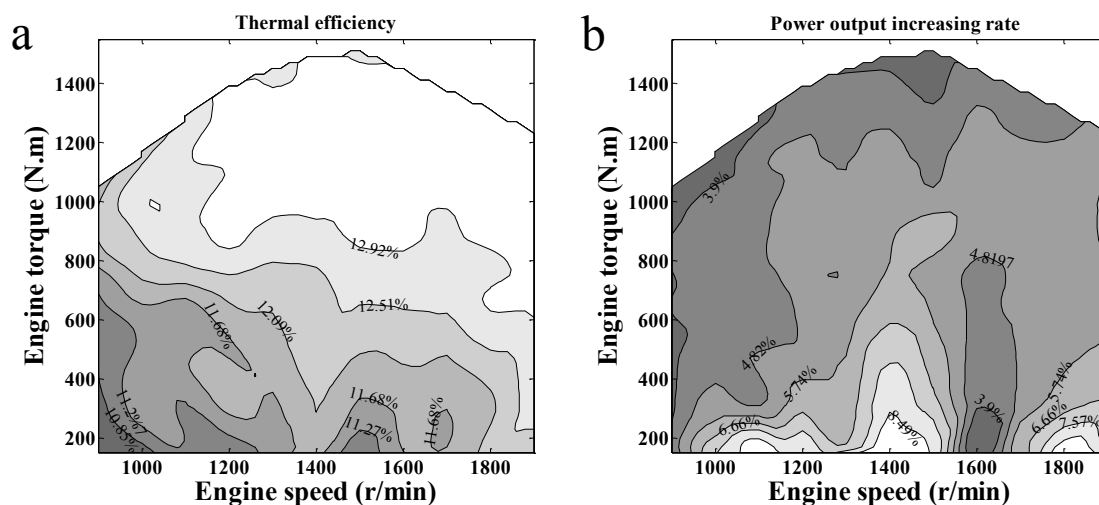
Figure 7: Thermal efficiency of the ORC system and the POIR compared with the diesel engine

Figure 8 shows the ratio of effective heat transfer area to actual area of the evaporator over the whole operating range of the diesel engine. It can be observed that when the diesel engine operates under the medium-low speed or medium-high torque conditions, the ratio of effective heat transfer area to actual area of the evaporator increases with the engine speed and torque. In addition, when the diesel engine operates under the medium-high speed and medium-low torque conditions, the ratio of effective heat transfer area to actual area of the evaporator is mainly affected by the engine torque. That is to say, the operating conditions of the diesel engine have a great effect on the performance of the evaporator. The performances of the evaporator, including heat transfer rate, heat transfer temperature difference, heat transfer coefficient, and heat transfer surface area will vary with the operating conditions of the diesel engine. Over the whole operating range of the diesel engine, the ratio of effective heat transfer area to actual area of the evaporator is in the range of 17.78% to 69.19%.
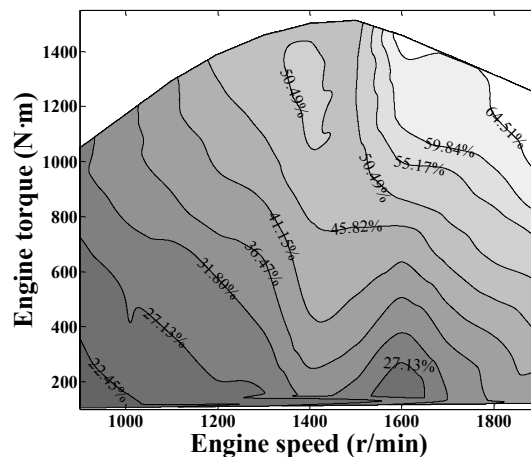
Figure 8: The ratio of effective heat transfer area to actual area of the evaporator

7. CONCLUSIONS

In this study, the parametric optimization and performance analysis of the ORC system using genetic algorithm for recovering exhaust waste heat of a diesel engine are conducted. Based on the first and second laws of thermodynamics, the effects of three key parameters, including evaporation pressure, superheat degree and condensation temperature on the system performances are conducted with net power output per unit heat transfer area and exergy destruction rate as objective functions. The main conclusions can be drawn as follows:
- Over the whole operating range of the diesel engine, the maximum POPA and the net power output are influenced by the engine operating conditions significantly. At rated condition, the maximum POPA and the net power output of the ORC system are 0.74 kW/m^2 and 13.84 kW, respectively.
- The overall trend about the OEP increases with the increment of engine speed and engine torque. Over the whole operating range, the OEP for the working fluid is in the range of 1.09 MPa to 2.81 MPa. The OCT has a small variation in its range, which is nearly kept constant at 298.15 K. The OSD is in the range of 0 K to 2.13 K. Under the most operating conditions of the diesel engine, the OSD values are in the range between 0 K to 1 K.
- For a selected fin-and-tube evaporator, the preheated zone has the maximum heat transfer rate and surface area. Over the whole operating range of the diesel engine, the ratio of effective heat transfer area to actual area of the evaporator is in the range of 17.78% to 69.19%. Considering the OSD almost equals 0, therefore the heat transfer rate and surface area in the superheated zone can almost be neglected.

NOMENCLATURE

$\dot{W}$	power	(kW)
$\dot{Q}$	heat transfer rate	(kW)
$\dot{m}$	mass flow rate	(kg/s)
h	specific enthalpy	(kJ/kg)
s	specific entropy	(kJ/kg.K)
$\dot{I}$	exergy destruction rate	(kW)
T	temperature	(K)
P	pressure	(MPa)
A	area	(m^2)

Greek letters

η	efficiency

Subscript

0	reference state
1-7,2s,5s	state points in the cycle
exp	expander
wf	working fluid
con	condenser
p	pump
eva	evaporator
exh	exhaust
eff	effective
act	actual

REFERENCES

Heberle, F., Preißinger, M., Brüggemann, D., 2012, Zeotropic mixtures as working fluids in Organic Rankine Cycles for low-enthalpy geothermal resources, *Renew. Energy*, vol. 37, no. 1: p. 364-370.

Holland, J. H., 1992, *Adaptation in nature and artificial systems: an introductory analysis with applications to biology, control and artificial intelligence*, MIT Press, Massachusetts.

Li, Y.R., Du, M.T., Wu, C.M., Wu, S.Y. Liu, C., 2014, Economical evaluation and optimization of subcritical organic Rankine cycle based on temperature matching analysis, *Energy*, vol. 68, p. 238-247.

Mago, P.J., Chamra, L.M., Srinivasan, K., Somayaji, C., 2008, An examination of regenerative organic Rankine cycles using dry fluids, *Appl. Therm. Eng.*, vol. 28, no. 8-9: p. 998-1007.

Tong, H., Regner, G., Cowland, C., 2006, Achieving high engine efficiency for heavy-duty diesel engines by waste heat recovery using supercritical organic-fluid Rankine cycle, *SAE paper*, no. 2006-01-3522.

Vaja, I., Gambarotta, A., 2010, Internal Combustion Engine (ICE) bottoming with Organic Rankine Cycles (ORCs), *Energy*, vol. 35, p. 1084-1093.

Walraven, D., Laenen, B., D'haeseleer, W., 2015, Economic system optimization of air-cooled organic Rankine cycles powered by low-temperature geothermal heat sources, *Energy*, vol. 80, p. 104-113.

Wang, E.H., Zhang, H.G., Fan, B.Y., Ouyang, M.G., Zhao, Y., Mu, Q.H., 2011, Study of working fluid selection of organic Rankine cycle (ORC) for engine waste heat recovery, *Energy*, vol. 36, p. 3406-3418.

Wang, T.Y., Zhang, Y.J., Zhang, J., Peng, Z.J., Shu, G.Q., 2014, Comparisons of system benefits and thermo-economics for exhaust energy recovery applied on a heavy-duty diesel engine and a light-duty vehicle gasoline engine, *Energy Convers. Manag.*, vol. 84, p. 97-107.

Zhai, H.X., Shi, L., An, Q.S., 2014, Influence of working fluid properties on system performance and screen evaluation indicators for geothermal ORC (organic Rankine cycle) system, *Energy*, vol. 74, p. 2-11.

Zhang, H.G., Wang, E.H., Fan, B.Y., 2013, Heat transfer analysis of a finned-tube evaporator for engine exhaust heat recovery, *Energy Convers. Manag.*, vol. 65, p. 438-447.

ACKNOWLEDGEMENT

INNOVATIVE ORC SCHEMES FOR RETROFITTING ORC WITH HIGH PRESSURE RATIO GAS TURBINES

Vinayak .Hemadri [1]*, P.M.V Subbarao [2]

[1] Indian Institute of Technology Delhi,
Department of Mechanical Engineering,
New-Delhi, Delhi, India.
vinayakhemadri@gmail.com

[2] Indian Institute of Technology Delhi,
Department of Mechanical Engineering,
New-Delhi, Delhi, India.
pmvs@mech.iitd.ac.in
* Corresponding Author

ABSTRACT

Combined cycle mode of power generation is one of the efficient ways of generation of power. Combined cycles generally use gas turbine in the toping cycle. However, steam is a standard working fluid in bottoming cycle in present units. Recent studies show that Organic working fluids are most suitable for bottoming cycles under certain range of exhaust gas temperatures. Gas turbines with retrofits like intercooling between the compressor stages and regenerator are not suitable for conventional combined cycle operations. Tapping higher amounts of gas turbine exhaust thermal energy for power generation for high pressure ratio, recuperative gas turbine are feasible with organic working fluids.
Present research work aims at introduction of organic Rankine cycle (ORC) as a bottoming cycle in a conventional combined cycle unit. Commercially available gas turbine models like SGT200 (small capacity) and GE LM -6000 (medium capacity) have been considered for the toping cycle. Saturated Toluene, cyclopentane, butane, MM, MDM, MD_2M, D_4, D_5 are studied parametrically to understand energy recovery potential from the gas turbine exhaust. The working fluid with higher potential for power generation is best suited for ORC.
Use of dry working fluids can achieve the same efficiency as that of other organic working fluids, as they create a scope for use of Internal Heat Exchange (IHE). The advantage of IHE can be understood with reduced condenser loads and enhanced potential for waste heat recovery from the source fluid. It can be either used for thermal applications or power applications depending upon its availability. As siloxanes are deep dry working fluids, their internal regeneration capability is good and hence another bottoming cycle can be thought of with lower boiling point organic working fluid in conjunction with primary bottoming cycle. A very innovative scheme with R-245fa and butane bottoming cycles are studied in conjunction with MM saturated cycle. The power recovery potential by using both the bottoming cycle schemes is studied. This scheme increases complexity of the combined cycle. Hence a dual pressure bottoming cycle scheme is developed using MM as the working fluid. Saturated MM is injected with expanding vapor in the turbine (which is in superheated state). Studying the potential of energy recovery in this arrangement is very creative.

1. INTRODUCTION

Efficiency of power generating cycle improves, if the heat rejection occurs at lowest feasible temperature. This is better achieved by generating power in a combined cycle mode. The commercial combined cycles generally use gas turbine in the toping cycle. The exhaust gas from the toping cycle is used to generate steam for the generation of power in the bottoming cycle. Heavy duty gas turbines with higher exit temperatures from the turbine are techno-economically viable for combined cycle applications.

Combined cycle efficiency depends upon the optimal selection of the gas turbine efficiency. Improving gas turbine efficiency does not necessarily improve the combined cycle efficiency. It is useful only if it does not cause high reduction in steam cycle efficiency. For the same gas turbine inlet conditions, the toping cycle attains higher efficiency at higher pressure ratio. But the efficiency of combined cycle with moderate pressure ratio toping cycle is better than the high pressure ratio toping cycle. This is because steam turbine operates with higher inlet pressure and temperature and contributes greater output. Chacartegui *et al.* (2009a) observed that, gas turbines with retrofits like intercoolers and regenerators are not found suitable in conventional gas and steam combined cycles. Jaheeruddien (2004) observed that steam and gas combined cycles with triple pressure bottoming cycle achieve highest efficiency.

Nazzar *et al.(*2003) carried out review of cogeneration opportunity using gas turbine exhaust. Tapping gas turbine exhaust heat to power for a high pressure ratio, recuperative gas turbines needs organic working fluid. It can perform better in the given exhaust temperature range. The integration of ORC with high efficiency, recuperative turbines is carried out by Chacartegui *et al.* (2009b). Bianchi *et al.* (2011) carried out study of different alternative waste heat recovery arrangements like ORC, Stirling engine, inverted Bryton cycle for low to moderate temperature heat sources. Srinivasan *et al.* (2010) and Vaja and Gambarotta (2010) studied integration of ORC with I C engine exhaust.

Colonna *et al. (2006a) (2008a)* developed multi parameter Span and Wagner equations for determination of thermodynamic properties of selected siloxanes. The same authors recommend siloxanes for high temperature ORC applications. Drescher and Bruggemann (2007a) and Fernández *et al.* (2011a) suggested use of intermediate thermo oil (recoverer) circuit to exchange energy with source fluid and organic fluid.

This paper presents introduction of ORC as a bottoming cycle in a combined cycle mode. Commercially available gas turbine models of medium to small power capacity are selected for the toping cycle. Saturated toluene, cyclopentane, butane, MM(Hexamethyldisiloxane), MDM(Octamethyl trisiloxane),MD$_2$M(Decamethyaltetrasiloxane),D$_4$(Octamethylcyclotetrasiloxane),D5(Decamethylcycl opentasiloxane) are studied parametrically to understand energy recovery potential from the gas turbine exhaust. Thermodynamic analysis of the cycle is carried out with the help of software program developed in C++.Thermodynamic properties of the working fluids calculated using Peng Robnsion cubic equations, the constants required to calculate vapor pressure and ideal gas isobaric heat capacity taken from Colonna *et al.* (2006b) (2008b) and Nanan and Colonna (2009) for siloxanes. For toluene, cyclopentane and butane the constants have been referred using Lai Ngoc Anh (2009).

To avail the advantage of internal regeneration using IHE, another bottoming cycle in conjunction with MM bottoming cycle has been discussed in sections to follow. A creative multi pressure evaporative scheme is developed to understand the complete power recovery potential from MM

2. DESCRIPTION OF COMBINED CYCLE

Retrofitting high pressure ratio gas turbine toping cycle with ORC bottoming cycle is certainly a challenging task. An intermediate thermo oil circuit (recoverer) circuit is preferred over direct exchange of energy from gas turbine exhaust to the organic working fluid, keeping the safety aspect in focus. Siemens, SGT 200 and high efficiency aero derivative GE LM -6000 are considered for toping cycle. The energy recovery potential for the bottoming ORC cycle using different working fluids is studied for saturated turbine inlet conditions of the bottoming cycle.

2.1 Description of Toping Cycle

The modern heavy duty gas turbine models are not preferred for integration with ORC. The specifications of the gas turbine toping cycles used in this work are provided in Table 1 High efficiency, intercooled and recuperated toping gas turbine cycles produce exhaust gas temperature in the range 355 to 450ºC. When there is no process steam requirement, taping this potential could be possible effectively through organic working fluids.

Figure 1. represents block and *T-s* diagram for combined cycle power plant with gas turbine toping cycle and ORC bottoming cycle with intermediate thermal (thermo) oil circuit. The atmospheric air enters the compressor at point 1$_{GT}$ and it is pressurized to 2$_{GT}$ and then enters the combustor, where it helps to combust the fuel. The hot gases from the combustor 3$_{GT}$ enter the gas turbine, after passing

through the turbine it leaves at 4_{GT} and enter the recoverer (known as heat recovery steam generator HRSB in steam based combined cycle). Dow therm A, thermo oil is used to exchange energy with turbine exhaust. After exchanging energy to the thermo fluid the exhaust gases move to stack and is let out to the atmosphere at prescribed conditions. Thermo fluid after receiving energy from the hot exhaust gases enter the vapor generator of ORC circuit.

Table 1: Specifications of different gas turbine models [Siemens web page, Chacartegui *et al.* (2009c)]

Parameter	SGT200	GE LM-6000
$\dot{m}_{ex}$(kg/s)	29.3	127
PR	12.2	29.1
TIT(K)		1533
TET(K)	739.15	711
$\dot{W}$(MW)	6.75	43.4
η (%)	31.5 (ele)	41.8

2.2 Description of ORC Bottoming Cycle

For high pressure ratio recuperative gas turbine toping cycles, steam based bottoming cycle is least efficient. In this scenario, using an organic working fluid in bottoming cycle is a novel idea. The organic working fluid enters the pump at point 1 and it is pressurized to turbine pressure at point 2. Then it flows through the internal heat exchanger (if provided in the circuit) and receives energy from the turbine exhaust of bottoming cycle and leaves at point 2a. It enters the vapor generator and leaves at point 3. After expansion in the turbine point 4, it is in superheated state and made to pass through internal heat exchanger (IHE). It leaves IHE at 4a and passes through condenser; after condensing it enters pump at point 1.
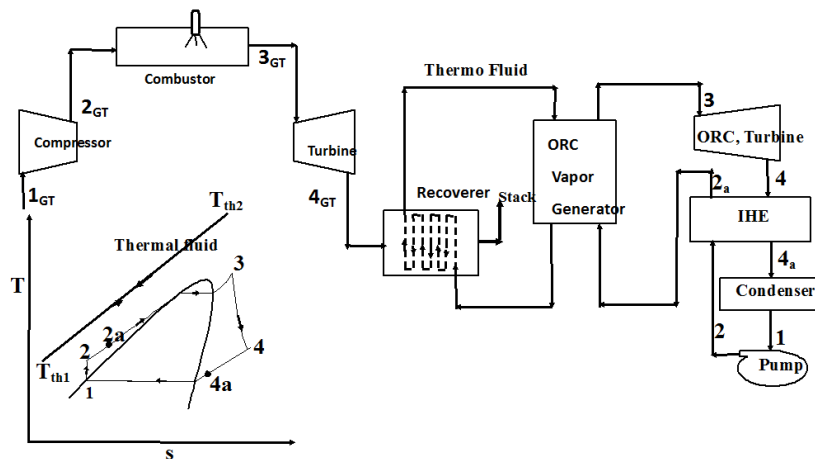

Figure 1: T-s and block diagram for combined cycle power plant

Figure 2. shows temperature T-ΔH diagram for the generalized combined cycle for bottoming cycles without IHE. It represents heat exchange between exhaust gas to intermediate thermo oil as well as thermo oil to the organic working fluid. The exhaust gas and intermediate thermo oil temperatures for different working fluids is given in Table 2 for SGT 200 integration with organic working fluids. It also explains the operating conditions of the condenser of the ORC circuit. The exhaust gas inlet temperature to the recoverer circuit is denoted by T_{4GT}, it is the exit temperature of the flue gas from the toping cycle. The exhaust gas outlet temperature from the recoverer circuit (T_{stack}) is taken as 423.15 K (150ºC) based on the suggestions by Meherwan (2002).The inlet and outlet temperature of the thermo oil at the recoverer circuit is denoted by T_{th1} and T_{th2}. T_{th2} is the inlet temperature of the thermo oil to the vaporizer section of ORC and it leaves the vaporizer at a temperature T_{th1}. The maximum temperature of the working fluid is governed by stability and safety criterion of the working fluid. It is given by T_3 in the Figure 2. Since we have carried out a parametric study it is not presented in Table 2. The minimum

temperature of the working fluid is given by condenser conditions. Minimum condenser pressure of 5kPa is recommended by Drescher and Bruggemann (2007b) and Fernández *et al.* (2011b). The condenser temperature ($T_{con}=T_1$) of 323.15K (50°C) is selected for toluene, cyclopentane, butane and MM as their saturation pressure i.e. condenser operating pressure ($P_{con}=P_1$) is above 5kPa. For the working fluids MDM, MD$_2$M, D$_4$, D$_5$ the condenser temperatures (T_1) is elevated to maintain the minimum acceptable condenser pressure.
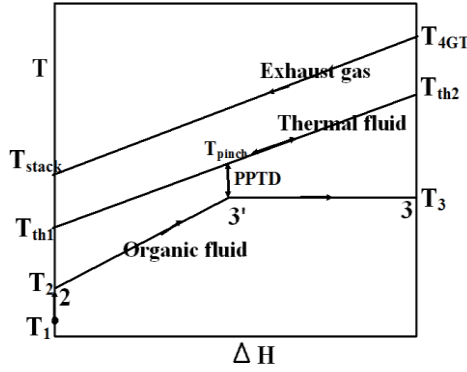

Figure 2: T-ΔH diagram for recoverer and vaporizer

Table 2: Operating temperatures of exhaust gas, thermo oil & working fluid [Refer Figure 2]

Working fluid	T_{4GT} (K)	T_{stack} (K)	T_{th1} (K)	T_{th2} (K)	T_1 (K)	P_1 (kPa)
Toluene	739.15	423.15	343.15	648.15	323.15	9.19
Cyclopentane	739.15	423.15	343.15	648.15	323.15	103.92
Butane	739.15	423.15	343.15	648.15	323.15	494.27
MM	739.15	423.15	343.15	648.15	323.15	17.72
MDM	739.15	423.15	363.15	648.15	343.15	5.83
MD$_2$M	739.15	423.15	393.15	648.15	375.15	5.00
D$_4$	739.15	423.15	383.15	648.15	363.15	5.68
D$_5$	739.15	423.15	410.15	648.15	390.15	5.29

3. INTEGRATION OF SATURATED ORC BOTTOMING CYCLE WITH TOPING GAS TURBINE CYCLE

Saturated ORC schemes are widely accepted schemes in ORC technology in various applications. These are simple and show good efficiency and preferred over superheated and supercritical schemes for dry working fluids. Different dry type of working fluids like toluene, cyclopentane, butane, MM, MDM, MD$_2$M, D$_4$, and D$_5$ are studied parametrically to understand the energy recovery potential from gas turbine exhaust. The condition of the vapor leaving the turbine is superheated for dry type working fluids. Hence cycles with internal heat recovery using IHE is also studied. An innovative R-245fa bottoming cycle in conjunction with MM bottoming cycle is also studied to understand total recovery potential from gas turbine exhaust. The following assumptions are made in the analysis of the cycle.

- Isentropic efficiency of turbine and pump are assumed as 0.88 and 0.80
- The effectiveness of IHE is 0.8
- PPTD ≥10°C

3.1 Thermodynamic analysis of the cycle

Selection of pinch point is one of the important parameters in the combined cycle analysis. It can be defined as the temperature difference between the exhaust gas (thermo oil in this case) leaving the evaporator section and saturation temperature of the working fluid at the turbine inlet pressure. It is the lowest temperature difference existing in the evaporator. The calculation of the pinch point and mass flow rates of working fluid is carried out by conducting energy balance. Refer Figure 2. For the notations.

A) Energy exchange in recoverer to calculate mass flow rate of thermal fluid:

Energy lost by the exhaust gas= Energy gained by the thermal fluid

$$\dot{m}_{ex} \times C_{p,ex} \times (T_{4GT} - T_{stack}) = \dot{m}_{th} \times C_{p,th} \times (T_{th2} - T_{th1}) \qquad (1)$$

B) Energy exchange in vaporizer section of ORC bottoming cycle to calculate mass flow rate of working fluid:

Energy lost by thermal fluid=Energy gained by the working fluid

$$\dot{m}_{th} \times C_{p,th} \times (T_{th2} - T_{th1}) = \dot{m}_{wf} \times (h_3 - h_2) \qquad (2)$$

C) Energy exchange in the evaporator section of the vaporizer to calculate PPTD

$$\dot{m}_{th} \times C_{p,th} \times (T_{th2} - T_{pinch}) = \dot{m}_{wf} \times (h_3 - h_3') \qquad (3)$$

$$PPTD = T_{pinch} - T_3' \tag{4}$$

D) The first law efficiency for heat engine can be expressed as:

$$\eta_{th} = \frac{Net\ work\ output}{Heat\ input} = \frac{\dot{m}_{wf} \times (w_t - w_p)}{\dot{Q}_{in}} \tag{5}$$

3.1 Integration of Toping Cycle SGT200 with Bottoming ORC Saturated Cycles

In this section integration of different ORC schemes with small capacity gas turbine SGT200 is discussed. Toluene, cyclopentane, butane, MM, MDM, MD$_2$M, D$_4$, D$_5$ working fluids have been studied parametrically to understand the potential for power generation, when connected with gas turbine exhaust. The working fluid with higher potential for power generation is best suited for ORC integration.

The integration with gas turbine cycle for all working fluids considered are studied parametrically at various reduced pressures (P$_r$) (0.6-0.9). Initially cycles without internal regeneration have been studied followed by cycles with internal regeneration.

Table 3 shows the results obtained for saturated cycles at the maximum permissible temperature limit for individual fluid, expressed in the form of reduced temperature T$_r$ (T$_{max}$/T$_c$). The corresponding saturation pressure is also expressed in the form of reduced pressure P$_r$ (P$_{max}$/P$_c$). T$_{max}$ =T$_3$, is permissible maximum inlet temperature for the working fluids for integration with SGT200. Toluene is considered at 0.85 P$_{max}$/P$_c$, understanding its safe limit of evaporation for saturated cycles as provided by Chacartegui *et al.* (2009d).

Power produced by any power generating cycle is a function of the mass flow rate of the working fluid and the specific net work output (w_{net}=w_t- w_p) of the working fluid. It can be observed that mass flow rate of toluene cycle is less compared to other working fluids, but specific net work output is considerably high over other working fluids. This can be shown with higher level of power recovery from integration with a particular heat source. After toluene, cyclopentane and MM show better exhaust heat to power conversion capabilities. The efficiency of the cycle without IHE is studied initially. Except for butane the potential for internal heat exchange using turbine exhaust is good for all the working fluids considered and hence cycles with IHE have been studied for other working fluids. It can be observed that toluene shows highest efficiency of 25.75% and D$_5$ exhibits lowest efficiency with a value of 11.38%. The combined cycle efficiency is calculated for gas turbine and ORC integration. The efficiency of the toping gas turbine cycle is referred from Siemens web page and its value is taken as η_{GT} = 0.334. Highest combined cycle efficiency of 54.11% is observed for toluene with integration with SGT 200.

$$\eta_{cc} = \eta_{GT} + \eta_{ORC} - (\eta_{GT}.\eta_{ORC}) \text{ [Murugan and Subbarao (2010)]} \tag{6}$$

Table 3: Results for saturated ORC cycles for all working fluids at 0.9P$_r$

Working fluid	T$_r$	P$_r$	$\dot{m}_{wf}$ (kg/s)	w$_{net}$ (kJ/kg)	$\dot{W}$ (MW)	$\eta_{(-IHE)}$ %	$\eta_{(+IHE)}$ %	η_{cc} %
Toluene	0.978	0.850	14.847	183.401	2.723	25.75	31.09	54.11
Cyclopentane	0.984	0.900	18.622	117.574	2.189	20.71	22.49	48.38
Butane	0.985	0.900	25.601	57.082	1.461	13.82	----	42.60
MM	0.988	0.900	20.656	78.364	1.619	15.31	24.59	49.78
MDM	0.990	0.900	20.196	76.060	1.536	14.53	27.44	51.68
MD$_2$M	0.989	0.900	21.035	63.105	1.327	12.55	25.53	50.41
D$_4$	0.988	0.900	23.191	63.058	1.462	13.83	26.53	51.07
D$_5$	0.989	0.900	22.908	52.552	1.204	11.38	24.11	49.46

Parametric study of all the working fluids is done for the P$_r$ range 0.6-0.9. Figure 3(a). shows power recovery potential of all the working fluids. Toluene shows highest power recovery at all the reduced pressures and power recovered by the D$_5$ is least. This makes toluene most competent working fluid for the integration at all inlet conditions of the turbine. The contribution of bottoming cycle to the total power produced by the combined cycle is expressed by ratio of % $\dot{W}_{bot}$ /$\dot{W}_{tot}$. Figure 3(b) shows % $\dot{W}_{bot}$/$\dot{W}_{tot}$ for toluene, cyclopentane and MM the top three power recovery working fluids. As toping cycles for all the working fluids is same it is obvious that toluene shows higher ratio compared to other

two. Similarly combined cycle efficiency at various reduced pressures is shown in Figure 3(c). The combined cycle efficiency with toluene as the bottoming cycle is highest at all the reduced pressure ranges and it is followed by MM and cyclopentane.
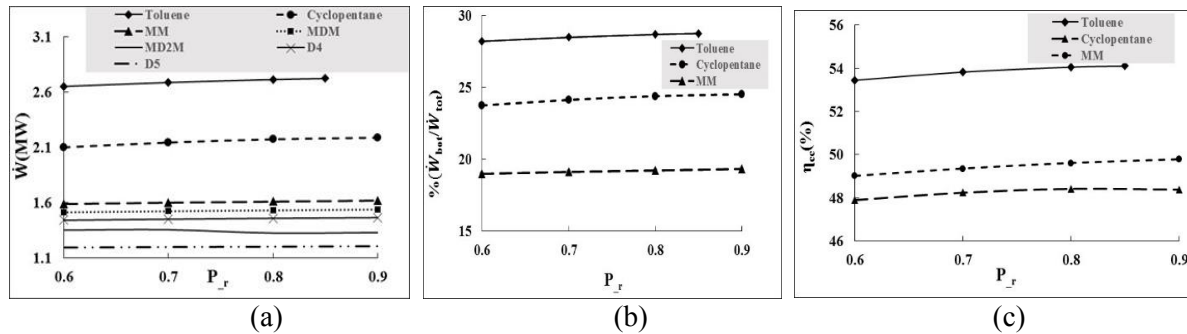

(a)   (b)   (c)

Figure 3 (a, b, c): Total power recovered, $\% \dot{W}_{bot}/\dot{W}_{tot,}$ η_{cc}

3.2 Integration of Toping Cycle GELM-6000 with Bottoming ORC Saturated Cycles

The integration of the saturated ORC with different working fluids with medium capacity gas turbine GE LM- 6000 is done in a similar way to SGT 200. The exhaust gas enters the recoverer at 711K at a mass flow rate of 127kg/s and enters the stack at a temperature of 150°C. Thermo fluid is maintained at a temperature of 343.15K and 648.15K at the inlet and out let of the recoverer. Table 4 shows the results obtained for the parametric integration of GE LM- 6000 with different working fluids at $0.9P_{\_r}$. Power recovery potential of toluene is highest as compared to other working fluids, similar to SGT 200 integration.

Table 4: Results for the parametric integration of GELM-6000 with different working fluids

Working fluid	$T_{\_r}$	$P_{\_r}$	$\dot{m}_{wf}$ (Kg/s)	$\dot{W}$ (MW)	$\eta_{(-IHE)}$ %	$\eta_{(+IHE)}$ %	η_{cc} %	$\%(\dot{W}_{bot}/\dot{W}_{tot})$
Toluene	0.978	0.85	58.43	10.72	25.07	30.10	59.32	19.80
Cyclopentane	0.984	0.9	73.28	8.62	20.70	22.49	54.89	16.56
MM	0.988	0.9	81.28	6.37	15.31	24.59	56.11	12.80
MDM	0.990	0.9	79.47	6.04	14.53	27.44	57.77	12.22
MD$_2$M	0.989	0.9	82.77	5.22	12.55	25.53	56.66	10.74
D$_4$	0.988	0.9	91.26	5.75	13.83	26.53	57.24	11.70
D$_5$	0.989	0.9	90.15	4.74	11.38	24.11	55.83	9.84

3.3 Impact of Internal Heat Exchange on Power Recovery:

The advantage of IHE can be understood with reduced condenser loads and enhanced potential for waste heat recovery from the source fluid. It can be either used for thermal applications or power applications depending upon its availability.

Figure 4. shows the advantage of using IHE to the circuit. The temperature of the working fluid increases from T_2 to T_{2a}. And due to this heat addition in a constant pressure process is h_3-h_{2a} instead of h_3-h_2 as represented in the diagram. The effect of this can be observed in thermo oil circuit also, the thermo oil leaves the vaporizer at $T_{th1'}$ instead of T_{th1}. This potential generated due to IHE effect, can be availed either by utilizing it for thermal application or else for power generation. This potential is very small for toluene and cyclopentane and it can be used for small process heat requirement of the industry. As siloxanes are deep dry working fluids, their internal regeneration capability is good and hence another bottoming cycle can be thought with lower boiling point organic working fluid. For the sake of analysis, MM cycle at $0.9P_{\_r}$ is considered to integrate with another bottoming cycle. R-245fa and butane bottoming cycles are studied in conjunction with MM saturated cycle at $0.9P_{\_r}$ by using the potential $T_{th1'}$-T_{th1}. As R-245fa produces higher power with the integration and it is presented in the next section.
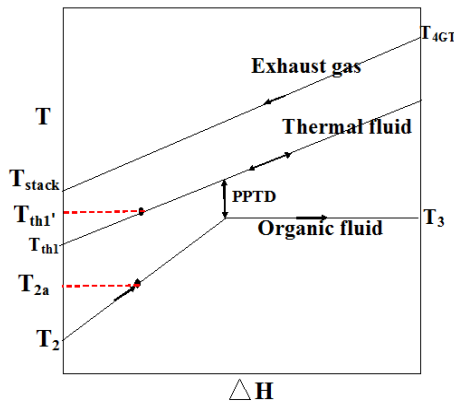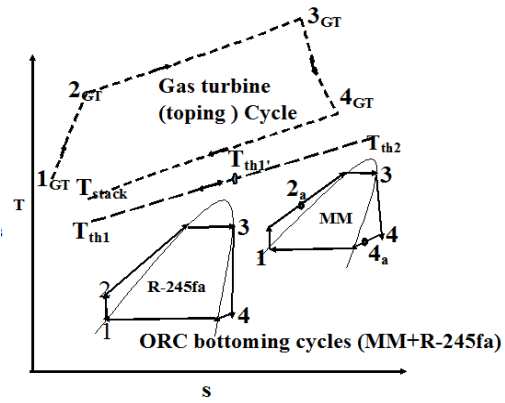
Figure 4: IHE effect on thermal oil circuit

Figure 5: Integration of MM+R-245fa bottoming cycles

3.4 Saturated R-245fa Bottoming Cycle in Conjunction with MM at 0.9P_r for Integration of GE-LM 6000

A very innovative cycle has been developed by understanding the extra potential created due to IHE effect. Figure 5. Shows T-s diagram for saturated R-245fa bottoming cycle which is used in conjunction with MM cycle. The thermo oil leaving the vaporizer of the MM circuit ($T_{th1'}$) is made pass through another vaporizer in which it interacts with low boiling point working fluid R-245fa. After exchanging energy it leaves the vaporizer of R-245fa at T_{th1}, which is the inlet temperature to the heat recoverer. The saturated R-245fa vapor enters the turbine at point 3 after expansion in the turbine the state of the working fluid is slightly superheated. Hence the use of internal heat exchanger is eliminated. The turbine exhaust vapor enters the condenser at point 4.After condensing at point 1 it is pumped to turbine pressure. As this bottoming cycle uses two ORC circuits, it increases complexity of the design, it also adds extra capital investment on all ORC components. The cost associated with this arrangement is not being discussed in this work.

Table 5 shows the parametric study carried for R-245fa cycle for the reduced pressure range of 0.6 to 0.9 P_r. It can be observed that saturated R-245fa at a reduced pressure of 0.9 P_r contributes power of 1.76MW, it is the maximum power obtained from the arrangement. Total power obtained by the two bottoming cycles (MM+R-245fa) is 8.13MW. The efficiency of the combined cycle improves considerably by converting this potential into power. A combined cycle efficiency of 69.57 % is reached by the combination of MM at 0.9 P_r and R-245fa also at 0.9 P_r. The contribution of the bottoming cycle to the combined cycle power is also improved by incorporating this scheme.

Table 5: Results for parametric optimization of R-245fa bottoming cycle used in conjuction with MM at 0.9P_r for integration with GE LM-6000

P_r	$\dot{m}_{wf}$ (kg/s)	$\eta_{(-IHE)}$ %	$\dot{W}$ (MW)	$\dot{W}_{bot}$ (MM+R245fa)	η_{cc} (%)	%($\dot{W}_{bot}/\dot{W}_{tot}$)
0.90	58.22	12.63	1.76	8.13	69.57	15.77
0.80	57.24	13.27	1.72	8.09	70.16	15.72
0.70	57.10	13.73	1.67	8.04	70.58	15.63
0.60	57.36	13.99	1.58	7.95	70.82	15.49

4. MULTI PRESSURE EVAPORATION FOR ORC BOTTOMING CYCLES

In this section multi pressure evaporative scheme for bottoming cycle ORC plant is being studied for MM as the working fluid. A very innovative case has been developed and analyzed by using MM as the working fluid.

Due to internal heat exchange between turbine exhaust vapor and exit liquid from pump, the temperature of the thermo oil leaving the vaporizer section of the ORC is increased. This potential has

been utilized by running another bottoming cycle (R-245fa in conjunction with MM cycle). The total power produced by the bottoming cycle by both MM and R245fa is 8.13MW at 0.9P_r as discussed in previous section. It is the maximum power recovery from the combination. Of course it increases the power recovery potential of the bottoming cycle, but it also increases complexity and cost of the cycle by adding one more ORC cycle (components) to the circuit.

4.1. Discussion of Dual Pressure Evaporative MM Cycle

The idea of generating MM vapor and injecting it in the turbine, instead of R-245fa was futile because the condition of MM at lower pressures is superheated and it is not supported by thermodynamics. Therefore a new idea is developed in which instead of generating superheated vapor at the lower pressure (pressure of injection), saturated vapor is being generated and injected in MM turbine. It does lead to slight reduction in exergy of expanding vapor, but it is important that it should produce power comparable to MM and R-245fa combination. After studying feasibility of evaporation at different pressures, it is decided to evaporate MM at 0.3269P_r (0.639MPa) for injection into the turbine.

The block and T-s diagram for the scheme is shown in Figure 6.The condensate from the condenser with flow rate $\dot{m}_{wf}$ at point 1 is divided into two streams: mass $\dot{m}_{wf1}$ and $\dot{m}_{wf2}$. The mass $\dot{m}_{wf1}$ is pressurized to high pressure in high pressure pump, (2). It is internally regenerated by using the vapor from the exit of the turbine to point, (2a). The regenerated high pressure fluid then enters the high pressure vapor generator at point 2a. It leaves the vapor generator in a saturated state with respect to the turbine inlet pressure, (3). At the same state it enters the turbine and expands till point 4. The condensate $\dot{m}_{wf2}$ is pumped through low pressure pump at 2', the fluid leaving the low pressure pump is internally regenerated using turbine exhaust in the low pressure regenerator to point 2a'. It then enters the low pressure vapor generator and heated till point 4. It is injected into the turbine at the same state. The state of low pressure vapor at point 4 is saturated and the state of the expanding vapor is superheated at point 4. It leads to small amount of exergy destruction of expanding vapor. The temperature of the mixed stream is calculated by this approximation.

Mass flow rate of vapor expanding in turbine at high pressure: $\dot{m}_{wf1}$ =81.284kg/s

Mass flow rate of low pressure vapor: $\dot{m}_{wf2}$ =10.8kg/s

Total mass:$\dot{m}_{wf} = \dot{m}_{wf1} + \dot{m}_{wf2} = 92.084$kg/s $\qquad$ (7)

Temperature of the expanding vapor at point 4:$T_{4,sup}$=480K

Temperature of the low pressure saturated vapor:$T_{4,sat}$=451.98K

Mass fraction high pressure expanding vapor: $x_h = \dfrac{\dot{m}_{wf1}}{\dot{m}_{wf}}$ $\qquad$ (8)

Mass fraction of low pressure vapor:$x_l = \dfrac{\dot{m}_{wf2}}{\dot{m}_{wf}}$ $\qquad$ (9)

Hence temperature of the mixed stream is approximated as:
$$T_4 = x_h \times T_{4,sup} + x_l \times T_{4,sat} \approx 477\text{K}$$
$\qquad$ (10)

As both the streams mixing at the same pressure, P$_4$=0.639MPa

The further expansion of the mixed stream is considered from P$_4$, T$_4$ to condenser condition till point 5. At point 5 the total mass flow rate of working fluid is divided into two steams. $\dot{m}_{wf1}$ goes to high pressure regenerator and $\dot{m}_{wf2}$ enters low pressure regenerator. After exchanging energy with feed fluid in IHE, both the streams mix together and enter the condenser at point 1' and the cycle continues.

4.2. Thermodynamic analysis of the cycle

Rate of work obtained from high pressure vapor before mixing (3-4) in the turbine:
$$\dot{W}_{t1} = \dot{m}_{wf1} \times (h_3 - h_4)$$
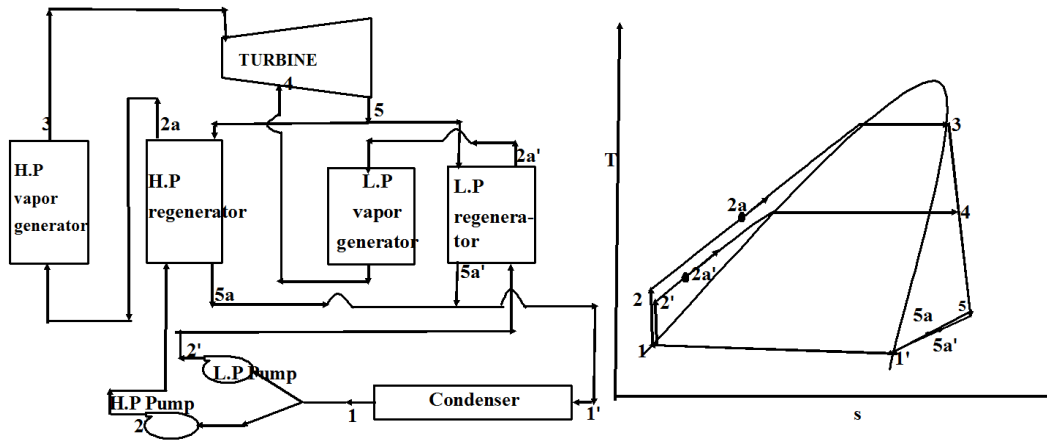$\qquad$ (11)

Figure 6: Block and T-s diagram for multi pressure evaporation

Rate of work obtained from the mixed stream (4-5) the turbine:

$$\dot{W}_{t2} = \dot{m}_{wf} \times (h_4 - h_5) \tag{12}$$

Total rate of work obtained: $\quad \dot{W}_t = \dot{W}_{t1} + \dot{W}_{t2}$ (13)

Rate of work in put to high pressure pump: $\quad \dot{W}_{p1} = \dot{m}_{wf1} \times (h_2 - h_1)$ (14)

Rate of Work in put to low pressure pump: $\dot{W}_{p2} = \dot{m}_{wf2} \times (h_2' - h_1)$ (15)

Total rate of pump work: $\quad \dot{W}_p = \dot{W}_{p1} + \dot{W}_{p2}$ (16)

Net rate of work obtained : $\quad \dot{W}_{net} = (\dot{W}_t - \dot{W}_p)$ (17)

Rate of energy input to the cycle: $\dot{Q}_{in} = \dot{m}_{wf1} \times (h_3 - h_{2a}) + \dot{m}_{wf2} \times (h_4 - h_{2a}')$ (18)

Efficiency of the cycle: $\eta_{th} = \dfrac{Net\ rate\ of\ work\ obtained}{Total\ rate\ of\ Energy\ input} = \dfrac{W_{net}}{\dot{Q}_{in}}$ (19)

Table 6: Results for multi pressure evaporation for MM

$T_{\_r3}$	$P_{\_r3}$	$T_{\_r4}$	$P_{\_r4}$	$\dot{m}_{wf1}$ (kg/s)	$\dot{m}_{wf2}$ (kg/s)	$\dot{W}_t$ (kW)	$\dot{W}_p$ (kW)	$\dot{W}_{net}$ (kW)	$\dot{Q}_{in}$ (kW)	η (%)
0.98	0.90	0.87	0.33	81.28	10.80	7540.50	251.48	7289.00	28526.44	25.55

Table 6 shows the results obtained for multi pressure evaporation. It can be observed that net power produced from the multi pressure evaporation is 7.289 MW and the total power produced by bottoming cycle of saturated MM and saturated R245fa at 0.9P_r is 8.13 MW. There is a reduction of power by 841kW by injecting MM saturated vapor in to the turbine, but this cycle is less complicated and simple as it consists only single ORC in the bottoming cycle.

5. CONCLUSIONS

The potential for power recovery using different organic working fluids for saturated ORC schemes is studied for high pressure ratio recuperative gas turbine toping cycles. The cycles are studied for both without IHE and with IHE schemes. Toluene shows highest recovery potential over all the working fluids considered. It generates a power of 2.723MW for integration with SGT200. The advantage of using IHE not only improves efficiency but also creates opportunity for extra power generation using low boiling point working fluid. MM bottoming cycle in conjunction with another low boiling point working fluid (R245fa) recovers a power of 8.13MW(MM+R245fa) for integration with GE-LM 6000. This is lower than toluene bottoming cycle which produces 10.72 MW of power from integration .A multi pressure cycle using MM as the working fluid is discussed at the end for the integration of GE-LM 6000. The advantage of IHE is utilized to generate saturated vapors of MM and injected into the expanding vapor of MM bottoming cycle. The power recovery capability of this innovative idea is compared with (MM+R245fa) combined bottoming cycle. Even though multi pressure evaporation of MM produces less power but it reduces complexity of the cycle.

NOMENCLATURE

List of Symbols				Subscripts	
$\dot{m}$	Mass flow rate	kg/s		cc	Combined cycle
PR	Pressure ratio	(-)		GT	Gas turbine
h	Enthalpy	kJ/kg		th	Thermo
P	Pressure	MPa		wf	Working fluid
T	Temperature	K		sup	Superheated
s	Entropy	kJ/(kg-K)		sat	Saturated
TIT	Turbine inlet temperature	K		bot	Bottoming
TET	Turbine exit temperature	K		tot	Total
IHE	Internal heat exchanger	(-)		t	Turbine
$\dot{W}$	Power	MW		p	Pump
w	Specific work output	kJ/kg		c	Critical
C_p	Specific heat	kJ/(kg-K)		sup	Superheated
T_r	Reduced temperature	(-)		sat	Saturated
P_r	Reduced pressure	(-)			
Greek Symbols					
η	Efficiency	(%)			

REFERENCES

Bianchi M., De Pascale A., 2011, Bottoming cycles for electric energy generation: Parametric investigation of available and innovative solutions for the exploitation of low and medium temperature heat sources, *Applied Energy*, 88, 1500–1509.

Chacartegui R., Sánchez D., Muñoz J.M., Sánchez T., 2009, Alternative ORC bottoming cycles FOR combined cycle power plants, *Applied Energy*, 86, 2162–2170.

Colonna P., Nannan N.N., Guardone A., Lemmon E.W.,2006, Multiparameter equations of state for selected siloxanes*, Fluid Phase Equilibria*, 244, 193–211.

Colonna P., Nannan N.N., Guardone A., 2008, Multiparameter equations of state for selected siloxanes*, Fluid Phase Equilibria*, 263, 115-130.

Drescher U., Bruggemann D., 2007, Fluid selection for the Organic Rankine Cycle (ORC) in biomass power and heat plants, *Applied Thermal Engineering*, 27, 223–228.

Fernández F.J., Prieto M.M., Suárez I.,2011, Thermodynamic analysis of high-temperature regenerative organic Rankine cycles using siloxanes as working fluids, *Energy,*36, 5239–5249.

Jaheeruddien S.K., 2004, Optimization of Erection of Steam Side of a Combined Cycle Power Plant, M-Tech Thesis, Indian Institute of Technology, Delhi.

Lai Ngoc Anh.,2009, Thermodynamic data of working fluids for energy engineering, Ph.D. Thesis, University of Natural Resources and Applied Life Sciences, Vienna.

Meherwan P.B., 2002, Hand book for cogeneration and combined cycle power plants, ASME Press, New York.

Murugan R.S., Subbarao P.M.V., 2008, Efficiency enhancement in a Rankine cycle power plant: combined cycle approach. Proc. Inst. Mech. Eng. Part A J. Power Energy. 222:753–760.

Nannan N.R., Colonna P., 2009, Improvement on multiparameter equations of state for dimethylsiloxanes, *Fluid Phase Equilibria*, 280,151–152.

Najjar Y.S.H., Akyurt M., Alrabghi O.M., Alp T., 1993, Cogeneration with gas turbine engines, *Heat Recovery Systems and CHP*, vol.13, no.5:p.471-480.

Siemens Gas Turbine, Website: http://www.energy.siemens.com/hq/en/fossil-power-generation/gas-turbines/sgt-200.htm, [accessed on 01.12.2014].

Srinivasan K.K.,Mago P.J., Krishnan S.R.,2010, Analysis of exhaust waste heat recovery from a dual fuel low temperature combustion engine using an Organic Rankine Cycle, *Energy,*35, 2387-2399.

Vaja I., Gambarotta A., 2010, Internal Combustion Engine (ICE) bottoming with Organic Rankine Cycles (ORCs), *Energy,* 35, 1084–1093.

UTILIZATION OF WASTE HEAT FROM INTERCOOLED, REHEAT AND RECUPERATED GAS TURBINES FOR POWER GENERATION IN ORGANIC RANKINE CYCLES

Xurong Wang, Yi Yang, Mingkun Wang, Ya Zheng, Jiangfeng Wang, Yiping Dai*

Xi'an Jiaotong University, School of Energy and Power Engineering,
Xi'an, Shaanxi, P.R. China
*ypdai@mail.xjtu.edu.cn

ABSTRACT

Organic Rankine cycle (ORC) is a very attractive technology for the conversion of low-grade thermal energy into electrical and/or mechanical energy. As the ORC has a wide range of power, it can recover the waste heat from power cycles such as turbines and/or microturbines of gas. The ORC bottoming cycle is currently incorporated into the exhaust of recuperative gas turbines to further lower the temperature of the exhaust gas, yielding similar overall efficiency to that of conventional gas turbine and steam combined cycles. However, a certain amount of thermal energy in the intercooler is not effectively utilized in the intercooled gas turbine cogeneration cycles. The temperature of the compressed air at the intercooler inlet could be found about 120 ℃-250 ℃. This is an ideal energy source to be used in an ORC for power generation.

In this investigation, a thermodynamic analysis was carried out on combined cycles comprising recuperated, intercooled and reheat gas turbines and two ORCs (recuperated ICRHGT-ORCs) to recover waste heat from the intercooler and the exhaust of recuperated gas turbine. Three existing gas turbines were performed as the topping cycles with appropriate modifications. The following organic fluids were considered as the working fluids in ORCs: R123, R245fa, toluene and cyclohexane. A computer program was then designed for computations of system performance. Thermodynamic analyses were performed to study the effects of parameters including evaporator temperatures and degrees of superheat at the ORC turbine inlet on the combined cycle performance. These parameters were then optimized with thermal efficiency as the objective function by means of a genetic algorithm. It was found that all the three modified gas turbines with bottoming ORCs had higher performance, with thermal efficiency increase of 7.8% to 15.2%, in comparison to their original values.

1. INTRODUCTION

In the low-grade waste heat recovery field, the organic Rankine cycle (ORC) gives a good performance to convent low and medium temperature heats such as renewable energies like solar, wind and geothermal power, low enthalpy heat rejected by industry and exhaust gas of gas turbines into electrical or/and mechanical energy. Much work has been carried out on the application and performance of ORCs (Angelino *et al.*, 1998, Hung, 2001, Wei *et al.*, 2007, Tchanche *et al.*, 2011, Vélez *et al.*, 2012). Typically, the ORC as a bottoming cycle in combined power plants is a promising process to enhance the system efficiency and reduce the fossil fuel consumption. For gas turbine applications, the combination of an ORC bottoming cycle can reduce design and development cost.

The modularity and wide range of power of the ORC system allow repowering of the existing gas turbines to use the thermal power of the exhaust gases typically available in the temperature range of 250 – 300 ℃ and produce electricity by acting a bottoming cycle. Najjar and Radhwan (1988) proposed a cogeneration system by combining a gas turbine cycle with an ORC bottoming cycle. The results showed that a global combined cycle efficiency slightly below 45.2% with an efficiency improvement of about 54% by using R22 as the organic fluid. Invernizzi *et al.* (2007) investigated the

performance of a 100 kW size micro-gas turbine and ORC combined cycle. They reported that the micro-gas turbine could obtain an additional 45 kW of electricity and an efficiency improvement of 30% to 40%. Yari (2008) conducted parametric analysis and comparison of the micro turbine ORC with or without internal heat exchanger combined cycles. The effects of several parameters on the combined cycle performance were also discussed. Clemente *et al.* (2013) studied a number of different expanders for ORCs with the aim to design a bottoming cycle for a 100 kW recuperated gas turbine. A careful review of these numerous works shows that the bottoming ORC cycle is designed to recover waste heat from the flue gases of a small recuperative gas turbine. However, combined cycles comprising high efficiency heavy duty gas turbines and ORCs in the medium and large scale power generation have not been carefully analyzed. Chacartegui *et al.* (2009) found this shortage and then studied the use of ORC bottoming cycles incorporated into the exhaust of recuperated gas turbines or very high pressure ratio gas turbines, which are characterized by their very high efficiency but low exhaust temperature. Moreover, they modified the topping gas turbines by adding intercooled compression and reheat, showing that the efficiency of the modified combined cycle was up to 3% points higher than conventional single pressure steam combined cycles, depending on the working fluid.

By adding an intercooled compression to the modern high efficiency gas turbines, the low pressure compressor (LPC) outlet temperature varies from 120 ℃ to 250 ℃, depending on the LPC pressure ratio (Bhargava *et al.*, 2002). This amount thermal energy currently is rejected to the coolant like atmospheric air, cooling water or sea water. It is noticed that there may be a continuous increase of efficiency improvement of the current gas turbine and ORC combined cycle by designing an additional ORC bottoming cycle to recover the heat from the intercooled compression. In addition, a limited amount of work has been done on the evaluation of a combined cycle comprising a recuperated, intercooled and reheat (ICRH) gas turbine and two ORC bottoming cycles in cogeneration applications.

This paper investigated the possibility of increasing the performance of recuperated ICRH gas turbines by combining two ORCs which recover the waste heat from the intercooler and the exhaust of recuperated gas turbine. Three existing gas turbines with appropriate modifications were performed as the topping cycles. For the ORC bottoming cycles, the following organic fluids were considered as the working fluids: R123, R245fa, toluene and cyclohexane. A computer program was designed for computations of system performance. Four key parameters in the bottoming cycles including evaporator temperatures and degrees of superheat at the ORC turbine inlet were evaluated to analysis their effects on the combined cycle thermal efficiency. These parameters were then optimized with thermal efficiency as the objective function by means of a genetic algorithm (GA).

2. RECUPERATED ICRHGT-ORCS COMBINED CYCLE DESCRIPTION

In this section, two ORC bottoming cycles are incorporated into the exhaust and two successive compression stages, respectively, of a recuperated ICRH gas turbine cycle, as shown in Figure 1. The purpose of such analysis is to evaluate the interest of the proposed bottoming cycles when integrated with the recuperated ICRH gas turbines. In order to use the exhaust waste heat, an ORC is employed through an evaporator to further decrease the exhaust temperature. Additionally, a second ORC is designed through a suitable evaporator 2 to recover waste heat from the compressed air leaving the LPC.

For the topping cycle, three existing gas turbines are selected and modified to be converted into the recuperated ICRH gas turbine cycles. The selected gas turbines include a modern heavy duty gas turbine Alstom GT 24, a high efficiency aeroderivative gas turbine GE LM-6000 (dry) and a recuperated and intercooled gas turbine Rolls-Royce WR 21. The examples give a large power range from 25 MW to 179 MW. This study converted each of the selected gas turbines into a recuperated ICRH cycle system using the design methodology presented in Bhargava *et al.* (2002). Note that for the Rolls-Royce WR 21 gas turbine, a low pressure turbine (LPT), which is not presented in Figure 1,

is included between the high pressure turbine (HPT) and the combustion chamber 2 (CC2). The calculated main performance of each modified gas turbine is presented in Table 1.
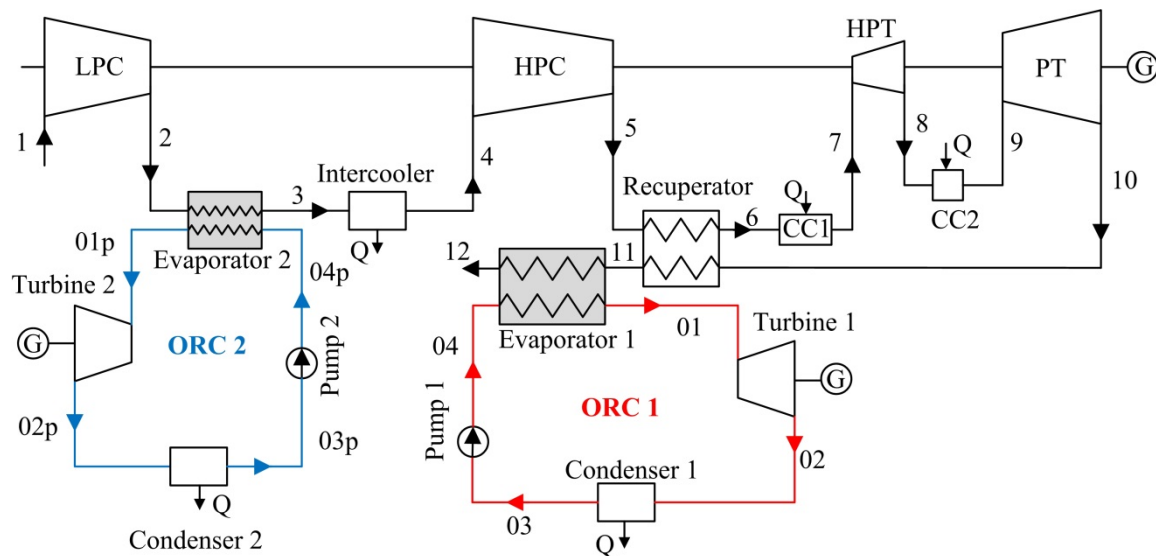

Figure 1: Schematic diagram of reference combined recuperated ICRH gas turbine with two ORC cycles

Table 1: Recuperated ICRH Gas turbines main characteristics

Parameter	GE LM-6000	Alstom GT 24	RR WR 21
Power Output (MW)	96.84	249.75	35.76
Overall Efficiency (%)	47.59	47.32	47.5
Turbine Inlet Temperature (℃)	1260	1260	982
Exhaust Temperature (℃)	462	384	307
LPC outlet temperature (℃)	117	211	152
Exhaust Gas Flow (kg/s)	148.7	391	73.1
Overall Pressure Ratio	34.1	31	16.2
LPC Pressure Ratio	2.65	4.48	3.3
HPT Pressure Ratio	3.44	2.03	1.97
LPT Pressure Ratio	-	-	1.64
PT Pressure Ratio	9.88	15.27	4.94

Data in Table 1 show that each of the recuperated ICRH cycle had impressive efficiency and power output. The modified LM-6000 machine achieved efficiency and power of 47.59% and 96.84 MW, respectively. For the modified GT 24 gas turbine, the efficiency and power were 47.32% and 249.75 MW, respectively. Additionally, the recuperated ICRH cycle derived from WR 21 machine attained efficiency and power of 47.5% and 35.76 MW, respectively. Although the value of exhaust temperature for modified gas turbines is not particularly high due to the presence of the recuperator, it can further drop by addition of an evaporator to transfer its heat to the bottoming cycle. For the modified LM-6000, GT 24 and WR 21 the LPC outlet temperatures were 117, 211 and 152 ℃, respectively. The difference in values of LPC outlet temperature for modified gas turbines is due to the fact that the optimum LPC pressure ratio varies.

For the bottoming cycle, two simple configuration of ORC are considered. The ORC uses organic working fluids with low boiling points to recover heat from low- and medium temperature heat sources. The selection of the working fluid substantially affects the performance of the ORC. Table 2 presents a list of some common working fluids considered in this paper along with their critical properties and maximum operating temperatures. The limitation of maximum operating temperature for each working fluid guarantees that fluid degradation is avoided. The working fluid at the ORC

turbine inlet can be either saturated or superheated. The effect of degree of superheat on the combined cycle thermal efficiency will be later discussed.

Table 2: Properties of working fluids used in this study

Working fluid	T_c (℃)	P_c (MPa)	T_{max} (℃)
R123	183.68	3.66	175
R245fa	154.05	3.64	140
Toluene	318.6	4.13	300
Cyclohexane	280.45	4.075	270

3. THERMODYNAMIC ANALYSIS

In this section, the thermodynamic model of combined cycles that use commercially modified gas turbines and ORC bottoming cycles was developed on the basis of available resource in literature (Bhargava *et al.*, 2002, Chacartegui *et al.*, 2009, Yari and Mahmoudi, 2010). It must be noted that the same working fluid is used in both bottoming ORCs for certain recuperated ICRHGT-ORCs combined cycle.

3.1 Assumptions
The following assumptions for the combined cycle are considered in this study:
(1) The system operates in a steady-state condition; kinetic and potential energy changes are neglected.
(2) The pressure drops throughout the pipes and heat exchangers are negligible.
(3) The general assumptions of ORC are listed in Table 3. Saturated liquid is supposed at the condenser outlet with a conservative temperature of 40 ℃.
(4) In thermodynamic calculations special attention is paid to the values of pinch point in evaporator which is not below 2 ℃.
(5) The effectiveness of 0.9 was considered for the intercooler and the recuperator.

Table 3: ORC data assumption

Pump Efficiency (%)	Turbine Efficiency (%)	Evaporator Efficiency (%)	Condensation Temperature (℃)
80	85	90	40

3.2 Performance evaluation
The net power output of the recuperated ICRHGT-ORCs can be expressed as:

$$\dot{W}_{net} = \dot{W}_{net, REC\ ICRHGT} + \dot{W}_{net,\ ORCs}$$
$$= (\dot{W}_{HPT} + \dot{W}_{PT} - \dot{W}_{LPC} - \dot{W}_{HPC})_{REC\ ICRHGT} + (\dot{W}_T - \dot{W}_P)_{ORC,\ 1} + (\dot{W}_T - \dot{W}_P)_{ORC,\ 2} \tag{1}$$

The overall efficiency of the combined cycle is given by

$$\eta_I = \frac{\dot{W}_{net}}{\dot{Q}} = \frac{\dot{W}_{net}}{\dot{m}_{air}(h_7 - h_6) + \dot{m}_{mix,1}(h_9 - h_8)} \tag{2}$$

The power ratio is defined as the ratio of bottoming cycles to combined cycle power, which is given as follows

$$\text{Power Ratio} = \frac{\dot{W}_{net,ORCs}}{\dot{W}_{net}} \tag{3}$$

3.3 Optimization method
In order to recover as much waste heat as possible, it is necessary to optimize the combined cycles. The parameters chosen for optimizing recuperated ICRHGT-ORCs combined cycle are evaporator temperatures, pitch point temperature difference and degrees of superheat at the ORC turbine inlet.

The equation of the mathematical model reveal that the optimum value for overall efficiency (η_I) can be expressed as a function of these five operating parameters, as shown in the equation:

$$\text{Maximize} \quad \eta_I(T_{e,1}, T_{e,2}, \Delta T_E, \Delta T_{sup,1}, \Delta T_{sup,2}) \tag{4}$$

Subject to:

$$
\begin{aligned}
&90 \le T_{e,1} \le T_{max} \\
&60 \le T_{e,2} \le T_2 - 10 \quad \text{or} \quad T_{max} \\
&2 \le \Delta T_E \le 15 \\
&0 \le \Delta T_{sup,1} \le 10 \\
&0 \le \Delta T_{sup,2} \le 10
\end{aligned}
\tag{5}
$$

where $T_{e,1}$ is the evaporator temperature of the organic fluid in ORC 1, $T_{e,2}$ is the evaporator temperature of the organic fluid in ORC 2, T_2 is the LPC outlet temperature, ΔT_E is the pitch point temperature difference in the evaporator, $\Delta T_{sup,1}$ is the superheat degree at the ORC 1 turbine inlet, $\Delta T_{sup,2}$ is the degree of superheat at the ORC 2 turbine inlet, T_{max} is the maximum operating temperature of the organic fluid.

The constraints as listed in Equation (5) were applied by setting the bounds on each variable. Note that the upper bound of $T_{e,2}$ was limited to either LPC outlet temperature subtracted 10 ℃ or maximum operating temperature of the organic fluid. This is because the critical temperature of the organic working fluid like R245fa may below the LPC outlet temperature. In the present study, the genetic algorithm (Holland, 1992) is applied to the optimization process to obtain the maximum overall efficiencies for each combined cycle.

4. RESULTS AND DISCUSSION

The results of parametric analysis of the recuperated ICRHGT-ORCs combined cycles are presented in this section. Reference data from the NIST REFPROP database (Lemmon *et al.*, 2007) are used to calculate the working fluid thermodynamic properties. In addition, a code of the recuperated ICRHGT-ORCs combined cycles was developed to perform the simulation of these combined cycles. As toluene has higher critical properties and turbine specific enthalpy than R123, R245fa and cyclohexane, it is used as the working fluid of the bottoming cycles to evaluate effects of key parameters of ORCs on the performance of three modified gas turbine and ORCs combined cycles. Optimizations of recuperated ICRHGT-ORCs combined cycles for different organic working fluids were then conducted.
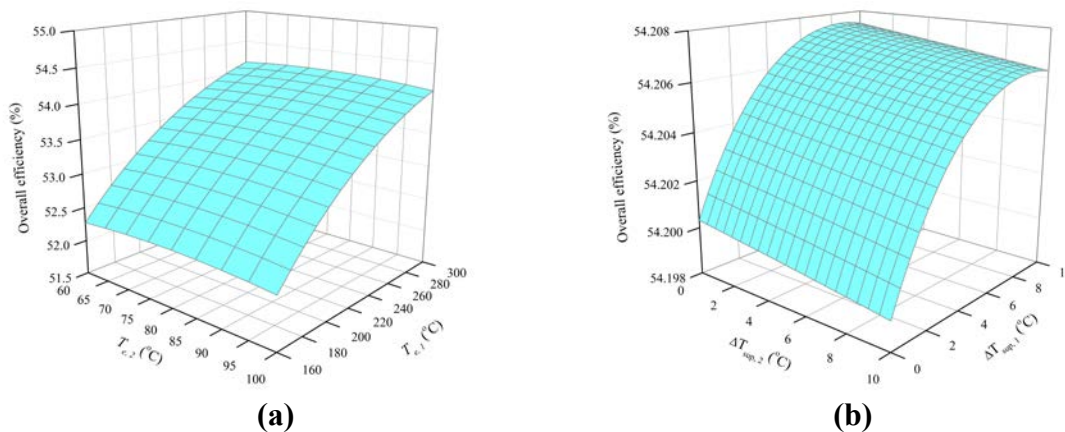

| (a) | (b) |

Figure 2: Overall efficiency versus evaporator temperatures (a) and degrees of superheat (b) with toluene as the organic working fluid and the recuperated ICRH LM-6000 gas turbine as the topping cycle

The effect of the evaporator temperatures and degrees of superheat on the overall efficiency of toluene LM-6000-ORCs combined cycle is shown in Figure 2. It can be seen that the overall efficiency strongly increased with an increase in the evaporator temperature $T_{e,1}$. It seems that a greater overall efficiency can be obtained by a higher evaporator temperature in the evaporator 1. This result is understandable because the exhaust temperature of LM-6000 was as high as 465 ℃. However, the evaporator temperature $T_{e,2}$ had slight effect on the overall efficiency. It can be seen from Figure 2(b) that there is an optimum value of superheat degree at the ORC 1 turbine inlet with which the efficiency is found to be maximum.

Figure 3 shows the variation of modified GT 24-ORCs combined cycle with evaporator temperatures and degrees of superheat in bottoming cycles with toluene as the working fluid. It can be observed that an increase in evaporator temperature 1 ($T_{e,1}$) led to an increase in overall efficiency. However, an increase in evaporator temperature 2 ($T_{e,2}$) led to an increase and then a decrease in the combined cycle efficiency. These results indicate that the ORC 2 plays an important role in the enhancement of the overall efficiency. This is expected because the LPC outlet temperature of GT 24 was up to 211 ℃, and, as a result, the heat recovery from LPC exhaust in evaporator 2 section increased significantly. From Figure 3(b) it can be seen that the overall efficiency decreased with an increase in degree of superheat at ORC 2 turbine inlet. An increase in degree of superheat at ORC 1 turbine inlet, however, led to an increase in the overall efficiency.
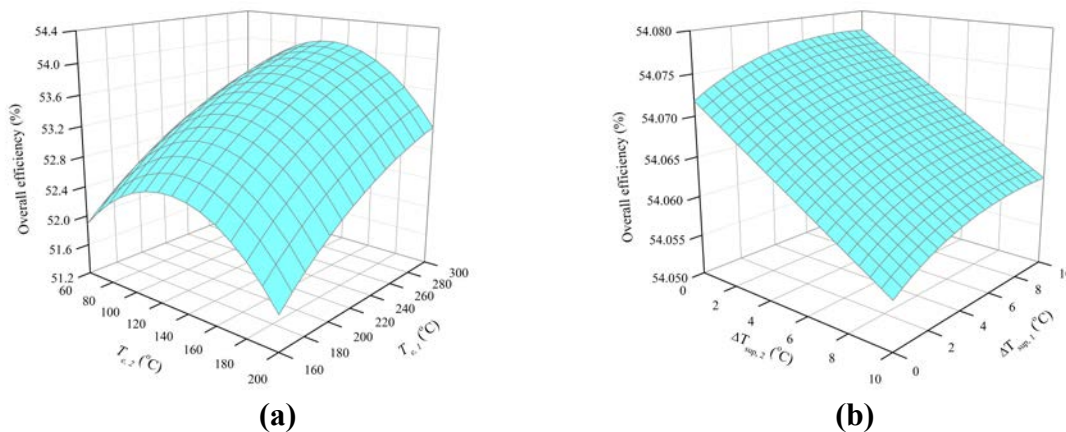

| (a) | (b) |

Figure 3: Overall efficiency versus evaporator temperatures (a) and degrees of superheat (b) with toluene as the organic working fluid and the recuperated ICRH GT 24 gas turbine as the topping cycle

Figure 4 presents the effects of evaporator temperatures and ORC turbine inlet vapour superheating on the toluene WR 21-ORCs combined cycle efficiency. It can be seen from Figure 4(a) that an optimum evaporator temperature 2 ($T_{e,2}$) existed and could be found by parameter optimization of the combined cycle. For a higher evaporator temperature 1 ($T_{e,1}$), greater waste heat is transferred to the ORC 1 resulting in an increase of power generation in ORC turbine and therefore the combined cycle efficiency. Figure 4(b) shows that by increasing the degrees of superheat at the turbine inlet both in the ORCs the overall efficiency decreased. It appears that saturated vapour of the organic working fluid is expected at the turbine inlet in both ORCs for the WR 21 and ORCs combined case.

In order to investigate the interest of combining low temperature bottoming cycle with low exhaust temperature intercooled gas turbines, a parametric optimization of the bottoming cycles is now presented depending on the modified gas turbines as described in Table 1 and working fluid in the bottoming cycles. Results are shown in Tables 4, 5 and 6 for different topping gas turbines.
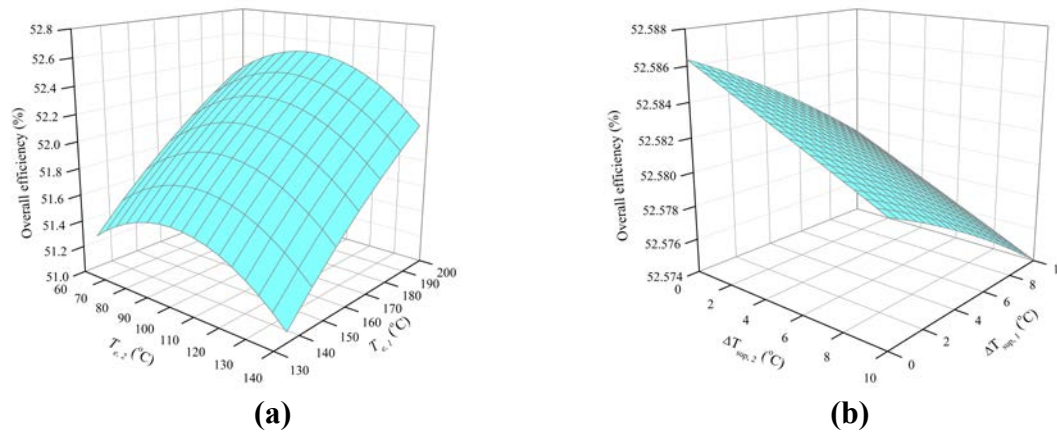
Figure 4: Overall efficiency versus evaporator temperatures (a) and degrees of superheat (b) with toluene as the organic working fluid and the recuperated ICRH WR 21 gas turbine as the topping cycle

Table 4 shows the optimization results of the recuperated ICRH LM-6000-ORCs combined cycle for different organic fluids. It is found that the modified LM-6000-ORCs combined cycle had higher performance, with thermal efficiency increase of 8.75% - 15.18% depending on the organic fluid, in comparison to the original value of stand-alone recuperated ICRH LM-6000. Note that the efficiency enhancement is the overall efficiency of the combined cycle relative to the efficiency of single modified gas turbine. The maximum overall efficiency was obtained by using toluene as the ORC fluid, i.e., 54.81%. Moreover, the toluene REC ICRHGT-ORCs had an overall power output of 111.54 MW with a power ratio of 13.18%. These findings are understandable because the turbine specific work or enthalpy drop of toluene in ORCs is higher when compared with R123, R245fa and cyclohexane. The net additional power produced by the ORCs was about 8.5 - 14.7 MW. The R123 and R245fa ORCs combined cycles demanded mass flow rates of about 231 and 216 kg/s in ORC 1, respectively, which were almost 3 times greater than that the toluene or cyclohexane ORCs combined cycle demanded. The ORC 2 recovering waste heat from the intercooler produced electricity of about 0.5 MW on average for each organic fluid. This amount of power is relatively smaller than the power generated by the ORC 1 due to the limitation of LPC outlet temperature. The optimum operating parameters using the GA are also presented in Table 4. It can be seen that the pitch point temperature difference approached a value of 2 ℃ for all the organic working fluids, which means that the evaporator size would be large or the evaporator should be well designed to meet the demand of heat transfer. On the other hand, the degree of superheat at the ORC 1 turbine inlet was as high as 10 ℃ using R123 as the organic fluid, while the degree of superheat at the ORC 2 turbine inlet was relatively small for each organic fluid.

Table 4: Summary of optimization results for maximum overall efficiency of the modified GE LM-6000-ORCs cycle

Parameter	R123	R245fa	Toluene	Cyclohexane
Overall Efficiency (%)	52.62	51.75	54.81	53.89
Efficiency Enhancement (%)	10.57	8.75	15.18	13.24
ORC 1 Power Output (MW)	9.72	7.95	14.21	12.33
ORC 2 Power Output (MW)	0.52	0.53	0.49	0.49
Overall Power Output (MW)	107.08	105.32	111.54	109.66
Power Ratio (%)	9.56	8.05	13.18	11.69
$T_{e,1}$ (℃)	169.9	140	299.7	263.8
$T_{e,2}$ (℃)	80.3	78.1	80.3	75.6
ΔT_E (℃)	2.3	2.1	2.2	2.9
$\Delta T_{sup,1}$ (℃)	10	8	5.7	1.4
$\Delta T_{sup,2}$ (℃)	0.7	2.1	1.2	3.4
ORC 1 Mass Flow Rate (kg/s)	231.4	215.7	72.8	76.7
ORC 2 Mass Flow Rate (kg/s)	31.6	31.4	12.1	14.1

Table 5 shows the optimization performance of the recuperated ICRH GT 24-ORCs combined cycle. It is found that the modified GT 24-ORCs combined cycles had efficiencies of 52.13% - 54.07%, with thermal efficiency increase of 10.17% - 14.26%, in comparison to the original value of stand-alone recuperated ICRH GT 24. The maximum overall efficiency was obtained by using toluene as the ORC fluid, i.e., 54.07%, which is close to the overall efficiency of toluene REC ICRH LM-6000-ORCs combined cycle. Moreover, the toluene REC ICRH GT 24-ORCs had a maximum overall power output of 284.47 MW. The net additional power produced by the ORCs was about 25.4 - 35.6 MW. Furthermore, the power ratios were 9.96%, 9.23%, 12.48% and 10.6% for R123, R245fa, toluene and cyclohexane combined cycles, respectively. The ORC 2 could produce electricity of about 9 MW by using R245fa as the ORC fluid. This amount of power is more than a half of the power generated by the ORC 1 due to the high inlet temperature of ORC turbine 2. Correspondingly, large amount of R245fa is desirable to run the R245fa REC ICRH GT 24-ORCs combined cycle, which, however, may increase the system capital cost. Conversely, organic fluids with high turbine specific enthalpy like toluene and cyclohexane had few mass flow rates in ORCs. The optimum operating parameters using the GA are also presented in Table 5. It can be seen that, similar to the case of modified LM 6000-ORCs combined cycle, the pitch point temperature difference approached a value of 2 ℃ for all the organic working fluids. On the other hand, the degree of superheat at the ORC 1 turbine inlet ranged from 0.2 ℃ to 8.2 ℃, while the degree of superheat at the ORC 2 turbine inlet was close to zero for all the organic fluids.

Table 5: Summary of optimization results for maximum overall efficiency of the modified Alstom GT 24-ORCs cycle

Parameter	R123	R245fa	Toluene	Cyclohexane
Overall Efficiency (%)	52.55	52.13	54.07	52.93
Efficiency Enhancement (%)	11.06	10.17	14.26	11.85
ORC 1 Power Output (MW)	19.83	16.34	28.99	23.13
ORC 2 Power Output (MW)	7.78	9.06	6.63	6.48
Overall Power Output (MW)	277.36	275.15	284.47	279.36
Power Ratio (%)	9.96	9.23	12.48	10.60
$T_{e,1}$ (℃)	175	140	297	225.7
$T_{e,2}$ (℃)	139	129.4	126.1	150.6
ΔT_E (℃)	2.2	2.2	2	2
$\Delta T_{sup,1}$ (℃)	6.6	8.2	4	0.2
$\Delta T_{sup,2}$ (℃)	0.4	0	0.7	0
ORC 1 Mass Flow Rate (kg/s)	477.6	442.7	150.3	161.9
ORC 2 Mass Flow Rate (kg/s)	230.9	280.9	82.1	68.2

Table 6 shows a summary of optimization performance of the recuperated ICRH WR 21-ORCs combined cycle for different organic working fluids. It is found that the modified WR 21-ORCs combined cycles had efficiencies of 51.19% - 52.62%, with thermal efficiency increase of 7.77% - 10.76%, in comparison to the original value of single recuperated ICRH WR 21. The maximum overall efficiency was obtained by using cyclohexane as the ORC fluid, i.e., 52.62%, which is slightly higher than that by using toluene as the ORC working fluid. Moreover, the cyclohexane REC ICRHGT-ORCs had an overall power output of 39.61 MW with a power ratio of 9.72%. The minimum power ratio was obtained by using R245fa, i.e., 7.21%, where the overall power output was equal to 38.55 MW. The ORC 2 produced electricity of about 0.5 MW on average for each organic fluid. This amount of power is relatively smaller than the power generated by the ORC 1 due to the limitation of LPC outlet temperature and minimum pitch point temperature difference. The optimum operating parameters using a GA are also presented in Table 6. It can be seen that the pitch point temperature difference approached a value of 2 ℃ for all the organic working fluids. On the other hand, the degree of superheat at the ORC 1 turbine inlet could be as high as 7.8 ℃ using R123 as the organic fluid, while the degree of superheat at the ORC 2 turbine inlet was relatively small for all the organic fluids in absence of cyclohexane. It can be noticed that the mass flow rate of the working fluid

in ORC 1 in this case was much lower than that of corresponding working fluid in ORC 1 in LM-6000 and GT 24 combined cases as given in Tables 4 and 5. This is because both of the exhaust temperature and the exhaust flow rate of the WR 21 gas turbine were relatively lower, i.e., 307 ℃ and 73.1 kg/s, respectively, which leads to a decrease in heat transfer to the ORC 1. Compared to the other two high efficiency gas turbines, the modified WR 21 is more suitable to couple ORC bottoming cycles with reasonable operating conditions.

Table 6: Summary of optimization results for maximum overall efficiency of the modified RR WR 21-ORCs cycle

Parameter	R123	R245fa	Toluene	Cyclohexane
Overall Efficiency (%)	51.77	51.19	52.55	52.62
Efficiency Enhancement (%)	8.99	7.77	10.61	10.76
ORC 1 Power Output (MW)	2.68	2.2	3.3	3.34
ORC 2 Power Output (MW)	0.53	0.56	0.5	0.51
Overall Power Output (MW)	38.97	38.55	39.56	39.61
Power Ratio (%)	8.25	7.21	9.59	9.72
$T_{e,1}$ (℃)	170.6	140	205.8	235.7
$T_{e,2}$ (℃)	98	104	95.3	92.7
ΔT_E (℃)	2.2	2	2	2
$\Delta T_{sup,1}$ (℃)	7.8	5.6	0.9	0.8
$\Delta T_{sup,2}$ (℃)	0	0.4	0.4	2.9
ORC 1 Mass Flow Rate (kg/s)	64.8	61.4	23.4	22.5
ORC 2 Mass Flow Rate (kg/s)	23.9	22	9.2	10.1

5. CONCLUSIONS

The main conclusions drawn from this study are the following:
- The analysis of combined cycles based on commercial gas turbines and two ORCs shows that ORCs are an interesting and impressing option when combined with high efficiency gas turbines with low exhaust temperatures. Among the organic fluids in the bottoming cycles, toluene ORC combined cycles for each modified gas turbines present a very attractive overall efficiency.
- The efficiencies of recuperated ICRH gas turbines when coupled with two ORC bottoming cycles were improved by about 7.8% to 15.2% depending on the exhaust temperature and LPC outlet temperature of the topping gas turbine cycle and organic working fluid in ORCs. The use of different organic fluid in the two bottoming cycles may further improve the combined cycle efficiency.
- The heavy duty gas turbines like modified LM-6000 and GT 24 are not preferable to be used in combined cycles with R123 or R245fa ORC as the bottoming cycles resulting from the demand for large amount of mass flow rate in bottoming cycles and further high system capital cost. Gas turbine with relatively small power like WR 21 is more suitable to combine bottoming ORCs with reasonable mass flow rate of the organic fluid.
- The ORC 2 yielded about 0.5 and 0.53 MW on average of the power output for LM-6000 and WR 21 gas turbine combined cycles, respectively. The power could be further increased by using a high pressure ratio LPC and a newly designed HPC of the topping recuperated ICRH gas turbine.

NOMENCLATURE

CC   combustion chamber
G   generator
GT   gas turbine

HPC	high pressure compressor	
HPT	high pressure turbine	
LPC	low pressure compressor	
ORC	organic Rankine cycle	
PT	power turbine	
Q	heat transfer rate	(kW)
REC	recuperator	
T	temperature	(℃)
$\dot{W}$	power generation	(kW)
$\dot{m}$	mass flow rate	(kg/s)

Greek letters

η_I	first-law efficiency	(%)

Subscript

1,2,3…	cycle locations
c	critical
E	evaporator
I	first law
max	maximum
mix	mixture
sup	superheating

REFERENCES

Angelino G., Colonna P., 1998, Multicomponent working fluids for Organic Rankine Cycles (ORC), *Energy*, vol. 23, no. 6: p. 449-463.

Bhargava R., Bianchi M., Peretto A., Spina P.R., 2002, A feasibility study of existing gas turbines for recuperated, intercooled and reheat cycle, *Proc. ASME Turbo Expo Amsterdam*: GT-2002-30558.

Chacartegui R., Sánchez D., Muñoz J.M., Sánchez T., 2009, Alternative ORC bottoming cycles FOR combined cycle power plants, *Appl. Energy*, vol. 86: p. 2162-2170.

Clemente S., Micheli D., Reini M., Taccani R., 2013, Bottoming organic Rankine cycle for a small scale gas turbine: A comparison of different solutions, *Appl. Energy*, vol. 106: p. 355-364.

Holland J.H., 1992, *Adaptation in nature and artificial systems: an introductory analysis with applications to biology, control and artificial intelligence*, MIT Press, Massachusetts.

Hung T., 2001, Waste heat recovery of Organic Rankine Cycle using dry fluids, *Energy Convers. Manage.*, vol. 42: p. 539–553.

Invernizzi C., Iora P., Silva P., 2007, Bottoming micro-Rankine cycles for micro-gas turbines, *Appl. Therm. Eng.*, vol. 27: p. 100-110.

Lemmon E.W., Huber M.L., McLinden M.O., 2007. "NIST standard reference database 23: reference fluid thermodynamic and transport properties-REFPROP", version 9.0.

Najjar Y.S.H., Radhwan A.M., 1988, Cogeneration by combine gas turbine engine with organic Rankine cycle, *Heat Recovery Syst. CHP*, vol. 8, no. 3: p. 211-219.

Tchanche B.F., Lambrinos G., Frangoudakis A., Papadakis G., 2011, Low-grade heat conversion into power using organic Rankine cycles – A review of various applications, *Renew. Sust. Energ. Rev.*, vol. 15: p. 3963-3979.

Vélez F., Segovia J.J., Martín M.C., Antolín G., Chejne F., Quijano A., 2012, A technical, economical and market review of organic Rankine cycles for the conversion of low-grade heat for power generation, *Renew. Sust. Energ. Rev.*, vol. 16: p. 4175-4189.

Wei D., Lu X., Lu Z., Gu J., 2007, Performance analysis and optimization of Organic Rankine Cycle (ORC) for waste heat recovery, *Energy Convers. Manage.*, vol. 48: p. 1113–1119.

Yari M., 2008, Thermodynamic analysis of a combined micro turbine with a micro ORC, *Proc. ASME Turbo Expo Berlin*: GT2008-51163.

Yari M., Mahmoudi S.M.S., 2010, Utilization of waste heat from GT-MHR for power generation in organic Rankine cycles, *Appl. Therm. Eng.*, vol. 30: p. 366-375.

TECHNICAL AND ECONOMICAL STUDY OF AN ORC DEDICATED TO THE PRODUCTION OF ELECTRICITY FROM A GEOTHERMAL SOURCE

Stéphane Schuller[1*], Morgan Da Silva[1], Christophe Josset[2], Bruno Auvity[2], Jérôme Bellettre[2]

[1] Cryostar, Clean Energy,
Hésingue, France
stephane.schuller@cryostar.com, morgan.dasilva@cryostar.com

[2] Laboratoire de Thermocinétique de Nantes, UMR-CNRS 6607 Université de Nantes,
Nantes, France
christophe.josset@univ-nantes.fr, bruno.auvity@univ-nantes.fr, jerome.bellettre@univ-nantes.fr

* Corresponding Author

ABSTRACT

This paper presents an original method to design equipment of an organic Rankine cycle power plant. It is based on the entropy production equipartition theorem in the geothermal heat exchanger. The criterion of best pressure in favor of exergy at turbine inlet at given temperature is also used to initialize the problem at an ambient design temperature. According to these design criteria, the price of each main pieces of equipment is estimated. Then the equipment are simulated throughout a typical year, the net electrical production is deduced. The same method is repeated with different ambient temperatures chosen as design temperature. Then the product price per kWh is calculated and compared to the one obtained at the average design temperature. The methods is revealed not monotonous and so a filter is applied to results in order to keep the best cases regarding economical criteria. Three sites are studied. Regarding the ambient temperature climate distribution, a temperature where design appear to be the best, is found. Finally the developed simulation tool of ORC power plant allows to test the relevance of different design criteria.

1. INTRODUCTION

ORCs are proving to be an effective solution to produce mechanical or electrical power from low temperature heat source. These low temperature sources also make them sensitive to the sizing of their equipment (Schuller et al., 2014). Indeed, due to the evolution of the Carnot efficiency for ORCs influenced by ambient temperature (see figure 1 where equation (1) is plotted), the pinches involved in the evaporators or condensers have high consequences. This particular point must be carefully addressed. In these specific conditions, technical and economical trade-offs must be determined in order to make ORC competitive. This paper focuses on the technical-economic study of a supercritical ORC with propane, without regenerator, dedicated to the production of electricity from a geothermal source. The supercritical cycles are chosen for their ability to extract the heat from the hot source and the absence of the phase change plateau that avoids a large pinch inside the steam generator (Schuster et al., 2010). We firstly describe how the four main pieces of equipment (pump, geothermal heat exchanger, turbine and condenser) are designed by applying the entropy production equipartition theorem in the geothermal heat exchanger (Schuller et al., 2014). In the same time a specific criterion (Schuller et al., 2014) regarding working fluid in the turbine is used to constrain the problem and avoid liquid formation in the turbine. The costs of the four main items of equipment are estimated in relation to their sizing parameters (surface of exchanger, turbine power,...) designed at an arbitrarilly chosen ambient temperature. The effect of this temperature selection on the design and the overall efficiency (energetic and economic) will be dis-
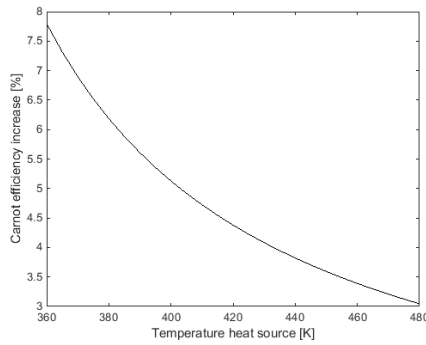
$$f(T_{hot}) = \frac{(1 - \frac{277}{T_{hot}}) - (1 - \frac{283}{T_{hot}})}{1 - \frac{283}{T_{hot}}} * 100 \quad (1)$$

Figure 1: Carnot efficiency rise for a temperature drop from 283 **to** 277 **K**

cussed. Secondly, this paper describes how equipment performances change according to the weather variation throughout the year. A typical ambient temperature distribution along the year is estimated with Meteonorm (Remund and Kunz, 1997)(see figure 2) and is used to calculate the yearly production. Thirdly, the same geothermal source is virtually placed in three sites in the world with different climates. By the previously described method three different ORC plants are designed. The comparison of the three plants is presented. This opens a discussion about the consequence of heat sink temperature variations. The consequence on the characteristics of equipment, designed at a fixed ambient temperature, but used at a variable ambient temperature is observed.

The three places chosen to illustrate the influence of the ambient air as heat sink are:

- Site 1, East of France
- Site 2, Turkey
- Site 3, Caribbean Island

The typical distribution of temperature given by Meteonorm (Remund and Kunz, 1997) for each site is presented in the figure 2 and the mean values are given in table 1
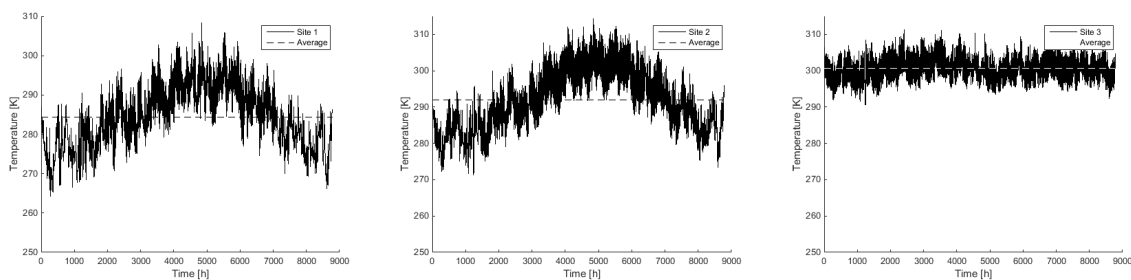
Figure 2: Hourly ambient temperature on typical year

Site	Average temperature (K)	Standard deviation (K)
1	284.5	8.0
2	292.0	8.6
3	300.6	3.5

Table 1: Average and standard deviation of ambient temperature distribution along a typical year

In the present work, the results are obtained by numerical simulations performed with a dedicated simulator developped with Matlab (Schuller et al., 2014).

2. THERMODYNAMICS MODEL

The thermo-physical fluids characteristics are calculated by Refprop (Lemon, 2013), directly linked to Matlab The main physical properties taken account are summarized in the table 2.

Physical properties	value	unit
Geothermal inlet temperature	435.15	K
Geothermal outlet temperature	273.15	K
Geothermal inlet pressure	2000	kPa
Geothermal mass flow	45	kg/s
Geothermal fluid	pure water	
Working fluid	propane	
Superheating margin (regarding cricon)	≥ 200	kPa
Hex Working fluid outlet entropy	$\geq$ Cricondentrope entropy	
Pinch Hex	≥ 5	K
Expander inlet temperature	$> T_{crit} + 10$	K
Expander inlet pressure	$> P_{crit} + 50$	kPa
$\Delta T_{Condensation-Ambient\ air}$ (approach design)	18	K
Condenser working fluid pressure drop	20	kPa
Evaporator working fluid pressure drop	100	kPa
Evaporator geothermal fluid pressure drop	200	kPa

Table 2: Hypothesis summary

2.1 Details of equipment model

This supercritical ORC has four main items of equipment [1]:

- a pump transferring and pressurizing the working fluid in liquid phase.
- a geothermal heat exchanger transferring heat from the geothermal source, toward the working fluid.
- a turbine expanding the working fluid to remove the mechanical energy, which coupled to a generator via a gear box will produce electricity then injected on the electrical network.
- a condenser, which desuperheats and then condensates the expanded working fluid, in contact with the cold source, i.e. the ambient air.

Propane is chosen as a working fluid because adapted to the temperature of the hot source (Marcuccilli, 2010) (Sauret, 2011).

2.2 Condenser, cold source

The air cooled condenser is a classic model similar to API661 models that are found in ORC facilities for geothermal applications. The working fluid flows in finned tubes. Air is driven by fans. The power of the fans is calculated according to Robinson and Briggs correlation (Nir, 1991). Fan speed is assumed constant. Fan power depends only on ambient air temperature and its density (calculated directly by Meteonorm). Geometry is fixed, i.e tube length, diameter, fin width, height, fin density, as well as the number of tube rows. Only the number of tubes required by the condensation power is considered for the design calculation, whereas the condensation pressure and temperature will be considered for the off-design calculation.

2.3 Pump

The pump is of centrifugal type. Because of high fluid pressure (beyond its critical pressure), the variation in density between the input and output of the pump is significant. The model considers therefore, for the

---

[1]No regenerator is considered in this study

pump power consumption calculation, a polytropic compression with efficiency depending on its variable speed, head and flow (Troskolanski, 1977). The power and the speed are assumed to be sufficient to reach all the requirements for all off-design points.

2.4 Geothermal heat exchanger, hot source

The geothermal heat exchanger is of the shell and tube type. For cleaning considerations, geothermal water flows in the tubes. The exchanger is discretized in intervals of equally exchanged heat power . The diameter of tubes is considered constant, as well as pitch and baffles spacing and number. The number of parallel tubes depends only on water flow. The length of these tubes is calculated from the required exchange surface at design point.

2.5 Turbine

The turbine is of radial inflow type (Marcuccilli, 2007). The wheel diameter and the speed of rotation are determined to maximize isentropic efficiency (Balje, 1981). Pressure and temperature at turbine inlet are determined according to an optimization procedure (Schuller et al., 2014). The turbine is equipped with variable inlet guide vanes. The turbine inlet pressure is controlled by the position of these inlet guide vanes whereas the inlet temperature is governed by the working fluid mass flow rate (i.e. controlled by the pump).

3. ALGORITHM OF DESIGN AND OFF-DESIGN CALCULATION

The program contains a multitude of parameters. A lot of them are geometric, such as diameter of heat exchanger tube, fin height etc. In this study we focus on the following parameters:

- Ratio of mass flows, water over propane
- Pressure at turbine inlet
- Temperature at turbine inlet
- Design ambient temperature

Simulations are performed in two steps: design step and off-design step. In the design step, a specific ambient design temperature and condenser approach are chosen. Then the four main items of equipment previously presented are designed with respect to some optimization processes (Schuller et al., 2014) (Schuller, 2011). Optimal values of pressure and temperature at turbine inlet (see figure 3) and mass flows ratio are obtained at this stage. In figure 3, the thermal path of water is scaled to propane enthalpy as described in Augustine et al. (2009). In the second step, with off-design calculation, the performances of the designed plant are predicted keeping all the geometrical parameters constant. In this stage, the influence of the varying ambient temperature can be estimated. The flow of propane is calculated to reach the same turbine inlet temperature than at design. In real control scenario, it would be done by varying the speed of the pump. Finally, two different indicators are predicted, one with respect to the annual energy production, the other with respect to the economic efficiency of the plant, depending on the chosen business plan (see paragraph 5). The algorithm is detailed as follows (see figure 4): first, the temperature, at three quarter from supercritical to geothermal source temperature is chosen as the turbine inlet temperature. Thus the corresponding pressure on the curve EMTD[2] (see figure 3) is deduced for turbine inlet. The turbine outlet pressure is the condensation pressure corresponding to the ambient temperature plus the chosen approach shift from an arbitrary pressure drop. We consider no subcooling [3]. Then optimization is launched on the turbine inlet pressure and temperature and mass flow of propane, in order to minimize the variance of the reduced temperature difference to the average reduced temperature difference along the geothermal heat exchanger. In other words, the optimization makes the two thermal

---

[2]Maximal exergy at given temperature: for a given temperature, there exists a corresponding enthalpy or pressure where the exergy reaches a maximum (Tondeur, 2006)

[3]The NPSH, net pressure suction head, required by the pump is supplied by the height of the condenser
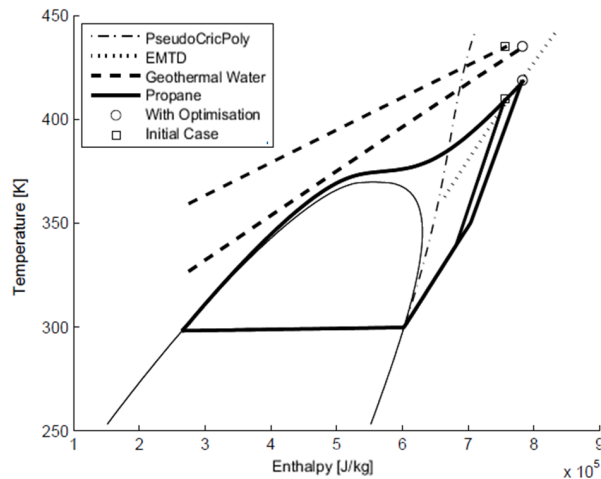
Figure 3: Thermal path of cycles before and after optimization to minimize the criterion of entropy production equipartition

paths (water and propane) as parallel as possible in a diagram of reduced temperature[4] versus enthalpy. The pinch point is not fixed as recommended byWalraven et al. (2014) for optimum issue, but it is a consequence of using the equipartition criterion. Furthermore, the turbine inlet point should be on the right hand side (in the H,T diagram) of the pseudocricondentropic curve (PseudoCricPoly in figure 3) in order to avoid liquid ingress during the expansion through the turbine, with respect of constraints and condition summarized in table 2. At this step, the design is fixed and equipment characteristics are defined. Off-design turbine inlet temperature and pressure are set to the design value. Temperature data from Meteonorm are implemented at condenser inlet, and at fixed characteristics, equipment performances are calculated:

- condenser approach
- condensation pressure
- fans power consumption
- pump speed
- pump efficiency and losses
- pump power consumption
- turbine nozzle opening
- turbine efficiency
- turbine, gearbox, generator losses
- generator power
- propane mass flow
- Hex pinch

This off-design is calculated hourly and production is assumed constant during one complete hour. Annual production is the sum of the power at each hour. In the figure 5, the example of site 1, design at average temperature is given. Power and production are reduced by the power and respectively production, produced at the average temperature. The coldest temperature gives the greatest power, but a poor occurrence. Average temperatures give average power values but have the highest occurrences. Hottest temperatures give the lowest power values but have poor occurrences. The consequence is illustrated in figure 6. The power and contribution to annual production are not correlated. Then at which temperature should equipment be designed: at a frequent temperature or at a temperature that gives the best power? To find out, different design temperatures are tested in the paragraph 4.

4. OFF-DESIGN REGARDING THE CHOSEN DESIGN TEMPERATURE

The method described in the paragraph 3 is applied for different design temperatures. These temperatures are chosen among temperature site occurrences, every 0.5 K. All results are reduced by a reference production. This reference is the production of a complete year in site 1, in the case of design at the average temperature of this site. These results are shown in figure 7. The shape of curves are non monotonous. This is due to the chosen criterion of entropy production equipartition. This is different to minimizing the entropy production. The algorithm of optimization is based on a simplex method, with

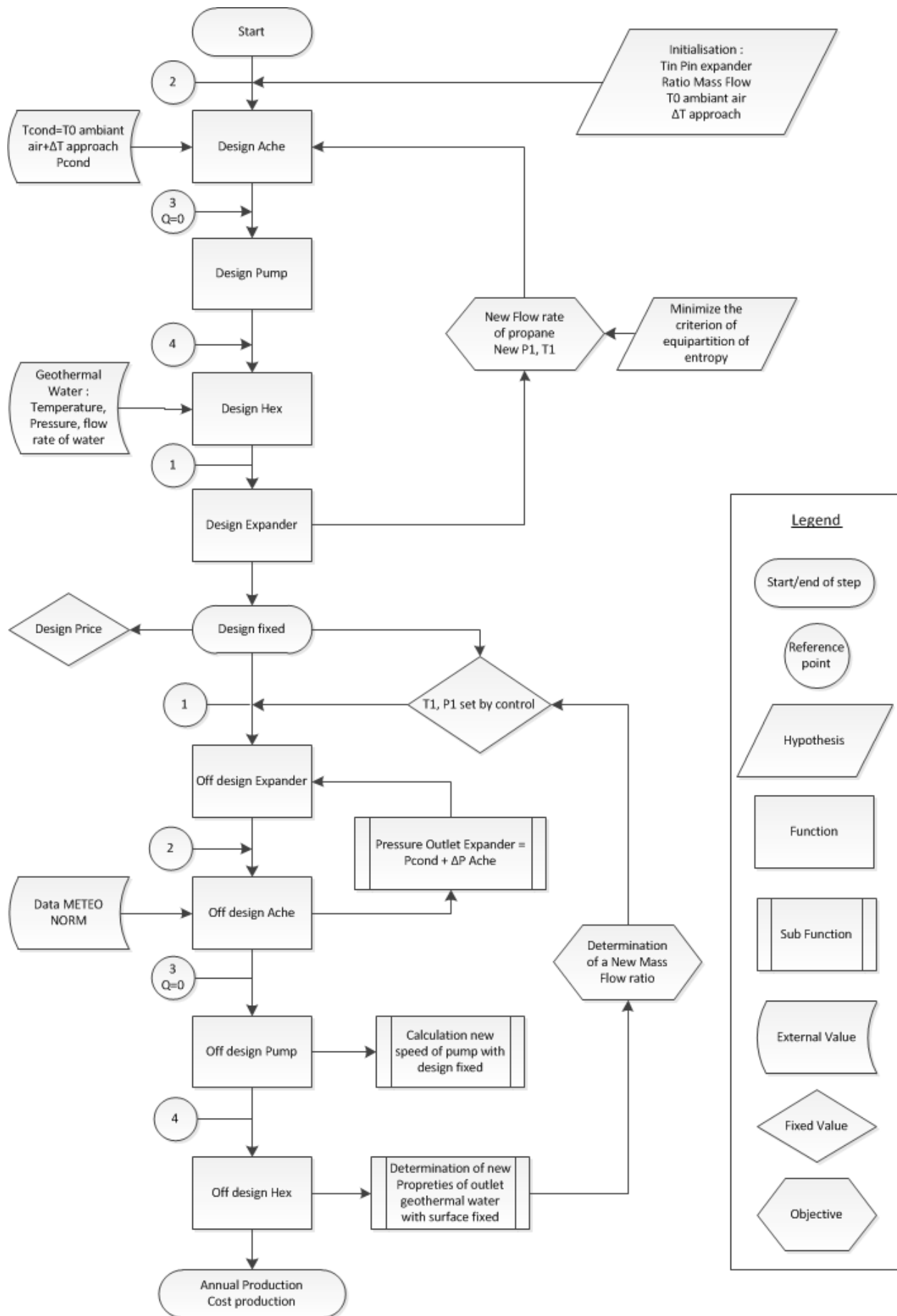---

[4]temperature reduced by the Carnot factor

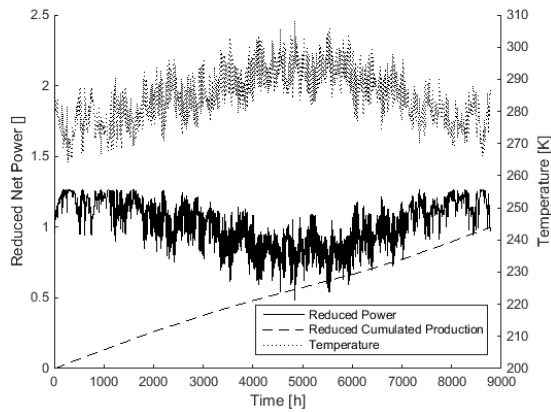**Figure 4: Algorithm logic diagram**

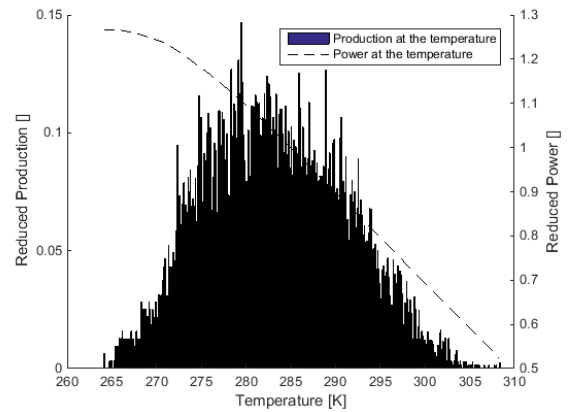**Figure 5: reduced power and production and temperature throughout the year**

Figure 6: Reduced power and contribution to production vs ambient temperature

three parameters: turbine inlet pressure and temperature and water over propane mass flow ratio. Entropy production is illustrated by the gap between both thermal paths. On the other hand, entropy production equipartition is illustrated by the parallelism between both thermal paths. Sometimes, regarding the equipartition, it is preferable to move the thermal paths away from each other rather than bringing them together while keeping them parallel. This is clearly shown in the example of figure 8:

- The point 1 of figure 7 corresponds to the annual production of a power plant designed at 269.6 K and running at site 1. Its design case is shown with a dotted line in figure 8.

- The point 2 of figure 7 corresponds to the annual production of a power plant designed at 273.6 K and running at site 1. Its designed case is shown with a continuous line in figure 8.

The characteristics of both cases are summarized in the table 3. For only 4 K of design temperature difference, the gap between the two thermal paths of the continuous line case shows that the heat exchanger is smaller than the one of the doted line case. In consequence the heat exchanger surface of case 1 is three times bigger than that of case 2. Both annual productions are coherent regarding heat exchanger sizes. More generally, pressure rise flattens isobaric curves, while flow ratio changes the slope of the water thermal path. A temperature rise increases the length of the thermal path, thus the range of temperatures taken into account to calculate the average gap between the two fluid temperatures. Finally, by using the equipartition criterion to design equipment and if we assess the production of the designed cycle, we realize that it is not the best method to design equipment that will finally mainly work at off-design conditions. The method is missing a criterion to distinguish between plants that are designed at different ambient temperatures. Thus in paragraph 5, we add some economical criteria.

Case	Design ambient temperature	Propane reduced mass flow	Heat exchanger reduced surface	Turbine inlet temperature	Turbine inlet pressure	Reduced annual production
(Units)	(K)	( )	( )	(K)	(kPa)	( )
1	270	0.91	2.43	421	6900	1.19
2	274	1.28	0.81	408	4500	0.94

Table 3: Comparison between two different design ambient temperature
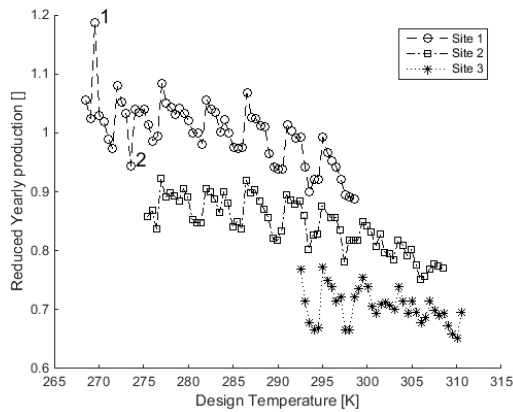
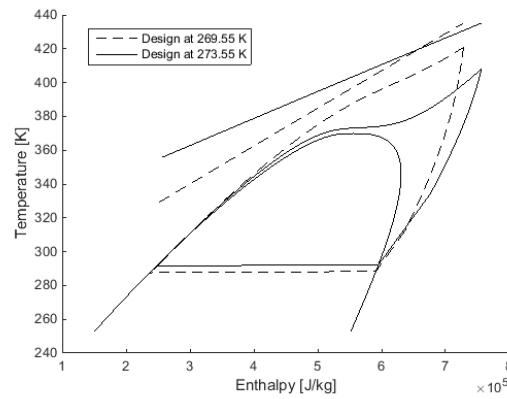**Figure 7: Reduced annual production ("Sum of net kWh produced in one year")**

Figure 8: Thermal path of cycles after optimization for two different design ambient temperatures

5. BUSINESS PLAN

One kind of business plan is now implemented. The prices of the four main items of equipment are evaluated by means of Marshall and Swift Index (Turton et al., 2008), then shifted to match some MW ORC scale. From the sum of these items of equipment, by a Lang method (Lang, 1947), updated by Peters et al. (2003), the rest of the cost is estimated by adding rate of this sum. Of course, the business plan depends very sensitively to the place where the plant is built, the local fee, and the price for the kWh sold. The average ambient temperature of site 1 is taken as reference. The results for the other case are then reduced by this reference. The reduced production cost of the reference is then equal to 1, the sames goes for its production at the end of one year. As previously done for the calculation of yearly production in paragraph 4, the cost of production is also estimated at different design temperatures. The results are shown in figure 9. This business plan is done for a period of twenty years. The life time of the power plant is assumed to be equal to this duration. The cost of production (see equation 2) is the sum of all cost of charges, salaries and fees to be payed during one year in the power plant. One twentieth of the plant cost is added as depreciation. This amount is divided by the number of kWh produced in one year.

$$Cost_{Production} = \frac{\sum_{year}(fees,\ charges,\ salaries) + \frac{1}{20}(capital\ investment)}{\sum_{year}(sold\ electricity)} \qquad (2)$$

6. FILTER APPLIED TO DESIGN TEMPERATURE REGARDING BUSINESS PLAN

As shown in figure 7, the yearly production is non monotonous with regards to the design temperature when entropy production equipartition is the optimization criterion chosen. However, once the design is done, off-design is regular and follows the ambient temperature. The business plan brings a new criterion for the evaluation of the results obtained at different design temperatures. Especially the cost of production reveals some more interesting design temperature. We decide to focus on the low production cost plants and the ambient temperature at which they have been designed, as shown in figure 9. The filter keeps all local minima [5]. We plot them with a continuous line for each site. These continuous line reveal more monotonous shapes, with global minima. These minima appear at average minus 1.5 times the standard deviation for site 1 and 2, and the average minus 2 times the standard deviation for site 3. A best design temperature found below the average temperature is coherent with figure 6 data [6].

---

[5] the filtered points correspond to the lower bound of the points cloud

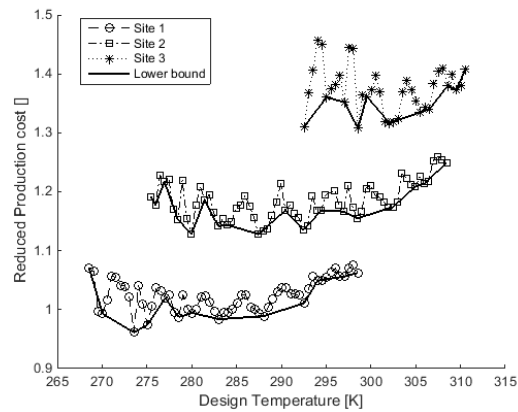[6] The ambient air distribution is symmetric around average, but power is higher at below average temperature

Figure 9: Reduced cost of production ("production cost of kWh")

7. CONCLUSION

Focusing production and comparing between sites, as expected, the coldest site reaches the best result. The entropy production equipartition, used only for design does not have regular trend. Despite this non monotonous characters, it is possible to extract a global regular behavior by filtering data. Due to the sensitivity of the equipartition criterion, it remains necessary to perform the calculations on the entire range of ambient temperature. Each climate has its own optimum. However, based on these three tests, no generic law (rule of thumb) seems to be able to predict a priori the optimal design temperature. Thus, the use of such numerical simulator, coupled with an optimization method seems to be essential in the context of the design of plant like ORC system. The results presented here are closely linked to the choice of the steam generator design criterion, but taking into account other constraints or criteria is easily implementable in the simulator. Thus, in forthcoming publication, we intend as well to test the following points:

- Use a particle swing optimization method to determine the best power plant design.
- Do a systematic calculation on the neighborhood of the assumed optimum found in paragraph 6.
- Use the criterion of entropy production equipartition in off-design control setting [7].
- Add a constrain to the equipartition criterion to force the mean to reach a target value, figuring indirectly the size of the heat exchanger.
- Calculate the best approach[8] on the condenser regarding the cost of production.

The combination of multiple criteria is interesting to study. Especially when thermodynamics criterion have benefit to economical optima, which finally is one of the most efficient means to deploy ORC with the support of policymaker.

NOMENCLATURE

T	temperature	(K)		Ache	condenser
T_0	temperature of cold sink	(K)		Hex	geothermal heat exchanger
Q	mass quality			**Subscript**	
P	pressure of working fluid,	(kPa)		*cond*	condensation
Δ	difference			*in*	inlet
EMTD	maximal exergy at given temperature			*hot*	hot source

---

[7] Actual control is at fixed turbine inlet temperature and pressure.
[8] Differential temperature between ambient air and condensation temperature.

REFERENCES

Augustine, C., Field, R., Dipippo, R., Gigliucci, G., Fastelli, I., and Tester, J. (2009). Modeling and analysis of sub- and supercritical binary rankine cycles for low- to mid-temperature. In *Geothermal resource council*, volume 33, pages 689--693.

Balje, O. (1981). *Turbomachines: A guide to design selection and theory*. Wiley-Interscience.

Lang, H. (1947). Cost relationships in preliminary cost estimation. *Chemical Engineering*.

Lemon, E. (2013). *NIST Standard Reference Database 23: Reference Fluid Thermodynamic and Transport Properties (REFPROP),Version 9.1*.

Marcuccilli, F. (2007). Benefits of using radial inflow turbines for organic rankine cycles. In *Proceeding of World Geothermal congress*. World Geothermal Congress, Geothermal Resource Council.

Marcuccilli, F. (2010). Optimizing binary cycles thanks to radial inflow turbines. In *Proceeding of World Geothermal congress*. Proceedings European Geothermal Congress.

Nir, A. (1991). Heat transfer and friction factor correlations for crossflow over staggered finned tube banks. *Heat Transfer Engineering*, 12(1):43--58.

Peters, M., Timmerhaus, K., and West, R. (2003). *Plant Design and Economics for Chemical Engineers*. Companies, The Mcgraw-hill, 5th edition.

Remund, J. and Kunz, S. (1997). *METEONORM: Global meteorological database for solar energy and applied climatology*. Meteotest.

Sauret, E. (2011). Candidate radial-inflow turbines and high-density working fluids for geothermal power systems. *Energy*, 36-7:4460--4467.

Schuller, S. (2011). Best exergy point for orc. In *Proceeding of European Geothermal congress*, volume 35, pages 1343--1349. European Geothermal Congress.

Schuller, S., Josset, C., Auvity, B., and Bellettre, J. (2014). Optimisation par le critère d'équipartition de production d'entropie d'un cycle orc supercritique équipant une source d'eau chaude géothermale et influence sur les performances.

Schuster, A., Karellas, S., and Aumann, R. (2010). Efficiency optimization potential in supercritical Organic Rankine Cycles. *Energy*, 35(2):1033--1039.

Tondeur, D. (2006). Optimisation thermodynamique Équipartition de production d'entropie. In *Thermodynamique et Énergétique*, number 8017 in BE, pages 1--15. Techniques de l'ingénieur.

Troskolanski, A. (1977). *Les turbopompes*. Eyrolles.

Turton, R., Bailie, R., Whiting, W., and Shaeiwitz, J. (2008). *Analysis, synthesis and design of chemical processes*. Pearson Education.

Walraven, D., Laenen, B., and D'haeseleer, W. (2014). Optimum configuration of shell-and-tube heat exchangers for the use in low-temperature organic rankine cycles. *Energy Conversion and Management*, 83:177--187.

ORC BOTTOMING FOR COMBINED CYCLE SYSTEMS FED BY BIOMASS

M. Gaia [1], F. Mowill[2] and C. Pietra[1*],

[1]Turboden s.r.l.,
Via Cernaia, 10
I-20124 Brescia

[2]OPRA Turbines BV,
Opaalstraat 60
NL-7554 TS Hengelo

e-mail: claudio.pietra@turboden.it
Web page: http://www.turboden.it, http://www.opraturbines.com/en/

ABSTRACT

In the last two decades ORCs have been largely used to convert the heat from biomass combustion into electric energy. The success of the ORC technology for this application is mainly due to its low maintenance requirements, ease of operation and good partial load performance.

In the quest for higher efficiency systems, biomass gasification, followed by conversion to electric power in a small scale combined cycle, is very promising.

Indeed several gasification systems, integrated with gas cleaning and gas engines for power production, have been put into operation in the past, with different results depending on the adopted solution.

The paper suggests a different approach featuring an innovative gasification device, a gas turbine prime mover, and an Organic Rankine Cycle as bottoming system, typically for a power output of the combined system up around 5 MW. A preliminary study of the system performance is presented.

1.   INTRODUCTION

Biomass is a very interesting source for power generation, thanks to a number of reasons, which we try and summarize here:

- it allows storage over extended periods of time, without substantial loss of energy. Hence it allows to cope with a varying power demand, in particular with a seasonally varying power demand.
- it can be transferred to other sites, though at a higher cost than fossil fuels.
- it is, or it can be made, substantially neutral concerning the introduction of carbon dioxide in the atmosphere.
- its cost is strongly related to its origin (residual biomass from agriculture and forestry, energy crop, waste from wood industry etc.), however in many cases the cost per unit of energy content is much lower than the equivalent in a fossil fuel.
- biomass can be transformed into power by quite small power units, down to about one MW of electric power and even less. Hence the related investment can be sustained by small enterprises and limited local resources can be exploited.
- due to the low power level, it is often possible to find, at least for a fraction of the year,

a suitable consumer for the thermal power associated with the generation of electric power.

- On the other hand, if the conversion to power is referred to a Rankine Cycle power plant (steam or ORC), a number of critical aspects have often hindered a more widespread utilisation of biomass for power:
- the cost per kW electric installed is rather high, typically in the range 4000 to 8000 €/kW except for large systems, which are less attractive, for the reasons considered above. An important fraction of the cost is often related to the need to reduce the emission of particulate and of gaseous/VOC pollutants into the atmosphere.
- the efficiency of conversion is up to now rather low in most installations, typically around 15 to 20%, taking into account the whole process, that is the ratio between electric energy produced and the energy content of biomass. Even lower figures can be met for co-generative plants. This low efficiency obviously has the adverse effect of reducing the amount of electric energy which can be produced by a given low cost biomass source, so that in practice, only relatively large sources can be exploited for power generation.
- moreover the ability of today's plants to follow a fast varying load is limited. Hence in the case of an isolated grid, either a mix of power sources is introduced into the grid, or the biomass power unit has to be kept running at high power condition, and the excess power is wasted.

2. DISCUSSION OF GASSIFICATION

Gasification has been proposed as an alternative solution to straight combustion, in order to overcome the problems listed above. In fact, notwithstanding a number of tentative tests, starting back to Rudolf Diesel experiments with pulverized coal, direct utilisation in internal combustion engines of solid biomass, even very finely divided, does not seem to be promising, due to the uneven properties, the energetic cost of pulverisation, the alkali content in ashes, and in general the difficulties of feeding a solid product.

Gas feeding of reciprocating engines on the contrary has been the subject of many analyses and it has been put in to effect in a large number of real applications. A large number of different solutions have been proposed and experimented for the gasifier itself, for the cleaning of the produced gas and the overall implementation of the power plant. Gas turbine systems have been considered too, mostly at larger power level than reciprocating engines.

Specific solutions for gasification are discussed in detail, e.g. in [1] and [2].

The large number of proposed solutions indicate that none is in fact totally satisfactory.

The scope of the present paper is to describe a solution involving an innovative concept gasifier, feeding a combined cycle, composed by a gas turbine and an ORC bottoming unit.

Traditionally the solutions are classified according to the following schemes:
- fixed bed Updraft in which the descending biomass moves counter-current to the ascending gaseous phase, so that the subsequent steps of the process, from the point of view of biomass, are ordered as Drying, Pyrolysis, Reduction, Oxidation (as reported in fig.1-a)
- fixed bed Downdraft in which the descending biomass moves co-current to the descending gaseous phase, so that the subsequent steps of the process, from the point of view of biomass, are ordered as Drying, Pyrolysis, Oxidation, Reduction (fig 1-b)
- fluidized bed of various kinds. In many cases the process cannot be divided in zones and it takes place instead on the surface and within each particle of solid biomass, hence all four transitions take place substantially at the same time in parallel.
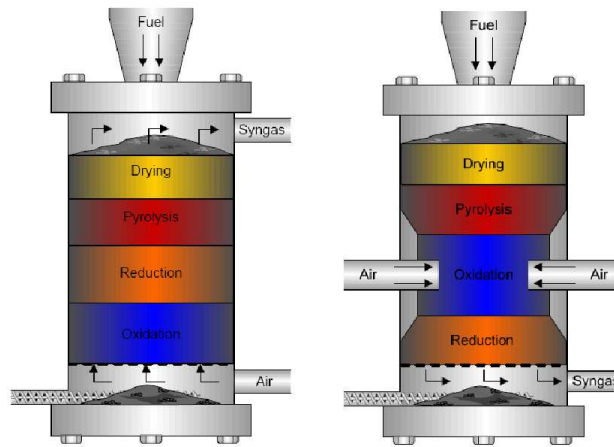
Figure 1 - Traditional fixed bed gasifier schemes [3]

In fixed bed gasifiers, Reduction is the most characterising step, which takes place in the bed of char resulting from the Pyrolysis. In Downdraft gasifiers reduction involves a given dwell time and interaction between the gases and tars resulting from the pyrolysis. As a consequence, besides the main scope of obtaining a gas composition including high H_2 and high CO, the reduction step is very effective at achieving thermal decomposition of tars. In Updraft gasifiers, the produced gas is substantially clean at the top of the reduction zone, but then it flows through the pyrolysis zone and it becomes heavily loaded with tar and moisture.

Apparently, a Downdraft solution is preferable in any case. However in practice the transfer of heat to the upper layers undergoing pyrolysis is rather ineffective and it is difficult to keep a uniform flow through the bed, in particular if the bed has a large cross section. Hence the Updraft solution, though not attractive from the tar content point of view, is preferable for relatively large systems.

Moreover so as in fact the counter-current flow of hot gas allows an efficient pre-drying of the biomass before it enters the pyrolysis zone and the separated water is added to the produced gas instead of being put to the high temperature reaction zone, allowing to feed the Updraft gasifier with high moisture biomass (up to 50% vs 20% for the Downdraft). [3]

The fluidized bed gasifiers are intermediate, for what concerns both the tar content in the gas point of view and the acceptance of high humidity feed. [4-5]

Fixed bed gasifiers are attractive due to the low parasitic power required and their tolerance of eneven quality biomass. However, the required volume of the reactor is large and the quality of the produced gas is less predictable than with fluidized bed gasifiers.

3. PRESENT PROPOSAL FOR THE GASIFIER

A different approach to the flow within fixed bed gasifiers is here proposed in conjunction with ORC bottoming solution. The new approach should allow to solve the problems reported, that is it should lead to an efficient transfer of heat to the pyrolysis zone and an efficient cleaning of gas thanks to flow within the char bed at high temperature.

The present proposal concerns an innovative co-current fixed bed gasifier, characterized by the fact of utilizing two vessels in parallel, and having an alternate flow of gasifying agent. In this way the produced gas flows back and forth through the bed, ensuring a larger volume of high temperature reactive zones, compared to a conventional downdraft gasifier. Moreover the increase of velocity through the bed activates both the heat exchange between gas and solids and the gasification reactions.

The proposed solution has been given the acronym "Twingas" by the authors of the relevant patent [6], hence here the same name is adopted, too.

A sketch of the Twingas is reported in fig. 2, concerning a system with top to bottom flow of biomass as well as an alternating co-current and counter-current flow of gas.
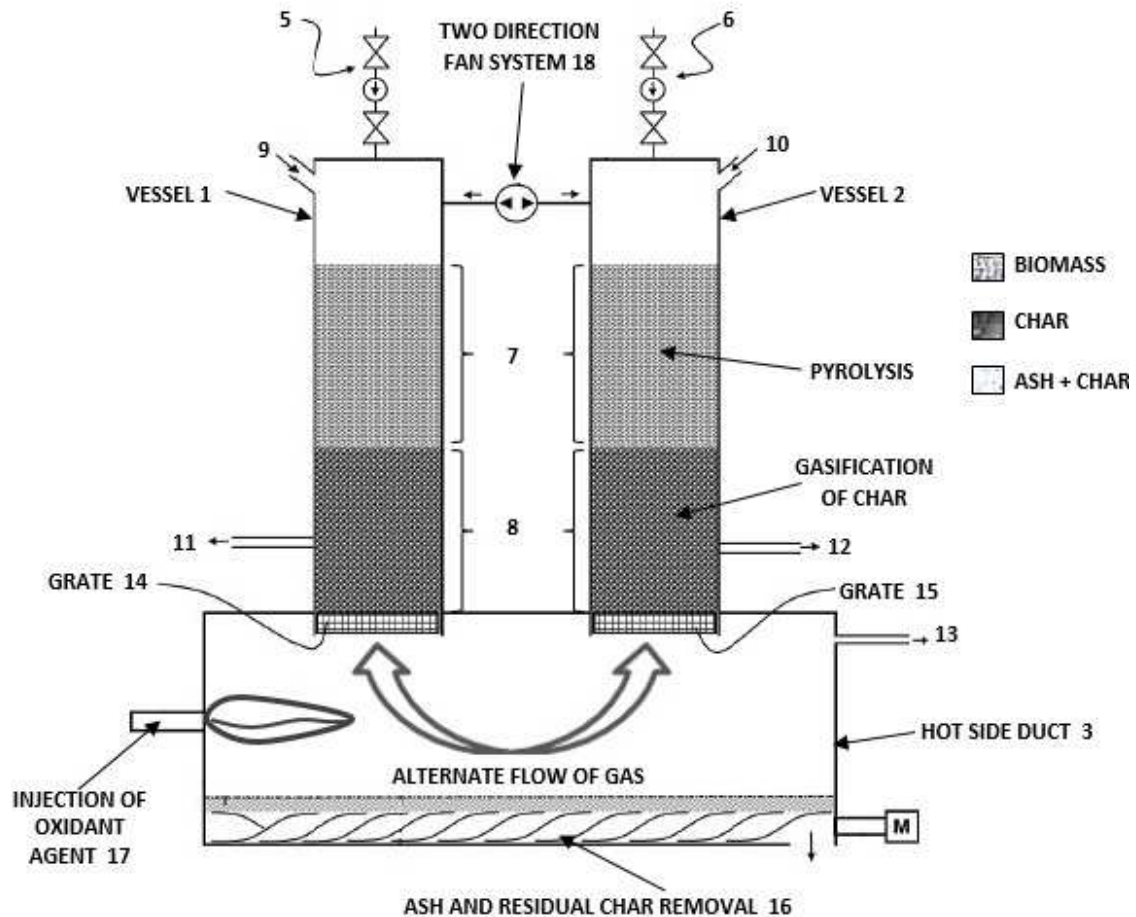
Figure 2 - TWINGAS gasifier solution, with two vessels and alternated flow of gas

The expected results are a higher production per unit of volume of gasifier, a better quality gas and a good tolerance towards non-uniform charge. Twingas is reported more in detail in Appendix I.

4. UTILIZATION OF PRODUCED GAS

The syngas produced by the gasifier can be utilized to generate power according to one of the following schemes:

1) Gas is burned in a boiler to generate organic vapour (or steam) for a Rankine cycle, preferably after some treating of the gas, e.g. to reduce the particulate content (fig. 3). Though organic vapour or steam could be also generated by burning the initial solid biomass in a suitable boiler, burning syngas gives some definite advantages, compared to a solid fuel powered furnace and boiler: the combustion can be better controlled, drastically reducing the pollutants in the exhaust, the boiler heat exchange surfaces remain clean, it is possible to change fast the flow of generated vapour/steam, in particular it is possible to reduce/shut-off quickly the combustion, in order to adapt to a the fast load change of a stand-alone unit. Moreover, the inventory of fluid in the boiler is lower, compared to a solid fuel boiler, this feature can be important if a direct exchange between combustion gas and organic working fluid is envisaged.
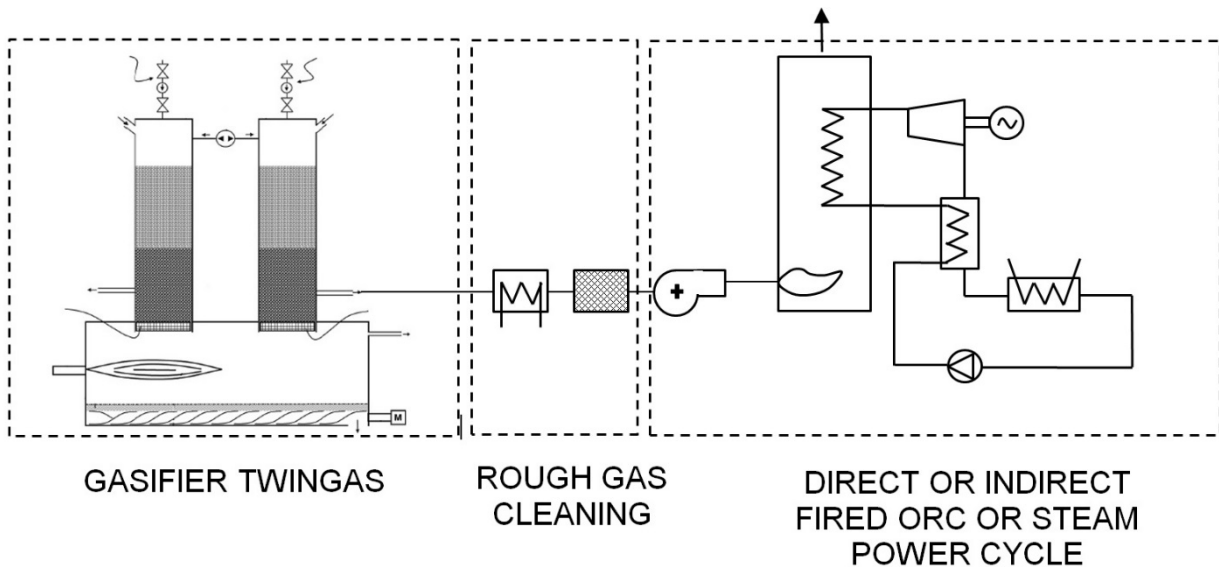
GASIFIER TWINGAS   ROUGH GAS   DIRECT OR INDIRECT
CLEANING   FIRED ORC OR STEAM
POWER CYCLE

Figure 3 - Utilization of syngas for evaporation of working fluid (ORC or Steam plant)

2) Gas is thoroughly cleaned and fed to a reciprocating internal combustion engine (ICE). From the point of view of efficiency this solution is very effective, however past experience has shown that it is difficult to clean the gas consistently to a high purity level, such as to avoid a heavy maintenance burden. The thermal power available in the exhaust downstream from the engine is not large, hence a combined cycle ICE + ORC (fig.4) would get a minor increase of power and efficiency from the ORC itself (the power of the bottoming cycle amounts to some 10% of engine power).
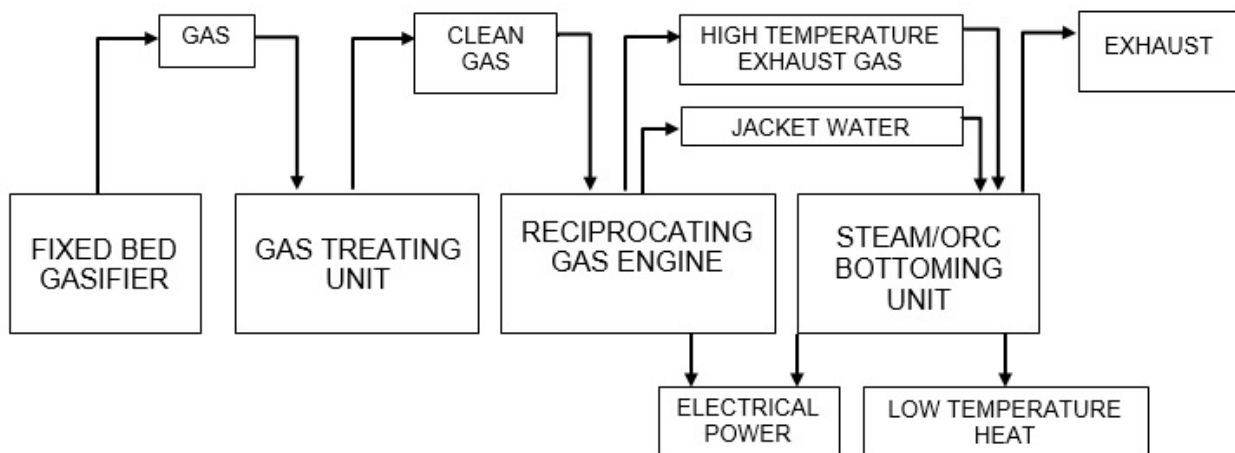
Figure 4 - Schematic of power production from fixed bed gasifier by ICE.

3) Gas is thoroughly cleaned, and fed to a compressor which in turn feeds the combustor of a gas turbine (GT). The required purity level for the gas is substantially lower for a gas turbine then for an ICE. The footprint of the gas turbine is small compared to the ICE, its exhaust gas is cleaner, the maintenance load is lower while availability and realiability are higher.

The amount of thermal power at high temperature in the exhaust is much larger than in a reciprocating engine, and the addition of a bottoming cycle is instrumental to obtain a high overall efficiency. The bottoming cycle can produce some 30% of the overall power.

The rationale for adopting an ORC solution, rather than steam are the following:

- an ORC, if properly designed and constructed is a very reliable, long lasting, and easy to operate unit, featuring a moderate pressure and low rpm turbine,
- the maintenance cost for ORC is low compared to steam system,

- the ORC concept allows to exploit efficiently low power sources, by adopting suitable working fluid and optimized cycle for the specific heat source,
- fast and repeated start/ stop operation and load variation can be easily fulfilled.

A schematic of the solution is reported in fig.5, with reference to an ORC bottoming unit.
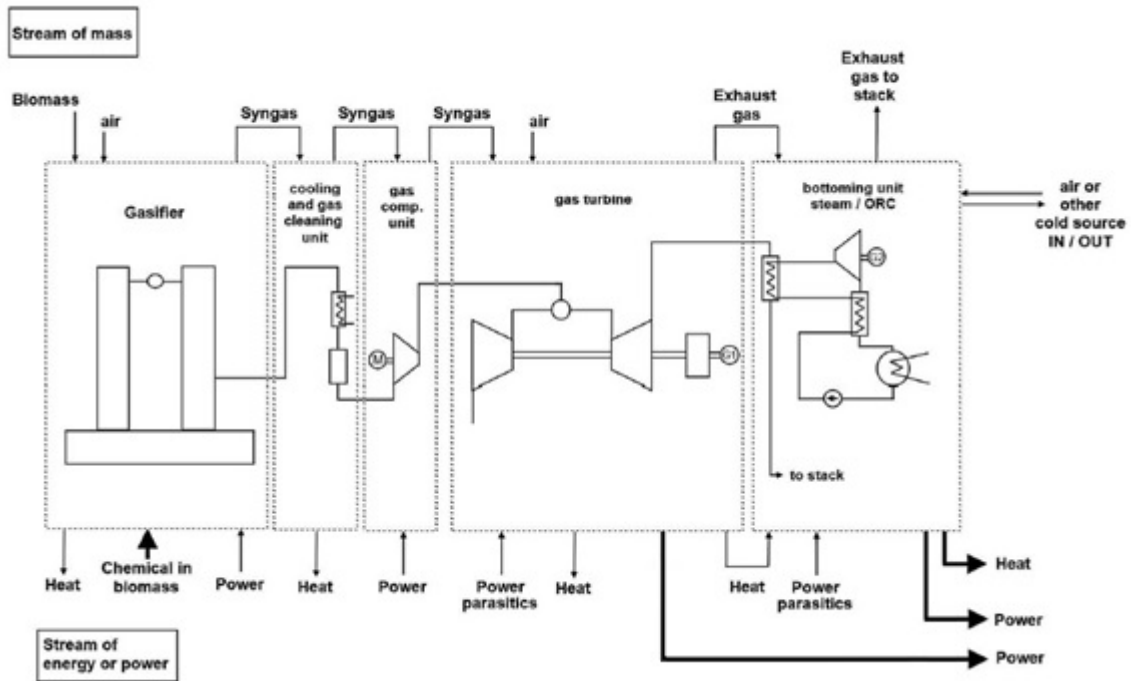

Figure 5 - Schematic of combined cycle fed by gasifier: mass and power streams

The proposed solution for the gasifier should allow to obtain a reliable, low tar, low particulate gas source.
In fact, the best option from the energy efficiency point of view involves the production in the gasifier itself of a pressurized high temperature syngas, hence the whole gas production and supply line to the gas turbine combustor must be under sufficient pressure for power modulation of the gas turbine. To avoid the deposition of its (albeit small) tar content, the temperature of the gas should be kept above some 400 °C.
A preliminary calculation has been performed for a power plant utilizing an OPRA OP16 Gas Turbine [7], organized in a combined cycle, fed by a pressurized Twingas fixed bed gasifier. The bottoming cycle for the combined cycle has been identified as a standard unit (TD 7 by Turboden, with direct recovery from gas turbine exhaust). The working fluid adopted in this case hexamethyldisiloxane.

A simplified scheme is reported in fig.6, featuring direct heat exchange between turbine exhaust gas and ORC working fluid.
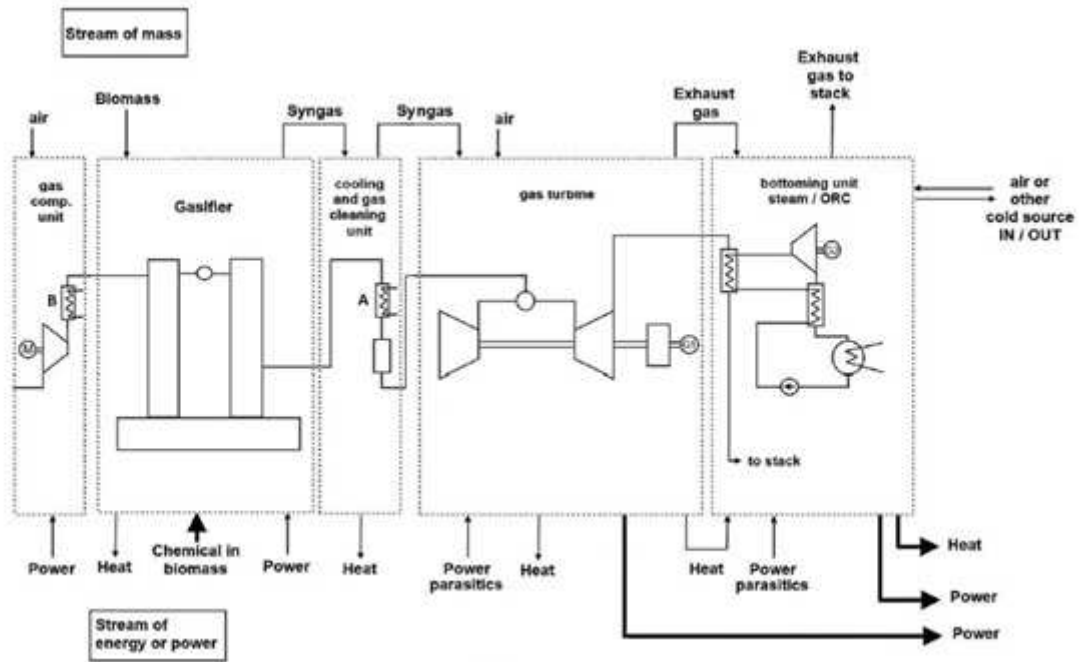
Figure 6 - Schematic of ORC combined cycle fed by pressurized Twingas gasifier: list of mass and power streams

The data adopted for a preliminary evaluation of performance for a case of power only production are reported in Table I ("Standard ORC"), while the preliminary performance is reported in Table II. The design point characteristics for the TD 7 ORC are reported in Tab III [8].

5. ENHANCED ORC BOTTOMING SOLUTIONS

The example reported in the previous chapter concerns the adoption of a standard unit of Turboden as bottoming. In order to explore the power which could be recovered by an ORC system put to the limits, an optimized recovery system has been considered, with two units in series on the exhaust. Moreover, a very high temperature supercritical cycle has been envisaged. The purpose is both to increase the temperature level of the heat input the "high side" of the exhaust flow and to lower the temperature of the exhaust gas leaving the unit, on the "low side". The same working fluid, hexamethyldisiloxane, is adopted in the two cycles, which can be linked in order to take advantage of a number of shared auxiliaries.

The exchanged power vs temperature diagram is reported in fig.7, and the expected performance is summarized in Table I to III and fig. 8 ("Enhanced ORC"). The power increase is obvious, besides the uncertainties linked to the thermal endurance of the working fluid, in any case the power increase would be obtained at the expense of increased capital cost, and complexity of system.
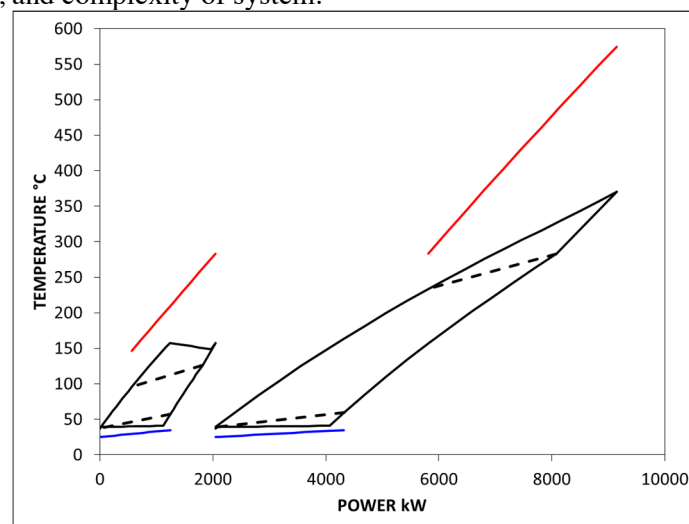

Figure 7 - Q-T diagram for enhanced ORC bottoming solution

Table I: Preliminary data for power-only operation   **Standard ORC** **Enhanced ORC**

			Standard ORC	Enhanced ORC
Gasifier	**Fuel power input (rel. To NCV)**	**kW**	**8362**	**8362**
	NCV fuel (moisture content wood chips 27.5 wt.% w.b.	*kJ/kg w.b.*	12701	12701
	Fuel input	*kg/h*	2370	2370
	Ash	*kg/h*	9,5	9,5
	NCV producer gas (gasifier outlet)	*kJ/kg w.b.*	5100	5100
	Temperature producer gas out of gasifier	*℃*	400	400
	Total power outpu gasifier	**kW**	**8224**	**8224**
	Heat losses producer gas	**kW**	**8**	**8**
	Temperature producer gas after heat loss	*℃*	396	396
Gas Turbine	**Total power input turbine**	**kW**	**8216**	**8216**
	Pressure producer gas into turbine	*barg*	14	14
	Mass flow producer gas into turbine	*kg/s*	1,47	1,47
	Mass flow air into turbine	*kg/s*	8,73	8,73
	Electric power output turbine - gross	**kW**	**2054**	**2054**
	Thermal power exhaust gas out of turbine	**kW**	**5916**	**5916**
	Mass flow exhaust gas	*kg/s*	10,2	10,2
	Temperature exhaust gas out of turbine	*℃*	575	575
	Heat losses exhaust gas	**kW**	**36**	**36**
	Temperature exhaust gas into ORC	*℃*	572	572
ORC	**Thermal power input ORC - from exhaust gas**	**kW**	**4284**	**4906**
	Thermal power input ORC - from cooling PG	**kW**	**-**	**-**
	Conversion losses ORC	**kW**	**27**	**27**
	Electric power output ORC - gross	**kW**	**966**	**1328**
	Thermal power output ORC (not used)	**kW**	**3291**	**3705**
Heat recovery	*Temperature exhaust gas out of ORC*	*℃*	197	129
	Low-temperature heat recovery exhaust gas (used)	**kW**	**-**	**-**
	Temperature exhaust gas leaving heat recovery	*℃*	197	129
	Heat content exhaust gas rest (not used)	**kW**	**1632**	**1010**
	Ambient temperature	*℃*	15	15

Table II: Preliminary performance data for power-only operation   **Standard ORC** **Enhanced ORC**

			Standard ORC	Enhanced ORC
Overall plant	**Total electric power output - gross**	**kW**	**3020**	**3382**
	Auxiliary power consumption gasifier plant	**kW**	**82**	**82**
	Auxiliary power consumption air cooler	**kW**	**11**	**11**
	Auxiliary power consumption gas turbine	**kW**	**16**	**16**
	Auxiliary power consumption ORC	**kW**	**43**	**93**
	Auxiliary power consumption pumps	**kW**	**10**	**15**
	Auxiliary power consumption compression (air, producer gas)	**kW**	**281**	**281**
	Total electrical power output - net	**kW**	**2577**	**2884**
	Total utilized thermal power output	**kW**	**-**	**-**
	Total electric efficiency - gross	**%**	**36,1**	**40,4**
	Total electric efficiency - net	**%**	**30,8**	**34,5**

Table ⅠⅠⅠ: Load case data for power only module		Standard ORC	Enhanced ORC
Net thermal power processed by ORC	kW	4270	4906
Exhaust gas temperature into ORC	℃	575	575
Exhaust gas temperature out of ORC	℃	197	138
Total exhaust gas flow rate	kg/s	10,2	10,2
Exhaust gas average heat capacity	kJ/kgK	1,1	1,1
Heat losses (on gas-fluid exchanger)	%	-	-
ORC overall net output	kW	920	1237
Thermal power to cooling source	kW	3280	3607
Average air temperature (Dry bulb)	℃	15	15
Cooling water inlet temperature	℃	23	23
Cooling water outlet temperature	℃	35	31
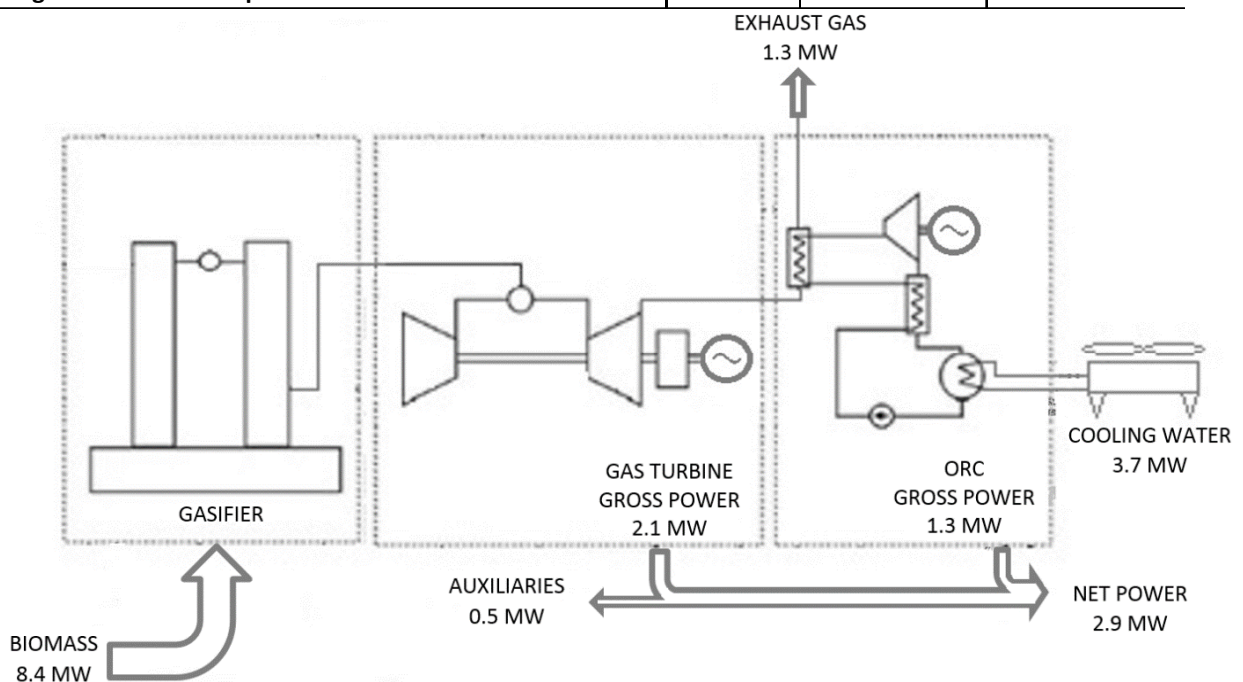
Figure 8 – Simplified block diagram and performance

6. CONCLUSIONS AND FINAL REMARKS

The solution outlined here would allow to obtain a plant, well adapted to converting wood biomass to electric power in the few MW power range, featuring some very attractive points:

- A high overall efficiency of conversion, around 30% for a power-only system with standard ORC.
- Low pollutant content of the exhaust gases.
- Fast modulation of power produced, which could become an important feature for a stand-alone unit.
- Good tolerance concerning the characteristics of the biomass fed to the gasifier, similar to the one of an updraft gasifier.
- Performance with an ORC bottoming system featuring very high temperature supercritical cycle could exceed 34%.

Up to now the solution has been the subject of a number of studies and preliminary evaluations, the technical feasibility, expected performance and cost effectiveness shall be ascertained in the frame of the future activity. If the expected results are confirmed, the proposed solution could give an important contribution to spreading the practical use of small scale biomass sources for power, (typically around 5 MW of electric power produced, by adopting two OPRA Gas Turbine units in parallel), all around the world.

REFERENCES

[1] Obernberger I., Thek G., Combustion and gasification of solid biomass for heat and power production in Europe – state of the art and relevant future developments, *Proceeding of the 8th European Conference on Industrial Furnaces and Boilers (keynote lecture)*, April 2008, Vilamoura, Portugal, ISBN 978-972-99309-3-5, CENERTEC (Ed.), Portugal.

[2] Obernberger I., Thek G., Cost assessment of selected decentralized CHP applications based on biomass combustion and biomass gasification, *Proceeding of the 16th European Biomass conference & Exhibition*, June 2008, Valencia, ETA-Renewable Energies (Ed.), Italy.

[3] Chopra S., Jain A., A review of fixed bed gasification systems for biomass, Agricultural Engineering International: *the CIGR Ejournal*. Invited Overview n° 5. Vol. IX. April, 2007.

[4] P. Basu, Combustion and gasification in fluidized beds, Taylor & Francis, ISDN 0849333962, pp. 335-357, 2006.

[5] S. Kern, C. Pfeifer, H. Hofbauer, Gasification of wood in a dual fluidized bed gasifier: influence of fuel feeding on process performance, Chemical Engineering Science, vol. 90, pp. 284-298, 2013

[6] R. Bini, M. Gaia, inventors; Turboden srl, assignee. Method for gasifying a biomass and respective gasifier. Patent application N° PCT/IB2015/0502238

[7] OPRA turbines – Nederland – Technical specification sheets, available online: http://www.opra.nl/upload/Products/Spec%20sheet%20-%20general%20description.pdf [Last accessed March 2015]

[8] Obernberger I., Thonhofer P., Kerchbaumer C., Thechnical and economic pre-assessment of a biomass gasification coupled with a gas turbine and a ORC, Turboden internal study

APPENDIX I- Description of the TWINGAS concept.

With reference to figg.2 and 9, the proposed gasifier is composed of at least two reactors (vessels 1, and vessel 2) and two connecting vessels or ducts, the hot side duct 3, and the cold side duct.
Biomass feed (wood chips, or any other biomass of interest) are fed through the gated feed mechanisms 5 and 6, and flow down in the twin vessels to the high temperature zone at the bottom. The biomass is pyrolyzed to char in zone 7. In the subsequent zone 8 the char reacts with the volatiles generated in the pyrolysis and air from the top air feeds 9,10 (if present) to produce syngas.
The syngas is extracted through ports 11, 12 in the vessels, or through port 13 in the bottom duct. The charcoal column is retained by grates 14, 15 while the ash falling to the bottom of the bottom duct 3 is extracted by a suitable mechanism 16 (screw or other mechanism).
The temperature of the gas in the bottom duct 3 is held at the value required for proper reaction within the vessels by a burner 17, introducing in the gas the correct amount of oxidizing agent (air, oxygen or any oxygen containing gas). The temperature set is one of the main variables in gasifier operation, in principle it should be as high as possible without exceeding the ash melting threshold.
The whole system is characterized by the pumping device 18, a fan which pushes alternatively the gas in the vessel 1 towards the vessel 2 and viceversa. As the head loss through the biomass columns is low compared to the average pressure of the gas, the pumped gas will behave as a nearly incompressible fluid , and a substantially alternate flow of gas will be established throughout the whole system.
This alternate flow involves that the high temperature at the bottom is easily transferred by the flowing gas to the reacting char bed in the twin vessels, thus supplying the required energy for the gasification reactions.
The following advantages are expected from the alternated flow in the two vessels: each vessel is operated, for about half time, as an updraft gasifier. In this phase a gas flow is established from the high temperature zone to the pyrolysis zone and, further up, to the drying zone. This phase allows an effective transfer of heat to the colder zones following a substantially counter-flow scheme. The gas exiting the top layer of biomass of this "updraft" gasifier, is not sent to utilizer, on the contrary it flows through the other vessel, acting in this phase as a "downdraft" gasifier. Flowing down, the gas becomes loaded with steam from the drying section and then with tar, from the pyrolysis zone. It gets progressively at higher temperature, taking heat from the layers it

goes through. It transfers steam and tar to the char bed, where they participate to the gasifying reactions. Tars are decomposed in the bed, CO and H_2 levels are enriched: the typical effects of a downdraft scheme.

In order to have this scheme running sustainably, an energy input is required as well as an extraction of the useful product, syngas. Like in most gasifiers, fresh energy is supplied by introducing a sub-stoichiometric amount of oxidizer, typically air, or oxygen-enriched air. A number of different options are possible concerning the site of introduction, the most obvious position being the connecting drum at the bottom of the two vessels. In this area the temperature is high, typically around 800 °C, in order to achieve fast going reactions in the char bed, while avoiding ash softening. Introduction of the oxidizer in this area involves the development of immediate reaction with the gas and allows a good control on the temperature in this area, too.

Extraction of produced gas is more tricky, as it should be extracted in a low tar content zone. Also, the temperature should not be too high, to reduce the duty of the heat exchanger preheating of the oxidizer. A position along the two vessels, corresponding to the lower half of the char bed is most probably the best solution. However, due to the pressure drop within the bed, the gas will preferably flow out from the "downdraft" vessel. Hence a gas with a good combination of tar removal and temperature should be obtained. An alternated extraction, controlled by a valve or a fan, can give a number of interesting control strategies.
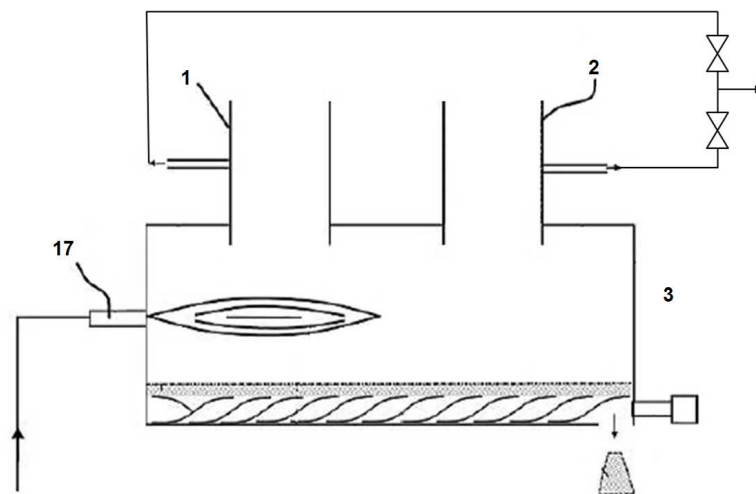
Figure 9 - Extraction points and control values for syngas in Twingas gasifier

In summary, the Twingas solution is expected to allow an effective combination of the advantages of both updraft and downdraft fixed bed gasifiers: moreover so, as it gives new tools for controlling the process, that is the frequency and the intensity of the alternate flow, which are independent from the flow of oxidizer.

Moreover it can be expected that, by keeping a larger thickness of char bed at high temperature, the Twingas solution should allow a much faster modulation of load, and in particular a much faster load increase after an extended low load period. This aspect can be very important for systems supplying an isolated grid.

The Twingas solution has been here summarized, its analysis is in fact complex and involves a time dependent simulation, much more demanding than the already complex simulation of conventional gasifiers.

DEVELOPMENT AND TEST OF A 100KW CLASS ORC POWER-GENERATOR FOR LOW TEMPERATURE GEOTHERMAL APPLICATIONS

Dong Hyun Lee[1], Young Min Yang[1,2,3], Chun Dong Park[1], Si Woo Lee[2], Byung-Sik Park[1,3]*

[2]Energy Efficiency Research Division, Korea Institute of Energy Research,
152 Gajeong-ro, Yuseong-gu, Daejeon 305-343, Republic of Korea
http://www.kier.re.kr (e-mail: dhlee@kier.re.kr)

[2]Jinsol Turbomachinery Co., Ltd.,
94-17 Techno2-ro, Yuseong-gu, Daejeon, 305-509, Republic of Korea
http://www.jinsolturbo.co.kr (e-mail: impentacle@jinsolturbo.co.kr)

[3]Advanced Energy and Technology, Korea University of Science and Technology,
217 Gajeong-ro, Yuseong-gu, Daejeon 305-333, Republic of Korea
e-mail: ymyang@kier.re.kr

ABSTRACT

The major portion of the heat sources is in the lower end of the temperature spectrum. Therefore, the successful utilization of low-grade heat is very essential to energy. The organic Rankine cycles (ORCs) are one of the appropriate technologies to convert low grade heat to power. Korea Institute of Energy Research (KIER) and Jinsol Turbomachinery have jointly developed an ORC power-generator applicable to very low-temperature heat sources. This paper deals with the design, fabrication and test results of the ORC power generator. The ORC system was designed the maximum electric power output of 100kW utilizing geothermal hot water. The ORC has a simple configuration with an evaporator, an expander, a condenser and a pump. The completely hermetic turbo-generator was developed by Jinsol Turbomachinery and applied to the system. The turbo-generator has twin radial inflow turbines connected with high-speed synchronized generator. Two plate heat exchangers are used for evaporator and condenser. The performance test was conducted and the resulted gross electric power output was 91.22kW with cycle efficiency of 7.14%.

1. INTRODUCTION

An organic Rankine cycle (ORC) is a type of a Rankine cycle, which uses organic compounds as a working fluid instead of water. Thanks to the low evaporation temperature of the organic compounds, ORCs could be applied to lower temperature heat sources compared to the steam Rankine cycle. Low grade waste heat, geothermal hot water, solar thermal heat, and biomass combustion can be the heat source for ORCs (Lecompte et al., 2015). There are a couple of alternative technologies for converting low-temperature heat to power, such as Kalina cycle (Kalina, 1984), Uehara cycle (Uehara et al., 1994), Goswami Cycle (Goswami, 1995), trilateral Flash cycle (TFC) and thermoelectric generator. Despite of the high potential of TFC, a lack of efficient two-phase expander is the main obstacle of the TFC. Many researchers have been compared the ORCs and Kalina cycles (Yari et al., 2015, Bombarada et al., 2009, Zare and Mahmoudi, 2015, Yue et al., 2015 and Victor et al., 2013) from a thermodynamic and/or economical perspective. There is still controversy about the best heat recovery power generation technique. However, simple configuration, low pressure level and high freedom of design (selection of working fluids including mixtures, transcritical/supercritical cycle) make the ORS to the most practical technology.

Designing ORC power-generator is quite complex problem due to excessively high freedom of design. Selection of working fluids, configuring a cycle, choosing an expander and heat exchanger types, and etc. Colonna, P. (2013) pointed out that there are 1.6 million alternatives in designing ORCs. Various ORC power-generators are already developed and commercialized in the market. The power ranges of ORCS are from a few kW to tens of MW. Most of the ORCs adopt turbines as expanders, except very small systems due to relatively high isentropic efficiency of turbine. In spite of the long history and successful commercialization of ORCs (Mario Gaja, 2011), many researchers have been making efforts to develop a new and advanced ORC system. Many researchers introduced novel cycles and/or new optimization design method to enhance the cycle efficiency of ORCs (Xiao et al., 2015, Feng et al., 2015 and Imran et al., 2015) and adopting new working fluids (Lecompte et al., 2014 and Mavrou et al., 2015). Several researchers built their own ORCs with various configurations. Yun et al. (2015) designed parallel-expanders ORC for the application with large heat source variations. . Yamada et al (2015) developed a prototype of 10W ORC with a scroll expander. They showed the possibility of micro-scaled ORC in spite of low cycle efficiency. Fu et al. (2015) designed and constructed a simple cycle 250kW class ORC with turbine expander and achieved 9.5% thermal efficiency using 120°C hot water.

In the present work, KIER and Jinsol Turbomachinery jointly developed a 100 class ORC power generator for the commercialization purpose. A simple cycle was selected to avoid complexities in construction/maintenance. Instead of that, we focused on improving and optimizing the performances of the ORC system. An originally designed turbo-generator and hybrid type plate heat exchangers are developed and integrated to the present system. This paper will describe the design, fabrication procedures and test results of the system.

2. CYCLE DESIGN

2.1 Design conditions
To design an ORC system, the conditions of heat source and heat sink should be defined. In the present work, one of the hot spring wells in Seokmo Island is selected as a heat source. The heat source temperature is 75°C and the well is expected to produce about 1,400ton of geothermal hot water per day. For a heat sink, dry cooling tower was chosen. The power output of ORCs changes with external temperature and the maximum power is achieved during the winter season. When designing an ORC power generator, not only the rated power but also maximum power output should be considered due to the safety reasons. Therefore, the cooling water temperature of 5°C was assumed for the winter season.
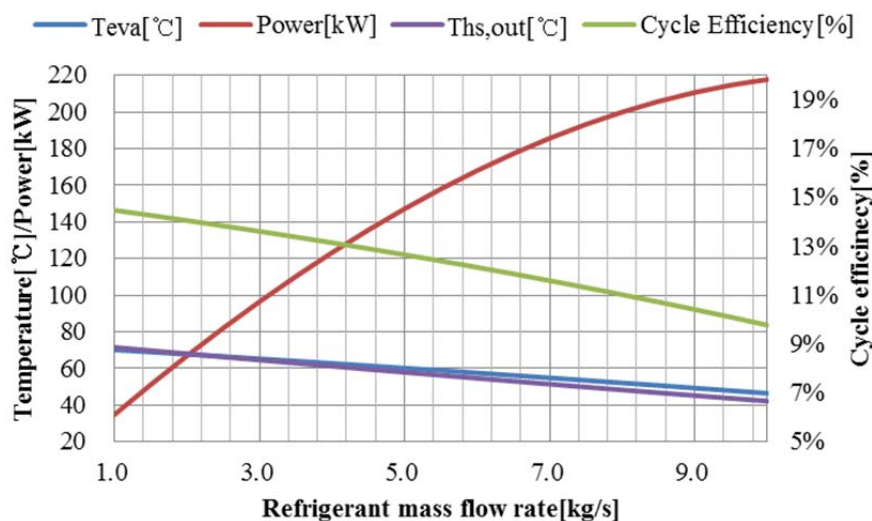

Figure 1: Effects of working fluid flow rate

For the given heat source conditions, the output power of the ORCs increases with the mass flow rate of working fluid, while the cycle efficiency reduces. Therefore, there is no correct answer in deciding a mass flow rate. Hot water in Suokmo Island is planned to be used in hot springs, so the water temperature after the power generation should be high enough for hot springs. Figure 1 shows the effect of mass flow rate of working fluid on evaporation temperature, power output, cycle efficiency and heat source outlet temperature. The working fluid is refrigerant R245fa and the pinch point temperature difference (PPTD) is 2.5°C. For quick estimation, no loss was assumed. Form the calculation, the mass flow rate was determined to 5kg/s with the heat source outlet temperature of 57.9°C.

2.2 System configuration and cycle design
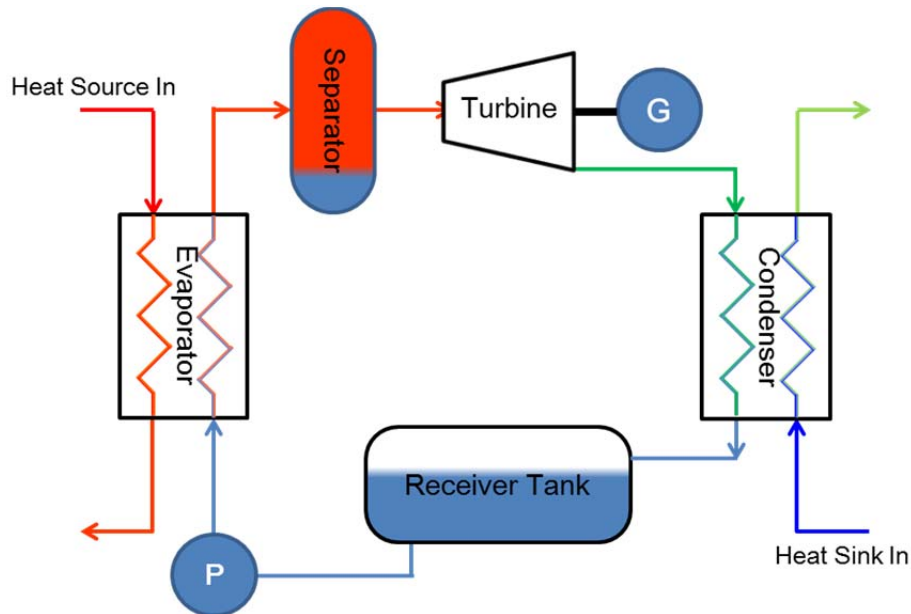
Figure 2: Schematic diagram of ORC power generator
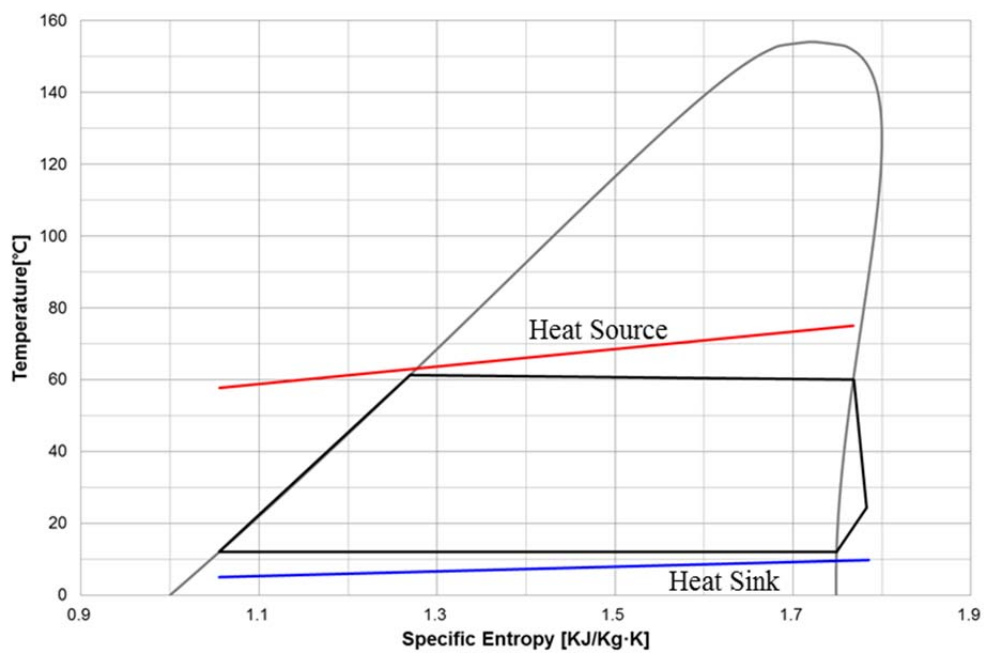
Figure 3: T-s diagram of the present ORC cycle

Figure 2 shows the schematic diagram of the present ORC power generator. The system is consisted of a pump, an evaporator, a separator, turbines, a generator, a condenser and a receiver tank. The R245fa in the receiver tank is assumed an equilibrium state and the temperature and pressure are the same with the condensing condition. For cycle design, efficiencies of the pump, motor, turbine and the generator are assumed to be 0.700, 0.895, 0.850 and 0.950, respectively. And the pressure losses through each component and pipes are considered. The pinch point temperature differences of 2.5°C were applied for both the evaporator and condenser. Required mass flow rate of heat source and heat sink were calculated from the PPTD and were 16.0kg/s and 52.3kg/s, respectively. The *T-s* diagram of the calculated ORC cycle is shown in Fig. 3. The red and blue lines refer the heat source and heat sink, respectively. The generator power output is 113.1kW with 2.268kW of pumping power consumption. The expected gross cycle efficiency is 9.74% (Net: 9.55%).

3. SYSTEM FABRICATION AND TEST

3.1 Component selection and system fabrication

Design requirements for each component are fixed from the cycle design and summarized in Tables 1 and 2.

Table 1: Design requirements of evaporator and condenser

		Evaporator		Condenser	
		Cold side	Hot side	Cold side	Hot side
Working Fluid		R245fa	Water	Water	R245fa
$\dot{m}$[kg/s]		5.0	16.0	52.3	5.0
Inlet	T[°C]	12.2	75.0	5.0	24.2
	P[kPa]	479.4	-	-	91.5
Outlet	T[°C]	60.0	-	-	12.0
	P[kPa]	462.3	-	-	89.2
Heat duty	Q[kW]	1161.0		1044.0	

Table 2: Design requirements of turbine and pump

		Turbine	Pump
Working Fluid		R245fa	
$\dot{m}$[kg/s]		5.0	
Inlet	T[°C]	59.8	12.0
	P[kPa]	456.6	102.6
Outlet	T[°C]	24.3	-
	P[kPa]	95.2	492.8
PR/ΔP[kPa]		4.8/361.4	4.8/390.2

Hybrid type heat exchangers, developed by Innowill, are adopted for both the evaporator and condenser. A Grundfos pump (CRN15-4) was chosen for the present system. A twin radial type turbo-generator was designed and fabricated by Jinsol Turbomachinery. The turbo-generator has twin radial turbines directly coupled with a high speed synchronous generator (Fig. 4). The yellow arrows in Fig. 4 indicate the flow direction of the vapor refrigerant. Details of the turbo-expander are discussed by Yang (2015).
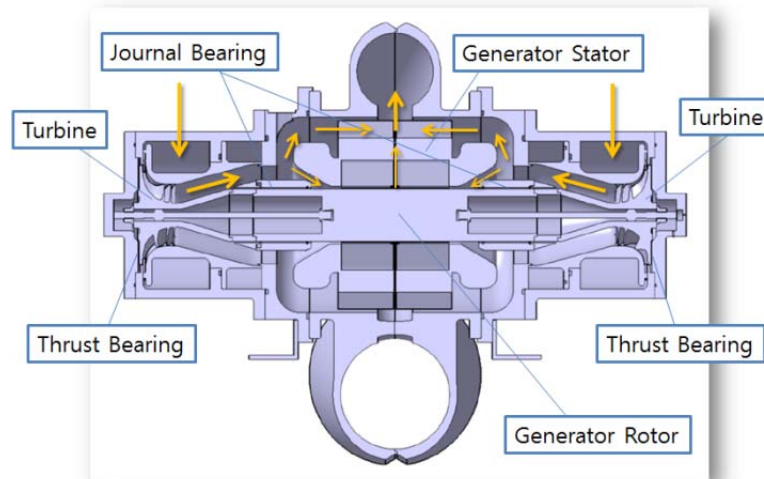
Figure 4: Mechanical Layout of the 100kW turbo-generator for ORC plant (Yang et al., 2015)

A 3ton/hr steam boiler and a plate heat exchanger and hot water tank are used to simulate heat source in Seokmo Island (Fig. 4). The hot water temperature to evaporator was adjusted by controlling steam valve, and the hot water flow rate is fixed. A 500RT cross-flow cooling tower supplies cooling water.
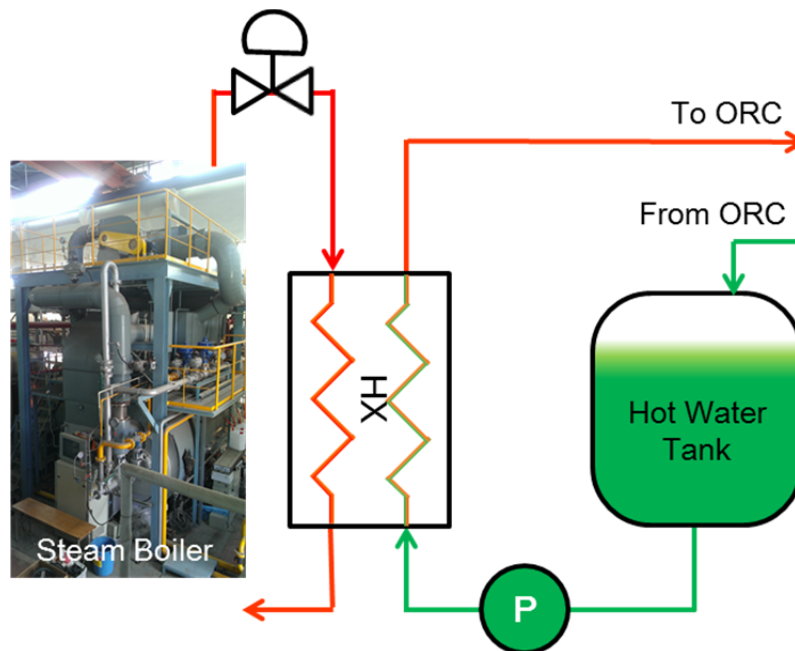

Figure 5: Schematics of hot water supply system

Figure 6 presents the photo of a 100kW ORC turbo-generator installed at KIER. A separator is located just downstream of the evaporator to remove liquid droplet and prevent the possibility of flooding. A small tank is positioned beneath the separator. If the tank is filled with liquid R245fa, an automated control valve opens, so liquid refrigerant can be discharged to receiver tank. Then, hot refrigerant vapor enters the turbines and expands. Since the expanded vapor has very low temperature, it designed to cool the generator instead of external air. Therefore, the vapor refrigerant flows through the generator as shown in Fig. 4. After that it reaches to the condenser and returns to the receiver tank. The receiver tank secures acceptable pump operation pressure for avoiding cavitation and keeps the system stable during unexpected transient behavior, such as over heat input and/or failures in cooling system. A bypass pipe is installed parallel to the turbine.

Figure 6: Photo of a 100kW Geothermal ORC Turbo-generator

3.2 Performance test

For the test and control, pressure transducers with the full scale range of 10bar (GE Druck, PT5072), and RTDs (PT100, 3-wire) are installed as shown in Table 3. The full scale range of the selected pressure transducers is more than double of the operating range. The reason is that the system is pressurized up to 10bar with N_2 gas during the leakage test. The refrigerant flow rate was measured by using Coriolis mass flow meter (OVAL, CA010L) located between the pump and the evaporator. The flow rates of the heat source and cooling water are measured by using magnetic flow meters. The generated electric power was measured at the generator outlet. Precision power analyzer (Yokogawa, WT3000) is used to measure the high frequency electric power.

Figure 7 shows the generator power output (P), refrigerant mass flow rate ($\dot{m}$) and cycle efficiency (η) during the startup test. When the turbine starts, the bypass valve was partially opened, and part of the refrigerant flows through the bypass line. Therefore, the measured flowrate is higher than that enters the turbines. With increasing of the refrigerant mass flow rate, both the power output and the cycle efficiency increase. When the power output increases up to 70kW, the cycle efficiency reaches maximum value and then stays constant. The effects of mass flow rate are shown in Fig. 8. The condensing temperature rose slightly during the test run. The maximum power output (gross) was recorded 91.22kW and the cycle efficiency was 7.14% at 4.17kg/s of mass flow rate. Both the power output and the cycle efficiency are lower than expected. One of the possible reasons is the absence of insulation. The disagreement between heat release of the source and heat gain of the working fluid is about 10~15% during the test. Based on heat gain of the working fluid, the cycle efficiency was rises up to 9.17%.

Figure 9 compares the designed cycle and test results. Dashed lines indicated designed cycle and solid lines refers the test results. During the test, heat sink temperature was higher than that of design condition. To keep the temperature difference between the heat source and heat sink, the heat source temperature. As a result, the tested condition shifted upward compared to the designed cycle, due to higher heat sink temperature. As shown in Fig. 9, unexpected superheating and subcooling are observed. The degrees of superheat and subcooling were 10.2°C and 5.6°C, respectively. The estimated uncertainty of the measured electric power and calculated cycle efficiency were less than ±1.0% and ±1.46%, respectively (Kline and McClintock, 1995).
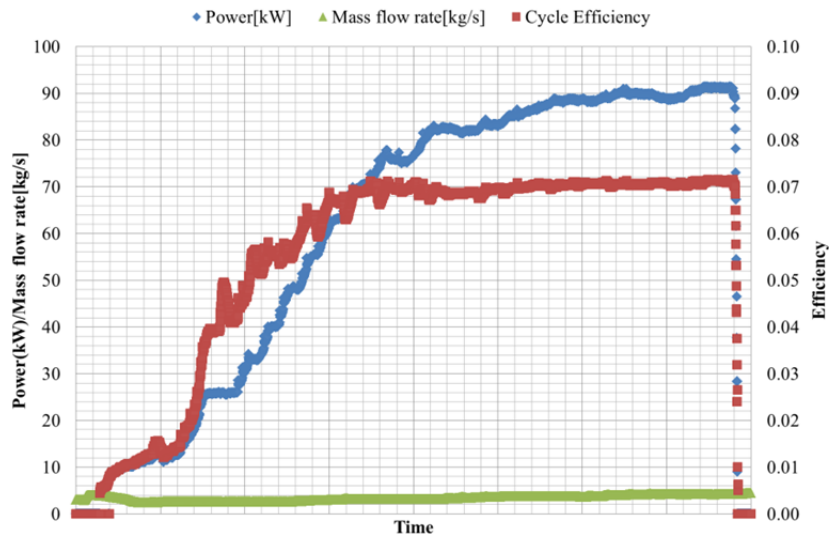
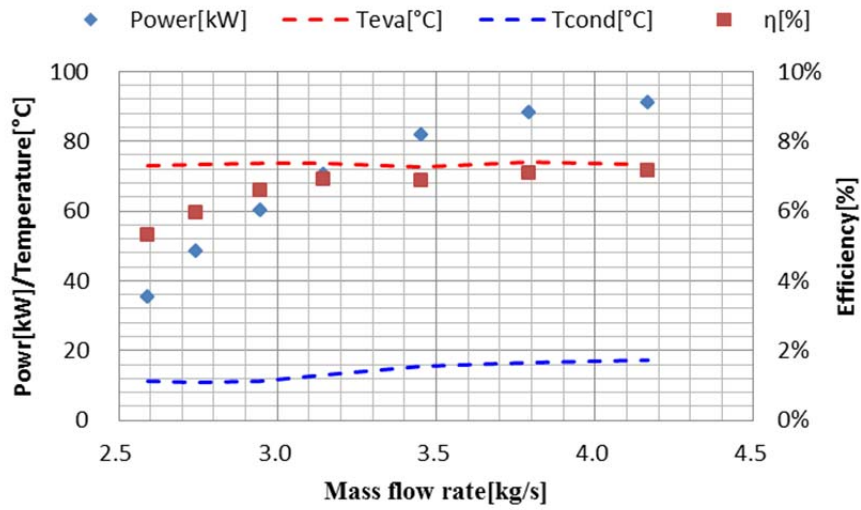**Figure 7:** Power and efficiency change during startup

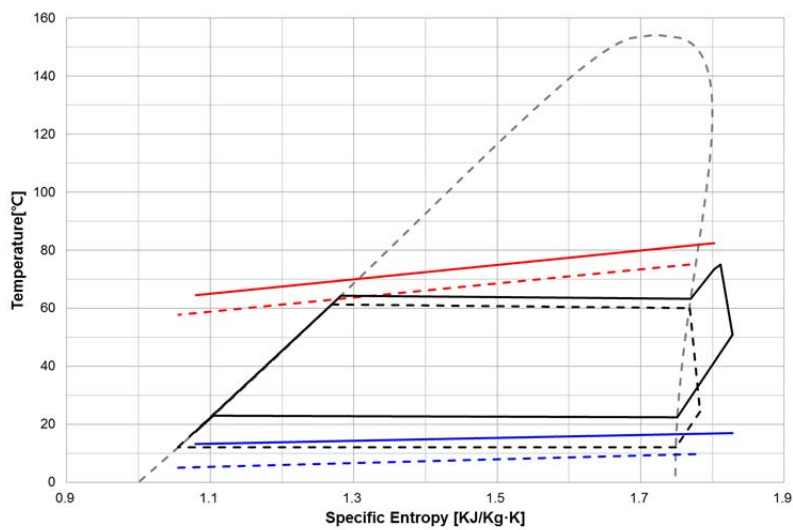**Figure 8:** Performance results of 100kW ORC generator

Figure 9: Comparison of designed and tested cycles

6. CONCLUSIONS

A 100kW ORC system adopting a high speed turbo expander was developed for low temperature geothermal heat applications. Performance test has been made and the results are follows:

- The ORC turbo-generator is designed for 113.1kW of gross electric power and 9.74% of cycle efficiency with the refrigerant mass flow rate of 5kg/s.
- The performance test show maximum electric power output was 91.22kW with the cycle efficiency of 7.14%, and the measured refrigerant flow rate was 4.17kg/s.
- High heat sink temperature and heat losses of the evaporator are the possible reason of low cycle efficiency. Based on heat gain of R245fa, the cycle efficiency was 9.17%, which is almost the same with expected value.

NOMENCLATURE

T	temperature	(°C)
P	pressure	(kPa)
$\dot{m}$	mass flow rate	(kg/sec)
η	cycle efficiency	(%)

Subscript

eva	evaporation
cond	condensation
h	heat source
c	heat sink

ACKNOWLEDGEMENTS

REFERENCES

Bombarada, P., Invernizzi, C.M., Pietra, C., 2010, Heat recovery from Diesel engines: A thermodynamic comparison between Kalina and ORC cycles, *Applied Thermal Engineering*, vol. 30, no 2-3: p. 212-219.

Colonna, P., 2013, ORC power systems: the path from the concept to current applications and an outlook to the future, *Proc. of 2nd Int. Seminar on ORC Power Systems*, Rotterdam, The Netherlands.

Goswami, D.Y., 1995, Solar thermal power-status of technologies and opportunities for research, *Int. Proc. of the 2nd ASME-ISHMT Heat and Mass Transfer Conference*, Tata-McGraw Hill Publishers, New Delhi, India.: p. 57-60.

Feng, Y. Zhang, Y., Li, B., Yang, J., Shi, Y., 2015, Comparison between regenerative organic Rankine cycle (RORC) and basic organic Rankine cycle (BORC) based on thermoeconomic multi-objective optimization considering exergy efficiency and levelized energy cost (LEC), *Energy Conversion and Management*, vol. 96: p. 58-71.

Fu, B.-R., Lee, Y.-R., Hsieh, H.-C., 2015, Design, construction, and preliminary results of a 250-kW organic Rankine cycle system, Applied Thermal Engineering, vol. 80:, p. 339-346.

Gaja, M., 2011, 30 years of organic Rankine cycle development, *Proc. of ORC 2011*, Delft, the Netherlands.

Imran, M., Park B.S., Kim, H.J., Lee, D.H., Usman, M., Heo, M., 2015, Thermo-economic optimization of regenerative organic Rankine cycle for waste heat recovery applications, *Energy Conversion and Management*, vol. 87: p. 107-118.

Kalina, A.I., 1984, Combined-Cycle System with Novel Bottoming Cycle, *J. Eng. Gas Turbines Power*, vol. 106, no. 4: p. 737-742.

Kline, S.J., McClintock F.A., 1953, Describing uncertainty in single-sample experiments, *Mech. Eng.* vol. 75: p. 3-8.

Lecompte, S., Ameel, B., Ziviani, D., van den Broek, M., De Paepe, M., 2014, Exergy analysis of zeotropic mixtures as working fluids in organic Rankine cycles, Energy Conversion and Management, vol. 85: p. 727-739.

Lecompte, S., Huisseune, H., van den Broek, M., Vanslambrouck, B.,DE Paepe, M., 2015, Review of organic Rankine cycle (ORC) architectures for waste heat recovery, Renewable and Sustainable Energy Reviews, vol. 47: p. 448-461.

Mavrou, P., Papadopoulos, A. I., Stijepovic, M. Z., Seferlis, P., Linke, P., Voutetakis, S., 2015, Novel and conventional working fluid mixtures for solar Rankine cycles : Performance assessment and multi-criteria selection, *Applied Thermal Engineering*, vol. 75:, p. 384-396.

Uehara, H., Lkegami, Y., Nishida, T., 1994, OTEC system using a new cycle with absorption and extraction process, *Proc. of 12th Int. COnf. on the Properties of Water and Steam*, pp. 862-869.

Victor, R.A., Kim, J.K., Smith, R., 2015, Composition optimization of working fluids for organic Rankine cycles and Kalina cycles, *Energy*, vol. 55: p. 114-126.

Yamada, N., Tominaga, Y., Yoshida, T., 2014, Demonstration of 10-W_p micro organic Rankine cycle gererator for low-grade heat recovery, *Energy*, vol. 78: p. 806-813.

Yari, M., Mehr, A.S., Zare, V., Mahmoudi, S.M.S., Rosen, M.A., 2015, Exergoeconomic comparison of TLC (trilateral Rankine cycle), ORC (organic Rakine cycle) and Kalina cycle using a low grade heat source, *Energy*, vol. 83: p. 712-722.

Yang, Y.M., Park, B.S., Lee, S.W., Lee, D.H., 2015, Development of a turbo-generator for ORC system with twin radial turbines and gas foil bearings, *Proc. of ASME ORC 2015*, Brussels, Belgium.

Yue, C., Han, D., Pu, W., He, W., 2015, Comparative analysis of a bottoming transcritical ORC and a Kalina cycle for engine exhaust heat recovery, *Energy Conversion and Management*, vol. 89: p. 764-774.

Yun, E., Kim, D., Yoon, S.Y., Kim, K.C., 2015, Experimental investigation of an organic Rankine cycle with multiple expanders used in parallel, *Applied Energy*, vol. 145: p. 246-254.

Zare, V., Mahmoudi, S.M.S., 2015, A thermodynamic comparison between organic Rankine and Kalina cycles for waste heat recovery from the gas turbine-modular helium reactor, *Energy*, vol. 79: p.398-406.

Xiao, L., Wu, S.-Y., Yi, T.-T., Liu, C., Li, Y.-R., 2015, Multi-objective optimization of evaporation and condensation temperatures for subcritical organic Rankine cycle*, Energy*, vol. 83; p. 723-733.

MINI-ORC TURBOGENERATOR: THE UPCOMING LEAP FORWARD?

Piero Colonna

TU Delft
P.Colonna@tudelft.nl

ABSTRACT

Much R&D is currently devoted to obtain commercial ORC power systems generating few kilowatts up to few tens. The driver application is currently waste heat recovery from long-haul truck engines, but many other applications can be envisaged, once these units successfully reach the market. This is not a new idea, and a brief history will illustrate past developments, useful for the context. The design paradigm of such systems is bound to be quite different from mainstream stationary ORC power plants, as mini systems will be designed for standardized large series production. The small capacity offers at the same time challenges and opportunities. The small and fast turbine is one such challenge, and options and concerned research are briefly addressed. Several new applications based on these miniature power plants are described, and ideas for the path forward proposed.

THERMO-ECONOMIC ANALYSIS OF ZEOTROPIC MIXTURES AND PURE WORKING FLUIDS IN ORGANIC RANINKE CYCLES FOR WASTE HEAT RECOVERY

Florian Heberle* and Dieter Brüggemann

University of Bayreuth, Center of Energy Technology (ZET),
Lehrstuhl für Technische Thermodynamik und Transportprozesse (LTTT),
Universitätsstraße 30, 95447 Bayreuth, Germany
e-mail: zet@uni-bayreuth.de
Web page: http://www.zet.uni-bayreuth.de

* Corresponding Author

ABSTRACT

We present a thermo-economic analysis of an Organic Rankine Cycle (ORC) for waste heat recovery. A case study for a heat source temperature of 150 °C and a subcritical, saturated cycle is performed. As working fluids R245fa, isobutane, isopentane and the mixture of isobutane and isopentane are considered. The minimal temperature difference in the evaporator and condenser as well as the mixture composition are chosen as variables in order to identify the most suitable working fluid in combination with optimal process parameters under thermo-economic criteria.

In general, cost-effective systems show a high minimal temperature difference $\Delta T_{PP,C}$ at the pinch-point of the condenser and a low minimal temperature difference $\Delta T_{PP,E}$ at the pinch-point of the evaporator. In case of R245fa, the design parameters $\Delta T_{PP,E} = 1$ K and $\Delta T_{PP,C} = 13$ K lead to minimal costs of 56.8 €/GJ. Choosing isobutane as working fluid leads to the lowest costs per unit exergy with 52.0 €/GJ ($\Delta T_{PP,E} = 1.2$ K; $\Delta T_{PP,C} = 14$ K). Considering the major components of the ORC, specific costs range between 1150 €/kW$_{el}$ and 2250 €/kW$_{el}$. For the mixture isobutane/isopentane, a mole fraction of 90 % isobutane leads to lowest specific costs per unit exergy. Despite an increased efficiency an overcompensation of the additional expenses for the heat exchange equipment is not achieved compared to isobutane. The pure working fluid is 3.3 % more cost-effective. A sensitivity analysis for the ORC system using isobutane as working fluid shows high sensitivity of the costs per unit exergy to the costs of process integration and the isentropic efficiency of the turbine.

1. INTRODUCTION

Organic Rankine Cycle (ORC) systems for waste heat recovery have a high growth potential (Tchanche *et al.*, 2011). Numerous investigations are performed in order to maximize the efficiency of such power plants by working fluid selection with respect to the heat source temperature. Particularly, the use of zeotropic fluid mixtures is a promising optimisation approach due to a good glide match of the temperature profiles at phase change. In this context, Angelino and Colonna di Paliano (1998) show for a low-temperature application that mixtures of natural hydrocarbons (n-butane/n-hexane) lead to an efficiency increase of 6.8 % compared to the pure working fluid n-pentane. Other case studies for geothermal heat sources prove the potential of zeotropic mixtures as working fluids in ORC systems (Demuth, 1981; Iqbal *et al.*, 1976). For subcritical cycles an increase in efficiency by up to 16 % is obtained compared to pure working fluids, like isobutane or isopentane. More recent investigations include sensitivity analyses for crucial parameters (Borsukiewicz-Gozdur and Nowak, 2007; Wang and Zhao, 2009; Chen *et al.*, 2011; Garg *et al.*, 2013; Dong *et al.*, 2014; Lecompte *et al.*, 2014; Shu *et al.*, 2014). In addition, Heberle *et al.* (2012b) show high second law efficiencies for mixture compositions which lead to an good match of the temperature profiles at

condensation. However, these concentrations show a significant increase in heat exchange capacity. Similar results are obtained by Andreasen *et al.* (2014) considering pure components and their zeotropic mixtures as working fluids for subcritical and transcritical cycles in case of a low-temperature heat source. For a heat source temperature of 120 °C, mixtures of propane and higher boiling natural hydrocarbons as well as isobutane/isopentane show high first law efficiency for the subcritical cycle. At the same time, an increase of the heat exchange capacity for the condenser is presented, which is an indicator for the requirement of high heat transfer areas. Angelino and Colonna di Paliano (2000) compare an equimolar mixture of n-butane/n-hexane and pure n-pentane as ORC working fluids in a case study for waste heat recovery. Fan power savings of the air-cooling system of 49 % by using the zeotropic mixture are determined. However, an additional heat transfer area of 73 % is required. Weith *et al.* (2014) have recently shown for a waste heat recovery unit that the use of a siloxane mixture leads to an efficiency increase of 3 % compared to the most efficient pure component. In consequence, a 14 % higher heat transfer area of the evaporator is determined for the zeotropic mixture.

The described dependence suggests a thermo- or exergo-economic analysis of ORC systems in order to evaluate the increased power output and the additionally required heat exchange area for fluid mixtures. Existing thermo-economic analyses of ORC systems are focused on pure working fluids (Tempesti and Fiaschi, 2013; Astolfi *et al.*, 2014; Heberle and Brüggemann, 2014). Regarding small-scale waste heat recovery ORC units, Quoilin *et al.* (2011) determine specific investment costs for 8 working fluids in the range of 2136 €/kW and 4260 €/kW. For an electric capacity between 30 kW and 120 kW, Imran *et al.* (2014) considered different plant schemes and working fluids. In this context, specific investment costs in the range of 3556 €/kW and 4960 €/kW are obtained. Quoilin *et al.* (2013) indicate specific investment costs between 8000 €/kW and 1000 €/kW for an ORC waste heat recovery module in the range of 10 kW and 7500 kW electrical power output. In case of an geothermal resource, Heberle *et al.* (2012a) identify isobutane as a cost-efficient working-fluid compared to isopentane. The lowest specific costs are obtained for a minimal temperature difference of 3 K in the evaporator and 7 K in the condenser.

Under the consideration of zeotropic mixtures as potential ORC working fluids, we provide a thermo-economic analysis of waste heat recovery ORCs. In order to clarify if an efficiency increase overcompensates the additional heat transfer requirements. A case study is performed for a heat source temperature of 150 °C. In this context, a second law analysis for the ORC working fluids R245fa, isobutane and isopentane as well as for the zeotropic mixture isobutane/isopentane is conducted. Based on processes parameters the required heat exchange equipment is designed. Finally, the specific costs for the generated electricity are calculated. Depending on the working fluid composition and the minimal temperature difference in the condenser and evaporator, the most cost-efficient system is identified.

2. METHODS

2.1 Exergy analysis

For the exergy analysis, steady-state simulations are performed using the software Cycle Tempo (Woudstra, N. and van der Stelt, T.P., 2002). Fluid properties are calculated by RefProp Version 9.1 (Lemmon, E.W. *et al.*, 2013). Process simulations are conducted for a subcritical and saturated cycle. The scheme of the module and the corresponding *T,s*-diagram in case of a pure working fluid is illustrated in Figure 1.

The present case study is conducted for a low-temperature waste heat source of 150 °C. As a heat transfer medium pressurized water is assumed ($p_{HS} = 6$ bar). The mass flow and the outlet temperature of the heat source are chosen according to a thermal heat input of 3 MW. For the analysis, an air-cooled system is considered. R245fa, isobutane and isopentane as well as the zeotropic mixture isobutane/isopentane are examined as ORC working fluids. For the considered mixture, the composition is varied in discrete steps of 10 mole-%. The temperature difference in the evaporator and condenser is chosen as independent design variables in order to identify the most cost-efficient

process parameters. The analysis is conducted neglecting pressure and heat losses in the pipes and components. In Table 1 the boundary conditions for the cycle simulations are shown.
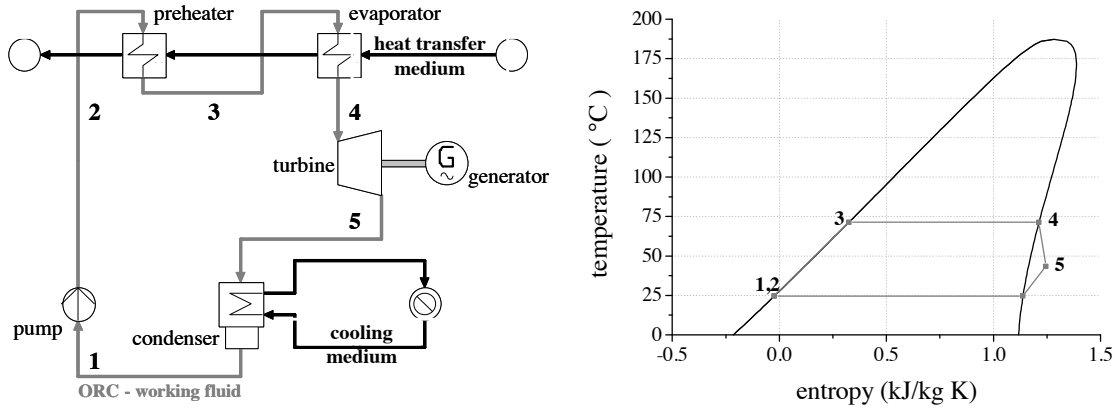

Figure 1: Scheme of ORC system and corresponding *T,s*-diagram for the working fluid isopentane

Table 1. Boundary conditions assumed for the second law analysis

parameter	
mass flow rate of heat source $\dot{m}_{HS}$	10 kg/s
outlet temperature of heat source $T_{HS,in}$	80 °C
inlet temperature of cooling medium $T_{CM,in}$	15 °C
temperature difference of cooling medium ΔT_{CM}	15 °C
maximal ORC process pressure p_2	$0.8 \cdot p_{crit}$
isentropic efficiency of feed pump $\eta_{i,P}$	75 %
isentropic efficiency of turbine $\eta_{is,T}$	80 %
efficiency of generator η_G	98 %

To evaluate the cycle efficiency, the net second law efficiency η_{II} of the ORC is calculated by

$$\eta_{II} = \frac{\left| P_G + P_{Pump} + P_{Fans} \right|}{\dot{E}_{HS}} = \frac{P_{net}}{\dot{m}_{HS} \cdot e_{HS}} \tag{1}$$

where P_G and P_{Pump} correspond to the power of the generator and the pump. P_{Fans} is related to the power of the air cooler fans. The exergy flow of the heat source $\dot{E}_{HS}$ is obtained by multiplying the specific exergy e_{HS} with the mass flow rate $\dot{m}_{HS}$. The specific exergy could be calculated by

$$e_{HS} = h - h_0 - T_0(s - s_0) \tag{2}$$

where the subscript 0 corresponds to the reference state ($T_0 = 15$ °C and $p_0 = 1$ bar). Corresponding to (Bejan et al., 1996), the exergy analysis is extended by an exergy balance for each component k of the system

$$\dot{E}_{F,k} = \dot{E}_{P,k} + \dot{E}_{L,k} + \dot{E}_{D,k} \tag{3}$$

where $\dot{E}_F$ and $\dot{E}_P$ describe the exergy flow rate of the fuel and the product. The exergy flow rate $\dot{E}_L$ includes heat losses to the surrounding or exergy that leaves the system in a physical way, like exhaust gases. Here $\dot{E}_L = 0$, due to neglected heat losses. The exergy flow rate $\dot{E}_D$ represents the exergy destruction rate associated to irreversibilities. Exemplarily, the exergy destruction rate of the preheater can be calculated as

$$\dot{E}_{D,PH} = \dot{m}_{ORC} T_0 \left[(s_3 - s_2) - \frac{h_3 - h_2}{T_{m,PH}} \right] \qquad (4)$$

where $T_{m,PH}$ corresponds to the thermodynamic mean temperature of the heat source in the preheater.

2.2 Component design and economic analysis

For the major components of the ORC module, the purchased equipment costs (PEC) are estimated based on cost data of Turton *et al*. (2003). Purchased equipment costs C_0 based on ambient operating conditions and a carbon steel construction are calculated in US $ depending on parameter Y:

$$\log_{10}C_0 = K_1 + K_2 \log_{10}(Y) + K_3 \left(\log_{10}(Y) \right)^2 \qquad (5)$$

where Y represents the capacity or size of a component. The parameters K_1, K_2 and K_3 are listed in Table 2. To convert the PEC in Euro a conversion ratio of 0.815 is considered. Due to maximal ORC pressures below 35 bar, additional cost factors depending on system pressure are not considered.

Table 2. Equipment cost data used for Equation (5) according to Turton *et al*. (2003)

component	Y; unit	K_1	K_2	K_3
Pump (centrifugal)	kW	3.3892	0.0536	0.1538
Heat exchanger (floating head)	m^2	4.8306	-0.8509	0.3187
Heat exchanger (air cooler)	m^2	4.0336	0.2341	0.0497
Turbine (axial)	kW	2.7051	1.4398	-0.1776

By setting the corresponding Chemical Engineering Plant Cost Index (CEPCI$_{2001}$) of 397 into relation to the value of 2014 with 575, the inflation and the development of raw material prices are taken into account Turton *et al*. (2003). For the costs $C_{tot,ORC}$ of the major components of the ORC power plant the PEC are summarized. The total investment costs of the power plant are calculated by multiplying $C_{tot,ORC}$ by the factor $F_{costs} = 6.32$. According to Bejan *et al*. (1996) this parameter represents additional costs like installation, piping, controls, basic engineering and others. The heat exchange area A is determined for the shell and tube heat exchanger in counter flow. Therefore, the overall heat transfer coefficient U_{tot} of each heat exchanger is calculated by

$$\frac{1}{U_{tot}} = \frac{1}{\alpha_o} + \frac{1}{\alpha_i}\frac{r_o}{r_i} + \frac{r_o \, ln\left(r_o / r_i\right)}{\lambda_t} \qquad (6)$$

where α_o represents the heat transfer coefficient at the outside of the tube, respectively, the shell side and α_i corresponds to the heat transfer coefficient at the inside of the tube. The inner and outer radius of the tube are represented by r_i and r_o. The thermal conductivity of the tube corresponds to λ_t. The outer diameter of the tubes is 20 mm and the wall thickness of the tube is 2 mm. In order to calculate the required diameter of the shell and the number of tubes, the maximal flow velocities of 1.5 m/s for liquid flows and 20 m/s for gaseous flows are assumed according to chapter O1 of the VDI Heat Atlas (VDI-GVC, 2010). In general, the ORC working fluid is led inside the tubes. Regarding the tube layout, a squared pitch and a pitch to diameter ratio of 1.22 are assumed. The considered heat transfer correlations for the calculation of α_i, depending on phase state and flow configuration are listed in Table 3. In case of the preheater and the evaporator, the method of Kern (1950) is applied for the shell side (α_o). For the air-cooled condenser a tube bank staggered arrangement is applied. In this context, a cross-flow heat exchanger with finned tubes is considered and the following design parameters are assumed: fin height of 3 mm, a fin thickness of 0.3 mm, a fin spacing of 2 mm and a transversal tube pitch of 60 mm. The air-side heat transfer coefficient is determined by the method of Shah *et al*. (2003). For all considered heat exchangers, the heat transfer surface is finally calculated by

$$\dot{Q} = U_{tot} A F_{LMTD} \Delta T_{log} \tag{7}$$

where ΔT_{log} is the logarithmic mean temperature difference. In general, the logarithmic mean temperature difference correction factor F_{LMTD} is equal 1 for condensation and boiling heat transfer. In this study, the simplifying assumption of $F_{LMTD} = 1$ is also met for single phase heat transfer.

Table 3. References for the considered heat transfer correlations

heat exchanger	tube side
preheater	(Sieder and Tate, 1936)
evaporator (pure working fluid)	(Steiner, 2006)
evaporator (zeotropic mixture)	(Schlünder, 1983)
condenser (pure working fluid)	(Shah, 1979)
condenser (zeotropic mixture)	(Bell and Ghaly, 1973; Silver, 1964)

2.3 Exergy costing

The thermo-economic analysis combines thermodynamic and economic aspects. In this context, the product of the energy conversion as well as each component can be evaluated according to the cost formation process. For the presented analysis, the method by Tsatsaronis and Winhold (1985), also known as exergo-economic method, is used. The exergy costing converts an exergy stream $\dot{E}$ to a cost stream $\dot{C}$, by multiplying the exergy with corresponding average costs per unit of exergy, respectively, specific costs c. In this context, a system of equations is set up consisting of the cost balance for each component k of system (Bejan *et al*., 1996), (Heberle *et al*., 2012a):

$$\dot{C}_{P,k} = \dot{C}_{F,k} - \dot{C}_{D,k} + \dot{Z}_k \tag{8}$$

The cost streams $\dot{Z}_k$ describe the costs of the k-th component depending on operation and maintenance $\dot{Z}_{O\&M}$ and capital investment $\dot{Z}_{CI}$. In order to calculate the described cost streams the economic boundary conditions listed in Table 4 are assumed.

Table 4. Economic parameters for the calculation of the cost streams $\dot{Z}_k$

parameter	
lifetime	20 years
interest rate *ir*	4.0 %
annual operation hours	7500 h/year
Cost rate for operation and maintenance	$0.02 \cdot \dot{Z}_{CI}$
Costs for process integration C_{PI}	$0.2 \cdot C_{tot,ORC}$
Power requirements of the air-cooling system	5 kW$_e$/MW$_{th}$
Electricity price €/kWh	0.08 €/kWh

The selected optimization criteria for the system is the minimization of the costs per unit exergy of the total system $c_{P,tot}$. In this study, the generated electricity is considered as the product of the system and the $\dot{E}_{P,tot}$ correspond to the power output of the generator. In this context, the auxiliary power requirements are covered by electricity from the grid. Alternatively, the net power output of the system can be considered in the denominator of Equation (9). The exergy rate of the fuel $\dot{E}_{F,tot}$ represents the exergy rate of the waste heat source transferred to the ORC system.

$$c_{P,tot} = \frac{\dot{C}_{P,tot}}{\dot{E}_{P,tot}} = \frac{(c_{F,tot} \dot{E}_{F,tot} + \sum_k \dot{Z}_k)}{\dot{E}_{P,tot}} \tag{9}$$

In addition, the specific investment costs *SIC* are calculated:

$$SIC = \frac{C_{tot,ORC}}{P_{net}} \tag{10}$$

3. RESULTS AND DISCUSSION

3.1 Identification of cost-efficient design parameters

For each working fluid the minimal costs per unit exergy $c_{p,tot}$ are identified depending on the minimal temperature difference ΔT_{PP} in the evaporator and condenser. In order to vary the minimal temperature difference, the corresponding upper and lower ORC pressure is adapted. In Figure 2, the resulting specific costs of the product are shown exemplarily for R245fa. The most cost-efficient design parameters for this ORC working fluid are $\Delta T_{PP,E} = 1$ K and $\Delta T_{PP,C} = 13$ K. For these parameters, costs per unit exergy of 56.8 €/GJ are obtained. Considering a minimal temperature difference between 0.5 K and 6 K for the evaporator and 8 K and 14 K for the condenser, the maximum costs per unit exergy of 60.0 €/GJ are calculated ($\Delta T_{PP,E} = 6$ K; $\Delta T_{PP,C} = 8$ K). In general, the cost minimum is a compromise between rising power output and increasing costs with decreasing minimal temperature difference in the heat exchangers. The results show that the condenser is crucial for the total PEC. Due to the highest amount of transferred thermal energy combined with the lowest logarithmic mean temperature difference, the highest heat transfer areas and component costs are obtained for the condenser. Therefore, the most cost-effective parameters show a low ΔT_{PP} for the evaporator and a high value in case of the condenser.
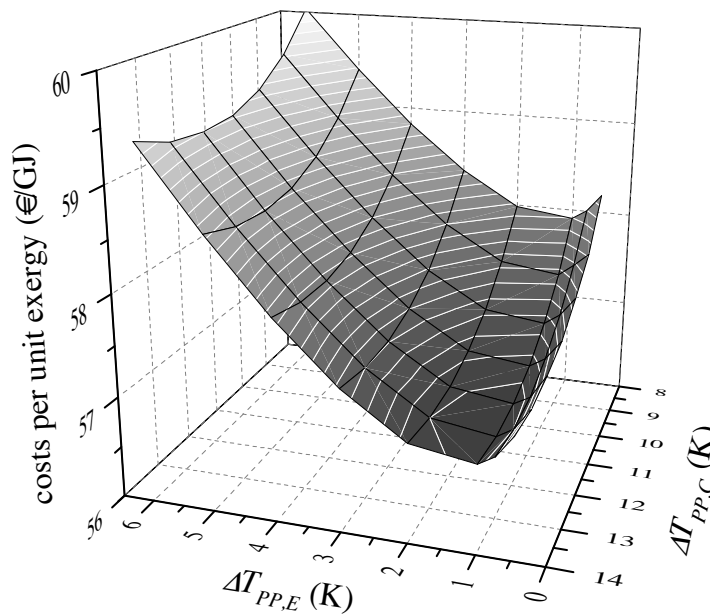
Figure 2: Costs per unit exergy for R245fa as ORC working fluid depending on minimum temperature difference in the evaporator and condenser

3.2 Comparison of ORC working fluids

Power output, heat transfer area and, therefore, capital investment costs for the ORC modules may considerably vary due to the working fluid selection and the corresponding fluid properties. In this context, Figure 3a illustrates the costs per unit exergy for the pure ORC working fluids isopentane, isobutane and R245fa as function of the minimum temperature difference in the condenser. For

$\Delta T_{PP,E}$, always the most cost-effective parameter is shown. In Figure 3b specific costs of the product are shown for selected mole fractions of the zeotropic mixture isobutane/isopentane.

Isobutane is identified as the most cost-effective working fluid for the considered case study with costs per unit exergy of 52.0 €/GJ. The corresponding design parameters are $\Delta T_{PP,E} = 1.2$ K and $\Delta T_{PP,C} = 14$ K. R245fa and isopentane lead to 9.2 % and 15.0 % higher costs per unit exergy (see Table 4). Although, these alternative pure working fluids show optimal design parameters with a lower minimum temperature difference, the power output is 10.8 % and 14.6 % lower. Net second law efficiency is between 1.0 % and 3.0 % lower compared to isobutane. The total heat exchange area differs only slightly and is 0.3 % lower for R245fa and 2.1 % higher for isopentane.
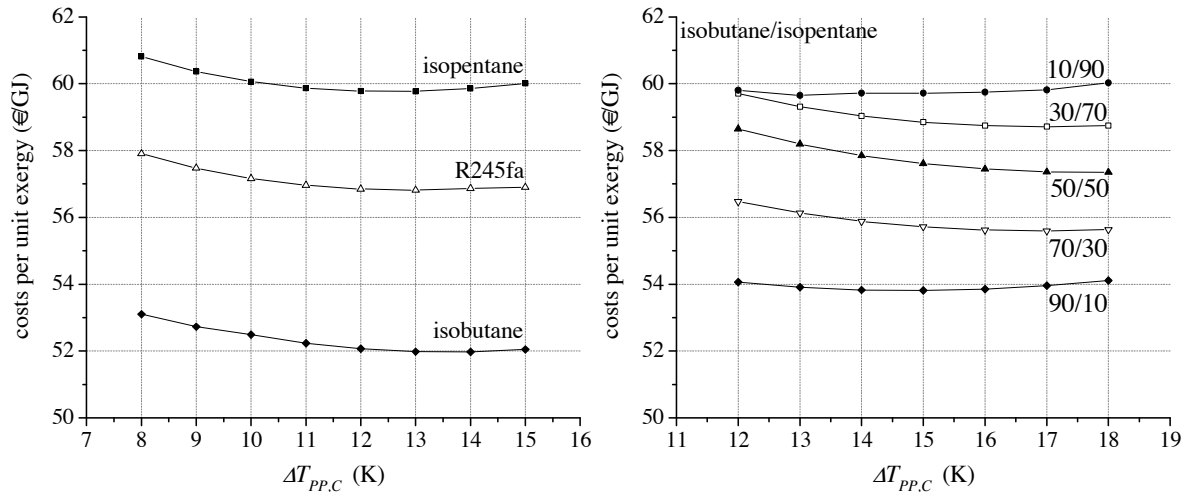
Figure 3: Costs per unit exergy for the pure ORC working fluids (**3a**) and for the zeotropic mixture isobutane/isopentane (**3b**) depending on the minimum temperature difference in the condenser

Regarding the mixture isobutane/isopentane, a mole fraction of 90 % isobutane leads to the lowest costs. In case of $\Delta T_{PP,E} = 2$ K and $\Delta T_{PP,C} = 15$ K specific costs of 53.8 €/GJ are obtained. However, the costs per unit exergy are 3.5 % higher compared to the most efficient component isobutane. This is due to a 5.5 % lower power output. At same time the total heat exchange area is only 3.6 % lower for 90/10 compared to isobutane.

Table 4. Selected ORC parameters for the most-effective cycles depending on fluid selection

parameter	isobutane	R245fa	isopentane	isobutane/isopentane
A_{PH} (m^2)	173.2	100.0	90.8	108.1
A_E (m^2)	123.1	118.1	118.6	112.8
A_C (m^2)	747.1	821.7	856.0	785.0
P_G (kW)	387.8	345.9	331.0	366.4
P_{Pump} (kW)	60.1	21.6	12.1	41.4
$\Delta T_{PP,E}$ (K)	1.2	1.0	1.0	2.0
$\Delta T_{PP,C}$ (K)	14.0	13.0	13.0	15.0
η_{II} (%)	30.3	30.0	29.4	30.0
SIC (€/kW)	1161.9	1270.1	1336.23	1203.0
$c_{p,tot}$ (€/GJ)	52.0	56.8	59.8	53.8

3.3 Sensitivity analysis for selected boundary conditions

In order to identify the most cost-important parameters of the estimated boundary conditions, Figure 4 illustrates the costs per unit exergy as function of interest rate, turbine efficiency, costs for process

integration, costs for operation and maintenance and *F*-factor. The specific costs per unit exergy show the highest sensitivity for the isentropic efficiency of the turbine and the costs for process integration.
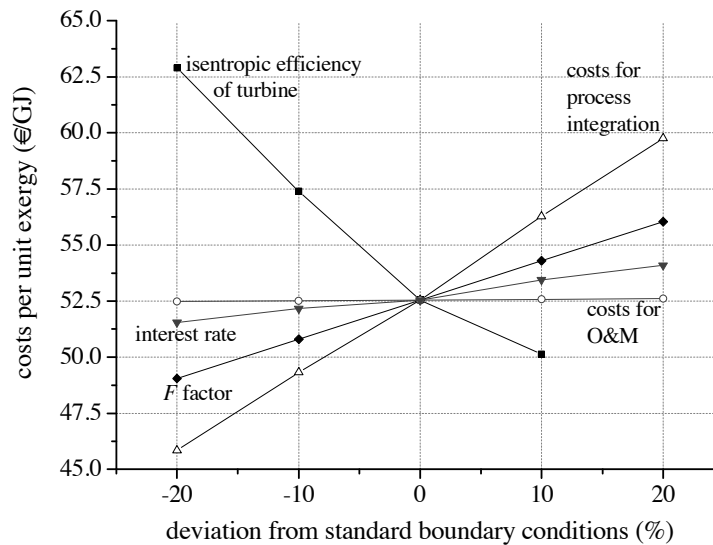

Figure 4: Cost per unit exergy as function of selected parameters for the working fluid isobutane

4. CONCLUSIONS

A thermo-economic case study for waste heat recovery by ORC is conducted. Cost-efficient design parameters concerning the temperature difference at the pinch point are identified in the case of pure working fluids and mixtures. In general, low minimum temperature differences in the evaporator and high values in the condenser are suitable for a cost-efficient ORC system. Isobutane as a working fluid leads to the most cost-effective ORC ($\Delta T_{PP,E}$ = 1.2 K; $\Delta T_{PP,C}$ = 14 K). Regarding the considered mixture isobutane/isopentane, a mole fraction of 90 % isobutane leads to the lowest costs per unit exergy. The economic parameters show a high sensitivity with respect to the estimated isentropic efficiency of the turbine and the costs for process integration. For further work, a variation of the heat source temperature and the heat exchanger design will be considered. In the context of a reliable estimation of the turbine efficiency, a detailed turbine model will be implemented in the analysis.

NOMENCLATURE

A	heat transfer area	(m^2)
c	costs per unit exergy	(€/GJ)
C	costs	(€)
$\dot{C}$	cost rate	(€/h)
e	specific exergy	(kJ/kg)
$\dot{E}$	exergy flow	(kW)
F	cost factor	(-)
h	specific enthalpy	(kJ/kg)
K	constant	(-)
$\dot{m}$	mass flow	(kg/s)
p	pressure	(bar)
P	power	(kW)
r	radius	(m)
s	specific entropy	(kJ/(kgK))
SIC	specific investment costs	(€/kW)
T	temperature	(°C)
U	overall heat transfer coeff.	(W/(m^{2}K))

Y	capacity/size parameter	(kW) or (m^2)
$\dot{Z}$	cost rate	(€/h)
α	heat transfer coefficient	(W/(m^{2}K))
$\varDelta T$	temperature difference	(K)
η	efficiency	(%)

Subscript

C	condenser		*log*	logarithmic
CI	capital investment		*m*	mean
CM	cooling medium		*net*	net
D	destruction		*o*	outer
E	evaporator		*out*	outlet
F	fuel		*O&M*	operation and
G	generator			maintenance
HS	heat source		*P*	product
i	inner		*PH*	preheater
is	isentropic		*PP*	pinch point
II	second law		*Pump*	pump
K	k-th component		*t*	tube
L	loss		*tot*	total
$LMTD$	logarithmic mean temperature difference		*0*	reference state

REFERENCES

Andreasen, J.G., Larsen, U., Knudsen, T., Pierobon, L., Haglind, F., 2014. Selection and optimization of pure and mixed working fluids for low grade heat utilization using organic rankine cycles. *Energy* 73, 204–213.

Angelino, G., Colonna di Paliano, P., 1998. Multicomponent Working Fluids For Organic Rankine Cycles (ORCs). *Energy* 23, 449–463.

Angelino, G., Colonna di Paliano, P., 2000. Air cooled siloxane bottoming cycle for molten carbonate fuel cells, *Proceedings of 2000 Fuel Cell Seminar*. Portland (USA).

Astolfi, M., Romano, M.C., Bombarda, P., Macchi, E., 2014. Binary ORC (Organic Rankine Cycles) power plants for the exploitation of medium–low temperature geothermal sources – Part B: Techno-economic optimization. *Energy* 66, 435–446.

Bejan, A., Tsatsaronis, G., Moran, M., 1996. *Thermal Design & Optimization*. John Wiley & Sons, New York.

Bell, J., Ghaly, A., 1973. An approximate generalized design method for multicomponent/partial condensers. *AIChe Symp Ser. Heat Transf.* 69, 72–79.

Borsukiewicz-Gozdur, A., Nowak, W., 2007. Comparative analysis of natural and synthetic refrigerants in application to low temperature Clausius-Rankine cycle. *Energy* 32, 344–352.

Chen, H., Goswami, D.Y., Rahman, M.M., Stefanakos, E.K., 2011. A supercritical Rankine cycle using zeotropic mixture working fluids for the conversion of low-grade heat into power. *Energy* 36, 549–555.

Demuth, O.J., 1981. Analyses of mixed hydrocarbon binary thermodynamic cycles for moderate temperature geothermal resources, *Proceedings of IECEC Conference*. Atlanta (USA).

Dong, B., Xu, G., Cai, Y., Li, H., 2014. Analysis of zeotropic mixtures used in high-temperature Organic Rankine cycle. *Energy Convers. Manag.* 84, 253–260.

Garg, P., Kumar, P., Srinivasan, K., Dutta, P., 2013. Evaluation of isopentane, R-245fa and their mixtures as working fluids for organic Rankine cycles. *Appl. Therm. Eng.* 51, 292–300.

Heberle, F., Bassermann, P., Preissinger, M., Brüggemann, D., 2012a. Exergoeconomic optimization of an Organic Rankine Cycle for low-temperature geothermal heat sources. *Int. J. Thermodyn.* 15, 119–126.

Heberle, F., Brüggemann, D., 2014. Thermoeconomic Analysis of Hybrid Power Plant Concepts for Geothermal Combined Heat and Power Generation. *Energies* 7, 4482–4497.

Heberle, F., Preißinger, M., Brüggemann, D., 2012b. Zeotropic mixtures as working fluids in Organic Rankine Cycles for low-enthalpy geothermal resources. *Renew. Energy* 37, 364–370.

Imran, M., Park, B.S., Kim, H.J., Lee, D.H., Usman, M., Heo, M., 2014. Thermo-economic optimization of Regenerative Organic Rankine Cycle for waste heat recovery applications. *Energy Convers. Manag.* 87, 107–118.

Iqbal, K.Z., Fish, L.W., Starling, K.E., 1976. Advantages of using mixtures as working fluids in geothermal binary cycles. *Proc. Okla. Acad. Sci.* 56, 110–113.

Kern, D.Q., 1950. Process Heat Transfer. McGraw-Hill, New York.

Lecompte, S., Ameel, B., Ziviani, D., Van Den Broek, M., De Paepe, M., 2014. Exergy analysis of zeotropic mixtures as working fluids in Organic Rankine Cycles. *Energy Convers. Manag.* 85, 727–739.

Lemmon, E.W., Huber, M.L., McLinden, M.O., 2013. *NIST Standard Reference Database 23 – Version 9.1.* Physical and Chemical Properties Division. National Institute of Standards and Technology, Boulder, Colorado, US Department of Commerce, USA.

Quoilin, S., Broek, M.V.D., Declaye, S., Dewallef, P., Lemort, V., 2013. Techno-economic survey of Organic Rankine Cycle (ORC) systems. Renew. Sustain. *Energy Rev.* 22, 168–186.

Quoilin, S., Declaye, S., Tchanche, B.F., Lemort, V., 2011. Thermo-economic optimization of waste heat recovery Organic Rankine Cycles. *Appl. Therm. Eng.* 31, 2885–2893.

Schlünder, E.U., 1983. Heat transfer in nucleate boiling of mixtures. *Int.Chem. Eng.* 23, 589–599.

Shah, M.M., 1979. A general correlation for heat transfer during film condensation inside pipes. *Int. J. Heat Mass Transf.* 22, 547–556.

Shah, R.K., Sekulic, D.P., 2003. *Heat Exchanger Design Procedures, in Fundamentals of Heat Exchanger Design,* John Wiley & Sons, Inc., Hoboken, NJ, USA

Shu, G., Gao, Y., Tian, H., Wei, H., Liang, X., 2014. Study of mixtures based on hydrocarbons used in ORC (Organic Rankine Cycle) for engine waste heat recovery, *Energy* 74, 428-438.

Sieder, E.N., Tate, G.E., 1936. Heat transfer and pressure drop of liquids in tubes. *Ind. Eng. Chem.* 28, 1429–1435.

Silver, R.S., 1964. An approach to a general theory of surface condensers. *Proc. Inst. Mech. Eng. Part 1,* 179, 339–376.

Steiner, D., 2006. Wärmeübertragung *beim Sieden gesättigter Flüssigkeiten. (Part H3.1), in: VDI Heat Atlas.* Springer Verlag, Berlin.

Tchanche, B.F., Lambrinos, G., Frangoudakis, A., Papadakis, G., 2011. Low-grade heat conversion into power using organic Rankine cycles – A review of various applications. *Renew. Sustain. Energy Rev.* 15, 3963–3979.

Tempesti, D., Fiaschi, D., 2013. Thermo-economic assessment of a micro CHP system fuelled by geothermal and solar energy. *Energy* 58, 45–51.

Tsatsaronis, G., Winhold, M., 1985. Exergoeconomic analysis and evaluation of energy-conversion plants—I. A new general methodology. *Energy* 10, 69–80.

Turton, R., Bailie, R.C., Whiting, W.B., 2003. *Analysis, synthesis and design of chemical processes,* 2nd edition. Prentice Hall, Old Tappan, NJ.

VDI-Gesellschaft Verfahrenstechnik und Chemieingenieurwesen (GVC) (Ed.), 2010. *VDI Heat Atlas.* Springer Verlag, Berlin.

Wang, X.D., Zhao, L., 2009. Analysis of zeotropic mixtures used in low-temperature solar Rankine cycles for power generation. *Sol. Energy* 83, 605–613.

Weith, T., Heberle, F., Brüggemann, D., 2014. Performance of Siloxane Mixtures in a High-Temperature Organic Rankine Cycle Considering the Heat Transfer Characteristics during Evaporation. *Energies* 7, 5548–5565.

Woudstra, N., van der Stelt, T.P., 2002. *Cycle-Tempo: a program for the thermodynamic analysis and optimization of systems for the production of electricity, heat and refrigeration.* Energy Technology Section, Delft University of Technology, The Netherlands.

ACKNOWLEDGEMENT

TECHNO-ECONOMIC ANALYSIS OF THE SUB-CRITICAL ORC WITH OPTIMIZED HEAT TRANSFER PROCESS

Wei Liu[1,*], Dominik Meinel[1], Christoph Wieland[1] and Hartmut Spliethoff[1,2]

[1]Institute for Energy Systems, Faculty of Mechanical Engineering, Technische Universität München
Boltzmannstrasse 15, 85748
Garching, Germany
[2]The Bavarian Center for Applied Energy Research (ZAE Bayern), Division 1: Technology for Energy Systems and Renewable Energy, Walther-Meissner-Str. 6, 85748
Garching, Germany
wei.liu@tum.de

* Corresponding Author

ABSTRACT

A techno-economic analysis of a sub-critical ORC designed for the utilization of geothermal heat is performed. The thermodynamic optimization of the investigated ORC system is based on a new approach, in which thermal match between the heat source and the working fluid is improved by operating an optimal working fluid at near-critical pressures. The Optimal Heat Source Temperature (OHST) method is used to identify suitable fluids for which the pinch point is located at the inlet (or an intermediate point) of the preheater. As a result, R227ea is selected, which performs best under certain defined conditions, while R245fa is also considered as a reference fluid for further thermo-economic comparison. A heat transfer model is proposed for the plate heat exchanger system in order to determine the pinch point position in the case of near-critical fluid parameters, as well as to obtain the heat transfer area which is required for the calculation of Purchased Equipment Cost (PEC). The economic optimization is based on the minimization of the Levelized Cost of Electricity (LCOE) for the considered fluids. Results from the techno-economic optimizations show that for R245fa the optimum is obtained with a system efficiency of 7.306% and a LCOE of 205.7 €/MWh. In comparison, the proposed approach for R227ea leads to an optimum with a system efficiency of 8.607% and a LCOE of 185.9 €/MWh. The comparison suggests that although the proposed approach aims to improve the thermodynamic performance of the sub-critical ORC, it is also promising in terms of the economic profitability.

1. INTRODUCTION

Interests on power generation from low temperature geothermal heat have grown rapidly in the past decades due to the increase in the electricity consumption worldwide. The Organic Rankine Cycle (ORC) system has been considered as one of the most suitable technologies for the exploitation of such heat source because of several advantages, such as simplicity and relatively high efficiency compared to the conventional water/steam Rankine cycle. However, a great limitation of improving the system efficiency of ORC is the isothermal evaporation which leads to a high exergy destruction in the heat transfer process. Several methods are available, aiming at a better thermal match between the heat source and the working fluid, such as using triangular ORC (Khennich and Galanis, 2012) or super-critical ORC to bypass the isothermal evaporation (Schuster *et al*., 2010), or using fluid mixtures in order to obtain a non-isothermal evaporation (Heberle *et al*., 2012). Although these techniques are effective under certain working conditions, the complexity of the ORC system or of the component is increased, causing higher manufacturing costs.

To reduce the exergy destruction caused by isothermal evaporation, an interesting approach is proposed in this paper, where a very high evaporation temperature is applied in order to reduce the absolute heat amount transferred during the evaporation process. The drawback of this approach is, however, obvious: the pinch point which is in most cases located at the evaporator inlet can greatly

limit the mass flow rate of the working fluid, leading to a reduced power output. To overcome this drawback, it is prerequisite for the proposed approach to find a suitable working fluid, for which the pinch point is located not at the evaporator inlet but the preheater inlet. As a result, the whole heat transfer process is optimized, leading to a better thermal match and hence a higher system efficiency (Liu *et al.*, 2014, 2015).

Although the proposed approach has been proven to be an effective method for improving the thermodynamic performance, its impact on the economic performance is still uncertain: the better thermal match in the preheating process does lead to a higher system performance; however, it requires a larger heat transfer area, which increases the purchase cost of the heat exchanger system. Therefore, the main task of the present paper is the thermo-economic investigation of the ORC which is optimized using the proposed approach for the geothermal power generation.

2. Modeling and Thermodynamic Description of Subcritical ORC

Figure 1(a) shows the considered subcritical ORC, which includes the most fundamental components: pump, preheater, evaporator, turbine and condenser. The working fluid at the saturated liquid state (state 1) is pressurized in the pump to a high pressure (state 2). Then it is led to the preheater where the sub-cooled fluid is heated until being liquidly saturated (state 3). Afterwards, the saturated liquid is evaporated under isothermal condition to the saturated vapor (state 4). The vapor then expands in the turbine, which rotates the shaft and generates electricity. At last, the loop is closed by condensing the super-heated vapor (state 5) to the saturated liquid (state 1).

| (a) | (b) |
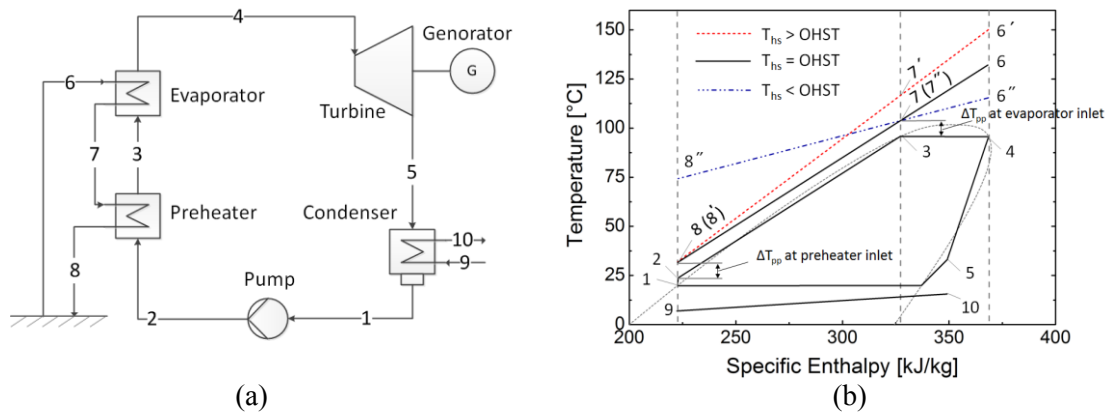
Figure 1: (a) Schematic diagram of a standard ORC, (b) Demonstration of OHST in T-h diagram

The static cycle simulation is performed in Matlab, using fluid properties from REFPROP 9.0 (Lemmon *et al.*, 2012). Simplifications are made that (1) there is no heat loss and no pressure drop through the cycle; (2) auxiliary power consumption, e.g. power required for circulating pump is neglected. The balance strategy is to vary the mass flow rate for the working fluid and the cooling water until the pinch point meets the design criteria in the heat exchanger and condenser, respectively. Unlike the common cycle simulations, the pinch point in the heat exchanger is considered as variable. Table 1 summarizes all boundary conditions for the cycle simulation.

Table 1: Boundary conditions for the investigated subcritical ORC.

Heat source temperature	T_{hs}	140 °C	Cooling water temperature	T_{cw}	8 °C
Heat source pressure	p_{hs}	10 bar	Cooling water pressure	p_{cw}	1 bar
Heat source thermal amount	$\dot{Q}_{hs}$	50 MW	Isentropic efficiency Turbine	$\eta_{is,turbine}$	0.85
Evaporating pressure	p_{evp}	< 30 bar	Isentropic efficiency Pump	$\eta_{is,pump}$	0.75
Pinch point in heat exchanger	$\Delta T_{pp,HE}$	Variable	Mechanical efficiency	η_{mech}	0.98
Condensation temperature	T_{cond}	20 °C	Generator/Motor efficiency	η_G/η_M	0.95
Pinch point in the condenser	ΔT_{cond}	5 K	Reference state	p_0, T_0	1 bar, 8 °C

Global system efficiency which combines both thermal efficiency η_{th} and heat transfer efficiency η_{HT} of the ORC system is used in this study for the evaluation of the thermodynamic performance. It is given by (Schuster *et al.*, 2010):

$$\eta_{sys} = \eta_{th} \cdot \eta_{HT} \tag{1}$$

Where η_{th} and η_{HT} are equal to:

$$\eta_{th} = \frac{P_{el,net}}{\dot{Q}_{HT}} = \frac{\eta_{mech} \cdot \eta_G \cdot (h_4 - h_5) - (h_2 - h_1)/\eta_{mech}/\eta_M}{h_4 - h_2} \tag{2}$$

$$\eta_{HT} = \frac{\dot{Q}_{HT}}{\dot{Q}_{hs}} = \frac{h_6 - h_8}{h_6 - h_0} \tag{3}$$

Where $P_{el,net}$ is the net power output [kW]; $\dot{Q}_{HT}$ is the heat flow transferred from the heat source to the ORC unit [kW]; $\dot{Q}_{hs}$ represents the available heat of the considered heat source [kW].

Therefore, to increase the thermal efficiency η_{th} of the investigated ORC system with a constant condensation temperature it is practical to increase the evaporating pressure p_4. To increase the heat transfer efficiency η_{HT}, the heat source outlet temperature T_8 should be lowered as much as possible. More specifically, the maximum of η_{HT} can be observed when the pinch point is located at the preheater inlet.

3. Optimal Heat Source Temperature

The Optimal Heat Source Temperature (OHST) is defined as a heat source temperature, for which the pinch point is evenly located in the preheater (Liu *et al.* 2015). By comparing the OHST with the available heat source temperature, the pinch point position for the investigated ORC can be identified, which is demonstrated by figure 1(b). In the case where T_{hs} < OHST, the pinch point is located at the evaporator inlet (states 3-7(7″)). In the case where T_{hs} > OHST, however, the pinch point is shifted to the preheater inlet (states 2-8(8′)). As the proposed approach requires a pinch point position at the preheater inlet, the working fluid selection should be based on a condition that the OHST is lower than the available heat source temperature.

Assuming a constant specific heat capacity for the homogeneous liquid, the OHST can be estimated as a state quantity depending only on the evaporating pressure (Liu *et al.*, 2015), provided that the pinch point and the condensation temperature are constant:

$$OHST = \frac{h_{evp}}{\bar{c}_{p,wf}} + T_{evp} + \Delta T_{pp,evp} \tag{4}$$

Where the mean specific heat capacity for the working fluid is calculated by:

$$\bar{c}_p = \frac{h_3 - h_2}{T_3 - T_2} \tag{5}$$

Where T_2 is assumed equal to the condensation temperature of the working fluid, since temperature changes only slightly for a homogenous liquid after compression.

The fluid screening is performed based on the OHST theory mentioned above. Firstly, 35 pure fluids with the critical temperatures between 90 and 160 °C are selected out of 121 fluids from the REFPROP database. Afterwards, the OHSTs are calculated for all the considered fluids using equation (4) and (5) given a constant pinch point of 10 K and the evaporating pressure of $0.9 \cdot p_c$, which are summarized in figure 2. It is noted that the constant pinch point is considered in this section only for the purpose of the screening of fluids. Next, taking into account the boundary conditions that p_{evp} < 30 bar and OHST < T_{hs} (140 °C), the only fluid, i.e. R227ea which is located near the bottom left corner of figure 2 can be selected for the further cycle simulations. In addition, R245fa which has been widely used in the ORC industry is also selected as a reference fluid for comparison.

It should be noted that in the case of near-critical fluid parameters the pinch point can be located neither in the preheater inlet nor the evaporator inlet, since the heat capacity is strongly dependent on

the temperature. Figure 3(a) presents a possible scenario where the pinch point is located at an intermediate point of the preheater. In order to predict such pinch point position, it is necessary to partition the preheating process into finite number of elements assuming an equal amount of transferred heat, which is detailed in section 4.
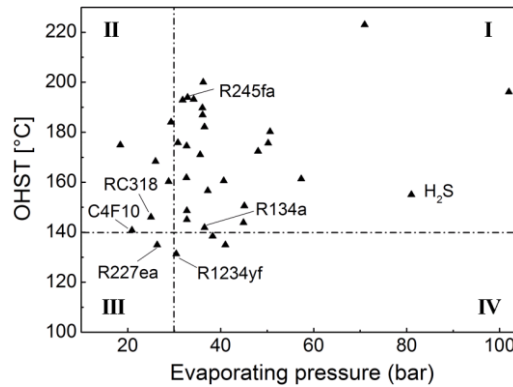

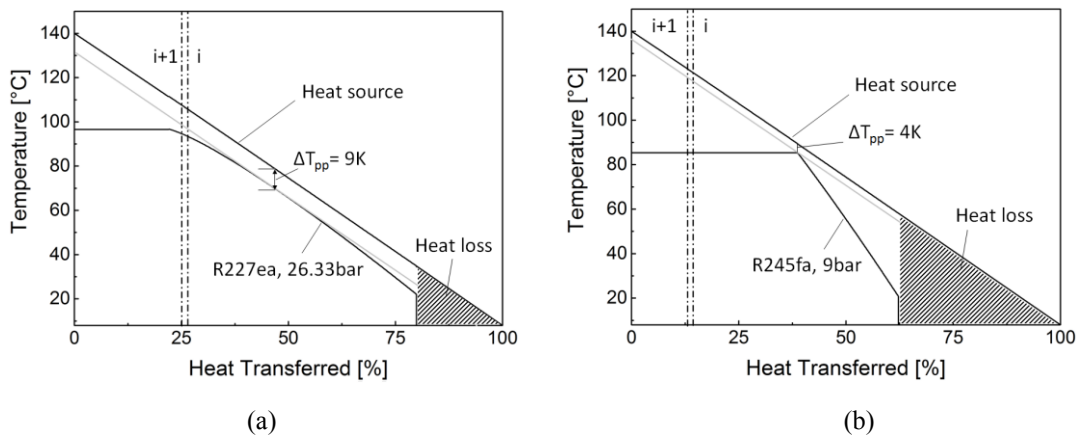**Figure 2:** OHST versus evaporating pressure for the considered fluids.

| (a) | (b) |

Figure 3: Demonstration of TQ-diagram and pinch point position for (a) R227ea and (b) R245fa, respectively.

4. Heat Transfer calculation

The main aims of the heat transfer calculations are 1) the determination of the pinch point location demonstrated similar to figure 3, and 2) the calculation of the heat transfer coefficient and the required surface area for a counter-flow plate heat exchanger system. The preheater and evaporator are considered as a whole in order to simplify the system components. Assumptions are made that the heat transfer process is stationary and both of the pressure drop and the fouling factor are negligible.

Based on the given geometric parameters of the plate (see table 2), the sizing of a Plate Heat Exchanger (PHE) system requires only few characteristics, i.e. plate arrangement, plates (channel) number and the channel spacing. Figure 4 demonstrates the plate arrangement of the considered PHE system, where plates are arranged into three blocks to form equal number of parallel channels. The channel spacing is set to 3.6 mm. The channel number for each fluid is related to the total required surface area.

Taking into account the temperature dependency of heat capacity, the assumption of an overall temperature difference between the hot and cold fluids cannot be acceptable for the investigated preheating process. For this reason, both of the preheating and evaporating processes are discretized respectively into a number of elements with equal amount of heat flow, as demonstrated in figure 3 and 4. For reduction of the calculation error, the number of elements N_{ele} is set to 500 (Karellas *et al.* 2012).

Table 2: Input parameters for plate.

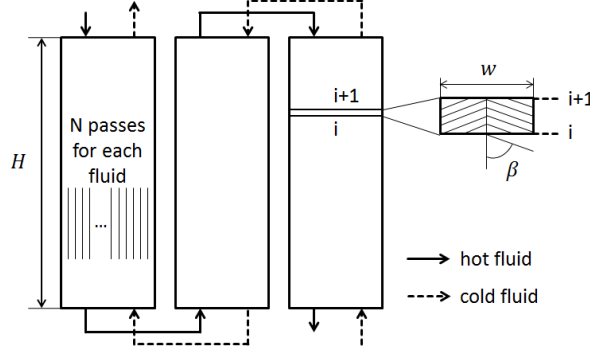|		
Plate width	W	0.7 m
Plate height	H	2.31 m
Channel space	b	3.6 mm
Corrugation angle	β	60°
Plate thickness	d_{plate}	0.7 mm
Thermal conductivity	λ_{plate}	15 W/m·K

Figure 4: Schematic overview of the plate heat exchanger system.

Within each element, the transferred amount of heat flow is thus given by:

$$\dot{Q}_i = \frac{\dot{Q}_{HT}}{N_{ele}} = U_i \cdot A_i \cdot \Delta T_i$$

$$= \dot{m}_{hs,i} \cdot c_{p,hs,i} \cdot (T_{hs,i+1} - T_{hs,i}) = \dot{m}_{wf,i} \cdot c_{p,wf,i} \cdot (T_{wf,i+1} - T_{wf,i})$$

(6)

Where $\dot{m}_i$ is equal to $\dot{m}/N_{ch}$ [kg/s]; and ΔT_i is simplified for each element by assuming:

$$\Delta T_i = T_{hs,i} - T_{wf,i}$$

(7)

On this account, the pinch point can be obtained by:

$$\Delta T_{pp} = \min_{1 \le i \le N_{ele}} \Delta T_i$$

(8)

Assuming the convective heat transfer is dominant, the overall heat transfer coefficient is given by:

$$\frac{1}{U_i} = \frac{1}{h_{wf,i}} + \frac{d_{plate}}{\lambda_{plate}} + \frac{1}{h_{hs,i}}$$

(9)

To calculate the convective heat transfer coefficient at an arbitrary point i, it is necessary to obtain the Nusselt number which is defined as the ratio of convective to conductive heat transfer across the elementary boundary:

$$Nu_i = \frac{h_i \cdot D_h}{\lambda_i} \rightarrow h_i = \frac{Nu_i \cdot \lambda_i}{D_h}$$

(10)

Where λ_i is the thermal conductivity at point i [W/m²K]; D_h [m] is the hydraulic diameter which is equal to $2Wb/(W + b)$ referring to the investigated plate channel.

Depending on the type of the heat transfer process, the Nusselt numbers are calculated using various empiric correlations. For the single-phase heat transfer process, the Chisholm and Wanniarachchi (Chisholm and Wanniarachchi, 1990) correlation is employed where Nusselt number is given by:

$$Nu = 0.724 \cdot \left(\frac{6\beta}{\pi}\right)^{0.646} \cdot Re^{0.583} \cdot Pr^{0.33}$$

(11)

Where Pr is the dimensionless Prandtl number, given by $Pr = c_p \cdot \mu/\lambda$.

For the multi-phase heat transfer, the working fluid undergoes the liquid-gaseous phase transition. Specifically for the evaporating process, Nusselt number is calculated using Yan and Lin's correlation (Yan and Lin, 1999):

$$Nu = 1.926 \cdot Pr_l^{0.33} \cdot Bo_{eq}^{0.3} \cdot Re_{eq}^{0.5} \left[(1 - x) + x \cdot \left(\frac{\rho_l}{\rho_v} \right)^{0.5} \right] \tag{12}$$

Where Bo_{eq} is the equivalent boiling number; Re_{eq} is the equivalent Reynold number; ρ_l is the density for saturated liquid [kg/m^3]; ρ_v is the density for saturated vapor [kg/m^3]; x is vapor fraction. It should be noted that for obtaining the continuous heat transfer coefficient the Nusselt number for the evaporative heat transfer is modified by multiplying equation (12) by a factor X_{Nu} given by:

$$X_{Nu} = \frac{Nu_{pre,i=N_{ele}}}{Nu_{evp,i=1}} \tag{13}$$

For the condensation process, Nusselt number is calculated using Yan's correlation (Yan *et al.*, 1999):

$$Nu = 4.118 \cdot Re_{eq}^{0.4} \cdot Pr_l^{0.33} \tag{14}$$

With the rated U_i and ΔT_i, the total heat transfer area A_{tot} can be given by:

$$A_{tot} = \sum_{i=1}^{N_{ele}} A_i \tag{15}$$

However, this calculated surface area must satisfy the input condition, i.e. the plate height of 2.31 m, which is achieved by varying the number of channels for each fluid until the objective error function (equation (16)) is minimized.

$$\Delta H(N_{ch}) = \frac{A_{tot}}{3 \cdot W} - H_{plate} \tag{16}$$

The total number of plates is thus given by:

$$N_{plate} = 3 \cdot (2 \cdot N_{ch} - 1) \tag{17}$$

5. Levelized Cost of Electricity

The economic performance of the considered geothermal ORC system is evaluated by means of the Levelized Cost of Electricity (LCOE) method. Based on the Net Present Value (NPV) method, LCOE is given by (Konstantin, 2013):

$$LCOE = \frac{I_0 + \sum_{t=1}^{t=n} \dfrac{A_t + I_t}{(1+r)^t}}{\sum_{t=1}^{t=n} \dfrac{W_{el}}{(1+r)^t}} \tag{18}$$

Where I_0 is the initial investment cost [€]; A_t is the expenditures for Operation & Maintenance (O&M) in the year t [€]; I_t is the investment costs for replacement of equipment in the year t [€]; W_{el} is the Electricity generation in the year t [MWh]; r is the annual discount rate [%]; n is the lifetime of the project in years [a].

Factors accounting for the initial investment cost I_0 are manifold, such as the costs for drilling, purchasing equipment, and other expenses such as site preparation, instrumentation, control, insurance, etc. For a drilling depth of 3.5 km, the drilling cost is estimated to about 21 Mio. € using the correlations from (Schlagermann, 2014). The Purchased Equipment Cost (PEC) related to the component parameters is described in detail see section 5.1. The other expenses for the initial investment are mainly dependent on the drilling process, which approximately accounts for 40% of the total drilling cost (Schlagermann, 2014).

Apart from the initial investment costs in equation (18), the annual expenditures for O&M are estimated to be about $0.03 \cdot I_0$ based on the proposed correlations (Schlagermann, 2014). The investment costs caused by the replacement of system components depend on the lifetime of each component (see table 3). The annual electricity generation is calculated with the consideration of 8000

full-load hours. The annual discount rate is set to 8%. Finally, the lifetime of the project is considered to be 25 years.

It is noted that the correlations used for the economic evaluation are based on an existing geothermal ORC plant in Germany. For more details, the reader is referred to Schlagermann (2014).

Table 3: Constants in equation (19), bare module factors and lifetimes for different system components (Turton *et al.*, 2013) (Schlagermann, 2014)

Equipment	K_1	K_2	K_3	F_B	Lifetime
Pump	3.3892	0.0536	0.1538	4.05	10
Preheater + Evaporator	4.6656	-0.1557	0.1547	3.86	10
Turbine	2.6259	1.4398	-0.1776	6.10	25
Condenser	4.6656	-0.1557	0.1547	3.86	10

5.1 Purchased Equipment Cost (PEC)

The PEC for each component of the ORC system is calculated using the empirical correlations based on a number of industrial data (Turton *et al.*, 2013), which is given by:

$$\log_{10} PEC_0 = K_1 + K_2 \cdot \log_{10} X + K_3 \cdot (\log_{10} X)^2 \tag{19}$$

Where K_1, K_2, K_3 are constants depending on the system component (see table 3) and X is the size or capacity for the corresponding component. The calculated PEC_0 is converted into Euro with the average exchange rate of 1.2 for the recent years.

The multiplication factor F_B is used to account for the indirect costs and the use of specific materials (Turton *et al.*, 2013). Therefore, the modified PEC is given by:

$$PEC = PEC_0 \cdot F_B \tag{20}$$

Where F_B is listed in table 3 for each of the system equipment.

The Chemical Engineering Plant Cost Index (CEPCI) is used to evaluate the cost deviation due to inflation. The PEC calculated using equation (20) is based on the CEPCI value of 382 for the year of 1996 (Turton *et al.*, 2013). In the present economic analysis, the updated value of 578.1 for the year of 2014 is employed.

6. Results

The main aim of the thermo-economic optimization is to obtain the minimum of LCOE for the considered two fluids, i.e. the selected R227ea and the reference fluid R245fa.

For R227ea with a constant evaporating pressure in the investigated ORC system, the influence of the pinch point (depicted in figure 3(a)) on the ORC system performance is threefold. Firstly, according to equation (4), increasing the pinch point temperature results in a higher OHST value, which can change the pinch point position to the evaporator inlet in the case of OHST > T$_{hs}$. In order to avoid such changes, the pinch point value is limited up to 15 K for which the OHST is equal to 139.93 °C. Secondly, increasing the pinch point temperature corresponds to a worse thermal match between the thermal water and the working fluid, which reduces the system efficiency. Such influence is illustrated in figure 5 where the global system efficiency for R227ea decreases monotonically with the increase of the pinch point value. Thirdly, the benefit of increasing the pinch point is that it requires a smaller heat transfer area, leading to a lower PEC value particularly for the preheater and the evaporator. Particularly for R227ea, it can be seen from figure 5 that the total PEC for the preheater and the evaporator decreases significantly with the increase of the pinch point value. A small decrease in the other costs mainly referring to the instrumentation & controlling is also observed for a higher pinch point value. The PEC for condenser, turbine and pump are relatively less affected by varying the pinch point. Conclusively, it is reasonable to consider the pinch point in the heat exchanger as the optimization parameter for R227ea.

It is necessary to note that due to the consideration of the constant condensation temperature the variation of the pinch point for the condenser affects only the condenser size but not the power output. Therefore, its influence on the LCOE is relatively limited so that it is not considered in the present techno-economic optimization.
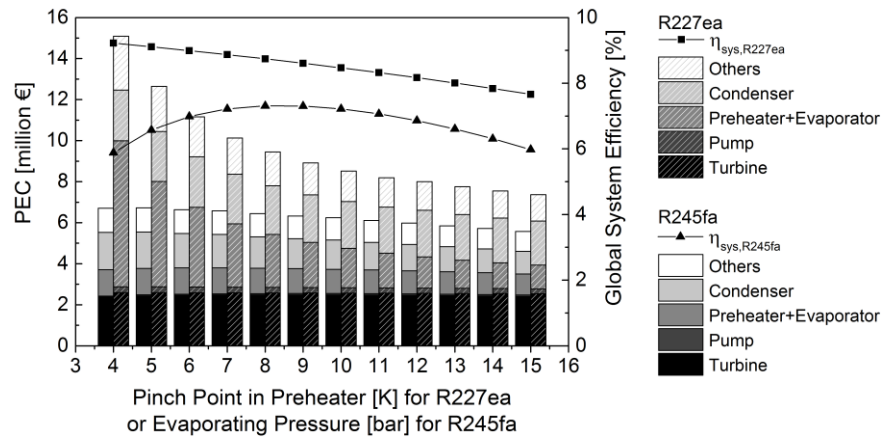
Figure 5: PEC and system efficiency as functions of $\Delta T_{pp,evp}$ and p_{evp} for R227ea and R245fa, respectively.
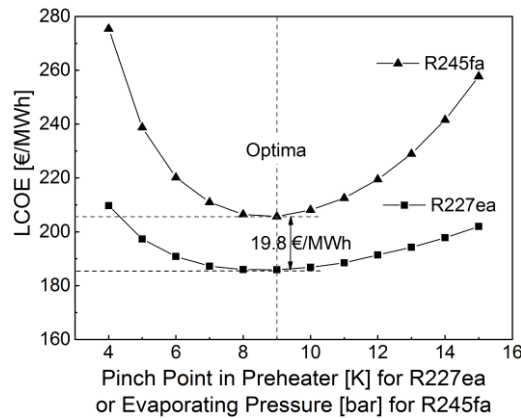

Figure 6: LCOE as functions of $\Delta T_{pp,evp}$ and p_{evp} for R227ea and R245fa, respectively.

Figure 6 shows the resulting LCOE with the variation of pinch point. For R227ea, the minimum of LCOE is observed around 185.9 €/MWh for the pinch point of 9 K. In order for such minimum to make sense, it is required to compare it to the optimum LCOE for some other fluid, e.g. the reference fluid R245fa. The optimization parameter for R245fa, however, is different from that for R227ea. According to equation (4), the OHST for R245fa is significantly higher than the available heat source temperature, indicating that the pinch point is located at the evaporator inlet (see figure 3(b)). In such case to obtain the minimum LCOE, the evaporating pressure is chosen as the optimization parameter (Quoilin *et al*., 2011). In contrast to R227ea, the pinch point in the preheater is fixed at 4 K for R245fa. In figure 5, the PEC and global system efficiency for R245fa are shown as a function of evaporating pressure, where a maximum global system efficiency can be observed. The LCOE for R245fa is given in figure 6 as a function of evaporating pressure, where a minimum is observed for the evaporating pressure of 9 bar.

For further comparisons, the T-Q diagrams for the optimized R227ea and R245fa are given, illustrating their heat transfer processes, respectively. In addition, table 4 summarizes the parameters resulting from the thermo-economic optimizations for both working fluids. Although the use of R227ea requires higher PEC, more electricity can be produced annually, which leads to reduce the LCOE by 9.63%.

Table 4: Results from the thermo-economic optimizations for R227ea and R245fa

Fluid	Thermodynamic						Economic	
	T_{evp} [°C]	p_{evp} [bar]	$T_{pp,evp}$ [K]	η_{sys} [%]	η_{HT} [%]	W_{el} [MWh]	*PEC* [m. €]	LCOE [€/MWh]
R227ea	96.60	26.33	9.000	8.607	79.47	29006	8.739	185.9
R245fa	85.33	9	4.000	7.306	63.51	23762	7.306	205.7

7. Conclusions

In the present paper, a new approach for the heat transfer optimization has been developed and thermo-economically investigated for a sub-critical ORC designed for geothermal power generation. The working fluid considered is R227ea, for which the pinch point is not located at the evaporator inlet for the available heat source temperature. A detailed heat transfer model is proposed, aiming at the precise determination of the pinch point position and the calculation of the required heat transfer area. Compared to common works, the optimization parameter considered for R227ea is not the evaporating pressure but the pinch point for the heat transfer process. The results show that the pinch point in the preheater has a great influence on both of the system efficiency and the PEC. An optimum pinch point value is obtained for R227ea, corresponding to a global system efficiency of 8.607% and a minimum LCOE of 185.9 €/MWh. Compared to the optimization results for R245fa, an increase of system efficiency of 17.81% and a reduction of LCOE of 9.63% are observed.

In general, the proposed approach leading to both higher system efficiency and economic profitability seems promising. However, further challenges remain. The numerical results should be compared with the experimental results in the near future. In addition, it is necessary to further include pressure drops through the ORC loops and to investigate their influences on the heat transfer mechanism particularly for the working fluid at the near-critical states.

NOMENCLATURE

A	Surface area or annual cost	(m^2 or €)
b	Channel space	(mm)
c_p	Specific heat capacity	(kJ/kg·K)
d	Plate thickness	(mm)
D_h	Hydraulic diameter	(m)
e	Specific exergy flow	(kJ/kg)
F_B	Multiplication factor for PEC	(-)
h	Specific enthalpy	(kJ/kg)
h	Convective heat transfer	(W/kg·m^2)
H	Plate height	(m)
I	Investment cost	(€)
K	Constants for PEC	(-)
m.	million	(€)
$\dot{m}$	Mass flow rate	(kg/s)
n	Lifetime of project	(a)
Nu	Nusselt number	(-)
p	Pressure	(bar)
P	Power	(kW or MW)
Pr	Prandtl number	(-)
$\dot{Q}$	Heat flow	(kW)
r	Annual discount rate	(%)
Re	Reynold number	(-)
t	Operation year	(-)
T	Temperature	(°C)
U	Overall heat transfer coeff.	(W/kg·m^2)
W	Plate width	(m)
W	Electricity generation	(MW)
x	Vapor fraction	(-)
X	Size or capacity	(m^2 or kW)
β	Corrugation angle	(°)
η	Efficiency	(%)
λ	Thermal conductivity	(W/m·K)

| μ | Viscosity | (kg/s·m) |
| ρ | Density | (kg/m^3) |

Subscript

0,1,2, ... 10	Reference or working states	*pre*	Preheater
el	Electricity	*sys*	System
ele	Element	*th*	Thermal
eq	Equivalent	*tot*	Total
evp	Evaporation	*v*	Saturated vapor
G	Generator	*wf*	Working fluid
hs	Heat source	**Acronyms**	
HT	Heat transferred	*LCOE*	Levelized Cost of Electricity
l	Saturated liquid	*ORC*	Organic Rankine Cycle
mech	Mechanical	*OHST*	Optimal Heat source temperature
M	Motor	*PEC*	Purchased Equipment Cost
pp	Pinch point	*PHE*	Plate Heat Exchanger

<div align="center">

REFERENCES

</div>

Chisholm, D., Wanniarachchi, A.S., Plate heat exchangers: plate selection and arrangement, *AIChE Meeting*, 18-22.

Heberle,F., Preißinger,M., Brüggemann, D, 2012, Zeotropic mixtures as working fluids in Organic Rankine Cycles for low-enthalpy geothermal resources, *Renewable Energy,* vol. 37, no. 1, p. 364–370.

Karellas, S., Schuster,A., Leontaritis, A., 2012, Influence of supercritical ORC parameters on plate heat exchanger design, *Applied Thermal Engineering,* vol. 33-34, p. 70–76.

Khennich, M., Galanis, N., 2012, Optimal Design of ORC Systems with a Low-Temperature Heat Source, *Entropy,* vol. 14, no. 12, p. 370–389.

Konstantin, P., 2013, *Praxisbuch Energiewirtschaft. Energieumwandlung, -transport und -beschaffung im liberalisierten Markt,* Springer Vieweg , Berlin, 474.

Lemmon E.W., Huber, M.L., Nist reference fluid thermodynamic and transport properties-refprop, NIST standard reference database 23-Version 9.0.

Liu, W., Meinel, D., Wieland, C., Spliethoff, H., 2014: Investigation of hydrofluoroolefins as potential working fluids in organic Rankine cycle for geothermal power generation, *Energy,* vol. 67, p. 106-116.

Liu, W., Meinel, D., Wieland, C., Spliethoff, H., 2015: Optimal Heat Source Temperature for Optimization of the Organic Rankine Cycle (ORC) process. Submitted In *Energy* 2015.

Quoilin, S., Declaye, S,. Tchanche, B.F., Lemort, V., 2011, Thermo-economic optimization of waste heat recovery Organic Rankine Cycles, *Applied Thermal Engineering,* vol. 31, p. 2885–2893.

Schlagermann, P., 2014, *Exergoökonomische Analyse geothermischer Strombereitstellung am Beispiel des Oberrheingrabens,* Dr. Hut, Munich, 168.

Schuster, A., Karellas, S., Aumann, R., 2010, Efficiency optimization potential in supercritical Organic Rankine Cycles, *Energy,* vol. 35, no. 2, p. 1033–1039.

Turton, R., Bailie, R.C., Whiting, W.B., Shaeiwitz, J.A., Bhattacharyya, D., 2013, *Analysis, Synthesis, and Design of Chemical Processes*, Pearson, NY, 965.

Yan, Y.Y., Lin, T. F., 1999, Evaporation Heat Transfer and Pressure Drop of Refrigerant R-134a in a Plate Heat Exchanger, *Journal of Heat Transfer,* vol. 121, p. 118–127.

Yan, Y.Y., Lio, H.C., Lin, T.F., 1999, Condensation heat transfer and pressure drop of refrigerant R-134a in a plate heat exchanger, *International Journal of Heat and Mass Transfer,* vol. 42, no. 6, p. 993–1006.

INFLUENCE OF THE HEAT-SOURCE COST ON GEOTHERMAL ORCS

Daniël Walraven[1,3], Ben Laenen[2,3], William D'haeseleer[1,3*]

[1] University of Leuven (KU Leuven) Energy Institute,
TME Branch (Applied Mechanics and Energy Conversion)
Celestijnenlaan 300 Box 2421, B-3001 Leuven, Belgium
daniel.walraven@kuleuven.be, william.dhaeseleer@kuleuven.be

[2] Flemish Institute for Technological Research (VITO),
Boeretang 200, B-2400 Mol, Belgium
ben.laenen@vito.be

[3] EnergyVille (Joint Venture of VITO and KU Leuven),
Dennenstraat 7, B-3600 Genk, Belgium

* Corresponding Author

ABSTRACT

The influence of the cost of the heat source on the performance and configuration of the economically optimal ORC is investigated in this work. This optimal ORC is obtained by performing a system optimization, in which the most important components (heat exchangers, cooling system and turbine) are optimized together with the configuration of the cycle. Minimization of the LCOE (Levelized Cost of Electricity) is chosen as the objective function.

As a result, the LCOE for both water and air-cooled ORCs is given as a function of the heat-source cost and heat-source-wellhead temperature. With these data, an estimation of the LCOE of a geothermal project can be made, based on the depth of the wells and the expected wellhead temperature. By comparing the obtained LCOE with expected electricity prices, the profitability of the project can be estimated.

1. INTRODUCTION

Low-temperature geothermal heat sources are widely available (Tester et al., 2006; IEA, 2011), but the heat-to-electricity conversion efficiency is very low due to the low temperature of the heat source. In many regions in the world, the geothermal heat sources do not manifest at the surface, but drilling of wells is necessary. These wells are often very expensive due to the relative high drilling depth.

In this paper, the combined influence of the drilling costs of the heat source and the temperature of the heat source is investigated. Contour maps of the LCOE (Levelized Cost of Electricity) of economically optimal ORCs are calculated as a function of these two parameters. This LCOE is the fixed electricity price needed to obtain break even at the end of the project. Also the influence of these parameters on the design and performance of the power plants is investigated.

A system optimization is performed, so that the configuration of the main components (heat exchangers, turbine and cooling system) are optimized together with the configuration of the cycle itself. The results in this paper are calculated with a previously developed code and the details of the modeling can be found in Walraven et al. (2015b).

2. MODEL

2.1 ORC

Organic Rankine cycles (ORCs) with different configurations (recuperated, subcritical or transcritical) are modeled in this paper, of which the scheme is given in figure 1. All the possible heat exchangers (economizer, evaporator, superheater and recuperator) are shown, but they are not always necessary. Air-cooled condensers (ACC) or wet cooling towers (WCT) connected to a condenser, and if necessary a desuperheater, can be used for cooling.
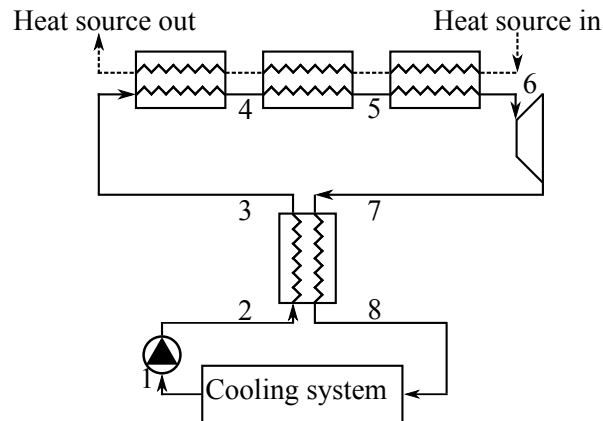

Figure 1: Scheme of a single-pressure, recuperated ORC.

It is assumed that state 1 is saturated liquid and that the isentropic efficiency of the pump is 80%. More information about the modeling of the cycle can be found in Walraven et al. (2013). An axial-inflow, axial-outflow turbine is modeled, based on the results of Macchi and Perdichizzi (1981).

2.2 Shell-and-tube heat exchangers

Figure 2 shows a TEMA E shell-and-tube heat exchanger with its basic geometrical characteristics, which is the only type of heat exchanger used in this paper. The geometrical characteristics are the shell outside diameter D_s, the outside diameter of a tube d_o, the pitch between the tubes p_t, the baffle cut length l_c and the baffle spacing at the inlet $L_{b,i}$, outlet $L_{b,o}$ and the center $L_{b,c}$. More information about the modeling of the heat exchangers can be found in Walraven et al. (2014).
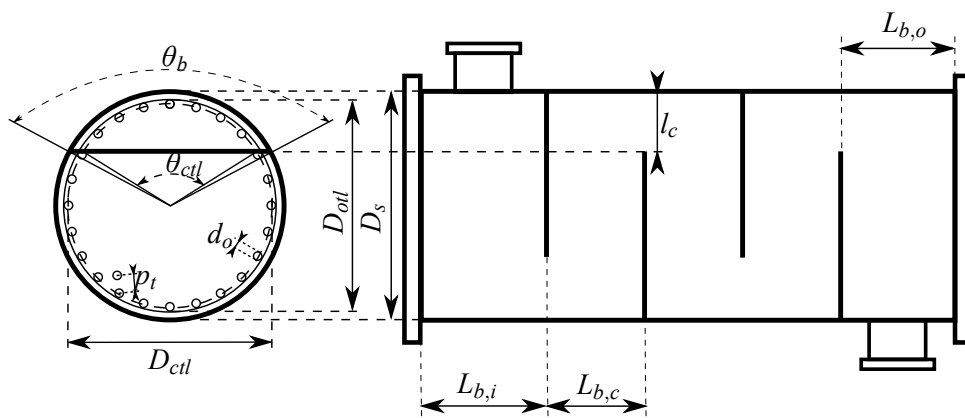
Figure 2: Shell-and-tube geometrical characteristics. Figure adapted from Shah and Sekulić (2003). See also Walraven et al. (2014).

2.3 Cooling system

Figure 3 shows the geometry of the air-cooled condenser (ACC) modeled in this paper. The tube-bundle geometry is determined by the tubes' small width W_s, the fin height H, the fin pitch S, the tubes' large width W_l and the length of the tubes L_t. In an A-frame ACC the tube bundles are placed at an angle θ with the horizontal. More information about the modeling can be found in Walraven et al. (2015a).
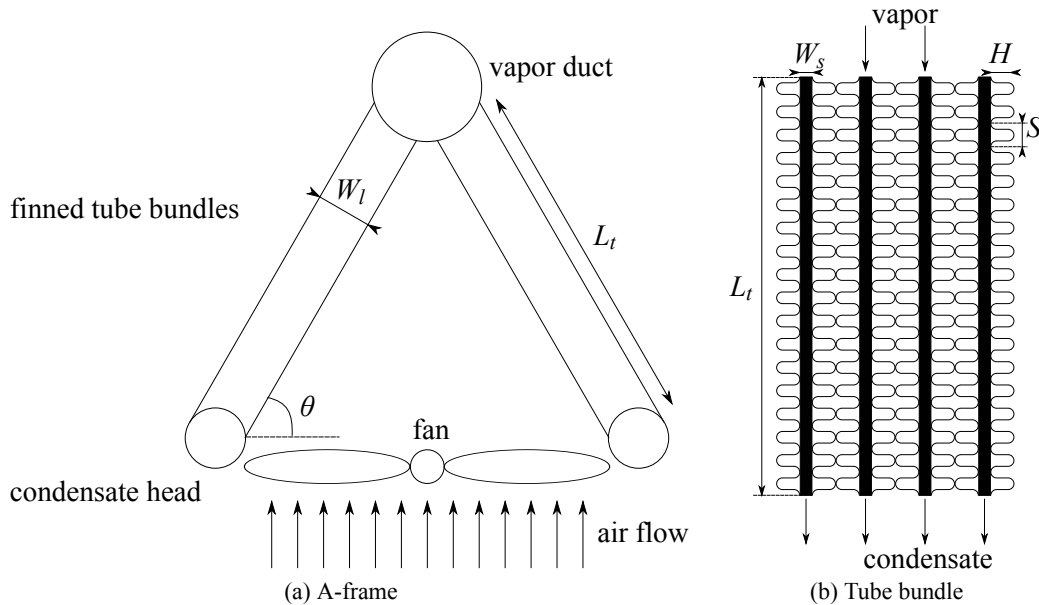
Figure 3: Geometry of an A-frame air-cooled condenser (a) and the bundle geometry of flat tubes with corrugated fins (b).

Another cooling option is the use of a wet cooling tower (WCT) connected to a condenser and, if necessary, a desuperheater. A mechanical-draft wet cooling tower is shown in figure 4. The height of the inlet H_i, the height of the fill H_{fi}, the height of the spray zone H_{sp} and the width of the tower W_t are shown in the figure. The reader is referred to Walraven et al. (2015b) for more information.
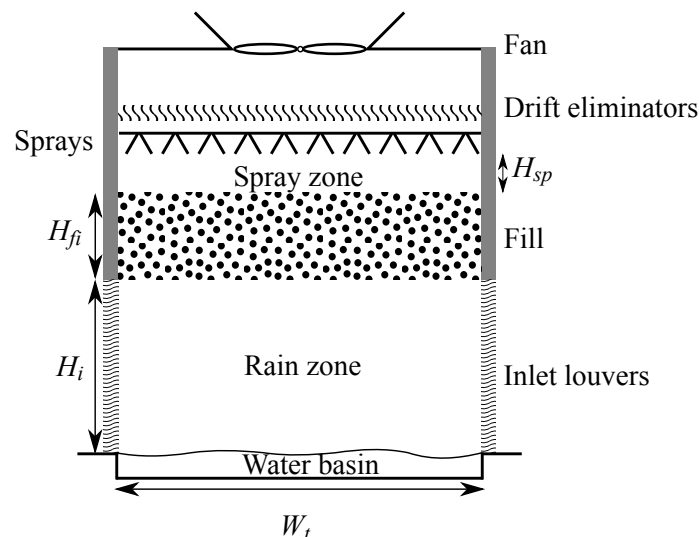
Figure 4: Geometry of an induced mechanical-draft wet cooling tower. Figure adapted from Kloppers (2003).

3. OPTIMIZATION

A *system* optimization is performed by optimizing the cycle parameters and the configuration of all the components together. The software packages CasADi (Andersson et al., 2012) and WORHP (Büskens and Wassel, 2013) are used for the optimization. The models themselves are developed in Python and the fluid properties are obtained from REFPROP (Lemmon et al., 2007).

3.1 Objective function

The objective of the optimization is to minimize the levelized cost of electricity (LCOE). This LCOE is the constant electricity price needed during the lifetime of the power plant to reach break even over the lifetime of the project. The LCOE is calculated in €/MWh$_e$ as (D'haeseleer, 2013)

$$\text{LCOE} = \frac{C_{EPC} + \sum_{t=1}^{t_{LT}} \left[\left(C_{O\&M,t} + C_{water,t} \right) (1+i)^{-t} \right]}{\sum_{t=1}^{t_{LT}} \dot{W}_{net} \, N \, (1+i)^{-t}}, \tag{1}$$

with C_{EPC} the engineering, procurement & construction overnight cost (EPC) of the installation, t_{LT} the lifetime of the installation, $C_{O\&M,t}$ the operations and maintenance cost in year t which is assumed to be 2.5% of the investment cost of the ORC per year (IEA, 2011), $C_{water,t}$ the water cost in year t, $\dot{W}_{net}$ the net electric power output, which takes an electric generator efficiency of 98% into account, expressed in MW$_e$, N the number of full-load hours per year (an availability of 95% is assumed) and i the discount rate. The EPC cost consists of two parts: the cost of the drilling $C_{drilling}$ and the cost of the ORC C_{ORC}. More information about the cost of the ORC can be found in Walraven et al. (2015b).

3.2 Optimization variables

The optimization variables of a single-pressure, recuperated cycle are the temperature before the turbine, the saturation temperature at the pressure before the turbine, the pressure at the inlet of the pump, the mass flow of the working fluid and the effectiveness of the recuperator (Walraven et al., 2013).

The optimization variables of each shell-and-tube heat exchanger are the shell diameter D_s, tube-outside diameter d_o, tube pitch p_t, baffle cut l_c and the distance between the baffles $L_{b,c}$ (Walraven et al., 2014).

The fin height H, the fin pitch S, the air velocity at the minimum cross section V_{Amin} and the number of tubes n_{tubes} are the optimization variables of the ACC and a non-linear constraint is used to limit the length of the tubes, as done in Walraven et al. (2015a).

The tower width W_t, the inlet height H_i, the relative mass flow of air $\dot{m}_{air}/\dot{m}_{brine}$, the relative cooling-fluid mass flow $\dot{m}_{cf}/\dot{m}_{brine}$ and the minimum cooling-fluid temperature T_{cf}^{min} are the optimization variables of the WCT, as explained in Walraven et al. (2015b).

4. RESULTS AND DISCUSSION

4.1 Reference parameters

The parameters of our "reference" case are given in Table 1, which are based on a proposed geothermal demonstration project in Belgium. In the next subsections, the influence of the well costs and the brine-wellhead temperature on the performance of the ORC is investigated. For each of the parameter variations, a new design optimization is performed with the optimization variables described in Section 3.2 to obtain the minimum LCOE.

4.2 LCOE

In this subsection, the optimal LCOE is given as a function of the brine-inlet temperature and the cost of the wells. They are varied between 100° - 150°C and between 0 - 50 M€, respectively.

Figure 5a shows the LCOE for air-cooled ORCs. As expected, does the LCOE increase for an increasing cost of the wells and a decreasing heat-source-inlet temperature. For the current electricity price of about

Table 1: Parameters of the reference case

Well parameters	
Brine-wellhead temperature	125°C
Brine production	194 kg/s
Well-pumps consumption	600 kW$_e$
Wells cost	27.5 M€

Economic parameters	
Lifetime plant	30 years
Discount rate	4 %/year
Water price	0.5 €/m^3

Environmental conditions	
Dry-bulb temperature	10.3°C
Wet-bulb temperature	8.6°C
Air pressure	1016 hPa

50 €/MWh$_e$, only a small part of the investigated temperature-cost range is economically interesting for the investigated reference parameters (Table 1). This "profitable" area is hatched in figure 5. For low heat-source-inlet temperatures, the distance between the LCOE contour lines as a function of the cost of the wells is very low. This is due to the low efficiency of the optimal ORCs for low temperatures.

(a) Air-cooled
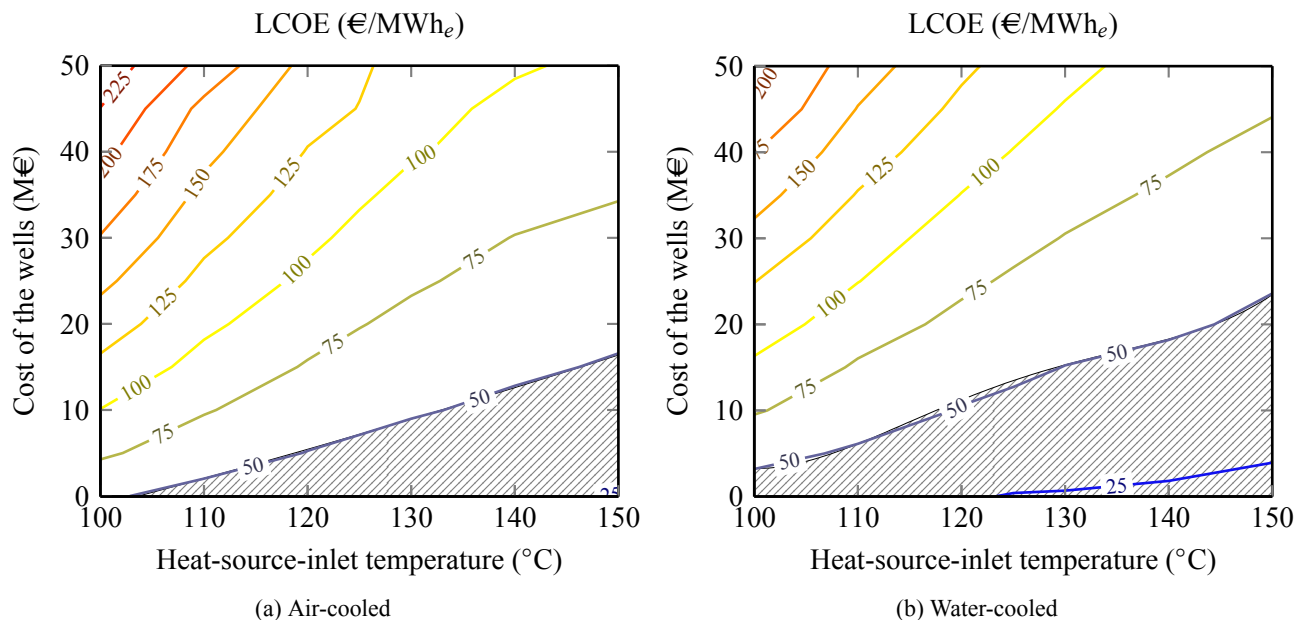
(b) Water-cooled

Figure 5: LCOE for air-cooled ORCs (a) and water-cooled ORCs (b) as a function of the heat-source-inlet temperature and the cost of the wells. The hatched area shows the region where the LCOE is lower than the assumed current electricity price of 50 €/MWh$_e$.

Figure 5b shows the LCOE for water-cooled ORCs. Comparison with Figure 5a shows that the LCOE for water-cooled ORCs is lower than the one for air-cooled ORCs, for the same heat-source-inlet temperature and cost of the wells. So, for the chosen reference parameters, it is better to select water cooling than air cooling.

4.3 Net power output and cost ORC
Figures 6a and 6b give contour lines of the net power output of air and water-cooled ORCs, respectively, as a function of the heat-source-inlet temperature and the cost of the wells. The net power output increases with increasing temperature and with increasing cost of the wells. The former evolution is the consequence of the increasing cycle efficiency with increasing temperature (Carnot). The latter evolution

Net power output (MW$_e$)

Net power output (MW$_e$)

(a) Air-cooled
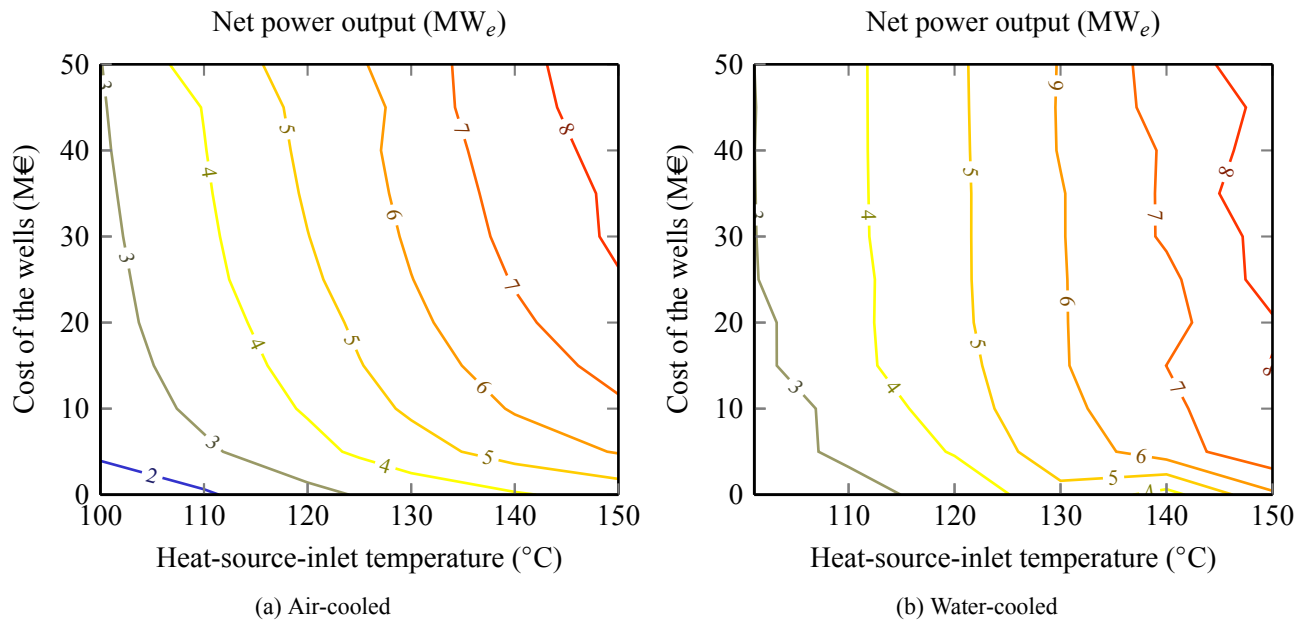
(b) Water-cooled

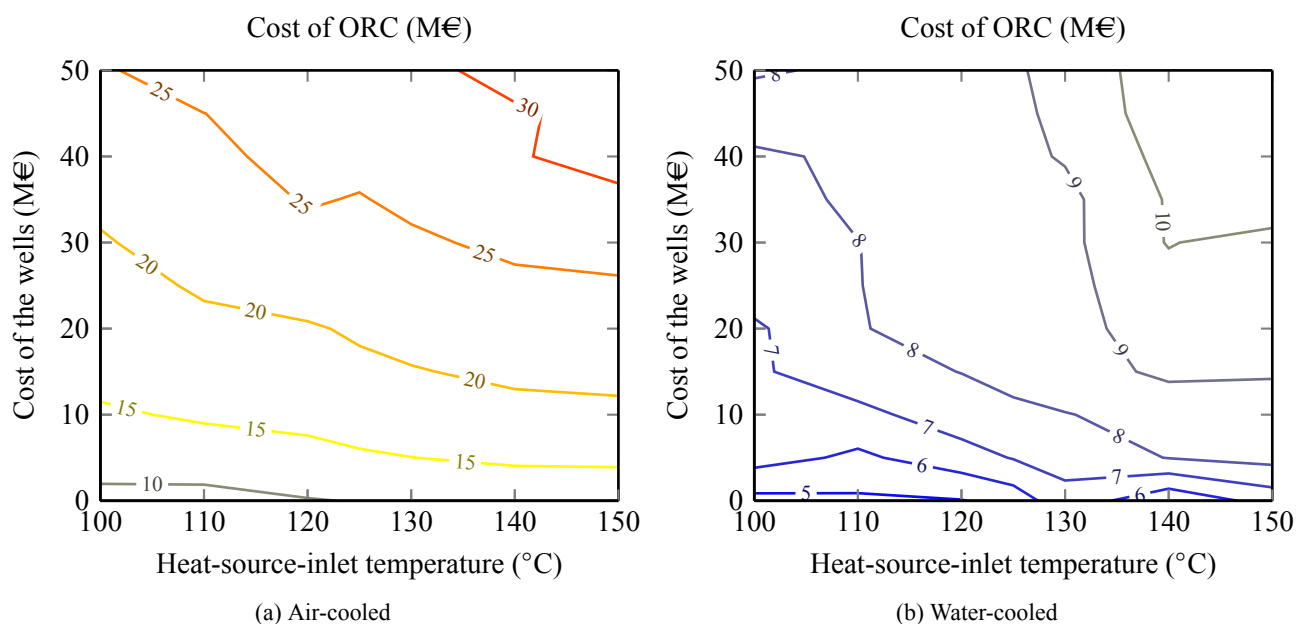**Figure 6: Net power output for air-cooled ORCs (a) and water-cooled ORCs (b) as a function of the heat-source-inlet temperature and the cost of the wells.**

is harder to explain. When the cost of the wells $C_{drilling}$ increases, the numerator in equation (1) increases. For an unchanged plant configuration, the LCOE would increase too. The only way to counteract this increase, is by trying to improve the net electric power of the cycle (denominator in equation (1)). This increase of the cycle efficiency can typically be done by decreasing the pinch-point-temperature differences and decreasing the condenser temperature. The consequence of these adaptations is of course that the cost of the ORC C_{ORC} will increase too. For higher well costs, a new optimum is found: the ORC generates more electric power, but also costs more.

Table 2 gives some results of the optimal configurations obtained for air-cooled ORCs at a wellhead temperature of 125°C and for different well costs. From this data, it is clearly seen that the cycle efficiency increases from 7 to almost 10% when the well costs increase from 0 to 50 M€. This is a consequence of the decreasing pinch-point-temperature difference (8 to 4°C) and the decreasing condenser temperature (42 to 28°C).

Well cost (M€)	0	10	30	50
Energetic cycle efficiency (%)	7.3	8.4	9.4	9.6
Pinch-point-temperature-difference in evaporator (°)	7.6	4.7	3.8	3.7
Condenser temperature (°)	41.7	34.4	28.7	27.7
Net electric power output (MW$_e$)	3.1	4.6	5.7	5.9
Brine-outlet temperature (°C)	73.3	57.3	49.8	48.9
Exergetic plant efficiency (%)	20.6	31.1	38.4	39.5
Cost ORC (M€)	10.2	17.0	26.0	28.2
Specific cost ORC (€/kW$_e$)	3326	3668	4539	4773
Total project cost (M€)	10.2	27.0	66.0	78.2
Specific cost total project (€/kW$_e$)	3326	5820	11 521	13 243
Cost ORC/total project cost (%)	100.0	63.0	39.4	36.0
LCOE (€/MWh$_e$)	32.2	56.4	94.4	128.3

Table 2: Data of the optimal configurations obtained at different well costs at a temperature of 125°C for ORCs with an ACC.

The relative increase of the net electric power output is larger than the relative increase of the cycle efficiency, because the brine-outlet temperature decreases too with increasing well costs. This is again a consequence of decreasing pinch-point-temperature differences and decreasing condenser temperature, but also because of a decrease in the turbine-inlet temperature.

The consequence of the decreasing pinches and condenser temperature and the increased heat input to the cycle is that the heat exchangers become larger and more expensive. The cost of the ORC increases from 10 to 28 M€ for well costs ranging from 0 to 50 M€, or an increasing cost of the ORC with almost 200%. At the other hand does the specific cost of the ORC "only" increase with 44%.

At the other hand, does the fraction of the cost of the ORC to the total cost of the plant decrease strongly (100-36%) for the investigated increase in the well costs, which is in fact the main reason why the a more efficient and expensive ORC is optimal for higher well costs. As shown by the values of the LCOE in table 2, is the increase in the LCOE also very high due too this increase of the well costs. The increased net electric power output does not manage to compensate for this increased cost to keep the LCOE constant (equation (1)).

Going back to figure 6, it is seen that water-cooled ORCs generate more net electricity than air-cooled ORCs, but the difference is not high enough to explain the large difference in LCOE (Figure 5). This is explained by the difference in cost between the two. Figures 7a and 7b show the contour plot of the costs of the ORC. The difference is cost is a factor of two or more, in favor of the water-cooled ORCs. This is due to the very large cost of an ACC in comparison with a WCT.

(a) Air-cooled   (b) Water-cooled

Figure 7: Cost of air-cooled ORCs (a) and water-cooled ORCs (b) as a function of the heat-source-inlet temperature and the cost of the wells.

The optimal ORC becomes more expensive with increasing cost of the wells, as explained above, and with increasing heat-source-inlet temperature. The latter evolution is due to the increased net power output (bigger turbine) and more heat flow (larger heat exchangers, etc.).

5. CONCLUSIONS

The influence of the cost of the wells and the heat-source-inlet temperature on the LCOE, the net power output and the cost of geothermal ORCs is investigated in this paper by performing an economic system optimization. The configuration of the components and the configuration of the cycle are optimized together to obtain the minimum LCOE.

Contour plots of the LCOE are given as a function of the heat-source-inlet temperature and the cost of the wells. With these plots, a first estimate can be made of the electricity price needed for a specific project to become economically profitable.

It is shown that the LCOE of water-cooled ORCs is lower than the one of air-cooled ORCs for the investigated parameters. This is mainly caused by the much higher cost of an ACC in comparison with a WCT, and to a lesser extent by the higher net power output of the water-cooled ORC.

NOMENCLATURE

ACC	Air-cooled condenser	
C	Cost	($€$)
d_o	Diameter of a tube	(m)
D_S	Diameter of the shell	(m)
H	Fin height	(m)
H_i	Inlet height	(m)
H_{fi}	Hight fill	(m)
H_{sp}	Height spray zone	(m)
L_b	Baffle spacing	(m)
L_t	Length of the tubes	(m)
LCOE	Levelized Cost of Electricity	($€$/MWh$_e$)
N	Full-load hours per year	(-)
p_t	Pitch between tubes	(m)
S	Fin pitch	(m)
WCT	Wet cooling tower	
W_l	Tubes' large width	(m)
$\dot{W}_{net}$	Net electric power output	(MW$_e$)
W_S	Tubes' small width	(m)
W_t	Tower width	(m)

Subscript

EPC	Engineering, procurement & construction
O&M	Operations and maintenance
ORC	Organic Rankine cycle

REFERENCES

Andersson, J., Åkesson, J., and Diehl, M. (2012). CasADi -- A symbolic package for automatic differentiation and optimal control. In Forth, S., Hovland, P., Phipps, E., Utke, J., and Walther, A., editors, *Recent Advances in Algorithmic Differentiation*, volume 87 of *Lecture Notes in Computational Science and Engineering*, pages 297--307. Springer Berlin Heidelberg.

Büskens, C. and Wassel, D. (2013). The esa nlp solver worhp. In *Modeling and Optimization in Space Engineering*, pages 85--110. Springer.

D'haeseleer, W. (2013). Synthesis on the economics of nuclear energy. Study for the European Commission, DG Energy. available at: `http://ec.europa.eu/energy/nuclear/forum/doc/final_report_dhaeseleer/synthesis_economics_nuclear_20131127-0.pdf`.

IEA (2011). Technology Roadmap: Geothermal Heat and Power. Technical report, International Energy Agency.

Kloppers, J. C. (2003). *A critical evaluation and refinement of the performance prediction of wet-cooling towers*. PhD thesis, Department of Mechanical Engineering, University of Stellenbosch.

Lemmon, E., Huber, M., and Mclinden, M. (2007). *NIST Reference Fluid Thermodynamic and Transport Properties REFPROP*. The National Institute of Standards and Technology (NIST). Version 8.0.

Macchi, E. and Perdichizzi, A. (1981). Efficiency prediction for axial-flow turbines operating with nonconventional fluids. *Journal for Engineering for Power*, 103(4):718--724.

Shah, R. K. and Sekulić, D. P. (2003). *Fundamentals of heat exchanger design*. John Wiley and Sons, Inc.

Tester, J., Anderson, B., Batchelor, A., Blackwell, D., DiPippo, R., Drake, E., Garnish, J., Livesay, B., Moore, M., and Nichols, K. (2006). The Future of Geothermal Energy: Impact of Enhanced Geothermal Systems (EGS) on the United States in the 21st Century. Technical report, Massachusetts Institute of Technology, Massachusetts, USA.

Walraven, D., Laenen, B., and D'haeseleer, W. (2013). Comparison of thermodynamic cycles for power production from low-temperature geothermal heat sources. *Energy Conversion and Management*, 66(C):220--233.

Walraven, D., Laenen, B., and D'haeseleer, W. (2014). Optimum configuration of shell-and-tube heat exchangers for the use in low-temperature organic rankine cycles. *Energy Conversion and Management*, 83(C):177--187.

Walraven, D., Laenen, B., and D'haeseleer, W. (2015a). Economic system optimization of air-cooled organic rankine cycles powered by low-temperature geothermal heat sources. *Energy*, 80(C):104--113.

Walraven, D., Laenen, B., and D'haeseleer, W. (2015b). Minimizing the levelized cost of electricity production from low-temperature geothermal heat sources with orcs: water or air cooled? *Applied Energy*, 142(C):144--153.

A PERSPECTIVE ON COSTS AND COST ESTIMATION TECHNIQUES FOR ORGANIC RANKINE CYCLE SYSTEMS

Sanne Lemmens[1]*

[1]University of Antwerp, Department Engineering Management,
Antwerp, Belgium
sanne.lemmens@uantwerpen.be

* Corresponding Author

ABSTRACT

The potential of organic Rankine cycle (ORC) systems is acknowledged by both the considerable amount of ongoing research efforts and the increased occurrence of its applications in practice. A large share of research in this field strives to improve ORC systems by analyzing the performance of various cycle architectures and numerous working fluids. These technical feasibility and optimization studies are at the core of ORC development. Yet, when it comes down to considering practical instalments the economic feasibility of the project is often decisive. Complementary to research efforts on these technical issues this paper approaches the matter from an economic point of view. The costs-dimension of ORC systems is discussed from various perspectives. First of all, this paper provides a brief review of literature knowledge on ORC investment costs. Technical publications on ORC development increasingly include estimates of the costs associated with the system design, but knowledge on actual ORC module and project costs remains scarce. Secondly, this paper takes a closer investigation into the methods used to estimate ORC project costs from the bottom up and the expected accuracies associated with these estimates. Finally, these insights are used to estimate the costs of a known ORC system applied for waste heat recovery. The comparison of the estimated and the actual specific investment costs confirms the existence of a wide accuracy range. The purchased equipment costs obtained with the bottom-up estimate diverge from the actual costs by almost 44% and the deviation leads to differing interpretations on the share of equipment items in the total purchased equipment costs. The results of this analysis are not generalizable since only one real-life study is used for comparison. The main conclusion of the paper is to be cautious when interpreting estimated ORC plant costs.

1. INTRODUCTION

The interest for organic Rankine cycle (ORC) systems is growing increasingly. The concept of using an organic fluid instead of water dates back from right after the invention of the Rankine cycle in 1859, yet it was not until the 1960s and 1970s that ORC technology got more prominent research attention. By today, ORC systems constitute a flourishing research field and its practical possibilities have been proven. The reasons for this success are manifold. Rankine cycles operate with organic fluids, which allows conversion of energy sources in much lower temperature ranges than suitable for conventional steam cycles. ORCs can generate electricity from energy sources such as geothermal wells, biomass, solar and oceanic sources and industrial waste heat. Hence, ORC systems have potential to generate electricity from renewable energy sources as well as to enhance industrial energy efficiency. Both are essential in the transition of energy sectors to more streamlined, efficient, secure and climate-friendly systems. Research on ORC systems is very technical in nature and includes i.a. architecture design and optimization (e.g. Chen, Goswami, and Stefanakos (2010); Lecompte, Huisseune, van den Broek, Vanslambrouck, and De Paepe (2015)), the quest for suitable working fluids (e.g. Hung (2001); Lakew and Bolland (2010)) and the design of new expander types (e.g.

Declaye, Quoilin, Guillaume, and Lemort (2013)). Technical invention and optimization are a necessary first step in the technological innovation process. The subsequent steps are innovation (where the product goes from lab tests to real applications) and diffusion (gradual adoption by firms). The final degree of utilization may impact energy demand. Innovation processes typically follow an s-shaped figure: adoption occurs gradually in the beginning, then with increasing rapidity until the point of saturation. However, there is no guarantee for an invention to go through the entire innovation process and yield market success, even while interesting. For instance, the rate of technological invention and innovation of energy-efficient technologies is found to correlate with energy price increases. The gradual character of the diffusion process stems from the heterogeneity of (potential) adopters, which have a differing expected return. Those firms expecting the investment to be profitable will adopt first. Over time, more firms will adopt due to technology cost reduction, quality improvements and improved information availability. The adoption of energy-efficient technologies is likewise encouraged by higher energy prices, but decreased by adoption costs. Finally, energy-efficient technology adoption is found to be sensitive to the cost of equipment more than to the expected energy costs. (Jaffe, Newell, & Stavins, 2004) Seeing the importance of the economic perspective in technology development and diffusion, the aim of this paper is to complement the large body of literature on technical aspects with an economic viewpoint on ORC installations. A literature review gives insight in current knowledge on the investment costs of ORC systems (section 2). Section 3 elaborates on bottom-up cost estimation techniques and accuracies. In section 4 the investment costs of an actual ORC project are compared to those obtained from a bottom-up estimate. A final chapter discusses the results and conclusions.

2. ORC COSTS: A LITERATURE REVIEW

The body of literature on ORC systems and applications is extensive. The importance of the economic perspective is recognized and increasingly taken along in the engineering studies. At the basis of the economic analysis are the capital costs, particularly important for ORC projects since the annual costs are fairly low. Figure 1 displays the specific investment costs (SIC) estimated for various types of ORC input sources: solar, waste heat recovery (WHR), biomass and geothermal. The references are not included in the figure for clarity, but are included in the reference list. The values in the graph stem from literature and have been adjusted to 2013 Euros to allow for comparison. Geothermal ORC systems are most reported in the larger power output ranges. Figure 2 displays the same values but without the geothermal systems to provide a better view on the other costs. Similarly, Figure 3 limits the graph to smaller size (< 1.2 MW) ORC units. Solar ORC systems appear to be more costly, but most of the other costs are within the 2000 to 4000 €/kW range. Figure 1 suggests lower SIC values for higher power output systems, but additional references would be needed for a more detailed analysis.
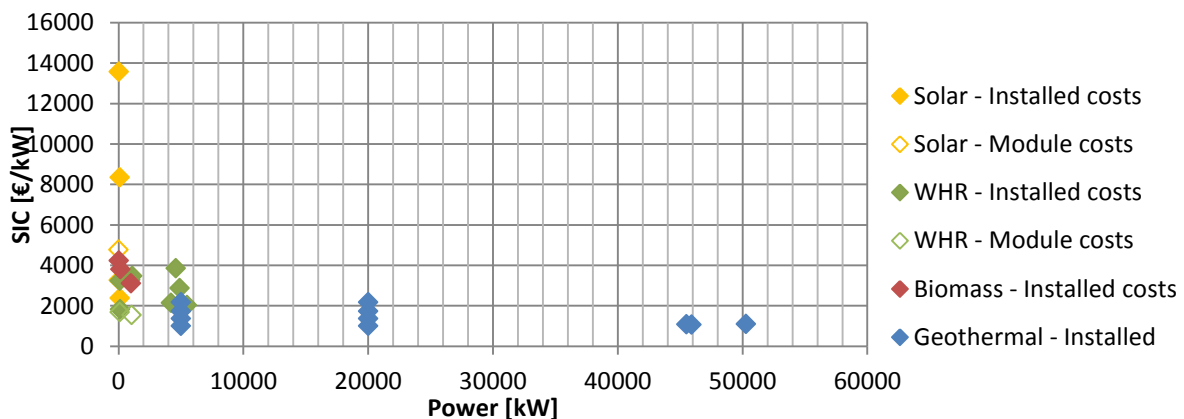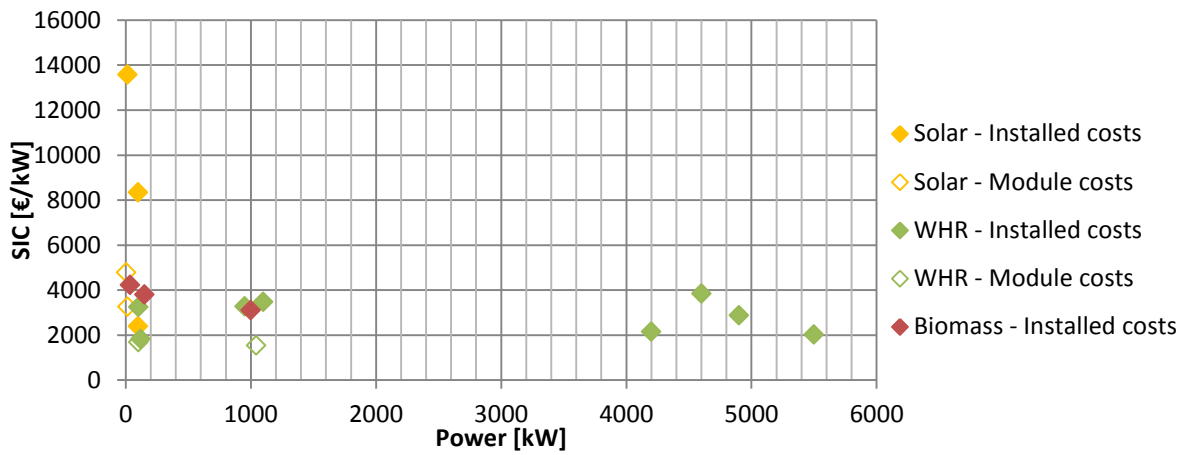

Figure 1: ORC costs in literature

Figure 2: ORC costs in literature - without geothermal references
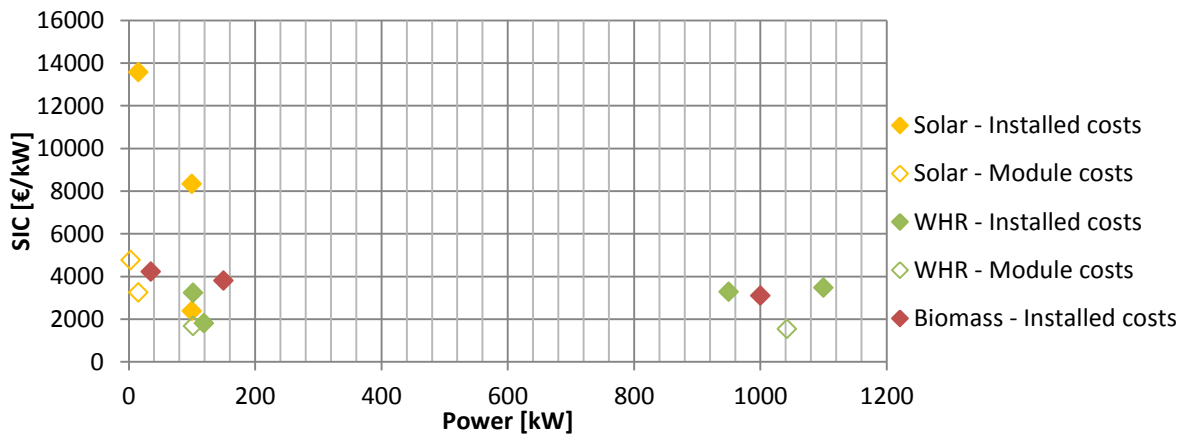

Figure 3: ORC costs in literature – small to medium sized

Not all references reporting ORC costs can be included in such summary graphs, e.g. because only SIC values are given and not the power output. For instance, Quoilin et al. (2011) perform a thermo-economic optimization of ORCs for waste heat recovery. They obtain SIC values between 2136 €/kW and 4260 €/kW, depending on the fluid operated, for small scale (< 5 W_{net}) systems. An important conclusion from their work is that the operating point yielding maximum power does not coincide with that of minimal SIC. Similarly, Imran et al. (2014) utilize thermo-economic optimization to compare cycle setups. The SIC values are in the range of 3274 to 4155 €/kW for the basic ORC, 3453 to 4571 €/kW for the single stage regenerative ORC and 3739-4960 €/kW for the double stage regenerative ORC, depending on the working fluid operated. Unfortunately no indication was given on the power range. Walraven, Laenen, and D'Haeseleer (2015) investigate air-cooled geothermal ORC systems. No exact specific investment costs numbers are presented, but the impact of various factors, such as brine inlet and outlet temperatures, pressure levels, electricity prices, discount rates and electricity price evolutions, on the economics of the ORC project are demonstrated. Other studies are not included here because the economic values are expressed in €/kWh rather that €/kW, such as in Meinel, Wieland, and Spliethoff (2014) who perform a considerate comparison of architecture designs at various sizes. The results were calculated for heat sources of 0.5 MW_{th}, 1 MW_{th} and 5 MW_{th}.

The references in Figure 1 all concern estimates of ORC costs rather than reporting of real ORC costs. Real ORC costs are provided by e.g. Leslie et al. (2009) who report the findings of a 5.5 MW ORC system applied for heat recovery from a gas turbine driving a natural gas pipeline compressor. The system was monitored extensively for one year, the capital costs of the system constitute approximately 2500 €/kW. Prices for biomass fuelled ORC systems are published in the range of 4500 €/kW for a 1803 kW system to 10,200 €/kW for a 345 kW system in 2009 (Duvia, Guercio, & Rossi di Schio, 2009).

3. COST ESTIMATION FOR ORC PLANTS

The up-front estimation of the costs of a new plant is a challenging task. Capital costs, or capital investment, refer to the one-time costs occurring at the beginning of the project. These total investment costs include the costs directly associated with the system (equipment, materials, labor etc. required for the equipment and the installation thereof), indirect costs (engineering, construction costs and contingencies) and other outlays (such as startup costs, working capital, etc.) (Bejan, Tsatsaronis, & Moran, 1996). The estimate of plant capital costs is a practice iterating as the design evolves to increased detail. Plant estimates are classified according to their level of detail and thus their accuracy (Table 1). The accuracy ranges indicate variations regarding technological complexity of the project, suitable reference information, and an appropriate determination of project contingencies (AACE International, 2005). The ranges represented in Table 1 are applicable for process industry projects (AACE International, 2005). Underestimation of capital costs occurs mainly due to incomplete listing of all the equipment needed in the process (Turton, Bailie, Whiting, Shaeiwitz, & Bhattacharyya, 2013, p. 160). An increasing level of detail implies a smaller accuracy range, but similarly an increasing amount of effort and labor hours to make the estimate. Estimates performed in research are generally order-of-magnitude, study and preliminary design estimates.

Table 1: Classification of capital cost estimates (AACE International, 2005; Turton et al., 2013).

Class	Type of estimate	Description	Accuracy ranges
5	Order-of-magnitude estimate (also Ratio / Feasibility)	Based on limited information. Concept screening.	Low: -20% to -50% High: +30% to +100%
4	Study estimate (also Major Equipment / Factored)	List of major equipment. Project screening, feasibility assessment, concept evaluation, and preliminary budget approval.	Low: -15% to -30% High: +20% to +50%
3	Preliminary Design estimate (also Scope)	More detailed sizing of equipment. Budget authorization, appropriation, and/or funding.	Low: -10% to -20% High: +10% to +30%
2	Definitive estimate (also Project Control)	Preliminary specification of all the equipment, utilities, instrumentation, electrical and off-sites. Control or Bid/Tender.	Low: -5% to -15% High: +5% to +20%
1	Detailed estimate (also Firm / Contractor's)	Complete engineering of process and related off-sites and utilities required. Check Estimate or Bid/Tender.	Low: -3% to -10% High: +3% to +15%

The equipment needed for construction of the plant is at the core of most cost estimates. The best approach for the purchase cost of a piece of equipment is a current vendor's price quote. Data from previously bought but similar equipment is next best. (Turton et al., 2013) When the costs of a component are known but its capacity differs from that of the to-be-estimated component, the costs can be roughly estimated using the correlation

$$\frac{c_a}{c_b} = \left(\frac{A_a}{A_b}\right)^n \tag{1}$$

where c and A respectively represent the purchase costs and the equipment cost attribute of the required component (c_a and A_a) and the known component (c_b and A_b) and n is the exponent used to correlate the costs. This exponent n differs per type of equipment, but it is often close to 0.6 for the chemical industry and therefore sometimes referred to as the six-tenths rule. This extrapolation method provides only rough approximations of the actual costs. In case no purchased equipment costs are known, but technical details are available, the costs can be estimated using equipment cost correlations. Guidance, exponents and correlations for various types of process equipment are

provided by i.a. Bejan et al. (1996), Couper, Penney, Fair, and Walas (2012), Smith (2005), Towler and Sinnot (2008), Turton et al. (2013).

The total capital investment of a project can be estimated using various techniques. A simple method is to use a capacity exponent ratio, similarly as previously described for equipment costs estimates. The costs of a planned plant are estimated using the known costs of a similar previously constructed plant. The accuracy of this method is rather low. It should be used for order-of-magnitude or study estimates only. (Peters, Timmerhaus, & West, 2004) Step Count methods take a different approach and utilize the number of functional units or plant sections as a basis to estimate total investment costs. This method is designed for use in the chemical process industry and not so suitable for usage in other manufacturing fields. The accuracy would be in the range of order-of-magnitude estimates. (Towler & Sinnot, 2008) Thirdly, factorial estimation techniques are based on the costs of the major purchased equipment items and apply multiplication factors to obtain the total capital investment. The Lang Factor method is probably the first factorial method. Lang suggested to multiply the total delivered costs of the major equipment parts with a factor that differs according to the type of process. The factors are available for solid, fluid and mixed fluid-solid processing chemical plants. (Towler & Sinnot, 2008) The Lang Factor technique utilizes only one multiplication factor and is therefore expected to yield lower accuracies, it is suggested to use for order-of-magnitude estimates (Peters et al., 2004, p. 252). The Lang Factor method has been adapted numerous times since then. For instance, Hand suggested to utilize multiplication factors for the equipment types instead of the plant type. (Towler & Sinnot, 2008) The utilization of multiple factors implies more detail, but this method would probably still not provide very good accuracies. The detail of the estimate can be improved further using cost factors for different items related to direct costs (erection of equipment, piping, electrical, instrumentation and control, buildings and structures, ancillary buildings, storage, utilities, site preparation). Dividing the process into subunits and applying factors per subunit function improves the estimate's accuracy and reliability. (Towler & Sinnot, 2008) An even more detailed estimate is suggested by Guthrie and accounts the installation, piping and instrumentation costs of each equipment item individually. Inclusion of a factor for the equipment materials used would improve accuracy even more. (Towler & Sinnot, 2008) Still, these estimates would remain within the accuracy of preliminary estimates. Another, somewhat different, factorial method calculates the direct fixed costs and total investment costs as percentages of the delivered-equipment costs. The factors used depend i.a. on the process type, design complexity, location, experience. This percentage of delivered-equipment method is suitable for study and preliminary estimates. (Peters et al., 2004) When the goal is to achieve more detailed estimates than the ones formerly described, this requires more detailed information and engineering effort. For instance, the unit cost method is used for preliminary and definitive estimates. The method requires accurate information on costs from previous projects, detailed estimates of equipment prices, installation labor, instrumentation, electrical and other miscellaneous items. Also engineering hours, drawing efforts, construction, contractor's fee and contingencies are included. This can yield relatively accurate results but requires sufficiently detailed information and engineering time. (Peters et al., 2004) Detailed item estimates, with high accuracies, generally concern advanced project plans. At this stage most details of the project are known, the drawings are finished and the estimates are based preferably on delivered quotations. For most research and development projects, both definitive and detailed cost estimates would range beyond the scope of the project and the information available. Preliminary estimates are feasible, but the accuracy of the results relies strongly on the quality of the information (i.a. factors) used.

Finally, the costs of materials and labor are subject to inflation which implies cost figures from different years are not directly comparable. The most straightforward manner to update historical data is by means of composite cost indices, using equation

$$c_j = c_i * \left(\frac{I_j}{I_i}\right) \tag{2}$$

where c_j and c_i refer to the costs in year j and i respectively, and I_j and I_i are the cost indices for the respective years. These composite indices are a weighted average index of various components costs

commonly used in a particular industry. Updating cost data using cost indices is acceptable for only shorter periods of time, some say four to five years (Jelen & Black, 1983, p. 339). The accuracy of the results decreases when longer time periods are used.

4. A NUMERICAL EXAMPLE

To demonstrate the precarious exercise of bottom-up cost estimation for ORC-plants, this paper compares the costs of an actual case study with the costs obtained from a rough bottom-up estimate. The case study concerns a waste heat recovery ORC installation. The heat source is a low-medium temperature (range 150 – 250°C) flue gas stream from an industrial plant. The ORC system was integrated into the plant using an intermediate thermal oil circuit including a flue gas heat exchanger. The ORC itself has a gross power output of 375 kW and is composed of a centrifugal pump, a one-step radial expander and a generator. The evaporator is a plate heat exchanger and condensation occurs air-cooled. The project has a SIC of 4216 €/kWgross, including installation (in 2013). The partitioning of the costs for this project (Figure 4) demonstrates a major share stems from the ORC unit itself, including pump, expander and generator. The intermediate thermal oil circuit represents about 11% of total investment costs.
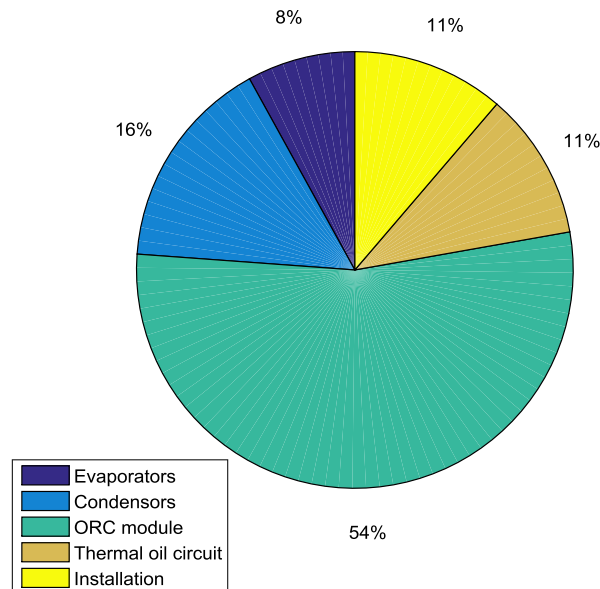
Figure 4: Diagram of the real ORC project costs

Knowing most technical details of the real plant, a rough bottom-up cost estimation was performed using the module costing technique. The module costing technique is a commonly used factorial cost estimation method based on the approach of Guthrie. (Turton et al., 2013). This technique is suitable for preliminary estimates in the range of -20% to +30% accuracy. The costs of the major purchased equipment parts are estimated using available correlations. These base costs are multiplied with the bare module cost factor, that accounts for operating pressures and specific materials of construction, as well as direct and indirect project expenses. This yields the bare module costs. To obtain the total module costs, estimated for integration of the plant into an existing facility, the bare module costs are adapted with another multiplication factor. (Turton et al., 2013) All estimates are converted to 2013 Euros to allow for comparison with the real system. The cost correlations published in Turton et al. (2013) are utilized to estimate most purchased equipment costs, the correlation by Smith (2005) for estimation of the fan costs and the generator costs stem from the correlation given by Toffolo, Lazzaretto, Manente, and Paci (2014). The results obtained from Turton et al. (2013) are in USD_{2001}, they are converted to EUR using a 1.1162 exchange rate (average 2001) and updated to 2013 using the Chemical Engineering Plant Cost Index (CEPCI), with $CEPCI_{2001}$ and $CEPCI_{2013}$ values of 397 and 587.3 respectively. Results obtained from Smith (2005) are converted from $USD_{Jan,2000}$ to EUR_{2013}

using an exchange rate of 0.9857 (average Jan 2000) and $CEPCI_{2000}$ equal to 394.1. The correlation from Toffolo et al. (2014) was first published in 1993, so a $CEPCI_{1993}$ of 359.2 was used.

In case only the essential ORC components are considered, and the thermal oil circuit is not accounted for, the estimate yields a result of 1843 €/kW for the purchased equipment costs. In the module costing technique, the purchased equipment costs are used to estimate the total plant costs. An intermediate step is the calculation of the bare module costs. These costs include the direct (equipment, installation materials and labor) and indirect (freight, insurance, taxes, overhead and engineering expenses) costs associated with the project. Accounting for these expenses additional to the purchased equipment costs yields a bare module cost of 4390 €/kW. Finally, the total module costs include also contingencies and contractor fees and auxiliary facilities and are estimated at 5180 €/kW. Note that these estimated costs do not yet include the costs of the thermal oil circuit. Simply adding the costs of the thermal oil system (real costs, not estimated) gives a total module cost of 5642 €/kW. The costs of the thermal oil system are taken as such and not manipulated with bare module or total module factors. Manipulation of the costs for the thermal oil system with a bare module factor of 1.5 and a 1.18 multiplication factor to obtain the total module costs would give a SIC of 5997 €/kW. The bare module factor given for this latter estimate was not given by any reference but expected in line with other bare module factors, a 1.5 factor seems not unreasonable knowing the amount of piping involved with the installation of the system.

Figure 5 displays the real (a) and the estimated (b) purchased equipment costs of the components of the ORC system, excluding installation and thermal oil circuit. The partitioning of purchased equipment costs differs strongly from that of the actual costs. Whereas the evaporators constitute only 10% of purchased equipment costs in reality, the cost estimation leads to a 45% share. The ORC module (expander, generator and pump) represents 69% of actual purchased equipment costs but is estimated at 47%.
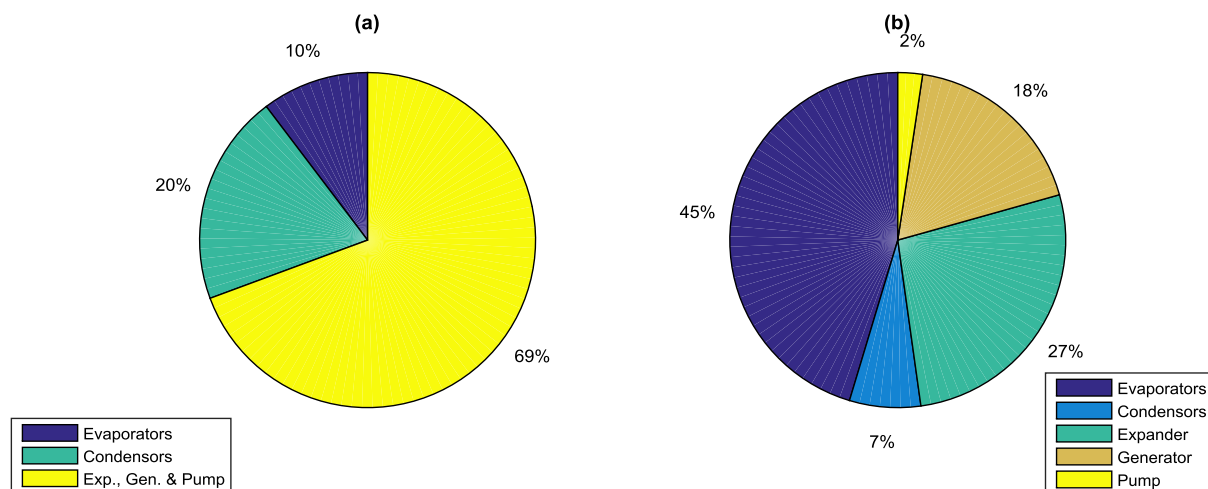
Figure 5: Real (a) and estimated (b) purchased equipment costs

The estimated PEC of 1843 €/kW is significantly lower than the actual PEC of 3280 €/kW (-44 %). If the total module costs are estimated, including the thermal oil circuit but with no adaption of the real costs of the thermal oil system, the obtained costs (5642 €/kW) are 34% higher than the actual total project costs (4216 €/kW). If the thermal oil circuit is included and adapted with bare and total module factors, the estimated cost (5997 €/kW) is even higher and deviates more from the actual costs.

5. DISCUSSION AND CONCLUSIONS

The aim of this paper is to give insight into ORC systems from an economic point of view. Technical invention and innovation are key for evolution to more streamlined and renewables-based energy sectors, but the adoption and diffusion processes of innovative technologies are strongly influenced by

economic factors. There is still not much published information about the actual costs of ORC systems. A brief review of literature knowledge on the investment costs of ORC modules and ORC projects reveals most are in the 2000 – 4000 €/kW range. Geothermal projects tend to be larger with lower SIC values, solar projects are mostly small and can have very high specific investment costs. An increasing number of references utilize thermo-economic and techno-economic optimization techniques and apply bottom-up estimation techniques to estimate the costs of ORC modules or projects. Component cost estimates can simply be made using scale exponent methods, more detailed estimates use factorial estimation techniques. In any bottom-up estimate it is important to consider the expected accuracy range. Simpler methods require less effort but yield lower accuracy. High accuracies are possible making definitive and detailed estimates, but these require a level of plant detail which is commonly not achieved in research estimates. The precariousness of using factorial techniques to approach real plant costs is demonstrated and confirmed for an existing ORC applied for waste heat recovery. The estimated specific purchased equipment costs deviate from the actual project costs by almost 44%. The purchased equipment costs distribution differs largely between the actual and the estimated costs of the components. There are many potential reasons for this deviation. First of all, factorial estimation methods are suitable for preliminary estimates. A deviation of -20% to +30% is therefore not uncommon. The accuracy of factorial estimation methods depends strongly on the quality of the information that was used to establish the multiplication factors. Additional inaccuracies and uncertainties may stem from treatment of costs over time periods. Extrapolation of costs over large periods of time decreases the accuracy of the results. Most of the open-source correlations available in text books are at least nine years old and thus provide less accurate results. Additionally, some of these references refer back to original factors and correlations published in by Guthrie in 1969 or 1974 and updated with few recent data points or using cost indices. This makes these correlations less reliable. Finally, also the choice of indicator for cost escalation and local conditions may have an influence and create additional deviations. This implies that results in such settings should not be interpreted as final, but rather as giving an idea on the expected range of investment costs. This type of estimate can be useful to mutually compare various system designs, where the proportional comparison is more important than the exact outcomes. Finally, it is important to take the difference between costs and prices into consideration in this type of studies. Costs reflect the amount that is required to produce a certain item, the price is the amount you pay to purchase it. The costs associated with producing an ORC system will thus differ from the price paid to acquire that system. Many correlations used to estimate costs are obtained using vendor prices. In case the ORC developer would purchase most equipment instead of developing it this is not a problem. For innovative system designs (e.g. expanders) this method would be less suitable. The main conclusion from this study is to be careful when interpreting results obtained from preliminary bottom-up cost estimates. This is also the case for the results obtained from the estimates in this study. The results confirm a wide accuracy range. Rather than being used as exact results, these estimates could give guidance when comparing several alternatives, estimated with the same method.

NOMENCLATURE

A	equipment cost attribute	
c	cost of component	(€)
CEPCI	Chemical Engineering Plant Cost Index	
ORC	organic Rankine cycle	
n	exponent for cost correlation	
SIC	specific investment costs	(€/kW)
WHR	waste heat recovery	

Subscript

a	required component
b	known component
i	year i
j	year j

REFERENCES

AACE International. (2005). Recommended Practice No. 18R-97. Cost estimate classification system - As applied in engineering, procurement, and construction for the process industries. TCM Framework: 7.3 – Cost Estimating and Budgeting (pp. 10): AACE International.

Angelino, G., Gaia, M., & Macchi, E. (1984, 13-15 February). *Medium temperature 100kW ORC engine for total energy systems - Experimental results.* Paper presented at the International Seminal of the Commission of the European Communities on Energy Conservation in Industry, Düsseldorf.

Arslan, O., Ozgur, M. A., & Kose, R. (2012). Electricity Generation Ability of the Simav Geothermal Field: A Technoeconomic Approach. *Energy Sources, Part A: Recovery, Utilization, and Environmental Effects, 34*(12), 1130-1144. doi: 10.1080/15567031003773254

Barber, R. E. (1978). Current costs of solar powered organic Rankine cycle engines. *Solar Energy, 20*(1), 1-6.

Bejan, A., Tsatsaronis, G., & Moran, M. (1996). *Thermal design and optimization* New York: Wiley & Sons.

Chen, H., Goswami, D. Y., & Stefanakos, E. K. (2010). A review of thermodynamic cycles and working fluids for the conversion of low-grade heat. *Renewable and Sustainable Energy Reviews, 14*(9), 3059-3067. doi: 10.1016/j.rser.2010.07.006

Couper, J. R., Penney, R. W., Fair, J. R., & Walas, S. M. (2012). *Chemical Process Equipment: Selection and Design* (Third ed.): Butterworth-Heinemann.

Declaye, S., Quoilin, S., Guillaume, L., & Lemort, V. (2013). Experimental study on an open-drive scroll expander integrated into an ORC (Organic Rankine Cycle) system with R245fa as working fluid. *Energy, 55*, 173-183. doi: 10.1016/j.energy.2013.04.003

Duvia, A., Guercio, A., & Rossi di Schio, C. (2009). *Technical and economic aspects of Biomass fuelled CHP plants based on ORC turbogenerators feeding existing district heating networks*.

Forni, D., Vaccari, V., Di Santo, D., Rossetti, N., & Baresi, M. (2012, 11–14 September 2012). *Heat recovery for electricity generation in industry.* Paper presented at the ECEEE 2012 Summer Study on energy efficiency in industry, the Netherlands.

Forsha, M. D., & Nichols, K. E. (1991). Factors affecting the capital cost of binary power plants. *Geothermal Resources Council Transactions, 15*, 99-105.

Georges, E., Declaye, S., Dumont, O., Quoilin, S., & Lemort, V. (2013). Design of a small-scale organic Rankine cycle engine used in a solar power plant. *International Journal of Low-Carbon Technologies, 8*(suppl 1), i34-i41. doi: 10.1093/ijlct/ctt030

Huang, Y., McIlveen-Wright, D. R., Rezvani, S., Huang, M. J., Wang, Y. D., Roskilly, A. P., & Hewitt, N. J. (2013). Comparative techno-economic analysis of biomass fuelled combined heat and power for commercial buildings. *Applied Energy, 112*, 518-525. doi: 10.1016/j.apenergy.2013.03.078

Hung, T.-C. (2001). Waste heat recovery of organic Rankine cycle using dry fluids. *Energy Conversion and Management, 42*, 539-553.

Imran, M., Park, B. S., Kim, H. J., Lee, D. H., Usman, M., & Heo, M. (2014). Thermo-economic optimization of Regenerative Organic Rankine Cycle for waste heat recovery applications. *Energy Conversion and Management, 87*, 107-118. doi: 10.1016/j.enconman.2014.06.091

Jaffe, A. B., Newell, R. G., & Stavins, R. N. (2004). Economics of Energy Efficiency. *Encyclopedia of Energy, 2*, 79-90.

Jelen, F. C., & Black, J. H. (1983). *Cost and optimization engineering* (Second ed.): McGraw-Hill, Inc.

Kosmadakis, G., Manolakos, D., Kyritsis, S., & Papadakis, G. (2009). Economic assessment of a two-stage solar organic Rankine cycle for reverse osmosis desalination. *Renewable Energy, 34*(6), 1579-1586. doi: 10.1016/j.renene.2008.11.007

Lakew, A. A., & Bolland, O. (2010). Working fluids for low-temperature heat source. *Applied Thermal Engineering, 30*(10), 1262-1268. doi: 10.1016/j.applthermaleng.2010.02.009

Law, R., Harvey, A., & Reay, D. (2013). Techno-economic comparison of a high-temperature heat pump and an organic Rankine cycle machine for low-grade waste heat recovery in UK industry. *International Journal of Low-Carbon Technologies, 8*(suppl 1), i47-i54. doi: 10.1093/ijlct/ctt029

Lecompte, S., Huisseune, H., van den Broek, M., Vanslambrouck, B., & De Paepe, M. (2015). Review of organic Rankine cycle (ORC) architectures for waste heat recovery. *Renewable and Sustainable Energy Reviews, 47*, 448-461. doi: 10.1016/j.rser.2015.03.089

Lee, K. M., Kuo, S. F., Chien, M. L., & Shih, Y. S. (1988). Parameters analysis on organic rankine energy recovery system. *Energy Conversion and Management, 28*(2), 129-136.

Leslie, N. P., Sweetser, R. S., Zimron, O., & Stovall, T. K. (2009). Recovered Energy Generation Using an Organic Rankine Cycle System. *ASHRAE Transactions, 115*(Part 1).

Meinel, D., Wieland, C., & Spliethoff, H. (2014). Economic comparison of ORC (Organic Rankine cycle) processes at different scales. *Energy, 74*, 694-706. doi: 10.1016/j.energy.2014.07.036

Peters, M. S., Timmerhaus, K. D., & West, R. E. (2004). *Plant Design and Economics for Chemical Engineers* (Fifth ed.): McGraw-Hill

Quoilin, S., Declaye, S., Tchanche, B. F., & Lemort, V. (2011). Thermo-economic optimization of waste heat recovery Organic Rankine Cycles. *Applied Thermal Engineering, 31*(14), 2885-2893.

Rentizelas, A., Karellas, S., Kakaras, E., & Tatsiopoulos, I. (2009). Comparative techno-economic analysis of ORC and gasification for bioenergy applications. *Energy Conversion and Management, 50*(3), 674-681. doi: 10.1016/j.enconman.2008.10.008

Schuster, A., Karellas, S., Kakaras, E., & Spliethoff, H. (2009). Energetic and economic investigation of Organic Rankine Cycle applications. *Applied Thermal Engineering, 29*(8), 1809-1817.

Smith, R. (2005). *Chemical Process Design and Integration*. West Sussex, England: John Wiley & Sons, Ltd.

Toffolo, A., Lazzaretto, A., Manente, G., & Paci, M. (2014). A multi-criteria approach for the optimal selection of working fluid and design parameters in Organic Rankine Cycle systems. *Applied Energy, 121*, 219-232. doi: 10.1016/j.apenergy.2014.01.089

Towler, G., & Sinnot, R. (2008). *Chemical Egineering Design: Principles, Practice and Economics of Plant and Process Design*: Butterworth-Heinemann.

Turton, R., Bailie, R. C., Whiting, W. B., Shaeiwitz, J. A., & Bhattacharyya, D. (2013). *Analysis, Synthesis, and Design of Chemical Processes* (Fourth ed.). Upper Saddle River, New Jersey: Pearson Education International.

Walraven, D., Laenen, B., & D'Haeseleer, W. (2015). Economic system optimization of air-cooled organic Rankine cycles powered by low-temperature geothermal heat sources. *Energy, 80*, 104-113. doi: 10.1016/j.energy.2014.11.048

ACKNOWLEDGEMENT

DESIGN OF WASTE HEAT RECOVERY SYSTEMS BASED ON SUPERCRITICAL ORC FOR POWERFUL GAS AND DIESEL ENGINES

Oleksii Rudenko[1], Leonid Moroz[2], Maksym Burlaka[3], Clement Joly*[4]

[1]SoftInWay, Engineering,
Burlington, MA, USA
o.rudenko@softinway.com

[2]SoftInWay, Engineering
Burlington, MA, USA
l.moroz@softinway.com

[3]SoftInWay, Engineering
Burlington, MA, USA
m.burlaka@softinway.com

[4]SoftInWay, Engineering
Burlington, MA, USA
clement.joly@softinway.com

* Corresponding Author

ABSTRACT

Nowadays the scientific world community is strongly concerned about problems of efficiency increase and emissions reduction of Internal Combustion Piston Engines (ICPE). The equipment of ICPE with Waste Heat Recovery Systems (WHRS) is an effective solution for the aforementioned problems. This paper focuses on finding the maximum possible heat recovery from the available high and low temperature waste heat flows of a powerful ICPE to produce the maximum amount of additional power while decreasing the load on the engine's cooling system.

Having considered and analyzed existing works devoted to the development of WHRS the most effective ideas were combined to design several thermodynamic cycles for new WHRS of a powerful piston engine (here a G3612 CAT gas petroleum engine is considered). The proposed WHRS is based on a Supercritical Organic Rankine Cycle (SORC) using R245fa as the working fluid where heat is extracted from the waste heat sources by a refrigerant at different pressure levels. Internal recuperation is used to further improve the cycle performances and increase the waste heat recovery. The thermodynamic analysis of the new WHRS showed that up to 19.73% of power boost for the internal combustion engine can be achieved without burning additional fuel which represents significant gains in terms of specific power.

In order to quantify the estimation of the performances for proposed cycles the design of a traditional, high efficiency, a WHRS based on double pressure water steam cycle for the same engine's conditions was performed. This comparison of performances between the steam cycle and the SORC R245fa cycles confirmed a high potential for the designed cycles.

1. INTRODUCTION

Internal combustion piston engines are among the largest consumers of liquid and gaseous fossil fuels all over the world. Despite the introduction of new technologies and constant improving of engines

performances they still are relatively wasteful. Indeed, the efficiency of modern engines rarely exceeds 40-45% (Seher et al. (2012), Guopeng et al. (2013)) and the remainder of the fuel energy usually dissipates into the environment in the form of waste heat. The heat balance diagram of typical engine is given in Figure 1. As is evident from Figure 1, besides the mechanical work energy the heat balance includes a heat of exhaust gas, a heat of charge air, a Jacket Water (JW) heat, a heat of lubricating oil and a radiation heat. The energy from all the heat sources except the last one (radiation), due to its ultra-low waste heat recovery potential, can be used as heat sources for WHRS (Paanu et al. (2012)) and are considered here.
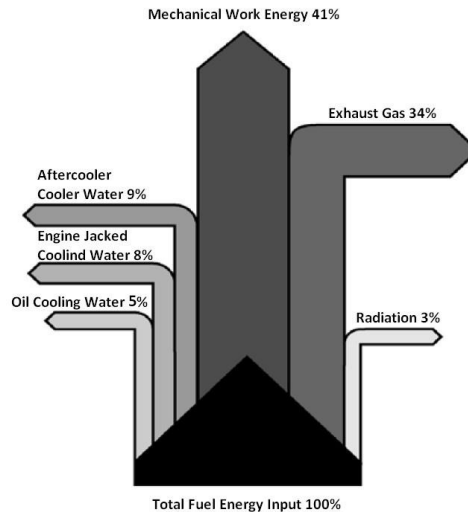
Figure 1: Typical heat balance diagram for CAT engine (Caterpillar (2011))

Waste heat utilization is a very current task because it allows to reduce the harmful influence of ICPE operation on the environment as well as to obtain additional energy and to reduce the load on the engine's cooling system. Different WHRS can produce heat energy, mechanical energy or electricity and combinations of the converted energy forms exist as well. In general, the type of WHRS to be used is determined by the engine type, fuel cost, available energy customers and other factors. In the present paper only WHRS for mechanical power and electricity production were considered because these kinds of energy are preferable for this type of applications and they can be easily converted into other forms of energy.

For vehicle engines the WHRS based on Organic Rankine Cycle (ORC) are the most commercially developed (Paanu et al. (2012)). Because of strict restrictions on weight and dimensions, the mentioned systems typically operate on the base of a simple or recuperated ORC and utilize only high temperature waste heat from the exhaust gases and the exhaust gas recirculation. They usually produce mechanical power or electricity. More complex cycles and a larger number of heat sources are used for waste heat recovery from powerful internal combustion engines where additional weight and dimensions are not crucial factors. Waste heat from stationary, marine and another more powerful ICPE can be recovered using a typical steam bottoming cycle. Steam WHRS allow utilizing almost all a high temperature waste heat and partially utilizing a low temperature heat. The high efficiency steam WHRS are presented in (MAN Diesel & Turbo (2012), Petrov (2006)), they provide up to 14.5% of power boost for the engine.

From the existing works devoted to waste heat recovery range of problems the following methods of efficiency increase can be highlighted:

- Addition of the internal heat recuperation to a WHR cycle;
- Appropriate working fluid selection;
- Increment of initial parameters of bottoming cycle up to supercritical values;
- Maximize waste heat utilization due to the usage of low temperature heat sources;
- Bottoming cycle complexification or usage of several bottoming cycles with different fluids (Maogang (2011)).

This paper focuses on the development of new WHRS as an alternative to high efficiency steam bottoming cycles by accounting for the latest progress in the field of waste heat recovery. The application range of the proposed system extends to powerful and super powerful ICPEs.

2. DEVELOPMENT OF NEW WHRS

The goal of the present work is the development of a new, high efficiency WHRS for powerful and super powerful ICPEs based on ORC principles. To solve the assigned task, a thorough study of the currently existing works was performed and the best ideas were combined. The principles of the maximum waste heat utilization, maximum possible initial cycle parameters, recuperation usage and single working fluid were assumed as a basis for the new WHRS design.

It is well known that the fluid saturation temperature depends on the pressure and the higher the pressure level the higher the saturation temperature. This why the extraction of the waste heat from available sources by a refrigerant at different pressure levels is more effective to achieve a maximum waste heat utilization. The thermodynamic efficiency of a Rankine cycle mainly depends on its maximum cycle parameters (pressure and temperature) and minimum pressure. In the works (Jadhao and Thombare (2013), Braimakis et al. (2014)) is shown that ORC operation with a supercritical top pressure has a positive effect on cycle performances. The internal recuperation, in turn, increases WHRS efficiency due to returning part of the heat after the expander to the cycle.

The process of design of recovery system for waste heat flows from the G3612 CAT gas petroleum piston engine is described hereafter. The process is divided into 4 steps and includes: working fluid selection, definition of main cycle parameters, cycle design and thermodynamic simulation, preliminary design of High Pressure and Low Pressure Turbines (HPT, LPT, respectively). The used engine's data is given in Table 1 and the engine's heat balance is shown in Figure 1.

Table 1: Waste heat flows from G3612 CAT gas petroleum engine (Caterpillar (2011))

Energy Flow	Value, kW	Temperature Potential	Recoverability by WHRS
Total Input Heat From the Fuel	7192	High	-
Mechanical Work	2948.72	-	-
Heat Rejection to Exhaust (Recoverable Exhaust Heat at 120°C)	2445.28 (1644.62)	High	Yes
Heat Rejection to the Aftercooler	647.28	Middle	Yes
Heat Rejection to the Jacket Water	575.36	Low	Yes
Heat Rejection to the Oil Cooler	359.6	Low	Yes
Heat Rejection to the Atmosphere	215.46	Lowest	No

2.1 Working Fluid Selection

Unfortunately, a universal organic working fluid that can be used for a wide range of ORC does not seem to exist and the working fluid selection is one of the most important design steps. There are a lot of works devoted to the mentioned problem (Jadhao & Thombare (2013), Braimakis et al. (2014), DiCarlo & Wallace (2011), Jadhao & Thombare (2013), Nouman (2012)). As a rule, the working fluids are considered according to such criteria as thermodynamic properties, environmental impact, thermal stability and safety. Water, ethanol, R245fa and R134a are among the most popular organic working fluids at the moment. Besides, for a recuperated ORC it is recommended to use either an isentropic or a dry fluid. Here, the working fluid was selected according to its potential to remove heat from the selected sources, at different temperatures, in a pressure range from 1 to 45 bars.

Maogang (2011) used in his work for this purpose the combined thermodynamic cycle. It consists of two cycles: an ORC is used to recover the waste heat of the lubricant and exhaust gas and a Kalina cycle for the recovery of the waste heat of the low-temperature cooling water. Of course, the combined WHRS is effective enough but the use of 2 working fluids essentially complicates the system. For these reasons the Kalina cycle is eliminated here in order to simplify the system.

Based on aforementioned thoughts the R245fa (pentafluoropropane) was selected as the working fluid. Due to its low condensation temperature and relatively high decomposition temperature (higher than 250 °C (Honeywell (2014))) R245fa fits the basic criteria of this study. R245fa fluid properties

were calculated based on the NIST RefProp library (version 9.1). The fluid reference state corresponds to the International Institute of Refrigeration (IIR) convention.

2.2 Main ORC Parameters

The design parameters of the cycle components used in this study are presented in Table 2. The maximum cycle temperature was limited to 240 °C to avoid fluid decomposition. The maximal cycle pressure was set to 45 bars. The subsequent pressure increase does not lead to essential cycle performance increase but it leads to an increase of the WHRS production cost and complication of the HPT design. At the HPT inlet the R245fa is at a supercritical pressure which allows for an increase in the cycle efficiency. The comparison of performances between the SORC and subcritical ORC is given in (Jadhao and Thombare (2013), Braimakis et al. (2014)). For this case the condenser pressure was fixed to 1.3 bars to prevent air ingression into the closed cycle.

Table 2: Design parameters of cycle components

Parameter	Units	Value
Efficiency of HPT and LPT	-	0.8
Efficiency of High and Low Pressure Pumps	-	0.8
Minimal Pinch Point for Heat Exchangers	°C	10
Hydraulic Losses in the Pipelines and Heat Exchangers	-	Ignored

2.3 WHRS Cycle Design and Thermodynamic Simulation

At the initial stage of the ORC design waste heat flows from the G3612 CAT engine (see Figure 1 and Table 1) were considered to provide optimal heat utilization with moderate system complexity. In Figure 2 the distribution of the waste heat flows according to their temperatures and the option of their utilization to generate superheated working fluid for ORC are shown.
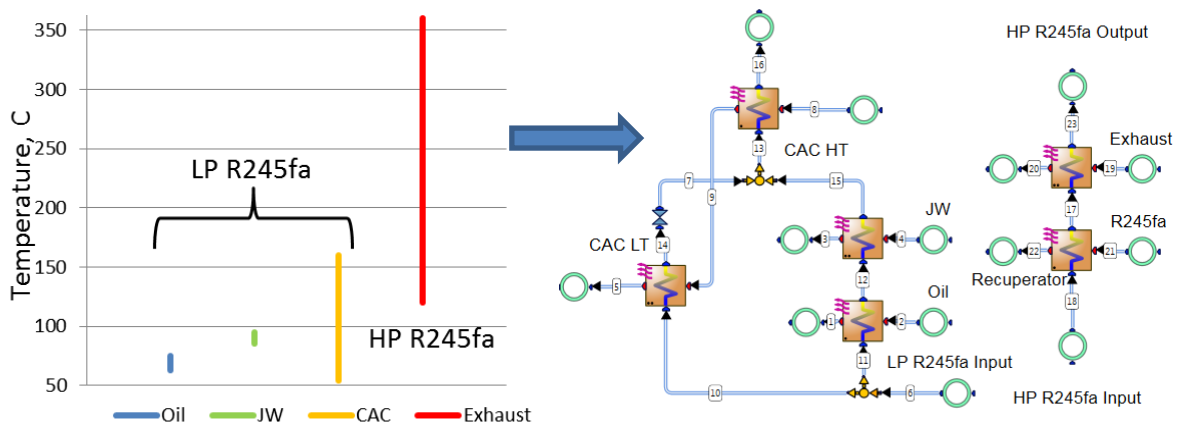
Figure 2: The distribution of heat flows according to their temperatures and the option of their utilization (where LP and HP – low pressure and high pressure; LT and HT – low temperature and high temperature; CAC – charge air cooler)

As is clear from Figure 2, the waste heat from the lubrication oil, the JW and the charge air has a lower temperature potential than the exhaust. It is then rational to use the heat from these sources to preheat the LP flow of R245fa to the necessary conditions. The heat exchangers which transfer heat from the oil and the JW to the low pressure flow of R245fa are connected in series according to their temperature ranges. The Charge Air Cooler (CAC) is divided into two temperature zones; The low temperature CAC (CAC LT heat exchanger in Figure 2) which operates in parallel with the JW and the oil coolers and the high temperature CAC (CAC HT) which is intended for the whole LP flow of R245fa superheat. The pressure of the LP R245fa loop was determined so that the temperature of the working fluid at high temperature CAC outlet is slightly higher than the saturation temperature at the given pressure. Due to the use of a dry working fluid the expansion process in the LPT will take place in the superheated region. In the designed ORC the low pressure loop operates under 7 bars of pressure.

The high pressure loop of the WHRS operates at a maximum pressure of 45 bars. The ORC working fluid is heated through two heat exchangers connected in series (internal recuperator and exhaust gas exchanger). The internal recuperator is used to return to the cycle the part of the heat rejected into condenser. The developed distribution of heat flows for this CAT engine allows utilizing the extra heat in the ORC cycle; almost all of the waste heat can be transferred to the WHRS, the CAC has minimum heat utilization (584.4 kW from the 647 kW available heat). Two alternative cycle concepts for this CAT engine were designed: with separate turbines and with a shared LPT. Both concepts were simulated with the use of the heat balance calculation tool AxCYCLE^{TM} (SoftInWay Inc. (2014)).

2.3.1 Dual loop SORC concept with separate turbines

The flow diagram of the dual loop SORC with the separate turbines is presented in Figure 3. The cycle consists of 6 heat exchangers, 2 turbines (HPT and LPT), 2 pumps (HPP and LPP) and the condenser. Both turbines operate with the same backpressure – 1.3 bars. The flows of R245fa are mixed at the condenser inlet and split at its outlet. The temperature – entropy diagram for the presented cycle is shown on Figure 4. The process 1-2-3-4-5-1 corresponds to the high pressure loop operation and the process 10-20-30-40-10 is for the low pressure loop operation.
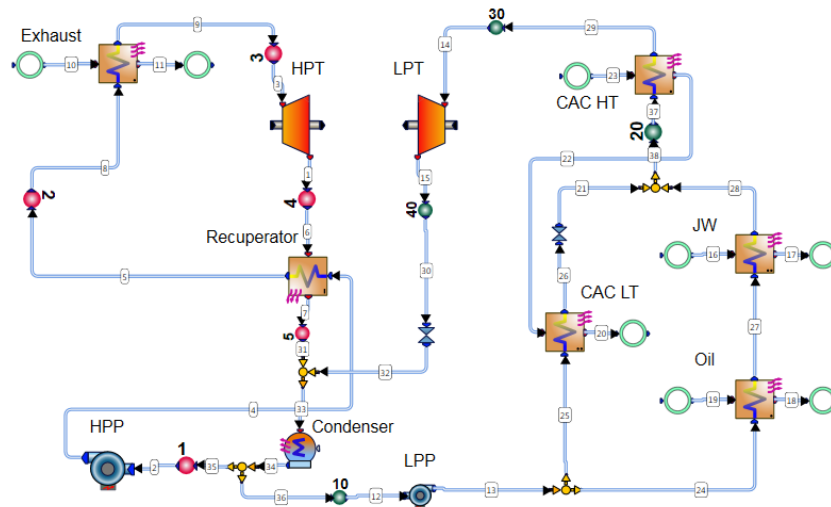
Figure 3: The flow diagram of the SORC with separate turbines
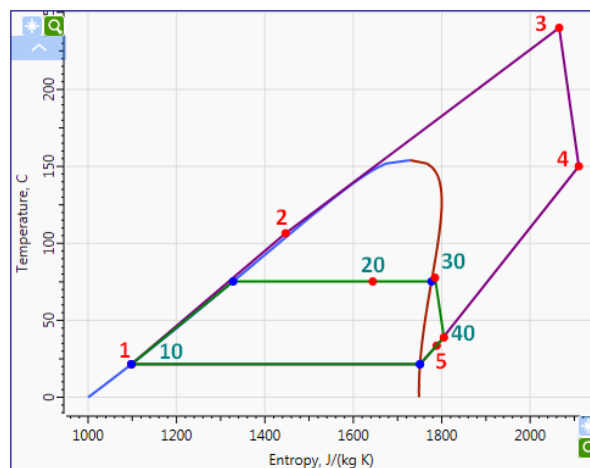
Figure 4: The t-s diagram for the SORC with separate turbines

2.3.2 Dual loop SORC concept with shared LPT

The flow diagram of the dual loop SORC with shared LPT is presented on Figure 5. The considered cycle has the same set of components as the previous one. Unlike in the previous cycle, here the working fluid expands in the HPT up to the pressure of the LP loop (7 bars). After that the flows from the different loops mix and expand in the shared LPT. This means that the mass flow through the LPT is equal to the sum of the HP and LP flows. Flows are again split at the condenser outlet.

The temperature – entropy diagram for the cycle with the shared LPT is shown on Figure 6. In the process 1-2-3 the heat is transferred to the high pressure R245fa flow (45 bars), the process 3-4 is the expansion in the HPT, the process 10-20-30 corresponds to the heat addition to the low pressure flow (7 bars), at point 5 the flows from the different loops mix, between 5 and 6 – the expansion in the LPT occurs and for 6-7 happens a heat transfer in the internal recuperator.
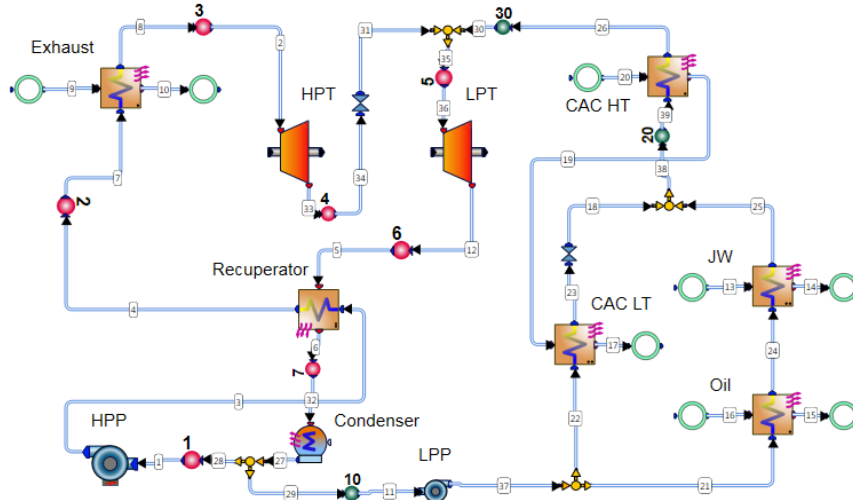
Figure 5: The flow diagram of the SORC with shared LPT
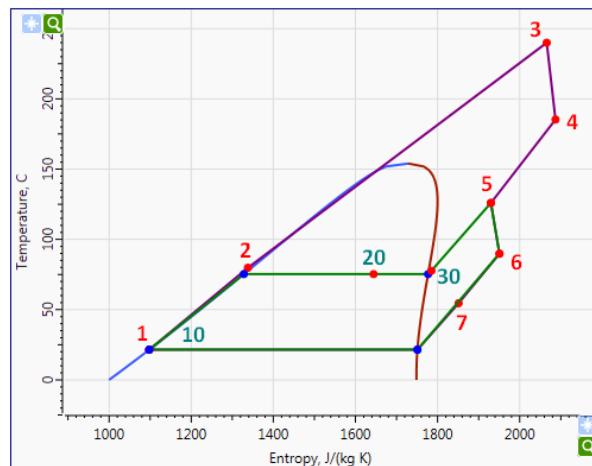
Figure 6: The t-s diagram for the SORC with shared LPT

2.3.3 Performance comparison
In order to quantify the estimation of the performances for the proposed embodiments of the SORC the comparison of their performances with the integral parameters of WHRS based on the double pressure water steam cycle was performed.
The bottoming steam cycle was designed according to materials from (MAN Diesel & Turbo (2012)) for the same CAT engine's conditions given in Table 1. The design parameters used for the steam cycle components are presented in Table 2. The maximum cycle temperature and pressure were limited to 258 °C and to 9 bars, respectively. The pressure at the HPT outlet was set to 3 bars and the condenser pressure was taken as 5.7 kPa. The steam cycle flow diagram and its process in the t – s coordinates are shown on Figure 7. As is evident from Figure 1Figure 7, the use of a steam WHRS allows covering only two sources of the engine's waste heat. This is connected to the thermodynamic properties of water. In this cycle a huge part of the heat is absorbed by the working fluid in the two-phase region under pretty high temperatures (175.35 °C at pressure of 9 bars and 133.52 °C at 3 bars respectively) and the heat of most of the low-temperature sources remains unclaimed. The use of heat from the low temperature sources as well as the steam mass flow is limited by the high temperature source (by the exhaust gas temperature and mass flow).

On the t-s diagram (see Figure 7) between 1 and 2 the total water flow is preheated. After this the flows splits, in the process 2-3-4 the heat is transferred to the high pressure loop and the process 2-8 corresponds to the heat addition to the low pressure flow. The processes 4-5 and 6-7 are for the expansion in the HPT and LPT, respectively.
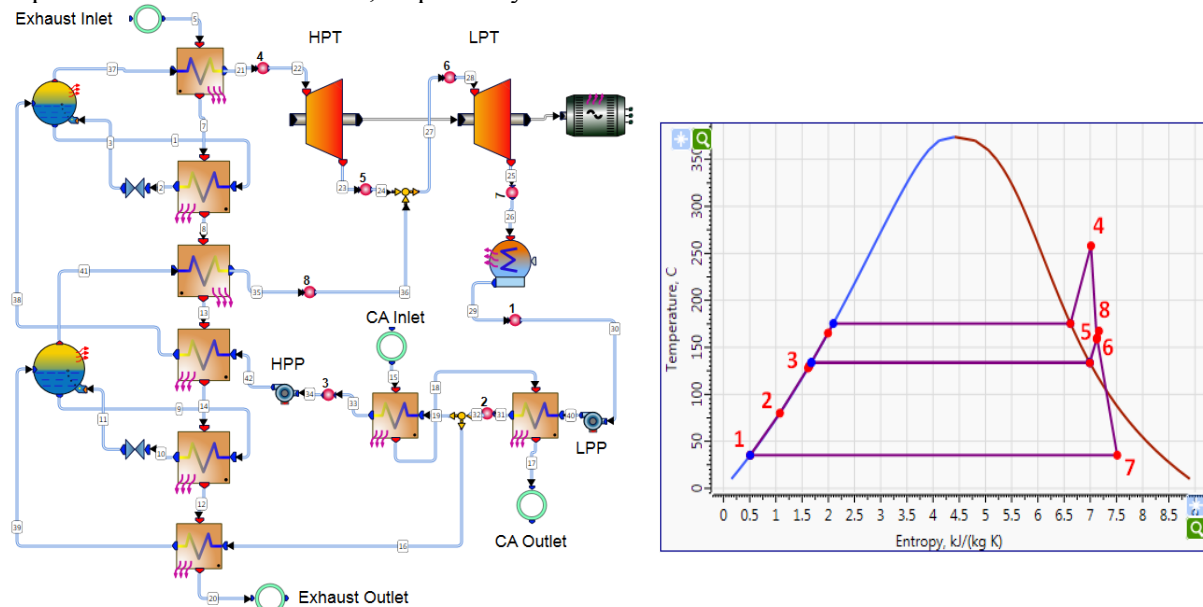
Figure 7: Flow diagram and process in t-s coordinates of the steam cycle

Table 3: The main thermodynamic parameters and the calculated performances of considered cycles

Parameter	Unit	Cycle Embodiments		
		R245fa with Separate Turbines	R245fa with Shared LPT	Steam Cycle
Total Mass Flow	kg/s	12.53	11.77	0.63
Pressure at HPT inlet	bar	45.0	45.0	9.0
Temperature at HPT inlet	°C	240.0	240.0	258.0
Pressure at HPT outlet	bar	1.3	7.0	3.0
Temperature at HPT outlet	°C	150.0	185.3	158.8
Pressure at LPT inlet	bar	7.0	7.0	3.0
Temperature at LPT inlet	°C	77.7	126.0	160.0
Pressure at LPT outlet (Condenser Pressure)	bar	1.3	1.3	0.057
Temperature at LPT outlet	°C	39.0	89.8	35.2
Saturation Temperature at Condenser Pressure	°C	21.5	21.5	35.2
Total Heat Transferred to Cycle	kW	3162.46	3162.46	1750.96
Net Power Production	kW	575.824	531.102	395.728
Power Boost for the CAT Engine	%	19.53	18.01	13.42
Total System Efficiency (ICE+WHRS)	%	49.01	48.38	46.50

The main thermodynamic parameters and the calculated performances of the aforementioned cycles are summarized in Table 3. It can be seen that the steam cycle has the lowest net power production of the three embodiments studied. This fact can be explained by the lowest total amount of waste heat transferred to the WHR cycle. At the same time this cycle has the largest thermal efficiency; it produces 395.728 kW from 1750.96 kW of transferred heat. However, for a WHRS cycle the Net Power Production (NPP) is more attractive since the waste heat is free.

The SORC with separate turbines has a higher NPP due to its higher internal heat recuperation. In that cycle the working fluid temperature at the recuperator inlet (HPT outlet) is 150 °C versus 90 °C in the cycle with the shared LPT. It allows increasing the working fluid mass flow at the HPT inlet (6.02 vs. 5.25 kg/s) which therefore leads to a rise in the mechanical power production. However, the operation of the turbine of the HP loop in the pressure range of the low pressure turbine (cycle concept with

separate turbines) is not a very rational solution. Despite the NPP, the cycle embodiment with the shared LPT is more preferable in the terms of HPT design, production costs and off-design operation. The results of the preliminary design of the HPT and LPT for the SORC with shared LPT are given below.

2.4 Preliminary Design of High Pressure and Low Pressure Turbines

In order to estimate performance and dimensions of these turbines, it was decided to perform a preliminary design for them using SoftInWay turbomachinery design/analysis tool AxSTREAM (Moroz et al. (2005) and (2006)). The boundary conditions for the turbines design are presented in Table 4.

Table 4: Boundary conditions

Parameter	Unit	HPT	LPT
Inlet total pressure	bar	45.00	7.000
Inlet total enthalpy	kJ/kg	621.87	515.63
Static pressure at outlet	bar	7.000	1.300
Mass flow rate	kg/s	5.249	11.77

Rough preliminary estimations showed that both turbines will be rather small in size. For example, the LPT turbine of axial type has 10 stages with a 1st stage nozzle height of about 2 cm and a constant hub diameter of 26 cm. The HPT turbine has up to 20 stages and even smaller blade heights and diameter. It is obvious that it is not reasonable to use axial turbines in these conditions. Taking into account the aforementioned preliminary results it was decided to select a radial turbine type for the further steps. Turbines evaluation was performed in two steps:

1. Turbine design utilizing simplified 1D axisymmetric calculation models by automatic generation of thousands of designs and selection of the best design.
2. Turbine analysis utilizing precise 2D axisymmetric models to get realistic turbine performance.

The Mitrohin-Stepanov loss model was utilized for impeller losses calculation.

Thousands of turbine designs were automatically generated using AxSTREAM's preliminary design tool. At this step an optimum rotational speed and diameter were selected. After this, 2D calculations were performed for both turbines to obtain their performance. A meridional view of the turbines with some performance data and density field are shown on Figure 8. It should be noted that the turbines picture on Figure 8 are presented using a different scale. Real dimensions can be seen on the vertical and horizontal rulers on the left and the bottom sides of the pictures, respectively. Three-dimensional views of the turbines are presented on Figure 9. Both turbines are of a non-nozzles design type (only impellers and volute). The required inlet angle on impeller blades is achieved by using a special volute design. All performance data and crucial dimensions are collected in Table 5.
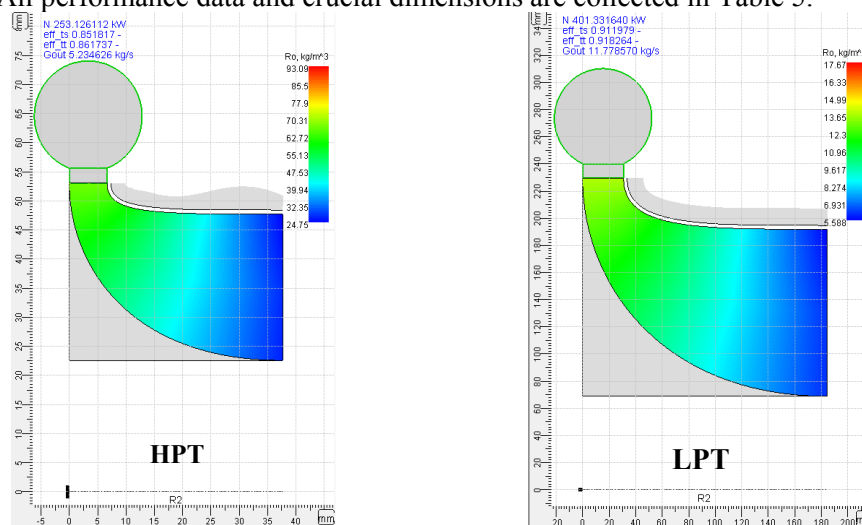
Figure 8: Turbines meridional view with density field
(where, eff_ts – turbine internal total-to-static efficiency, eff_tt – turbine internal total-to-total efficiency, N – turbine power, Gout – turbine mass flow rate, Roh – density)

The HPT is about 4 times smaller than the LPT but its shaft rotational speed is about 5 times higher than for the LPT. The HTP gives 211 kW of mechanical power while the LPT turbine provides about 395 kW. It should be noted that the obtained geometry and performance should not be considered as final. Final configurations might have slightly different performance and dimensions but the difference will not be significant.
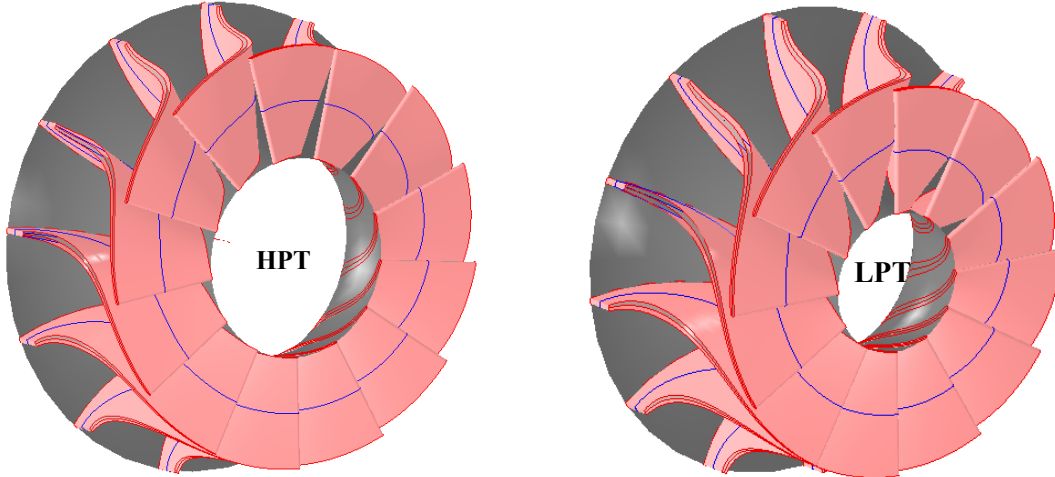

Figure 9: 3D view of the turbines

Table 5: Performance data and crucial dimensions of the turbines

Parameter	Unit	HPT	LPT
Internal total-to-static efficiency	%	85.18	91.33
Power	kW	211.4	394.6
Shaft rotational speed	rpm	40000	7914
Impeller diameter at inlet	mm	106.1	459.2
Mean impeller diameter at outlet	mm	70.3	260.6
Blade height at inlet	mm	6.7	30.9
Blade height at outlet	mm	25.1	122.8
Blade number		13	12

As is evident from Table 5, the obtained turbines efficiency values exceed the previously assumed values (see Table 2). The thermodynamic simulation of the SORC with shared LPT while accounting for the new turbines efficiencies gave 581.86 kW of net power production and 19.73% of power boost for the CAT Engine.

3. FUTURE WORK

The current paper represents a feasibility study and all the received results are not final. In the future, our works on the theme of WHR will be continued in the following directions: off-design WHRS simulation, control system design, estimation of cost and dimensions and more.

4. CONCLUSIONS

- The proposed concepts of dual loop Supercritical Organic Rankine Cycles are a promising technology for maximum waste heat utilization with moderate system complexity. The WHRS designed on the basis of the proposed concepts for powerful and super powerful ICPEs can be either adopted for electricity or mechanical power production.
- The simulation of the new WHRS in AxCYCLE showed that up to 19.73% of power boost for the G3612 CAT gas petroleum engine can be achieved without burning additional fuel which represents significant gains in terms of specific power.
- The comparison of performances between the traditional, high efficiency steam cycle and the SORC R245fa cycles confirmed a high potential for the designed cycles. Both proposed cycles embodiments have a higher net power production compared to the one for the steam cycle in net

power production due to the deep utilization of the low temperature waste heat sources that is not possible using steam.

- For one of the proposed ORC embodiments (the SORC with shared LPT) the evaluation of the turbines size and performance prediction was performed. The designed turbines have high efficiency levels with reasonable dimensions. The internal total-to-static efficiency of the HPT is equal to 85.18 % while it is 91.33% for the LPT. The maximum impeller diameters are equal to 106.1 and 459.2 mm, respectively. The strength characteristics and manufacturability of the designed turbines were not considered in the scope of the present study.

REFERENCES

Braimakis, K., Leontaritis, A.-D., Preißinger, M. , Karellas, S., Brüggeman, D., Panopoulos, K., 2014, Thermodynamic investigation of waste heat recovery with subcritical and supercritical low-temperature organic Rankine cycle based on natural refrigerants and their binary mixtures, *The 27th Int. Conf.of efficiency, cost, optimization, simulation and environmental impact of energy systems*.

Caterpillar, 2011, *Cooling system*.

DiCarlo J., Wallace J., 2011, Feasibility study of an organic Rankine cycle system coupled to a diesel engine, *ASME 2011 5th International Conference on Energy Sustainability*, ES2011-54579.

Guopeng Yu, Gequn Shu, Hua Tian, Haiqiao Wei, Lina Liu, 2013, Simulation and thermodynamic analysis of a bottoming Organic Rankine Cycle (ORC) of diesel engine (DE), *Int. J. Energy*, vol. 51, p. 281-290.

Honeywell, Revision Date 04/03/2014, *Genetron 245fa Safety Data Sheet*.

Jumel S., Feidt M., Kheir K., Long Le V., 2012,Working fluid selection and performance comparison of subcritical and supercritical Organic Rankine Cycle (ORC) for low-temperature waste heat recovery, *ECEEE Summer Study on Energy Efficiency in Industry*.

MAN Diesel & Turbo, 2012, Waste heat recovery system (WHRS) for reduction of fuel consumption, *Emission and EEDI*, no.5510-0136-01ppr.

Moroz L., Govoruschenko Y., Pagur P., 2006, A uniform approach to conceptual design of axial turbine / compressor flow path, *The Future of Gas Turbine Technology. 3rd International Conference*, Brussels, Belgium.

Moroz L., Govoruschenko Y., Pagur P., Axial turbine stages design: 1d/2d/3d simulation, experiment, optimization, *Proceedings of ASME Turbo Expo 2005*, Reno-Tahoe, Nevada, USA, GT2005-68614.

Maogang He, Xinxin Zhang, Ke Zeng, Ke Gao, 2011, A combined thermodynamic cycle used for waste heat recovery of internal combustion engine, *Int. J. Energy*, vol. 36, p. 6821-6829.

Nouman, J., 2012, Comparative studies and analyses of working fluids for Organic Rankine Cycles – ORC*, Master of Science Thesis EGI-2012-086MSC*.

Paanu, T., Niemi, S., Rantanen P., 2012, Waste heat recovery – bottoming cycle alternatives, ISSN 1238–7118, *Proc. of the University of VAASA*.

Petrov, M., 2006, Steam bottoming cycles for the W20V34SG gas engine, *KTH Energy Technology*.

Seher, D., Lengenfelder, T., Gerhardt, J., Eisenmenger, N., Hackner, M, Krinn, I., 2012, Waste heat recovery for commercial vehicles with a Rankine process, *21st Aachen Colloquium Automobile and engine technology*.

SoftInWay Inc, 2014, *AxCYCLE user documentation*.

ACKNOWLEDGEMENT

PERFORMANCE ANALYSES OF SUPERCRITICAL ORGANIC RANKINE CYCLES (ORCS) WITH LARGE VARIATIONS OF THE THERMOPHYSICAL PROPERTIES IN THE PSEUDOCRITICAL REGION

TIAN Ran[1], AN Qingsong[2] , SHI Lin[1,*] , ZHAI Huixing[1] and DAI Xiaoye[1]

[1]Key Laboratory for Thermal Science and Power Engineering of Ministry of Education, Department of Thermal Engineering, Tsinghua University,
Beijing, 100084, China
[2]Key Laboratory of Efficient Utilization of Low and Medium Grade Energy, MOE, School of Mechanical Engineering, Tianjin University, Tianjin 300072, China
e-mail: rnxsl@mail.tsinghua.edu.cn   and   tianr13@mails.tsinghua.edu.cn

ABSTRACT

Transcritical Organic Rankine cycles (ORCs) are more attractive than subcritical ORCs in terms of their lower exergy losses, higher thermal efficiencies and higher work outputs. This study analyzed the influence of the thermophysical properties variations in the pseudocritical region on the transcritical ORCs performance. For various turbine inlet temperatures and vapor generation pressures, the operating parameters were optimized simultaneously considering the net work output, the thermal efficiency and the total vapor generator area. The results show that the total vapor generator area varied with the turbine inlet temperature along an N-shaped curve. For any heat source temperature, the suitable working fluid should have a pronounced N-shaped curve of the total vapor generator area to guarantee the existence of the optimal parameter region in which all three indicators are optimized. This provides a working fluid selection criterion for heat sources of different temperatures. The analysis simplifies the selections of the operating parameters and the working fluids.

1. INTRODUCTION

Organic Rankine Cycles and their many applications for heat recovery from medium and low temperature heat sources have been widely investigated. Much research interest has been focused on transcritical ORCs because of their high thermal efficiencies, exergy efficiencies and work outputs (Schuster e*t al.*, 2010, Karellas and Schuster, 2008, Saleh *et al.*, 2007).
Many studies have considered the working fluid selection and parameter optimization of transcritical ORCs. Maraver *et al.* (2014) provided a general overview of the working fluid selection and optimal design of ORC for different heat sources. They concluded that supercritical cycles are justified for lower critical temperature working fluids if there is no high pressure limitation. However the author did not take into account the working fluid's heat transfer rates. Some researchers have used heat transfer models in heat exchanger area calculations to make economic analyses. Baik *et al.* (2011) compared the transcritical ORC performance of CO_2 and R125 systems using a discretized heat exchanger model to show that R125 has the higher net power output. Li *et al.* (2014) performed thermo-economic analyses with CO2, R123, R600a, R245fa and R601. Zhang *et al.* (2011) compared the performance of subcritical and transcritical power cycles using optimized cycle parameters. R125 in a transcritical power cycle gave excellent economics and maximized the heat source utilization. Guo *et al.* (2014) investigated the

performance of subcritical and transcritical ORCs based on the pinch point locations in the evaporators. Their results showed that transcritical ORCs have better performance when heat source outlet temperatures are lower.

Although much work has been done on optimizing the thermodynamics and economics of ORC cycles, there are few studies of the heat transfer characteristics or the influence of the thermophysical properties. The thermophysical properties in the supercritical pressure region undergo significant changes in the pseudocritical region (Pioro *et al.*, 2011) as shown in Figure 1. These changes affect the working fluid temperature profile and the pinch point location which greatly influence the operating parameter selection and add new requirements to the heat exchanger designs (Karellas *et al.*, 2012). Therefore, the thermophysical properties changes are the key issue for optimization and heat exchanger designs but there are few studies on this topic.

The aims of this study are to investigate the influence of the significant thermophysical property changes in the pseudocritical region on the ORC performance to provide guidance for system designs. First, the turbine inlet temperature, T_3, and the vapor generation pressure, P_{vap}, were optimized using the net work output W_{net} and the thermal efficiency as the indicators. Then, the variations of the vapor generator surface area, A_{total}, that are related to the changes in T_3 and P_{vap} were analyzed based on the thermophysical property changes. An optimal region was discovered by considering all three indicators, W_{net}, the thermal efficiency and A_{total}. A working fluid selection criterion was then developed based on an analysis of the N-shaped curve for A_{total} at various heat source temperatures.

2. SYSTEM MODELING

2.1 System Description

The basic ORC cycle includes a turbine, condenser, pump and vapor generator. As shown in Figure 2, the working fluid is pressurized to supercritical pressures in the pump and heated by the heat source from point 2 to point 3. In the turbine, the working fluid expands to low pressure to produce work. Finally, the lower pressure vapor is condensed to liquid in the condenser. The working fluid R134a was used as an example.
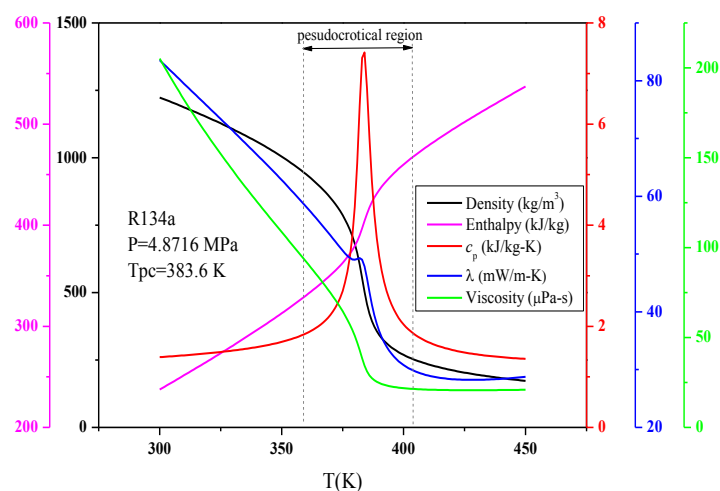
Figure 1: Thermophysical property variations in the pseudocritical region.
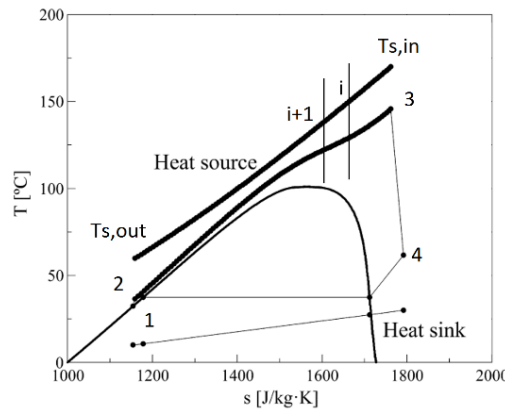
Figure 2: *T-s* diagram for a transcritical ORC system

2.2 Vapor Generator Model

The working fluid is heated in the vapor generator from liquid to vapor without phase change at supercritical pressures. Due to the significant changes in the thermophysical properties, the vapor generator was divided into n sections in a discretized model assuming equal enthalpy differences as shown in Figure 2. The vapor generator was divided into 100 sections, which has been shown to be reasonable in the literature (Karellas *et al.*, 2012). Section 1 was at the heat source inlet and the working fluid outlet with section 100 as the heat source outlet and the working fluid inlet.

The Nusselt number was calculated using the Jackson correlations (Jackson, 2002) for supercritical pressure fluids:

$$Nu = 0.0183\,\mathrm{Re_b}^{0.82}\,\mathrm{Pr_b}^{0.5}\left(\frac{\rho_w}{\rho_b}\right)^{0.3}\left(\frac{\overline{c_p}}{c_{pb}}\right)^{n} \tag{1}$$

Exponent n is:

$$n = 0.4, \qquad\qquad\qquad \text{for } T_b<T_w<T_{pc} \text{ and for } 1.2T_{pc}<T_b<T_w;$$

$$n = 0.4 + 0.2\left(\frac{T_w}{T_{pc}}-1\right), \qquad\qquad \text{for } T_b<T_{pc}<T_w;$$

$$n = 0.4 + 0.2\left(\frac{T_w}{T_{pc}}-1\right)\left[1-5\left(\frac{T_b}{T_{pc}}-1\right)\right], \text{ for } T_{pc}<T_b<1.2T_{pc} \text{ and } T_b<T_w$$

Where b refers to the bulk fluid temperature and w refers to the wall temperature and T_{pc} is the pseudocritical point temperature. The average specific heat of the working fluid was defined as:

$$\overline{c_P} = \frac{h_w - h_b}{T_w - T_b} \tag{2}$$

The convective heat transfer coefficient in the working fluid was:

$$\alpha_{ORC} = \frac{Nu\lambda}{d} \tag{3}$$

The mean overall heat transfer coefficient was:

3rd International Seminar on ORC Power Systems, October 12-14, 2015, Brussels, Belgium

$$\frac{1}{U} = \frac{1}{\alpha_{ORC}} + \frac{1}{\alpha_{HS}} + \frac{\delta}{\lambda} \tag{4}$$

α_{HS} was calculated using the Dittus Boelter correlation (Sharabi *et al.*, 2008):

$$Nu = 0.023 \, \mathrm{Pr}^n \, \mathrm{Re}^{0.8} \tag{5}$$

Where n=0.4 is for heating processes.

The model assumed no heat losses with the logarithmic mean temperature difference (LMTD) used in each element instead of a global temperature difference:

$$Q_{1-i} = \dot{m}_{ORC} \cdot (h_1 - h_i) = \dot{m}_{HS} \cdot c_{p,HS} \cdot (T_{HS,1} - T_{HS,i}) \tag{6}$$

The total vapor generator area, A_{total}, was:

$$A_{total} = \sum_{i=1}^{i=n} A_i \tag{7}$$

2.3 Global Model

There is no isothermal boiling in the transcritical ORC, so the pinch point location cannot be determined as easily as for the subcritical ORC. The temperature profiles in both the heat source fluid and the working fluid in the vapor generator were calculated using the vapor generator model for the model parameters listed in Table 1. The pinch point location was then determined by modifying the working fluid mass flow rate to get the designed pinch point temperature difference.

Table 1: Simulation parameters for ORC model

Part	Items	Values
Heat source	Inlet temperatures (°C)	160, 170, 180, 190
	Mass flow rate (kg/s)	1
	Pipe pressure (MPa)	1.3
ORC cycle	Pinch point temperature difference (°C)	10
	Condensing temperature (°C)	30
	Isentropic pump efficiency	0.65
	Isentropic turbine efficiency	0.85

3. RESULTS AND DISCUSSION

The calculation used R134a as the working fluid and a 170°C heat source for the parameter optimization (section 3.1) and vapor generator area analysis (section 3.2). R152a and R245fa were used for higher heat source temperatures in section 3.3.

3.1 Parameter optimization based on W_{net} and the thermal efficiency

W_{net} and the thermal efficiency were optimized by changing the turbine inlet temperature, T_3, and the vapor generation pressure P_{vap}. As shown in Figure 3(a), an optimal W_{net} exists at each P_{vap}. Further, the peak W_{net} move towards higher T_3 as P_{vap} increases. The maximum W_{net} was reached at $1.6P_c$ with only small differences in the maximum W_{net} for various P_{vap}. For example, the maximum W_{net} at $1.3 P_c$ is only 1.14% smaller than that at $1.6 P_c$. Therefore, lower vapor generation pressures should be used to reduce the component requirements and the initial cost with little difference in the work output.

As shown in Figure 3(b), the thermal efficiency increases with T_3 as has been seen in many studies. The thermal efficiency variations with P_{vap} depend on the turbine outlet conditions. For lower T_3 ($T_3 <$ 393.15K), the thermal efficiency decreases with P_{vap} while higher T_3 ($T_3 >$ 393.15K) have maximum thermal efficiency as P_{vap} varies.

Figure 4 shows the variations of W_{net} and the thermal efficiency in response to T_3 and P_{vap}. The shaded area in Figure 4(c) is the optimal region for both W_{net} and the thermal efficiency.

(a)　　　　　　　　　　　　　　　　　　(b)
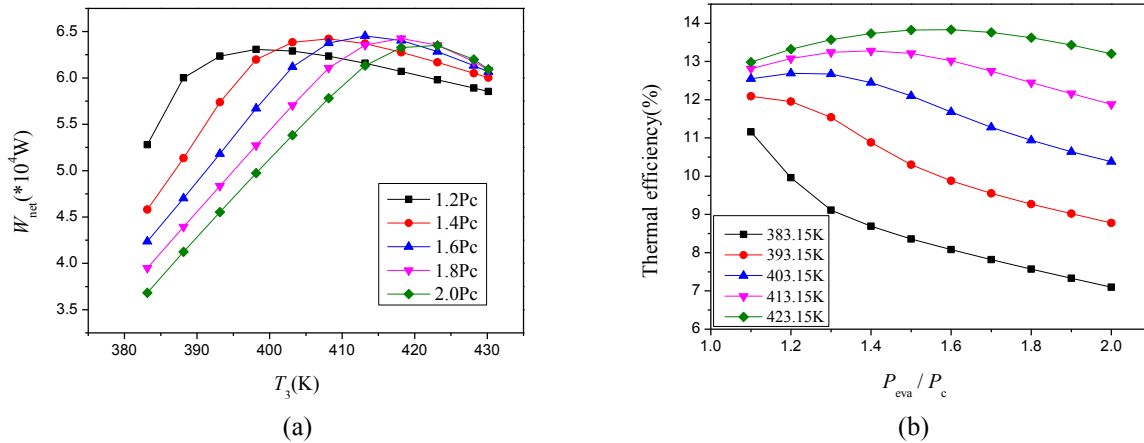
Figure 3: (a) Net work outputs for various turbine inlet temperatures and vapor generator pressures and (b) thermal efficiencies for various vapor generator pressures and turbine inlet temperatures (R134a, T_s=170°C)

(a)　　　　　　　　　　　(b)　　　　　　　　　　　(c)
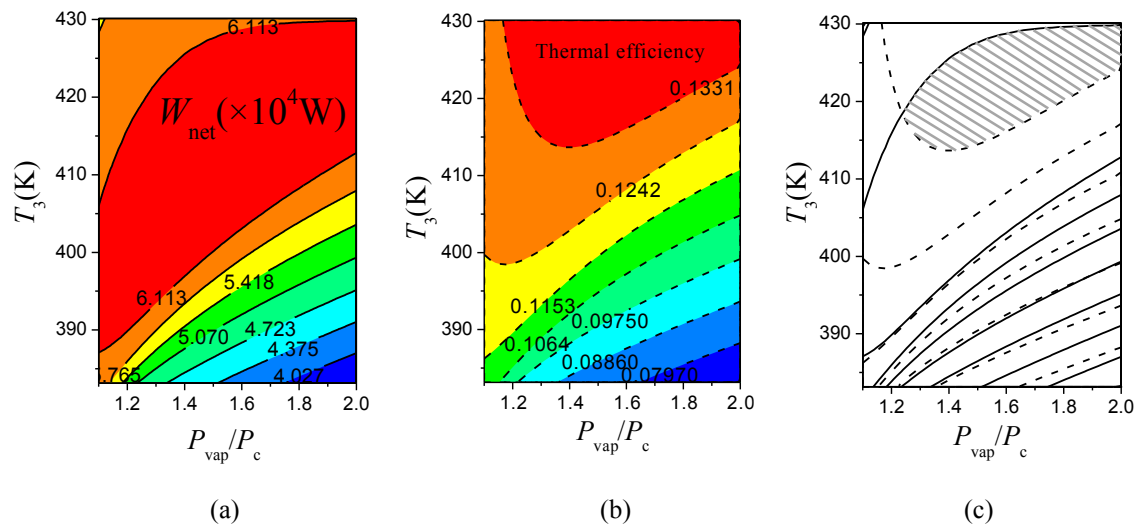
Figure 4: (a) W_{net} for various T_3 and P_{vap}, (b) thermal efficiency for various T_3 and P_{vap} and (c) the optimal operating conditions.

3.2 Vapor Generator Area Analysis

The vapor generator heat exchanger area is the third optimization indicator. The special characteristics of heat transfer at supercritical pressures need to be illustrated by showing the influence of the ORC parameters on the heat exchanger area. Figure 5 shows that the total vapor generator area varies with the turbine inlet temperature along an N-shaped curve.

The N-shaped curve is caused by the variations of the heat transfer coefficient and the LMTD in the pseudocritical region and the movement of the pinch point location. The heat transfer is strongly

affected by the significant changes in the thermophysical properties. As shown in Figure 6(a), the convection heat transfer coefficient of R134a has a peak at temperatures slightly lower than the pesudocritical point and then decreases sharply. The enthapy sharply increases in the pseudocritical region as shown in Figure 1, so the working fluid temperature gradient, dT/dn, is almost equal to zero, resulting in the temperature profile shown in Figure 6(b). This temperature profile means that the pinch point cannot move across the pseudocritical region. With increasing T_3, the pinch point moves from the heat source outlet towards the middle, staying at the lower temperature side of the pseudocritical region in the end as shown in Figure 7. The variation of LMTD shown in Figure 8(a) coincides with the temperature profile shown in Figure 6(b), which is the result of the enthalpy variation in the pseudocritical region. In each section of the vapor generator, the elementary area A_i is inversely proportional to the heat transfer coefficient and LMTD, so A_i varies as shown in Figure 8(b). A_{total} is the sum of A_i. Thus, the variations of the heat transfer coefficient and the LMTD in the pseudocritical region and the movement of the pinch point location result in the N-shaped curve for A_{total}.

| (a) | (b) |
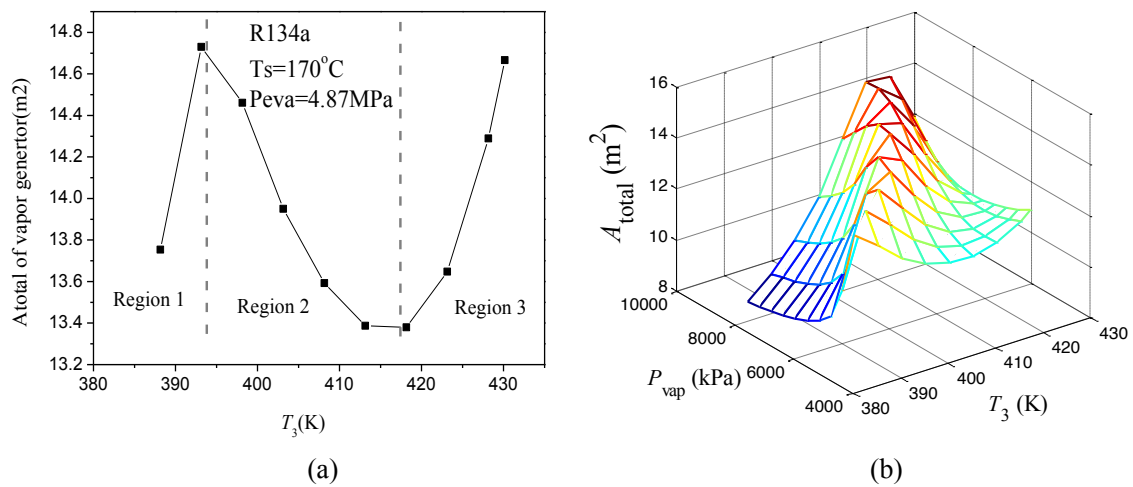
Figure 5: (a) Variation of the vapor generator area A_{total} with the turbine inlet temperature and (b) the variation of A_{total} with the vapor generation pressure and turbine inlet temperature.

A_{total} can be used as the third optimization indicator along with W_{net} and the thermal efficiency. The N-shaped curve in Figure 5(a) can be divided into three regions:

Region 1: T_3=388.15-393.15 K. The pinch point moves from the heat source outlet to the inlet with increasing T_3 as shown in Fig. 8. A_{total} increases with T_3 with the minimum at 388.15 K. However, the transcritical ORC has low W_{net} and thermal efficiency in this region. Therefore, the system should not operate in this region.

Region 2: T_3=393.15-418.15 K. The pinch point moves to the heat source inlet and A_{total} begins to decrease with T_3. In this region, both W_{net} and thermal efficiency are relatively high, so the system should operate in this region.

Region 3: T_3>418.15 K，A_{total} increases rapidly in this region due to the higher T_3 and the heat transfer coefficient in this region being much lower than in the other two regions so the heat exchanger area is wasted . For economic reasons, the system should not operate in this region.

The influence of pressure on A_{total} is shown in Figure 5(b). A higher vapor generation pressure results in a larger heat exchanger. Therefore, higher pressures are not economical. The final optimization results considering all three indicators, W_{net}, η_{th} and A_{total}, are shown in Figure 9(b) as the shaded area.
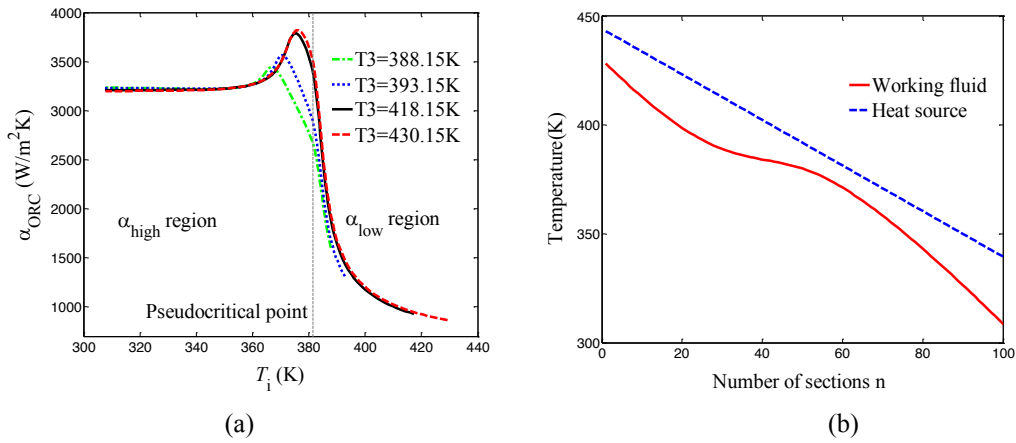
Figure 6: (a) Convection heat transfer coefficient of working fluid in the vapor generator for various turbine inlet temperatures and (b) working fluid and heat source temperature profiles in the vapor generator.
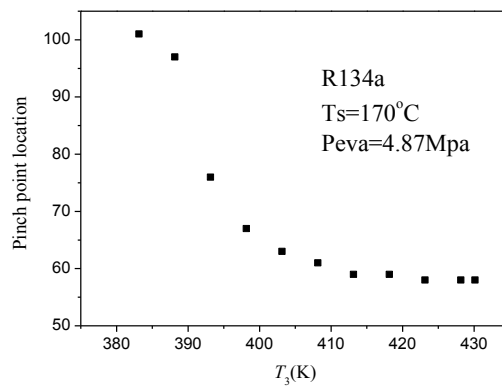

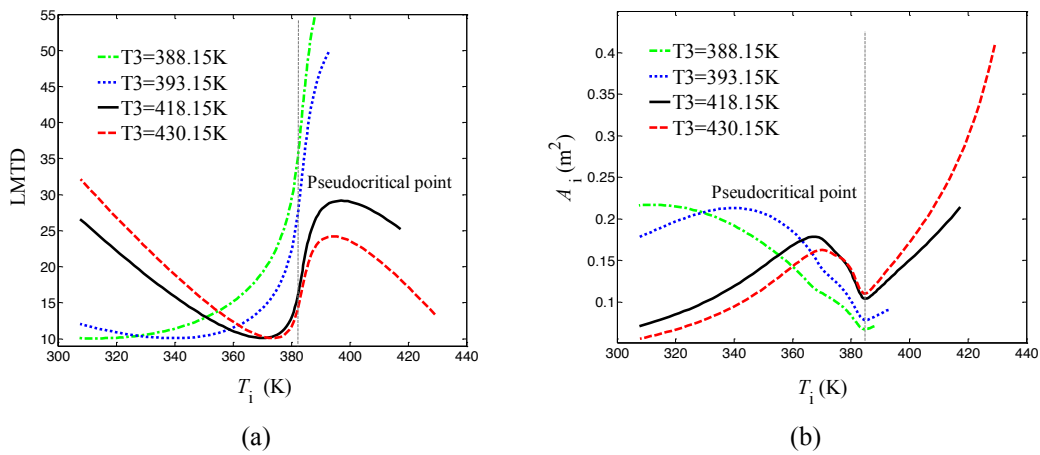**Figure 7:** Pinch point locations for various turbine inlet temperatures

Figure 8: (a) LMTD variations in the vapor generator for various turbine inlet temperatures and (b) the elementary surface area A_i variations in the vapor generator for various turbine inlet temperatures.

3.3 Working Fluid Selection Criterion at Various Heat Source Temperatures

The system performance was also investigated for various heat source temperatures. R134a was used in sections 3.1 and 3.2 with a 170°C heat source. Other heat source temperatures will require other working fluids so that the system has an optimal region as in Figure 9(b). As shown in Table 2, when

the heat source temperature increases from 160°C to 190°C, the higher temperature heat source gives a larger maximum W_{net}, but the corresponding optimal pressure increases from 6.09 MPa to 7.71 MPa. The higher pressure make the system more dangerous and difficult to maintain. As shown in Figure 10, the N-shaped curve of A_{total} for R134a is less pronounced with A_{total} in region 2 increasing significantly with the increasing heat source temperature. Moreover, the higher heat source temperature keeps the pinch point at the heat source outlet as shown in Figure 11. Since the system performance is worse when the pinch point is adjacent to the heat source outlet, the higher heat source temperature will lead to poor performance and there is no optimal shaded area as in Figure 9(b).

In conclusion, when the heat source temperature is much higher than T_c of the working fluid, the optimal area does not exist. While R134a performs well with a 170°C heat source, R134a is not suitable for higher temperature heat sources of 180-190°C. The results in Table 2 show that $W_{net,max}$ and the thermal efficiency of R152a, R245fa, whose T_c are higher than that of R134a, are both higher than that of R134a. The optimal pressures are also much lower than that of R134a for the same heat source temperature. Figures 10 and 11 show that the A_{total} in region 2 using R152a and R245fa are much lower than that of R134a and the pinch point quickly moves to the lower temperature side of the pseudocritical region. The performance is greatly improved by using R152a and R245fa with the 190°C heat source. Thus, if the N-shaped curve for A_{total} is less pronounced or disappears and the pinch point is always stay near heat source outlet, then the current working fluid cannot match the heat source and working fluids with higher critical temperatures are suggested.
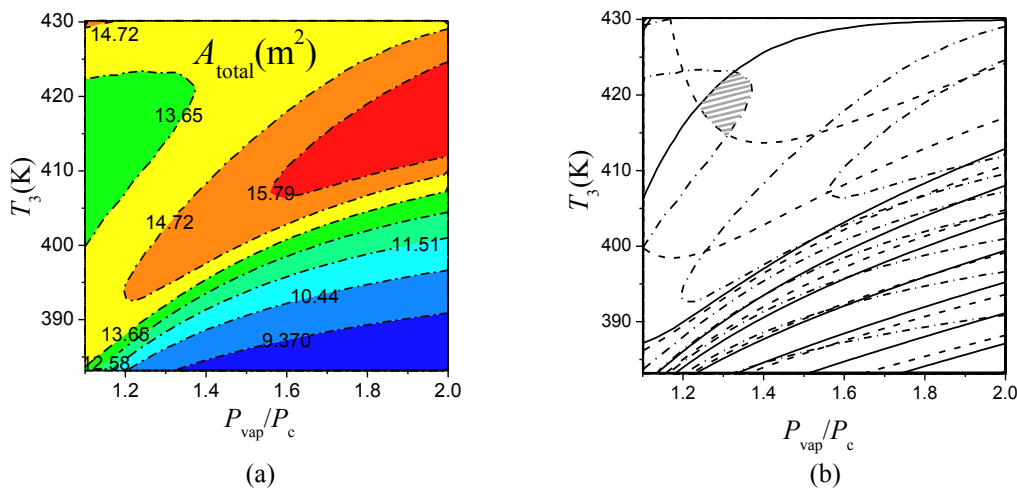

Figure 9: (a) A_{total} variations with T_3 and P_{vap} and (b) the optimal operating region

Table 2: Optimal operating parameters with W_{net} as the optimization objective

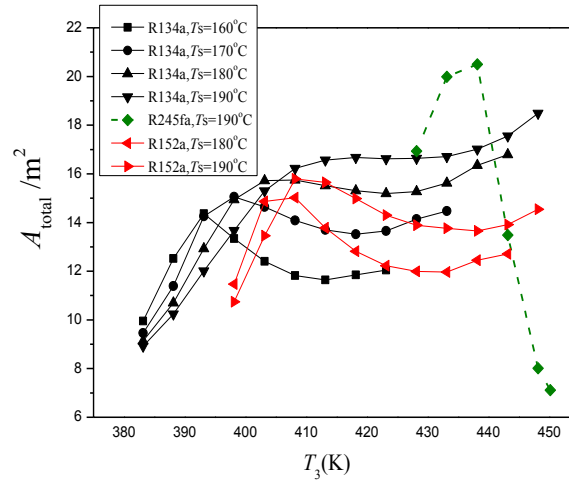|	T_c (°C)	P_c (MPa)	T_s (°C)	$W_{net,max}$ (kW)	P_{vap} (MPa)	η_{th} (%)
R134a	101.06	4.0593	160	55.4	6.089	12.10
			170	64.5	6.495	13.02
			180	73.9	6.901	13.76
			190	83.4	7.713	14.29
R152a	113.26	4.5168	180	73.5	6.324	13.85
			190	83.6	6.775	14.70
R245fa	154.01	3.651	190	90.4	4.746	15.22

Figure 10: A_{total} variations with the turbine inlet temperature for various heat source temperatures
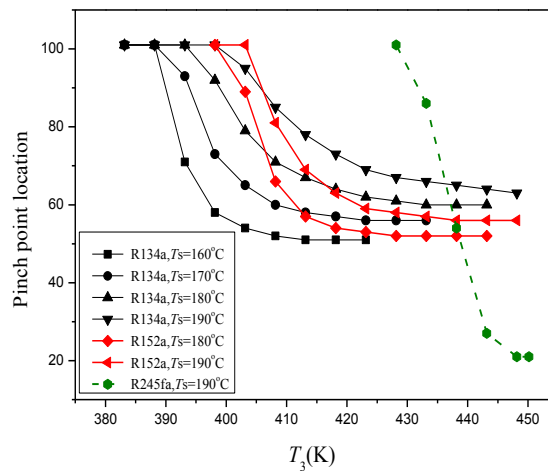

Figure 11: Pinch point location variations with the turbine inlet temperature

4. CONCLUSION

The influence of the large changes in the thermophysical properties in the pseudocritical region was investigated. An optimization method was developed using the net work output, the thermal efficiency and the total vapor generator area. The optimal turbine inlet temperature and vapor generation pressure were found for various operating conditions. The results obtained in this study will simplify working fluid selection for various heat source temperatures. The main conclusions can be summarized as:

1. The thermophysical properties of the working fluid in transcritical ORCs operating at supercritical pressure undergo significant changes, resulting in considerable variations in the heat transfer coefficient and LMTD. Therefore, studies of transcritical ORCs should pay much more attention to the thermophysical property changes in the pseudocritical region. The heat transfer mechanisms at supercritical pressure must be further understood for system optimization and proper heat exchanger design.

2. The total vapor generator area, A_{total}, varies with the turbine inlet temperature T_3 along an N-shaped curve due to the variations of heat transfer coefficient and LMTD in the pesudocirtical region and the changes of the pinch point location. The optimal operating conditions should be in region 2 of

the N-shaped curve to give the best area with the best W_{net} and thermal efficiency.

3. A working fluid selection criterion was developed for various heat source temperatures. A suitable working fluid should have a pronounced N-shaped curve for A_{total} to guarantee the existence of the optimal parameter region. When the N-shaped curve for A_{total} is less pronounced or non-existent and the pinch point is always near the heat source outlet, the working fluid cannot match the heat sources, and working fluids with higher critical temperatures are suggested.

REFERENCES

Baik, Y. J., Kim, M., Chang, K. C., & Kim, S. J. (2011). Power-based performance comparison between carbon dioxide and R125 transcritical cycles for a low-grade heat source. *Applied Energy*, *88*(3), 892-898.

Guo, C., Du, X., Yang, L., & Yang, Y. (2014). Performance analysis of organic Rankine cycle based on location of heat transfer pinch point in evaporator. *Applied Thermal Engineering*, *62*(1), 176-186.

Jackson JD. Consideration of the heat transfer properties of supercritical pressure water in connection with the cooling of advanced nuclear reactors, Proc. 13th Pacific Basin Nuclear Conference, Shenzhen City, China, October 21 – 25, 2002

Karellas, S., & Schuster, A. (2008). Supercritical fluid parameters in organic Rankine cycle applications. *International Journal of Thermodynamics*, *11*(3), 101-108.

Karellas, S., Schuster, A., &Leontaritis, A. D. (2012). Influence of supercritical ORC parameters on plate heat exchanger design. *Applied Thermal Engineering*, *33*, 70-76.

Li, M., Wang, J., Li, S., Wang, X., He, W., & Dai, Y. (2014). Thermo-economic analysis and comparison of a CO 2 transcritical power cycle and an organic Rankine cycle. *Geothermics*, *50*, 101-111.

Maraver, D., Royo, J., Lemort, V., &Quoilin, S. (2014). Systematic optimization of subcritical and transcritical organic Rankine cycles (ORCs) constrained by technical parameters in multiple applications. *Applied energy*,*117*, 11-29.

Pioro, I., Mokry, S., & Draper, S. (2011). Specifics of thermophysical properties and forced-convective heat transfer at critical and supercritical pressures. *Reviews in Chemical Engineering*, *27*(3-4), 191-214.

Saleh, B., Koglbauer, G., Wendland, M., & Fischer, J. (2007). Working fluids for low-temperature organic Rankine cycles. *Energy*, *32*(7), 1210-1221.

Schuster A, Karellas S, Aumann R. (2010) Efficiency optimization potential in supercritical Organic Rankine Cycles[J]. Energy, 35(2): 1033-1039.

Sharabi M., W. Ambrosini, S. He, J.D. Jackson, (2008) Prediction of turbulent convective heat transfer to a fluid at supercritical pressure in square and triangular channels, Annals of Nuclear Energy 35 993e1005

Zhang, SJ, Wang, HX, & Tao, G. (2011). Performance comparison and parametric optimization of subcritical Organic Rankine Cycle (ORC) and transcritical power cycle system for low-temperature geothermal power generation. *Applied Energy*, *88*(8), 2740-2754.

ACKNOWLEGEMENTS

3rd International Seminar on ORC Power Systems, October 12-14, 2015, Brussels, Belgium

INVESTIGATION AND EFFICIENCY MAXIMIZATION OF THE OPERATION AND DESIGN OF A SMALL SCALE EXPERIMENTAL TRIGENERATION SYSTEM POWERED BY A SUPERCRITICAL ORC

Tryfon Roumpedakis*, Konstantinos Braimakis[†], Sotirios Karellas[†]

*National Technical University of Athens,
Heroon Polytechniou 9, 15780 Zografou
Greece
e-mail: roumpedakis_t@hotmail.com

ABSTRACT

In this work, the detailed investigation and the optimization of the operational parameters of an experimental, small scale trigeneration system encompassing a supercritical Organic Rankine Cycle (ORC) and a heat pump are presented. Both the ORC and the heat pump jointly operate with the same working fluid (R227ea). The heat input to the ORC is provided by a 85 kW_{th} biomass boiler. The electricity produced by the ORC, which has a nominal power output of 5 kW_e, is used to power the heat pump, capable of covering a cooling load of 4 kW_{th}, while any surplus electricity is exported to the grid. Meanwhile, the heat generated during the condensation of the working fluid (around 70 kW_{th}) is utilized to produce hot water. The system has therefore the potential to produce combined cooling, heating and electricity, depending on the load requirements, by utilizing a renewable energy source with zero net CO_2 emissions.

The investigation carried out includes the selection process of the working fluid of the system through the comparison of its performance with that of other typical working fluids and by taking into account environmental and safety factors. Furthermore the study presents the optimization procedure for selecting the working temperatures and pressures in order to maximize the cycle's efficiency, given the technological limits of the elements of this system (heat exchangers, scroll expanders etc.). In addition, a supercritical plate heat exchanger model, used for the design of the heat exchanger of the unit, is presented.

1. INTRODUCTION

In the recent years, a significant amount of interest has been focused on multigeneration systems aiming to convert a primary energy source (fossil, solar, waste heat) into combined electricity, cooling and heating. This is in part driven by the fact that traditional electricity generation systems have a restricted efficiency (around 30-40 % [1], [2]), so a great deal of the original heat is rejected to the environment unexploited in the form of waste heat. Due to the policies followed worldwide in order to increase overall system efficiencies and restrain the emissions of greenhouse gas (GHGs), a lot of research focuses on the design of cost competitive co-generation and combined cooling, heating and power systems is carried out. Furthermore, small scale cogeneration and trigeneration systems that use renewable energy sources have gathered significant attention, since they can potentially contribute to a further reduction of emissions, while also ensuring sustainability and fuel independence.

The Organic Rankine Cycle (ORC) has lately gathered substantial interest as a promising technology in the field of power generation from low temperature heat sources, such as solar and geothermal energy and industrial waste heat. The traditional water-steam Rankine cycle, implemented in the conventional high-temperature thermal power plants, is in many cases not economic or technically feasible. This is because its implementation is not favorable for low grade applications and small-scale power outputs [3], such as those encountered in solar thermal plants. The Organic Rankine

Cycle (ORC), on the other hand, poses certain advantages compared to the conventional cycle. Some of these include the potential of low temperature heat recovery due to the lower boiling point of the working fluids used, the overall smaller component size as well as the capability of expander operation under smaller temperatures [4]. Moreover, due to the "dry" organic fluids having a positive dT/dS saturation vapor line, it is not in principle necessary to superheat them [5]. Meanwhile, the supercritical ORC (SORC), in which the working fluid is pressurized to supercritical pressures before its entrance to the heater has been shown to exhibit several advantages, such as improved thermal and also exergetic efficiency [6-8]. The most important characteristic of supercritical ORCs is the fact that, because of the supercritical heating pressures, the working fluid does not gradually evaporate into the gaseous phase. Instead, it changes from the liquid to the supercritical state when its temperature increases above its critical value. Despite, the fact that, compared to a subcritical, the supercritical ORC results in higher operating pressures in the cycle, it is worthy evaluating its competiveness for small scale systems in a practical way.
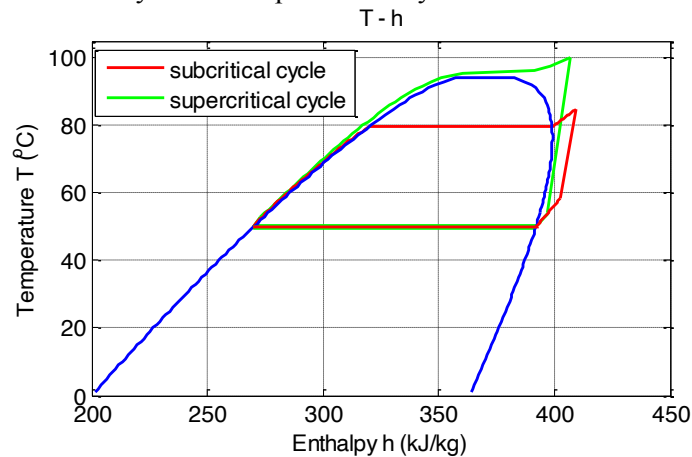
Figure 1: Sub- and supercritical ORC. Example of R1234yf

In this study an experimental trigeneration unit currently under construction in the Laboratory of Steam Boilers and Thermal Plants (LSBTP) in the National Technical University of Athens (NTUA), Greece, is introduced. The system consists of a supercritical Organic Rankine Cycle (SORC) interconnected with a Vapor Compression Cycle (VCC). Heat is provided to the system by a biomass boiler. The two systems are capable of combined electricity, cooling and heating generation, as can be seen in the simplified process diagram of Figure 2. In the present work, the preliminary design and decision process regarding the working fluid selection, the adjustment of some key thermodynamic operational parameters and the selection of equipment is presented and justified.
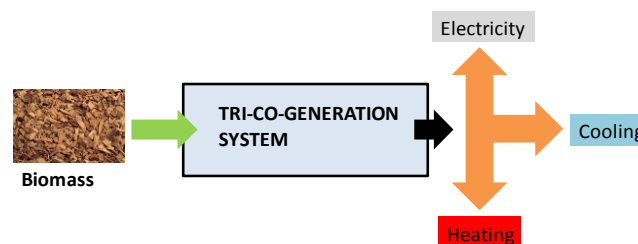

Figure 2: Simple process diagram of the ORC-VCC system under construction

2. SYSTEM DESCRIPTION

2.1 SORC and VCC modules

The system under design and construction consists of three main subsystems, the SORC module, the VCC module and the biomass boiler-heating oil module. The SORC is interconnected to the VCC and both cycles use the same working fluid. The SORC includes a pump and a series of heat exchangers, where energy is transferred from the heat sources to the working fluid. After reaching its maximum temperature the working fluid flows through the expander, producing useful work, which is used to cover the power needs of the system, while any surplus is exported to the grid

The supercritical fluid exiting the expander of the SORC is mixed with the stream exiting the compressor of the VCC and the mixture both enter the condenser of the system. In this way, the condensation step of both cycles takes place in a single condenser under a common pressure, providing the heat output of the system which is used for producing hot water. Apart from the compressor, the VCC is comprised of an expansion valve and an evaporator, where it absorbs heat, thus generating the cooling output of the system.

The power required for the compression of the cooling cycle is provided by the generator of the SORC, while any surplus power can be exported to the electricity grid.

During the winter, when there is no demand for cooling, the VCC can be disconnected from the rest of the system, giving an increased potential for electricity generation. In this manner, the operation mode can alternate between trigeneration and cogeneration. On trigeneration mode, it is necessary that the power produced by the ORC is adequate for the operation of the compressor in order for the system to be independent from external power sources. It must be mentioned, that this system is to operate at steady state conditions, besides the inevitable fluctuations of the biomass boiler.

2.2 Biomass boiler-heating oil circuit

The heat input to the SORC originates from the combustion of biomass in a boiler. The combustion heat is provided to a heating oil which then flows through an intermediate heat transfer loop (HTL) in order to deliver its energy content to the working fluid in the heater of the SORC. The heating oil then returns to the biomass boiler to increase its temperature.

3. MATHEMATICAL MODELING AND SIMULATION

3.1 Mathematical formulation

The first step of the design of the experimental unit is its thermodynamic modeling, which will subsequently allow to select the optimal values of some of its key operational parameters. The simulation of the system is carried out by numerically solving a set of mathematical equations that describe the operation of its components. For the simulation of the system, a steady state operation is assumed, while heat and pressure losses along the equipment are neglected. The equilibrium thermodynamic properties of the working fluid in each state are calculated with the CoolProp database [9] incorporated in the Matlab Software [10]. The most important system performance evaluation indexes used for the design of the facility are the thermal efficiency of the SCORC $\eta_{th,ORC}$, the electrical efficiency of the ORC $\eta_{el,ORC}$, the Coefficient of Performance (COP) of the VCC, the heat production efficiency of the system $\eta_{heat,sys}$ as well as its overall cogeneration efficiency $\eta_{CHP,sys}$. These are described by the following equations:

$$\eta_{th,ORC} = \frac{P_{turb} - P_{pump}}{Q_{ORC,in}} \tag{1}$$

$$\eta_{el,ORC} = \frac{P_{el,net}}{Q_{ORC,in}} \tag{2}$$

$$COP = \frac{Q_{cool}}{P_{el,comp}} \tag{3}$$

$$\eta_{heat,sys} = \frac{Q_{cond}}{Q_{ORC,in}} \tag{4}$$

$$\eta_{CHP,sys} = \frac{Q_{cond} + P_{el,net}}{Q_{ORC,in}} \tag{5}$$

In the above equations, P_{turb} is the work derived in the turbines, P_{pump} is the work consumed in the pump, $P_{el,net}$ is the net electric output of the SORC expander, Q_{cool} is the cooling duty of the VCC, $P_{el,comp}$ is the electricity consumed by the VCC compressor, Q_{heat} is the heat generated in the condenser of the system and $Q_{ORC,in}$ is the heat provided to the working fluid in the heater of the SORC.

3.2 Assumptions

Further assumptions made regarding the operation and the technical specifications of the basic components of the system are summarized in Table 1. The upper pressure level of the SORC was determined by considering the capability to use an open-drive scroll expander, which is commonly proposed for small scale applications such as the one investigated in the current study. The preference towards this type of expander instead of an expander of the hermetic type is justified by its lower cost. Moreover, high pressures (beyond 40 bar) inhibit the use of plate heat exchangers, which are relatively cheap and provide a very attractive heat transfer area-to-volume ratio. The maximum temperature limit of the working fluid of the SORC is imposed by the maximum temperature of the heating oil and the pinch point value of the heater that are assumed to be equal to 120 °C and 10 K respectively. Moreover, it is known that the thermal efficiency of ORCs increases as the condensation temperature decreases. The impact of the condensation temperature on the COP of the VCC is similar. However, it is not possible to decrease this temperature below a certain limit. On one hand, the condensation temperature cannot be lower than the temperature of the cooling water. On the other hand, since the system is intended to produce useful heat, the temperature of the water at the condenser outlet must be at least equal to 50 °C.

Table 1: Heating system and SORC assumptions

Biomass boiler-Heat Transfer Loop	
Boiler efficiency	82.9 %
Biomass Low Heating Value	16920 kJ/kg
Heat duty	85 kW$_{th}$
Heating oil	BP Transcal N
Heating oil maximum temperature	120 ºC
Heating oil temperature difference in boiler	15 K
SORC module	
Pinch point heater	10 K
Pinch point condenser	5 K
Maximum pressure of working fluid	40 bar
Maximum temperature of working fluid	110 °C
Isentropic efficiency of pump	50 %
Isentropic efficiency of expander	65 %
Electromechanical efficiency	85 %
Cooling water temperature at the condenser inlet	
Summer	30 °C
Winter	20 °C
Minimum cooling water temperature at the condenser outlet	40 °C
VCC module	
Pinch point evaporator	5 K
Nominal cooling load	4 kW$_{th}$
Evaporation temperature	10 °C
Condensation temperature	50 °C
Isentropic efficiency of compressor	75 %

4. WORKING FLUID SELECTION AND THERMAL EFFICIENCY MAXIMIZATION

The selection of the most appropriate working fluid is the first goal of the thermodynamic optimization. In the design process of the experimental unit, the screening method, which is commonly used in the literature, was followed. The two primary criteria used for selecting working fluid candidates are the critical temperature and pressure. Given the operational range of the temperatures and pressures of the system, as given in Table 1, a short list of 11 working fluids was created. These fluids are given in Table 2.

A second group of fluids were chosen from the working fluids of Table 2, by taking into account their Ozone Depletion Potential (ODP), their Global Warming Potential (GWP) as well as their ASHRAE safety group categorization. More specifically, R123 has a high ODP and is to be substituted by HFE7000 by 2030, R1234yf, R143a, R41, Propylene and n-Propane were rejected because of their high inflammability, R134a because of its high critical pressure and R161 because of its very limited market availability. Thus a final list of three working fluids, R125, R227ea and R404a, is assembled (in bold format in Table 2). The optimal working fluid is ultimately chosen by performing a thermodynamic investigation of their performance. The purpose of the optimization process is to determine which fluid exhibits the highest thermal SORC efficiency, when varying certain independent operation variables within the acceptable ranges specified in Table 1. The independent variables are the maximum pressure and temperature of the SORC and the condensation temperature. The evaporation temperature of the VCC is set at 7.5 °C, while a cooling load of 0 (cogeneration mode) and 3 kW (trigeneration mode) is assumed. The results of the optimization process for the three final working fluids are summarized in Table 3.

Table 2 : Preliminary selection of working fluid candidates (P_{crit}<40bar, T_{crit}<110°C)

Working fluid	Critical temperature °C [11]	Critical pressure (bar) [11]	ODP [12]	GWP [12]	ASHRAE safety group [13]
R125	**66.02**	**36.18**	**0**	**3500**	**A1**
R134a	101.06	40.59	0	1430	A1
R143a	72.71	37.61	0	4470	A2L
R1234yf	94.70	33.82	0	4	A2L
R227ea	**101.75**	**29.25**	**0**	**3220**	**A1**
Propylene	92.42	46.65	0	1.8	A3
R41	44.13	58.97	0	92	---
N-Propane	96.70	42.48	0	3.3	A3
R161	102.22	47.02	0	12	--
R410a	72.80	48.60	0	2088	A1
R404a	**72.07**	**37.32**	**0**	**3300**	**A1**

As can be seen from Table 3, R227a exhibits both the highest SORC efficiency and the highest COP among the fluids examined. For this reason, it is selected for the experimental unit. It deserves to be noted that, despite it being commonly investigated as a working fluid for ORC applications in the literature [3, 14, 15], R227ea has not been very often used in actual ORC plants or experimental rigs. Moreover, it is rarely used in commercial refrigeration applications. Its market availability is relatively scarce and its cost significantly high, since its price is about eight times the price of R134a.

Table 3 Optimization results of the SORC thermal efficiency for the three final working fluids

	R125	R404a	R227ea
P_{max} (bar)	40	40	30.4
T_{max} (°C)	110	110	110
T_{cond} (°C)	50	50	50
T_{cool} (°C)	10	10	10
$\eta_{th,orc}$	2.16	2.81	4.92
$\eta_{el,net}$ (Q_c=0)	0.71	1.17	2.72
$\eta_{el,net}$ (Q_c=1)	0.23	0.73	2.30
COP	3.24	3.57	3.78

It can be thus considered as a "novel" working fluid. Based on the optimization results, the operational data of the system are summarized in Table 4.
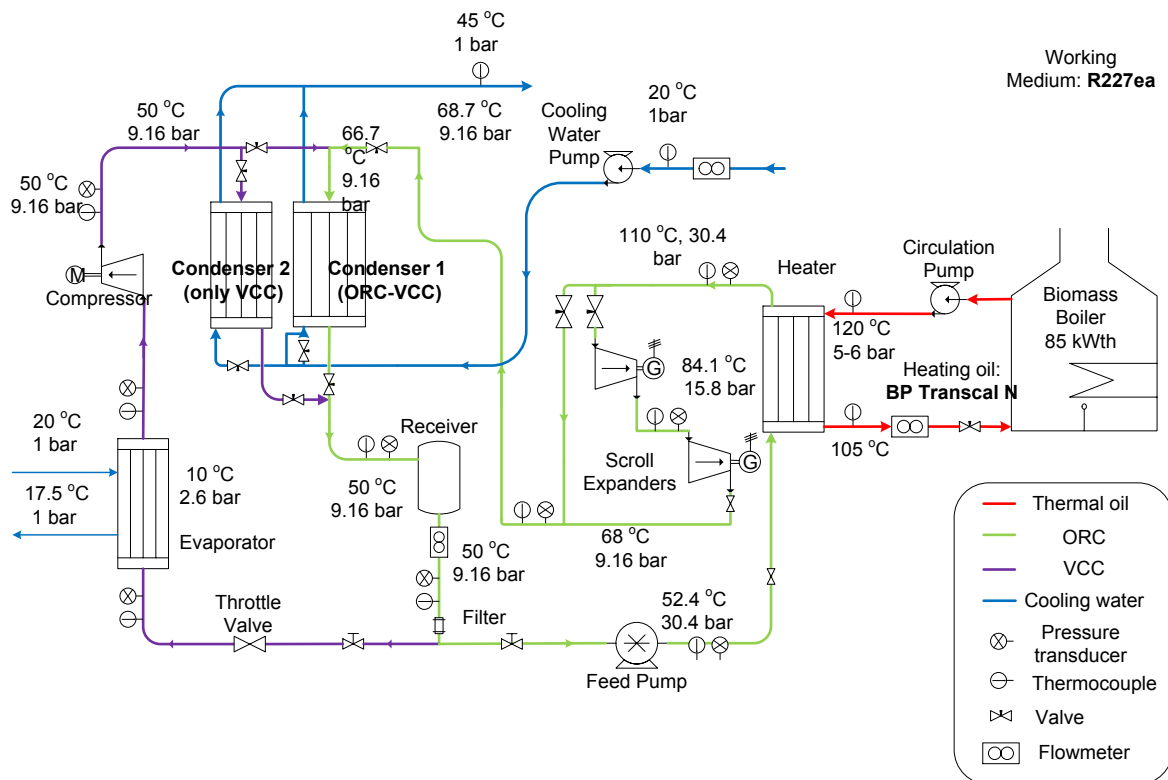
Figure 3: Process flow diagram of the experimental trigeneration facility

5. EQUIPMENT SELECTION

5.1 Overview

A process flow diagram of the experimental unit to be constructed along with operational data and design pressures and temperatures is presented in **Error! Reference source not found.**. The right part of the figure depicts the heating oil circuit along with the biomass boiler (red color) and the left part depicts the VCC (purple color). The SORC is in between these two circuits (green color). Two streams of water (blue color) are used for the cooling and the heating of the working fluid in the Condensers 1 and 2 as well as in the evaporator of the VCC respectively.

As can be seen, it was decided that two identical scroll expanders serially positioned will be used for the expansion process of the working fluid. Each one of these expanders is directly coupled to a generator. This is because of the limited volume flow ratio that is technically possible for these volumetric expanders. According to the literature [16], its value must not be higher than 5. Following a more conservative approach, the volume flow ratio for the expanders of the experimental rig is set between 2 and 3. During the start-up of the operation of the system, the working fluid does not flow through the expanders but goes through a by-pass loop until the vapor reaches the desired pressure and temperature.

Table 4: Design point operational data of the system at trigeneration mode

SORC module	
Mass flow rate	0.699 kg/s
Maximum pressure/temperature	30.4 bar/110 °C
Condensation pressure/temperature	9.16 bar/50 °C
Pressure/temperature after expanders	9.16 bar/68 °C
SORC net electric power output	2.40 kW$_e$
Overall net electric power output	0.99 kW$_e$
VCC module	
Mass flow rate	0.056 kg/s
Evaporation pressure/temperature	2.79 bar/10 °C
Condensation pressure/temperature	9.16 bar/50 °C

Pressure/temperature after compressor	9.16 bar/50 °C
Nominal cooling load	4 kW$_{th}$
Cooling system	
Water inlet temperature (summer/winter)	30 °C/20 °C
Water outlet temperature	45 °C
Mass flow rate	0.730 kg/s
Nominal heating load	85.8 kW$_{th}$
Heating system	
Heating oil inlet temperature	120 °C
Heating oil outlet temperature	105 °C
Mass flow rate	3.12 kg/s

Furthermore, the system includes two condensers, a large and a small one. The large one is intended for the trigeneration and cogeneration modes, during which the SORC is operational. Due to the significantly lower mass flow rate of the VCC, it is necessary to install a second small condenser, in the case that only the VCC is operational.

A description of the selection process of the equipment of the unit follows.

5.2 Boiler-heating oil circuit

The boiler has the capability to use both biomass pellets and natural gas as combustion fuel. The addition of gas burners is made in order to ensure the versatility of the system and its flexible response to rapidly varying loads. The gas burner consists of two stages. Its heat duty can be varied between 65 to 85 kW$_{th}$ and its maximum fuel flow rate is 6.5 to 18.9 Nm^3/h. The flue gas temperature is between 220-230 °C. The pellet burner heat duty ranges between 40 to 80 kW$_{th}$ and its fuel consumption rate between 8 to 20 kg/h. The wood pellets to be used as fuels must have a size around 6-8 mm.

The heating oil circuit includes a centrifugal pump of fixed rotational speed and volume flow rate and is able to handle fluids of temperatures of up to 350 °C. Moreover, the heating oil is stored in a round expansion vessel with a capacity of 250 liters.

The heating system will be automatically controlled through an electronic control panel. The user adjusts the desired heating oil maximum temperature. Since the volume flow rate of the heating oil has a fixed value, the control of this temperature is achieved by automatically shutting down starting up the burners of the boiler based on the readings of a thermostat. In order to investigate the performance of the system at off-design conditions, it is possible to change the heat duty of the burners.

5.3 Heat exchangers

The system includes four heat exchangers: a heater for the heating of the working fluid of the SORC by the heating oil, two cooling water condensers for condensing the working fluid (the requirement for two condensers was explained previously), as well as an evaporator for the VCC module, where the cooling output of the system is produced. All the heat exchangers to be installed are of the plate type. This is because these types of heat exchangers have a number of advantages compared to other types (i.e. shell and tube) for the operational range (pressures, temperatures, heat duty) of the unit under construction. Their advantages include the efficient heat transfer because of the development of high heat transfer coefficients between the fluid streams low volume to heat transfer area ratio and low cost. All heat exchanger models, except for the supercritical refrigerant-heating oil heater were readily proposed on-demand from manufacturers based on their technical specifications. However, most manufacturers were not able to dimension the supercritical heater of the working fluid. This is in part because of the lack of experience with the specific fluid (R227ea) and because of the supercritical conditions of the heat transfer. For this reason, a MATLAB code was used in order to estimate the required heat transfer surface of the heater. Geometrical data of commercially available heat exchanger models were input to the program and the heat transfer area was estimated using the heat exchanger partitioning method [17] and implementing method presented in [18] for calculating the overall heat transfer coefficient. Through a loop computational procedure, a specific plate heat exchanger model with defined number of plates was tested in order to estimate if its available heat

transfer surface would be sufficient for the process. If the available heat transfer surface was estimated to be lower than the required surface, more plates were added and a new loop started. The loop ended when the number of plates ensured that the heat transfer area of the heat exchanger would be higher than the required one. A safety factor was also considered, in order to ensure that the heat exchanger surface would suffice for completing the heat transfer under the desired conditions. The technical characteristics of all heat exchangers are summarized in Table 5.

Table 5: Technical specifications of heat exchangers

Heat exchanger	SORC heater		VCC evaporator		Condenser 1 (large)		Condenser 2 (small)	
Side	Hot	Cold	Hot	Cold	Hot	Cold	Hot	Cold
Fluid	BP Transcal N	R227ea	Water	R227ea	R227ea	Water	R227ea	Water
Mass flow rate (kg/s)	3.12	0.699	0.382	0.0522	0.643	0.737	0.067	0.062
Inlet pressure (bar)	5.5	30.4	1.013	2.58	9.115	1.013	9.126	1.013
Pressure drop (bar)	-	-	0.0073	0.007	0.062	0.026	0.0051	0.007
Inlet temperature (°C)	120	53	20	8.48 (x=0.4)	66.7	20	50	20
Outlet temperature (°C)	105	110	17.5	7.5	47.336	45	47.407	45
Heat duty (kW$_{th}$)	85		4		77		6.5	
Heat transfer area (m^2)	4.71		0.39		4.32		0.31	

5.4 SORC expanders and VCC compressor
As stated previously, the expanders and the compressor are of the scroll type. Scroll expanders and other positive displacement type machines have been consistently proposed in the literature as ideal for ORCs with outputs in the scale between a few hundred Watts to 10 kW [19-22]. The expanders to be used in the SORC of the experimental unit are commercially available scroll compressors used in trucks, which are modified to enable their reverse operation as expansion machines. The most important considerations to be taken into account when selecting scroll expanders are their maximum operating pressure, their volume flow rate which greatly impacts their rotational speed, the latter being also directly influenced by their swept volume and their expansion ratio. The decision to use open drive scroll expanders instead of hermetic ones was made because of the lower cost and customization capability of the former versus the latter. Two same expanders were chosen to operate at different speeds. The reason for this choice was the fact that this commercial model of scroll compressor has a well-documented performance in expansion mode. The selection of the VCC compressor was simpler, since the operation data of the working fluid at its design point are typical for scroll compressors available in the market.

Table 6: Technical specifications of SORC expanders and VCC compressor

		Built-in swept volume (cc/rev)	Maximum rotational speed (rpm)	Rotational speed at design point (rpm)	Volume flow ratio at design point	Power at design point (kW)
SORC expander	HP	121.1	10000	1384	2.47	2.86
SORC expander	LP	121.1	10000	2632	1.90	2.89
VVC compressor		53.9	10000	1755	3.52	1.06

5.5 SORC pump

The feed pump increases the pressure level of the working fluid before its entrance to the heater. It is also used to control its mass flow rate. This control is achieved by varying the rotational speed of the motor coupled with the pump. The pumps that are commonly used and proposed in ORC units are of the positive displacement type [4]. For this type of pumps, the flow rate is almost proportional to their rotational speed. For the experimental unit, a diaphragm pump will be used. The SORC pump will have a design power output of 2.2 kW at 1450 rpm, which corresponds to a working fluid volume flow rate of around 29 lt/min. As can be seen in **Error! Reference source not found.**, the inlet and outlet pressures of the pump are 9.2 bar and 30.4 bar respectively. The pump is coupled with an electric motor of a nominal power of 3 kW.

5.6 Receiver

The receiver is a feed tank that is positioned after the condensers of the system. It provides a buffer storage of the working fluid during the operation of the unit, since only a certain percentage of its total quantity is circulating through the equipment components and the tubes at any given time (depending on the operating conditions). The feed tank also serves another purpose: it ensures that the working fluid at its outlet is at liquid state and has zero vapor fraction. For the sizing of the working fluid the total mass of the working fluid flowing through the equipment and piping was estimated. The tube diameters at each location of the unit were estimated by considering the proper fluid velocities (1-2 m/s for liquid and 8-10 m/s for gases). An additional volume for the sizing of heat exchangers, as well as an overall safety factor were taken into account. The total required volume of the receiver was thus estimated at around 50 lt.

5.7 System control equipment

The automated control of the system will be realized with the implementation of Programmable Logic Controllers (PLC). The PLC will be programmed to open and close the valves of the system. The PLC will also govern the coupling and the de-coupling between the generators and the scroll expanders. Moreover, they will be responsible for adjusting the rotational speed of the feed pump motor and the generators of the expanders, by the use of power inverters.

6. CONCLUSIONS

The thermodynamic optimization procedure (selection of working fluid, expander inlet pressure and temperature) of a trigeneration experimental unit combining an ORC with a VCC based on the heat input of a 85 kW$_{th}$ biomass/natural gas boiler was developed. The working fluid found to be optimal for the unit is R227ea, while the optimal pressure and temperature are 30.4 bar and 110 ºC. At its design point (trigeneration mode), the system will produce 0.99 kW$_e$, a heating load of 85.8 kW$_{th}$ and a cooling load of 4 kW$_{th}$.

The selection process of the basic equipment (biomass/natural gas boiler/heating oil circuit, heat exchangers, expanders/compressor, feed pump, receiver and system control equipment) of the experimental unit was also presented. The construction of the experimental system will be completed by the end of 2015 year and measurements on its operation will be carried out in order to evaluate its performance.

ACKNOWLEDGEMENT

NOMENCLATURE

η	efficiency	
P	power	kW
Q	heat duty	kW
P	pressure	bar
S	entropy	kJ/K
T	temperature	°C

Subscript

CHP	combined heat and power
comp	compressor
cond	condenser
cool	cooling
crit	critical
el	electric
heat	heat
in	input
max	maximum
net	net value
ORC	ORC working fluid
sys	system
th	thermal

REFERENCES

[1] Cho H, Mago PJ, Luck R, Chamra LM. Evaluation of CCHP systems performance based on operational cost, primary energy consumption, and carbon dioxide emission by utilizing an optimal operation scheme. Applied Energy. 2009;86(12):2540-9.

[2] Martins LN, Fábrega FM, d'Angelo JVH. Thermodynamic Performance Investigation of a Trigeneration Cycle Considering the Influence of Operational Variables. Procedia Engineering. 2012;42(0):1879-88.

[3] Rayegan R, Tao YX. A procedure to select working fluids for Solar Organic Rankine Cycles (ORCs). Renewable Energy. 2011;36(2):659-70.

[4] Quoilin S, Broek MVD, Declaye S, Dewallef P, Lemort V. Techno-economic survey of Organic Rankine Cycle (ORC) systems. Renewable and Sustainable Energy Reviews. 2013;22(0):168-86.

[5] Pei G, Li J, Ji J. Analysis of low temperature solar thermal electric generation using regenerative Organic Rankine Cycle. Applied Thermal Engineering. 2010;30(8–9):998-1004.

[6] Schuster A, Karellas S, Aumann R. Efficiency optimization potential in supercritical Organic Rankine Cycles. Energy. 2010;35(2):1033-9.

[7] Vetter C, Wiemer H-J, Kuhn D. Comparison of sub- and supercritical Organic Rankine Cycles for power generation from low-temperature/low-enthalpy geothermal wells, considering specific net power output and efficiency. Applied Thermal Engineering. 2013;51(1–2):871-9.

[8] Mikielewicz D, Mikielewicz J. A thermodynamic criterion for selection of working fluid for subcritical and supercritical domestic micro CHP. Applied Thermal Engineering. 2010;30(16):2357-62.

[9] Bell IH, Wronski J, Quoilin S, Lemort V. CoolProp Database.

[10] TheMathWorks I. MATLAB and Statistics Toolbox Release 2012b,. Natick, Massachusetts, United States.

[11] Technology NIoSa. REFPROP

[12] United States Environmental Protection Agency. Official Website of the United States Environmental Protection Agency, http://www.epa.gov, Accessed on August 19th, 2014.

[13] American Society of Heating Refrigerating and Air-Conditioning Engineers. Addenda to Designation and Safety Classifications of Refrigerants. Atlanta, GA 303292000.

[14] Quoilin S, Declaye S, Tchanche BF, Lemort V. Thermo-economic optimization of waste heat recovery Organic Rankine Cycles. Applied Thermal Engineering. 2011;31(14–15):2885-93.

[15] Delgado-Torres AM, García-Rodríguez L. Analysis and optimization of the low-temperature solar organic Rankine cycle (ORC). Energy Conversion and Management. 2010;51(12):2846-56.

[16] Ibarra M, Rovira A, Alarcón-Padilla DC, Zaragoza G, Blanco J. Performance of a 5 kWe Solar-only Organic Rankine Unit Coupled to a Reverse Osmosis Plant. Energy Procedia. 2014;49(0):2251-60.

[17] Karellas S, Schuster A, Leontaritis A-D. Influence of supercritical ORC parameters on plate heat exchanger design. Applied Thermal Engineering. 2012;33–34(0):70-6.

[18] Walraven D, Laenen B, D'haeseler W. Optimum Configuration of Plate-Type Heat Exchangers for the Use in ORCs for Low-Temperature Geothermal Heat Sources. Katholieke Universiteit Leuven; 2013.

[19] Bao J, Zhao L. A review of working fluid and expander selections for organic Rankine cycle. Renewable and Sustainable Energy Reviews. 2013;24(0):325-42.

[20] Qiu G, Liu H, Riffat S. Expanders for micro-CHP systems with organic Rankine cycle. Applied Thermal Engineering. 2011;31(16):3301-7.

[21] Clemente S, Micheli D, Reini M, Taccani R. Energy efficiency analysis of Organic Rankine Cycles with scroll expanders for cogenerative applications. Applied Energy. 2012;97(0):792-801.

[22] Lemort V, Quoilin S, Cuevas C, Lebrun J. Testing and modeling a scroll expander integrated into an Organic Rankine Cycle. Applied Thermal Engineering. 2009;29(14–15):3094-102.

EXPERIMENTAL TESTING OF A SMALL-SCALE SUPERCRITICAL ORC AT LOW-TEMPERATURE AND VARIABLE CONDITIONS

George Kosmadakis[*], Dimitris Manolakos and George Papadakis

Department of Natural Resources and Agricultural Engineering,
Agricultural University of Athens, Iera Odos Street 75, Athens 11855, Greece
E-mail: gkosmad@aua.gr, dman@aua.gr, gpap@aua.gr
Web page: http://www.renewables.aua.gr/

ABSTRACT

The detailed experimental investigation of an organic Rankine cycle (ORC) is presented, which is designed to operate at supercritical conditions. The net capacity of this engine is almost 3 kW and the temperature of the hot water is always lower than 100 ^{o}C. The laboratory testing of the engine includes the variation of the heat input and of the hot water temperature. The maximum heat input is 48 kW, while the hot water temperature ranges from 65 up to 100 ^{o}C.

The tests are conducted at the laboratory and the heat source is a controllable electric heater, which can keep the hot water temperature constant, by switching on/off its electrical resistances. The expansion machine is a modified scroll compressor with major conversions, in order to be able to operate with safety at high pressure (max. pressure around 40 bar). The ORC engine is equipped with a dedicated heat exchanger of helical coil design, suitable for such applications. The speeds of the expander and ORC pump are regulated with frequency inverters, in order to control the cycle top pressure and heat input. The performance of all components is evaluated, while special attention is given on the supercritical heat exchanger and the scroll expander.

The performance tests examined here are the ones for hot water temperature of 95 ^{o}C, with the aim to examine the engine performance at the design conditions, as well as at off-design ones. Especially the latter are very important, since this engine will be coupled with solar collectors at the final configuration, where the available heat is varied to a great extent.

The engine has been measured at the laboratory, where a thermal efficiency of almost 6% has been achieved, while supercritical operation did not show superior performance as expected, due to the oversized expander. A smaller expander would allow operation at even higher pressures for higher speed with increased electric efficiency, which would probably reveal the full potential of the supercritical operation.

1. INTRODUCTION

The organic Rankine cycle (ORC) technology is suitable for heat recovery applications for low-temperature of even lower than 100 ^{o}C (Manolakos *et al*., 2009a). At such conditions its efficiency is rather low, usually in the range of 3-5%, but still there are cases where its cost-effectiveness can be secured, especially when the heat input comes from waste energy sources. The main advantage at this temperature range is the simple and low-cost heat source circuit, since even pure water can be used with low-pressure piping, while the use of glycol or thermal oil is avoided, as well as a simple ORC configuration with a single expansion machine and no internal heat exchangers (Kosmadakis *et al*., 2013a).

Supercritical cycles have some interesting features, since a better thermal match exists between the hot source and the organic fluid (Schuster *et al*., 2010). This aspect is beneficiary for thermal and exergy efficiency, while at the same time some restrictions are introduced to the components selection due to the high pressure operation. This is the common case for steam cycles, which tend towards such configuration, since in large-scale utility steam power plants the use of supercritical cycles has

been already accomplished. But the largest challenges are for the small-scale systems using an ORC, since it is difficult to find and select the appropriate components for such heat-to-power engines. Moreover, low-temperature operation (below 100 ^{o}C) brings some additional restrictions, since a limited number of fluids can be used for such purposes and the cycle configuration does not allow any flexibility.

The most important component in ORC engines is the expansion machine and there is intensive research effort for producing expanders (of positive displacement type or even turbines for larger systems). For small-scale systems with power production lower than around 20 kW, scroll expanders have been widely used and showed adequate performance and expansion efficiency (Lemort *et al.*, 2012). The present authors have also used the same expansion technology (both open-drive and hermetic ones) and revealed the good performance at a wide range of pressure ratios (Manolakos *et al.*, 2009a). This brings confident that such expander can be also used at a supercritical cycle, where the biggest challenge is the increased pressure. One positive aspect is that for low-temperature applications, the pressure ratio for both cycle types (supercritical and subcritical) is low and usually in the range of 2-3 (Kosmadakis *et al.*, 2013a). In such pressure ratio range the scroll expander operates with good efficiency.

There are various studies focusing on supercritical ORC at theoretical level (Karellas *et al.*, 2012). Most of the studies provide a thermodynamic overview, focusing on the performance potential of such cycles, while others focus on the fluid selection under such conditions (Chen *et al.*, 2011). These theoretical studies treat some key components as black boxes, providing few details about their performance and operation at off-design conditions (Li *et al.*, 2013), such as the pump and expander, while more focus is given on the heat transfer at supercritical conditions (Lazova *et al.*, 2014).

Such aspects, especially in small-scale systems, are very important, in order to evaluate and compare the performance of a supercritical ORC. Here, an experimental study is implemented, testing a small-scale supercritical ORC with a net capacity of 3 kW under various conditions (Kosmadakis *et al.*, 2014). The heat input is varied, while the hot source temperature is held constant. The first series of measured data are presented, focusing on the whole engine operation, as well as its capability to reach supercritical operation at some conditions.

Such study is very important, since real test data are presented, and the advantages and potential of such technology can be identified. Also, this study provides some first proof, whether a supercritical ORC can be indeed more efficient than a subcritical cycle, and if the theoretical results can be verified. Focus is also given on the expansion machine, evaluating the converted scroll expander at such conditions.

2. THE INSTALLED ENGINE

A small-scale ORC engine has been designed and constructed. One of its biggest challenges during its construction was the modification of a scroll compressor (manufactured by Copeland, type ZP137KCE-TFD with swept volume 127.15 cm^3/rev, maximum isentropic efficiency 75.2%, and built-in volume ratio of around 2.6 at compressor mode) to operate as scroll expander (reverse operation). A new casing had to be made, while many internal parts have been re-designed for better matching its operation as expander (such as the inlet volume before the fluid enters the steady scroll). The internal design has been optimized and all issues have been resolved, such as to find an efficient way to get the three wirings of the asynchronous motor out of the casing, ensuring at the same time electrical insulation and pressure sealing. An electric brake is connected with a frequency inverter of the expander, in order to control the test conditions and evaluate this expansion machine. This dynamic brake has a 100% duty cycle and is connected to the frequency inverter of the expander. Its main operation is to convert the variable frequency AC power through transistors into DC electricity, which is then dissipated to heat through a bank of appropriate electrical resistances. This method is followed, in order to have the full control of the expander speed, and find its performance maps.

Also, a dedicated evaporator has been developed for this application, following a helical-coil design. The organic fluid is R-404a. The cooling of the ORC engine is accomplished with a cooling water circuit, using a conventional shell and tube heat exchanger. Cold water with temperature around 16 ^{o}C is circulated and drawn from a large water reservoir with capacity of 320 m^3, rejecting the heat of the

ORC engine. The condensation temperature of the organic fluid with this method is around 25 ^{o}C (fluctuating according to the engine load).

The ORC engine has been then installed at the laboratory for performance tests under controlled conditions. The heat input is provided by an electric heater and its heat production can be altered covering a large range of its capacity (from 25% of the total heat capacity: 12-48 kW$_{th}$) by operating different number of electric resistances and switching on/off the heater. For the investigation of the ORC engine, the maximum heat produced by the electric heater is around 48 kW$_{th}$, while the hot source temperature is held constant and equal to 95 ^{o}C. The heat transfer fluid (HTF) is pressurized water at around 2.5 bar at such temperature, and circulated with an inline centrifugal pump, operating at constant speed (2900 rpm). A simplified design of the system installed at the laboratory is depicted in Figure 1, together with the heating and cooling circuits (Kosmadakis *et al.*, 2013b).
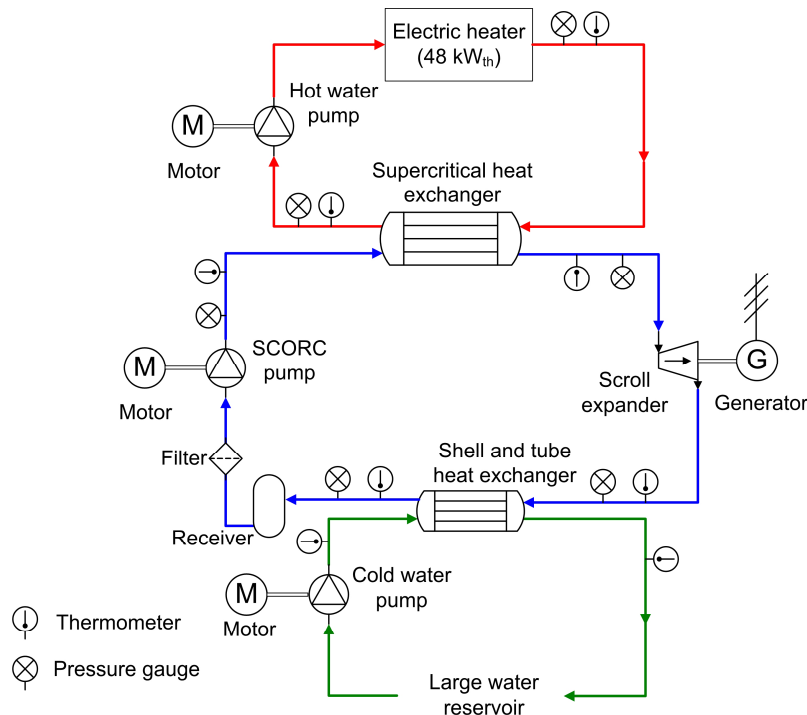
Figure 1: Supercritical ORC design

In Figure 1, the location of the measurement instruments is also depicted at the three circuits (hot water circuit, ORC engine, cold water circuit), in order to measure the key properties and evaluate the performance of this engine at controlled conditions. These instruments are mainly temperature (Pt100 thermocouples, accuracy up to ±0.2 ^{o}C) and pressure sensors (pressure transducers, Keller 21Y type, accuracy 1% of the pressure scale), in order to calculate the thermodynamic state of the organic fluid and hot/cold water at each location. With the above uncertainties, the thermodynamic properties are calculated with an accuracy of around 1.2% (Manolakos *et al.*, 2009b). Flow meters are not used, since steady-state conditions are examined, after the engine has reached a balanced operation at each case. The heat input is calculated from the ORC side, since the organic fluid pump is of diaphragm type and has a linear correlation of flow rate/speed, which is provided by the manufacturer (accuracy estimated at 2%). The accuracy of the calculated parameters is given in Table 1 (Manolakos *et al.*, 2009b), with the maximum error concerning the thermal efficiency, since it includes many calculated parameters. Nevertheless, this error is still low and does not influence the relative differences of the results. The installed engine at the laboratory is depicted in Figure 2.

Table 1: Accuracy of calculated parameters

Parameter	Maximum error (%)
Heat input to ORC	2.62

Expander power production	2.62
Pressure ratio	1.40
Expansion efficiency	2.66
Thermal efficiency	3.71
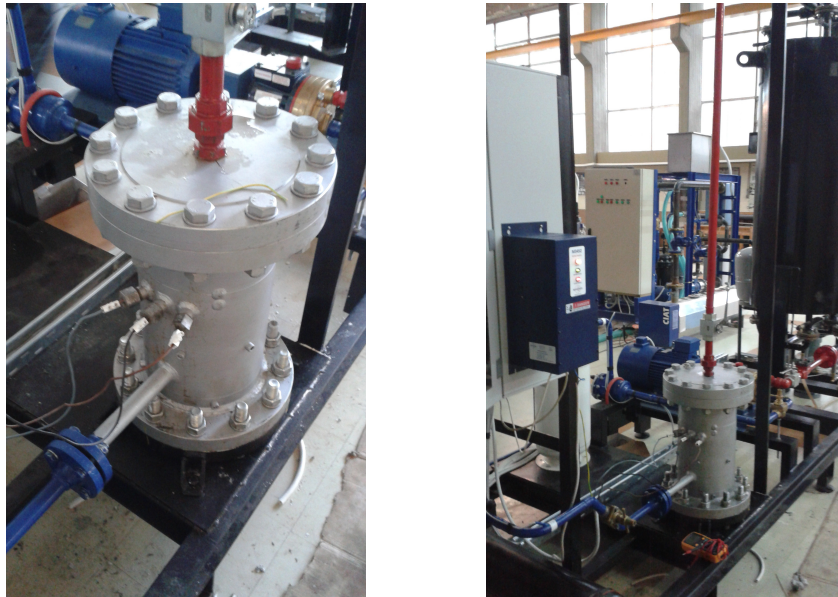
Figure 2: Installed ORC engine. Left: converted hermetic scroll expander. Right: Side view of the ORC engine

3. PERFORMANCE TESTS

The HTF temperature is set constant to 95 ^{o}C, while the heat input is varied. The goal is to examine and evaluate the ORC engine performance at these conditions, while supercritical operation is also attempted, in order to identify if and how much the efficiency can be increased at such conditions.

The pump frequency is altered from 15 Hz up to 50 Hz (from 288 up to 960 rpm) and the expander frequency is regulated from 10 Hz up to 45 Hz (from 580 up to 2610 rpm). By regulating the pump speed, the heat input is varied up to almost 50 kW$_{th}$, which is depicted in Figure 3. The variation of the expander speed has just a minor effect on the absorbed heat (see right hand side of Figure 3).
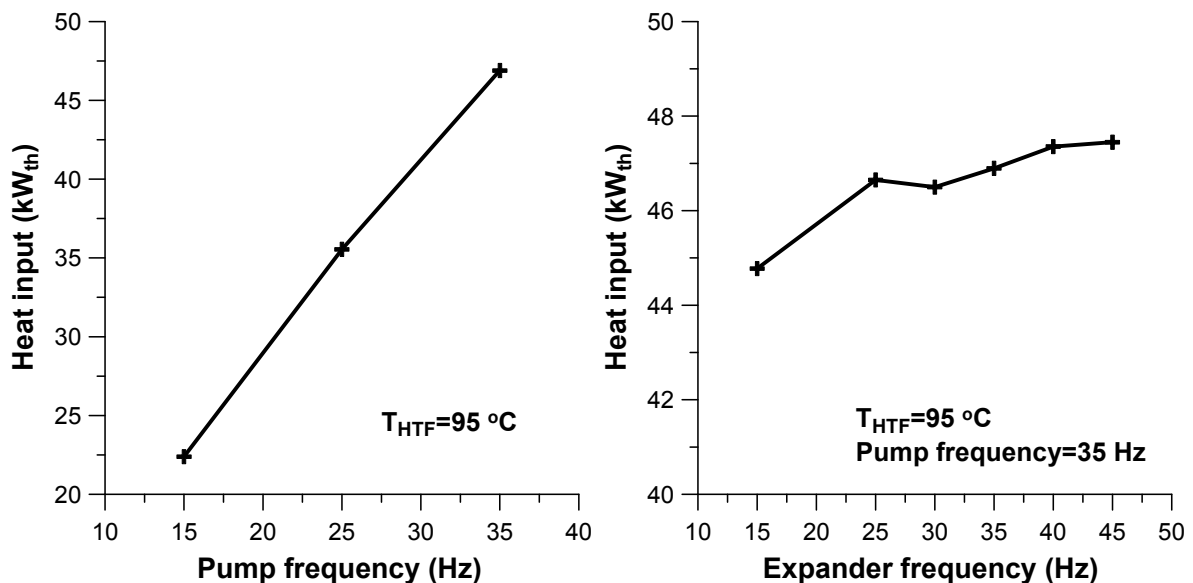
Figure 3: Heat input as a function of the pump and expander frequency

The regulation of the organic fluid pump speed is an effective way to control the heat absorbed by the ORC, while at the same time the flow rate of the organic fluid is adjusted. Therefore, there is the option to keep the speed of the hot water pump constant, simplifying the overall control. In that case, the temperature difference of the HTF would change according to the operating condition (large difference for high heat input). The regulation of the organic fluid pump speed has an important effect on high pressure as well, especially when the expander speed is kept constant, as it will be shown later in this section.

In Figure 4 is shown the expander power production as a function of expander and pump speed, covering a very wide range of operation.
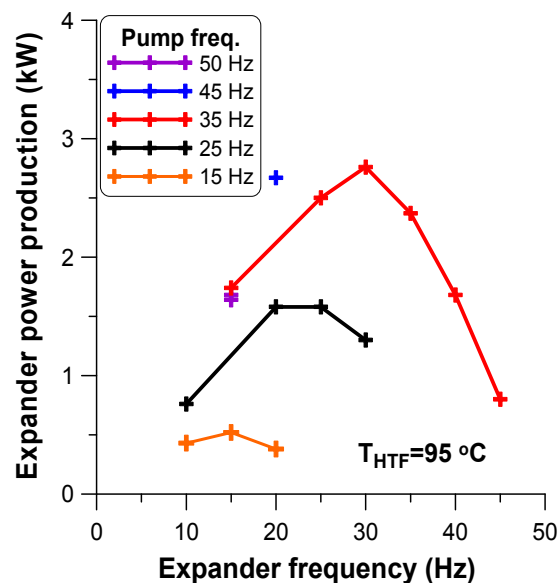
Figure 4: Expander power production as a function of the expander and pump speeds

This power production is actually electricity, since the scroll expander is directly coupled with a three-phase asynchronous motor/generator (capacity of around 10 kW) inside the hermetic casing. This motor operates up to around half of its nominal power, avoiding overheating, due to the absence of cooling (in compressor mode it is cooled by the refrigerant itself).

The power production here reaches 3 kW for the moderate pump frequency of 35 Hz (see Figure 4). For higher pump speed the power production decreases, while additionally more pump power is required. For the pump frequency of 35 Hz and for high expander speed, the power decreases due to lower pressure ratio, while the temperature at the expander outlet is increased. This temperature is shown in Figure 5, together with the expander inlet temperature, which slightly decreases as the expander speed increases.

For high expander speed, the temperature difference across the expander is just 15 ^{o}C, which is very low, leading to a poor power production, as already shown in Figure 4. Also, such high outlet temperature provides a first view of the low process efficiency, since large quantities of heat are rejected in this case at the condenser, having to de-superheat the organic fluid. One interesting solution would be to recover this heat, either by using an internal heat exchanger, although it is not recommended for low-temperature applications, or even use this heat for heating purposes (e.g. operation at CHP mode). But the most efficient way is to further adjust and optimize the engine operation, by avoiding operation at such conditions.

The decrease of pressure and pressure ratio for higher expander speed is presented in Figure 6, where the expander inlet pressure and pressure ratio are shown as a function of the expander frequency for pump frequency of 35 Hz. The low cycle pressure is almost constant and equal to 11-12 bar (higher condensation pressure for high load operation). Therefore, the main effect on the pressure ratio is introduced with the variation of the high cycle pressure.
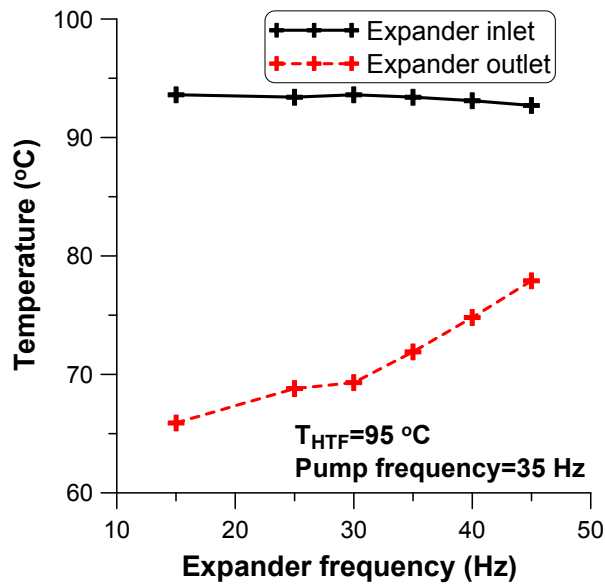
Figure 5: Expander inlet and outlet temperature as a function of the expander speed for pump frequency of 35 Hz
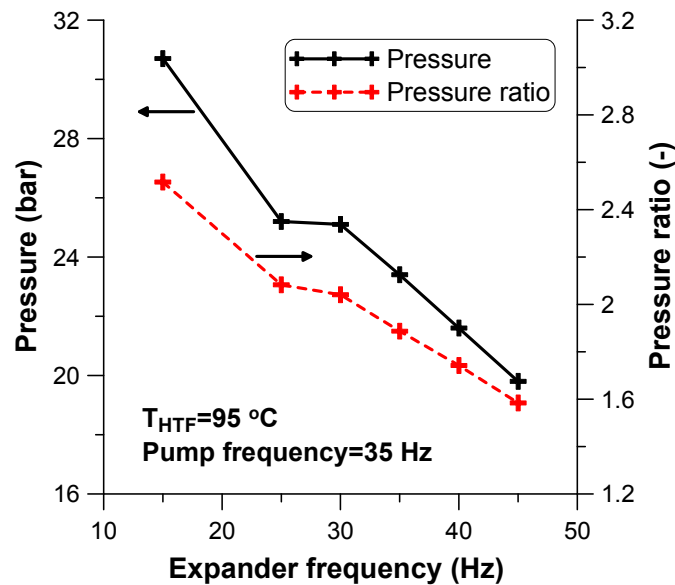

Figure 6: Expander inlet pressure and pressure ratio as a function of the expander speed for pump frequency of 35 Hz

There is a large variation of pressure ratios as the expander speed changes. The maximum pressure ratio is almost 2.6, while the maximum expansion efficiency is observed at a lower expander speed/pressure ratio (equal to around 85%), due to the low electrical efficiency of the asynchronous generator at low speeds, as shown in Figure 7 for three different pump frequencies. It should be mentioned that expansion efficiency is used here as the actual electric power produced divided by the theoretical power produced if the expansion was isentropic. This parameter includes all possible losses (electrical, friction, heat transfer, etc.) and provides a reliable evaluation parameter of all types of expansion machines.

The maximum expansion efficiency is observed for a pressure ratio of 2 (for pump frequency of 35 Hz), which is highly relevant to the built-in volume ratio of the original compressor (Declaye *et al.*, 2013). This pressure ratio value is lower than usual (common values for maximum expansion efficiency are around 3-4), since this compressor is intended for air-conditioning applications, where the pressure/temperature differences are not high. For lower pump speeds and pressure ratios, the

expansion efficiency is decreased. For pump frequency of 25 Hz the pressure ratio with the maximum expansion efficiency of around 80% is 1.87, while for pump frequency of 15 Hz is even lower and equal to 1.62. But again for lower pump speeds, the maximum expansion efficiency is high enough and shows good production potential within a narrow range of operating conditions.
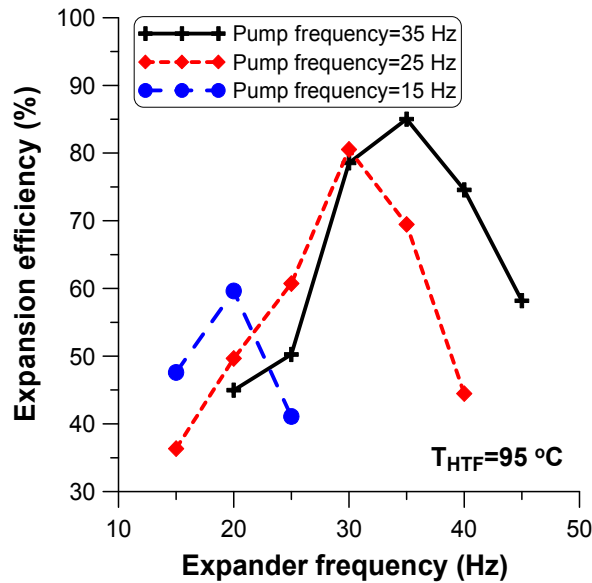
Figure 7: Expansion efficiency as a function of the expander speed for three pump frequencies

The thermal efficiency as a function of pump and expander speeds is depicted in Figure 8. The thermal efficiency is expressed as the net power output (power produced minus the pumping work) divided by the heat input. The maximum values of thermal efficiency are in the range of 5.5%, and are observed for pump frequency of 35 Hz and expander frequency of 30 Hz, which correspond to the conditions, where the maximum expansion efficiency was noticed as well.
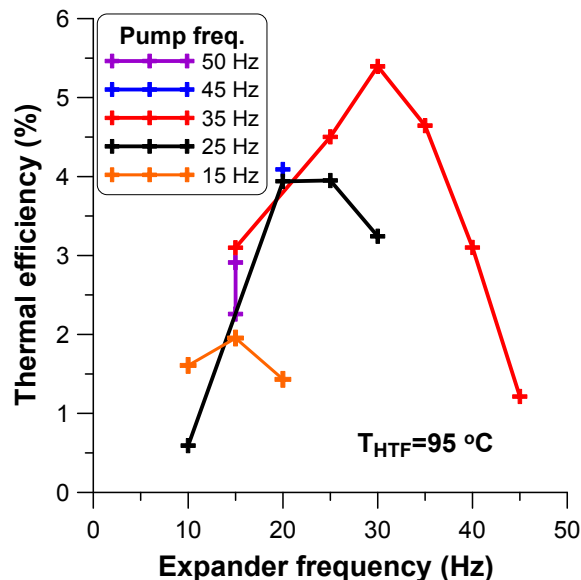
Figure 8: Thermal efficiency as a function of the expander and pump speeds

In all previous tests, supercritical operation was very difficult to be achieved. Although the temperature was over the critical fluid's temperature, the pressure was lower and around 80% of the critical pressure. Such high pressure could be reached only for very large pump speed and low expander speed. One such condition (pump frequency: 50 Hz, expander frequency: 15 Hz) that has

been also recorded showed that the high pressure is 40 bar, which is actually the design pressure, and the expander operated with a pressure ratio of 2.64. The thermal efficiency is equal to 2.9%, due to the low expansion efficiency, being equal to 25% (the low expander speed leads to a low electric efficiency of the generator). Nevertheless, this efficiency value is much higher than all the other recorded for such low expander speed (usually in the range of 1.5-2%), and provides a first positive aspect of the supercritical cycle, although such conditions were difficult to be reached.

The next tests included a lower cooling water flow rate, decreasing the cooling capacity and increasing the condensation pressure/temperature. Such conditions are realistic, since the cooling water had low temperature (around 16 ^{o}C), and much higher temperatures are expected to be reached with either air-cooled condenser or evaporative condenser. The pump frequency was high (45 Hz) and the condenser pressure was around 16-17 bar (close to the pump inlet pressure limit). The pressure ratio was not high (equal to 2.2) and the expander frequency varied from 16 up to 30 Hz. The expansion efficiency is observed in Figure 9, where it is shown that the maximum value is almost 80%, which is achieved for moderate expander speed. Moreover, for the supercritical condition (for expander frequency of 16 Hz) the expansion efficiency is low and around 45%, mainly due to the low electrical efficiency of the generator at such conditions.
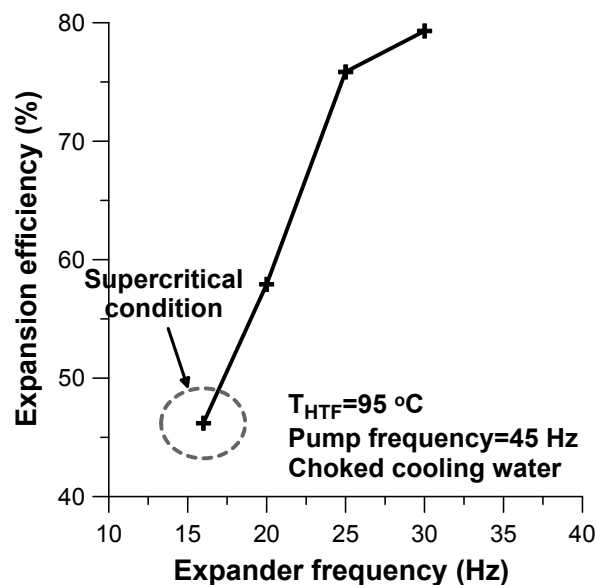
Figure 9: Expansion efficiency as a function of the expander frequency

The thermal efficiency is depicted in Figure 10, where it is shown that the maximum efficiency reached is almost 6% for subcritical operation.

It should be reminded that this high value is reached, when the condensation pressure and temperature are increased, decreasing the power production capability. Therefore, the potential can be even higher than that, which can be achieved with an improved design, especially of the expander, and further testing and development.
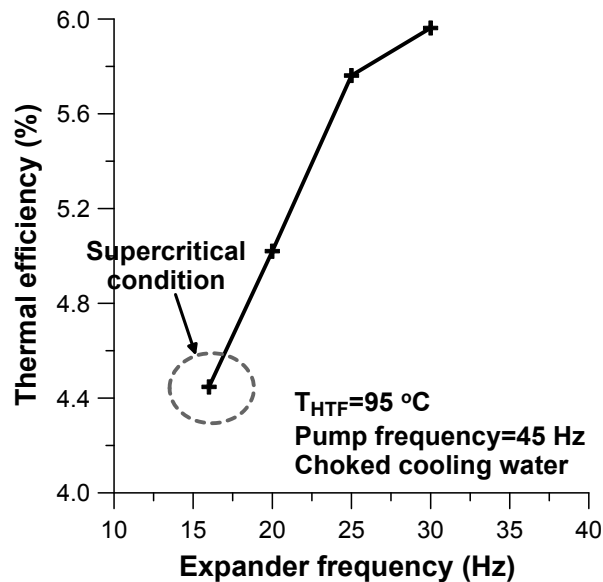
Figure 10: Thermal efficiency as a function of the expander frequency

The efficiency at supercritical condition is lower, mainly due to the low expansion efficiency (see Figure 9). If this condition had a higher expansion efficiency (by including a smaller expander with lower swept volume) and extrapolating the performance curves, then the efficiency would even reach the value of 7%, which is very promising for such small-scale engine at low-temperature and much higher than any other value observed during the current performance tests.

4. CONCLUSIONS

The detailed experimental results of the ORC engine testing at the laboratory have been presented, revealing its performance capability. The tests here concern a constant HTF temperature and equal to 95 °C with variable heat input. This heat is provided by an electric heater and is controlled with the speed variation of the organic fluid pump. A converted hermetic scroll expander is used for power production, showing increased expansion efficiency at some favorable conditions. Various parameters have been examined, mainly when regulating the expander and pump speed, showing the heat-to-power conversion efficiency of such engine.

Moreover, supercritical operation was difficult to be achieved and only when the cooling water flow rate was decreased, could the engine operate at supercritical conditions and maintain such operation. At these conditions, the expander frequency/speed was low (around 15 Hz), keeping a pressure ratio close to the designed one, but leading to a low expansion efficiency, due to the low electric efficiency of the asynchronous generator at these conditions. If the expansion efficiency could be increased (mainly having to do with the frequency operation and the increase of the electrical efficiency), by using a smaller expander, then the thermal efficiency at supercritical conditions seems to be superior to the one at subcritical ones, and fully exploit the theoretical performance.

REFERENCES

Chen, H., Goswami, D. Y., Rahman, M. M., Stefanakos, E. K., 2011, A supercritical Rankine cycle using zeotropic mixture working fluids for the conversion of low-grade heat into power, Energy, vol. 36, no. 1: p. 549-555.
Declaye, S., Quoilin, S., Guillaume, L., Lemort, V., 2013, Experimental study on an open-drive scroll expander integrated into an ORC (Organic Rankine Cycle) system with R245fa as working fluid, Energy, vol. 55: p. 173-183.
Karellas, S., Schuster, A., Leontaritis, A. D., 2012, Influence of supercritical ORC parameters on plate heat exchanger design, Applied Thermal Engineering, vol. 33: p. 70-76.

Kosmadakis, G., Manolakos, D., Papadakis, G., 2013a, An investigation of design concepts and control strategies of a double-stage expansion solar organic Rankine cycle, Int J of Sustainable Energy, DOI: 10.1080/14786451.2013.827682, in press.

Kosmadakis, G., Manolakos, D., Bouzianas, K., Papadakis, G., 2013b, Heat recovery in low-concentration PV/thermal units using a low-temperature supercritical organic Rankine cycle for improved system performance, Presented at the *2nd Int. Seminar on ORC Power Systems* (ASME-ORC2013), Rotterdam, The Netherlands, 7-8 October 2013.

Kosmadakis, G., Manolakos, D., Olsson, O., Ntavou, E., Bystrom, J., Papadakis, G., 2014, Design and implementation of a hybrid low-concentration PV/thermal system, including a bottoming supercritical ORC engine, Presented at the *29th European PV Solar Energy Conference and Exhibition* (29th EU PVSEC, 2014), Amsterdam, The Netherlands, 22-26 September 2014.

Lazova, M., Daelman, S., Kaya, A., Huisseune, H., De Paepe, M., 2014, Heat transfer in horizontal tubes at supercritical pressures for organic rankine cycle applications, 10th International Conference on Heat Transfer, Fluid Mechanics and Thermodynamics (HEFAT 2014), Proceedings (pp. 1044–1051). Presented at the 10th International Conference on Heat Transfer, Fluid Mechanics and Thermodynamics, Orlando, Florida, USA.

Lemort, V., Declaye, S., Quoilin, S., 2012, Experimental characterization of a hermetic scroll expander for use in a micro-scale Rankine cycle, Proceedings of the Institution of Mechanical Engineers, Part A: Journal of Power and Energy, vol. 226, no. 1: p. 126-136.

Li, C., Kosmadakis, G., Manolakos, D., Stefanakos, E., Papadakis, G., Goswami, Y., 2013, Performance investigation of concentrating solar collectors coupled with a transcritical organic Rankine cycle for power and seawater desalination co-generation, Desalination, vol. 318, no. 3: p. 107–117.

Manolakos, D., Kosmadakis, G., Kyritsis, S., Papadakis, G., 2009a, Identification of behaviour and evaluation of performance of small scale, low-temperature Organic Rankine Cycle system coupled with a RO desalination unit, Energy, vol. 34, no. 6: p. 767-774.

Manolakos, D., Kosmadakis, G., Kyritsis, S., Papadakis, G., 2009b, On site experimental evaluation of a low-temperature solar organic Rankine cycle system for RO desalination, Solar Energy, vol. 83: p. 646-656.

Schuster, A., Karellas, S., Aumann, R., 2010, Efficiency optimization potential in supercritical Organic Rankine Cycles. Energy, vol. 35, no. 2: p. 1033-1039.

ACKNOWLEDGEMENT

EXPERIMENTAL OBSERVATION OF NON-IDEAL NOZZLE FLOW OF SILOXANE VAPOR MDM

Andrea Spinelli[1][*], Alberto Guardone[2], Fabio Cozzi[1], Margherita Carmine[1], Renata Cheli[1], Marta Zocca[2], Paolo Gaetani[1], Vincenzo Dossena[1]

[1] Politecnico di Milano, Department of Energy
Via Lambruschini 4, 20156 Milano, Italy
e-mail: andrea.spinelli@polimi.it

[2] Politecnico di Milano, Department of Aerospace Science and Technology
Via La Masa 34, 20156 Milano, Italy
e-mail: alberto.guardone@polimi.it

* Corresponding Author

ABSTRACT

The first experimental results from the Test-Rig for Organic Vapors (TROVA) at Politecnico di Milano are reported. The facility implements an Organic Rankine Cycle (ORC) where the expansion process takes place within a straight axis convergent-divergent nozzle, which is the simplest geometry representative of an ORC turbine blade passage. In order to reduce the required input thermal power, a batch operating mode was selected for the plant. Experimental runs with air allowed to verify the throttling valve operation and the measurement techniques, which include total pressure and temperature measurements in the settling chamber, static pressure measurements along the nozzle axis. A double-passage Schlieren technique is used to visualize the flow field in the nozzle throat and divergent section and to determine the position of shock waves within the flow field. The first experimental observation of non-ideal nozzle flows are presented for the expansion of siloxane fluid MDM ($C_8H_{24}O_2Si_3$, octamethyltrisiloxane) for vapor expansion in the close proximity of the liquid-vapor saturation curve, at relatively low pressure of operation. A supersonic flow is attained within the divergent section of the nozzle, as demonstrated by the observation of an oblique shock wave at the throat section, where a 0.1 mm recessed step is located. Schlieren visualizations are limited by the occurrence of condensation along the mirror side of the nozzle. Pressure measurements are compatible with the observed flow field.

1. INTRODUCTION

Organic Rankine Cycle (ORC) is a well established and viable technology for the exploitation of energy from low/medium temperature sources, such as renewable or heat-recovery, with applications to low/medium electrical power generation and Combined Heat and Power (CHP) plants. For these applications, the ORC technology is usually preferred over steam cycle due to the simplicity of plant components, high reliability and low operational costs Gaia and Duvia (2002); Bini and Manciana (1996) and relatively high efficiency of the thermodynamic cycle Angelino et al. (1984).

Turbine efficiency in current ORC plants is around 75-85%, see Schuster et al. (2009); Duvia and Tavolo (2008) and recent researches in ORC technology are focused on blade geometry optimization to improve the turbine efficiency. This task is complicated by the fact that the use of organic compounds operating close to the vapor saturation curve in ORC results in highly

non-ideal compressible-fluid flows within the turbine passages, which are usually designed to operate in supersonic flow conditions due to the relatively low speed of sound which characterizes high molecular mass fluids, especially in close-to-saturation flow conditions Harinck et al. (2009). Moreover, the accurate prediction of the flow behavior requires the use of complex non-ideal thermodynamic models. Computational Fluid Dynamics (CFD) codes for non-ideal compressible-fluid dynamics (NICFD) are already available which implement the complex thermodynamics of fluids in ORC turbine passages Colonna and Rebay (2004); Guardone (2007); Cinnella and Congedo (2007); Colonna et al. (2008); Hoffren et al. (2002).

Currently, no experimental data of non-ideal compressible-fluid flows are available to support our understanding of the fluid dynamics of ORC plants and to assess the reliability and accuracy of available thermodynamics models and CFD tools.

To investigate experimentally the non-ideal compressible-fluid flows of organic compounds in typical operating conditions for ORC applications, the *Test Rig for Organic Vapors* (TROVA) was designed and constructed at the Politecnico di Milano, see Spinelli et al. (2013). In the facility, expansion flows of different organic compounds in non-ideal conditions in the close proximity of the liquid-vapor saturation curve can be investigated by independent measurements of pressure, temperature and velocity. The facility implements an ORC (either sub-critical or super-critical), where the expansion process take place within a nozzle replacing the turbine. A straight axis converging-diverging nozzle was chosen, being it the simplest geometry providing an expansion from subsonic to supersonic flow in the operating conditions of interest. The size of the nozzle is large enough to guarantee that within the expanding flow a large isentropic core is preserved, thus making it possible to measure temperature and pressure fields without the use of calibrated probes, see Spinelli et al. (2010). Total pressure and temperature are measured in the settling chamber ahead of the nozzle inlet; static pressure taps at different sections along the nozzle axis are used to follow the flow evolution as it expands from rest to supersonic conditions. In order to reduce the required input thermal power, a batch operating facility has been selected.

The structure of the paper is as follows. In section 2, the general set-up of the test-rig is presented and an overview of the measurement techniques is given. In section 3, experimental results with air are reported. In particular, the operation of the throttling valve is verified and the complete measurement system is tested. The possibility of using the Schlieren visualization to support the interpretation of the pressure measurement is assessed. In section 4, preliminary experimental results for siloxane fluid MDM ($C_8H_{24}O_2Si_3$, octamethyltrisiloxane) are reported. In particular, the heating and degassing procedure is tested and assessed against saturated data for MDM fluid. A very preliminary test run at low pressure (in the range 70-350 mbar) is described and the suitability of the set-up to investigate nozzle flows of non-ideal compressible flows of organic fluids is discussed. Final remarks and observations are gathered in section 5.

2. TROVA: SET-UP AND MEASUREMENT TECHNIQUES

The TROVA operates as a blow-down wind tunnel, namely, in a discontinuous way, to reduce the power requirements. The working fluid to be tested is stored in a high pressure vessel (HPV) (see figure 1) and isochorically heated up to saturated, superheated, or supercritical conditions (point 4 in figure 1) at a pressure P_4 and temperature T_4 above the nozzle stagnation conditions (point 6). The heating elements consist of electrical bands and wires externally clung to the vessel. The control valve (MCV) regulates the feeding total pressure P_{T6} at the inlet of the nozzle during the entire test. Small fluctuations in pressure around the set-point are acceptable since they are characterized by a time scale extremely large if compared to the nozzle characteristic
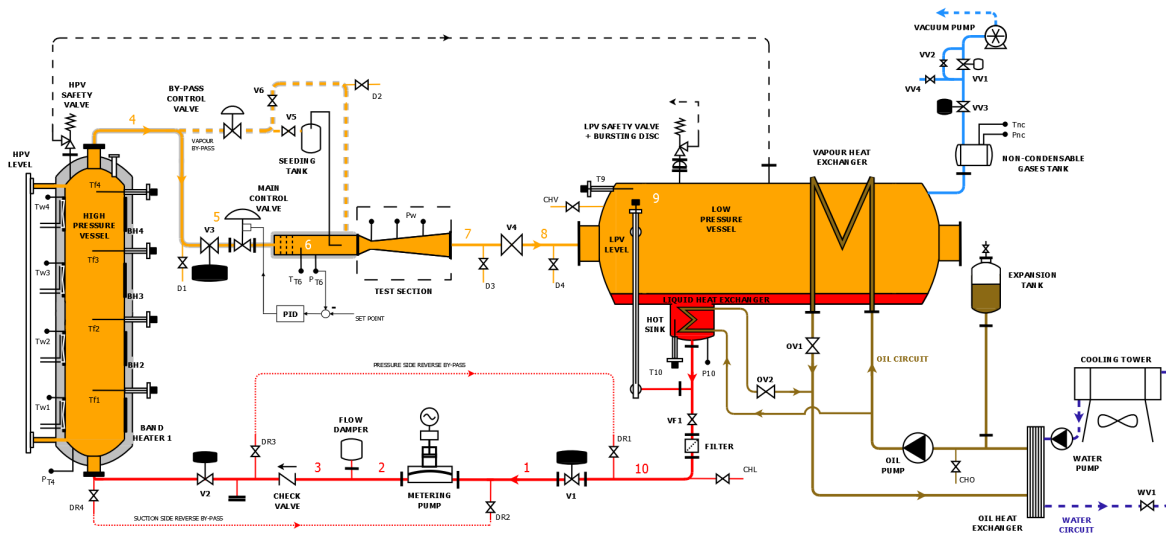
Figure 1: Scheme of the TROVA test-rig. The total pressure and temperature in the settling chamber are measured by sensors P_{T6} and T_{T6}, respectively. Static pressure taps in the test section are indicated by P_w.

Fluid	P_{T6} (bar)	T_{T6} (°C)	Z_{T6}	β	P_7 (bar)	M_7	t (s)
MDM	4.0	253.2	0.85	10.0	0.4	2.05	~ 40

Table 1: Operating conditions for the first MDM test and expected duration. The expansion ratio β, exit pressure P_7 and exit Mach number M_7 refer to adapted conditions.

time. Similarly, the reduction of the nozzle inlet total temperature T_{T6} due to the HPV emptying process is small, thanks to the high molecular complexity of the working fluid, i.e., large heat capacity, and occurs at a very small time rate. However, in the settling chamber ahead of the nozzle, the stagnation conditions data P_{T6} and T_{T6} are acquired at frequency of orders of magnitude higher with respect to the frequency content of each signal. The organic vapor is then expanded (to state 7) through the nozzle, where wall pressure measurements are performed. The vapor is discharged into a large area pipe (point 8), where it is slowed and brought in a low pressure vessel (LPV, state 9) where the fluid is collected and condensed (state 1). The loop is closed by the liquid compression to the HPV (point 2), performed by a membrane metering pump. Further details concerning all components can be found in Spinelli et al. (2013).

The design test scheduled for the TROVA concerns the expansion flow of siloxane MDM. Due to its relatively high critical temperature ($T_C = 290.94$ °C), its thermal stability, non-toxicity and low cost, this fluid is of particular interest for industrial ORC plant exploiting relatively high temperature sources (e.g. biomass, solar radiation). The operating conditions for this test have been selected as a compromise between the requirement of moderate temperatures, in order to avoid fluid decomposition during the early tests, and the need of expanding the vapor through thermodynamic regions where non-ideal compressible-fluid effects are appreciable. The resulting conditions are reported in table 1.

2.1 Test section and instrumentation

The test section is made of a planar converging-diverging nozzle (see figure 2); the diverging portion of the nozzle profile was designed by applying the method of characteristics coupled with state-of-the-art thermodynamic models for the siloxane MDM (Guardone et al. (2013),Colonna
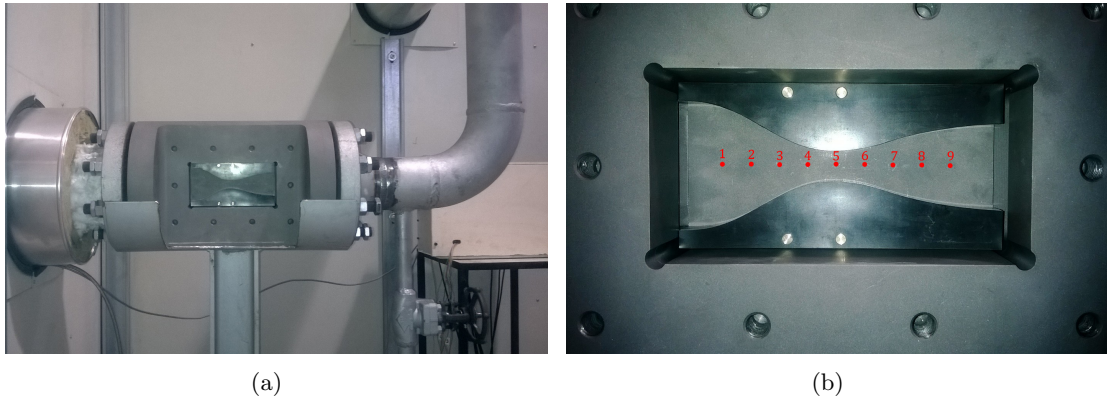
(a)

(b)

Figure 2: Overview of the test section (a) and details of the nozzle within the test section (b). The flow is from left to right. The settling chamber is on the left and it is enclosed in the white box which contains the TROVA and it is separated from the laboratory for safety. The front window is made of quartz to allow for optical access, the back closure is a mirror (not installed to take the picture). Static pressure taps are located along the symmetry axis and are marked with red dots.

Property	Sensor	Type	CR P (bar)	CR T (°C)	U_2 P (%FS)	U_2 T (°C)
T_T	Thermocouple	J (Fe - Cu/Ni)	-	25-250	-	0.4
P_T, P_w	Piezo-resistive	Kulite XTEH	1-FS (3.5-40)	25-250	0.07	-

Table 2: Type, calibration range (CR) and expanded uncertainty (U_2) of the instruments employed for pressure and temperature measurements. FS is the transducer full scale.

et al. (2006)), while the converging portion was represented by a 5th order polynomial profile which realizes a smooth transition from the inlet to the throat section. At the geometrical throat a recessed step of 0.1 mm depth (1.2% of the nozzle semi-height at the throat) was machined on both the top and bottom contoured profiles, in order to fix the location of the minimum nozzle area, independently from boundary layer unsteadiness.

The front planar wall is a quartz window which guarantees optical access, while the rear wall is made by a steel plate and it houses 9 pressure taps along the nozzle axis. Behind each tap a 25 mm long pneumatic line-cavity system is machined in the plate body, connecting the tap with the sensing element of a piezo-resistive pressure transducer. For the present experimentation, the plate surface has been mirror polished, in order to allow the implementation of the double-passage Schlieren visualization technique detailed in section 2.2. The stagnation conditions are measured in the settling chamber ahead of the test section. A wall pressure tap/line/transducer system (similar to the nozzle ones) is used for the total pressure, due to the very low flow velocity in the chamber; the total temperature is measured by a J type thermocouple whose hot junction is located at the chamber axis.

The pneumatic lines connecting each pressure measurement point with the corresponding transducer are characterized by very short length ($\sim$ 25 mm) and small diameter ducts (0.3 to 1.5 mm); similarly the volume of the capacities ahead of the transducer sensing element is extremely small ($\sim$ 45 mm^3). A natural frequency of about 900 Hz has been estimated for the transmission lines. All pressure sensors are piezo-resistive transducers (Kulite XTEH-7L series) operating at high temperature (up to 343 ℃) and chemically compatible with almost all working fluids of interest for the ORC industry. The data acquisition (DAQ) system consist
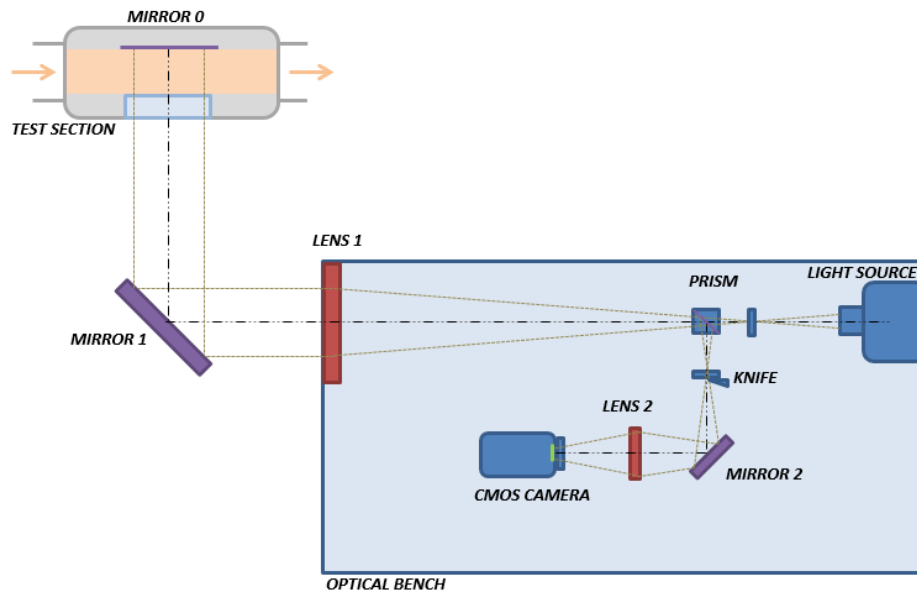
Figure 3: Functioning scheme of the double-passage Schlieren set-up.

of analog modules employed to provide the voltage supply to the transducers and to amplify the measurement signals (including the thermocouple output voltage) and of a high speed data acquisition board.

The J thermocouple has been calibrated in the temperature range 25-250 ℃. Due to the large sensitivity of the pressure transducers to temperature variation and the consequent uncertainty increase, the pressure sensors were calibrated both in pressure and in temperature in the range 1-FS bar for the pressure and 25-250 ℃ for the temperature. The final accuracy, expressed in terms of expanded uncertainty, obtained for each sensor is summarized in table 2. Notice that the acquisition channels and the supply/amplification modules are kept unchanged during both the calibration and the measurement processes.

2.2 Schlieren set-up

A double pass-type parallel light Schlieren system with the emitting and receiving optical components mounted on an optical table was used. This configuration is shorter and easier to align with respect to the classical Z-type system. A schematic sketch of the system is shown in figure 3. A 100 W Hg arc-lamp is used as the light source. The light from the lamp is focused by a F/1.5 silica lens into a circular spot of about 3 mm in diameter and then collimated to form parallel light rays by a Schlieren lens head (Lens 1 in figure 3). The latter has a diameter of 150 mm and a focal length of 1000 mm. The collimated light beam is deflected by a circular mirror (Mirror 1 in figure 3) before traversing the test section. It is then reflected back to the Schlieren head by the metallic mirror 0 (namely, by the polished nozzle back wall) and focused on the vertically aligned knife edge (knife in figure 3)). The knife orientation allows to visualize the density gradient along the nozzle axis. A cubic beamsplitter (prism in figure 3) separate the light beam originated by the light source and the reflected one. A lens of 160 mm focal lenght and 50 mm diameter is located behind the knife (Lens 2 in figure 3) and forms a real image of the test section on the sensor of a high speed CMOS camera. To allow a suitable long recording time the CMOS camera resolution and frame rate were respectively set to 1024 x 512 pixels and to 100 fps (frames per second), while the exposure time was set to 20 μs.

Fluid	P_{T6} (bar)	T_{T6} (°C)	Z_{T6}	β	P_7 (bar)	M_7	t (s)
Air	4.0	20-60	1.0	20.0	0.2	2.59	~ 40

Table 3: Operating conditions for the air test and expected duration. The expansion ratio β, exit pressure P_7 and exit Mach number M_7 refer to adapted conditions.
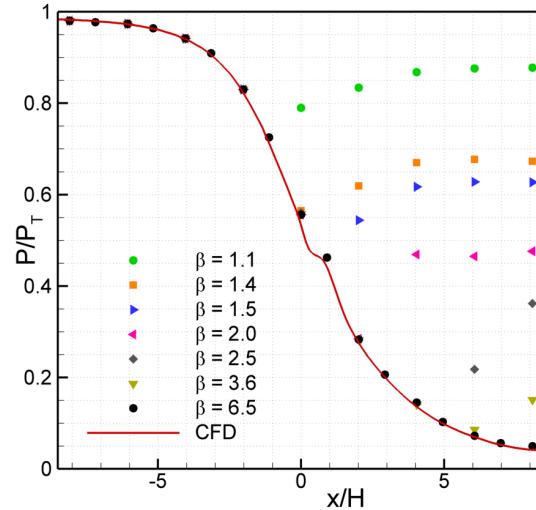

Figure 4: Pressure measurement along the nozzle axis for different values of the expansion ratio β. Pressure is made non-dimensional by the upstream total pressure P_T. The throat is located at $x/H = 0$. H is the nozzle semi-height at the throat.

3. EXPERIMENTAL RESULTS WITH AIR

3.1 Equivalent test with air

In order to verify the suitability of the test procedure and of the measuring strategy in giving reliable measurements and an accurate description the nozzle flow field, an equivalent test is designed and performed using dry air as working fluid. This allows for a comparison with theory based on the ideal gas model, with similar experiments in nozzle (available from the literature), and with standard CFD simulations. The equivalent test was designed in order to have a comparable duration with respect to the MDM 1st test (see table 1), thus a similar dynamic operation of the plant. Therefore, the capability of the control valve MCV in keeping a reasonably constant pressure at the nozzle inlet during the test can be verified. The converging-diverging nozzle profile designed for the MDM 1st test was used. However, when operated with air, the nozzle adapted expansion ratio and exit Mach number considerably differ from the corresponding design values for MDM expansion. The operating conditions of the equivalent test are summarized in table 3.

The air tests were performed by storing in the HPV air at a pressure of about $P_{T4} = 12$ bar and at a temperature in the range $T_{T4} = 20\text{-}160$ °C. The LPV pressure is brought to $P_{T9} = 0.08$ bar by evacuating the reservoir. Therefore, at the initial time ($P_7=P_{T9}$) the nozzle is under-expanded, since the expansion ratio is $\beta = P_{T6}/P_7 = 50$. The test start is dictated by the opening of the ball valve V3 (see figure 1) which also triggers the CMOS camera recording, in such a way that the pressure and temperature data are synchronized with the Schlieren images. The control valve operates with low frequency oscillations (of the order of 1 Hz) keeping the nozzle inlet total pressure at a value of about $P_{T6} = 4\pm0.1$ bar for approximately 25 s, than the MCV is fully opened and the pressure across the valve is balanced ($P_{T4}=P_{T6}$). The test
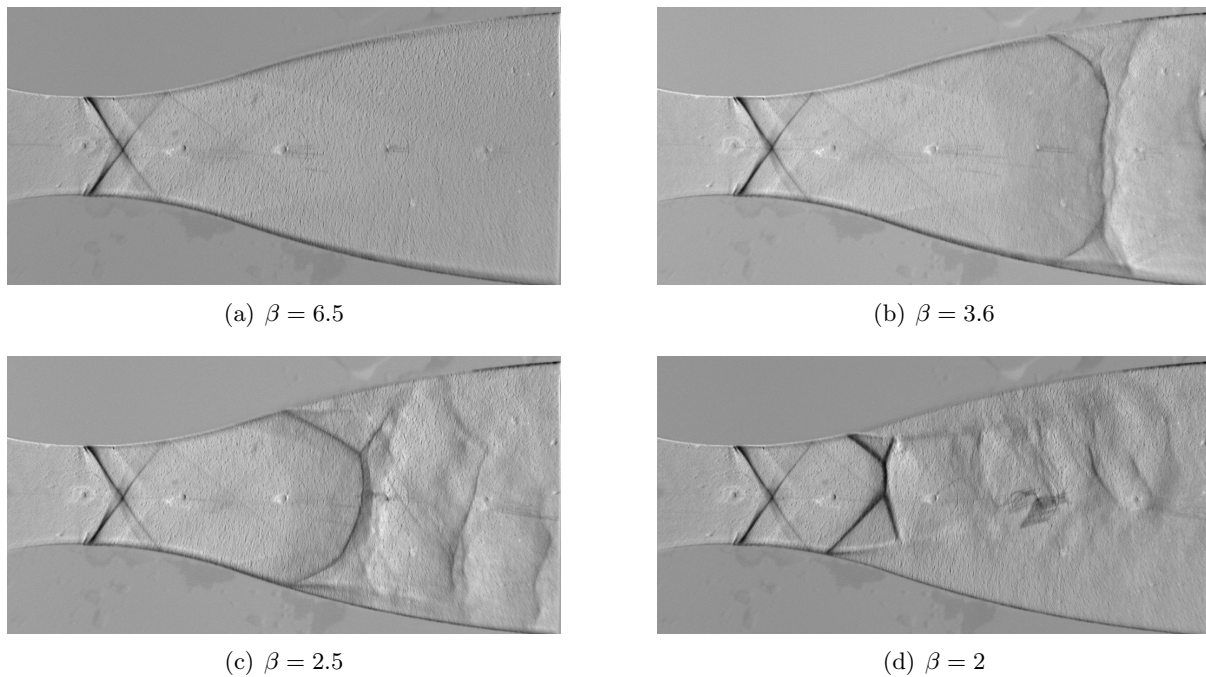
(a) $\beta = 6.5$

(b) $\beta = 3.6$

(c) $\beta = 2.5$

(d) $\beta = 2$

Figure 5: Schlieren visualization of nozzle operation in air in chocked conditions for four values of the expansion ratio β, corresponding to adapted conditions (a) and subsonic outflow with a shock wave in the divergent section (b,c,d). A recessed step 0.1 mm deep is machined at the throat section of geometry shown on top: a fan-shock-fan system originates at the step location. Pressure measurements are reported in figure 4.

proceeds for additional 15 s (with a reducing and uncontrolled P_{T6}) until the pressure of the two reservoirs are balanced ($P_{T4}=P_{T9}$) (due to the HPV emptying and the LPV filling). According to this test scheme, the entire range of possible flow regimes in the nozzle are observed during the test: from under-expanded/adapted/over-expanded to fully subsonic flow.

3.2 Test results

The values of the static to total pressure ratio are reported in figure 4 for all static pressure taps along the nozzle axis and for different values of the expansion ratio β. Note that pressure taps along the back plate are not symmetric and up to 17 different measurement station can be obtained if different tests are carried out by changing the plate orientation. Numerical simulations of the expansion process, including the geometry of the recessed step, agree fairly well with the adapted flow conditions within the nozzle ($\beta = 6.5$) in figure 4. Note that the isentropic expansion profile is perturbed by the presence of the recessed step at the nozzle throat, as confirmed by the numerical simulations as well as by the experimental results. At lower values of β, the measured pressure profiles departs from the adapted one, as expected from the gasdynamic theory of nozzle flows.

Indeed, as confirmed also by the Schlieren measurements in figure 5, shock waves occurs in the divergent portion of the nozzle for low enough expansion ratios. For $\beta = 1.1$ and $\beta = 1.4$ (see figure 4) a fully subsonic flow is observed in both the convergent and the divergent section of the flow; notice that in case of $\beta = 1.4$ sonic conditions are reached at throat. Remarkably, the recessed step at the nozzle throat produces significant perturbation in the flow field, which are clearly visible in all Schlieren visualizations in figure 5 and in the pressure profiles in figure 4. Supersonic flow expansion at the step location results in the formation of a Prandtl-Meyer fan
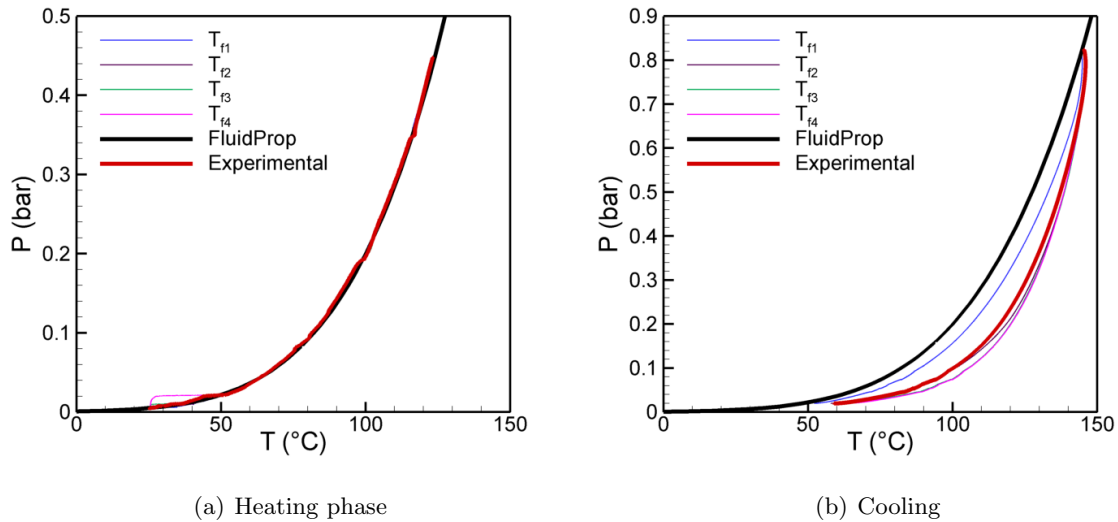
(a) Heating phase

(b) Cooling

Figure 6: Pressure-temperature profile during the heating (a) and cooling (b) phase and saturation curve of fluid MDM.

(light gray in the Schlieren images) and causes flow separation around the step corner. Flow re-attachment at the nozzle surface results in the formation of a shock wave (dark gray). A further expansion is visible at the geometric discontinuity at the end of the machined portion of the nozzle. The resulting fan-shock-fan combination is clearly seen to propagate and to interact with the nozzle walls in the adapted flow conditions shown in 5a).

4. PRELIMINARY RESULTS FOR MDM VAPOR

4.1 Fluid preparation and heating/cooling procedure

The preliminary steps required to prepare the MDM test include the fluid charge and the execution of cycles of isochoric heating and cooling within the HPV for removing incondensable gases, most notably air, from the fluid. The fluid was charged at the condenser (LPV) after a complete plant evacuation, which was carried out using the plant vacuum pump. The final pressure before the charge (at each section) was of the order of 1 mbar. Depending on the test conditions a proper fraction of the liquid is pumped to the HPV by the metering pump, whose operation was also verified. The mass of fluid charged at each section is such that, at room temperature, the fluid is always in saturated conditions, therefore at a pressure well below the atmospheric pressure.

The heating/cooling cycles were performed from room temperature ($\sim$ 20℃) to about 180 ℃, therefore below the critical point and always maintaining saturated conditions, namely by keeping the fluid within the two-phase region. It's worth reminding that the HPV is electrically heated from the vessel external walls and it is not equipped with a cooling system, therefore cooling can be obtained only by heat exchange with the external environment.

Figure 6 shows that the experimental *P-T* saturation curve obtained during the heating process is finely captured by the thermodynamic model Colonna et al. (2006), whereas the agreement is lost during the cooling process. Indeed, during the heating process the convective heat transfer between the fluid and the thermocouple (industrial K type) hot junctions (located at the reservoir axis) is promoted by the expected convective motion within the reservoir (activated by the liquid boiling in the lower portion of the reservoir, where most of the thermal energy enters the system). This heat transfer mechanism is expected to prevail over the conduction
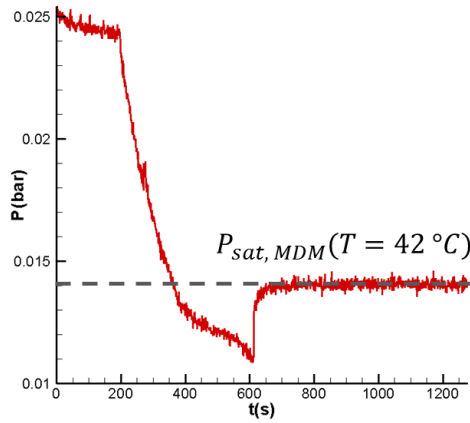
Figure 7: Pressure in the HPV during the degassing cycle at a temperature of 42 °C.

Fluid	P_{T6} (bar)	T_{T6} (°C)	Z_{T6}	β
MDM	0.35-0.07	120-80	0.97	50-10

Table 4: Operating conditions for the early MDM tests.

along the thermocouple stem and the radiation from the vessel wall. During the cooling process, convective motions are strongly inhibited, since the the entire HPV (and especially its top portion) is not provided with a cooling system and it is strongly insulated. Therefore, the thermocouple are presumably heated by conduction and radiation from the vessel wall at a temperature constantly higher than the condensing fluid temperature.

After each heating/cooling cycle, the HPV pressure is significantly higher than the saturation pressure at the fluid temperature (see figure 7, at $t < 200$ s). This could be related to the presence of air sucked by HPV from the surrounding environment, to liquid degassing or to fluid decomposition, since MDM is expected to form more volatile fractions after decomposition. For this reason, after each cycle the HPV has been degassed, by means of the vacuum pump. The process is depicted in figure 7. It can be seen that as the vacuum pumps is operating (staring at $t \simeq 200$ s) the HPV pressure reduces at a large rate (until $t \simeq 400$ s) this behaviour is probably related to volatile gas extraction (air, non-condensible gas, possible decomposition products). As the pressure diminishes the rate of decrease also reduces, indicating the approaching of the saturation pressure and the consequent probable extraction of MDM vapor. As the vacuum pump is stopped (at $t \simeq 600$ s), the pressure rapidly rise, reaching and keeping constant the saturation value, thus indicating that no fluid decomposition occurred. This matching is also a confirmation of the consistency between the experimental and the calculated P-T value at this saturation point ($P = 0.014$ bar, $T = 42$ °C).

4.2 Experimental results
Due to the difficulties related to the accurate setting of the MCV PID parameters, the early test with MDM are performed with a constant valve opening set at 25%. The resulting test conditions are reported in table 4.

A picture of the test section during the experimental runs with MDM is shown in figure 10. Condensation of MDM vapor occurred along the back plate, which is not heated, in all performed tests. Condensation prevented the use of the double-passage Schlieren techniques, since liquid
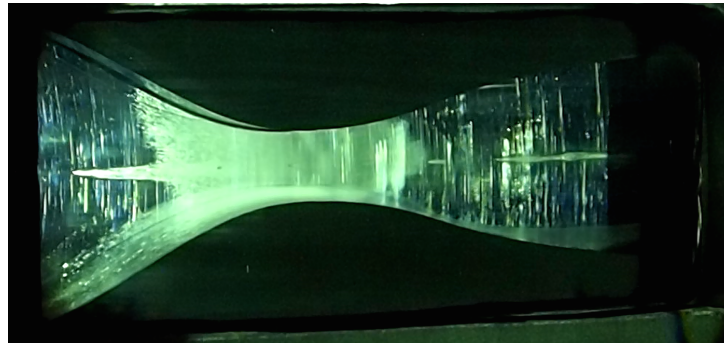
Figure 8: Picture of the test section during the experimental runs with MDM. The flow is from left to right. Condensation along the back plate is clearly visible. A liquid film is also visible in the convergent section of the nozzle.

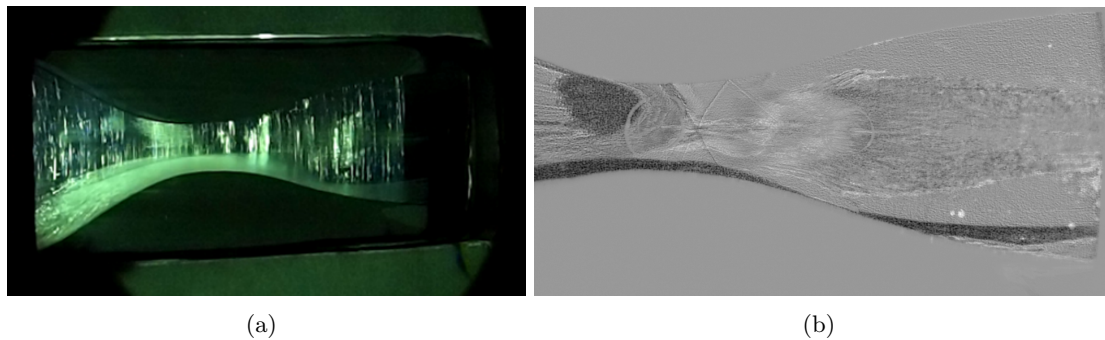(a)   (b)

Figure 9: Last part of the experimental run with MDM. The flow is from left to right. Total inlet conditions at this time are $P_{T6} = 100$ mbar, $T_{T6} = 84$ °C; the downstream pressure is $P_9 = 6$ mbar. (a) Picture of the test section; the liquid film is largely evaporated at the back plate. (b) Schlieren visualization; oblique shock waves immediately downstream of the recessed step are clearly visible.

drops and film over the back plate produced reflected rays featuring highly distortion in different directions, thus preventing the detection of the density gradients in the vapor phase. Direct observation of the test section revealed that indeed condensation occurs only along the metal plate. Moreover, two shock waves originating from step position were observed thus confirming the possibility of observing a supersonic nozzle flow in the vapor phase. This is also proved by partial Schlieren visualization of figure 9 obtained during the last part of the test, when the test section heating provided by the vapor flow is such that the liquid film is largely evaporated. The oblique shock waves originated immediately after the recessed step are clearly visible (together with their reflection at the contoured wall), thus confirming the occurrence of a supersonic flow of MDM vapor within the nozzle.

Figure 10 reports the instantaneous Mach number at the pressure tap located along the nozzle axis and at the throat section. The Mach number is computed from isentropic relations using the instantaneous values of the total and static pressure ratio and according to the pertinent thermodynamic model. From small-perturbation theory of transonic flows, the value of the Mach number in this peculiar location is independent from the fluid thermodynamics. Therefore the ideal-gas value measured for air (about 0.96) should be equal to that obtained for MDM in non-ideal conditions. Indeed a good agreement is observed during the first 15 s of the experiment, thus confirming the consistency of the pressure measurements. Departure from the expected value is believed to be related also to the presence of a thick liquid film along the bottom surface of the nozzle, probably caused by liquid entrainment within the main vapor flow from
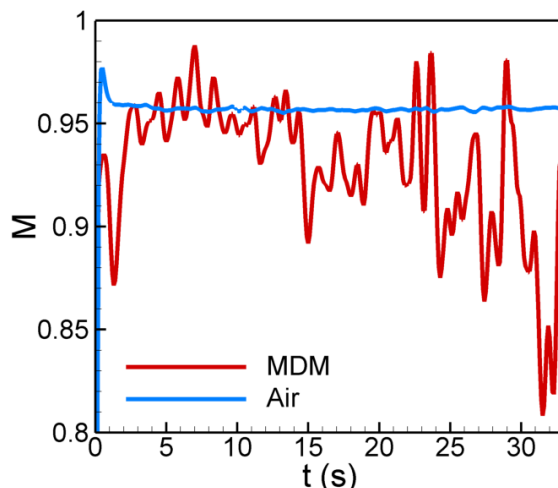
Figure 10: Mach number from the pressure tap located along the nozzle axis and at the throat section for the air and MDM test runs.

the settling chamber.

5. CONCLUSIONS

Preliminary results from the Test-Rig for Organic Vapors (TROVA) at Politecnico di Milano were reported. Pressure measurements are in good agreement with theoretical predictions for air, thus confirming the accuracy of the measurement chain and the efficiency of the throttling valve. The Schlieren bench is functional and provides an overview of the flow field, including the location of shock waves which is required to understand the pressure signal in the diverse operating conditions. Regarding the test run with the organic fluid MDM, the loading procedure and the liquid pump operation was verified. Degassing of the fluid is satisfactory: after vacuumising the HPV, the pressure immediately sets back to the vapor pressure at the considered temperature. The fluid follows the saturation curve while heating, thus indicating that no contaminants are present. Preliminary results for nozzle flow of MDM were found to be consistent with those obtained for air, though condensation along the back plate prevented its use as a mirror for the optical measurements. The appearance of shock waves induced by the recessed step confirms the occurrence of a supersonic nozzle flow of MDM in the vapor phase, during the last part of the test. The test-rig is currently being retrofitted with a new heating system to avoid condensation during the fluid heating phase, most notably in the piping connecting the HPV and the test section, and during the test runs.

REFERENCES

Angelino, G., Gaia, M., and Macchi, E. (1984). A review of italian activity in the field of organic rankine cycles. In *VDI Berichte - Proceedings of the International VDI Seminar, Zrich*, volume 539, Dsseldorf. VDI Verlag.

Bini, R. and Manciana, E. (1996). Organic rankine cycle turbogenerators for combined heat and power production from biomass. In *Energy Conversion from Biomass Fuels, Current Trends and Future System, Munich.*

Cinnella, P. and Congedo, P. M. (2007). Inviscid and viscous aerodynamics of dense gases. *J. Fluid Mech.*, 580:179–217.

Colonna, P., Harinck, J., Rebay, S., and Guardone, A. (2008). Real-gas effects in organic rankine cycle turbine nozzles. *J. Prop. Power*, 24:282–294.

Colonna, P., Nannan, R., Guardone, A., and Lemmon, E. W. (2006). Multi-parameter equations of state for selected siloxanes. *Fluid Phase Equilib.*, 244:193–211.

Colonna, P. and Rebay, S. (2004). Numerical simulation of dense gas flows on unstructured grids with an implicit high resolution upwind Euler solver. *Int. J. Numer. Meth. Fluids*, 46(7):735–765.

Duvia, A. and Tavolo, S. (2008). Application of orc units in the pellet production field: technical-economic considerations and overview of the operational results of an orc plant in the industry installed in madau (germany). Technical report, Turboden s.r.l., Italy.

Gaia, M. and Duvia, A. (2002). Orc plants for power production from biomass, 0.4-1.5 MWe: technology, efficiency, practical experiences and economy. In *7th Holzenergie Synposium*. ETH Zurich.

Guardone, A. (2007). Three-dimensional shock tube flows of dense gases. *J. Fluid Mech.*, 583:423–442.

Guardone, A., Spinelli, A., and Dossena, V. (2013). Influence of molecular complexity on nozzle design for an organic vapor wind tunnel. *ASME Journal of Engineering for Gas Turbines and Power*, 135:042307.

Harinck, J., Guardone, A., and Colonna, P. (2009). The influence of molecular complexity on expanding flows of ideal and dense gases. *Phys. of Fluids*, 21:086101, 1–14.

Hoffren, J., Talonpoika, T., Larjola, J., and Siikonen, T. (2002). Numerical simulation of real-gas flow in a supersonic turbine nozzle ring. *J. Eng. Gas Turbine Power*, 124:395–403.

Schuster, A., Karellas, S., Kakaras, E., and Spliethoff, H. (June 2009). Energetic and economic investigation of organic rankine cycle applications. *Applied Thermal Engineering*, 29(8-9):1809–1817.

Spinelli, A., Dossena, V., Gaetani, P., Osnaghi, C., and Colombo, D. (2010). Design of a test rig for organic vapours. In *Proceedings of ASME Turbo Expo, Glasgow, UK*.

Spinelli, A., Pini, M., Dossena, V., Gaetani, P., and Casella, F. (2013). Design, simulation, and construction of a test rig for organic vapours. *ASME Journal of Engineering for Gas Turbines and Power*, 135:042303.

ACKNOWLEDGEMENT

WAVE SPEED MEASUREMENTS IN NON-IDEAL COMPRESSIBLE FLOWS USING THE FLEXIBLE ASYMMETRIC SHOCK TUBE (FAST)

T. Mathijssen [1], M. Gallo [1], E. Casati [1], A. Guardone [2], P. Colonna [1*]

[1] Propulsion & Power, Delft University of Technology
2629 HS, Delft, The Netherlands
P.Colonna@tudelft.nl

[2] Department of Aerospace Science & Technology, Politecnico di Milano
Via La Masa 34, Milano 20156, Italy

* Corresponding Author

ABSTRACT

Non-ideal compressible fluid dynamics (NICFD) are defined as compressible fluid flows occurring in the dense vapour, dense vapour-liquid equilibrium or supercritical thermodynamic region. This type of flow can occur in expanders of organic Rankine cycle power plants. In order to study NICFD, a Ludwieg tube-type facility has been designed and constructed at Delft University of Technology. A large variety of fluids can be employed in the facility, but for this study D_6 siloxane is chosen as working fluid due to its high thermal stability and the possibility of encountering non-classical gasdynamic phenomena. This compound belongs to the siloxane class, which are also used as working fluids in ORC power systems. Gasdynamic experiments within the NICFD region are presented from which the wave speed and speed of sound can be inferred using the time-of-flight technique. These data can be used to improve and validate thermodynamic models.

1. INTRODUCTION

The field of fluid mechanics studying the motion of fluids in the dense-vapour, dense-vapour-liquid and supercritical thermodynamic region is called Non-ideal compressible fluid dynamics (NICFD). Such flows are characterized by, among other interesting phenomena, a quite different variation of the sound speed compared to that of ideal gases. This feature can be investigated by considering the fundamental derivative of gasdynamics Γ, defined by Thompson (1971) as

$$\Gamma \equiv 1 + \frac{\rho}{c}\left(\frac{\partial c}{\partial \rho}\right)_s,$$ (1)

in which ρ, c and s denote the fluid density, speed of sound, and entropy respectively. For an ideal gas, Γ is constant and equal to $(\gamma + 1)/2$ in ideal gases, in which γ is the ratio of specific heats. Whenever Γ is variable among the thermodynamic states of the fluid flow, NICFD occurs (Thompson, 1988).

The working-fluid flows within turbomachinery of Organic Rankine Cycle (ORC) power systems is one example where NICFD is encountered (Cramer, 1989; Brown and Argrow, 2000; Colonna et al., 2015). Other examples encompass supercritical carbon dioxide (scCO$_2$) power systems (Conboy et al., 2012; Rinaldi et al., 2015) and high temperature heat pumps (Zamfirescu and Dincer, 2009).

Flow measurements in the dense vapour region of complex organic fluids can contribute to the improvement of thermodynamic models and to the understanding of NICFD. ORC turbine designs benefit from better thermodynamic models through a more accurate prediction of flow patterns, such as shock waves. However, measurements in dense vapours of high molecular weight fluids are scarce (Nannan et al.,
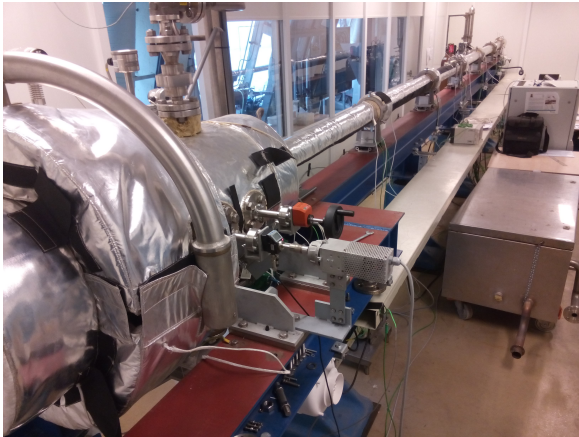
Figure 1: Picture of the FAST setup. In the foreground the LPP is visible, with the charge tube extending to the other side of the room. The vapour generator and condenser are not visible in this image.
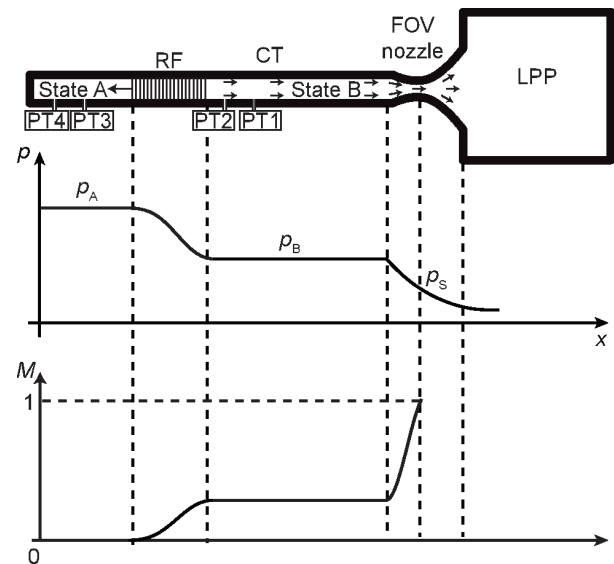

Figure 2: Schematic overview of a rarefaction wave experiment after opening the FOV. A rarefaction fan (RF) propagates into the charge tube (CT) at sonic speed *W*. The rarefaction starts a flow from stagnant condition A in the CT to condition B. It flows through a choked nozzle to the low pressure plenum (LPP). The pressure *p* and Mach number *M* along the tube are displayed qualitatively.

2007; Weith et al., 2014). In order to fill this gap, the flexible asymmetric shock tube (FAST), an unconventional Ludwieg tube, is designed and installed at Delft University of Technology (Colonna et al., 2008a), in the Netherlands, with the aim of studying wave propagation in the dense vapour of organic compounds.

This work documents the FAST set-up and the first experimental results of wave propagation measurements in the dense vapour of dodecamethylcyclohexasiloxane (D_6). Fig. 2 shows a schematic overview of a classical rarefaction wave experiment. The charge tube (CT) is filled with the dense organic vapour and kept at the desired pressure and temperature. The fast-opening valve (FOV), initially closed, is opened, thus allowing the fluid to flow towards the low pressure plenum (LPP), which is maintained at a lower pressure. Consequently a rarefaction travels into the CT.

A description of the set-up is provided in Sec. 2: it provides details about the components equipping the complete system as-built, the experimental procedure, and an overview of the control and data acquisition system. The results of the rarefaction wave experiments in a variety of incondensable gases are reported and discussed in Sec. 3. In Sec. 4 results from preliminary rarefaction wave measurements in D_6 are reported. Sec. 5 summarizes concluding remarks and outlines future work.

2. THE FAST AND THE EXPERIMENTAL PROCEDURE

The mechanical and heating equipment is described in Sec. 2.1 by outlining the procedure of a typical experiment. The measurement and monitoring instruments as well as the control system are briefly reported in Sec. 2.2.
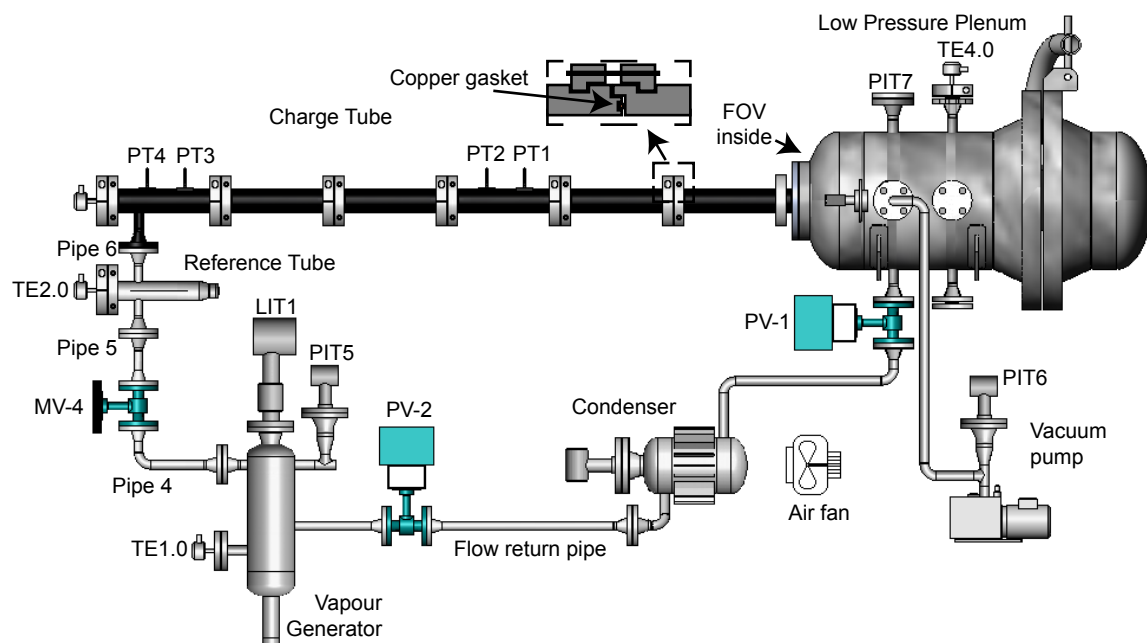
Figure 3: Overview of the FAST setup. Relevant labels are placed to the equipment and instruments. The fast-opening valve is placed inside the low pressure plenum.

2.1 Equipment & procedure

A schematic representation of the FAST is reported in Fig. 3. All pipes, vessels, and parts in contact with the working fluid are made of stainless steel (316Ti).

Before starting an experiment the working fluid needs to be purified in order to remove air and moisture deemed as the main causes of thermal decomposition of the adopted organic compounds at high temperature (Dvornic, 2004). The fluid, after being filtered with a 3Å molecular sieve and a paper filter, is inserted into a stainless steel Swagelok cylinder (type 304L-HDF-81CAL) and a Pfeiffer vacuum pump (type Duo 5 M) is used to extract any incondensable gases. By immersing the cylinder in a pool of liquid nitrogen, the fluid freezes and, as a consequence, releases the dissolved gases that are extracted by using a vacuum pump once the fluid has melted. This freezing-thawning procedure is repeated at least 2 times before filling the vapour generator through pipe 1, see Fig. 4.

The vapour generator is a custom made 5.9 liter vessel, designed to heat and evaporate the working fluid isochorically (valves MV-4 and PV-2 closed, see Fig. 3) up to the desired pressure and temperature by utilizing electric heaters. Most of the thermal energy is supplied to the vapour generator by a 1.5 kW Kurval ceramic band heater (custom built ETB HRHK-type) covering the bottom section, see Fig. 4, because the lower part of the vapour generator is always in contact with liquid. This ensures a high heat transfer coefficient between the heater and the liquid fluid inside the vessel and helps avoiding hot spots that could trigger thermal decomposition of the fluid. Preliminary tests revealed periodic instabilities of the thermal control induced by condensation phenomena occurring in the unheated section of the vessel (pipe 2 and 3, Fig. 4). By heating all the walls of the vapour generator, these instabilities were eliminated. Therefore, the main section of the vessel is heated by a 2.8 kW ceramic band heater (custom built ETB HRHK-type). The complex geometry of the top section made the implementation of a band heater impossible, so the upper section of the vapour generator is heated with a 6 m long 1 kW Welvy Joule dissipation heating wire (type HSQ/060). Another heating wire of the same type is wrapped around pipe 2 and 3, and a third wire around pipe 4, see Fig. 3. Where possible to apply, the heating element presses into a KWX 2 mm conducting graphite layer (type KU-CBGA2000-0H) to improve the thermal contact, which also ensures an even surface temperature distribution, thanks to its high in-plane thermal
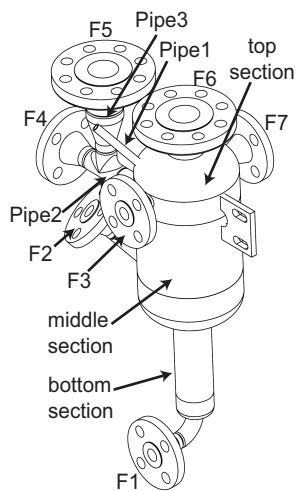
Figure 4: Drawing of the vapour generator. The numbers correspond to the flanges connecting with the following equipment: F1: outlet to extract liquid, F2: PT-100 sensor, F3: return pipe from the LPP, F4: burst disc, F5: static pressure transducer, F6: liquid level meter, F7: reference tube
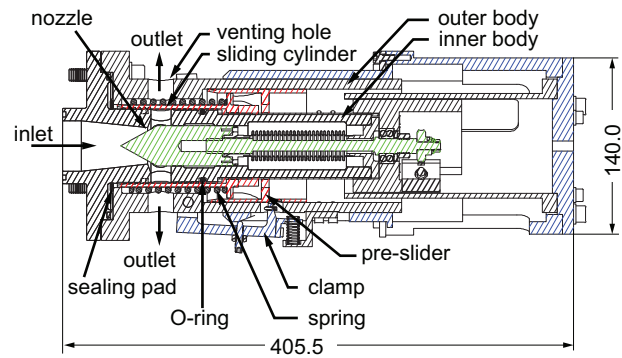

Figure 5: Drawing of the cross-section of the Fast Opening Valve. The actuation system (in blue) slides slowly to the right side, which pushes the clamps outward. Once the clamps release the pre-slider, the fast moving components (in red) come into motion because the compressed spring pushes the sliding cylinder and the pre-slider away. After the sliding cylinder is pushed across the venting holes, he fluid is free to flow from the inlet to the outlet. The nozzle insert (in green) can be moved in the longitudinal direction in order to control the throat area.

conductivity. This is required to obtain a uniform temperature and to prevent hot spots that could promote thermal decomposition. The entire vapour generator is covered with a layer of minimum 50 mm rockwool insulation to limit heat losses to the environment.

Once the desired pressure is attained in the vapour generator, a manually operated Tyco 19.05 mm globe valve MV-4 (type Megastar) is opened and vapour flows through pipe 4 to the reference tube (RT) and charge tube (CT), see Fig. 3. The purpose of the RT is to finely control the vapour superheating and to provide a reference for the thermal control of the CT, as further explained in Sec. 2.2. The RT is a 500 mm long tube with an internal diameter of 40 mm and 15 mm thick walls. The thickness of the walls enhances an even distribution of the thermal power. The thermal energy is supplied by two Tyco custom-made heating jackets around the tube, which includes a 25 mm glass silk insulation layer. A 335 W version is placed around the RT and a 180 W version around the flange of the RT. To prevent condensation in pipe 6, see Fig. 3, a 2.1 m long 370 W Welvy Joule dissipation heating wire (type HSQ/021) is applied with a 2 mm thick graphite layer placed underneath.

The geometry of the CT and of the RT are identical, except for their length. The CT is composed of six pipe segments, each 1520 mm long. The pipe segments feature a male-to-female connection and a red copper seal (see the zoomed section in Fig. 3) which allow for satisfactory sealing both in case the inner volume is at superatmospheric pressure, or under vacuum conditions. The CT assembly measures 9 m in total and is placed on a sliding support to allow for its thermal expansion when at high temperature. Each segment is fitted with a custom made Tyco 950 W Glass Silk heating jacket and the couplings between the elements are fitted with two 0.5m Welvy 180 W Joule heating electric wire (type: HBQ/005), all covered by a 25 mm glass silk insulation layer. Immersion of temperature sensors in the CT would inherently disturb the flow field of interest. Instead, the outside wall temperature is measured both in the RT and CT. Due to the geometric equivalence of the RT and the CT, imposing the same temperature on the walls results in the same fluid temperature inside the tube.

The end of the CT is closed off by a FOV, arguably the most complex mechanical part of the setup, see Fig. 5. This custom designed valve is able to operate at high temperatures without lubrication to

avoid contamination of the working fluid. It might however be expected that the siloxane working fluids act as a lubricant. The valve is contained in the LPP and can be operated remotely, keeping the entire facility hermetically sealed for multiple experiments. In the opened position, the working fluid can flow through venting holes present in the inner and outer body in the radial direction. In the closed position, a sliding cylinder is pushed between these bodies, obstructing the flow through the venting holes. The sliding cylinder presses into a Kalrez compound sealing pad on the flange to ensure sealing. On the other side, the sealing is performed by a Kalrez O-ring with a diameter of 47.22 mm and a thickness of 3.53 mm between the sliding cylinder and the inner body. Since the thermal swelling of the O-ring has a strong effect on the friction of the sliding cylinder during the fast opening, a 3 mm thermocouple (K-type) inserted in a hole in the mounting flange of the FOV monitors the temperature of the steel. An Inconel steel spring is compressed and three radial clamps engage the pre-slider to prevent the spring from being released. To open the valve, the clamps are moved in the outward direction, allowing the spring to push the sliding cylinder and the pre-slider away, thus leaving the venting holes open. A nozzle insert creates a throat area in order to choke the flow, thus preventing flow disturbances from travelling upstream. For this reason the throat is located upstream of the sealing, as opposite to solutions that are typical in Ludwieg tubes (Schrijer and Bannink, 2010; Knauss et al., 1999). The nozzle insert can be moved remotely in the longitudinal direction to change the throat area section, between approximately 420 mm^2 and 600 mm^2, and this allows to modulate the strength of the rarefaction waves.

The FOV is contained in the LPP, a 113 liter cylindrically shaped vessel, see Fig. 3, with an outer diameter of 406.4 mm and 9.53 mm thick walls. The electric motor triggering the FOV and the manual nozzle positioning gear are mounted on the LPP with feedthrough shaft connections sealed with copper gaskets. A lid gives access to the vessel interior for installation of the FOV, and is sealed by a graphite gasket. The LPP can be heated by 4 custom built Tyco heating jackets with a nominal power of 1450, 425, 960 and 490 W respectively.

The vapour flows from the LPP through globe valve PV-1 into a condenser. The condensed liquid accumulates in a flow return pipe and returns via globe valve PV-2 into the vapour generator, see Fig. 3.

2.2 Instruments & Control

The thermal energy supply to the various sections of the facility is regulated by digital PID controllers, which modulates the electrical voltage to the heating elements via RKC 1-phase thyristors (model: THV-1PZ-020-5*NN-6).

In the vapour generator, the static pressure had initially been used as process variable for the main heater at the bottom section, measured by a Klay pressure transmitter (type 2000-SAN-4-F(w)-I-HT-G43) with a specified accuracy of 0.1% of the full range of 30 bar. Because the operating pressure range of the vapour generator spans from very far from the critical point to close-to-critical conditions, the response in pressure to the supplied thermal power changes dramatically, due to the difference in the pressure derivative with respect to temperature at constant specific volume $\left(\frac{\partial P}{\partial T}\right)_v$. Consequently, the PID parameters should also be adapted depending on the operated pressure. This is avoided by converting the pressure into a saturation temperature with the help of in-house software (Colonna et al., 2012) implementing suitable fluid thermodynamic property models, (see, e.g. Nannan and Colonna 2009). Now the same PID parameters can be used throughout the entire operating range, because the change in specific heat capacity is sufficiently moderate. At the same time, the fast response of the pressure transmitter is still exploited for the control. The fluid saturation temperature is compared by a direct measurement of the liquid temperature as sensed by a Klay 4-wire Pt-100 sensor with insertion length of 180 mm and 6 mm diameter (type TT-E-D-F-L180xD6-S-P2-P13), which is calibrated using a Presys calibration oven (type T-350P) to within a tolerance of 0.12 °C. The other heaters on the vapour generator are each regulated based on the temperature difference as measured by the Pt-100 and a 1 mm thick thermocouple (K-type) applied underneath each heater.

The heat supply to the RT is regulated by a PID controller with as process variable the superheating of
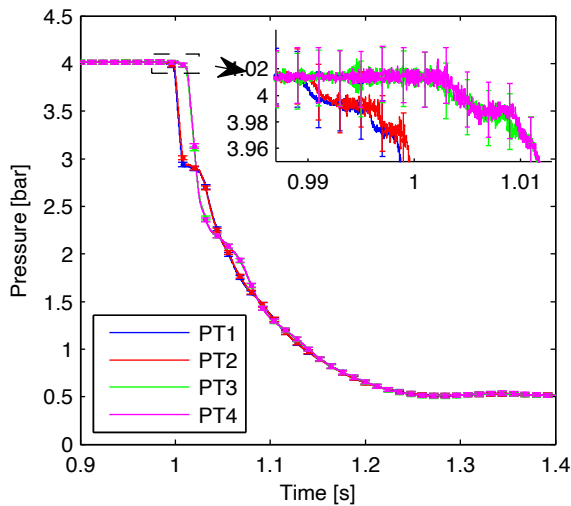
Figure 6: Pressure signals of experiment 25 measured by transducers PT1 to PT4. The valve opening results in a pressure drop from 3.97 bar to 2.88 bar, which is preceded by two other small pressure drops. These are attributed to an initial leakage flow that starts as soon as the FOV sliding cylinder detaches from the seal.
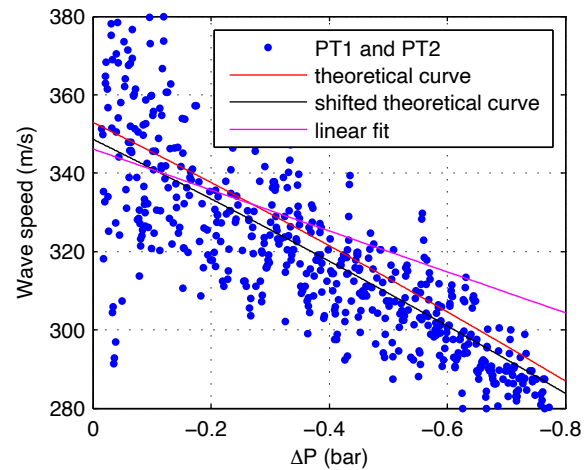

Figure 7: Wave Speed in N_2 as a function of the pressure drop. The blue dots are the experimental results obtained with the time-of-flight method. The red line is the theoretical curve. The black line is a shift of the theoretical curve with the average deviation from the theoretical curve. The magenta line is a linear fit of the data. The shifted theoretical curve and the linear fit are made based on 25 % of Δp_{rel} = -0.2 bar

the vapour, measured by the difference in temperature of the vapour in the RT and of the liquid in the vapour generator. The temperature in the RT is measured with a Klay 3-wire Pt-100 sensor (type TT-E-D-F-L250xD6-S-P2-P13) with 250 mm insertion length and 6 mm diameter, and is calibrated in the same manner as the one in the vapour generator. An identical resistance temperature detector (RTD) as the one in the RT is used to monitor the temperature in the CT.

The fluid temperature inside the CT is controlled by imposing the same wall temperature on the CT as on the RT, which are geometrically equivalent, except for the length. The process variable of each control loop is the difference in wall temperature between the RT and the respective CT pipe segment and coupling. Instead of measuring the temperature of the two thermocouples and calculating the difference in temperature, here the two thermocouples are connected to each other and the voltage difference is directly measured to reduce the measurement error. The 1 m long and 0.5 mm thick thermocouple (type K) is placed in a groove in the RT and in each CT element, bonded to the tube with Aremco silver-filled conductive ceramic adhesive (type 597A) to ensure the measurement of the wall temperature.

To measure the passing rarefaction, four dynamic pressure measurement stations PT1-PT4 are created by flush mounting a high-temperature Kulite fully active four arm wheatstone bridge pressure transducer (type XTEH-10LAC-190M-21bar-A) that measures the pressure with an accuracy of 0.5 % of the full scale of 21 bar along the CT at a distance of 4, 4.3, 8.4 and 8.7 m from the FOV respectively, see Fig. 3. The signals acquire at a frequency of 250 kHz and are scaled after each experiment with the more accurate value of the pressure before and after the experiment, measured by the static pressure transducers. The sensors are placed in pairs to give the possibility to have a time of flight measurement at two different locations in the tube.

nr	fluid	P_{CT} [bar]	T_{CT} [°C]	Γ [-]	ΔP_{wave} [bar]	A_{nozzle} [mm²]	c_{model} [m/s]	c_{fit} [m/s]	c_{shift} [m/s]
1	He	6.01	17.3	1.34	1.74	459	1006	998	964
2	He	4.90	22.7	1.34	0.28	79	1014	1014	1028
3	He	6.09	48.9	1.34	1.69	438	1059	1005	1072
4	He	6.50	50.0	1.34	0.32	67	1060	1121	955
5	He	6.66	99.2	1.34	2.01	483	1138	1274	1169
6	He	6.02	149.4	1.34	1.84	489	1212	1225	1182
7	He	7.29	269.4	1.34	0.33	62	1373	1547	1348
8	He	8.47	269.9	1.34	0.44	72	1374	1424	1483
9	air	6.31	17.6	1.21	1.62	456	343	341	341
10	air	4.08	18.0	1.20	0.97	418	343	338	339
11	air	7.01	19.1	1.21	1.81	459	344	338	339
12	air	4.86	20.0	1.21	0.21	67	344	359	350
13	air	5.39	20.0	1.21	0.23	68	344	344	353
14	air	7.13	22.0	1.21	0.30	67	345	338	347
15	air	6.15	49.1	1.21	1.62	468	361	353	356
16	air	6.98	95.0	1.20	0.27	61	386	375	388
17	air	6.80	99.5	1.20	1.76	461	388	390	384
18	CO_2	5.99	18.0	1.13	1.50	471	262	257	259
19	CO_2	6.42	50.0	1.12	1.59	465	275	274	273
20	CO_2	6.64	100.3	1.12	1.64	464	296	294	293
21	CO_2	6.13	149.7	1.11	1.50	459	314	321	315
22	N_2	1.09	25.3	1.20	0.35	576	352	337	338
23	N_2	1.12	25.4	1.20	0.33	531	352	379	349
24	N_2	4.00	25.7	1.20	1.00	443	353	360	353
25	N_2	4.01	25.8	1.20	1.08	481	353	346	349
26	D_6	1.26	264.2	0.86	0.09	169	89.8	89.5	88.4
27	D_6	1.26	293.7	0.91	0.15	278	94.3	94.0	94.1
28	D_6	1.27	298.0	0.91	0.18	328	94.8	96.9	93.9
29	D_6	1.27	300.1	0.92	0.14	254	95.1	98.3	94.0
30	D_6	2.52	301.1	0.79	0.26	254	84.6	84.9	83.5
31	D_6	2.38	302.3	0.81	0.21	220	86.2	83.5	82.7
32	D_6	2.53	305.1	0.79	0.29	286	85.4	84.3	83.5

Table 1: Results from rarefaction measurements. p_{CT} and T_{CT} are the measured initial pressure and temperature in the charge tube. Γ and c_{model} are the fundamental derivative of gasdynamics and speed of sound respectively calculated using the most accurate thermodynamic model for the measured conditions (uncertainty unknown). Δp_{wave} is the pressure difference across the rarefaction. A_{nozzle} is the nozzle area calculated using the pressure drop across the expansion. c_{fit} and c_{shift} are the speed of sound as measured by fitting the experimental time-of-flight results using a linear function and by shifting the theoretical curve with the average deviation respectively.

3. RAREFACTION WAVES IN INCONDENSABLE GASES.

In order to verify the correct functioning of the facility, a series of experiments are performed using incondensable gases in the ideal gas regime. The CT is filled with the gas under pressure, while the LPP is kept at vacuum conditions. The FOV is opened after which a rarefaction wave propagates into the CT, see Fig. 2. A flow starts from the CT into the LPP, which is attaining a sonic speed in the throat.

The pressure recordings of rarefaction experiment 25 (see Table 1) are displayed in Fig. 6. The working fluid in that experiment is nitrogen and the pressure is 4.01 bar in the CT and < 10 mbar in the LPP, both at an ambient temperature of 25.8 °C. The FOV opening sequence can be inferred from these pressure data: as soon as the FOV opening is initiated, the sliding cylinder is pushed by the compressed spring, see Fig. 5. A small opening is created when the sliding cylinder does not touch the seal anymore, and the flow gets choked close to this position. This causes a small pressure drop of approximately 20 mbar. As the slider moves further, the position of minimum cross-section of the flow changes to a section between the slider and the inner body, which is slightly larger than the initial choked section. This is revealed by

a second small drop in the pressure of approximately 20 mbar. Finally the sliding cylinder passes over the venting hole of the inner body, and the flow chokes at the designated nozzle. This is seen as the large pressure drop down to 2.88 bar.

The nozzle throat cross-sectional area is not easily recovered from the FOV geometry and therefore it is inferred from the measurements by assuming a steady flow from state B through the nozzle, see Fig. 2. The mass flow in state B is evaluated using the density calculated by using the isentropic relations from state A, the known cross-sectional area of the CT and the evaluated flow velocity using the Riemann invariant from state A. The isentropic relations are used to calculate the density and velocity in the throat. The calculated throat area ranges from 418 to 576 mm^2. Several experiments were performed using a special nozzle insert, for which the calculated throat area ranges from 61 to 79 mm^2, see Table 1.

The local wave propagation speed in the CT equals the local speed of sound minus the local flow velocity. A theoretical curve can be constructed by calculating the wave propagation speed as a function of the pressure drop of the rarefaction. At zero pressure drop, the wave propagation speed equals the speed of sound, since stagnant conditions are assumed in the CT before opening the valve, and is evaluated using the reference equation of state. For a given pressure drop, the wave propagation speed is evaluated by calculating the local speed of sound using the isentropic relations, while the local flow velocity is calculated by evaluating the Riemann invariant in the undisturbed state (Thompson, 1988).

By applying the time-of-flight method to the signals of two pressure transducers, an experimental value of the local wave propagation speed is obtained. This is done by first selecting the relevant part of the pressure signal as follows: the beginning of the wave at $t = t_{start}$ is formally identified as the time when the pressure departs more than 15 mbar from the initial value P_{CT}. The threshold is chosen such that it exceeds the noise level. The end of the unperturbed portion of the signal is chosen when the head of the wave is expected to reach the end of the CT at $t = t_{end}$. The estimate is performed by using the speed of sound from the accurate reference thermodynamic model, therefore $t_{end} = t_{start} + \Delta x / c_{model}$, where Δx is the distance between the sensor location and the end of the CT. The relevant portion of the signal ΔP_{rel} spans from P_{start} to P_{end}. This span is divided into intervals of two times the resolution of 0.32 mbar of the pressure signal of the current measurement system. The time-of-flight method is applied to corresponding subintervals from different sensors to compute the local wave propagation speed. The measurements of sensors PT3 / PT4 are quickly influenced by the reflection of the rarefaction from the CT end wall, so only the measurements of sensors PT1 / PT2 are considered.

Fig. 7 shows for the example of experiment 25 the charts that can be obtained, from which the speed of sound can be retrieved at $\Delta p \to 0$. Wave speed values as a function of the measured pressure drop are shown together with fitting curves used to estimate the speed of sound. To reduce inaccuracies introduced by the FOV in the determination of the speed of sound to a negligible level, only the first 25 % of the relevant pressure span is taken, while keeping a minimum of 40 mbar, such that $\Delta p_{max} = \max{(0.25 p_{rel}, 0.04\,bar)}$. Two methods are used to fit the experimental data: a simple linear fit and a fit obtained by shifting the theoretical curve with the average deviation of the measurement points with respect to this curve. The resulting speed of sound c_{fit} and c_{shift} are reported in table 1. For air, CO_2 and N_2, both methods deliver an accurate estimate of the speed of sound, compared to the value obtained from the reference thermodynamic model (Lemmon et al., 2013), which corresponds to the ideal gas model in this regime. The only exception is the linear fit for experiment 23. The average error and standard deviation with respect to the model are 2.1 ± 1.6 % and 1.1 ± 1.1 % for the linear fit and the shifted theoretical curve respectively. For helium, the average error and standard deviation with respect to the model are 5.1 ± 4.6 % and 4.0 ± 3.1 % for the linear fit and the shifted theoretical curve respectively. The reason for the larger error is due to the higher speed of sound of helium in combination with the finite process start-up time of the FOV resulting in a very small usable relevant portion of the signal.
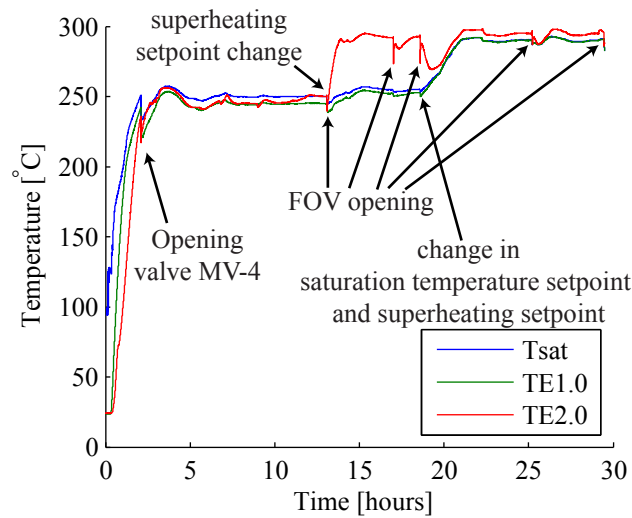
Figure 8: Temperature recordings during the experimental campaign on siloxane D_6. Tsat is obtained from the measured pressure in the vapour generator by means of the suitable thermodynamic model from Nannan and Colonna (2009). TE1.0 is the temperature measured by the PT-100 sensor in the vapour generator. TE2.0 is the temperature measured by the PT-100 sensor in the reference tube.

4. RAREFACTION WAVES IN SILOXANE D_6

Experiments to measure the expansion wave speed in D_6 (dodecamethylcyclohexasiloxane, $C_{12}H_{36}O_6Si_6$) are performed from which the speed of sound is estimated. Gaschromatographic analysis confirmed the specification of the supplier that the fluid has a 96 % purity. Experiments were conducted at several thermodynamic states, see experiments 26 to 32 in Table. 1. Fig. 8 shows the temperature of the fluid in the vapour generator and in the reference tube during the entire test campaign. Part of the liquid in the vapour generator is flashed each time valve MV-4 is opened after an experiment. The measured temperature fluctuations in the reference tube and charge tube had a period of approximately 2 hours with an amplitude of up to 3 °C for both temperature levels.

Pressure recordings of experiment 28 are displayed in Fig. 9. Calculations using the resulting pressure drop from the experiments result in a significantly lower nozzle area than the 460 to 600 mm^2 that was expected based on the geometry, see Table 1, which may indicate that there is accumulation of condensed fluid in the unheated FOV.

The wave propagation speed has been computed from the experimental data and compared with the theoretical curve, which is constructed in the same manner as for the incondensable gases. The ideal gas model can not be used in this case, and consequently the Riemann invariant can not be integrated analytically. The local flow velocity is instead evaluated by integrating the Riemann invariant numerically. Estimation of the speed of sound is obtained with the best available thermodynamic model for pure D_6, which shows a 30 % deviation on the speed of sound with the sole reliable measurement, which is performed in the liquid state (Colonna et al., 2008b). Results from experiment 28 are displayed in Fig. 10. The wave speed calculated from experimental data for this experiment is within 8 % of the value predicted by the thermodynamic model. Only for a pressure drop lower than 12 mbar the deviation is higher, because the pressure gradient is very low, thus the influence of noise more significant. By fitting the experimental data in the same manner as illustrated for the case of incondensable gases, i.e. using a linear fit, and by shifting the theoretical curve, the speed of sound c_{fit} and c_{shift} is obtained. The average error and standard deviation with respect to the value predicted by the thermodynamic model are 1.6 ± 1.2 % for the linear fit and 1.6 ± 1.1 % for the shifted theoretical curve. The experimental results are unexpectedly close to model predictions, considering that, differently from the case of incondensable
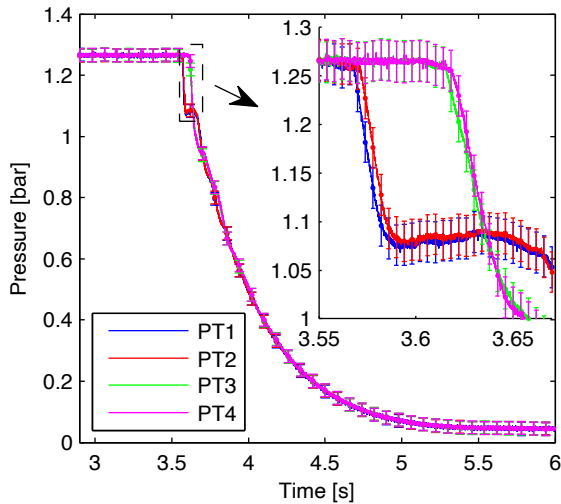
Figure 9: Pressure recordings during a D_6 experiment. The conditions in the CT are 1.27 bar and 298 °C. PT1 to PT4 are the pressure recordings of the sensor closest to the FOV to furthest away from the FOV, respectively.
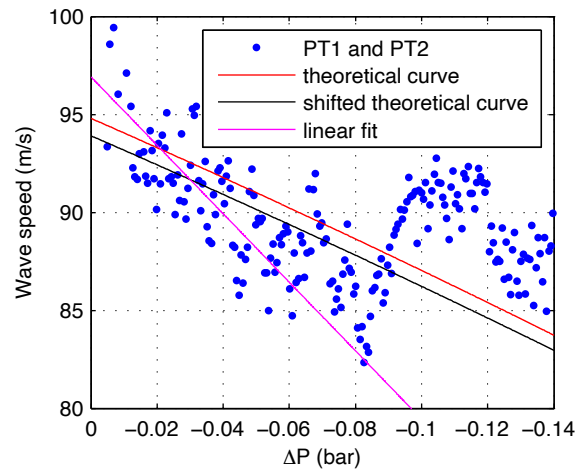

Figure 10: Wave speed in D_6 siloxane as a function of the pressure drop. The blue dots are the experimental results obtained with the time-of-flight measurements. The red line is the theoretical curve. The black line is a fit of the experimental data using a shift of the theoretical curve. The magenta line is a linear fit of the data.

gas, the D_6 thermodynamic model is expected to be rather inaccurate for states in the close proximity of the saturation curve.

5. CONCLUSION & FUTURE WORK

A novel Ludwieg-tube-type facility has been commissioned at Delft University of Technology, with the purpose of performing measurements on rarefaction waves in dense organic vapours. The pressure and temperature of the working fluid can be regulated independently from each other, such that any thermodynamic state can be achieved within the limits of the measurement system of 21 bar and 400 °C. Experiments on rarefaction waves in a number of incondensable gases have been conducted to validate the correct functioning of the facility. A novel algorithm is devised to estimate the speed of sound from rarefaction experiments. Experiments using siloxane D_6 show the feasibility of the original design concept up to 300 °C: rarefaction wave speed measurements were successfully performed, providing values of the speed of sound that are within 1.6% of the predictions of the best available thermodynamic model (the model itself is known to be affected by uncertainties of 30 % for the speed of sound).

REFERENCES

Brown, B. and Argrow, B. (2000). Application of Bethe-Zel'dovich-Thompson fluids in organic Rankine cycle engines. *J. Propul. Power*, 16(6):1118--1124.

Colonna, P., Casati, E., Trapp, C., Mathijssen, T., Larjola, J., Turunen-Saaresti, T., and Uusitalo, A. (2015). Organic Rankine cycle power systems: Fom the concept to current technology, applications and an outlook to the future. *J. Eng. Gas Turb. Power*, 137(10):100801.

Colonna, P., Guardone, A., Nannan, N., and Zamfirescu, C. (2008a). Design of the dense gas flexible asymmetric shock tube. *J. Fluids Eng.*, 130(3). 034501.

Colonna, P., Nannan, N. R., and Guardone, A. (2008b). Multiparameter equations of state for siloxanes:

$[(CH_3)_3\text{-Si-O}_{1/2}]_2\text{-[O-Si-}(CH_3)_2]_{i=1,\dots,3}$ and $[\text{O-Si-}(CH_3)_2]_6$. *Fluid Phase Equilib.*, 263(2):115--130.

Colonna, P., van der Stelt, T. P., and Guardone, A. (2012). FluidProp (Version 3.0): A program for the estimation of thermophysical properties of fluids.

Conboy, T., Wright, S., Pasch, J., Fleming, D., Rochau, G., and Fuller, R. (2012). Performance characteristics of an operating supercritical CO_2 Brayton cycle. *J. Eng. Gas Turb. Power*, 134(11).

Cramer, M. S. (1989). Shock splitting in single-phase gases. *J. Fluid Mech.*, 199:281--296.

Dvornic, P. R. (2004). High temperature stability of polysiloxanes. *Silicon Compounds: Silanes and Silicones, Gelest Catalog*, pages 419--432.

Knauss, H., Riedel, R., and Wagner, S. (1999). The shock wind tunnel of Stuttgart university - a facility for testing hypersonic vehicles. In *9th International Space Planes and Hypersonic Systems and Technologies Conference*, number AIAA 99-4959.

Lemmon, E., Huber, M., and McLinden, M. (2013.). NIST standard reference database 23: Reference fluid thermodynamic and transport properties-REFPROP, version 9.1.

Nannan, N. and Colonna, P. (2009). Improvement on multiparameter equations of state for dimethyl-siloxanes by adopting more accurate ideal-gas isobaric heat capacities: Supplementary to P. Colonna, N. R. Nannan, A. Guardone, E. W. Lemmon, Fluid Phase Equilib. 244, 193 (2006). *Fluid Phase Equilib.*, 280(1--2):151--152.

Nannan, N., Colonna, P., Tracy, C., Rowley, R., and Hurly, J. (2007). Ideal-gas heat capacities of dimethylsiloxanes from speed-of-sound measurements and ab initio calculations. *Fluid Phase Equilib.*, 257(1):102--113.

Rinaldi, E., Pecnik, R., and Colonna, P. (2015). Computational fluid dynamic simulation of a supercritical CO_2 compressor performance map. *J. Eng. Gas Turb. Power*, 137(7):072602.

Schrijer, F. and Bannink, W. (2010). Description and flow assessment of the delft hypersonic ludwieg tube. *J. Spacecraft Rockets*, 47(1):125--133.

Thompson, P. A. (1971). A fundamental derivative in gasdynamics. *Phys. Fluids*, 14(9):1843--1849.

Thompson, P. A. (1988). *Compressible Fluid Dynamics*. McGraw-Hill.

Weith, T., Heberle, F., Preißinger, M., and Brüggeman, D. (2014). Performance of siloxanes mixtures in a high-temperature organic Rankine cycle considering the heat transfer characteristics during evaporation. *Energies*, 7:5548--5565.

Zamfirescu, C. and Dincer, I. (2009). Performance investigation of high-temperature heat pumps with various BZT working fluids. *Thermochim. Acta*, 488(1–2):66 -- 77.

ACKNOWLEDGEMENT

SCALING OF GAS TURBINE FROM AIR TO REFRIGERANTS FOR ORGANIC RANKINE CYCLE (ORC) USIING SIMILARITY CONCEPT

Choon Seng Wong[1]*, Prof. Susan Krumdieck[2]

[1,2]Department of Mechanical Engineering, University of Canterbury,
Private Bag 4800, Christchurch 8041, New Zealand.
choon.wong@pg.canterbury.ac.nz[1], susan.krumdieck@canterbury.ac.nz[2]

* Corresponding Author

ABSTRACT

Organic Rankine Cycle (ORC) could be used to generate power from low temperature heat sources or improve overall cycle efficiency in waste heat applications with minimal environmental pollution. The design and development of an ORC turbine, however, is a complex and costly engineering problem. The common refrigerants for an ORC application exhibit non-ideal gas behaviour and some unfavourable characteristics, such as flammability and toxicity. These characteristics further increase the complexity of the design and laboratory testing process of a turbine. Similitude, or similarity concept, is an essential concept in turbomachinery to allow the designer to scale a turbine design to different sizes or different working fluids without repeating the whole design and development process. Similarity concept allows the testing of a turbo-machine in a simple air test bench instead of a full scale ORC test bench. The concept can be further applied to adapt an existing gas turbine as an ORC turbine using different working fluids.

This paper aims to scale an industrial gas turbine to different working fluids, other than the fluid the turbine was originally designed for. Three different approaches using the similarity concept were applied on the turbine performance data using compressed air to generate the performance curve for two refrigerants, namely R134a and R245fa. The scaled performance curves derived from the air performance data were compared to the performance map generated using 3D computational fluid dynamics (CFD) analysis tools for R134a and R245fa. The three approaches were compared in term of the accuracy of the performance estimation, and the most feasible approach was selected. The result shows that complete similarity cannot be achieved using two turbo-machines with different working fluids, even at the best efficiency point for particular expansion ratio. Constant $\Delta h_{0s}/a_{01}^2$ is imposed to achieve similarity, but the volumetric ratio is varying using different working fluids due to the variation of sound speed. The differences in the fluid properties and the expansion ratio lead to the deviation in turbine performance parameters, velocity diagram, turbine's exit swirl angle, and entropy generation. The use of $\Delta h_{0s}/a_{01}^2$ further limits the application of the gas turbine for refrigerants with heavier molecular weight to a pressure ratio less than the designed pressure ratio using air. The specific speed at the best efficiency point with different expansion ratio was shifted to a higher value if higher expansion ratio was imposed. A correction chart for R245fa was attempted to estimate the turbine's performance at higher expansion ratio as a function of volumetric ratio.

1. INTRODUCTION

The adaptation of an existing turbines for ORC application using different working medium can reduce the developmental effort involved in turbomachinery design aspects, such as re-designing the turbine wheel, prototyping and re-conducting the laboratory testing. The lack of documentation in literature about the adaptation of off-the-shelf turbines in applications other than the application for which they were originally designed has impeded the further development for ORC new-entrants. Turbines are usually designed for a particular set of specific speed and operating conditions, for a

specific working fluid and a specific application. The adaptation of an existing turbine for the ORC application using a different working medium is fundamentally subjected to the similitude of the design analysis of turbomachinery, which is also known as similarity concept.

. Non-dimensional parameters of turbomachines for similarity concept have been derived using the Buckingham Pi theorem. In turbomachinery there are numerous dimensionless groups possible from the seven fundamental variables, such as flow coefficient, head coefficient, power coefficient, and Reynolds number. These non-dimensional groups serve as fundamental parameters for turbomachines handling compressible or incompressible fluids. A number of other important turbine parameters include specific speed, specific diameter, and loading coefficients. The introduction of specific speed allowed the rapid development in the experimental testing of hydraulic turbines in the 1900s (Meher-Homji, 2000) and facilitated the selection of turbomachines' types for different applications (Balje, 1981). The performance mapping using flow coefficient and loading coefficient has facilitated the preliminary design process for both axial flow turbines (Dixon & Hall, 2010) and radial inflow turbines (Chen & Baines, 1994). These parameters also allow turbomachinery designers to scale a turbine from one application to another application, with different wheel size, different inlet operating conditions, and different working mediums (Aungier, 2006; Japikse & Baines, 1995).

Scaling of turbomachines using the previously discussed non-dimensional parameters is feasible if the machine is geometrically similar, which implies that the number of blades, blades thickness, blade angle, machine size, radii and operating clearance are scaled proportionally (Japikse & Baines, 1995). Scaling from large sizes to small sizes imposes some difficulties, attributed to the surface finish, the manufacturing limit and the increased cost for increased geometrical tightness at small size. The Reynolds number imposes the next major constraint, in which a correction factor has to be applied. A number of correction charts are recommended to take into account of the Reynolds number effect in the laboratory testing of centrifugal compressors at different operating conditions (Casey, 1985; Strub et al., 1987). The geometrical scaling of turbomachinery from one size to another requires the tip speed to be constant to maintain similar effects from windage loss, tip clearance loss, external losses and mechanical effects (Japikse & Baines, 1995).

Scaling of turbomachines for different operating conditions within the same working fluid is a common practice in turbomachinery testing. The inlet operating condition is scaled to reduce the pressure and temperature into the compressor or the turbine during the performance test. This practice can reduce the operational cost and the capital cost of the testing equipment. The Reynolds number cannot be scaled and a correction factor is required either from the published literature or based on in-house knowledge.

The increasing interest in Organic Rankine Cycles has prompted the need for ORC turbines that can operate with various working mediums. The most common working fluid in existing commercial installations is n-Pentane (working fluid patented by ORMAT) (S. Quoilin & Lemort, 2009). Other working fluids are actively proposed and recommended under different conditions for a better thermodynamic cycle efficiency (Bao & Zhao, 2013) and a more cost-efficient design of heat exchanger (Sylvain Quoilin, Declaye, Tchanche, & Lemort, 2011). The testing of the turbine, however, is not a simple task. A full scale ORC set-up is favorable for turbine performance test but it imposes high design, development, and installation cost and efforts in the concerns of system layout, pump, heat exchanger and piping. Refrigerants typically introduce some side effects to either the environment, atmosphere, and health and safety issues. The refrigerants have to be sealed properly with minimal leakage, which further increases the operational cost of the test facility. A simple compressed air test bench is favorable as the compressed air is safe to be released to the atmosphere without any environmental issues. The testing via compressed air, however, might introduce some important deviations, as the real gas effects cannot be accounted accurately. The variation of density of real gas across blade passage during the expansion process and the machine Reynolds number cannot be scaled precisely from one fluid to another, which further limits the similitude using real gas. The lack of published correction chart for Mach number and Reynolds number for different working mediums has further limited the application of the similarity concept. These issues make it difficult for the turbomachinery designers or the

engineers to apply the turbine performance curve generated using compressed air to an application using real gas, such as n-Pentane.

This study explores the feasibility of utilizing the similarity concept to estimate the turbine performance using real gas. Three different approaches using the similarity concept were proposed to scale air performance data to generate performance curves for two refrigerants, namely R134a and R245fa. A full computational fluid dynamic (CFD) analysis was then performed to generate the performances curves for the selected refrigerants. The approaches using the similarity concept were then compared to the result from the CFD analysis. The most feasible approach in scaling a turbine from air to refrigerants was selected. The accuracy of the performance prediction through the similarity analysis of the ORC turbomachine was estimated. The deviation in turbine's performance for different working fluids was presented and discussed.

2. METHODOLOGY

An industrial gas turbine with published turbine geometry (Sauret, 2012) was selected for this study. The selected gas turbine was initially designed for Sundstrand Power Systems (SPS) T-100 Multipurpose Small Power Unit (MPSPU) with a single-shaft configuration to accommodate the ground-based auxiliary power application (Jones, 1996). The nominal power of the selected turbine is 37 kW with a growth capability up to 75 kW (Jones, 1996). A CFD model was previously conducted on the gas turbine using air as the working medium and the result from the numerical modelling was compared to the experimental data (Jones, 1996; Wong & Krumdieck, 2014). The result from the CFD model agreed with the experimental data with less than 1% error in term of total-to-static efficiency. The CFD method was employed to generate the performance curve using two selected refrigerants, namely R134a and R245fa to validate the precision and accuracy of three different approaches of similarity concept in scaling the gas turbine from one working medium with ideal gas behavior to another working medium with real gas behavior.

The first part of this study re-generated the performance map of the selected gas turbine using air as the working medium and the performance curve served as a benchmark to determine the turbine performance using R134a and R245fa via similarity concept. The fluid properties of air were estimated using polytropic ideal gas equations. Three different approaches for similarity analysis were applied in this study. The performance curve scaled from the air data was plotted as a function of velocity ratio and specific speed for comparison.

The second part utilized the CFD methodology as outlined in previous study (Wong & Krumdieck, 2014) to generate the performance map of the selected gas turbine using R134a and R245fa. The performance map generated from the CFD tools was compared to the scaled performance map. The fluid properties of the refrigerants were extracted from REFPROP developed by National Institute of Standards and Technology (E. W. Lemmon, Huber, M.L., McLinden, M.O, 2013), and the details of the mathematical expressions to represent the real gas behavior of the selected refrigerants should be referred to the work by Lemmon (E. W. Lemmon & Span, 2006). The three different approaches were compared to the performance map by CFD tools, and the accuracy of each method was discussed.

The third part discusses the deviation in the turbine's performance using different working fluids at the best efficiency point. The fluid flow field and the blade loading across the blade passage, the velocity diagram at the turbine inlet and the outlet, and the Reynolds number effect on the turbine's performance were investigated. The limitation of the selected approach was presented, and a correction factor was generated to predict the best efficiency point of the turbine at higher expansion ratio (including super-sonic expansion).

2.1 Similarity Analysis

Similarity analysis, or similitude, provides a quick solution to scale a fluid machine for different operating conditions and different incompressible fluids without resorting to the full scale three-dimensional CFD methods. The performance of a turbomachine is dependent on the machine size, machine speed, and the fluid properties. Turbomachines are designed to handle either compressible or incompressible flow. Two extra terms are employed for turbomachines handling compressible flow, compared to the fluid machines handling incompressible flow, to take account of the compressible flow properties and the change of density during the expansion/compression process (Dixon & Hall, 2010). The performance parameters of a compressible flow turbomachine is expressed as a function of some variables, as listed in equation (1).

$$\Delta h_{0s}, P, \eta = f(N, D, \dot{m}, \rho_{01}, a_{01}, \gamma, \mu) \tag{1}$$

Where Δh_{0s} is the total-to-static enthalpy drop of the fluid across the turbine at the designed pressure ratio, P is the shaft power, η is the isentropic efficiency, and the efficiency is evaluated using the inlet stagnation and outlet static condition in this study, N is the rotational speed of the shaft, D is the diameter of the turbine wheel, $\dot{m}$ is the inlet mass flow rate, ρ_{01} is the density evaluated using the inlet stagnation condition, a_{01} is the sonic velocity at the inlet, γ is the specific heat, and μ is the dynamic viscosity. Buckingham π theorem was applied in equation (1) and three variables, density, ρ_{01}, shaft speed, N, and wheel diameter, D were selected to reduce the original expression into five dimensionless groups, as presented in equation (2). The full mathematical derivation should be referred to the work by Dixon (Dixon & Hall, 2010).

$$\frac{\Delta h_{0s}}{a_{01}^2}, \eta, \frac{P}{\rho_{01} a_{01}^3 D^5} = f\left\{\frac{\dot{m}}{\rho_{01} N D^3}, \frac{\rho_{01} N D^2}{\mu}, \frac{N D}{a_{01}}, \gamma\right\} \tag{2}$$

The current dimensionless group is not an explicit formulation where the parameters, such as density and sonic velocity, cannot be measured directly. The dimensionless groups can be reduced to a number of variables which allows direct measurement from the experiments if the compressible flow is modelled as a perfect gas. The dimensionless parameters were then reduced to a function of temperature and pressure at both inlet and outlet stations of the turbine, as listed in equation (3).

$$\frac{p_{02}}{p_{01}}, \eta, \frac{\Delta T_0}{T_{01}} = f\left\{\frac{\dot{m}\sqrt{\gamma R T_{01}}}{p_{01} D^2}, \text{Re}, \frac{N D}{\sqrt{\gamma R T_{01}}}, \gamma\right\} \tag{3}$$

Where p is pressure, T is temperature, Re is machine Reynolds number, and R is the gas constant. The mathematical simplification of the dimensionless groups using perfect gas model are available from the works by Baines, Aungier, and Dixon (Aungier, 2006; Dixon & Hall, 2010; Japikse & Baines, 1995). Complete similarity can be achieved when
1) complete geometrical similarity is achieved (Aungier, 2006; Japikse & Baines, 1995), in which the turbine is scaled up or scaled down proportionally, *and*
2) dynamic similarity is achieved, in which the velocity components and forces are equal (Aungier, 2006).

Three different approaches are trialed to scale the performance data using air into the performance map using refrigerants. The scaled performance curve from each approach was compared to the performance curve from CFD analysis and the accuracy for each method was evaluated.

The *perfect gas approach* assumes that the selected refrigerants, R245fa and R134a are perfect gas. Three non-dimensional groups are hold constant, which are pressure ratio, blade speed coefficient in equation (4), and mass flow coefficients in equation (5). The outlet static pressure of the refrigerants

is determined given the pressure ratio of the turbine using air. Equation (4) is employed to calculate the shaft's rotational speed whereas equation (5) is applied to determine the mass flow rate at the turbine inlet.

$$\frac{ND}{a_{01}} = \text{constant} \tag{4}$$

$$\frac{\dot{m}}{\rho_{01}ND^3} = \text{constant} \tag{5}$$

The *variable pressure ratio approach* is similar to the perfect gas approach, but the pressure ratio does not remain constant. The pressure ratio using the selected refrigerants is determined using the correlation in equation (6). Equation (4) and equation (5) are then employed to determine the shaft speed and the mass flow rate, respectively.

$$\frac{\Delta h_{0s}}{a_{01}^2} = \text{constant} \tag{6}$$

The *constant specific speed approach* assumes constant pressure ratio, velocity ratio, v and the specific speed, N_s for the selected working medium. The optimal velocity ratio and specific speed of a turbomachine typically fall in a narrow range of operation for maximum efficiency. Both are hold constant to determine the shaft speed and the mass flow rate by using equations (7) and (8), respectively.

$$v = \frac{U}{C_{is}} = \frac{U}{\sqrt{2\Delta h_{0s}}} \tag{7}$$

Where U is turbine inlet tip speed, and C_{is} is the fictitious velocity when the fluid is expanded in an isentropic process across a nozzle, with the pressure ratio equals to the pressure ratio of the turbine stage.

$$N_s = \frac{\omega\sqrt{\dot{m}/\rho_{exit}}}{\Delta h_{0s}^{0.75}} \tag{8}$$

Where ρ_{exit} is the density at the turbine outlet.

2.2 Evaluation of Aerodynamic Performance using CFD Analysis

CFD analysis was conducted on the gas turbine to determine the overall performance of the turbine stage and evaluate the fluid dynamics across the blade passage. The CFD analysis was performed using ANSYS CFX version 15.0 and the overall procedure is illustrated in Figure 1. The solid models of both nozzle and rotor blades were constructed in ANSYS BladeGen by providing the principal geometry and the distribution of the wrap angle along the meridional position. Hexahedral meshes were then applied on the fluid zone across both the nozzle and turbine blades. A two-dimensional topography was generated on the hub surface, mid span and close-to-shroud surface as a framework to smoothen the formation of meshes. The mesh quality was controlled by refining the mesh size and manipulating the number of elements across the boundary layer of the blade surface. The skew meshes were eliminated to avoid ill-meshes. The operating condition and the boundary condition were then set up at each stations (nozzle inlet, interface between nozzle and turbine rotor, and rotor outlet). A suitable working fluid was selected from the in-built fluid database or the fluid properties can also be imported from the external fluid database. k-ε model was selected to model the turbulence across the blade passage. The

Navier-Stokes equations were solved numerically and the result was evaluated as velocity vector field and distribution of thermodynamics properties across the blade passage.
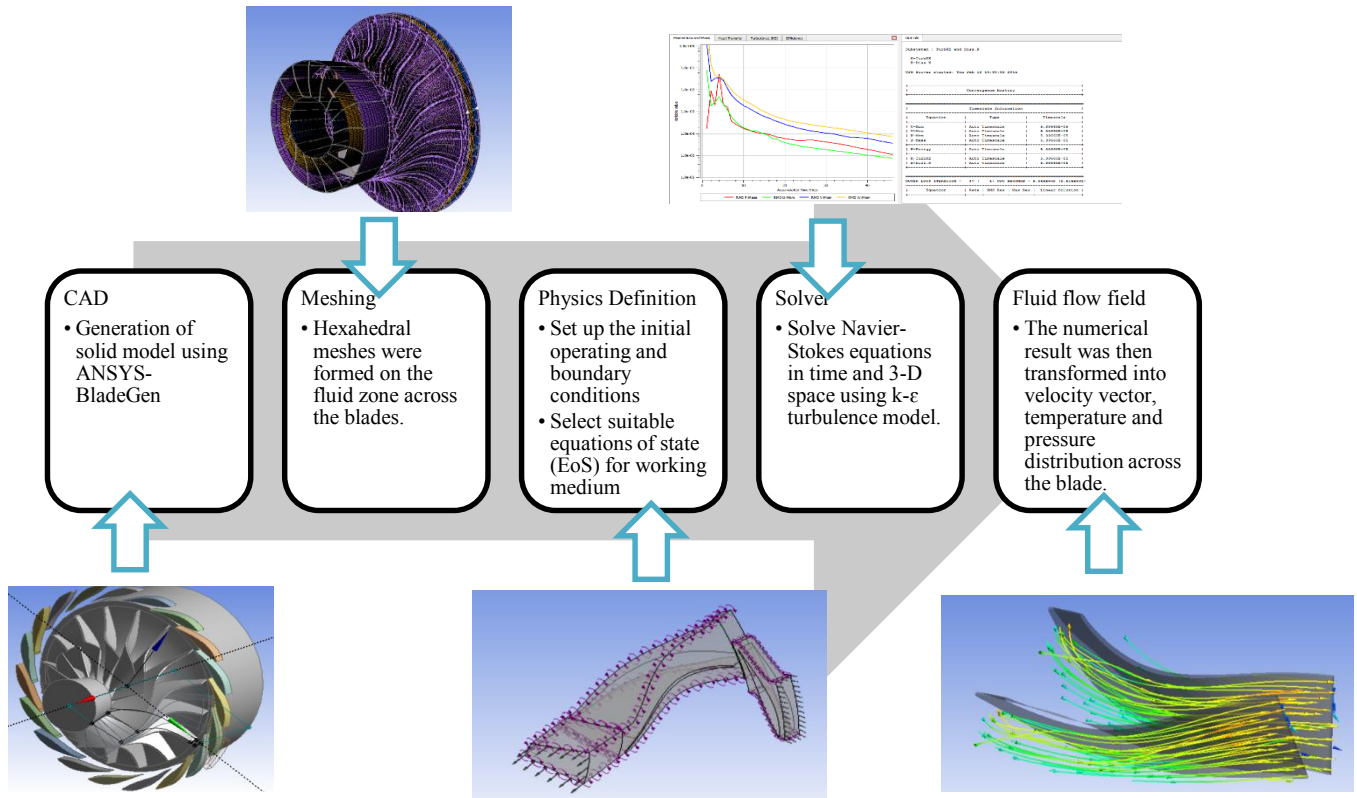

Figure 1: Overall procedures of CFD simulation using ANSYS Turbomachinery Package

3. RESULT

The three different approaches were applied to scale the performance curve from air to R134a and R245fa with the operating conditions in Table 1.

Table 1: Operating condition of air and selected refrigerants

	Unit	Air	R134a	R245fa
Molecular weight, M	g/mol	28.97	102.03	134.05
Inlet total temperature	K	1056.5	386	406.1
Inlet total pressure	kPa	580.4	2380	2334
Compressibility factor at inlet	-	1	0.786	0.630
Speed of sound at inlet	m/s	635	153.4	108.6
Outlet static pressure	kPa	101.3	420	420
Compressibility factor at outlet	-	1	0.931	0.904

R134a was superheated up to 35 degree before entering the turbine to avoid the formation of moisture at the end of the expansion process since it is a wet fluid. The scaled performance curves of R134a using the three approaches were compared to the result from the CFD analyses, in terms of velocity ratio in Figure 2, and specific speed in Figure 3. The three similarity approaches and the CFD analyses were compared in term of specific speed for R134a in Figure 3, and R245fa in Figure 4.

The *perfect gas approach* shows that the optimal velocity ratio is under-estimated. The optimal value from the *perfect gas approach* is 0.48, whereas the estimated value from the CFD analysis is 0.60.

The optimal velocity ratio from the *variable pressure ratio approach* and the *constant specific speed approach* agrees closely to the estimated values from the CFD analysis, with an error less than 10%, as illustrated in Table 1. The optimal operating shaft speed would be predicted incorrectly if the *perfect gas approach* was applied.

The overall trend of the turbine performance is similar between the CFD analysis and the *constant specific speed* approach, but the trend is different for the *variable pressure ratio* approach. The *variable pressure ratio* approach shows fairly flat efficiency for the range of velocity ratio between 0.55 and 0.70, and the range of specific speed between 0.33 and 0.42. However, the CFD analysis shows that the turbine is very sensitive to the operating point, as shown in Figure 2 and Figure 3. The turbine performance drops significantly at the operating points away from the best efficiency point. The best efficiency point is defined as the point with the maximum total-to-static isentropic efficiency at certain pressure ratio. The result shows that the *variable pressure ratio* approach provides a good prediction of optimal velocity ratio, optimal specific speed, and maximum efficiency. However, the approach does not provide a good estimation of performance for the operating points away from the best efficiency point, as presented in Table 2.

The *constant specific speed* approach assumes constant pressure ratio, specific speed and velocity ratio. The trend of the performance is similar between the *constant specific speed* approach and the CFD analysis for R134a and R245fa, based on Figure 3 and Figure 4. However, the turbine efficiency was over-estimated with errors between 10 and 20%, for the investigated range of velocity ratio and specific speed. This approach provides a better estimation in the turbine performance away from the best efficiency point, compared to another two approaches. However, the *constant specific speed* approach yields over 10% error in estimating the optimal velocity ratio, optimal specific speed, and maximum turbine efficiency, whereas the *variable pressure ratio* approach yields an error between 7% and 8%, as listed in Table 2.
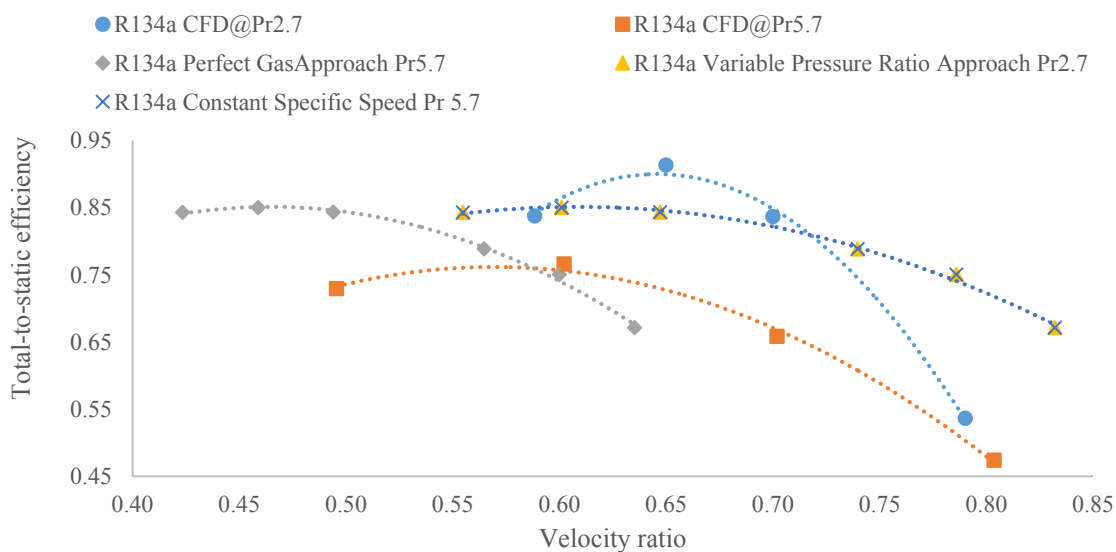

Figure 2: Comparisons of scaled performance from air data and CFD result for R134a as a function of velocity ratio
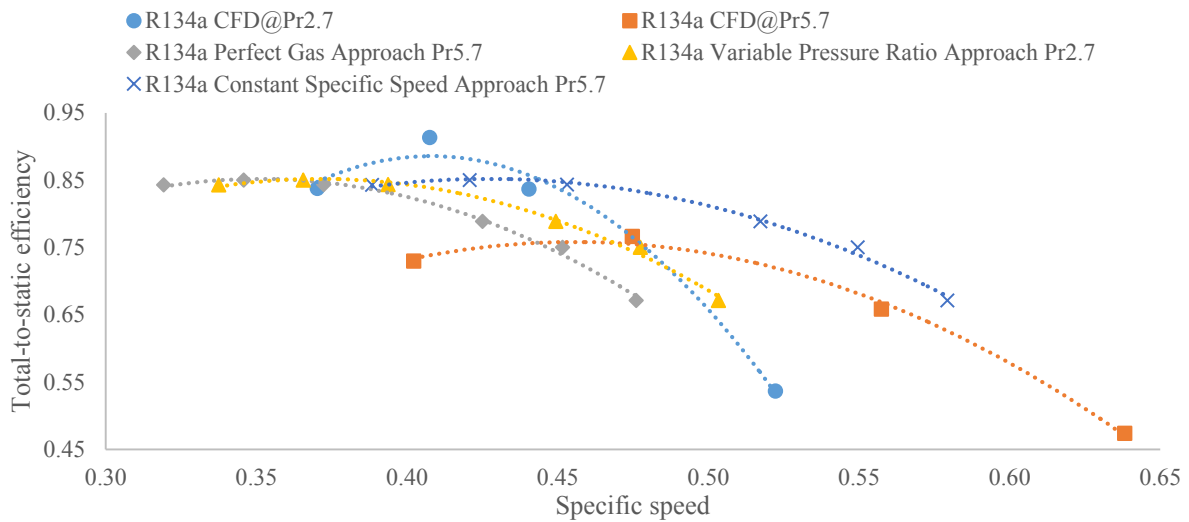
Figure 3: Comparisons of scaled performance from air data and CFD result for R134a as a function of specific speed
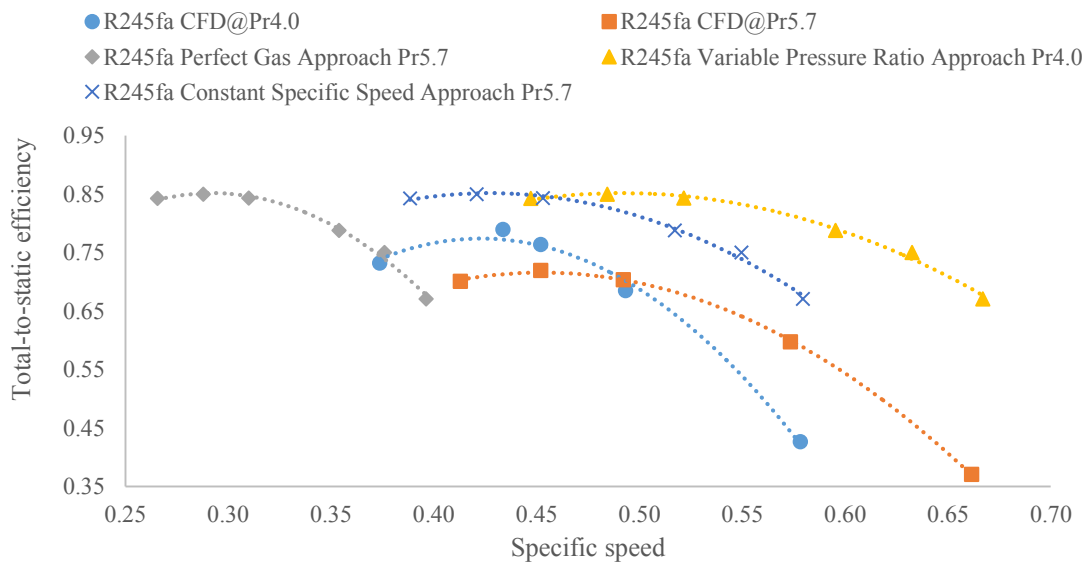

Figure 4: Comparisons of scaled performance from air data and CFD result for R245fa as a function of specific speed

The estimation of the inlet mass flow rate by the three similarity approaches and the CFD analysis was compared. The *perfect gas* approach and the *variable pressure ratio* approach utilize the mass flow coefficient in equation (5) whereas the *constant specific speed* approach uses the specific speed correlation in equation (8) to estimate the inlet mass flow rate. The result in Table 2 shows that the mass flow rate was under-estimated using all three approaches. The mass flow coefficient predicts the inlet mass flow rate with a better accuracy, with an error less than 10%, as opposed to the specific speed correlation, with error in the range of 15 and 25%. Hence, the *perfect gas* approach and the *variable pressure ratio* approach provide better estimations in the inlet mass flow, compared to the *constant specific speed* approach.

Table 2: Numerical error for different scaling approaches

	Working medium	Pressure ratio	Optimal velocity ratio	Optimal specific speed	Maximum total-to-static efficiency	Mass flow rate (kg/s)	Average Error (%)
Benchmark	Air	5.7	0.6	0.42	0.85	0.29	
Approach 1 (Perfect Gas)	R134a	5.7	0.46	0.35	0.85	3.46	
	Error (%)		23.3	25.5	11.8	4.6	16.3
	R245fa	5.7	0.38	0.29	0.85	3.75	
	Error (%)		31.9	35.9	18.4	9.0	23.8
Approach 2 (Variable Pressure Ratio)	R134a	2.7	0.6	0.37	0.85	3.46	
	Error (%)		7.7	9.8	6.6	4.7	7.2
	R245fa	4.0	0.6	0.48	0.85	3.75	
	Error (%)		2.9	13.5	9.4	9.0	8.7
Approach 3 (Constant Specific Speed)	R134a	5.7	0.6	0.42	0.85	2.99	
	Error (%)		0.0	10.6	11.8	17.6	10.0
	R245fa	5.7	0.6	0.42	0.85	3.15	
	Error (%)		7.5	7.2	18.4	23.5	14.1
CFD	R134a	2.7	0.65	0.41	0.91	3.63	
		5.7	0.60	0.47	0.76	3.63	
	R245fa	4.00	0.58	0.42	0.78	4.12	
		5.7	0.56	0.45	0.72	4.12	

4. DISCUSSION

The discrepancy in the turbine efficiency if a turbine stage is scaled from one operating condition into another is attributed to the variation in machine Reynolds number and Mach number. Various Reynolds number corrections were proposed for centrifugal compressors, such as ASME PTC-10 (PTC, 1997) and the efficiency-deficiency chart by Pampreen (Pampreen, 1973). The machine Reynolds number, however, does not have significant effect on the change in efficiency in this study as the effects of viscosity and thermal conductivity can be neglected at high Reynolds number (Harinck, Guardone, & Colonna, 2009). Reynolds number, $Re=\rho UD/\mu$ is a function of density, ρ, tip speed, U, wheel diameter, D, and dynamic viscosity, μ. The dynamic viscosity of the refrigerants is much smaller, rendering a higher value in the Reynolds number, in the magnitude of 100×10^6, as opposed to the Reynolds number of steam, air, and water in the magnitude of 1×10^6. The turbine inlet condition was varied using the CFD analysis to investigate the correlation between the machine Reynolds number and the turbine performance, as illustrated in Figure 5. The turbine's performance is fairly consistent in a wide range of Reynolds number, between 10 and 90. Hence, the Reynolds number effect can be neglected in this study.
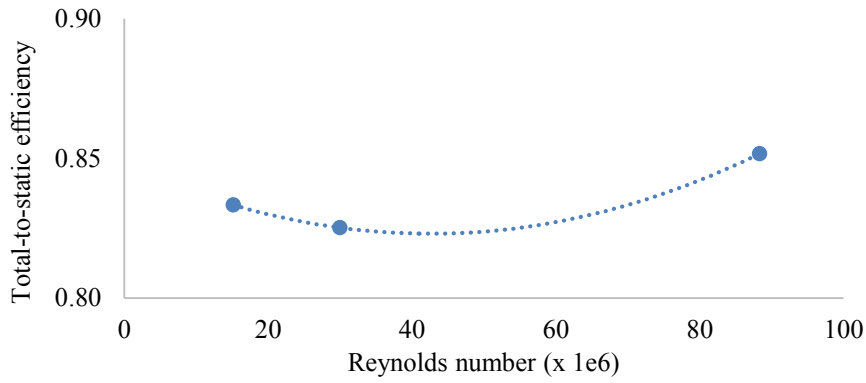
Figure 5: Effect of machine Reynolds number on turbine's performance using R134a
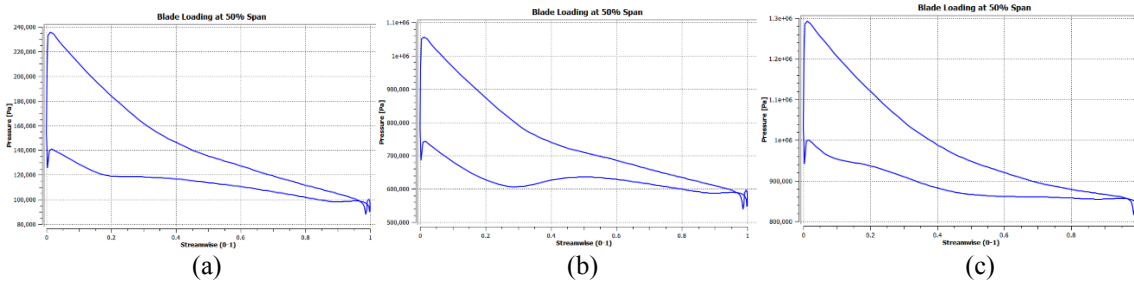

Figure 6: Blade loading and density at blade surface using air at pressure ratio of 5.7 (a), R245fa at pressure ratio of 4.0 (b) and R134a at pressure ratio of 2.7 (c)
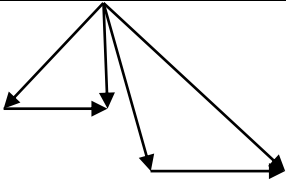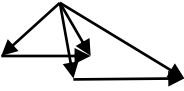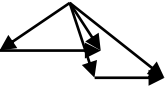
The blade loading along the pressure and suction surfaces at optimal specific speed using the *variable pressure ratio* approach are similar for all three working fluids; air, R134a and R245fa. Constant pressure drop was observed for air (modelled as ideal gas), R134a and R245fa (modelled as real gas) along pressure surface, but pressure fluctuation was observed for R245fa along the suction surface. The fluctuation is related to the adverse pressure gradient near the leading edge of the suction surface, which forms a vortex and local backpressure downstream of the vortex, as illustrated by the velocity vector in Figure 7. The flow re-attaches downstream of the vortex with gradual pressure drop along the blade passage.

The maximum isentropic efficiency for air, R134a and R245fa is different although the pressure loading along the blade passage at the optimal specific speed is similar. The highest turbine efficiency is achieved by R134a, followed by air, and R245fa. The deviation can be explained as a function of compressibility effect. The compressibility factor is a ratio of actual specific volume to the ideal volume of selected fluids. The compressibility effect of the expansion process across the turbine was measured qualitatively by volumetric flow ratio (Macchi & Perdichizzi, 1981). Macchi and Perdichizzi found that the increase in the volumetric flow ratio gives rise to a reduction in the turbine efficiency at optimal specific speed (Macchi & Perdichizzi, 1981), and the volumetric flow ratio has to be less than 50 to achieve a high turbine stage efficiency greater than 0.80 (Angelino, Invernizzi, & Macchi, 1991). The volumetric flow ratio is different for different working fluid using the *variable pressure ratio* approach. The volumetric flow ratio was determined as 5.7 for air, 4.9 for R245fa, and 2.7 for R134a. The use of equation (9) justifies the highest efficiency using R134a at low pressure ratio. Equation (9) is the change of entropy of a perfect gas in a closed system.

$$\Delta s = c_v \ln\left(T_3 \middle/ T_1 \right) + R \ln\left(v_3 \middle/ v_1 \right) \tag{9}$$

Where Δs denotes the entropy generation, c_V isochoric heat capacity, R specific gas constant, T temperature, and v specific volume. The increase in volumetric flow ratio generates a larger entropy difference. The larger the entropy differences, the larger the irreversibility of the system and the lower the turbine's efficiency. Hence, the highest efficiency is achieved by R134a with the lowest pressure ratio among all three working fluids. However, the turbine's efficiency using R245fa (expansion ratio of 4.9) is 78%, which is lower than air at 85% (expansion ratio of 5.7). This shows that the volumetric flow ratio is not the sole contributor to the drop in turbine performance using different fluids.

Table 3: Performance parameters for different working fluids, using Variable Pressure Ratio Approach

Fluids	Air	R134a	R245fa
Velocity triangle			
Pressure ratio	5.7	2.7	4.0
Volumetric flow ratio	5.7	2.7	4.9
Degree of Reaction	0.42	0.47	0.44
Flow coefficient	0.245	0.172	0.249
Stage loading coefficient	1.040	0.974	0.995

The differences in the volumetric flow ratio also gives rise to the change in a number of turbine parameters. Optimum degree of reaction decreases whereas optimal flow coefficient increases with increasing expansion ratio. These yield some changes in the velocity diagram at the turbine exit, as shown in Table 3. The complete similarity is not achieved as the velocity vector at the turbine exit is not conserved. Hence, the *variable pressure ratio* approach does not achieve complete similarity, and this gives rise to the error in estimating the velocity ratio, specific speed, and turbine performance.

The flow field diagrams of R245fa, R134a, and air using the *variable pressure ratio* approach were compared in Figure 7. The flow undergoes turning from axial direction to tangential direction, and gives rise to Coriolis effect in the radial direction (Moustapha, Zelesky, Baines, & Japiske, 2003). The flow undergoes a non-uniform velocity distribution in the spanwise direction, with lowest velocity near the end wall surface of the hub. The radial gradient of the flow velocity in the spanwise direction gives rise to the imbalance in the pressure gradient in the spanwise direction. The end result of the Coriolis effect and the non-uniform velocity give rise to a complex flow field, which is illustrated in Figure 7 in term of flow angle. The bulk flow moves from suction surface near the shroud to pressure surface near the hub. The flow is compensated by a number of passage vortices, and the flow vector diagram can be found in Kitton's work (also presented by Baines in his work (Moustapha et al., 2003)). This phenomena exists in the best efficiency point, attributed to the turning of the flow from axial to tangential direction. The distribution of the swirl angle at the trailing edge was averaged and the flow angle was determined as 1° for air, 33° for R134a and 37° for R245fa. The result implies that the turbine exit swirl angle might increase monotonically with the molecular weight of the working fluids, with the highest by R245fa and the lowest by air. Positive swirl angle is non-favorable as the fluid internal energy would be lost as kinetic energy. The specific work output would decrease with a positive swirl angle, based on Euler turbomachinery equation.

$$W_x = U_2 C_{\theta 2} - U_3 C_{\theta 3} = U_2 C_{m2} \tan \alpha_2 - U_3 C_{m3} \tan \alpha_3 \qquad (10)$$

Where W_X is specific work output, U_2 is rotor inlet tip speed, U_3 is rotor outlet tip speed, C_θ is tangential velocity component, C_m is meridional velocity component, and α is swirl angle.
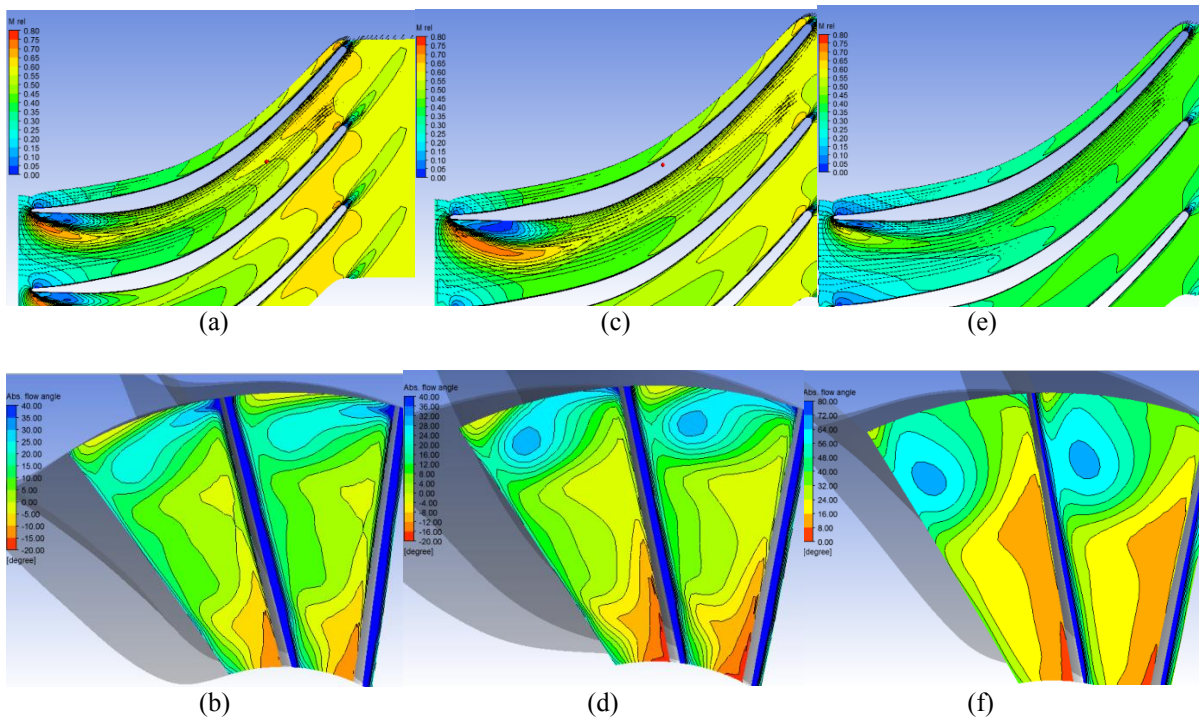
Figure 7: Distribution of relative Mach number in the meridional plane and distribution of absolute flow angle at the trailing edge using air at pressure ratio of 5.7 (a-b), R245fa at pressure ratio of 4.0 (c-d) and R134a at pressure ratio of 2.7 (e-f)

The conventional radial inflow turbine is typically designed for low pressure ratio application, which is between 1.2 and 3.0 for automotive turbochargers, and less than 10 for single stage gas turbines to avoid choking and shock waves in supersonic expansion. The selected gas turbine has a design pressure ratio of 5.7. Different pressure ratio was determined for R134a and R245fa assuming constant value of $\Delta h_{0s}/a_{01}^2$ (using the *variable pressure ratio* approach) and plotted in Figure 8. The limiting line on the left represents the saturation lines of the refrigerants. The calculated pressure ratio for the selected refrigerants is less than 5.7, which is the pressure ratio imposed on the turbine using air. The local sound speed of refrigerants with heavier molecular weight is less than the local speed of sound using air. The local speed of sound is between 90 and 190 m/s for R134a and between 75 and 160 m/s for R245fa for the temperature range of 300 and 450 K, and pressure range of 0.5 and 4.0 MPa, which is less than the local speed of sound of air at 635 m/s with the given operating condition in Table 1. The smaller the local speed of sound, the smaller the isentropic enthalpy drop and the smaller the pressure ratio across the turbine. Hence, the *variable pressure ratio* approach is limited to a pressure ratio less than the design pressure ratio using air. This limits the applicability of the approach in ORC application, which is characterized for high pressure ratio expansion.
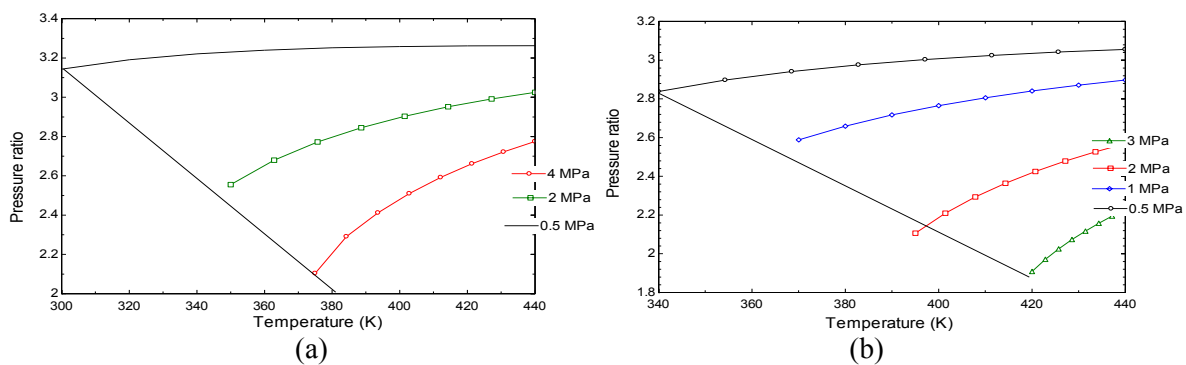

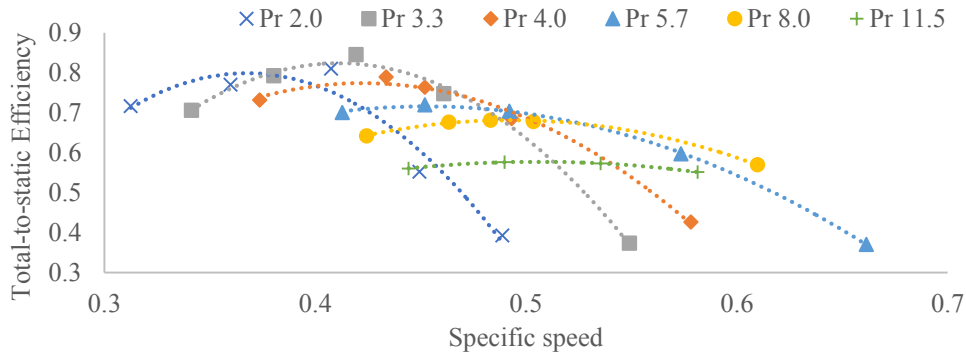**Figure 8**: Range of applicability using equation (6) for R134a (a) and R245fa (b)

Figure 9: Performance map of R245fa at different specific speed and pressure ratio

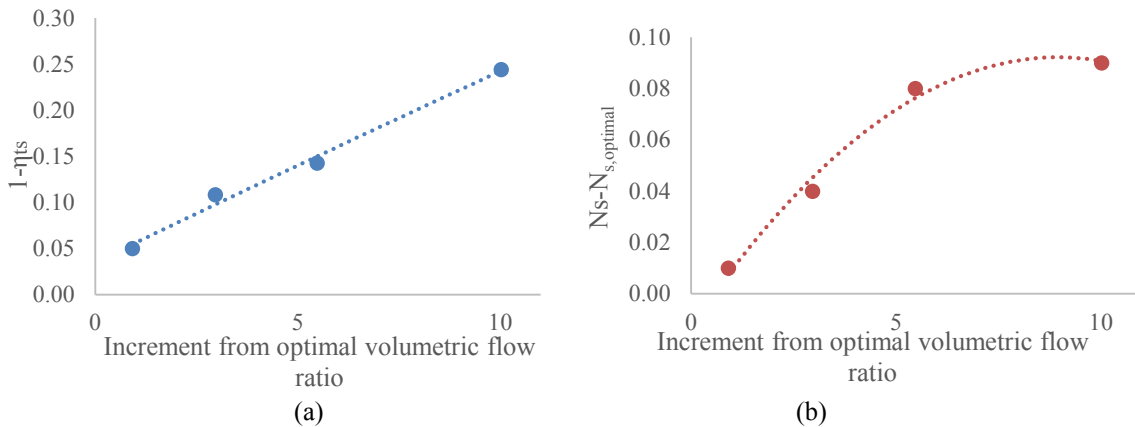(a)   (b)

Figure 10: Deviation of best efficiency point and the corresponding specific speed at increasing volumetric flow ratio

The prediction of the turbine performance at higher pressure ratio or expansion ratio is required for ORC application. A correction chart for R245fa at different expansion ratio was developed using Figure 9. The turbine's performance map for R245fa was generated for different pressure ratio (2 – 11.5) and specific speed (0.3 – 0.7), and plotted in Figure 9. The result shows that the maximum turbine performance was achieved at a pressure ratio of 3.3 (equivalent to volumetric flow ratio at 4.0). The maximum efficiency point at the pressure ratio of 3.3 iss used as a benchmark to calculate the deficiency in efficiency and deviation of optimal specific speed at higher volumetric flow ratio. The turbine losses increases linearly with increasing volumetric flow ratio as shown in Figure 10(a). The location of the specific speed for the best efficiency point at increasing volumetric ratio is increasing, as shown in Figure 9. The deviation in the optimal specific speed is plotted as a function of volumetric flow ratio in Figure 10. The result shows that the deviation in optimal specific speed increases with increasing volumetric flow ratio until the blade passage is choked (with the relative Mach number around 1). The further increment in volumetric flow ratio does not have any effect on the value of N_s-$N_{s,optimal}$, as illustrated in Figure 10.

5. CONCLUSION

Three different approaches using the similarity concept were proposed and investigated to scale the selected gas turbine from air to R134a and R245fa in this study. The *perfect gas* approach assuming the real gas as perfect gas provides the largest error in terms of optimal velocity ratio, optimal specific speed, and maximum efficiency. The *variable pressure ratio* approach shows the highest averaged accuracy in predicting the optimal velocity ratio, optimal specific speed, maximum efficiency and mass flow rate. The *constant specific speed* approach is recommended to estimate the turbine's performance away from the best efficiency point.

Constant value of $\Delta h_{0s}/a_{01}{}^2$ was imposed in the *variable pressure ratio* approach to achieve the similarity but a number of deviations was observed, including swirl angle at the turbine outlet, volumetric flow ratio, best efficiency point and the corresponding specific speed. The Reynolds number effect does not influence the scaling using refrigerants as the effect of viscosity is negligible at high Reynolds number using refrigerants with low viscosity. The swirl angle at the turbine outlet was observed as a function of molecular weight, in which the increment in molecular weight increases the swirl angle and reduces the specific work output. The *variable pressure ratio* approach does not ensure a constant volumetric flow ratio, hence the complete similarity cannot be achieved. The *variable pressure ratio* approach is limited to pressure ratio less than the design pressure ratio using air, which is not suitable to scale an ORC turbine. Therefore, a correction chart was developed to scale the performance of the gas turbine for higher volumetric ratio using R245fa. The deficiency in turbine efficiency is linearly correlated to the increased volumetric flow ratio. The correction chart provides a good estimation in selecting a suitable turbine for a particular ORC application. However, the correction chart has to be validated against the experimental data for better accuracy.

NOMENCLATURE

a	local speed of sound	(m/s)
C	absolute flow velocity	(m/s)
C_{is}	isentropic flow velocity	(m/s)
c_v	isochoric heat capacity	(J/kg.K)
D	turbine wheel diameter	(m)
Δh_0	enthalpy drop	(kJ/kg)
$\dot{m}$	mass flow rate	(kg/s)
N	shaft speed	(rev/min)
N_s	specific speed	(-)
p	pressure	(kPa)
P	shaft power	(kW)
R	gas constant	(J/kg.K)
Re	Reynolds number	(-)
T	temperature	(K)
U	tip speed	(m/s)

Greek letter

α	swirl angle	(degree)
θ	tangential direction	(-)
γ	ratio of specific heats	(-)
η	efficiency	(-)
ρ	density	(kg/m^3)
υ	velocity ratio	(-)
ω	shaft speed	(rad/s)

Subscript

01	nozzle inlet stagnation condition
02	rotor inlet stagnation condition
03	rotor outlet stagnation condition
1	nozzle inlet static condition
2	rotor inlet static condition
3	rotor outlet static condition
m	meridional plane
s	isentropic process

REFERENCES

Angelino, G., Invernizzi, C., & Macchi, E. (1991). Organic Working Fluid Optimization for Space Power Cycles. In G. Angelino, L. De Luca & W. A. Sirignano (Eds.), *Modern Research Topics in Aerospace Propulsion* (pp. 297-326): Springer New York.

Aungier, R. H. (2006). *Turbine aerodynamics: axial-flow and radial-inflow turbine design and analysis*: ASME Press.

Balje, O. E. (1981). *Turbomachines: A Guide to Design Selection and Theory*: Wiley.

Bao, J., & Zhao, L. (2013). A review of working fluid and expander selections for organic Rankine cycle. *Renewable and Sustainable Energy Reviews, 24*, 325-342.

Casey, M. V. (1985). The Effects of Reynolds Number on the Efficiency of Centrifugal Compressor Stages. *Journal of Engineering for Gas Turbines and Power, 107*(2), 541-548. doi: 10.1115/1.3239767

Chen, H., & Baines, N. C. (1994). The aerodynamic loading of radial and mixed-flow turbines. *International Journal of Mechanical Sciences, 36*(1), 63-79. doi: 10.1016/0020-7403(94)90007-8

Dixon, S. L., & Hall, C. (2010). Fluid Mechanics and Thermodynamics of Turbomachinery   Retrieved from http://canterbury.eblib.com.au/patron/FullRecord.aspx?p=534952

Harinck, J., Guardone, A., & Colonna, P. (2009). The influence of molecular complexity on expanding flows of ideal and dense gases. *Physics of Fluids (1994-present), 21*(8), 086101. doi: doi:http://dx.doi.org/10.1063/1.3194308

Japikse, D., & Baines, N. C. (1995). *Introduction to turbomachinery*: Concepts ETI.

Jones, A. C. (1996). Design and Test of a Small, High Pressure Ratio Radial Turbine. *Journal of Turbomachinery, 118*(2), 362-370. doi: 10.1115/1.2836651

Lemmon, E. W., Huber, M.L., McLinden, M.O. (2013). NIST Standard Reference Database 23: Reference Fluid Thermodynamic and Transport Properties-REFPROP, Version 9.1. Gaithersburg: Standard Reference Data Program.

Lemmon, E. W., & Span, R. (2006). Short fundamental equations of state for 20 industrial fluids. *Journal of Chemical & Engineering Data, 51*(3), 785-850.

Macchi, E., & Perdichizzi, A. (1981). Efficiency prediction for axial-flow turbines operating with nonconventional fluids. *ASME Journal of Engineering for Power, 103*, 718e724.

Meher-Homji, C. B. (2000). *'The Historical Evolution of Turbomachinery.* Paper presented at the Proceedings of the 29th Turbomachinery Symposium, Texas A&M University, Houston, TX.

Moustapha, H., Zelesky, M., Baines, N. C., & Japiske, D. (2003). *Axial and Radial Turbines*: Concepts Eti.

Pampreen, R. (1973). Small turbomachinery compressor and fan aerodynamics. *Journal of Engineering for Gas Turbines and Power, 95*(3), 251-256.

PTC, A. (1997). PTC 10-1997, Performance test code on compressors and exhausters. *American Society of Mechanical Engineers, New York, 3*.

Quoilin, S., Declaye, S., Tchanche, B. F., & Lemort, V. (2011). Thermo-economic optimization of waste heat recovery Organic Rankine Cycles. *Applied Thermal Engineering, 31*(14–15), 2885-2893. doi: 10.1016/j.applthermaleng.2011.05.014

Quoilin, S., & Lemort, V. (2009, 14-17 April). *Technological and economical survey of Organic Rankine Cycle systems.* Paper presented at the 5th European Conference Economis and Management of Energy in Industry, Algarve, Portugal.

Sauret, E. (2012). *Open design of high pressure ratio radial-inflow turbine for academic validation.* Paper presented at the Proceedings of the ASME 2012 International Mechanical Engineering Congress and Exposition, Houston, Texas.

Strub, R. A., Bonciani, L., Borer, C. J., Casey, M. V., Cole, S. L., Cook, B. B., . . . Strite, M. A. (1987). Influence of the Reynolds Number on the Performance of Centrifugal Compressors. *Journal of Turbomachinery, 109*(4), 541-544. doi: 10.1115/1.3262145

Wong, C. S., & Krumdieck, S. (2014). *Energy and Exergy Analysis of an Air-Cooled Geothermal Power Plant with Fixed Nozzle Turbine in Subsonic Expansion and Supersonic Expansion via CFD Analysis.* Paper presented at the 36th New Zealand Geothermal Workshop Auckland University.

ACKNOWLEDGEMENT

FAST DESIGN METHODOLOGY FOR SUPERSONIC ROTOR BLADES WITH DENSE GAS EFFECTS

Elio Antonio Bufi[1], Benoit Obert[2], Paola Cinnella[3*]

[1] Laboratoire DynFluid
Arts et Metiers ParisTech, Paris (France)
Polytechnic of Bari, Bari (Italy)
Email: elio-antonio.bufi@ensam.eu

[2] ENERTIME, Courbevoie (France)
Email: benoit.obert@enertime.com

[3] Arts et Metiers ParisTech, Paris (France)
Email: paola.cinnella@ensam.eu

* Corresponding Author

ABSTRACT

This work describes a fast 2-D design methodology based on the method of characteristics (MOC) for rotor blade vanes of supersonic axial Organic Rankine Cycle (ORC) impulse expanders. The MOC is generalized to gases governed by complex equations of state to fully account for dense gas behavior characteristic of ORC turbines. The fluid thermodynamic properties are described by highly accurate multiparameter equations of state based on Helmholtz free energy. Several working fluids are considered, including R245fa, R134a, R227ea, R236fa. The designs generated by the generalized MOC are compared with those obtained under the classical perfect gas model. Finally, CFD simulations of both isolated rotor blades and a full turbine stage are carried out to assess the performance of the designs using the ANSYS CFX solver.

1. INTRODUCTION

In recent years, the Organic Rankine Cycle (ORC) technology has received great interest from the scientific and technical community because of its capability of generating electric power using low temperature sources with good performances. For compactness, mechanical design simplicity and cost reasons, ORC plants often use single stage expander characterized by high pressure ratios, which leads to supersonic flow conditions. Furthermore, ORC working fluids are often characterized by the so-called dense-gas effects (see, e.g. (Congedo et al., 2011) and references cited therein).

The gas dynamics of dense gases can be described through a key thermodynamic property, known as the fundamental derivative of gas dynamics (Thompson, 1971):

$$\Gamma = 1 + \frac{\rho}{a}\left(\frac{\partial a}{\partial \rho}\right)_s \tag{1}$$

Equation (1) represents a measure of the rate of change for the local speed of sound with respect to density in isentropic transformation (Colonna et al., 2009). For light fluids, $\Gamma > 1$. This is the case of perfect gases, which have a constant $\Gamma = (\gamma + 1)/2$.

For fluid with sufficient molecular complexity and under specific thermodynamic conditions, $\Gamma < 1$, which leads to a reverse behaviour of the speed of sound in isentropic perturbations with respect to classical case: a decreases in isentropic compressions and grows in isentropic expansions.

The aerodynamic modelling of such a system is made difficult by dense gas effects characterizing the thermodynamic behaviour of the working fluid in the vicinity of the critical point and the saturation curve.

The need for a compact turbine working with high pressure ratios implies the choice of an impulse turbine architecture. This can be justified by considering a typical impulse blade and its velocity triangle (figure 4).
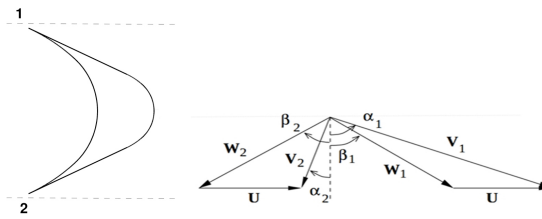

Figure 1: Example of impulse blade geometry and velocity triangles

By imposing an axial outlet flow for the impeller ($\alpha_2 = 0$), with the axial absolute velocity component kept constant, the work coefficient can be expressed as:

$$\psi = \frac{\Delta H_0}{U^2} = 2(1 - \Lambda) \tag{2}$$

In equation (2), U represents the peripheral velocity at a specified radius, ΔH_0 the total enthalpy drop per unit mass across the impeller and Λ the degree of reaction. For an impulse turbine ($\Lambda = 0$), the total enthalpy drop is two times greater than for a 0.5 reaction degree turbine. This property allows extracting a large amount of work from a single stage, with a maximum for a vane outlet swirl equal to 67° and rotor turning to 116° ($\beta_1 = \beta_2 = 58°$) (Paniagua et al., 2014). However, particular care must be addressed to the rotor and stator blades aerodynamic design because both behave as supersonic nozzles. Moreover, the typical operating conditions for an ORC turbine are in the proximity of the working fluid saturation curve or sometimes supercritical. Due to the presence of strong dense gas effects, models used to design the blade shapes have to be modified accordingly. Several authors in the past have addressed the design of dense gas nozzles and stator blades (Cramer and Tarkenton, 1992; Guardone et al., 2013; Wheeler and Ong, 2013; Bufi et al., 2015). All of them generally rely on extended versions of the Method of Characteristics (MOC) for 2D supersonic flows. The aim of this work is to develop, for the first time to the Authors knowledge, a methodology for the design of rotor blades of axial supersonic ORC impulse turbines, which takes properly into account dense gas effects. This is based on the MOC along with the vortex flow field approach, previously introduced for perfect gas flows (Goldman, 1968; Paniagua et al., 2014), extended to the dense gas case.

The performances of blade shapes obtained with MOC using different organic working fluids are then evaluated by means of numerical simulations carried out using the ANSYS CFX code, both for the isolated rows and for a supersonic turbine stage.

2. SUPERSONIC IMPULSE TURBINE BLADES DESIGN

In this Section we first recall the Method of Characteristics (MOC) for the design of perfect gas supersonic nozzles and its extension to dense gas flows. Then, we present its application to the design of supersonic rotor blades, in conjunction with a free-vortex methodology.

2.1 MOC for supersonic nozzle design

The MOC is a classical method for the design of the divergent part of supersonic nozzles under the hypotheses of 2D, steady and homentropic flow. Such a flow is governed by the 2D isentropic Euler equations, which represent an hyperbolic system of conservation laws characterized by two families of characteristic lines. These are defined by equations of the form (Délery, 2010; Zucrow and Hoffman, 1976):

$$\frac{dy}{dx} = tan(\varphi \mp \mu) \tag{3}$$

where φ is the local flow angle and $\mu = arcsin(M^{-1})$ is the Mach angle. Rewriting the governing equations in the characteristic reference frame, one gets the so-called compatibility equations, which are just ordinary differential equations, of the form:

$$d\varphi \pm \sqrt{M^2 - 1}\frac{dV}{V} = 0 \qquad (4)$$

where V is the velocity magnitude and the sign + or − denotes a left-running or − a right-running characteristic line, respectively. For a perfect gas, equations (4) can be integrated analytically after rewriting dV/V in terms of the Mach number and by making use of the equation of state, leading to the well-known Prandtl-Meyer relations:

$$\varphi \pm v(M) = constant \text{ (along a characteristic)} \qquad (5)$$

The preceding equations, along with the equations of the characteristic lines (3) are then used as described in (Délery, 2010) to design the nozzle wall contour. In the case of a dense gas, equation (4) can no longer be integrated analytically. Instead, we use a numerical method for ordinary differential equations, namely, Heun's second-order predictor-corrector method to carry out the integration along characteristic lines. The discretized compatibility equation is supplemented by dense gas equations of state to compute all of the required thermodynamic properties. Precisely, we make use of the thermodynamic library REFPROP (Lemmon et al., 2013), which contains reference multiparameter equations of state for many dense gases of potential interest as ORC working fluids. Extensions of the MOC to dense gases were proposed in the past by (Guardone et al., 2013; Wheeler and Ong, 2013) with focus on the design of De-Laval nozzles or radial turbine injectors, respectively. In (Bufi et al., 2015) the methodology is extended to dense gas models by using reference EOS and applied to axial turbomachinery design. Once the nozzle divergent has been designed via the MOC, a geometrical postprocessing procedure is applied to generate a supersonic turbine nozzle. Some geometrical parameters are imposed in order to control the final blade geometry (see figure 2): the stagger angle θ, the angular extension Φ and the radius of the leading edge arc cb, the radius R of the leading edge arc cd and the trailing edge thickness ef.
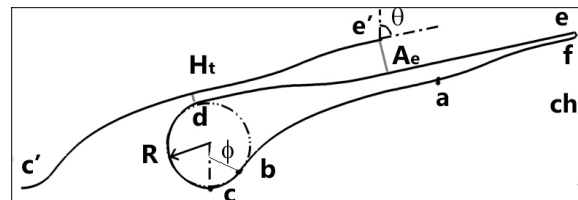

Figure 2: Example of supersonic stator blade geometry designed with MOC.

2.2 Design of dense gas supersonic rotor blades

For the design of supersonic rotor blades we follow the procedure described in (Paniagua et al., 2014; Goldman, 1968) for perfect gas flows and we extend it to dense gases.

The flow at the rotor inlet is assumed as a uniform one that is simply deflected by the rotor blades. To achieve this deflection, the flow passes through a transition region delimited by upper and lower transition arcs and by characteristic lines. For clarity, the transition region is sketched in figure 3, where AB and CD are transition arcs and the dashed lines are used to represent the characteristics. Through this region, the uniform inlet flow is converted into a free vortex flow, for which $V \cdot R = constant$, with R the radius of curvature of a streamline and V the constant velocity along it, following an isentropic transformation.

Figure 4 shows a schematic description of the rotor blade geometry designed with MOC. We use the same notation of the MOC for perfect gases reported in (Paniagua et al., 2014; Goldman, 1968) and we refer to them for details. In order to start with the design procedure for dense gases, the following input parameters are defined: inlet total pressure and temperature; inlet/outlet relative flow angle β_i/β_o;

AB Upper transition arc
CD Lower transition arc
CE Major expansion characteristic
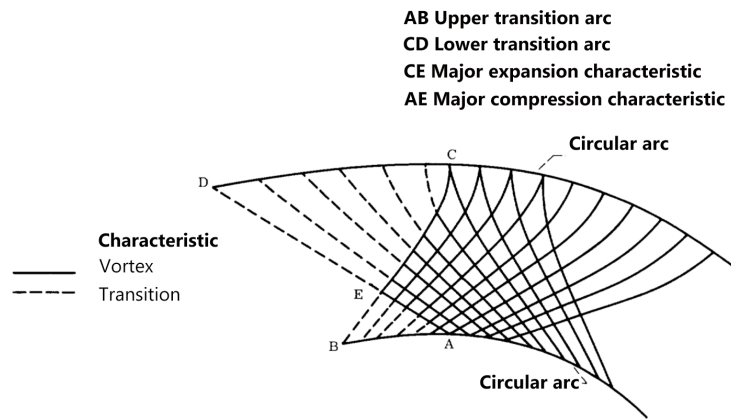AE Major compression characteristic

Figure 3: Scheme of the system of characteristic lines in the rotor vane. (Goldman, 1968)
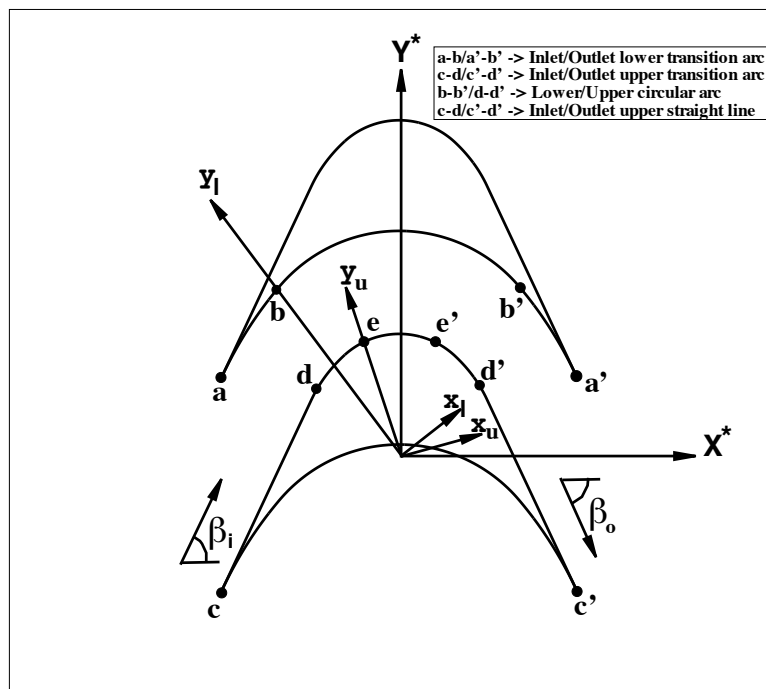
Figure 4: Schematic description of the rotor blade design.

inlet/outlet Mach number M_i/M_o; the lower arc Mach number M_l, assigned on the lower circular arc b-b'; the upper arc Mach number M_u, assigned on the upper circular arc d-d'. As for the perfect gas model, the lower and upper transition arcs (a-b/a'-b' and d-e/d'-e' for inlet and outlet, respectively) are determined in the unrotated lower/upper reference systems (denoted with subscripts l and u). The geometry is then rotated in the $X^* - Y^*$ reference system and completed with the straight line parts c-d/c'-d' and the circular arcs b-b'/d-d'.

The MOC for perfect gas algorithm makes use of the analytical expressions of the Prandtl-Meyer function $v = v(M)$ and of the critical Mach number $M^* = M^*(M)$ (with $M^* = V/a^*$ and a^* the critical speed of sound) for perfect gases. For a dense gas, no such analytical expressions are available.

The calculation of the critical Mach number is replaced by the following iterative procedure:

1. The critical speed of sound is first computed from the known values of the total pressure p_0 and temperature T_0 by using a thermodynamic library available in REFPROP

2. An initial tentative value $M^{*(0)}$ for the critical Mach number is prescribed.

3. At each iteration of the method, an updated value of the velocity magnitude is computed as $V^{(m)} =$

$$M^{*(m-1)}a^*$$

4. The latter is used to compute an updated value of the specific static enthalpy $h^{(m)}$, given the total enthalpy $h_0 = h_0(p_0, T_0)$.

5. The speed of sound is then updated by using the thermodynamic relation $a^{(m)} = f(h^{(m)}, s)$, where the entropy s is constant everywhere and is known from the prescribed inlet conditions.

6. Finally, an updated value of the Mach number $M^{(m)} = V^{(m)}/a^{(m)}$ is obtained.

7. If $M^{(m)} - M^{(m-1)}$ is below a given tolerance, the procedure is stopped. Otherwise, a new value is assigned for $M^{*(m+1)}$ (by using a bisection procedure) and the iteration is started again.

The design procedure above is completed by adding a finite leading-edge/trailing-edge thickness. Besides, non-symmetrical blades with various degrees of reaction can be designed if different inlet/outlet input parameters are imposed. In this work, unique incidence problems related to the supersonic relative flow on the rotor inlet are neglected on design stage, due to the interest on viscous effects which could make useless any incidence angle calculation based on inviscid theory.

2.3 Example of rotor blade designs
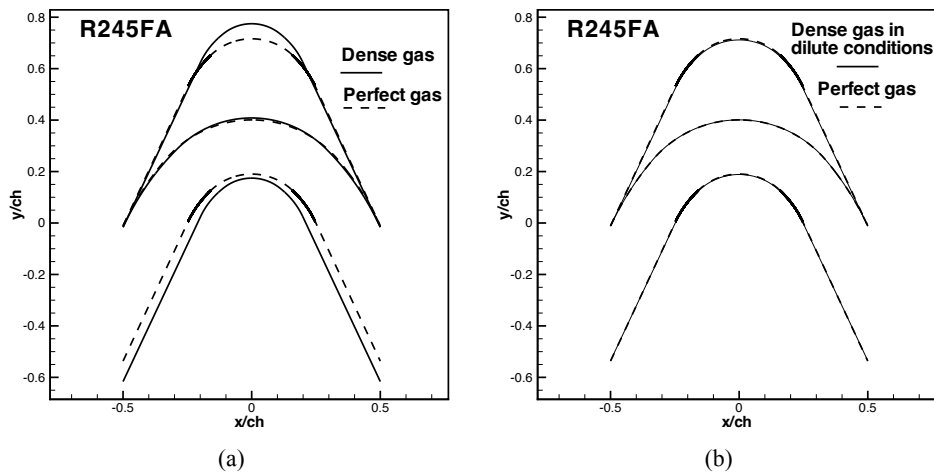

(a) (b)

Figure 5: Blade designs for R245FA at operating conditions ($p_r^0 = 1.05$, $T_r^0 = 1.05$) (a) and at conditions ($p_r^0 = 0.055$, $T_r^0 = 1.15$)(b). Dashed lines represent designs obtained under the perfect gas model.

Four organic working fluids are used to test the MOC. Their critical properties are shown in table 1, where γ is the specific heat ratio in the dilute gas limit along the critical isotherm curve (Guardone et al., 2013). The design algorithm for rotor blades has been run for a typical ORC working fluid, namely

Table 1: Thermophysical properties for different organic substances, based on reference EOS (from REFPROP ver. 9.1).

	R245fa	R227ea	R134a	R236fa
$p_c[MPa]$	3.651	2.93	4.06	3.2
$T_c[K]$	427.16	374.9	374.2	398.07
$\rho_c[kg/m^3]$	516.08	594.2	511.9	551.3
$M_w[g/mol]$	134.05	170.03	102.03	152.04
γ	1.061	1.056	1.092	1.059

R245FA, whose thermophysical properties are given in table 1 and used to investigate the impact of real gas effects on the resulting geometry. The degree of reaction is set to zero, so that the resulting geometry is symmetric. Figure 5 shows a comparison of geometries calculated with different operating

conditions and gas models. The first operation point (characterised by the reduced pressure $p_r^0 = 1.05$ and the reduced temperature $T_r^0 = 1.05$) is very close to the R245FA upper saturation curve and this affects the rotor geometry, leading to larger cross section variations with respect to perfect gas. Indeed, a greater generic area to throat area ratio is addressed to the REF geometry. This is a typical behavior already seen in supersonic stators (Guardone et al., 2013). It is due to the effect of Γ that, being lower than one in dense gas regions, provides higher exit-to-throat area ratios.

Figure 5b shows the design obtained for a lower total pressure ($p_r^0 = 0.055$) and higher total temperature ($T_r^0 = 1.15$), so that the thermodynamic conditions at rotor inlet lie far from the dese gas region. Here, the blade designed with a dense gas EOS is very similar to that obtained with the perfect gas model. Then,

Table 2: Geometrical output parameters for four different organic fluids under the same operating condition ($p_r^0 = 1.28$, $T_r^0 = 1.28$, $M_{in} = M_{out} = 1.5$, $M_l = 1$, $M_u = 2$,$\beta_{in} = \beta_{out} = 65°$).

	R245fa	R227ea	R134a	R236fa
σ	1.82	1.81	1.85	1.82
ch^*	2.31	2.32	2.30	2.31
ph^*	1.27	1.28	1.24	1.27

a parametric study for several working fluids suitable for ORC applications at the same reduced input conditions has been carried out. Fluid properties are also given in table 1. For all of the fluids, the input thermodynamic conditions and design parameters are set to ($p_r^0 = 1.28$, $T_r^0 = 1.28$, $M_{in} = M_{out} = 1.5$, $M_l = 1$, $M_u = 2$,$\beta_i = \beta_o = 65°$). Table 2 provides the following geometrical parameters for the resulting designs: blade solidity σ, defined as the axial chord to pitch ratio; the axial chord ch^* and pitch ph^* normalized respect to the critic radius r^*, the latter defined as the radius of the sonic streamline in the vortex flow field. It can be noticed that the lower is the fluid molecular complexity (as for the R134A fluid) the higher is the solidity.

3. NUMERICAL SIMULATIONS

Viscous 2-D numerical simulations have been carried out for both an isolated rotor blade row and a full turbine stage designed using the MOC methods presented in this paper. The CFD software used is the commercial code Ansys CFX 16.0. The turbulence model used is k-omega SST (Shear Stress Transport). The thermodynamic properties of the fluids are modelled using the real gas properties (rgp) library (AN-SYS, 2015). The rgp files contain property tables mapped as a function of temperature and pressure along the turbine expansion and allow accurately taking into account dense gas effects.

In table 3 the parameters used to design the blade shapes and to perform the simulations with the R245FA working fluid are shown. In order to assess the presence of dense gas effects it is important to evalu-

Table 3: Rotor blade design parameters.

Parameters	Values
Inlet total relative pressure [bar]	6
Inlet total relative temperature [K]	393.15
Inlet relative Mach number	1.5
Inlet relative flow angle [°]	60
Suction side circular arc Mach number	1.9
Pressure side circular arc Mach number	1.1

ate the position of the operating point on the working fluid state diagram. In figure 6a the isentropic evolution of the expansion on the T-S diagram is shown. The presence of strong dense gas effects is expected, since fundamental derivative Γ is below 1 throughout the expansion (see figure 6b). It can be noticed that, for this application, the strongest dense gas effects occur mainly inside the nozzle, where

the enthalpy drop is elaborated. This is due to the "dry" nature of R245FA fluid which allows to have the last part of expansion farther from the saturation curve. Simulations for an isolated supersonic rotor
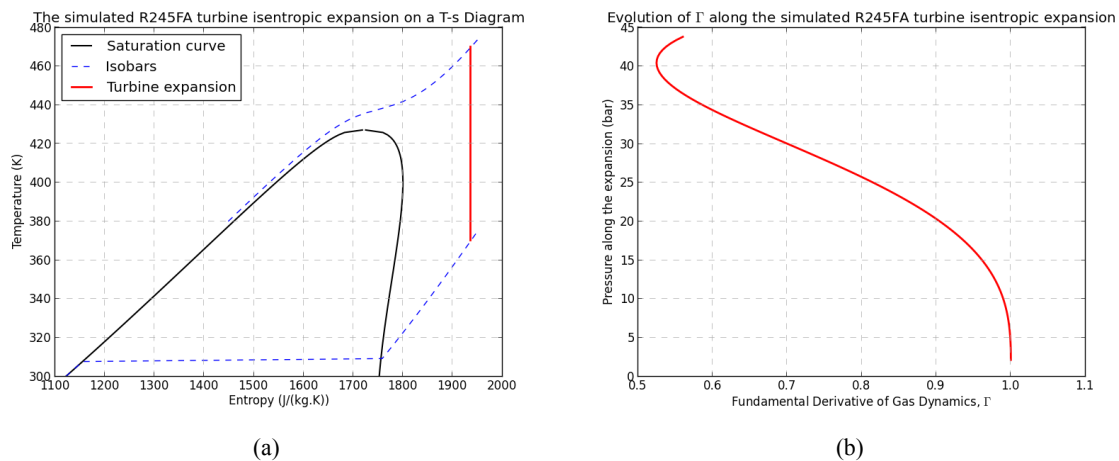

(a)   (b)

Figure 6: Isentropic turbine expansion on the R245FA T-S diagram (a); Fundamental Derivative of gas dynamics Γ evaluated along the turbine expansion (b).

blade row using fluid R245FA have been carried out in the relative reference system. The blade row considered is symmetric, so the outlet conditions are identical to the inlet conditions. The inlet rotor angle is prescribed according to the stator exit conditions.

By using the Zweifel empirical coefficient (Zweifel, 1945), the number of rotor to stator blades ratio is set to 2. The 2-D computational grid for the full stage simulation is composed of C-shaped blocks around the blades and of H-shaped blocks at stage inlet and outlet shown in figure 7a. It is generated using Ansys TurboGrid and refined to obtain y+ values less than 1 at the blade walls with 330066 total number of elements (121704 overall elements for the rotor row and 208362 elements for the stator row). Simulations for a full turbine stage involving a supersonic rotor blade row and a supersonic stator blade row both designed by the means of the MOC procedures presented in this paper are carried out. The total temperature, the total pressure and the velocity components are imposed at the inlet. Average static pressure is set at the outlet and a mixing-plane boundary condition is set at the stator-rotor interface. Table 4 presents the main turbine working parameters, taken from a real-world application (they are different from those used in the previous section 2.4). In order to maximize the impact of dense gas effects, we choose supercritical turbine inlet conditions (see figure 6a). Only the results for R245FA fluid are shown because of the absence of substantial differences among the other fluids considered in this paper (see table 1). Figure 7b presents the relative Mach number distribution for the full turbine stage simulation. The flow is accelerated in the stator vanes up to the design absolute Mach number of 2.4 and, thanks to the accurate design with the MOC algorithm, no normal shocks are formed in the divergent part of the nozzle. Thanks to the accurate design with the MOC algorithm, no normal shocks are formed in the divergent part of the nozzle. However, weak oblique shocks are generated at the trailing edge of the stator due the rounded trailing edge. These shocks interact with the viscous wake, visible on the stator outlet. Due to the mixing plane interface, interactions of the latter with the rotor row can not be observed. The flow in the rotor vanes is characterised by weak oblique shocks departing both from the leading and trailing edge of the blades due to the finite thickness of the actual rotor geometry. The turbine is found to be in a "started" configuration, since a normal shock at the inlet is avoided and the flow inside the rotor vanes is supersonic (Kantrowitz et al., 1945). The flow in the relative reference frame is then deflected by the blade vanes up to a relative Mach number slightly lower than the design one due to the set of oblique shocks departing both from leading and trailing edge. To better analyse the flow behaviour in the rotor vanes an isolated rotor simulation has been performed (see figure 8b). At the inlet of the rotor vanes, the presence of an oblique shock wave is noticed. Two oblique shocks depart also from trailing

edge: one impinges the suction side while the other one interacts with the viscous wake. The careful design of the rotor blade prevents the formation of a normal shock at the inlet that would slow down the flow to subsonic conditions within the blade passage. The calculated total to total isentropic efficiency for this turbine is 92.9%. In order to assess the main source of losses in the turbine stage, it is useful to analyse the entropy deviation $(S - S_{in})/S_{in}$, with S_{in} the specific entropy at inlet. The entropy deviation is shown in figure 8a for the isolated rotor. Entropy is mainly generated with the viscous boundary layers and wakes, whereas entropy generation across shocks is extremely weak. This demonstrates that the proposed methodology provides blade designs with negligible shock losses. The presence of viscous effects also modify the design degree of reaction, set to zero for the design here proposed. The actual degree of reaction evaluated after simulations is found to be 0.042. This effect can be addressed to the modification of the effective blade vane geometry due to the boundary layer thickness, which lead to lower passage sections going from inlet to outlet.

Table 4: Main turbine full stage working parameters.

Parameters	Values
Inlet total reduced pressure	1.2
Pressure ratio	20.6
Inlet total reduced temperature	1.1
Stator nozzle outlet design Mach number	2.4
Stator stager angle [°]	70
Rotor blade speed [m/s]	141.37

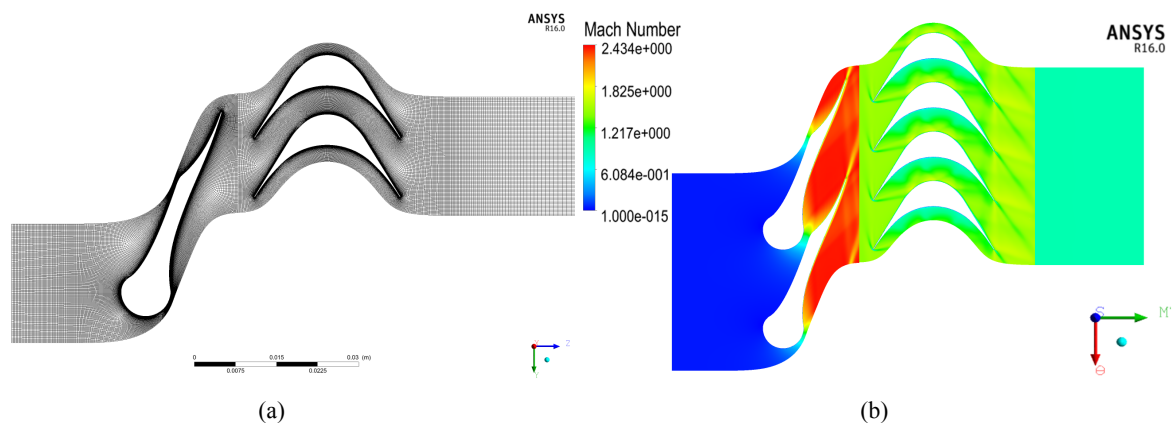(a)   (b)

Figure 7: Computational block structured grid for full turbine stage (330066 elements) (a); relative Mach number distribution for R245FA fluid (b).

4. CONCLUSIONS

An efficient design procedure for supersonic ORC turbine rotor blades taking carefully into account dense gas effects has been developed. It is based on the method of characteristics and allows designing blade vanes by imposing the momentum conservation through a free vortex flow condition. Significant differences are found between geometries obtained with the ideal and dense gas models. The numerical simulations show that the accurate blade design in dense gas flow regime allows accounting for the dense gas phenomena during expansion and avoiding the focusing of characteristic lines into strong right shocks inside the blade vanes. The main source of loss of performances can be then addressed to the viscous phenomena, as confirmed by the entropy deviation analysis.

Future developments of the supersonic ORC turbine stage design process will lead to the unsteady nu-
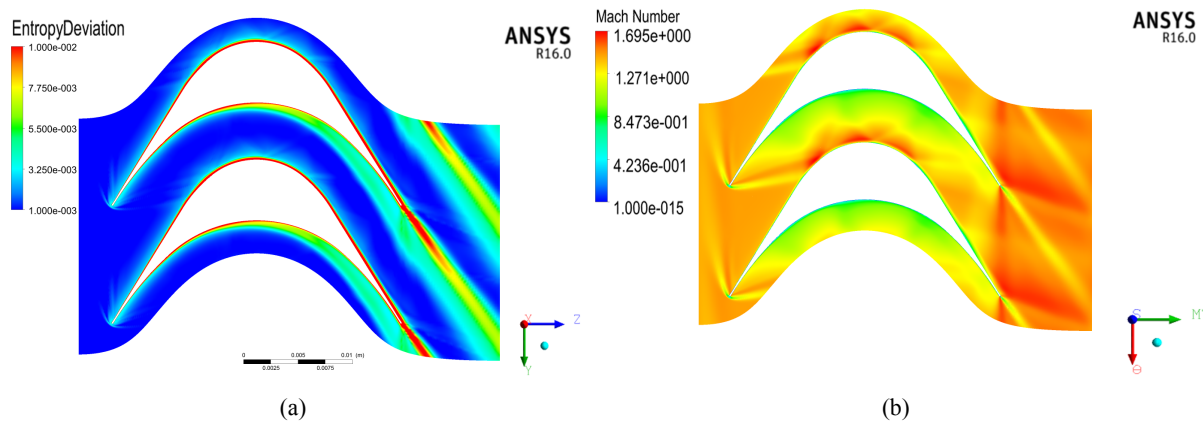
Figure 8: Entropy deviation contour plot for the isolated rotor (R245FA fluid) (a); Mach number distribution for the isolated rotor (R245FA fluid) (b).

merical analysis of the entire turbine stage in order to take into account the interactions between stator and rotor due to viscous phenomena along with the 3-D turbine full stage design.

ACKNOWLEDGEMENTS

REFERENCES

ANSYS, I. (2015). Ansys cfx-solver modeling guide.

Bufi, E. A., Cinnella, P., and Merle, X. (2015). Sensitivity of supersonic orc turbine injector designs to fluctuating operating conditions. *Proceedings of the ASME 2015 Turbo Expo Turbine Technical Conference, ASME TURBO EXPO 2015 June 15-19, 2015, Montreal, Canada (Submitted and accepted)*.

Colonna, P., Nannan, N., Guardone, A., and Van der Stelt, T. (2009). On the computation of the fundamental derivative of gas dynamics using equations of state. *Fluid Phase Equilibria*, 286(1):43--54.

Congedo, P., Corre, C., and Martinez, J.-M. (2011). Shape optimization of an airfoil in a BZT flow with multiple-source uncertainties. 200(1-4):216 -- 232.

Cramer, M. and Tarkenton, G. (1992). Transonic flows of bethe-zel'dovich-thompson fluids. *Journal of Fluid Mechanics*, 240:197--228.

Délery, J. (2010). *Handbook of compressible aerodynamics*. ISTE.

Goldman, L. J. (1968). Analytical investigation of supersonic turbomachinery blading. 1/2-analysis of impulse turbine-blade sections.

Guardone, A., Spinelli, A., and Dossena, V. (2013). Influence of molecular complexity on nozzle design for an organic vapor wind tunnel. *Journal of Engineering for Gas Turbines and Power*, 135(4):042307.

Kantrowitz, A., Donaldson, C., Laboratory, L. A., and for Aeronautics, U. S. N. A. C. (1945). *Preliminary Investigation of Supersonic Diffusers*. National Advisory Committee for Aeronautics.

Lemmon, E. W., Huber, M. L., and McLinden, M. O. (2013). *NIST Reference Fluid Thermodynamic and Transport Properties - REFPROP Version 9.1*. NIST.

Paniagua, G., Iorio, M., Vinha, N., and Sousa, J. (2014). Design and analysis of pioneering high supersonic axial turbines. *International Journal of Mechanical Sciences*, 89:65--77.

Thompson, P. A. (1971). A fundamental derivative in gasdynamics. *Physics of Fluids (1958-1988)*, 14(9):1843--1849.

Wheeler, A. P. and Ong, J. (2013). The role of dense gas dynamics on orc turbine performance. In *ASME Turbo Expo 2013: Turbine Technical Conference and Exposition*, pages V002T07A030--V002T07A030. American Society of Mechanical Engineers.

Zucrow, M. J. and Hoffman, J. D. (1976). Gas dynamics. *New York: Wiley, 1976*, 1--2.

Zweifel, O. (1945). The spacing of turbomachine blading, especially with large angular deflection. *Brown Bovery Review 32*.

NOMENCLATURE

a	Speed of sound	(m/s)
ch	Axial chord	(m)
p	Pressure	(Pa)
ph	Blade pitch	(m)
G	Mass-flow rate	(kg/s)
H	Specific enthalpy	(J/kg)
M	Mach number	
R	Radius for the design of the convergent	(m)
R_g	Specific gas constant	$(J/kg * K)$
S	Specific entropy	$(J/kg * K)$
T	Temperature	(K)
V	Velocity	(m/s)
β_a	Leading edge attach angle	(rad)
γ	Specific heat ratio	
η_{is}	Isentropic efficiency	
θ	Stagger angle	(rad)
μ	Mach angle	(rad)
v	Prandtl-Meyer function	
v_s	Specific volume	(m^3/kg)
ρ	Density	(kg/m^3)
σ	Blade solidity (chord to pitch ratio)	
φ	Flow angle	(rad)
Φ	Leading edge angular extension.	(rad)

Subscript

r	Reduced: normalised respect to critical conditions.
c	Critical thermodynamic property.
0	Total/reservoir thermodynamic property.

Superscript

$*$	Critic (sonic) parameter.

Acronyms/abbreviations

MOC	Method Of Characteristics.
REF	REFPROP model.
EOS	Equation Of State.
CFD	Computational Fluid Dynamics.
ORC	Organic Rankine Cycle.

DEVELOPMENT OF A TURBO-GENERATOR FOR ORC SYSTEM WITH TWIN RADIAL TURBINES AND GAS FOIL BEARINGS

Young Min Yang[1,2,3], Byung Sik Park[1,2*], Si Woo Lee[3], Dong Hyun Lee[2],

[1]Advanced Energy and Technology, Korea University of Science and Technology,
217 Gajeong-ro, Yuseong-gu, Daejeon 305-333, Republic of Korea
e-mail: ymyang@kier.re.kr

[2]Energy Efficiency Research Division, Korea Institute of Energy Research,
152 Gajeong-ro, Yuseong-gu, Daejeon 305-343, Republic of Korea
http://www.kier.re.kr (e-mail: bspark@kier.re.kr)

[3]Jinsol Turbomachinery Co., Ltd.,
94-17 Techno2-ro, Yuseong-gu, Daejeon, 305-509, Republic of Korea
http://www.jinsolturbo.co.kr (e-mail: impentacle@jinsolturbo.co.kr)

ABSTRACT

The interest in ORC plant is increasing over recent years in terms of the energy and the environment costs. But the capital cost and maintenance cost of an ORC plant are the main obstacles of the wide spread in the global market. To overcome them, it is necessary to decrease the manufacturing and maintenance cost, and to increase the turbine efficiency and the system availability.

Korea Institute of Energy Research (KIER) and Jinsol Turbomachinery have jointly developed a novel turbo-generator applicable to the low temperature heat sources to meet those needs.

The turbo-generator developed is almost maintenance-free, highly efficient and completely hermetic. A high speed permanent magnet synchronous generator (PMSG) was applied to get the high efficiency. Radial turbines were directly coupled with the PMSG without a gear box to reduce the power transfer loss and cost. The rotor shaft was supported by gas foil bearings to increase the system availability through the non-contacting bearings. Twin radial turbines were assembled with the rotor shaft in the way of face-to-face to cancel out the axial load caused by the pressure difference. This configuration made it possible to apply a gas foil bearing as a thrust bearing despite of its low load capacity. A gas foil bearings is the simple and cheap solution for the rotor support system and the completely hermetic turbo-generator. The high efficiency of the radial turbine was acquired by the real gas modelled turbine design with optimum specific speed.

The developed turbo-generator was integrated with the 100kWe ORC plant installed at KIER and it showed that the turbo-generator efficiency was about 80% as the result of the performance test with the temperature difference of 70℃ between the heat source inlet and the heat sink inlet.

1. INTRODUCTION

In terms of energy issues and environmental aspects, the interest in ORC (Organic Rankine Cycle) plant is increasing over recent years because of its applicability and availability for low temperature heat sources. An ORC has nearly the same components with a conventional steam Rankine cycle except using organic compounds instead of water. The organic compounds applicable to the low temperature heat source (<100~150℃) usually have lower boiling point than the water because ORC plants are applied to generate power from low-temperature heat sources (Quoilin *et al.*, 2013).

Although ORC power plant is considered as one of the promising technologies for generating power form low-temperature heat sources, its high capital cost and maintenance cost are the main obstacles in the wide spread on the global market (Quoilin *et al.*, 2013 and Wang *et al.*, 2011). Mainly the high capital cost and low cycle efficiency cause the low IRR for the ORC power plant. It is necessary to improve the capital cost, maintenance cost, cycle efficiency and system availability to obtain high IRR. In terms of cost, the capital cost of heat exchanges should be reduced at first because it is more than half of the total power plant capital cost and the costs of other components should be reduced secondly. The maintenance cost also should be reduced more. For revenue from the power generation, it is more important to obtain high cycle efficiency (by the components with high efficiency and system optimization) and high system availability (low maintenance shut-down by the robust components) to get more power from the given conditions.

In spite of its drawbacks, ORMAT, Turboden, BNI, UTC, Electratherm, Access Energy and so on have supplied their ORC power plant in the global market. And new manufacturers appear in the market continuously. Most of them select the turbines as their expanders while some others such as Electratherm and Kobelco use the screw type expanders especially in small power capacity plant (Kang, 2012, Takahashi *et al.*, 2013, Yuksek and Mrimobin, 2013). Many research studies were conducted with various types of expanders. According to the summary of Fu *et al.* (2015), a scroll expander is dominant in the ORC system with less than 50kW power output. But the reason is that the power capacities of the investigated studies are less than 10kW except some cases.

The expander and the generator are the most important components in the ORC power plant because they convert the electric power from the temperature difference between the heat source and heat sink. To overcome ORC's disadvantages, the expander and the generator must be highly efficient and robust at design point and off-design points. In addition, the expander-generator set must have the advantages such as high system availability, low manufacturing cost, light weight, small volume, easy maintenance, hermetic configuration, and excellent endurance performance.

This study presents the design and development of a novel turbo-generator applicable for low temperature heat sources in 100kW class ORC power plant to meet the needs suggested above. In addition, this paper presents the test results of the 100kW-class turbo-generator under some operation points.

2. DESIGN OF TURBO-GENERATOR

This 100kW power class turbo-generator was integrated to the 100kW class ORC power plant in the Korea Institute of Energy Research (KIER), Korea. R245fa was selected as the working fluid in the ORC system on the basis of the available heat source and heat sink temperature. Although various refrigerants were adopted in the numerous studies (Fu *et al.*, 2015, Bao and Zhao, 2013), there exists the proper refrigerant which might be used in the ORC system considering the various aspects such as cycle efficiency, fluid density, safety, and environmental effects.

2.1 Mechanical Layout
The turbo-generator was designed to meet the requirements listed above: high efficiency, high system availability, low manufacturing cost, light weight, small volume, easy maintenance, hermetic configuration, and excellent endurance performance. The turbo-generator was suggested to adopt the radial in-flow turbine, permanent magnet synchronous generator, gas foil bearing, and direct coupling between turbine and generator. The mechanical arrangement was that the twin radial in-flow turbines are located in the front-to front way and the generator is located between them as shown in Figure 1.
By selecting the radial in-flow turbine, the manufacturing cost can be reduced with the high efficiency. And compact size and light weight can be obtainable. The high rotational speed of turbine is inevitable to meet the optimum specific speed but this high speed makes the turbo-generator compact and small.
Due to the high speed, the high speed permanent magnet synchronous generator (PMSG) and the low

speed generator with a gear box can be the candidates. For this turbo-generator, the PMSG was selected as a generator. It has higher efficiency than other type generators, light weight, and small volume due to the high rotational speed. It can rotate at various speeds regardless the grid power frequency. That makes the radial turbine rotate at its optimum speed with the maximum efficiency. But its small volume has small surface area for its cooling. It makes hard to design the cooling system in spite of its low heat generation due to its high efficiency. Also it needs power converting system (PCS) to convert the generator side power-generating-frequency that depends on the rotational speed of generator to grid side one. But the power converting efficiency is higher than that of a gear box. PCS does not need the lubrication oil, an oil cooling system, and its maintenance such as oil change. It is more attractive to adopt the PMSG and PCS in the turbo-generator for ORC power plant.
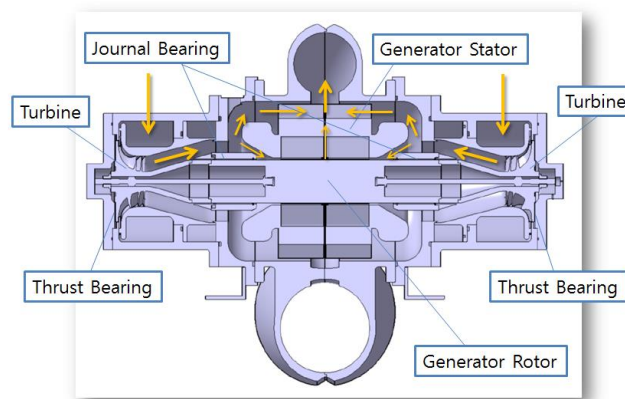
Figure 1: Mechanical Layout of the 100kW turbo-generator for ORC plant

A gas foil bearing was applied in the rotor support for the journal bearing and the thrust bearing. It is the gas foil bearing that is one of the non-contact bearing and oil free bearing. It makes the maintenance-free turbo-generator possible due to its special characteristics mentioned above. A magnetic bearing also has these characteristics but it has many complicate components (its own exclusive controller, position sensors and so on) and more power consumption. It may increase the cost of the ORC plant.

But the gas foil bearing has small load capacity. While it is not the problem in journal bearing, it can be a severe problem in thrust bearing because it should have the load capacity for the axial load caused by the pressure difference between the front side and back side of the radial turbine.

Table 1: Design requirements of radial turbine

Parameters	Unit	Values
Inlet Temperature	℃	59.8
Inlet Pressure	bar	4.56
Expansion Ratio	-	4.67
Mass Flow Rate	kg/s	2.5 (for each turbine) (total: 5 for twin turbines)
Output Power	kW	58.5 (for each turbine) (total: 117 for twin turbines)
Efficiency	%	85
Working Fluid	-	R245fa

As shown Figure 1, the turbine and the generator's rotor were coupled directly to skip the gear box and its oil handling system. And the twin turbines were arranged in the front-to front formation. It makes possible to cancel out the axial load caused by the pressure difference in each single turbine.

Theoretically the axial load caused by the turbine is zero, which allowed us to use the gas foil bearing as the thrust bearing. The thrust bearing was located at the back face of each twin turbines as shown in Figure 1. In addition, the generator was located between the twin turbines' exits. The relatively cool working fluid can flow into the generator from the turbine exit after expansion. It can cool down the generator by the cooling passage shown in Figure 1. It makes possible to omit the other cooling passage and to save the loss of working fluid for the cooling passage. Table 1 shows the design requirements of radial turbine on the basis of ORC plant cycle design.

2.2 Radial Turbine and PMSG

The radial turbine was designed on the basis of the thermodynamic properties of working fluid, R245fa to meet the specification shown in Table 1. The stage efficiency of the radial turbine was expected as high as 90% with Reynolds Number effect corrected. The rotational speed of the turbine was selected as an optimal value which corresponds to the optimal specific speed. The main flow sections of the turbine stage, i.e. rotor exit, rotor inlet were designed on the basis of optimum velocity triangles which makes the rotor exit relative flow velocity at the tip radius and the rotor inlet absolute flow velocity as minimum respectively and no swirl at the rotor exit. The minimum velocity design minimizes the aerodynamic losses and no swirl at the outlet of turbine rotor makes the radial component of the exit velocity negligible (Aungier, 2006). The dimension of the main flow path is shown in Table 2 for the designed radial turbine.

Table 2: Dimension of the main flow path from the design results of radial turbine

Items	Unit	Values
Stator Inlet Radius	mm	105
Stator Outlet Radius	mm	82
Stator Blade Height	mm	10.6
No. of Stator Blade	-	20
Rotor Inlet Radius	mm	76
Rotor Inlet Blade Height	mm	10.6
Rotor Outlet Tip Radius	mm	54.6
Rotor Outlet Tip Radius	mm	20
No. of Rotor Blade	-	14

The wall contour of the turbine rotor and the blade profiles were generated with the proprietary in-house design code on the basis of the main flow path shown in Table 2 and the real gas model of R245fa using REFPROP developed by NIST. The final radial turbine is shown in Figure 2. Figure 2 (a) shows one of the twin turbine rotors and Figure 2 (b) shows one of the twin turbine stators.
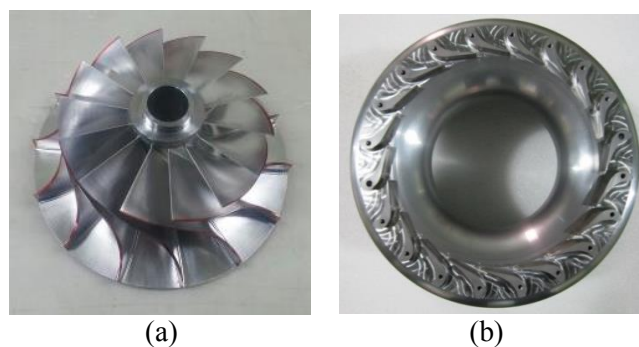

(a)   (b)

Figure 2: Radial Turbine Rotor (a) and Stator (b)

The generator was designed in the type of PMSG to obtain higher efficiency. A type of the rare earth magnet was used to get the strong permanent magnet. A samarium-cobalt magnet (Sm_2Co_{17}) is

preferred as the rotor magnet for PMSG because of its higher demagnetized temperature than others. Due to this, it can operate at higher temperature. The design specification and design results are shown in Table 3. The stator core was designed and constructed to have several cooling fins along the outside of it extended in the radial direction as shown in Figure 3 (a) to dissipate the heat generated by the iron loss and copper loss of the stator. It has also cooling passage in the middle of the stator core along the axial direction shown in the Figure 1 and Figure 3 (b). The cooling passage in the middle of the stator core is mainly the one for rotor shaft cooling, which can dissipate the heat from the can loss and the permanent magnet loss of the rotor shaft.

Table 3: Design specification and its result of PMSG

Items	Unit	Values
No. of Phase	-	3
No. of Poles	-	2
Rated Voltage(line-to-line)	V	480
Rated Current	A	137
Rated Power	kW	110
Efficiency	%	95
No. of Slots in Stator	-	24
Stator Outer Radius	mm	220
Stator Inlet Radius	mm	89
Rotor Radius	mm	85
Length of the Rotor Magnet	mm	150

(a)   (b)
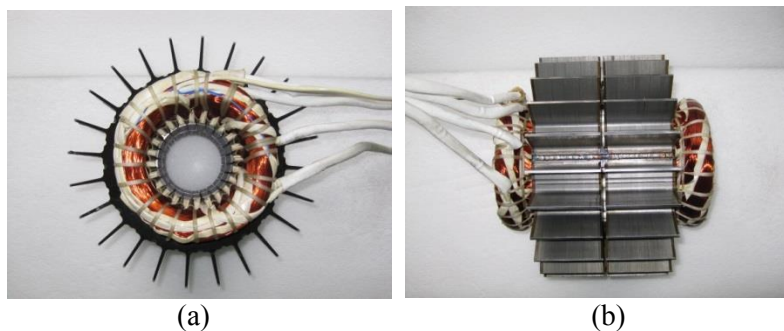
Figure 3: Stator for the PMSG Type Generator

2.3 Gas Foil Bearings

Twin turbine rotors were assembled at each end of the generator rotor shaft which was the part of the turbo-generator rotor to obtain the face-to-face configuration. The whole rotor was supported by the journal bearings and the thrust bearings as shown in Figure 1. The journal bearings support the radial load caused by the rotor weight and the thrust bearings support the axial load caused by the pressure difference between turbines, respectively. According to the literatures, the load capacity of a journal foil bearing is given by Equation (1) (Kus and Neksa, 2013).

$$C_{JB}=f_{JB}L_{JB}D_{JB}^2N \tag{1}$$

For the thrust bearing, the axial load on the rotor shaft could be ideally cancelled out to be zero because the rotor shaft is bilaterally symmetric. Therefore the axial load on the rotor is not significant. The thrust load capacity that can be supported by a thrust foil bearing, also is given by Equation (2) (Kus and Neksa, 2013).

$$C_{TB}=f_{TB}\pi w D_{TB}^2 N \tag{2}$$

According to the in-house design practice, the journal and thrust bearings were designed and made as shown in Figure 4. Figure 4 (a) is the top foil of the journal bearing and Figure 4 (b) shows the bump foil of the journal bearing placed between the top foil and the bearing housing. Figure 4 (c) is the thrust bearing located at the backside of each twin turbine.
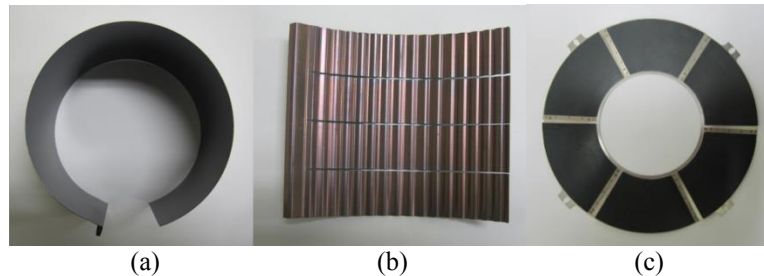

(a)   (b)   (c)

Figure 4: Gas Foil Bearing: Journal Bearing (Top Foil: a, Bump Foil: b) and Thrust Bearing (c)

3. TEST RESULTS AND DISCUSSION

Figure 5(a) shows the experimental apparatus for the turbine performance test. Actually the whole ORC power plant system was required to run the turbo-generator and to test its performance by the electrical power output from the generator. Then, the performance of the turbo-generator could be evaluated.

(a)   (b)
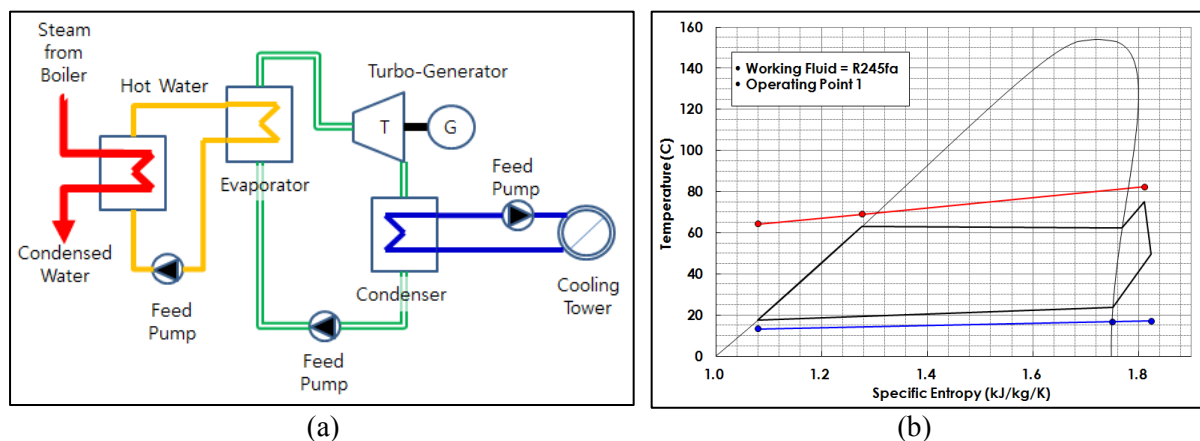
Figure 5: ORC power plant as a turbo-generator performance test rig

The orange line loop in Figure 5(a) is the hot water loop heated by the steam from the boiler as a heat source. The green line loop is the working fluid (R245fa) loop. The blue line loop is the cooling water line to absorb the heat rejection from the condensation of the working fluid. Steam line (red) and hot water loop (orange) were installed to simulate the hot-water type heat source. Figure 5(b) shows a plot of thermodynamic cycle in the temperature entropy diagram (T-S diagram) for an operating point Table 4 together with Figure 6 (a) show the operating conditions of the ORC power plant and the electrical power output at each operating point. The performance of the turbo-generator was evaluated on the basis of this power output. The mass flowrate of the heat source (hot water) was set to a constant value, 17kg/s. And the temperature difference between the heat source inlet and the heat sink inlet was also controlled to a constant value, about 70℃. Since the temperature difference was nearly

constant, the rotational speed of turbine was also kept nearly constant within 6% deviation. Figure 6 (a) also shows that the electrical power output was proportional to the mass flow rate of the working fluid.

The electrical power output was measured at the power output terminal of the generator. The (gross) cycle efficiency which is defined in Equation (3) increased from 5.2% to 7.3% while the mass flowrate increased. That means 40.4% increase along the flowrate increase. The efficiency of the turbo-generator means that of the total equipment composed of the turbine and generator. It is shown in Equation (4) that the efficiency is the ratio of the electrical power output to the ideal power output from the turbine.

Table 4: Electrical power output and control inputs at each measured operation point

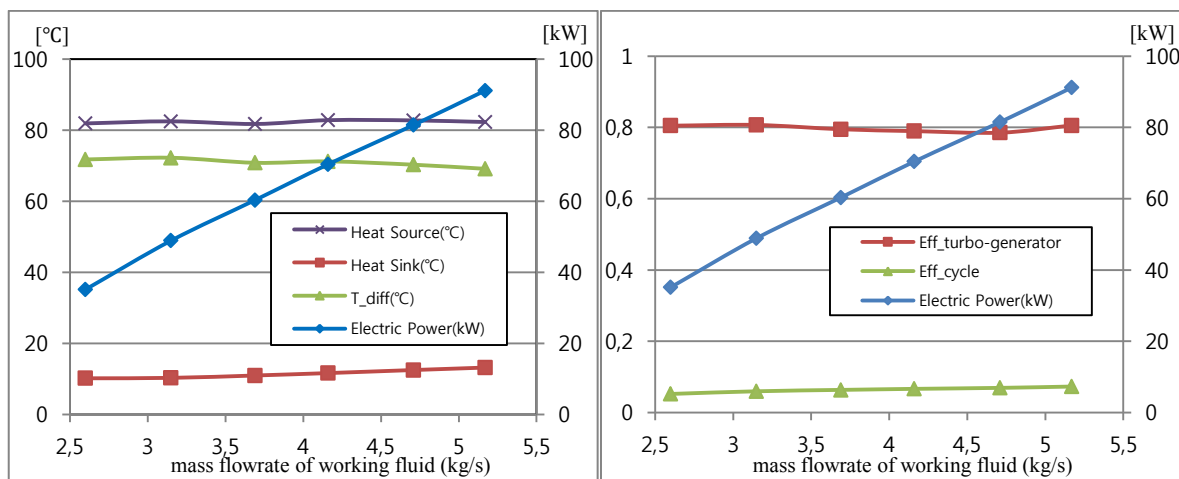| Operating Point	Electric Power Output (kW)	Control Inputs			
		Working Fluid Flowrate (kg/s)	Heat Source Inlet Temperature (℃)	Heat Sink Inlet Temperature (℃)	ΔT (℃)
1	91.20	5.17	82.32	13.17	69.14
2	81.50	4.71	82.78	12.48	70.30
3	70.43	4.16	82.85	11.62	71.23
4	60.34	3.69	81.77	10.94	70.84
5	48.93	3.15	82.52	10.27	72.26
6	35.17	2.60	81.93	10.15	71.78

Figure 6: Operation conditions and performance results

It was difficult to measure the temperature and pressure right after turbine exit because of the unique configuration of this turbo-generator. The temperature and the pressure were measure merely near the end-turn of the generator. Assuming that the pressure drop between them is negligible, ideal enthalpy drop can be calculated from the turbine inlet and outlet conditions. But the temperature difference was not negligible because of the temperature rise due to the generator loss and windage loss. Therefore only the turbo-generator efficiency was evaluated instead of the turbine efficiency. The calculated efficiencies of the turbo-generator ranged from 78.5% to 80.7% as shown in Figure 6. It matched well with the product of the design efficiency of the turbine and generator (0.85*0.95) without considering the windage loss.

$$\eta_{cycle} = \frac{P_e}{\dot{Q}_{in}} \tag{3}$$

$$\eta_{t-g} = \frac{P_e}{\Delta h_i \cdot \dot{m}_{ref}} \tag{4}$$

$$\eta_{t-g} = \eta_t \cdot \eta_g \cdot (1 - \xi_{wl}) \tag{5}$$

As shown in Equation (5), the efficiency of the turbo-generator is the product of the turbine efficiency, the generator efficiency, and the efficiency decrease due to the windage loss of the rest part of the rotor except the generator shaft. If the generator is designed with the specified efficiency (95%) and the windage loss is ignored, the turbine efficiency was 85% in the case of the maximum turbo-generator efficiency (80.7%).

4. CONCLUSION

The present study was the design and construction of a novel turbo-generator applicable for the low temperature heat sources to meet the market needs. It is almost maintenance free, highly efficient and completely hermetic. A unique configuration was developed including high speed permanent magnet synchronous generator (PMSG), twin radial turbines, and gas foil bearings. Twin radial turbines were assembled to the rotor shaft in the face-to-face configuration.

The performance test results of the turbo-generator showed that the maximum power output was 91.2kW. The maximal efficiency of the turbo-generator and cycle efficiency were 80.7% and 7.3%, respectively under the condition of 70℃ temperature difference between heat source and heat sink.

And the future study will focus on the clarification of the turbine and generator efficiencies, cost estimation compared with the other types, turbine efficiency change with respect to the operation points, and dynamic response of turbo-generator.

NOMENCLATURE

C	load capacity	(N)
D	diameter	(m)
f	bearing performance coefficient	(N/m^3/krpm)
L	axial length	(m)
$\dot{m}$	mass flow rate	(kg/sec)
N	rotor speed	(krpm)
P	power	(kW)
$\dot{Q}$	heat flow rate	(kW)
w	radial extent of the top foil	(m)
ξ	energy loss coefficient	(-)
η	efficiency	(-)
Δh	enthalpy difference	(kJ/kg)

Subscript

JB	journal bearing
TB	thrust bearing
t-g	turbo-generator

t	turbine
g	generator
e	electric
i	ideal
ref	refrigerant
wl	windage loss

REFERENCES

Aungier, R. H., 2006, *Turbine Aerodynamics; axial-flow and radial-inflow turbine design and analysis*, ASME Press, New York: p. 197-290

Bao, J., Zhao, L., 2013, A review of working fluid and expander selections for organic Rankine cycle, *Renewable and Sustainable Energy Reviews,* vol. 24: p. 325-342.

Fu, B., Lee, Y., Hsieh, J., 2015, Design, construction, and preliminary results of a 250-kW organic Rankine cycle system, *Applied Thermal Engineering*, vol. 80: p. 339-346

Kang, S., 2012, Design and experimental study of ORC and radial turbine using R245fa working fluid, *Energy*, vol. 41, no. 1: p. 514-524

Kus, B., Neksa, P., 2013, Development of one-dimensional model for initial design and evaluation of oil-free CO_2, *International Journal of Refrigeration*, vol. 36: p. 2079-2090.

Quoilin, S., Broek, M., Declaye, S., Dewallef, P., Lemort, V., 2013, Techno-economic survey of Organic Rankine Cycle(ORC) systems, *Renewable and Sustainable Energy Reviews,* vol. 22: p. 168-186.

Takahashi, K., et al., 2013, Binary Cycle Power Generation System for Hot Water, *"R&D" Kobe Steel Engineering Reports*, vol. 63, no. 2: p. 2-5

Wang, H., Peterson, R., Harada, K., Miller, E., Ingram, R., Fisher, L., 2011, Performance of a combined organic Rankine cycle and vapor compression cycle for heat activated cooling, *Energy*, vol. 36, no. 1: p. 447-458.

Yuksek, E., Mirmobin, P., 2013, High efficiency low temperature ORC system, *2nd International Seminar on ORC Power Systems*, Rotterdam

ACKNOWLEDGEMENT

EFFICIENCY CORRELATIONS FOR AXIAL FLOW TURBINES WORKING WITH NON-CONVENTIONAL FLUIDS

Marco Astolfi[1]*, Ennio Macchi[1]

[1]Politecnico di Milano, Energy Department,
Milano, Italy

*marco.astolfi@polimi.it

ABSTRACT

This work aims at defining a set of general correlations for the estimation of axial-flow turbine efficiency in Organic Rankine Cycle (ORC) field. A dedicated numerical tool is used for the optimization of several hundreds of turbines and the results are presented in specific parameters (SP, V_r and Ns) according to similarity rules. The analysis is carried out for single, two and three stages turbines. For each case a correlation of efficiency at optimal rotational speed is calibrated in function of the equivalent single stage SP and the total isentropic V_r. Three sensitivity analyses are proposed in order to highlight the effects of each single parameter on stage efficiency. Finally, the effect of fluid choice on turbine performance and dimension is discussed with a numerical example.

1. INTRODUCTION

The energy market is today more and more oriented to technical solutions able to exploit renewable energy sources and waste heat from industrial processes with the aim at reducing air and water pollution and increasing systems efficiency. In this context Organic Rankine Cycle (ORC) is one of the most reliable and mature solution for the exploitation of various energy sources characterized by a small available thermal power and/or a low maximum temperature. Typical fields of application of ORC technology are the geothermal energy, the solar energy, the biomass combustion and the heat recovery from industrial processes. ORCs have a simple layout characterized by a limited number of components; in addition they are extremely flexible showing good off-design performances in a large range of working conditions. The main advantage of ORCs is the possibility to select the most appropriate working fluid among a wide list of candidates guaranteeing high efficiency cycles in a large range of applications (Astolfi *et al*, 2014a). Despite their simplicity, the study of ORCs requires cross-functional expertise because the design and the optimization of these plants is largely influenced by the availability of (i) accurate equations of state (EoS), (ii) reliable cost correlations and (iii) efficiency correlations able to describe components performance. In particular, the expander is the key component of an ORC and the estimation of its efficiency and dimension is crucial to obtain a reliable evaluation of system performance and cost. The assumption of a fixed expander efficiency, independent of (i) the operative conditions (inlet and outlet thermodynamic states), (ii) the working fluid and (iii) the expected power output, may lead to unrealistic results (Astolfi *et al*, 2014b). In ORC field different types of expanders are used depending on the plant power output and the expansion ratio. Axial flow turbine is the most common choice and it is used by main market leaders like Ormat and Turboden, while Exergy has recently introduced high efficiency radial outflow turbines, especially suitable for high volume ratio expansions (Xodo *et al*, 2013). Radial inflow turbines are designed by Atlas Copco and by Calnetix GE in a large range of dimensions: from few tens of kW to tens of MW in geothermal applications. Finally, positive displacement expanders (scroll, pistons or screw devices) are proposed for small size applications like solar power plants and automotive ORC. This work is focused on axial-flow turbines because of their large market share and their capability to cover a large range of applications with high isentropic efficiency.

Various correlations, charts and diagrams for the estimation of axial turbine efficiency are proposed in literature but usually they lack in to account some variables of crucial interest in ORC field. The use of

1

complex and heavy fluids entails a design of ORC turbines which is different from either gas or steam turbines. Organic fluids generally operate at moderate temperatures and show a small isentropic enthalpy drop in expansion leading to the design of compact turbines with a reduced number of stages and low load coefficients (k_{is}). Peripheral speed is generally not a critical issue while in gas and steam turbines this is the key limiting factor in the selection of stage number due to both mechanical stresses and high temperatures. On the other hand, organic fluids usually have large volume ratios per stage and a low speed of sound. Both these aspects make the design of an ORC turbine a quite challenging task which cannot be faced without the support of a specific optimization software. Simple correlations such as Smith (1965) diagrams and Baljé and Binsley (1968) plots cannot catch these ORC turbines peculiarities. As already demonstrated by Macchi (1977), Macchi and Perdichizzi (1981) and Lozza *et al.* (1981), a rigorous design of an axial flow turbine should take into account real blade dimensions and the effects of Mach numbers especially if supersonic flows are present. These aspects are crucial for organic fluids, where blades are characterized by a large height variation, large flaring angles and supersonic velocities. In particular in Macchi (1977), the effect of both the volume ratio and the specific speed is analyzed for different single stage turbines operating with heavy and complex fluids while in Lozza *et al.* (1981) a sensitivity analysis is carried out varying the number of stages for turbines with two different size parameters. A further step ahead is provided in the work of Macchi and Perdichizzi (1981) with the definition of a map of efficiency for single stage turbines at optimized rotational speed as function of size parameter and volume ratio. The purpose of this paper is to propose an efficiency correlation for single, two and three stage axial flow turbines at optimized rotational speed in a wide range of volume ratios and dimensions.

2. SCOPE OF WORK AND METHODOLOGY

Except for some biomass applications, in ORC field each turbine is designed ex novo because each plant differs in the available thermal power and in the temperature of both the heat source and the cooling medium. Turbines in ORC can operate with different fluids in a large range of pressure and volume ratios, size and power output. For these reasons, it is interesting to adopt a non-dimensional approach which allows comparing optimal turbine designs on the basis of specific parameters. According to similarity rules (Dixon, 1998), the results achieved for a certain turbine stage can be extended to any other case if the stages respect the following conditions (Macchi and Perdichizzi, 1981):
  1. They have the same specific speed;
  2. The geometric similarity is fully verified (all the geometrical ratios are equal);
  3. The flow is fully turbulent so that the Reynold number effects are negligible
  4. the Mach numbers are similar;
  5. The volumetric behaviour of the two fluids is the same, namely the volume flow rate variation across the stage is equal for the two fluids. This condition is verified if the two fluids are incompressible or if they are ideal gas with the same pressure ratio and the same heat capacity ratio;

ORC turbines ranges from micro scale to very big machines and so the geometrical similarity cannot be always verified because of the presence of technological constraints like the minimum trailing edge thickness and the minimum tip clearance gap. Very small turbines are intrinsically less efficient because of the increase of profile and leakage losses. On the other hand, high value of volume ratios affect the turbine stage design which requires converging diverging blades and relevant variation of blade height in a single row with detrimental effects on stage efficiency.

The parameters suggested as independent variables for a parametric analysis are: the size parameter $\left(SP = \frac{V_{out,is}{}^{0.5}}{\Delta h_{is}{}^{0.25}} \right)$ and the volume ratio $\left(V_r = \frac{V_{out,is}}{V_{in}} \right)$ while the specific speed $\left(Ns = \frac{RPM}{60} \frac{V_{out,is}{}^{0.5}}{\Delta h_{is}{}^{0.75}} \right)$ will be optimized for each case. The physical significance of SP, V_r and Ns and their influence on the turbine efficiency will be discussed later.

2

In order to obtain efficiency maps with a sufficient detail and covering a large range of ORC applications, hundreds of turbines have been optimized. Independent variables range between a minimum and a maximum value which is 0.02 m -1 m for SP and 1.2-200 for Vr.

The optimizations presented in next sections are realized assuming a complex ideal gas with a γ value equal to 1.05 as representative of a generic organic fluid. We found this simplifying hypothesis appropriate for the scope of the present analysis, i.e. to obtain quite accurate preliminary prediction of turbine efficiency for a large variety of ORC cycles and working fluids. The results in section 6 confirm the validity of this assumption. Of course, in the final turbine design a proper EoS should be considered.

In this study, Reynolds numbers are not considered as independent variables since for Re greater than 10^6 the effect on stage performance is negligible, while the influence of Mach numbers on blade geometry, flow angles and losses are accounted for. Even if the Mach numbers resulting from the adopted ideal gas assumption differ from the real ones, these deviations cause minor effects on the predicted stage efficiency (Macchi and Perdichizzi, 1981).

All the results presented in the next sections are obtained with Axtur tool, an *in house* optimization code for axial flow and radial outflow turbines developed by Macchi and Lozza at the Energy Department of the Politecnico di Milano. The code is based on a pseudo 1D approach and both blade channels geometry and velocity triangles are defined at mean diameter for each blade row (see Fig 1 for nomenclature details). Blade heights are hence obtained from continuity equation and the actual blade geometry is considered in efficiency losses calculation. Efficiency loss for each row is computed using correlations from literature to take into account the presence of the boundary layer, supersonic flows, flow angle variations and other losses.

Axtur, starting from a feasible initial point, performs multivariable constrained optimizations of turbines with a maximum stage number equal to three. Every stage is fully defined by nine parameters. Three of them define stage quantities: the stage isentropic load (k_{is}), the isentropic degree of reaction (r^*) and the isentropic volume ratio (V_r). The other six (three for each row) parameters are representative of stage geometrical ratios (o/s, o/b and b/r_m). These parameters are the optimization variables of the problem and they can be varied by the optimization algorithm between a lower and an upper bound whose values are defined according to the limits of the correlations used to compute the efficiency losses.

In addition, nonlinear constraints are considered for other variables of interest, like maximum Mach numbers, maximum number of blades and flaring angles and for technological limitations. Penalty factors are introduced if the upper or the lower bounds are not respected.
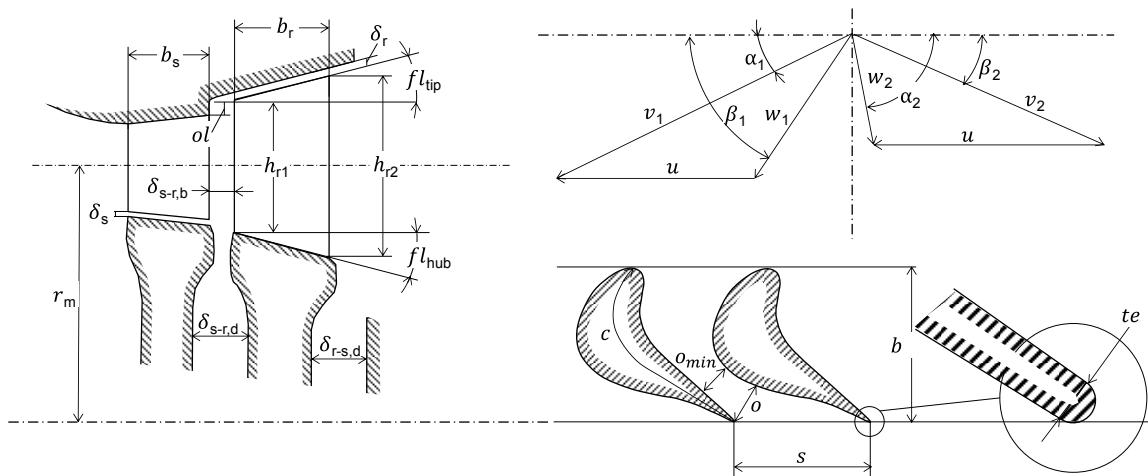

Figure 1 - Notation used in Axtur for the blade geometry and the velocity triangles. Converging-diverging blades are used by the code when Ma>1.4 otherwise $o = o_{min}$. In the velocity triangle the v vector represents the absolute velocity while w one the velocity relative to the rotor blade; u vector is the peripheral speed. Subscripts 1 and 2 refer to the inlet and the outlet of the rotor blade respectively.

3

For a single stage Axtur optimizes the total to static efficiency corrected by the fraction of kinetic energy recovered by the diffuser according to eq. 4.

$$\eta = \frac{W}{\Delta h_{T-S} - \varphi_E \frac{v_{2,a}^2}{2}}$$

(1)

Where φ_E is the efficiency of the diffuser; it is assumed that 50% of the kinetic energy of the discharge absolute velocity axial component can be recovered.

The approach is not completely rigorous because the recovery of kinetic energy entails a reduction of the pressure at turbine discharge and so a higher pressure drop and a higher power production while here the effect is accounted subtracting the same term from the denominator. As proved by Macchi [6], the approximation is generally valid and does not affect the quality of the solution in terms of turbine efficiency. For multistage turbine the code maximizes the power output imposing $\varphi_E = 1$ for all the stages except the last one, but introducing annulus losses between blade rows.

The results provided by Axtur consist in a complete characterization of blade geometry in both blade to blade and meridional planes and velocity triangles. Furthermore, the breakup of the efficiency losses is reported considering the following effects:

- *Profile loss* (Craig&Cox [10]): due to the blade shape and effects related to friction, fluid vane deflection and boundary layer dissipation. This loss mainly depends on blade pitch, blade axial chord length, trailing edge thickness and roughness of blade surface, angular deflection and relative velocity ratio.
- *Secondary losses* (Craig and Cox, 1970): caused by secondary flow structures mainly described by passage vortex, horseshoe vortex, trailing edge vortex and corner vortex. These losses are affected by the same parameters which have influence on profile losses plus blade height.
- *Annulus losses* (Craig and Cox, 1970 or Kacker and Okapuu, 1981): due to the passage of fluid in the gap between two blade rows. This loss is calculated for all the stages except for the last one.
- *Leakage losses* (Craig and Cox, 1970): caused by the unwanted passage of fluid above blade tip whose expansion does not contribute to power production. This kind of loss is mainly related to radial clearance, blade length and blade overlap. They can be null for the first stator blades only.
- *Disk windage losses*: due to velocity gradient in the clearance between stator and rotor disk walls. They are strongly affected by rotational speed and by both absolute disk clearance and disk diameter.
- *Kinetic energy loss*: it is the fraction of kinetic energy of discharge velocity which cannot be recovered with the diffuser. Usually it is defined with a coefficient φ_e smaller than unit respect to the kinetic energy of the axial component.

Exit flow angles are computed according with the flow condition: (i) Subsonic flow (Ainley and Mathieson, 1951), (ii) Supersonic flow with after expansion (Vavra, 1969), (iii) Supersonic flow with converging diverging nozzle (Deich, 1965). Experimental data from Deich (1965) are used for accounting of additional losses related to supersonic flows at blade exit, while an empirical correlation introduced by Macchi (1977) accounts for losses related to relative transonic velocities at rotor inlet.

3. SINGLE STAGE TURBINES

More than five hundreds of turbines are optimized varying SP and V_r and optimizing Ns. It is important to remember that, according to similarity rules, the results here obtained are representative of any other turbine stage with the same set of independent parameters. Different volumetric fluid behavior and molar mass affect variables like speed of revolution, pressure ratio, temperature and enthalpy drop and mass flow rate but they have small influence on the final optimal design which has the same geometrical aspect and the same isentropic efficiency. The validity of this assumption is verified in the test case presented in chapter 6.

4

In Fig 2.a each point represents the maximum efficiency attainable for any combination of SP, Vr and Ns. It is possible to notice that for each couple of SP and V_r parameters an optimal specific speed is found, while detrimental effects on the efficiency can be highlighted increasing the V_r and decreasing the SP. As a general consideration, there is a large range in SP and V_r where the optimal specific speed is between 0.1 and 0.15, as already pointed out in Macchi [6]. For small SP and for high V_r the optimal Ns decreases down to 0.05. This is justified by the presence of lower and upper bounds on some geometrical dimensions like minimum blade height and maximum h/D ratio at the discharge section. In these cases, a Ns value above 0.1 entails an almost unfeasible design of the blade with a strong increase of secondary losses due to fluid leakages and high flaring angles.

The maximum point for every curve is representative of the maximum attainable efficiency at optimized rotational speed and optimal results are collected in a contour map reported in Fig 2.b. For a better understanding of the effects occurring in the definition of optimized stage geometry, three parametric analyses are proposed in the following. The first focuses on the effect of Ns at fixed SP and V_r, while the other two are carried out varying one by one V_r and SP at optimized rotational speed.
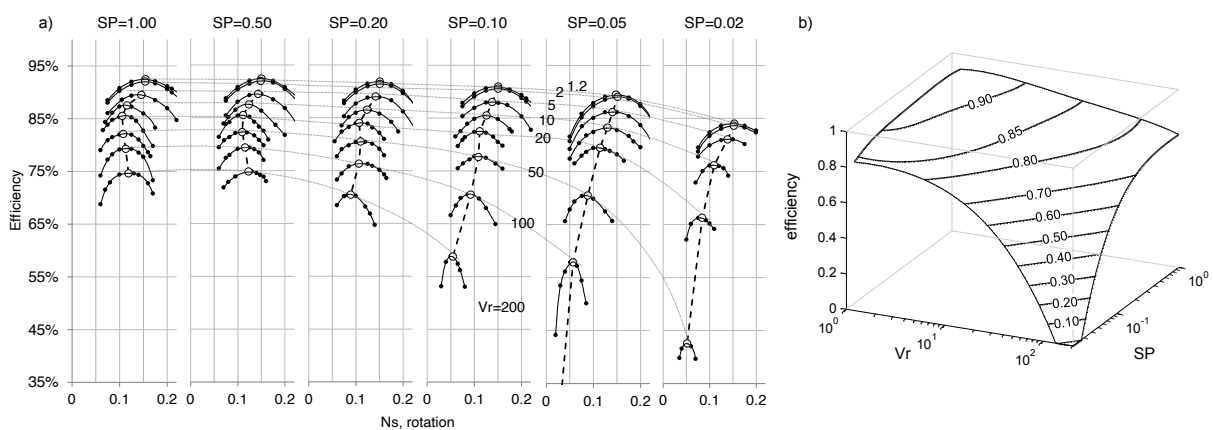
Figure 2 – a) Results for the single stage turbines. Black markers (●) are representative of the optimal turbine configuration for each combination of SP, Vr and Ns. White markers (○) identify the turbine designs at optimized rotational speed. b) map of efficiency for a single stage turbine at optimal Ns.

2.1. Effect of Ns

The first analysis regards the optimization of Ns for a single stage turbine at fixed SP and V_r equal to 0.4 m and 4 respectively (similar results are obtained for any other SP and Vr.combination) Results are reported in Fig 3. In this case, both the volume flow rate at turbine exit and the isentropic enthalpy drop are constant and so Ns parameter has a direct effect on the speed of revolution and turbine mean diameter. At low specific speed the turbine stages have large mean diameter because of the necessity to maintain optimal u velocity above a certain value, to reduce the stage load.

Stages in this region have small h/D parameters and they are affected by high leakage and secondary losses. Velocity triangles are representative of impulse stages with an almost axial absolute velocity v_2, thus the kinetic losses are minimized. Disk windage loss is noticeable because of the large diameter interested by this dissipation effect.

Increasing the rotational speed allows reducing both the secondary and leakage losses thanks to higher blades and a larger h/D ratio while the profile and the kinetic losses become more and more relevant. Optimal Ns value is equal to about 0.15 corresponding to well-proportioned turbine stages and an almost 50% reaction velocity triangle with an axial absolute velocity at turbine outlet.

On the other hand, for higher Ns values, the rotational speed is higher and the stage mean diameter is strongly reduced leading to high values of h/D parameter. Both the secondary and the leakage losses are

5

minimized but the distorted shape of the velocity triangles entails high values of discharge velocity which cannot be maintained in axial direction. As a consequence, kinetic energy losses increase because of the high value of v_2 and the presence of a tangential component which cannot be recovered by the diffuser. The trade-off between these opposite effects leads to the presence of an optimum value of Ns which yields the maximum efficiency.
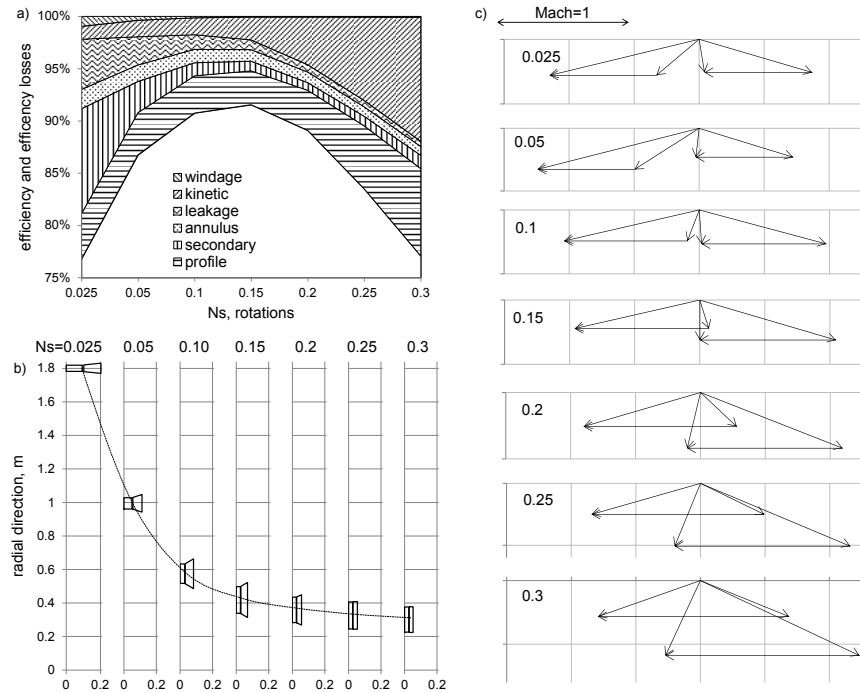

Figure 3 – Results of the parametric analysis varying Ns for a single stage turbine with SP=0.04 and Vr=4: a) Efficiency losses breakup, b) blade profiles and c) velocity diagrams. Mach numbers for inlet and outlet triangles are evaluated using the fluid SoS at stator and rotor outlet section respectively.

2.2. Effect of Vr at optimized Ns

Optimized results for single stage turbines, with different V_r and a fixed SP equal to 0.05, are presented in Fig 4. The breakdown of efficiency losses shows that the maximum attainable efficiency is a decreasing function of V_r. For really low volume ratios, namely values below twice than the $V_{r,crit} = 1.64$, velocity triangles are always subsonic, the load is limited and 50% reaction stages with high efficiency can be designed, h/D ratio is favourable, no flaring is required and both secondary and profile losses are small. Increasing V_r, Mach numbers greater than unit are obtained, in particular for v_1 and w_2 velocities, with an increase of profile losses. Converging-diverging stator nozzles are required for V_r above 5, while they are needed also for rotor blades for values beyond 10. For V_r greater than 20, a velocity close to the sonic one is obtained at w_1 vector with problems of shock waves at rotor inlet. The loss coefficient which takes into account this effect contributes to penalize the overall efficiency.

Velocity triangles become more and more distorted due to the necessity to handle higher volume flow variations and contextually maintaining a velocity vector v_2 close to the axial direction and limiting Mw_1. Increasing the volume ratio involves a higher isentropic enthalpy drop and optimized stages with a higher peripheral speed u and a larger mean diameter in order to limit the stage load. Solutions move toward impulse stages with very small blade heights and high secondary losses due to unfavorable h/D ratio and disk windage loss increases due to larger surface interested by the phenomena. In conclusion, adopting V_r higher than 5 for a small SP single stage turbine entails a strong limitation in the attainable efficiency and multistage turbines should be considered in order to contain the load on each stage.
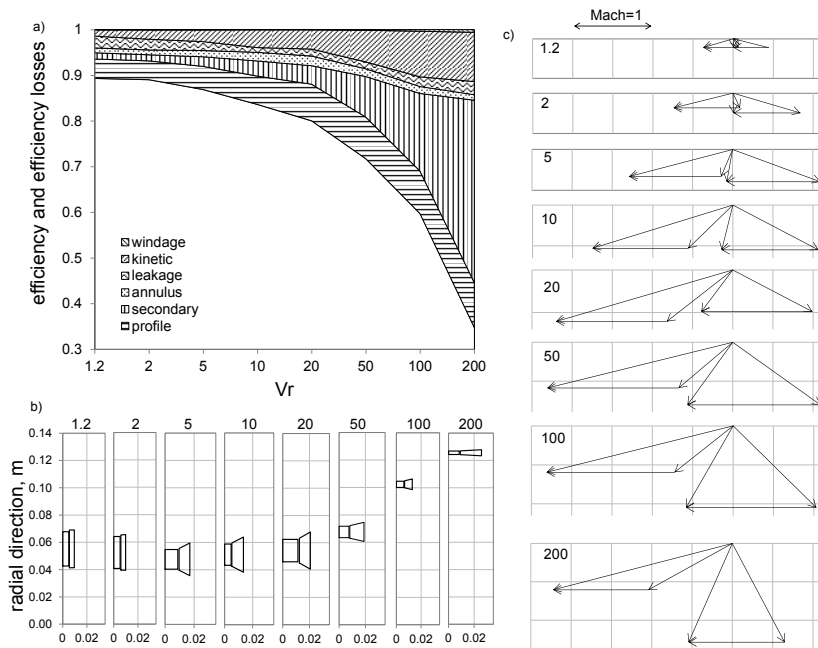
6

Figure 4 – Results of the parametric analysis for different single stage turbines having the same *SP*=0.05 m at the optimal specific speed: a) Efficiency losses breakup, b) blade profiles and c) velocity diagrams.

2.3. Effect of SP at optimized Ns

The last sensitivity analysis is realized for different single stage turbines with the same $V_r = 20$ but different *SP* and results are reported in Fig 5. Size parameter is varied from 0.02 m to 1 m which is a value representative of turbines close to the maximum size of normal ORC expanders. All the stages work with the same isentropic enthalpy drop but they notably differ in volumetric flow rate because of the quadratic dependence on the *SP*. Small size parameters lead to very small volume flow rates at turbine inlet section with a reduced passage area. Due to geometrical limits on minimum blade height and minimum δ_r/h ratio, the mean diameter gets smaller with an increase of rotational speed in order to maintain the optimal value of specific speed. These two effects result in a strong efficiency drop for small turbines with a considerable increase of secondary and leakage losses. Similar results are obtained for smaller V_r, even if the efficiency drop related to small SP decreases.
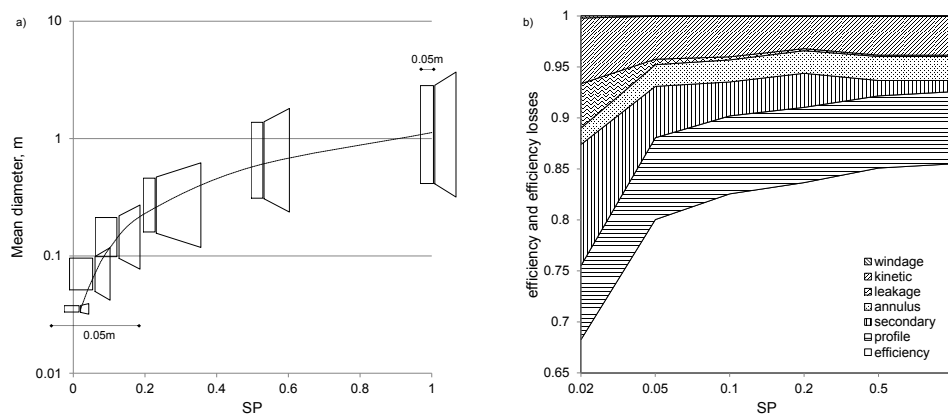

Figure 5 – Results of the parametric analysis for different single stage turbines having the same Vr=20 at the optimal specific speed: a) blade profiles and b) efficiency losses breakup.

7

4.   MULTI STAGE TURBINE

In previous section, single stage turbines have been considered highlighting that their efficiency is strongly penalized by high volume ratios with even more marked reduction at small size parameters. In ORC field, multistage turbines are commonly adopted because they can achieve a higher efficiency exploiting the repartition of the whole volume flow variation on two or more stages. In this work only two and three stage turbines are considered because in most of the applications the benefit in adopting a higher number of stages is limited with an increase of component cost and a higher cost of electricity. For common applications, axial turbines are usually overhung with rolling bearing on the generator side of the shaft. This design allows an easy inspection of the turbine during maintenance operation and it is generally preferred even if it limits the number of stages to three because of rotodynamic issues. For turbines directly coupled to generator, a rotodynamic analysis performed by Exergy (Spadacini *et al*, 2013) shows that for a number of stages greater than three the natural frequencies of the turbine shaft get closer to 50 (or 60 Hz) with the risk of resonance during normal operation. A technical solution to increase the number of stages and the overall volume ratio without incurring in these problems is represented by radial outflow turbines.

The same analysis presented in the previous section is repeated for both two and three stage machines. The results, obtained optimizing the rotational speed for each turbine, are presented in terms of V_r and SP calculated for the overall expansion as though it is exploited by a single stage.

In Fig 6.a the comparison between the maximum efficiencies achievable for a single stage and a two stage turbine is reported while in Fig 6.b the increment of efficiency is displayed.

Increases of efficiency are not constant over the considered range of SP and V_r. The most relevant increments are obtained for high overall volume ratios and small SP. For V_r equal to 5 the efficiency increment is greater than 2 percentage points independently of SP value: an increment that usually justifies a more expensive device with the adoption of a two stage turbine.

Benefits are obviously larger for higher V_r and the efficiency increase reaches values above 10% for medium-small machines and volume ratios greater than 50. Last observation regards the possibility to extend the domain of solution: in particular for a SP lower than 0.02 m and V_r of 100 and 200 it is not possible to design a full-admission single stage turbine with a reasonable efficiency. The high load on such a small stage and the presence of geometric constrains entail a non-feasible execution of the optimization algorithm with variables values always outside of the efficiency losses correlation limits.

This problem does not arise for two stage turbines and the whole range of SP and V_r is explored.

Similar considerations can be done comparing two stages and three stage turbines. Results are reported in Fig 7.a and Fig. 7.b. The attainable efficiency increase is lower than in the previous case but, once again, notable advantages are highlighted for high volume ratios and small turbines. Finally, a graphical comparison of the performance maps for the single stage, the two stage and the three stage turbine are reported in Fig 6.c and 7.c.
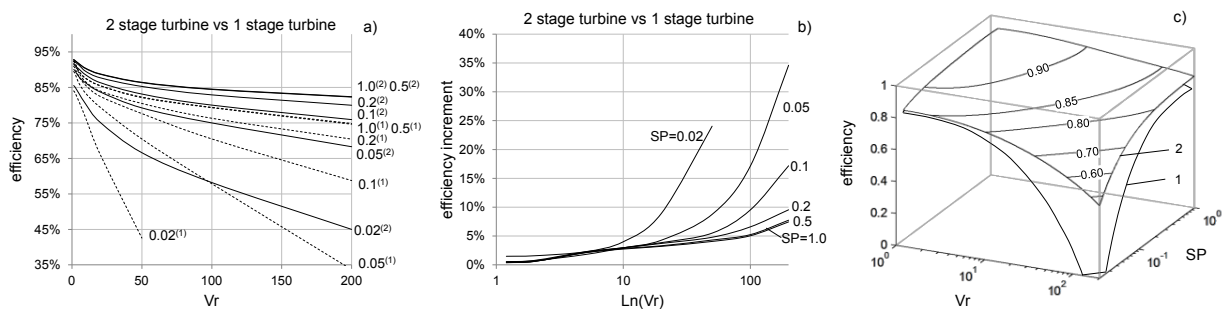

Figure 6 - Comparison between attainable efficiency adopting a two stage turbine instead of a single stage turbine (a) and corresponding efficiency increases (b). Graphical representation of maps of efficiency (c).
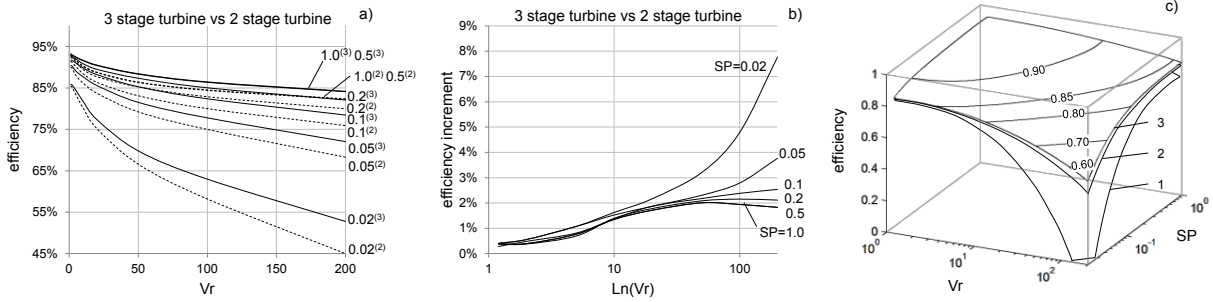
8

Figure 7 - Comparison between attainable efficiency adopting a three stage turbine instead of a two stage turbine (a) and corresponding efficiency increases (b). Graphical representation of maps of efficiency (c).

5. NUMERICAL CORRELATIONS OF EFFICIENCY

The set of data of maximum attainable turbine efficiency are regressed with a OLS regression performed in Gretl. The most suitable terms function of SP and V_r are selected and a process of exclusion of the less influencing ones is carried out in order to obtain the maximum value of the adjusted R^2 coefficient. All the proposed correlations have a functional form reported in eq 2 while the numerical values of the retrieved coefficients can be found in Table 1.

$$\eta = \sum_{i=0}^{15} A_i F_i \qquad (2)$$

Table 1 - Regressed coefficients to be used in the correlation of turbine efficiency for single, two and three stage turbines

Stages number		1	2	3
n	F_i		A_i	
0	1	0.90831500	0.923406	0.932274
1	$\ln(SP)$	-0.05248690	-0.0221021	-0.01243
2	$\ln(SP)^2$	-0.04799080	-0.0233814	-0.018
3	$\ln(SP)^3$	-0.01710380	-0.00844961	-0.00716
4	$\ln(SP)^4$	-0.00244002	-0.0012978	-0.00118
5	Vr	-	-0.00069293	-0.00044
6	$\ln(Vr)$	0.04961780	0.0146911	-
7	$\ln(Vr)^2$	-0.04894860	-0.0102795	-
8	$\ln(Vr)^3$	0.01171650	-	-0.0016
9	$\ln(Vr)^4$	-0.00100473	0.000317241	0.000298
10	$\ln(Vr)\ln(SP)$	0.05645970	0.0163959	0.005959
12	$\ln(Vr)^2\ln(SP)$	-0.01859440	-0.00515265	-0.00163
12	$\ln(Vr)\ln(SP)^2$	0.01288860	0.00358361	0.001946
13	$\ln(Vr)^3\ln(SP)$	0.00178187	0.000554726	0.000163
14	$\ln(Vr)^3\ln(SP)^2$	-0.00021196	-	-
15	$\ln(Vr)^2\ln(SP)^3$	0.00078667	0.000293607	0.000211
	Adjusted R^2	0.99790	0.99935	0.99954

9

6. MODEL VALIDATION

In this section an example about the capabilities of the proposed correlations is provided. In particular, the aim is underling how the volume ratio and the dimension of a real turbine stage can affect the turbine performance. To validate the proposed methodology two fluids (R125 and hexane) are considered and two turbine sizes (isentropic power of 5 MW and 250 kW) are analysed. Both fluids expand from a temperature of 155°C down to a pressure equal to the saturation at 30°C as representative of a low temperature heat source application with a cooling water condenser. A supercritical cycle is considered for R125 with a turbine inlet pressure of 36,2 bar while a saturated cycle is imposed for hexane according to its high critical temperature and the overhanging saturated vapour line which allows for a dry expansion. In Table 2 the main thermodynamic properties of the fluids are reported with other quantity of direct interest for the evaluation of turbine efficiency. Both R125 and hexane show real gas effects at turbine inlet with a compressibility factor equal to 0.85 and 0.79 respectively while a behaviour closer to ideal gas is founded at turbine discharge with values of 0.91 and 0.99. The overall expansion coefficients (γ) are different from the value assumed for the ideal gas in the previous sections and are equal to 1.10 and 1.06. The two turbine stage differ in both the Vr and the SP. The expansion of R125 shows a very limited variation of density because of the high condensation pressure and the high degree of superheating. On the contrary hexane according to the corresponding state principle (Poling and Prausnitz , 2000) has a lower condensing pressure (a vacuum pump is required at the condenser to remove air leakage) and a larger volume flow rate variation across the turbine. Hexane mass flow rate is lower than the R125 one but the SP is larger because of the very low density at turbine outlet section. Using the correlation of efficiency previously described the turbine efficiency is calculated: R125 turbine shows a very high (90%) efficiency while for hexane the presence of supersonic flows and limitation of flaring angles play a detrimental role in the final efficiency which is close to 83%. In this case the positive effect of a larger SP is not sufficient to compensate the difficulties in realizing a high Vr stage. Reducing the size of the turbines the presence of geometrical constraints (minimum o/s and maximum o/b) bound the final solution and leads to a decrement of about 3 point of efficiency confirming the overall trend presented in previous analyses.

Table 2 – Characteristics of the considered fluids and main results of the analysis

	R125		hexane	
critical properties				
MM	120.02		86.18	
T_{crit}, °C	66.02		234.67	
p_{crit}, bar	36.18		30.34	
expansion data				
W_{is}, kW	5000	250	5000	250
p_{in}, bar	36.200		8.290	
p_{out}, bar	15.685		0.250	
ΔT_{sh}, °C	88.980		0	
m, kg/s	237.71	11.89	40.78	2.04
$V_{out,is}$, m³/s	3.79	0.19	55.24	2.76
specific parameters				
V_r	2.293	2.293	34.389	34.389
SP, m	0.162	0.036	0.397	0.089
$\eta_{is}^{correlation}$	0.903	0.877	0.833	0.799
Axtur results				
η_{is}^{Axtur}	0.907	0.872	0.828	0.795
RPM	6000	31000	5500	2800
Ns	0.111	0.129	0.104	0.118
D, m	0.420	0.086	0.900	0.180

10

The four turbines are hence designed in Axtur considering real fluid properties (i.e. compressibility effects, Mach numbers, etc.) and optimizing the rotational speed. It is possible to highlight a good accordance among the efficiencies calculated with the two methods confirming the validity of the proposed approach. The optimal rotational speed, the optimal Ns and the resulting optimal diameter are reported in table as well.

7. CONCLUSIONS

In this work three correlations of performance are provided for axial turbines with a maximum number of stages equal to three. This study aims to complete the work done in previous publications about the estimation of maximum efficiency attainable with 1D optimization techniques. The correlations can be used for a preliminary estimation of turbine performance in the numerical optimization of ORC even if the results are affected by inaccuracy mainly related to the quality of efficiency losses correlations and the simplified volumetric behavior assumed in the generation of the performance maps.
On the basis of the present analyses the following conclusions can be addressed:

- Rotational speed must be always optimized since relevant efficiency decrements are highlighted for values lower and higher than the optimal one. The use of slow generators with more than two couple of poles is recommended for large turbines while a gearbox or a power electronic system is required for small size machines having an optimal rotational speed higher than 3000 RPM;
- Geometrical similarity cannot be always verified because of the presence of geometrical constraints related to blade machining and limits of loss correlations. Decreasing the size of the turbine the maximum efficiency is reduced mainly because of the increasing of profile and leakage losses;
- Isentropic volume ratio strongly affects stage design and efficiency. A single stage turbine with high Vr is penalized because of the presence of big flaring angles, supersonic flows and high kinetic losses and it is advantageous to split the expansion in two or more stages
- The contemporary presence of small SP and high VR strongly penalizes the attainable efficiency of single stage machines and suggests the adoption of multi-stage solutions.

NOMENCLATURE

Variables

A	coefficients for the efficiency correlations	(-)
b	axial chord	(m)
β	pressure ratio	(-)
η	efficiency	(-)
F	terms of the efficiency correlations	(-)
φ_E	kinetic energy recovery factor	(-)
γ	ratio of specific heats	(-)
k_{is}	Isentropic load coefficient	(-)
h	enthalpy or blade height	(m)
h/D	blade height-blade mean diameter ratio	(-)
m	mass flow rate	(kg/s)
Ns	specific speed	(-)
o	blade channels throat	(m)
p	pressure	(bar)
r	radius	(m)
ρ	density	(kg/m^3)
s	blade step	(m)

11

SP	Size Parameter	(m)
T	temperature	(°C)
V	volume flow rate	(m^3/s)
v	absolute velocity	(m/s)
u	mean peripheral speed	(m/s)
Vr	volume ratio	(-)
W	power	(kW)
w	relative velocity	(m/s)

Subscripts

crit	critical property
eva	evaporation
cond	condensation
is	isentropic
re	real
T-S	Total to Static

REFERENCES

Ainley, D.C., Mathieson, G.C.R., 1951, A method of performance estimation for axial-flow turbines, *British Aeronautical Research Council*, Vol. R&M 2974.

Astolfi, M., Romano, M., Bombarda, P., Macchi, E., 2014a, Binary Orc Power Plants For The Exploitation Of Medium-Low Temperature Geothermal Sources. Part A Thermodynamic Optimization, *Energy*.

Astolfi, M., Romano, M., Bombarda, P., Macchi, E., 2014b, Binary Orc Power Plants For The Exploitation Of Medium-Low Temperature Geothermal Sources. Part B Techno-Economic Optimization, *Energy*.

Baljè, O.E., Binsley, R.L., 1968, Axial turbine performace evaluation: part B - optimization with and without constraints, *ASME Journal of Engineering for Power*. pp. 349-360.

Craig, H.R.M., Cox, H.J.A., 1970, Performance estimation of axial flow turbines, *Proceedings of the institution of mechanical engineers*. pp. 407-423. Vol. 185 32/71.

Deich, M.E., Filippov, G.A., Lazarev, L.Y., 1965, Atlas of axial turbine blade characteristics. Moscow, *Maschinostromie Publishing House*.

Dixon, S. L., 1998, Fluid Mechanics, *Thermodynamics of turbomachinery*, Fifth Edition, Eselvier.

Kacker, S.C., Okapuu, U., 1981, A mean line prediction method for axial flow turbine performance prediction, *ASME* paper 81-GT-58.

Lozza, G., Macchi, E., Perdichizzi, A., 1981, On the influence of the number of stages on the efficiency of axial flow turbines, *Journal for Engineering for Power*.

Macchi, E., 1977, Design criteria for turbines operating with fluids having a low speed of sound. Closed cycle gas turbines, Von Karman Institute for Fluid-dynamics, lecture series 100.

Macchi, E., Perdichizzi, A., 1981, Efficiency prediction for axial flow turbines operating with non-conventional fluids, *J. Eng. Gas Turbines Power*.

Poling, E. B., Prausnitz, J. M., O'Connell. J. P., 2000, Properties of Gases and Liquids, Fifth Edition., *McGraw-Hill Education*.

Smith, M. H., 1965, A simple correlation of turbine efficiency, *Journal of Royal Aeronautical Society*.

Spadacini, C., Rizzi, D., Saccilotto, C., Salgarollo, S., Centemeri, L., 2013, The Radial Outflow Turbine Technology: Impact On The Cycle Thermodynamics And Machinery Fluid- And Rotordynamic Features. *2st International Seminar on ORC Power Systems*, Rotterdam.

Vavra, M.H., 1969, Axial flow turbines, *Von Karman Institute for Fluid-dynamics*, lecture series 15.

Xodo, G. L., Spadacini, C., Astolfi, M., Macchi, E., 2013, Comparison Of Axial And Radial Outflow Turbines In A Medium-High Enthalpy Waste Heat Recovery Orc Application. *2st International Seminar on ORC Power Systems*, Rotterdam.

12

VOLUMETRIC EXPANDER VERSUS TURBINE – WHICH IS THE BETTER CHOICE FOR SMALL ORC PLANTS?

Andreas P. Weiß

Competence Center for CHP Systems,
University of Applied Sciences Amberg-Weiden,
Kaiser-Wilhelm-Ring 23, 92224 Amberg, Germany
e-mail: a.weiss@oth-aw.de
Web page: http://www.oth-aw.de

ABSTRACT

Since the steam turbine replaced the steam reciprocating engine by the end of 19th century it has been the only expander type in Clausius Rankine Cycle (CRC) and Organic Rankine Cycle (ORC) power plants at least above 1 MW_{el}. Positive displacement expanders like scroll or screw machines have often been applied for smaller units – in particular below 100 kW_{el}. One reason for this is that in cooling or compressed air technology these machines are cheaply available as compressors which can be "easily" converted to expanders. In contrast, up to now small turbines are rather seldom in this market segment. One goal of this paper is to discuss whether there are others reasons than those already mentioned to justify the choice of volumetric expanders for small ORC plants and to clarify whether small turbines provide benefits which could not have been used in the past just due to the lack of appropriate machines.

The paper briefly introduces the working principles of positive displacement and turbine expanders and evaluates them concerning their application in small ORC-plants. In the author´s opinion, the advantages of turbines outweigh their disadvantages. Nevertheless, in the following the decision between e.g. impulse or reaction type, axial or radial, single or multistage turbine has to be made. The paper discusses and explains the "pro and cons" of these turbine types. This paper aims to identify the best expander for a given application and in addition evaluates the different expanders with regard to their suitability for a so-called "micro-expander-construction-kit" which should help to design and build an appropriate expander for any given application out of a wide range of boundary conditions and working fluids. Here, the single stage impulse turbine was identified as the best compromise

1. INTRODUCTION

By the end of 19th century the steam turbine had superseded the steam reciprocating engine in power generation as well as vessel propulsion because of its superiority with regard to power density and higher allowable steam temperatures and thus higher cycle efficiencies. Since that time, the turbine has been dominating the power generation at least above 1 MW power output. It is generally accepted that turbines outclass volumetric expanders regarding large power output and processing huge mass flows. However, on the lower end of the power generation range, i.e. 1 MW or even below 100 kW power output the situation seems to be different. For small ORC or CRC units very often volumetric expanders are applied (Figure 1, see Branchini et. al., (2013)). Many publications e.g. Glavatskaya *et.al* (2012), Lemort *et*. *al*. (2013) postulate that for small power output or rather small mass flow a piston, screw, scroll or rotating vane expander would be the better choice regarding efficiency, rotational speed, size, costs etc.. This statement will be discussed in the following.

The author is convinced that besides the above-mentioned reasons there is another very simple reason for the frequent use of small volumetric expanders for small plants: These machines were cheaply available in the past from refrigeration or compressed air technology where they acted as compressors. Compared to small compressors, small turbines appear rather seldom. There is one exception: Small radial inflow, (axial outflow) turbines which are typical for automotive

turbochargers. However, these turbines are designed for rather low expansion ratios (ER). Furthermore, they are only available as turbocharger units equipped with oil bearings which rely on the internal combustion engine´s oil system. Thus, the application of a turbocharger turbine as ORC expander is a bit elaborate.

The goal of the paper is to determine whether turbines can be a reasonable choice for small ORC units in the range of 3 to 100 kW$_{el}$. This question is in particular interesting for the development of a „micro-expander-construction kit" for small ORC expanders which has to cover different temperature levels, mass flow rates, as well as fluids.
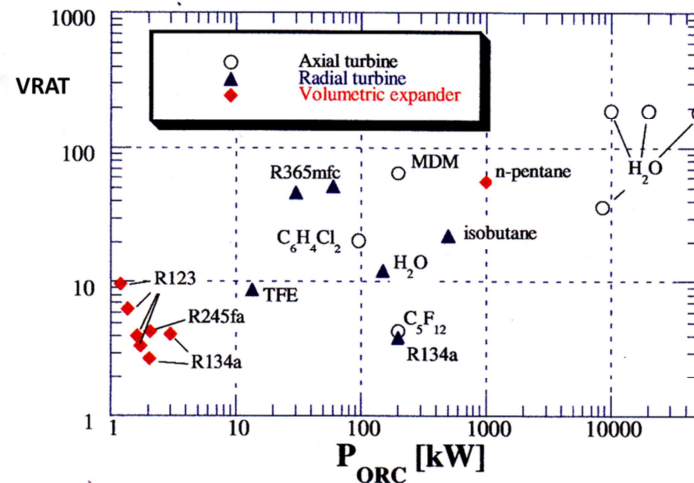
Figure 1: Actual VRAT values of existing ORC expanders with specified fluids (Branchini *et*. *al*., 2014)

Figure 1 suggests that the volumetric expanders seem to dominate the power range below 10 kW. Furthermore, a first limitation of the volumetric expander can be identified: It is obviously restricted to small volumetric expansion ratios VRAT < 10. This is due to their built-in volume ratio. This geometrical volume ratio is for screw or scroll expanders about 5 and in the range of 10 for piston expanders (Lemort *et*. *al*., 2013). However, higher expansions ratios may be advantageous e.g. for automotive waste heat recovery where small heat fluxes are combined with rather high temperatures or temperature differences, respectively. High temperature differences in an ORC usually result in high volume flow ratios for the expander.

2. VOLUMETRIC VERSUS DYNAMIC EXPANDER

2.1 Selection Criteria for Small Expanders
There are many criteria which may influence the choice of an expander for an ORC plant (Table 1). The design engineer tends to focus on efficiency, whereas for the „end-user" the return of investment is the most important issue. Thus, beside efficiency, costs are a major criterion, which are strongly influenced by the design of the expander, its complexity, number of parts, the expected wear maintenance etc..

Table 1: Selection criteria for small ORC expanders

Economic Criteria	Technical Criteria
• costs	• efficiency
• availability on market	• rotational speed (bearing, generator)
• reliability	• lubrication (pollution of working fluid)
• maintainability	• sealing
	• power level (volume flow rate)

	• working fluid
	• wear
	• complexity
	• adaptability (fluid, VRAT etc.)

Furthermore, if the focus is not only on one ORC unit for one set of boundary conditions but a „micro-expander-construction-kit"-system with the intention to cover different levels of heat source/heat sink temperature, power output and different fluids, the adaptability of the expander design has also to be taken into consideration.

2.2 Comparison of Working Principles
The working principles of a volumetric and a dynamic expander are quite different (Figure 2). Volumetric expanders use the expansion work directly by changing the volume of a working chamber. Therefore, they deal with high pressures, big forces and small velocities of flow and machine parts. The built-in volume ratio and the swept volume are the main design parameters of volumetric expanders which limit their reasonable application range. The built-in volume ratio determines the specific work and the volume flow ratio (VRAT) which can be implemented per stage. A multi-stage arrangement for high VRAT is conceivable, but also elaborate due to additional piping, clutches etc.. The swept volume in combination with the rotational speed results in the volume flow rate which can be processed. Furthermore, both parameters determine the required size of the expander. Usually, due to their relative low rotational speed volumetric expanders can drive a standard generator directly without a gear. Part load (p. l.) e.g. reduced mass flow in an ORC can easily be handled by adjusting the rotational speed. The working chamber of the volumetric expander must be closed. Hence, it needs a contact sealing, which generates friction losses and wear and requires lubrication.

In a first step, dynamic expanders i.e. turbines convert the vapor´s internal energy into kinetic energy by means of nozzles. Therefore, pressure and forces are rather small but flow velocities are high. In a second step the kinetic energy is converted into mechanical work by turning the flow within the rotor blading. The circumferential speed u of the wheel has to be in the magnitude of the flow velocity i. e. high. The high circumferential velocity u in combination with a small diameter D leads to a necessary rotational speed usually in the range of 10,000 to 100,000 rpm or even more (u ~ n*D). Thus, turbines cannot be coupled directly to a standard generator. In addition, a gear or a high-speed generator must be used. In a turbine the fluid volume change during expansion is not just implemented by changing a chamber volume but by simultaneously increasing flow velocity and area. High expansion ratios can be implemented even in a single stage if supersonic flow is accepted, which leads to lower achievable efficiency. This is the reason why a turbine design with fixed main dimensions (e. g. diameter, length) can cover a wide range of boundary conditions (mass flow rate, expansion ratio etc.) just by adapting nozzle length and area, blade height and/or degree of admission. Partial admission (p. a.) is a means to handle part load (see chapter 3). In a turbine there are no contact seals. Hence, no lubrication is necessary. However, there is a certain leakage which cannot be avoided. Due to the high flow velocities, the absence of valves and the continuously working principle, turbines can process high volume flows in a small construction volume.
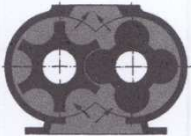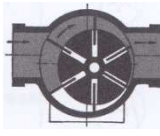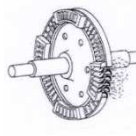
volumetric expanders				dynamic expanders		
$work = \int vdp$				$work \sim u^2$		
piston	screw	scroll	vane	axial	cantilever	radial

Figure 2: Expander types

2.3 Construction Types of Volumetric Expanders (Figure 2)

<u>Piston:</u> The classical volume expander is the reciprocating piston expander. It can show high expansion efficiencies (e.g. 70% in Eilts *et.al*. (2012)).The achievable volume ratios of volumetric expanders are in the range of 10 (Lemort *et. al*., 2013) or slightly higher. However, it needs a lot of bearings and in addition inlet and outlet valves which makes the design complex and costly. Liquid in the cylinder can cause damage. Thus, the piston expander should not be applied for wet expansion. The machine and the flow are oscillating. Hence, the machine needs balancing and is prone to vibrations.

<u>Screw:</u> The screw expander expands the fluid continuously. It does not need any valves but at least four bearings for the two rotors. The rotors are not in contact with each other. Lubrication is required for sealing purposes. Even lubricated the necessary rotational speed is the highest for volumetric expanders. Without lubrication the rotational speed must be high (> 10,000 rpm). Therefore, standard generators are not suitable. Possible volume ratios (VRAT) are in the range of 5, efficiencies of around 50% (Eilts *et.al*., 2012) might be acceptable. A certain amount of wetness can be handled by a screw expander.

<u>Scroll:</u> A scroll expander is a comparatively simple device: it consists of two spirals, one of which is rotating. It can be mounted directly on the shaft of the generator avoiding any additional bearing. Volume ratio is below 5 (Lemort et. al., 2013). Wang *et. al*. (2009) reported measured efficiencies in the range of 70% even for a quite small machine (< 1 kW). Droplets are no problem for a scroll expander.

<u>Vane:</u> The rotating vane expander is working continuously with a rather small rotational speed. Built in volume ratios are rather small (VRAT < 5). The vanes are in contact with the casing. Lubrication is required, which can spoil the working fluid. Furthermore, high friction losses and wear have to be expected. Rotating vane air motors are well known and widely used in industry. Their efficiencies are usually in the range of 30-40%. However, Badr *et.al*. (1984) report measured efficiencies of 80%.

<u>Dry Runners:</u> All the discussed volumetric expanders are available as dry runners, i. e. without lubrication, to avoid the spoiling of the working fluid. Usually, dry runners suffer from higher friction losses and leakages. Therefore, their efficiency is lower than that of their lubricated counterparts.

2.4 Construction of Small Dynamic Expanders - Turbines

Turbines are simple devices (Figure 2), comparable to volumetric expanders in terms of design. The turbine shaft needs two bearings. For small single stage turbines the rotor wheel can be mounted directly on the shaft of the high-speed generator. Because of the absence of contact seals, no lubrication is needed which could spoil the working fluid. Droplets at the end of expansion cause erosion in turbines. However, most of the applied organic working fluids show an isentropic or even dry saturation vapor curve. So, generally droplets are no problem in ORC applications. Small turbines suffer from a high relative surface roughness, big relative clearances and a big relative trailing edge thickness, etc.. Thus, they do not achieve efficiencies in the range of their bigger counterparts. All these statements hold true for axial and radial turbines of reaction or impulse type as well. The advantages and disadvantages of the different types of turbines will be discussed in more detail in chapter 3.

2.5 Which Expander Type for the "Micro-Expander-Construction Kit?

Table 2 summaries the results of this first evaluation. As long as efficiency is not the main focus or the only issue of consideration and as long as high speed generators are available, the turbine can compete with any volumetric expander. From the author´s point of view its main advantages are its simplicity, the possibility to adjust one basic turbine design quickly to different boundary conditions (e. g. VRAT) without changing the overall size and finally, that lubrication in contact with the working fluid can be avoided. Already Quoilin *et. al*. (2012) concluded that a turbine does have the broadest application map of all expander types. Hence, the author´s research group (Weith *et. al*., 2013) decided to build up the ORC "micro-expander-construction kit" based on turbines.

Table 2: Evaluation of small expander types

expander type	η	VRAT	n	p. l.	size	adapt-ability	lubri-cation	wear	wet-ness	vib-ration	com-plexity	Σ
volumetric												
piston	2	1	2	2	0	0	0	1	1	0	0	9
screw	1	0	1	2	0	0	0	2	2	2	0	10
scroll	1	0	2	2	1	2	0	1	2	2	2	15
vane	0	0	2	2	1	1	0	0	2	2	1	11
dynamic	1	2	0	1	2	2	2	2	1	2	2	17

3. COMPARISION AND ASSESSMENT OF DIFFERENT TURBINES

Although the decision was made in favor of a turbine expander there are still many different types of turbines e. g. impulse or reaction turbines, axial or radial turbines and radially inflow or outflow turbines which can be considered. In the following, these turbines will be compared and evaluated regarding their applicability as a basis for the "micro-expander-construction kit".

3.1 Impulse versus Reaction Turbine

Figure 3 compares the blading and the velocity triangles of an impulse stage and a 50% reaction stage. In an impulse stage the nozzles convert the entire required stage enthalpy drop Δh_{is} into kinetic energy. Thus, the nozzle exit velocity c_1 is very high. The rotor blades turn the flow without changing the magnitude of velocities ($|w_1|=|w_2|$). The pressure p in the rotor blading remains constant. In a 50% reaction stage the conversion of the stage enthalpy drop is equally distributed between nozzle and rotor blades. Thus, the nozzle exit velocity c_1 is not as high as in the impulse stage. The following acceleration ($|w_2| > |w_1|$) and pressure drop in the rotor blades has the same magnitude as in the nozzle blades. These differences in velocity triangles result in certain differences in stage characteristics:

- Higher velocities mean higher losses: the efficiency potential of an impulse stage is lower than that of a reaction stage.
- Thanks to the constant pressure via the rotor blading, impulse stages can be designed to work with partial admission (p.a.). This means that a portion of the total arc of the annulus is blocked off. Hence, the flow impinges only on-parts of the rotor blading. Partial admission is an option to implement part load with reasonable efficiency or to build turbines for very small power output without requiring blading heights that are too small to be manufactured with sufficient accuracy. Additionally, in this respect the impulse rotor blading benefits from the circumstance that it is subjected to the minimum pressure in the ORC plant and thus works with the maximal volume flow rate occurring in the cycle.
- The pressure drop via the reaction rotor blading generates non-negligible axial thrust. It either has to be balanced or the bearing must be able to withstand it.
- Furthermore, due to the pressure drop, the reaction stage efficiency is more sensitive to radial clearances.
- Applying the simplified Euler equation (1) for turbo machines ($u_1= u_2$)

$$\Delta h_{blading} = u * (c_{u1} - c_{u2}) \qquad (1)$$

it becomes obvious (Figure 3), that

$$\Delta h_{blading,impulse} = 2 * u^2 \text{ and } \Delta h_{blading,reaction} = 1 * u^2 \qquad (2), (3)$$

Since $\Delta h_{blading} \approx \Delta h_{is}$ it follows that

$$u_{opt,impulse} = \frac{1}{\sqrt{2}} * \sqrt{\Delta h_{is}} \text{ and } u_{opt,reaction} = 1 * \sqrt{\Delta h_{is}} \qquad (4), (5)$$

i.e. for an identical stage enthalpy drop Δh_{is} the impulse stage requires only a significantly lower optimal circumferential speed ($u_{opt,imulse} = u_{opt,reaction} /\sqrt{2}$) than the reaction stage. This is a big advantage of the impulse stage applied as a small expander.
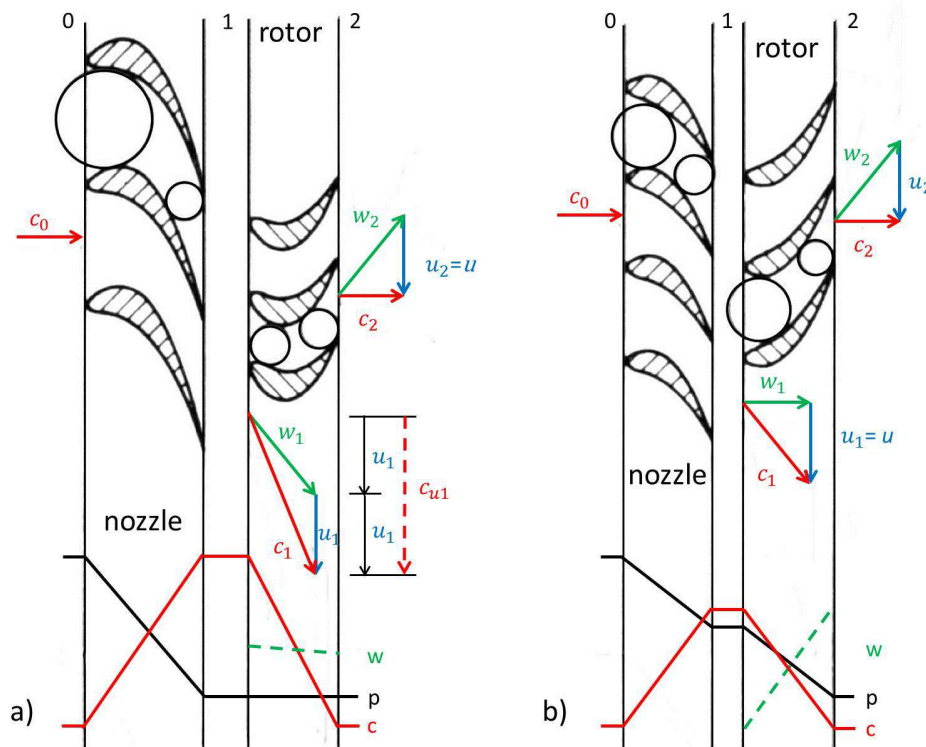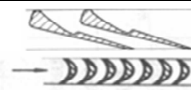
Figure 3: Comparison impulse (a) and reaction stage (b)

It has often been stated in literature - e. g. Bao and Zhao (2013) - that radial inflow turbines are better suited for low mass flow rates and high pressure ratios than axial ones. This is correct in principle. Nevertheless, for radial inflow turbines which are usually designed as reaction stages a maximal expansion ratio in the range 8 to 10 is reasonable (Moustapha *et. al.*, 2003). For higher values not only the nozzles but also the impeller would choke. That is why Bao and Zhao (2013) or Quoilin *et. al.* (2013) limit the rotor relative exit Mach number to 0.85 in their considerations. However, impulse stages can even cope with supersonic relative Mach number ($Ma_2 \approx Ma_1$) with acceptable efficiencies of 70%-80% (Vernau, 1987). As a consequence, very high stage expansion ratios ER >100 (Rinaldi *et. al.*, 2013)) or volume flow ratios (VRAT) can be put in practice.

Table 3: Impulse versus reaction turbines

turbine axial – cantilever - radial	impulse	reaction
efficiency potential (ts) ≈	80%	90%

turbine	η	VRAT	n	axial thrust	p. a.	leakages	minimal power/size	Σ
impulse	0	2	2	2	2	2	2	12
reaction	2	0	0	0	0	0	0	2

To summarize (Table 3), for small power output the impulse turbine (axial or radial) is obviously the more flexible and also a simpler approach for a micro ORC expander. The classical radial (reaction) inflow turbine might be more efficient for certain tasks but is probably less suitable for an ORC "micro- expander-construction-kit". The impulse turbine can be easily adapted to a wide range of

mass flow rate, fluids, inlet and exit pressures just by changing the nozzle area (-ratio), the blade height and/or the degree of admission.

3.2 Axial versus Radial Turbine (Figure 4)

Equation (6) below is valid for all types of turbines and shows the Euler work $\Delta h_{blading}$ processed in the rotor as difference between the squared rotor inlet (1) and exit (2) velocities (compare Figure 3). For an axial turbine, in particular for a small one with short blades the Δu^2-term is almost or exactly zero.

$$\Delta h_{blading} = \frac{1}{2} * [(c_1^2 - c_2^2) - (w_1^2 - w_2^2) + (u_1^2 - u_2^2)] \tag{6}$$

If the flow through a turbine wheel is subjected to a significant change in radius e.g. a change in circumferential velocity, the Δu^2-term contributes a substantial part to the overall enthalpy conversion like in a radial inflow reaction turbine. As a result, the radial inflow turbine can process higher expansion ratios than an axial stage without getting transonic or supersonic.

The radial inflow cantilever turbine benefits from this Δu^2-effect as well – however to a lesser extent. The author´s research group has recently developed small cantilever „quasi-impulse" turbines which do not work with acceleration in the rotor ($|w_1|= |w_2|$). Nevertheless, caused by the Δu^2-term there is a small amount of reaction. Thus, the nozzles are slightly relieved. The Mach numbers at nozzle exit and rotor inlet remain smaller than for the axial counterpart. Although a small amount of reaction is used, this type of cantilever turbine can be applied using partial admission. Of course, this benefit does have a disadvantage: the cantilever „quasi-impulse" turbine requires a slightly higher circumferential speed.

The significant advantages of radial outflow turbines are mainly twofold:
1. a flow direction from a smaller to a bigger radius corresponds to an area increase of the flow path which is helpful for expanding organic fluids with high volume flow ratios (VRAT)
2. centrifugal flow direction easily enables a multi stage arrangement if the expansion ratio of one stage is not sufficient.
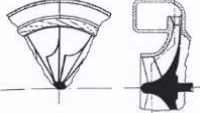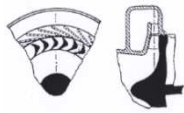
turbine type			
axial	radial inflow	cantilever inflow	cantilever outflow

turbine type	η	VRAT	n	axial thrust	p.a.	multi stage	complexity	Σ
axial (r ≈ 0)	1	2	2	2	2	2	2	13
radial inflow (r≈ 0,5)	2	0	0	0	0	0	1	3
cantilever inflow (r > 0)	2	1	1	1	2	0	2	9
cantilever outflow (r≈ 0,5)	2	2	0	0	0	2	1	7

Figure 4: Axial versus radial turbine

One main disadvantage of the radial outflow turbine stage is the fact that the Δu^2-term is working against the others terms (equation 6). I.e. in a radial outflow turbine the velocities (absolute, circumferential) and Mach numbers must be higher than in its inflow competitor for the same enthalpy drop.

The construction of a single stage axial turbine or a radial inflow cantilever turbine can be very simple. The manufacturing of the nozzle rings and the integral wheels does not need a 5-axis milling machine like for a radial inflow turbine. At least for small expanders the design and arrangement of a radial out-flow stage seems to be more challenging. Therefore, it was decided to rely on the single-stage impulse turbine for the "micro- expander-constructing-kit".

3.3 The Micro Turbo Generator Concept

Figure 5 displays the developed micro turbo generator concept which relies on the "micro expander construction kit". Its main features are:

- hermetically sealed turbine-generator (3 -100 kW_{el}, implemented with 5 manufactured sizes)
- single stage axial impulse turbine (10.000 – 70.000 rpm)
- integrally manufactured turbine wheel (Ø 50 – 250 mm)
- permanent magnet high-speed generator
- turbine wheel directly mounted on generator shaft: just one set of bearings required, no gear, no coupling
- roller bearings, slide bearings or aerodynamic bearings - depending on task
- compact design, low material usage
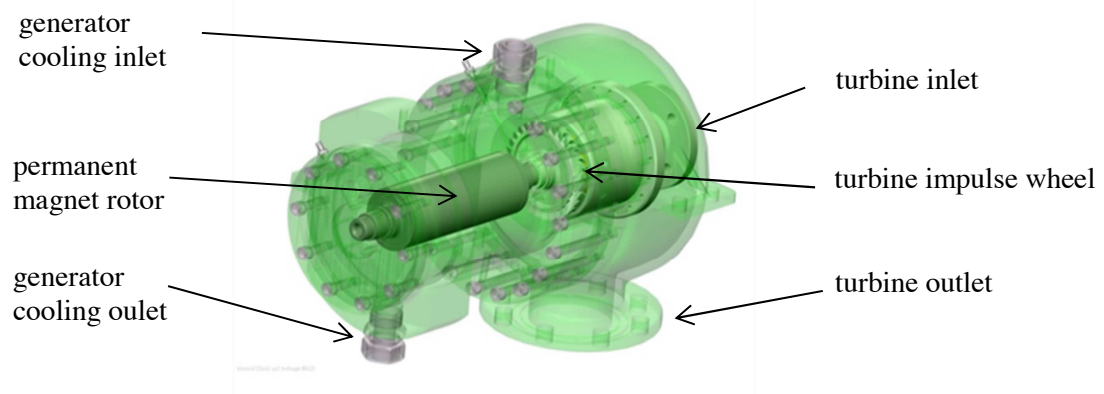- design can be easily adapted to different boundary conditions, fluids etc.

Figure 5: The micro turbo generator concept

3.4 Test Results of Developed Small Turbines

Based on the introduced concept several small axial and cantilevered turbines for steam, air and different organic fluids (Table 4) have already been built and successfully tested.

Table 4: Test results of built small turbines

#	turbine type		fluid	ØD	n	VRAT	p.a.	P	η_{ts}
				m	rpm	-	%	kW	%
❶	impulse	axial	steam	0,05	70000	3,9	30	1,0	40[1]
❷	impulse	axial	r245fa	0,08	21000	3,4	90	11,0	70[2]
❸	impulse	axial	cyclopentane	0,12	30000	16,0	55	11,0	65[3]
❹	impulse	axial	air	0,08	49000	6,4	60	5,4	60[1]
❺	low reaction	cantilever	air	0,08	49000	6,4	50	5,7	63[1]

[1]: brake efficiency [2]: including generator losses [3]: based on measured inlet/outlet temperatures and pressures

The small axial steam turbine ❶ was developed for automotive waste heat recovery. The r245fa- and the Cyclopentan-turbine (❷,❸) were designed and built for small waste heat recovery ORC plants as bottoming cycles for biogas engines. The air turbines (❹, ❺) are just demonstrators to investigate the pro and cons of the cantilever design compared to the axial design. The cantilever designed showed the expected higher efficiency. Nevertheless, the axial impulse design provides many other

advantages (see Figure 4) as discussed. Due to different constraints (e.g. maximum rotational speed of the bearing technology) none of the turbines could be designed to operate with its optimal circumferential speed (u_{opt}). Therefore, the efficiencies are rather too low but still acceptable for the given application.

4. CONCLUSIONS

For small and micro ORC plants costs per kW are usually high and it is questionable if those small units will work economically. Therefore, all components, especially the expander must be simple and cheap in series production. From the author´s point of view, this requirement rules out the reciprocating piston and screw expanders. The rotating vane expander has already been produced in big numbers for compressed air application. Due to the scrubbing (sealing) vanes it shows usually poor expansion efficiency and high wear. Using a scroll expander mounted on the standard generator shaft a very simple expander unit can be implemented. However, the scroll expansion ratios are limited to the lower end. Thus, only smaller temperature differences can be processed efficiently in an ORC if a scroll expander is to be applied.

The single stage axial impulse turbine can cope with small volume rates and high expansion ratios. Thus, a wide range of boundary conditions and working fluids can be covered with the introduced „micro-expander-construction-kit". Combined with a high-speed generator a compact, simple and cost-efficient turbo expander unit can be put into practice.

NOMENCLATURE

c	absolute velocity	(m/s)
D	diameter	(m)
ER	expansion ratio	(-)
h	enthalpy	(J/kg)
Ma	Mach number	(-)
n	rotational speed	(rpm)
P	power	(W, kW)
p	pressure	(N/m^2)
u	circumferential velocity	(m/s)
v	specific volume	(m^3/kg)
VRAT	volume flow ratio	(-)
w	relative velocity	(m/s)
Δ	difference	
η	efficiency	(-)

CRC	Clausius Rankine Cycle
ORC	Organic Rankine Cycle
p. a.	partial admission
p. l.	part load

Subscript

0	nozzle blading/stage inlet
1	nozzle blading outlet, rotor blading inlet
2	rotor blading/stage outlet
el	electric
is	isentropic
opt	optimal
ts	total to static
u	in circumferential direction

REFERENCES

Badr, O., O´Callaghan, P. W., Hussein M., Probert, S. D., 1984,
Multi-Vane Expanders as Prime Movers for Low-Grade Energy Organic Rankine Cycle Engines
Applied Energy 16, p129-146

Bao, J., Zhao, L., 2013,
A review of working fluid and expander selections of organic Rankine cycle
Renewable and Sustainable Energy Reviews 24, p 325-342

Branchini, L., De Pascale, A., Peretto, A., 2013,
Systematic comparison of ORC configurations by means of comprehensive performance indexes
Applied Thermal Engineering 61, p 129-140

Eilts, P., Seume, J., Brümmer A., 2012,
Zwischenbericht über das Vorhaben 1060 – C02-Sonderforschungsprogramm
Expansionsmaschine, *FVV Informationstagung 2012, Heft R558*, Bad Neuenahr

Glavatskaya, Y., Podevin, P., Lemort, V., Shonda O., Descombes G., 2012,
Reciprocating Expander for an Exhaust Heat Recovery Rankine Cycle for Passenger Car Application,
Energies, 5, p 1751-1765

Lemort, V., Ludovic, G., Arnaud, L., Declaye, S., Quoilin, S., 2013,
A comparison of piston, screw an scroll expander for small Rankine cycle systems
Proceedings of the 3rd International Conference on Microgeneration and Related Technologies, Naples, Italy

Moustapha, H., Zelesky, M. F., Baines, N. C., Japikse, D., 2003,
Axial and Radial Turbines
Concepts NREC, ISBN 0-933283-12-0

Quoilin, S., Declaye, S., Legros, A., Guillaume, L., Lemort, V., 2012
Working fluid selection and operation maps for Organic Rankine Cycle expansion machines
International Compressor Engineering Conference at Purdue, July 16-19

Rinaldi, E., Buonocore, A., Pecnik, R., Colonna, P., 2013,
Inviscid stator/rotor interaction of a single stage high expansion ratio ORC turbine
ASME Organic Rankine Cycle 2013, *2nd International Seminar on ORC Power Systems*, October 7-8, Rotterdam 2013

Verneau, A.. 1987,
Supersonic Turbines for Organic Fluid Rankine Cycles from 3 to 1300 kW
von Karman Institute for Fluid Dynamics, Lecture Series 1987-07, Brussels

Wang, H., Peterson, R. B., Herron, T., 2009,
Experimental performance of a compliant scroll expander for an organic Rankine cycle
Proc. IMechE Vol. 223 Part A: J. Power and Energy, pp 863-872

Weith T., Heberle F., Weiß A. P., Zinn G., 2013,
Development of a Small Scale ORC for Waste Heat Recovery
ASME Organic Rankine Cycle 2013, *2nd International Seminar on ORC Power Systems*, October 7-8, Rotterdam 2013

ACKNOWLEDGEMENT

STUDY OF A VOLUMETRIC EXPANDER SUITABLE FOR WASTE HEAT RECOVERY FROM AN AUTOMOTIVE IC ENGINE USING AN ORC WITH ETHANOL

José Galindo[1], Vicente Dolz[1]*, Lucía Royo[1], Regine Haller[2], Julien Melis[3]

[1]CMT – Motores Térmicos, Universitat Politècnica de València, Valencia, Spain

[2] Valeo Systèmes Thermiques, La Verriere, France

[3]Exoès, Gradignan, France

* Corresponding Author (vidolrui@mot.upv.es)

ABSTRACT

Waste Heat Recovery in exhaust gas flow of automotive engines has proved to be a path to increase the overall efficiency of automotive vehicles. Recovery potential of up to 7% are shown in several works in the literature. However, most of them are theoretical estimations. Some of them presents results from prototypes fed by steady flow generated in an auxiliary gas tank and not with actual engine exhaust gases.
This paper deals with the simulation model of a volumetric expander, integrated in an ORC mock-up, coupled to a 2 l turbocharged gasoline engine and using ethanol as working fluid. An experimental facility of an ethanol ORC using a swash-plate expander coupled to an Ecoboost 2.0 engine has then been used to correlate it.
The target is to understand the physical phenomena which are not predictable by simulation and can only be observed by experimentation and secondly, to carry out some parametric studies showing the potential for optimizing different elements of the expander machine.

1. INTRODUCTION

In the last years, the interest in improving energy efficiency in reciprocating internal combustion (ICE) engines of vehicles has increased, together with the entry into force of ever more stringent anti-pollution regulations. Many of these works are focused on the development of new technologies to recover waste heat from IC engines. Saidur et al. (2012) propose four different groups to classify these technologies: the thermoelectric generators (TEG) (Yang, 2005), organic Rankine cycles (ORC) (Apostol et al., 2015), six-stroke cycle IC engine (Conklin & Szybist, 2010) and new developments on turbocharger technology (Dolz et al., 2012) and (Serrano et al., 2012). The turbocharging technology has been deeply developed for vehicle IC engines in recent decades. In fact, turbochargers are used in practically all Diesel engines used in automotive vehicles. Regarding other present technologies and considering this classification, ORC technology is one of the most promising because of its implementation in the near future engines. ORC technology to recover low-grade heat sources has been wildly developed in biomass, geothermal or solar power plants and also in combined heat and power (CHP) in industrial processes. There are many studies about these facilities, both theoretical and experimental. Some of these theoretical studies describe mathematical models in different ORC facilities for the recovery of these low temperature heat sources. Table 1 presents a summary of several studies with the main characteristics of the described models.

Table 1: Summary of papers about ORC modeling

Reference	Model features	Software	Max. Power	Working fluid
(Bracco et al., 2013)	ORC with a scroll expander	AMESim	1.5kW (mechanical)	R245fa
(Lecompte et al., 2013)	ORC for CHP with a volumetric expander	Matlab with RefProp	207kW (output)	R152a, R1234yf, R245fa
(Manente et al., 2013)	Dynamic ORC model with a turbine	Matlab (Simulink)	8MW (net power)	Isobutene and R134a
(Quoilin et al., 2010)	ORC with a scroll expander	EES	1.8kW (mechanical)	HCFC-123
(Wei et al., 2008)	Dynamic ORC model with a turbine	Modelica and Dymola	100kW	R245fa
(Ziviani et al., 2014)	ORC with a scroll expander	AMESim	2.16kW (mechanical)	R245fa
(Carlos et al., 2014)	scroll expander	-	260W (mechanical)	air and ammonia
(Cipollone et al., 2014)	sliding vane rotary expander	-	2kW (mechanical)	R236fa
(Ferrara et al., 2013)	reciprocating expander	WAVE and EES	2.26kW (output)	water
(Giuffrida, 2014)	scroll expander	Matlab with Refprop	2kW (mechanical)	several fluids
(Lemort et al., 2009)	scroll expander	-	1.8kW (mechanical)	HCFC-123
(Wenzhi et al., 2013)	reciprocating expander	Matlab (Simulink)	11.5kW (output)	water

At present, some studies try to adapt this technology to waste heat recovery (WHR) on vehicle IC engines. In these engines, space and weight restrictions are higher than in industrial installations, which greatly hinders their adaptation. On the other hand, the thermal power available in these engines for WHR is lower than in industrial processes. So the optimized expander, mass flows and working fluids for heat recovery in IC engines can be different than the options considered in other applications. Typically, the expanders used in industrial ORC facilities are turbines, screws, scrolls or rotary vane expanders (Qiu et al., 2011). However, ORC design for automotive engines generally presents a reciprocating machine as the optimal solution to recover waste heat energy into mechanical energy, due to low working fluid flow, high values in expansion ratios and space restrictions.

Regarding the working fluids, ethanol is considered by several authors as a promising fluid due to its good features in the temperature range of a vehicle application (450ºC-100ºC). Although ethanol is positively evaluated taking into account environmental, thermo-physical properties and cost features, it has been classified as serious hazard by NFPA due to its high flammability. (Seher et al., 2012) concluded that ethanol is one of the most favorable solution when a reciprocating machine is used as expander. (Howell & Gibble, 2011) selected ethanol as the best working fluid for a successful ORC for a HD truck.

Despite of these theoretical studies, where the ethanol has proven to be the most suitable working fluid for this type of installations, experimental ORC works with this fluid have not been published due to the flammability properties. Therefore, it is necessary to take safety measures to prevent accidents arising from the use of this fluid.

In previous studies, some methodologies to design these cycles for vehicle IC engines have been proposed (Macián et al., 2013) and applied to define the main characteristics of an ORC facility for WHR in automotive IC engines. This experimental facility has been assembled and tested in order to estimate the viability of this technology. This installation uses a swash-plate reciprocating expander to recover heat losses into mechanical energy and ethanol as working fluid. The main objective of this

paper will consist in describing and validating a model in AMESim of this facility in order to evaluate the main thermo-physical magnitudes of these cycles.

2. SYSTEM LAYOUT

As the expander is the most innovative element of these cycles the description of this system layout has been divided in two parts: first part, where a general ORC layout is described and a second part, where the expander is characterized.

2.1 Organic Rankine Cycle layout

In order to perform an experimental evaluation of this system, an ORC test bench was designed and built at CMT-Motores Térmicos in Universitat Politècnica de València (
Figure 1) in a research project with the companies Valeo Systèmes Thermiques and Exoès. This facility can be coupled to different types of automotive combustion engines (an automotive diesel engine, a Heavy Duty diesel engine and an automotive petrol engine). The test bench recovers energy from exhaust gases of a turbocharged 2 l gasoline engine and exchanges thermal energy to the ethanol side.

Figure 1: ORC mock-up

Figure 2 shows the most relevant components of the ORC mock-up. The running principle is as follows: engine exhaust gases pass through the boiler to the working fluid, in this case, ethanol. Then, it is pumped into the high pressure loop and then is evaporated in the boiler and slightly superheated. Thus, working fluid under high temperature and high pressure is generated. After that, the vapor flows into the expander where enthalpy is converted into effective work measured by a torque measuring unit. Low pressure vapor is extracted from the expander and flows to the condenser, reducing its temperature by cooling water and producing condensed ethanol. Therefore, the cycle starts again. The ORC cycle contains as main elements: a boiler, a swash-plate expander, a condenser, a fluid receiver, a subcooler, an expansion vessel and a pump. The main elements have been carefully insulated to avoid heat losses to the ambient. The thermodynamic properties of the ethanol (pressure and temperature) have been measured upstream and downstream of all components, verifying energy balances and power estimations. Table 2 synthesizes the absolute uncertainties of all the sensors installed in the ORC mock-up.
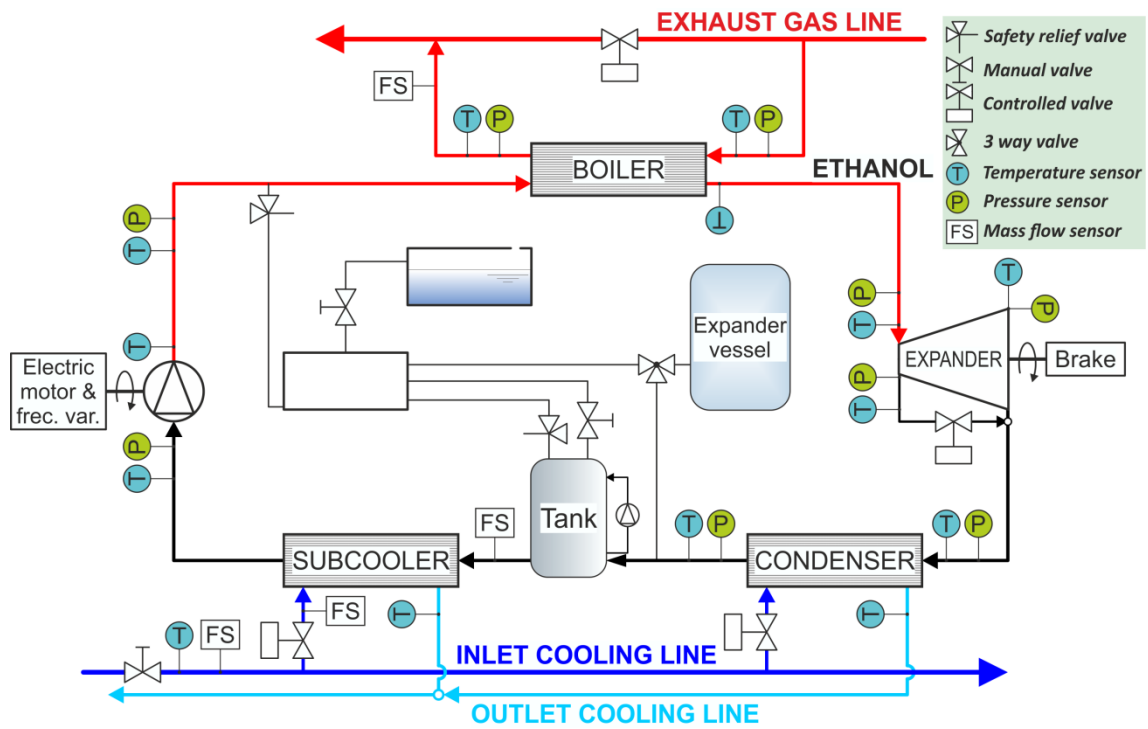
Figure 2: ORC scheme

Table 2: Range and accuracy of sensors

	Measurement principle	Range	Accuracy
Exhaust gas pressure	Piezoresistive	0-2 bar	0.05% FS
Ethanol high pressure loop	Piezoresistive	0-50 bar	0.05% FS
Ethanol low pressure loop	Piezoresistive	0-5 bar	0.05% FS
Temperatures	K-type thermocouples (Class 2)	(-270)-(1,372)K	±2.5°C
Ethanol flow meter	Coriolis flow meter	0-2,720 kg/h	±0.1%
Water flow meter	Electromagnetic flow sensor	0.3-1 m/s	±0.5% of rate
Expander rotational speed	Optical tachymeter	0-20,000 rpm	±1 rpm
Expander torque meter	Strain gauges	0-200 Nm	0.05%FS

2.2 Swash-plate expander layout

The expander machine used in this installation is a Swash-plate expander. Lower flow rates and higher expansion ratios could be reached in this machine, thus displacement expanders are considered the main technology for recovering waste heat from low temperature sources and low expander power in vehicle applications. The geometrical features of the expander are listed in Table 3 and
Figure 3 shows a picture of the Swash-plate expander delivered by Exoès.

Table 3: Swash-plate characteristics

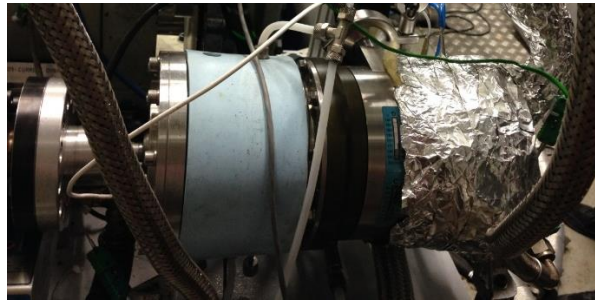| Swash-plate characteristics		
Pistons number	3	
Bore	40	mm
Stroke	31	mm
Maximum expander speed	4500	rpm

Figure 3: Swash-plate expander delivered by Exoès

The expander performance has been characterized through the calculation of the indicated diagram (P-V). One AVL GU13P piezoelectric pressure sensor was placed on the chamber of one of the pistons to evaluate the pressure variations. It allows tracking pressure variations during filling and emptying processes. The piezoelectric transducer was connected to a Kistler 5015 charge amplifier. The pressure-volume diagram is used to describe changes of volume and pressure of a system. A swash-plate expander is a positive displacement machine. It works as a two stroke machine, which means that during one revolution, with a piston movement from the Top Dead Centre to the Bottom Dead Centre and back again, one working cycle is completed. The superheated steam flows through the intake valve into the cylinder whose piston is near top dead center. Moving the piston downwards, the steam expands and lead out by exhaust ports in the cylinder (slits) situated near the bottom dead center. Finally, the upmoving piston closes the exhaust ports and compresses the steam remained in the cylinder and the cycle starts again. Furthermore, a TDC sensor is used to know the position of the BDC. TDC is an eddy current-Sensor which delivers a signal correlating to the distance between sensor and the swashplate. The piezoelectric pressure signal has been referenced using low frequency measurement (piezoresistive sensor). The analysis of P-V diagrams in different expanders could be very convenient to evaluate possible irreversibilities and improvements in the expansion machine. All the signals were recorded with a sampling frequency of 50 kHz and processed with Labview program. Each cycle was obtained as an average of at least 30 cycles to avoid dispersion in measurements.

3. MODELLING

A comprehensive theoretical model of both the Organic Rankine Cycle and the Swash-plate expander has been developed by the authors using AMESim®. The software package provides a 1D simulation suite to model and analyze multi-domain intelligent systems, and to predict their multi-disciplinary performances. This software consists of available object-oriented libraries, where the user should connect them properly and fix the parameters. The purpose of these models will be: Firstly, it should be used to help the understanding of those physical phenomena which are difficult to observe by means experimentation and secondly, in order to estimate the behavior of the cycle without the need for experimental tests under operating conditions that may cause danger to the installation and / or people. Both models have been validated using tests measured in the mock-up.

3.1 Organic Rankine Cycle model
A simple layout of the ORC consisting of a boiler, a positive displacement pump, a volumetric expander, a fluid receiver, a condenser and an expansion vessel is considered in this model.

Figure 4 shows the AMESim® model of the cycle based on the ORC installation. A detailed description for modelling each component will be presented in the following subsections.
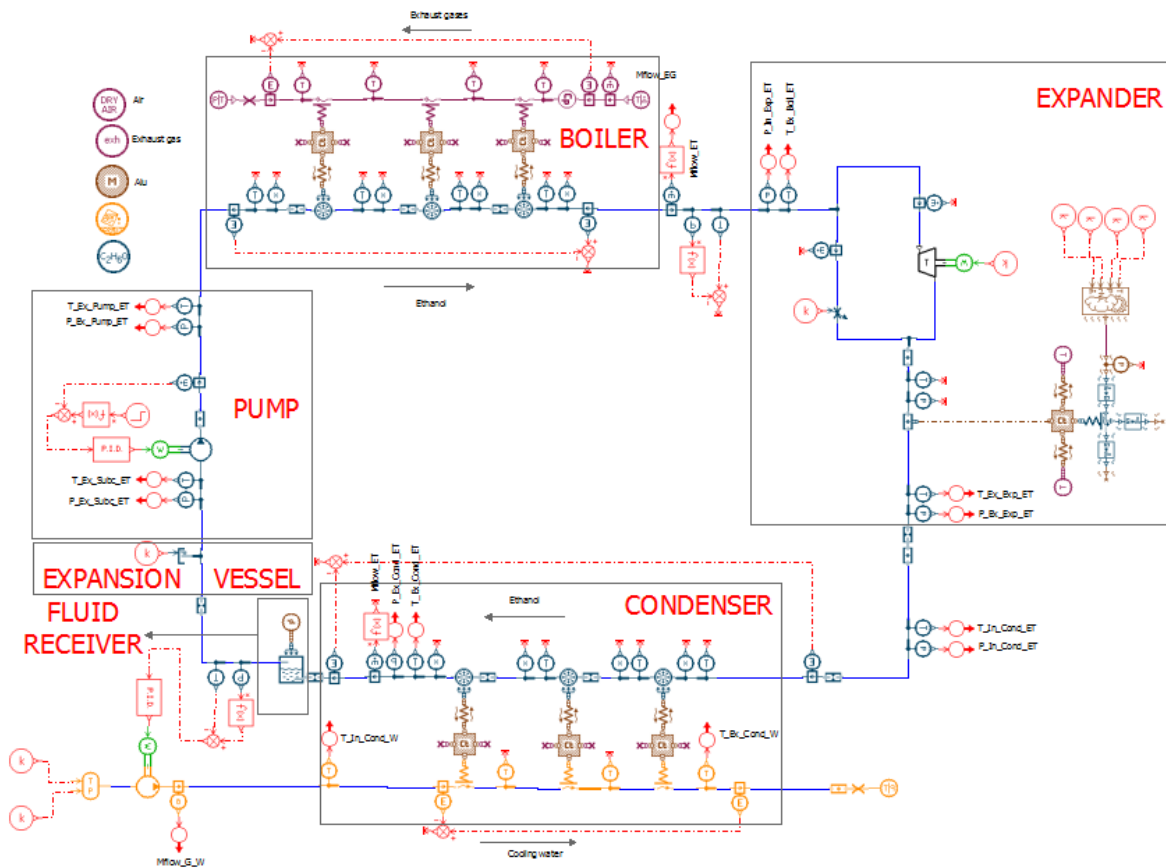
Figure 4: Organic Rankine Cycle model

3.1.1 Working fluid: In the modelling of a particular working fluid it is crucial to be able to reproduce both the thermodynamic and transport properties of the working fluid. AMESim® provides built-in physical-thermo property data of different fluids. In this case the working fluid is ethanol, which is considered by several authors as a promising fluid due to its great features in energy recovery aspect in the temperature range of a vehicle application. Table 4 summarizes the main characteristics of the working fluid.

Table 4: Properties of Ethanol

Chemical structure		C_2H_6O	
Critical Temperature	T_c	240.9	°C
Critical pressure	P_c	61.4	bar
Atmospheric boiling point	T_b	78.3	°C
Ozone depletion potential	ODP	0	-
Global Warming Potential	GWP	n/a	-
NFPA health hazard	H	2	-
NFPA flammability hazard	F	3	-
Auto ignition temperature	T_{ign}	363	°C

3.1.2 Heat Exchangers: The boiler ensures the heat transfer from exhaust gases to working fluid, based on plate and fin technology. A prototype was specifically designed for this application supplied by Valeo Systèmes Thermiques. The condenser and the subcooler are plate and fin heat exchangers chosen among industrial residential products. Plate and fin technology is preferred by the vast majority of the applications due to its compactness and high level of efficiency.

A 2D discretization model of both elements (boiler and condenser) is represented by a two-counter flow streams. In the case of the boiler, the exhaust gases and the ethanol represents the hot and cold source respectively. In the case of the condenser, the ethanol and the refrigerant (water) represent the hot and cold source respectively. In each element the volume has been divided in 3 small volumes, which in global terms exchanges the net thermal power of the global element. The heat exchange process takes into account both convective and conducting (just in longitudinal direction) process. Depending on the process (boiling or condensation) different correlations implemented in AMESim® have been taken into account.

3.1.3 Volumetric expander: The Swash-plate expander is the main element of the ORC system because it has a great impact in the overall system efficiency. Several tests have been done using turbines and expanders, most of them corresponds to scroll expanders and rotary vane ones. Between reciprocating machines, swash-plate expanders are increasingly taking into account due to its versatility and compactness. Swash-plate expanders could work with high pressure ratios, low flow regimes, lower rotational speeds and could tolerate fluid drops during its expansion. The expander model uses three parameters to characterize the performance of the expander, i.e. isentropic efficiency in Equation (1), mechanical efficiency in Equation (2) and volumetric efficiency in Equation (3).

$$\eta_{iso} = \frac{P_{ind}}{P_{iso}} \tag{1}$$

$$\eta_{mec} = \frac{P_s}{P_{ind}} \tag{2}$$

$$\eta_{vol} = \frac{\dot{m}_{ET}}{\rho_{ET} * N_{Exp} * Disp} \tag{3}$$

$$P_{iso} = \dot{m}_{ET} * \left(h_{in\_Exp\_ET} - h_{out\_Exp\_ET\_iso}\right) \tag{4}$$

$$P_{ind} = W_{cyl} * n_{cyl} * N_{Exp} * \frac{1}{60} \tag{5}$$

$$P_s = T_{Exp} * N_{Exp} \tag{6}$$

Where P_{iso}, P_{ind} and P_s are isentropic, indicated and shaft power respectively. They have been calculated using Equation (4), (5) and (6) respectively, where $\dot{m}_{ET}$ is the mass flow through the expander, $h_{in\_Exp\_ET}$ is the enthalpy at the inlet of the expander (calculated by using temperature and pressure at the inlet), $h_{out\_Exp\_ET_{iso}}$ is the isentropic enthalpy at the outlet of the expander (calculated by using pressure at the outlet and entropy at the inlet), W_{cyl} is the energy extracted from the system (calculated by integrating P-V diagram), N_{Exp} is the expander speed and n_{cyl} the number of cylinders of the expander. Regarding the volumetric efficiency, ρ_{ET} is the density of the ethanol at the inlet of the expander and Disp is the volume displaced by the expander.
No leakages and internal pressure drops have been taken into account in this expander model. Thermal conduction with internal walls of the swash-plate expander is considered to consider heat losses to the ambient.

3.1.4 Pump: A fixed displacement pump is used in this model. The mass flow rate is obtained from volumetric efficiency. The enthalpy increase is defined by the mechanical and isentropic efficiency and the swept volume. No correlations have been considered for efficiencies. Instead, some fixed values were specified for the points simulated.

3.1.5 Pipes and pressure drops: Internal piping losses in the system have been taken into account using hydraulic resistances. The transformation process is pretended to be isenthalpic. Using these elements both enthalpy and mass flow are computed.

Pressure drops in the system have been calculated using correlations available in AMESim®. The hydraulic diameter and the cross-sectional area were used to model different cross-sectional geometries. The pressure drops are regular and the friction factor depends on the flow regime and the relative roughness of the duct. Depending on the state of the fluid different correlations were applied: In a single phase flow (liquid or vapour) the Churchill (Churchill, 1977) correlation is used, while in a two phase flow correlation the user can choose between Mac Adams (McAdams, W.H., Woods, W.K., and Bryan, 1942), Cichitti (Cicchitti, Lombardi, Silvestri, Soldaini, & Zavattarelli, 1959), Dukler (Dukler, A.E., Wicks, M., and Cleveland, 1964), Friedel (Friedel, 1979) and Muller-Steinhagen-Heck (Müller-Steinhagen & Heck, 1986). In this case the Mac Adams correlation was implemented.

3.1.6 Expansion vessel: The expansion vessel is modelled using a tank with modulated pressure and constant specific enthalpy. The user must specify the low pressure value with a constant.

3.2 Swash-plate expander model

As shown in section 3, the volumetric expander tested in this installation is a Swash-plate expander. Although in the global ORC model an AMESim® submodel of the TPF library was used for modelling the expander using volumetric, isentropic and mechanical efficiencies, the need for a physical model of the expander has led to the development of a specific model for just the Swash-plate expander. Figure 5 shows the particular model of the Swash-plate expander in AMESim®. This model could be used as a design and optimization tool in future developments.
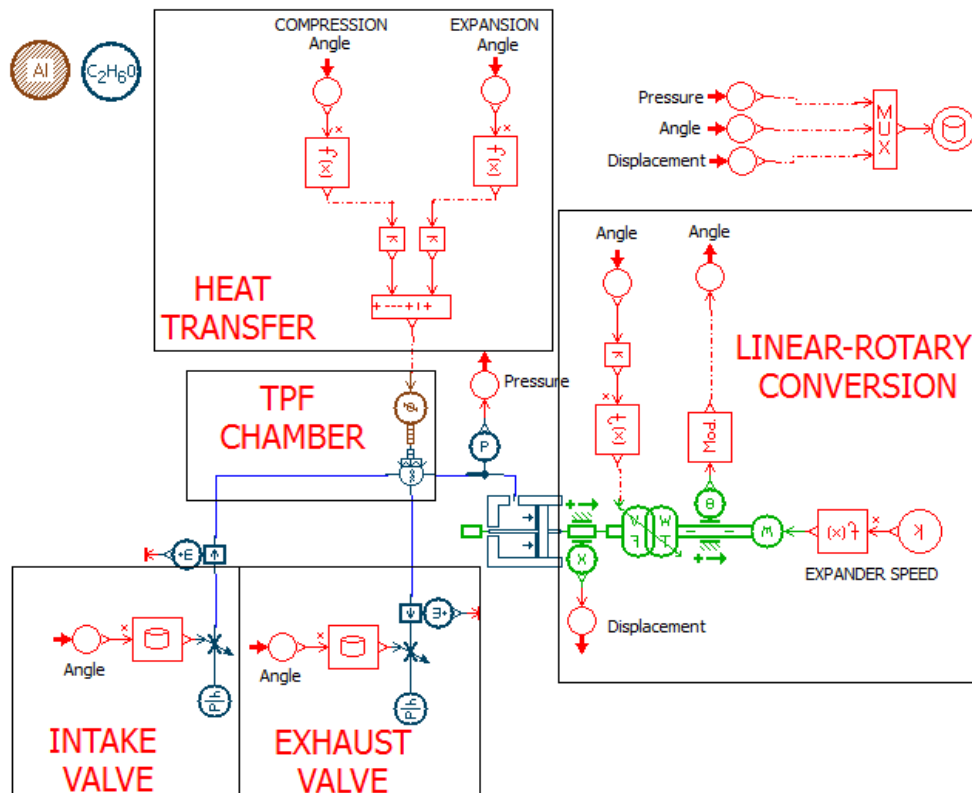

Figure 5: Swash-plate expander model

The fluid dynamic behavior of the Swash-plate was modelled using AMESim® and validated with the experimental tests developed in the expander. The comparison between P-V diagrams (simulated and tested) was used to quantify the error and accuracy of the model.

The main part of the model consists of a two phase flow chamber with variable volume and pressure and temperature dynamics. This submodel was modified respect the original model of the AMESim® library to take into account heat transfer during compression and expansion. The filling (Intake) and emptying (Exhaust) valves provide the mass and pressure exchanges during the process. The angle signal (obtained from the expander speed) is used in three parts of the model:

- In the heat transfer element: Although the expander was insulated, the expansion and compression process never follows an adiabatic law. The transformation is rather polytropic with a heat exchange between the working fluid and the expander walls due to friction, temperature differences and possible condensation effects in the piston chamber. Therefore, the angle signal was used to consider the angles of compression and expansion and to apply for each process a heat transfer coefficient.
- In the valves: The angle was considered to take into account the discharge coefficient for the intake and the exhaust valve at each particular angle. Thus, the valves were modeled as orifices with constant area and variable discharge coefficient.
- In the rotary-linear transformer: It was considered to calculate the absolute displacement in Equation (7) and therefore the volume variation in Equation (8) of the piston as a function of the Swash-plate angle.

$$X(\Phi) = R_{sw} * (1 - \cos(\Phi)) * tan(\alpha_{sw}) \tag{7}$$

$$V(\Phi) = V_d + \pi * \frac{A^2}{4} * X(\Phi) \tag{8}$$

Where R_{sw} is the radius of Swash Plate (m), α_{sw} is the swash plate angle (°), Φ is the angle covered by the piston, V_d is the dead volume (m³), A is the bore (m), $X(\Phi)$ is the displacement of the piston (m) and $V(\Phi)$ is the volume of the piston (m³). No leakages effects have been modelled.

4. RESULTS

4.1 Organic Rankine Cycle results

In order to characterize the ORC system three points have been tested at different steady working conditions of the ORC system. The points presented in this study aims to show the recovery features at different expander operating points. In these tests, the system has been controlled commanding three parameters: the speed of the pump, in order to control the mass flow of ethanol flowing through the installation, the balloon pressure of the expansion vessel, in order to control the outlet pressure of the expander, and the expander speed, in order to control the high pressure at the inlet of the expander.

These points correspond to a heat exchange in the boiler of 25 kW and three conditions of expander (expander speed of 2000, 2500 and 3000 rpm). Table 5 shows the inputs of the ORC model. For each point (P1, P2 and P3), the mass flow of the expander, the pressure at the inlet of the pump, the expander speed, the temperature at the inlet of the boiler at the EG side, the pressure at the boiler at the EG side, the mass flow of the EG and the temperature at the inlet of the condenser at the water side were fixed.

Table 5: Inputs of the ORC model

	P1	P2	P3	Units
Mf_ET	73.85	75.99	74.79	kg/h
P_in_P_ET	1.571	1.899	1.589	bar
N_Exp	2001	2502	3003	rpm
T_in_B_EG	749.48	740.28	748.92	°C
P_out_B_EG	1.018	1.024	1.018	bar
Mf_EG	154.98	159.47	155.25	kg/h
T_in_C_W	48.42	49.01	47.58	°C

Table 6 shows the volumetric, the isentropic, the mechanical efficiency (calculated using Equation (1),(2) and (3)) and the global efficiency of the expander (defined by the isentropic efficiency times the mechanical efficiency). They have been fixed in the model.

Table 6: Experimental efficiencies of the Swash-plate expander

	P1	P2	P3	Units
P_ind	1739	2007	1874	W
P_mec	1649	1543	1531	W
P_iso	3431	3413	3338	W
η_vol	19.37%	17.21%	14.54%	-
η_iso	50.68%	58.81%	56.14%	-
η_mec	94.81%	76.90%	81.72%	-
η_glob	48.05%	45.22%	45.88%	-

Table 7 presents the outputs of the model for the three points tested. For each point three columns are presented, the first one, called "P_i Exper.", corresponds to the experimental values, the second one, called P_i Sim., corresponds to the simulation values and the last one, called Error, corresponds the absolute error between both values. Temperatures are given in ºC, pressures in bar, torque in Nm and pump speed in rpm. As regards temperatures, the maximum deviation corresponds to the temperature at the inlet of the expander at medium expander speed (2500 rpm), with a value of 3.28%. The remainder temperatures of the cycle are obtained with an error lower than 3%. Regarding pressures, the maximum deviation corresponds to the pressure at the inlet of the condenser, with a value of 4.48%. The remainder pressures in the system are calculated with an error of 3%. The last two simulation parameters are the torque and the pump speed, in which the maximum deviation is 5%.

Table 7: Outputs of the ORC model

	P1 Exper.	P1 Sim.	Error	P2 Exper.	P2 Sim.	Error	P3 Exper.	P3 Sim.	Error
T_out_P_ET	47.39	46.39	0.31%	47.13	46.33	0.25%	48.60	46.33	0.70%
T_out_B_ET	210.23	208.65	0.33%	215.14	199.12	3.28%	208.29	201.34	1.44%
T_out_Exp_ET	104.74	116.21	3.04%	109.14	107.23	0.50%	111.05	109.89	0.30%
T_in_C_ET	103.79	102.55	0.33%	103.41	99.06	1.16%	102.26	97.12	1.37%
T_out_C_ET	48.27	48.58	0.10%	47.95	48.51	0.17%	47.88	48.60	0.22%
T_in_P_ET	46.67	45.76	0.28%	46.51	45.76	0.23%	47.47	45.76	0.53%
T_out_C_W	73.85	71.39	0.71%	67.25	69.03	0.52%	72.88	71.55	0.38%
P_out_P_ET	34.26	34.26	0.01%	31.01	31.48	1.51%	31.77	31.16	1.92%
P_in_Exp_ET	28.65	29.57	3.20%	27.00	26.53	1.74%	26.01	26.36	1.33%
P_in_C_ET	1.89	1.89	0.20%	2.01	2.10	4.48%	1.90	1.88	0.95%
T	7.81	7.98	2.18%	5.86	5.59	4.47%	4.87	4.96	1.85%
N_P	300	312	3.81%	305	321	5.14%	301	316	4.94%

4.2 Swash-plate expander results
The simulated and experimental curves of the pressure variation inside the expander chamber as a function of the volume were compared for the three points tested in previous sections.
Figure 6,
Figure 7 and

Figure 8 show the comparison carried out with the three expander speeds of 3000 rpm, 2500 rpm and 2000 rpm. Red and green crosses indicate the intake and exhaust valve closing angle (or volume) respectively. Red and green circles indicate the intake and exhaust valve opening angle (or volume) respectively. It was found a quite good agreement between experimental and simulation results in terms of indicated power delivered by the expander. In the right corner of these diagrams both the indicated power and the expander speed were added. Slight differences could be found in these simulations due to pressure drop in the valves and effects of pulsating flow, which cannot be modelled in AMESim® with the Two-Phase flow library.
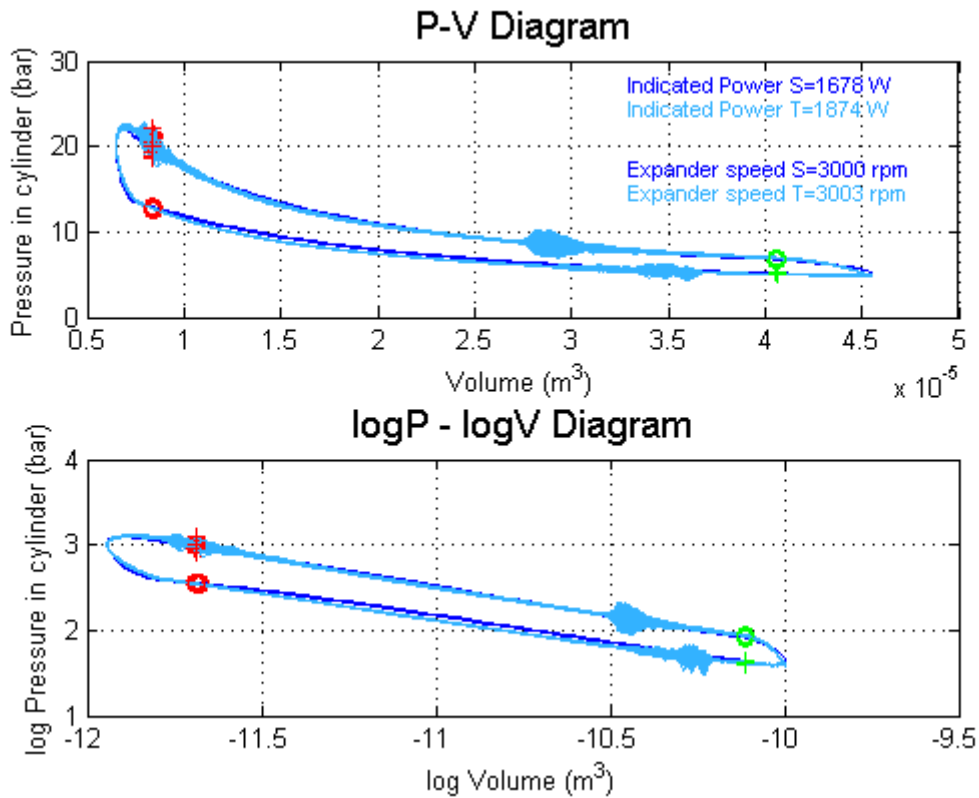
Figure 6: P-V and logP-logV Diagram 3000 rpm

P-V Diagram

Indicated Power S=1877 W
Indicated Power T=2007 W

Expander speed S=2500 rpm
Expander speed T=2502 rpm
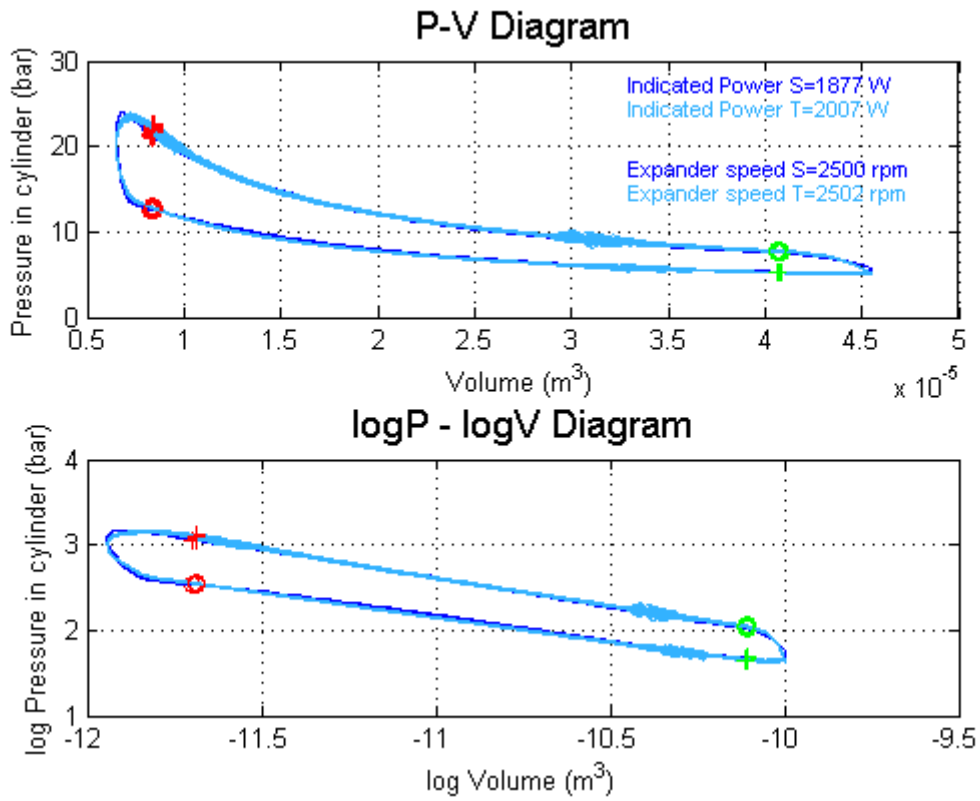
logP - logV Diagram

Figure 7: P-V and logP-logV Diagram 2500 rpm

P-V Diagram

Indicated Power S=1857 W
Indicated Power T=1739 W

Expander speed S=2000 rpm
Expander speed T=2001 rpm
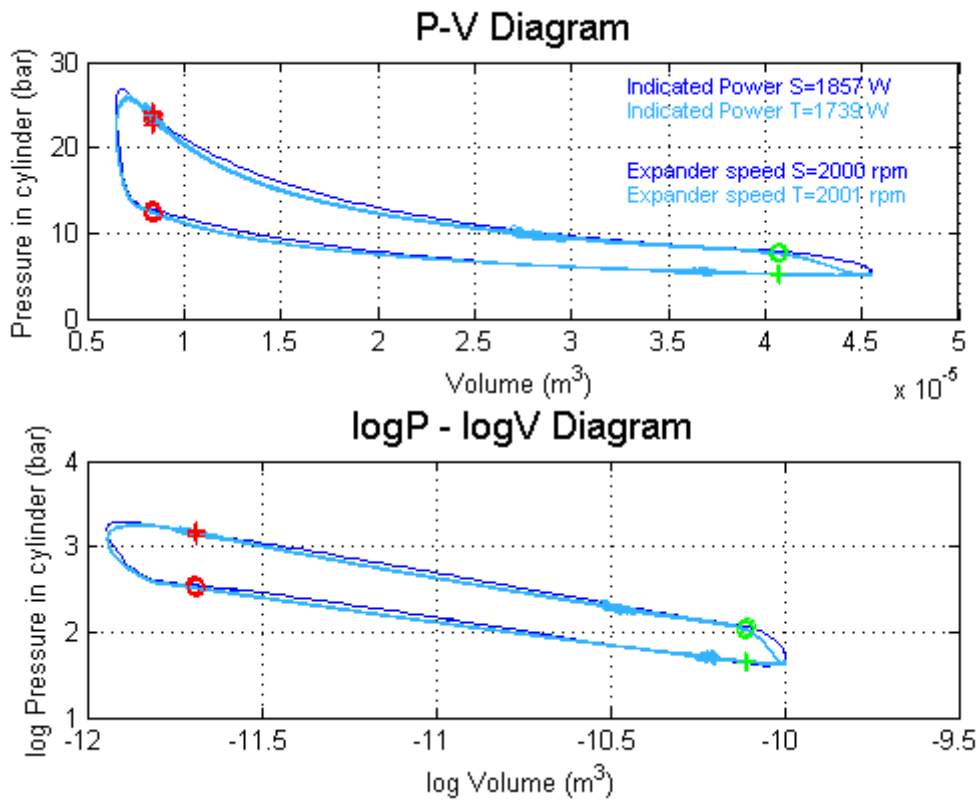
logP - logV Diagram

Figure 8: P-V and logP-logV Diagram 2000 rpm

Table 8 summarizes the results of the simulation. The inputs of the model were obtained from pressure measurements at the inlet of the expander and expander speed. In order to take into account differences between heat transferred in the three points, the coefficients of compression and expansion were modified. In this model the higher the expander speed is, the higher heat transfer rate should be imposed in the model. The maximum deviation of the model from measurements corresponds to 10% in the point of 3000 rpm, which is considered acceptable to predict flow behavior. Besides, the model predicts properly the filling and emptying processes as it can be seen in
Figure 6,
Figure 7 and
Figure 8.

Table 8: Results of the Swash-plate model

	P1	P2	P3	Units	I/O
P_B	25	25	25	kW	-
P_in_Exp_ET	28.65	27.00	26.01	bar	Input
N_Exp	2001	2502	3003	rpm	Input
P_ind_T	1739	2007	1874	W	-
P_ind_S	1857	1877	1678	W	Output
Error (%)	6.79%	6.48%	10.46%	-	-

5. CONCLUSIONS

The presented work describes and analyzes two models based on an experimental ORC installation installed in a turbocharged 2.0 l gasoline engine to recover waste heat in exhaust gases. These models correspond on one side to the global ORC cycle and on the other side the dynamic of the Swash-plate expander. The comparison of performance parameters have been made in three points by means of changing the inputs and obtaining the outputs of the model. The results are summarized in the following points:

- An ORC model is developed using the software AMESim®. This model allows to simulate the main parameters measured in the cycle. Comparing the three steady operating points, a maximum deviation of 4% regarding pressures and temperatures and a value of 5% regarding torque was attained.
- A Swash-plate expander model is presented using the software AMESim®. This model represents the fluid dynamic behavior of the Swash-plate using discharge coefficients, displacement laws and heat transfer coefficients. The P-V diagram was measured by a piezoelectric pressure sensor and compared to the simulation. Maximum deviation of 10% was achieved at point of 3000 rpm.

Waste heat recovery technologies seem to assume an essential role in the new regulations of the forthcoming decade. Therefore, ORC will be considered in increasingly growing markets to solve some of the actually environmental challenges, among which it can be pointed out ICEs. In these systems a large number of features should be contemplated, i.e. working fluid, heat exchangers, volumetric machine, pressure and temperature levels, etc….Thus, in order to optimize and improve these systems it is crucial the development of reliable models to avoid huge number of tests. The proposed models develop in this article using AMESim® are consistent due to its slight deviation between tests and simulation results. Thus, it could be considered a valuable tool in future ORC installed in ICEs.

NOMENCLATURE

ORC	Organic Rankine Cycle
P-V	Pressure Volume
TDC	Top Dead Center
BDC	Bottom Dead Center
T	Tested
S	Simulated
TPF	Two Phase Flow
Mf	Mass flow
N	Speed
T	Torque
P	Power

Subscript

ET	Ethanol
W	Water
EG	Exhaust Gases
P	Pump
Exp	Expander
C	Condenser
B	Boiler
in	inlet
out	outlet
iso	isentropic
ind	indicated
s	shaft
vol	volumetric
mec	mechanical
cyl	cylinder
sw	swash-plate
glob	global

REFERENCES

Apostol, V., Pop, H., Dobrovicescu, A., Prisecaru, T., Alexandru, A., & Prisecaru, M. (2015). Thermodynamic Analysis of ORC Configurations Used for WHR from a Turbocharged Diesel Engine. *Procedia Engineering*, *100*, 549–558. doi:10.1016/j.proeng.2015.01.402

Bracco, R., Clemente, S., Micheli, D., & Reini, M. (2013). Experimental tests and modelization of a domestic-scale ORC (Organic Rankine Cycle). *Energy*, *58*, 107–116. doi:10.1016/j.energy.2012.12.016

Carlos, L., Carles, J., Lemort, V., & Coronas, A. (2014). Characterization and modeling of a scroll expander with air and ammonia as working fl uid. *Applied Thermal Engineering*, *70*, 630–640. doi:10.1016/j.applthermaleng.2014.05.069

Churchill, S. W. (1977). Friction-factor equation spans all fluid flow regimes. *Chem. Eng.*, 91–92.

Cicchitti, A., Lombardi, C., Silvestri, M., Soldaini, G., & Zavattarelli, R. (1959). TWO-PHASE COOLING EXPERIMENTS: PRESSURE DROP, HEAT TRANSFER AND BURNOUT MEASUREMENTS. Retrieved from http://www.osti.gov/scitech/biblio/4181977

Cipollone, R., Bianchi, G., Di Battista, D., Contaldi, G., & Murgia, S. (2014). Mechanical energy recovery from low grade thermal energy sources. *Energy Procedia*, *45*, 121–130. doi:10.1016/j.egypro.2014.01.014

Conklin, J. C., & Szybist, J. P. (2010). A highly efficient six-stroke internal combustion engine cycle with water injection for in-cylinder exhaust heat recovery. *Energy*, *35*(4), 1658–1664. doi:10.1016/j.energy.2009.12.012

Dolz, V., Novella, R., García, A., & Sánchez, J. (2012). HD Diesel engine equipped with a bottoming Rankine cycle as a waste heat recovery system. Part 1: Study and analysis of the waste heat energy. *Applied Thermal Engineering*, *36*(1), 269–278.

Dukler, A.E., Wicks, M., and Cleveland, R. G. (1964). Pressure drop and hold-up in two-phase flow Part A: A comparison of existing correlations Part B: An approach through similarity analysis. *AIChE Journal*, *10*, 38–51.

Ferrara, G., Manfrida, G., & Pescioni, a. (2013). Model of a small steam engine for renewable domestic CHP (combined heat and power) system. *Energy*, *58*, 78–85. doi:10.1016/j.energy.2013.03.035

Friedel, L. (1979). Improved friction pressure drop correlations for horizontal and vertical two-phase pipe flow. In *European Two-Phase Group Meeting, Isra, Italy*.

Giuffrida, A. (2014). Modelling the performance of a scroll expander for small organic Rankine cycles when changing the working fl uid. *Applied Thermal Engineering*, *70*(1), 1040–1049. doi:10.1016/j.applthermaleng.2014.06.004

Howell, T., & Gibble, J. (2011). Development of an ORC system to improve HD truck fuel efficiency. *Deer 2011 Conference*, 1–21.

Lecompte, S., Huisseune, H., van den Broek, M., De Schampheleire, S., & De Paepe, M. (2013). Part load based thermo-economic optimization of the Organic Rankine Cycle (ORC) applied to a combined heat and power (CHP) system. *Applied Energy*, *111*, 871–881. doi:10.1016/j.apenergy.2013.06.043

Lemort, V., Quoilin, S., Cuevas, C., & Lebrun, J. (2009). Testing and modeling a scroll expander integrated into an Organic Rankine Cycle. *Applied Thermal Engineering*, *29*(14-15), 3094–3102. doi:10.1016/j.applthermaleng.2009.04.013

Macián, V., Serrano, J. R., Dolz, V., & Sánchez, J. (2013). Methodology to design a bottoming Rankine cycle, as a waste energy recovering system in vehicles. Study in a HDD engine. *Applied Energy*, *104*, 758–771.

Manente, G., Toffolo, A., Lazzaretto, A., & Paci, M. (2013). An Organic Rankine Cycle off-design model for the search of the optimal control strategy. *Energy, 58*, 97–106. doi:10.1016/j.energy.2012.12.035

McAdams, W.H., Woods, W.K., and Bryan, R. L. (1942). Vaporization inside horizontal tubes -II- Benzene-oil mixtures. In *Trans. ASME* (p. 193).

Müller-Steinhagen, H., & Heck, K. (1986). A simple friction pressure drop correlation for two-phase flow in pipes. *Chemical Engineering and Processing: Process Intensification, 20*(6), 297–308. Retrieved from http://www.sciencedirect.com/science/article/pii/0255270186800083

Qiu, G., Liu, H., & Riffat, S. (2011). Expanders for micro-CHP systems with organic Rankine cycle. *Applied Thermal Engineering, 31*(16), 3301–3307. doi:10.1016/j.applthermaleng.2011.06.008

Quoilin, S., Lemort, V., & Lebrun, J. (2010). Experimental study and modeling of an Organic Rankine Cycle using scroll expander. *Applied Energy, 87*(4), 1260–1268. doi:10.1016/j.apenergy.2009.06.026

Saidur, R., Rezaei, M., Muzammil, W. K., Hassan, M. H., Paria, S., & Hasanuzzaman, M. (2012). Technologies to recover exhaust heat from internal combustion engines. *Renewable and Sustainable Energy Reviews, 16*(8), 5649–5659. doi:10.1016/j.rser.2012.05.018

Seher, D., Lengenfelder, T., Gerhardt, J., Eisenmenger, N., Hackner, M., & Krinn, I. (2012). Waste Heat Recovery for Commercial Vehicles with a Rankine Process. *21 St Aachen Colloquium Automobile and Engine Technology 2012*.

Serrano, J. R., Dolz, V., Novella, R., & García, A. (2012). HD Diesel engine equipped with a bottoming Rankine cycle as a waste heat recovery system. Part 2: Evaluation of alternative solutions. *Applied Thermal Engineering, 36*(1), 279–287.

Wei, D., Lu, X., Lu, Z., & Gu, J. (2008). Dynamic modeling and simulation of an Organic Rankine Cycle (ORC) system for waste heat recovery. *Applied Thermal Engineering, 28*, 1216–1224. doi:10.1016/j.applthermaleng.2007.07.019

Wenzhi, G., Junmeng, Z., Guanghua, L., Qiang, B., & Liming, F. (2013). Performance evaluation and experiment system for waste heat recovery of diesel engine. *Energy, 55*, 226–235. doi:10.1016/j.energy.2013.03.073

Yang, J. (2005). Potential applications of thermoelectric waste heat recovery in the automotive industry. *ICT 2005. 24th International Conference on Thermoelectrics, 2005.*, 1–5. doi:10.1109/ICT.2005.1519911

Ziviani, D., Beyene, A., & Venturini, M. (2014). Advances and challenges in ORC systems modeling for low grade thermal energy recovery. *Applied Energy, 121*, 79–95. doi:10.1016/j.apenergy.2014.01.074

ACKNOWLEDGEMENT

COMBINED THERMODYNAMIC AND TURBINE DESIGN ANALYSIS OF SMALL CAPACITY WASTE HEAT RECOVERY ORC

Antti Uusitalo[*], Teemu Turunen-Saaresti, Aki Grönman, Juha Honkatukia, Jari Backman

[1] Larjola Laboratory of Turbomachinery, School of Energy Systems
Lappeenranta, Finland
Contact Information (antti.uusitalo@lut.fi)

* Corresponding Author

ABSTRACT

In this paper, the design of small-capacity ORC turbines for a waste heat recovery application is studied and discussed. A turbine design tool was coupled with a thermodynamic analysis tool in order to evaluate the effect of different working fluids and process parameters, not only by taking into account the thermodynamic aspects of the process design, but also evaluating the availability to design turbines with a relatively high efficiency and feasible geometry. The studied turbine type is a radial inflow turbine since radial turbines represent relatively simple geometries when compared to multistage configurations, can have a high expansion ratio over a single stage, and have a better efficiency at a low power capacity than the axial counterparts. The results indicate that the main difficulties in the design of small capacity ORC turbines are related to high rotational speeds, small dimensions, and large blade height ratios. In addition, the use of single stage turbines leads to highly supersonic flow in the stator even when adopting low or moderate flow velocities. The results of this study highlight the importance of combining both the thermodynamic process design and the turbine design when evaluating suitable working fluids and operational parameters.

1. INTRODUCTION

Organic Rankine Cycles (ORC) are a widely implemented technology in geothermal, biomass, and in different waste heat recovery applications. The use of organic working fluids allows to design small-scale power systems that are capable of utilizing efficiently low temperature heat sources. The current ORC applications and the most important design aspects of ORCs are presented and discussed e.g. in (Colonna et al., 2015). In small power output ORCs (about 10-50 kW) a volumetric expander, namely screw or scroll expanders, are typically preferred instead of a turbine whereas a turbine is typically used as an expansion machine in larger scale ORC applications (Colonna et al., 2015). The limitations of using volumetric expanders are related to the lower achievable expansion ratios over an expander when compared to the use of turbines and thus, the use of volumetric expanders disables the use of high molecular weight and high critical temperature fluids characterized by high expansion ratios and high thermodynamic efficiencies. Therefore, the use of turbines could enable the design of high efficiency small-scale ORCs, especially for high temperature applications.

The turbine types used in the ORCs are typically axial or radial turbines (Colonna et al., 2015). Studies on using multistage radial outflow turbines have been carried out in the recent years (Pini et al., 2013). The expansion ratio over the turbine can be very high, especially in high-temperature ORCs, which can result in high Mach numbers and significantly large rotor blade height ratio between the rotor outlet and inlet (Macchi, 1977; van Buijtenen et al., 2003; Uusitalo et al., 2013). In addition, the real gas effects in the expansion become significant, especially when fluids having a high molecular complexity are used and when the expansion occurs near the critical point of the fluid (Harinck et al., 2009; Guardone et al., 2013). In many ORC turbines, the flow is supersonic since the organic fluids have a low speed of sound. This causes losses related to the occurrence of shock waves in the flow passages. The design and flow

analysis of supersonic ORC turbine stators have been presented for radial turbines e.g. in (Harinck et al., 2010, Uusitalo et al., 2014) and for axial turbine stator e.g. in (Colonna et al., 2006). Geometry optimization methods by using automated CFD-design have been developed in the recent years in order to further improve the performance of supersonic ORC turbines (Harinck et al. 2013). The results by Harinck et al. (2013) indicated that the losses caused by the occurrence of shock waves can be reduced significantly by bending and turning the stator flow channels instead of using straight nozzles.

Few experimental works on small-scale ORC turbines are available in the literature. Verneau (1987) presented the experimental results for two high pressure ratio ORC turbines, having a power output of 50 kW and using FC 75 as the working fluid. The first turbine design was a supersonic two-stage axial turbine and the second design was a single-stage axial turbine. The pressure ratios of the designed turbines were about 150. The experiments showed that a relatively high turbine efficiency in a range of 70 to 80 % was achieved for both the two-stage and single-stage turbine designs. An experimental study on a small-scale ORC having a high speed radial turbine was presented by Kang (2012). The turbine and generator were assembled to a single shaft having a rotational speed of 63 000 rpm. The system used R245fa as the working fluid and the evaporation temperature was in a range from 70 ^{o}C to 90 ^{o}C. The measured power output was 32.7 kW and the turbine efficiency of 78.7 % was achieved. Additionally, Klonowicz et al. (2014) presented experimental results of a low-temperature ORC using R227ea. The system had a 10 kW hermetic turbogenerator and the designed turbine was a partial admission axial turbine. The electric efficiency of the turbogenerator of less than 60 % was measured including the losses in the turbine and in the generator.

Despite several studies on high-expansion ratio ORC turbines, guidelines to design such expanders, especially for small-scale systems are lacking and only few studies have presented experimental results on the performance of small ORC turbines. In addition, a large number of publications have discussed the working fluid selection from the thermodynamic point of view, but totally neglecting the effect of the working fluid on the turbine design. Maraver et al. (2014) included a preliminary turbine size evaluation for different working fluids in a thermodynamic study by using a size parameter (SP), but no further assessment on the turbine rotational speeds, geometry, or Mach numbers were included. This paper presents a method of combining the thermodynamic process analysis and preliminary turbine design tool to evaluate suitable working fluids and cycle design parameters for a small-scale ORC from the point of view of the turbine design. In addition, the most critical aspects of designing radial turbines for small-scale ORCs are highlighted and discussed. The studied application is exhaust heat recovery of small-scale gas turbines.

2. DESIGN METHODS

The design of an ORC process utilizing exhaust gas heat is studied by using exhaust gas values typical for small-scale gas turbines(Invernizzi et al., 2007). The exhaust gas temperature at the ORC evaporator inlet is 300 ^{o}C, and the mass flow rate of the exhaust gas was set to 1 kg/s. The exhaust gas temperature at the evaporator outlet was varied in the analysis in order to study the effect of the exhauts gas outlet temperature on the cycle power output and turbine design. A commercial thermodynamic library Refprop was used for calculating the fluid properties. The studied fluids are hydrocarbons toluene, cyclohexane, and pentane; siloxanes MDM and MM; and fluorocarbons R245fa and R365mfc. The main thermodynamic properties of the studied fluids are presented in Table 1.

In the thermodynamic analysis of the process, the evaporation pressure of the working fluid was optimized to reach a minimum pinch-point temperature difference of 15 ^{o}C in the evaporator with the given heat source values. If the temperature difference in the evaporator remained sufficient, a limit of $p_{ev}/p_{crit} = 0.95$ was used for the evaporation pressure. A condensing temperature of 60 ^{o}C was used, the cycle included a recuperator and all the studied fluids were superheated by 10 ^{o}C, since a flow through type of evaporator was considered. Turbine efficiency of 80 %, generator efficiency of 95 %, efficiency

Table 1: Studied working fluids and main thermodynamic properties.

fluid	T_{crit}, [^oC]	p_{crit}, [bar]	MW, [kg/kmol]	p_{cond} (@ 60 ^oC), [bar]
toluene	318.6	41.3	92.1	0.2
cyclohexane	280.5	40.75	84.2	0.5
pentane	196.6	33.7	72.1	2.1
MDM	290.9	14.2	236.5	0.04
MM	245.6	19.4	162.4	0.3
R245fa	154.0	36.5	134.0	4.6
R365mfc	186.9	32.7	148.1	2.0

of the frequency converter of 97 %, and the efficiency of feed pump of 60 % were used in the analysis. The design tool of radial turbines calculates the main dimensions and velocity triangles of the turbine. The turbine inlet and the outlet conditions were obtained as a result from the process thermodynamic design. The evaluation of the turbine rotational speed, n, was carried out by using the non-dimensional parameter, turbine specific speed N_s defined as,

$$N_s = \frac{\omega q_v{}^{0.5}}{\Delta h_s{}^{0.75}}. \tag{1}$$

According to the performance diagram for radial turbines operating with compressible fluids, the highest efficiencies are obtained with specific speeds in a range from 0.4 to 0.8 (Balje, 1981). The intermediate static pressure between the stator and rotor was selected by using the degree of reaction which is defined by dividing the enthalpy change in the turbine rotor by the total enthalpy change in the turbine stator and rotor

$$r = \frac{\Delta h_{rot}}{\Delta h_{tot}}. \tag{2}$$

The rotor outlet blade tip to rotor inlet diameter ratio D_{2t}/D_1, the blade hub-to-tip diameter ratio D_{2h}/D_{2t} at the outlet as well as the stator exit flow angle α_1 were evaluated by following the guide-lines of (Rohlik, 1972). The velocity calculations were based on the continuity equation and on the Euler turbomachine equation. The velocity vectors were solved at the rotor inlet and at the rotor outlet. An example of the turbine velocity triangle at the rotor inlet is presented in Fig. 1. The tangential component of the absolute velocity, c_u, was used in monitoring the shape of the velocity triangle at the rotor inlet by using a velocity ratio c_u/u while the radial component of the absolute velocity, c_r, was used in the continuity equation to calculate the blade height at the rotor inlet. The stator efficiency of 82 % was used in the calculations to estimate the static enthalpy at the stator outlet. The turbines were designed to have the rotor discharge in axial direction, and thus, the tangential component of the absolute velocity at the rotor outlet $c_{u2} = 0$. The calculations of the turbine geometry were based on the assumption that the flow velocity at the rotor discharge is relatively low and thus, an assumption of $h_{2,st} \approx h_{2,tot}$ was used and no analysis for the turbine diffuser was included.
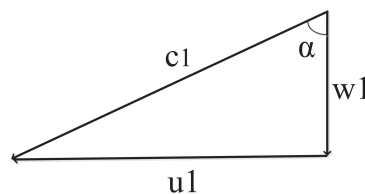
Figure 1: An example of a velocity triangle at the rotor inlet, having a radial relative velocity ($w_{u1} = 0$).

It should be noted that the results of the process calculations were based on the 80 % turbine efficiency

with all the studied fluids and process design parameters. This kind of approach can be well justified in the preliminary evaluation of turbine dimensions and rotational speeds, but it should be noted that the turbine efficiency has an effect on the size of the rotor wheel and on the optimal turbine rotational speed. Thus, a more accurate turbine design would be achieved in a case if the turbine efficiency used in the process design were iteratively changed based on the obtained turbine dimensions and Mach number at the stator outlet. However, this would require detailed numerical simulations of the turbine since there is very limited data available about the losses and applicable loss correlations for radial ORC turbines.

3. RESULTS

3.1 Comparison to radial turbine designs available in the literature

A comparison was made between the turbine geometries designed with the code used in this study and ORC radial turbine designs available in the literature to verify the design method. The working fluid mass flow rate, the turbine inlet state, the turbine efficiency and the turbine outlet pressure, as well as the degree of reaction and the specific speed if available, were set to the same values as presented in (Kang, 2012; van Buijtenen et al, 2003). The turbine isentropic efficiency of 75 % was used in the comparison of (Kang, 2012) and 80 % in the comparison of (van Buijtenen et al., 2003). The absolute flow angle at the stator outlet of 75 ^{o} was used for the both turbines designs. The results of the comparison are presented in Table 2. In general, based on the results of the comparison the developed turbine design code has a good agreement in the turbine diameter and rotational speed with the radial ORC turbine designs selected for the comparison. The found agreement shows the reliability of the design method and gives a good foundation for the analysis in the following sections.

Table 2: Comparison of the turbine rotor diameter and rotational speed between Turbine 1 (Kang, 2012), Turbine 2 (van Buijtenen et al., 2003), and the used turbine design code.

	fluid	$P_t,$ kW	$q_m,$ kg/s	$N_s,$ -	$r,$ -	$p_{t,in},$ bar	$T_{t,in},$ ^oC	$p_{t,out},$ bar	$D_{rot},$ mm	$n_{rot},$ rpm
Turbine 1	R245fa	≈ 30.0	1.58	na	na	7.3	80	1.78	125	20 000
comparison	R245fa	31.0	1.58	0.45	0.47	7.3	80	1.78	124.1	21 597
Turbine 2	toluene	≈ 200	1.24	0.44	0.26	32.3	325	0.27	224	28 300
comparison	toluene	191.6	1.24	0.44	0.26	32.3	325	0.27	227.5	28 081

3.2 Results with different working fluids

The process and turbine design results with different working fluids are presented in this section. The results presented in this section were calculated for turbines having the specific speed of 0.5 and the degree of reaction of about 0.5. The results of the cycle power output, the cycle efficiency and the evaporation pressure as a function of the exhaust gas temperature at the evaporator outlet are presented in Fig. 2a, Fig. 2b and Fig. 2c. The results for the power output show that the studied hydrocarbons represent the highest simulated cycle power output, above 30 kW, and the fluorocarbon R245fa represents the lowest power outputs, especially with the high exhaust gas temperatures at the evaporator outlet. The fluids with the highest critical temperatures represent the highest values for the power output with the higher exhaust gas temperatures at the evaporator outlet when compared to the fluids with the lowest critical temperatures. The highest cycle efficiencies are reached with hydrocarbons toluene and cyclohexane, and the lowest efficiencies with R245fa and R365mfc. It should be noted that these power output and efficiency results are based on the use of constant turbine isentropic efficiency with all the studied fluids and cycle parameters. Are more detailed analysis would require the turbine efficiency to be iteratively changed according to the obtained turbine geometries. The evaporation pressure limit of $p_{ev}/p_{crit} = 0.95$ is reached with fluids having the lowest critical temperatures, namely R245fa, R365mfc, pentane, and MM, since the temperature difference between the working fluid and the exhaust gas remains sufficient. Evaporation pressures well below the critical pressures are adopted with each fluid when the lowest ex-

haust gas outlet temperatures are considered in order to maintain a sufficient temperature difference of 15 ^oC in the evaporator.
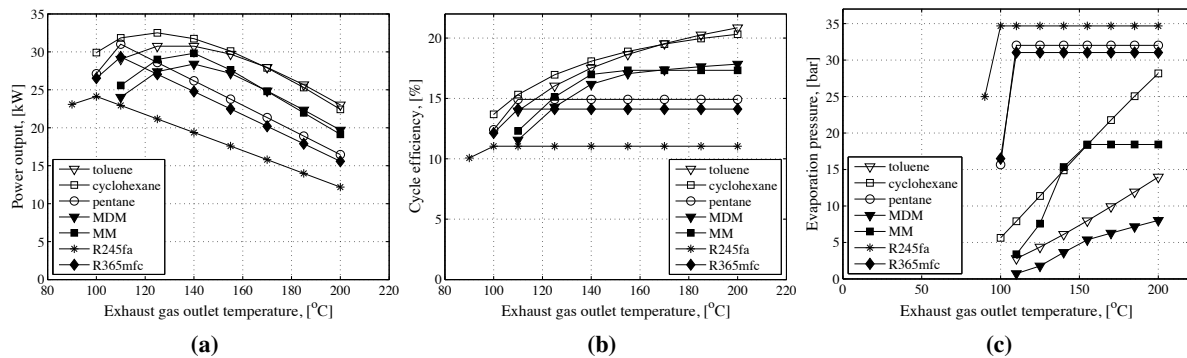

Figure 2: Results of a) power output, b) cycle efficiency, and c) evaporation pressure as a function of exhaust gas temperature at the evaporator outlet.

The working fluid mass flow rate is presented in Fig. 3a, the enthalpy change in the turbine in Fig. 3b, and the expansion ratio over the turbine in Fig. 3c as a function of the exhaust gas outlet temperature. The studied fluorocarbons, R245fa and R365mfc, represent the highest mass flow rates in the process, while the studied hydrocarbons, toluene, cyclohexane, and pentane represent the lowest mass flow rates. The studied hydrocarbons represent the highest enthalpy drop in the turbine and the studied fluorocarbons represent the lowest enthalpy drop. The studied siloxanes and high critical temperature hydrocarbons represent significantly higher expansion ratio over the turbine than the other fluids, especially when the exhaust gas temperature at the evaporator outlet is high. This can be explained by the low condensing pressure of these fluids and if the exhaust gas temperature is high at the evaporator outlet a high evaporation pressure was obtained, resulting in a large expansion ratio over the turbine. The studied fluorocarbons and pentane, which are the fluids having the lowest critical temperatures, represent the lowest expansion ratios over the turbine.
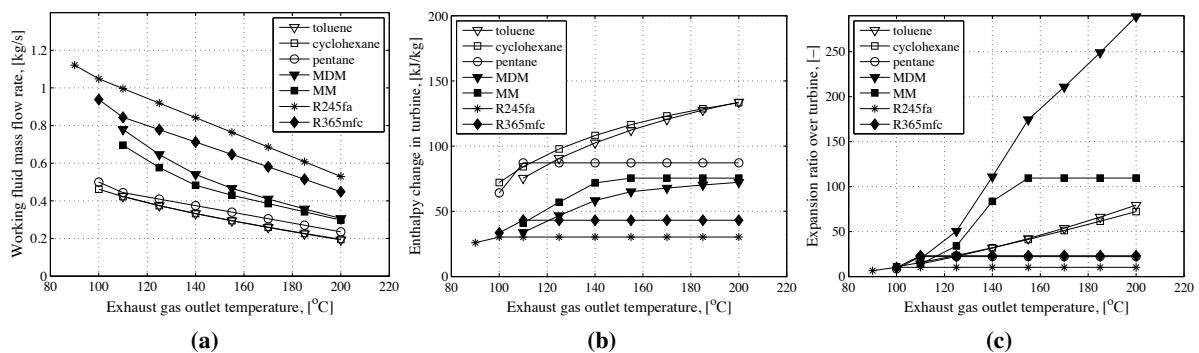
Figure 3: Results of a) working fluid mass flow rate, b) enthalpy change over the turbine, and c) expansion ratio over the turbine as a function of exhaust gas temperature at the evaporator outlet.

The calculated turbine diameters are presented in Fig. 4a, the blade height at the rotor inlet in Fig. 4b, and the rotor outlet-to-inlet blade height ratio in Fig. 4c. Based on the results, the fluids having the lowest critical temperatures presents the smallest turbine wheels and small blade heights at the turbine rotor inlet. The studied siloxanes and the hydrocarbons with the highest critical temperatures, toluene and cyclohexane, represent the largest rotor wheels and highest blade heights at the rotor inlet, especially when a low exhaust gas outlet temperature is used. These fluids also represent significantly large rotor blade

height ratios, especially with the high exhaust gas outlet temperatures. This can be mainly explained by the high expansion ratio over the turbine with these fluids, which requires a large change in the flow area over the turbine wheel. The blade heights at the rotor inlet are significantly small ranging from 1 mm to 2 mm when a high exhaust gas outlet temperature is adopted. The small blade height is estimated to cause turbine efficiency reductions due to the high tip clearance losses and relatively thick boundary layers when compared to the height of the flow channel, as well as difficulties in manufacturing the turbine wheel. On the other hand, the effect of the tip clearance at the rotor inlet on the radial turbine efficiency has been reported to be less significant when compared to significance of tip clearance loss in axial turbines (Dambach et al., 1999). The large rotor blade height ratio might cause flow separation in the rotor and thus, reducing the turbine efficiency.
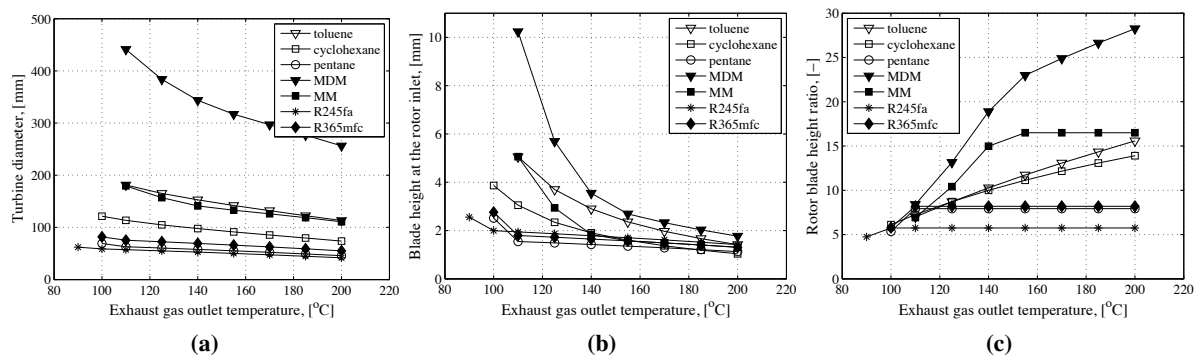
Figure 4: Results of turbine design values as a function of exhaust gas temperature at the evaporator outlet: a) rotor diameter, b) blade height at the rotor inlet, and c) rotor blade height ratio.

The Mach number at the stator outlet is presented in Fig. 5a, the peripheral speed at the turbine rotor inlet in Fig. 5b, and the turbine rotational speed in Fig. 5c. Fig 5a shows that all the studied fluids have a supersonic flow at the turbine stator outlet. The studied siloxanes and the hydrocarbons, toluene and cyclohexane, represent the highest Mach numbers at the stator outlet while the fluids with the lowest critical temperatures, namely R245fa, R365mfc, and pentane represent the lowest Mach numbers. The highly supersonic flow requires the use of accurate design methods for the stator flow channel in order to reduce the losses. In addition, the losses related to the stator-rotor interaction and to the reflection of shock waves from the rotor blades have been identified as a significant source of losses in this type of turbines (Rinaldi et al., 2013). The studied hydrocarbons represent the highest peripheral speed at the rotor inlet and the studied fluorocarbons represent the lowest values of peripheral speed. The high peripheral speed causes higher stresses for the turbine wheel, which should be taken into account in the mechanical design of the turbine wheel. The highest turbine rotational speed is achieved with pentane and the lowest rotational speed is achieved with the siloxane MDM. The high rotational speed increases the turbine shaft mechanical and windage losses and sets demands for the bearing design.

In general, the results indicate that by designing the cycle for low exhaust gas outlet temperatures and thus, resulting in a low evaporation pressure, several benefits can be achieved from the point of view of the turbine design. The working fluid mass flow rate and the blade height at the rotor inlet are higher and the turbine wheel is larger. In addition, the rotor blade height ratio, expansion ratio over the turbine, rotational speed and the Mach number at the stator outlet are lower when compared to a cycle designed with a higher evaporation pressure.

3.3 Effect of specific speed on turbine design

The effect of the turbine specific speed on the turbine design is presented and discussed in the following. The working fluid is toluene and the degree of reaction is about 0.5 in the calculated cases. The effect of the turbine specific speed on the rotor diameter is presented in Fig. 6a and on the turbine rotational
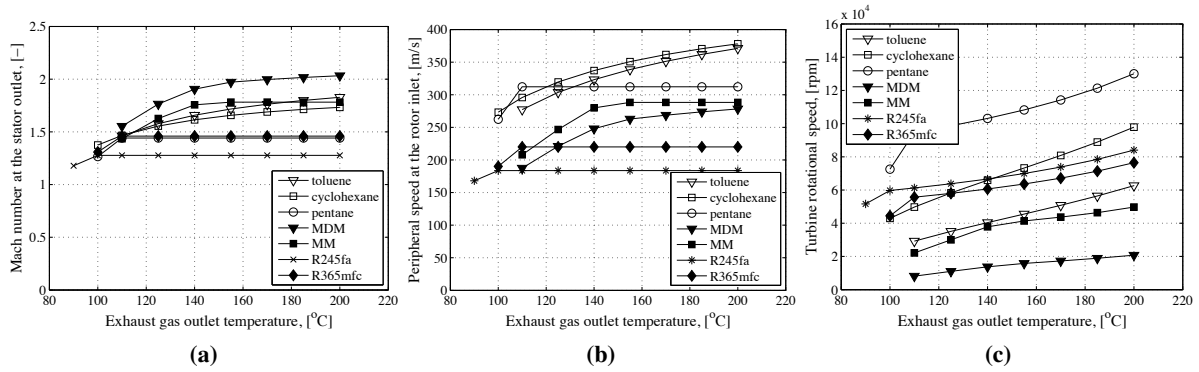
Figure 5: Results of a) Mach number at the stator outlet, b) peripheral speed at the turbine rotor inlet, and c) turbine rotational speed.

speed in Fig. 6b. The effect of the turbine specific speed on the blade height at the rotor inlet is presented Fig. 6c, and on the turbine rotor blade height ratio in Fig. 6d. The results presented in Figs. 6a-d, show
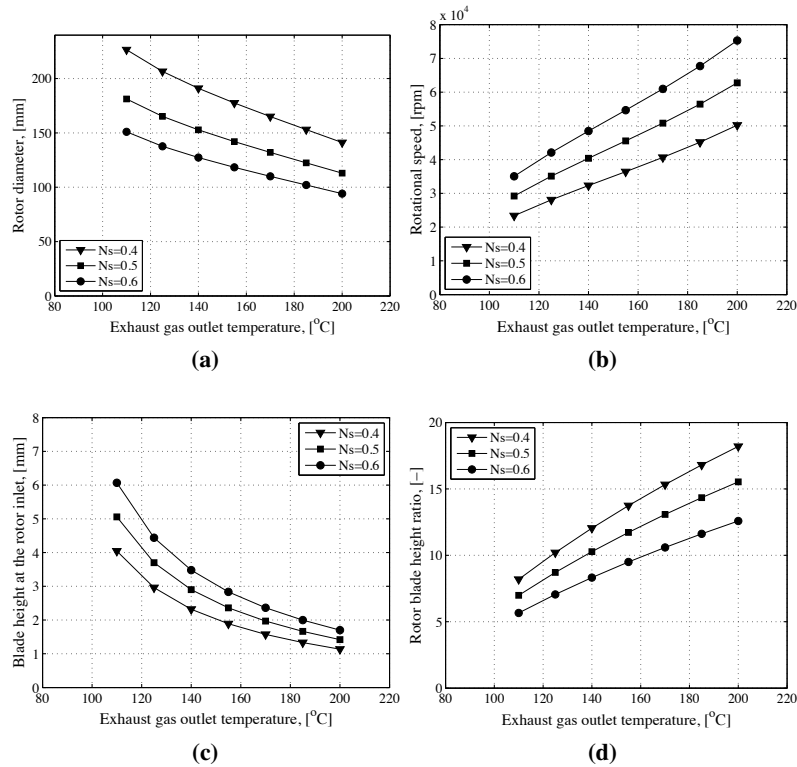

Figure 6: The effect of turbine specific speed on a) rotor diameter, b) rotational speed, c) blade height at the rotor inlet, and d) rotor blade height ratio. The working fluid is toluene.

that by selecting a low specific speed the turbine wheel is larger and the rotational speed is lower, when compared to a turbine design with a high specific speed. Thus, a turbine with a low specific speed can be considered if the turbine tends to be fast rotating and having a small diameter with a high specific speed. On the other hand, the results indicate that the blade height at the rotor inlet is smaller and the rotor blade height ratio is higher, possibly resulting to lower turbine efficiency when a low specific speed is selected, when compared to a turbine designed for higher specific speed.

3.4 Effect of degree of reaction on turbine design

The effect of the turbine's degree of reaction on the turbine design is presented and discussed in this section. The working fluid is toluene and the specific speed is 0.5 in the calculated cases. The effect of the degree of reaction on the rotor diameter, on the blade height at the rotor inlet, on the turbine rotor blade height ratio and on the Mach number at the stator outlet is presented in Fig. 7a, 7b, in Fig. 7c and 7d, respectively. The results presented in Figs. 7a-d, show that by selecting a low degree of reaction
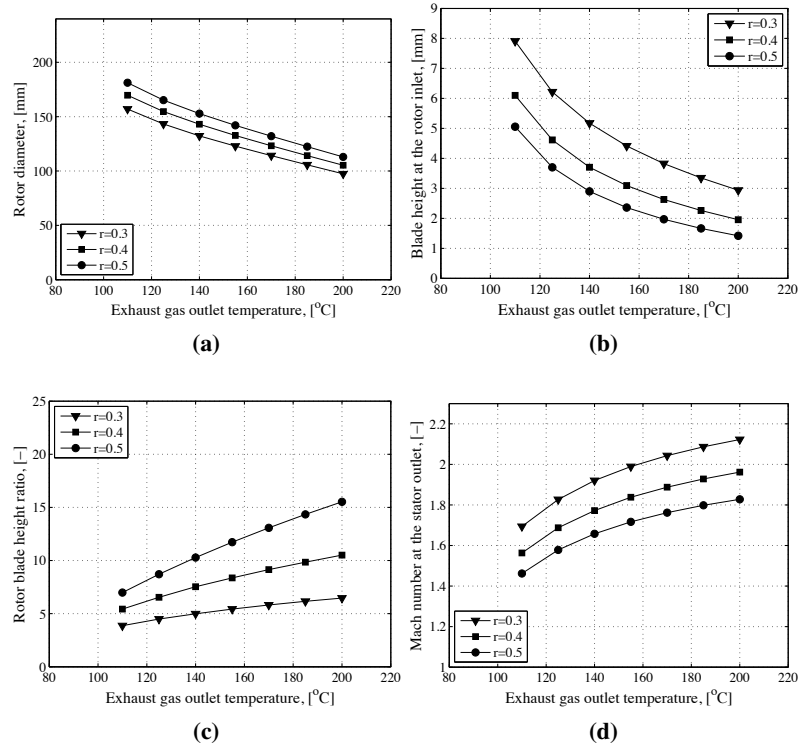
Figure 7: The effect of the degree of reaction on a) rotor diameter, b) blade height at the rotor inlet, c) rotor blade height ratio, and d) Mach number at the stator outlet. The working fluid is toluene.

the rotor wheel is smaller and the blade height at rotor inlet is higher when compared to a higher value of degree of reaction. In addition, the rotor blade height ratio is significantly reduced by selecting a low degree of reaction. However, the Mach number at the stator outlet is higher when a low degree of reaction is adopted. This can be explained by the fact that the pressure ratio over the turbine stator is high when a low degree of reaction is selected resulting in a high stator outlet velocity. In addition, the selection of low degree of reaction increases the velocity ratio c_{u1}/u_1 and there is a risk of a flow separation at the rotor inlet caused by a large incidence angle of the relative velocity if radial blades at the rotor inlet are considered. Thus, the use of bent blades at the rotor inlet, as were used e.g. in the turbine presented in (van Buijtenen et al. 2003), could be considered if a low degree of reaction is selected.

4. CONCLUSIONS

In this study, a simplified design tool of a radial turbine was coupled with a thermodynamic analysis tool to evaluate and compare different working fluids, not only from the thermodynamic point of view, but taking into account the turbine design considerations as well. Based on the results the selection of working fluid highly influences not only the thermodynamic performance of the cycle, but has a significant impact on the turbine dimensions and rotational speed as well. In general, the design of small-scale ORC turbines is difficult because the turbine wheels tend to be small and fast rotating, and represent small blade heights at the rotor inlet. The largest turbine wheels and the lowest rotational speeds were

obtained with fluids having the highest critical temperatures. However, the results indicate that the use of a fluid with a high critical temperature leads to a high expansion ratio over the turbine and thus, represents highly supersonic flow at the stator outlet and large rotor blade height ratio, which is estimated to reduce the achievable turbine efficiency. The results indicate that by designing the cycle for a low evaporation pressure several benefits can be achieved from the turbine design point of view. The working fluid mass flow rate and the blade height at the rotor inlet is higher and the turbine wheel is larger. In addition, the rotor blade height ratio, expansion ratio over the turbine, the rotational speed and the Mach number at the stator outlet are lower when compared to a cycle designed for a higher evaporation pressure. Thus, if a small-scale ORC adopting a single-stage turbine is considered, it might be beneficial to design the cycle for a low evaporation pressure despite the reduction in the cycle efficiency. It was also observed that the turbine dimensions are very sensitive on the choice of turbine specific speed and degree of reaction. Loss correlations for high expansion ratio radial turbines for ORC applications should be created and impelemented in the future. The authors suggest that more experimental work on ORC turbines should be carried out to provide knowledge on the performance and feasibility of small-scale ORC systems based on turbine technology.

NOMENCLATURE

c	absolute velocity	(m/s)
h	specific enthalpy	(kJ/kg)
P	power	(kW)
p	pressure	(bar)
q_m	mass flow rate	(kg/s)
q_v	volumetric flow rate	(m^3/s)
T	temperature	(°C)
c	absolute flow velocity	(m/s)
N_s	specific speed	(-)
n	rotational speed	(rpm,1/s)
w	relative velocity	(m/s)
u	tangential/peripheral velocity	(m/s)
D	diameter	(m)
r	degree of reaction	(-)
α	absolute flow angle	(deg)
ω	angular speed	(rad/s)

Subscript

ev	evaporation
s	isentropic
st	static
rot	rotor
t	turbine/blade tip
h	blade hub
0	turbine inlet
1	rotor inlet/stator outlet
2	rotor outlet
u	tangential component
r	radial component

REFERENCES

Balje, O.E., 1981, Turbomachines: A Guide to Design, Selection and Theory. John Wiley and Sons, New York.

Colonna P., Rebay S., Harinck J., and Guardone A., 2006, Real-Gas Effects in ORC Turbine Flow

Simulations: Influence of Thermodynamic Models on Flow Fields and Performance Parameters. Proceedings of ECCOMAS CFD, September 5-8.

Colonna P., Casati E., Trapp C., Mathijssen T., Larjola J., Turunen-Saaresti T., and Uusitalo A., 2015, Organic Rankine Cycle Power Systems: from the Concept to Current Technology, Applications and an Outlook to the Future.*J. Eng. Gas Turbines and Power*, vol. 137:10.1115/1.4029884.

Dambach R., Hodson H.P., and Huntsman I., 1999, An Experimental Study of Tip Clearance Flow in a Radial Inflow Turbine. *Journal of Turbomachinery*, vol. 121(4): 644-650.

Guardone A., Spinelli A., and Dossena V., 2013, Influence of Molecular Complexity on Nozzle Design for an Organic Vapor Wind Tunnel. *J. Eng. Gas Turbines and Power*, vol. 135:042307.

Harinck J., Guardone A., and Colonna P., 2009, The Influence of Molecular Complexity on Expanding Flows of Ideal and Dense Gases. *Physics of Fluids*, vol. 21:086101.

Harinck J., Turunen-Saaresti T., Colonna P., Rebay S., and van Buijtenen J., 2010, Computational Study of a High-Expansion Ratio Radial Organic Rankine Cycle Turbine Stator. *J. Eng. Gas Turbines and Power*, vol. 132:054501.

Harinck, J., Pasquale, D., Pecnik, R., van Buijtenen, J., and Colonna, P., 2013, Performance improvement of a radial organic Rankine cycle turbine by means of automated computational fluid dynamic design.*Journal of Power and Energy*, vol. 227(6), p.637-645.

Kang S.H., 2012, Design and experimental study of ORC (organic Rankine cycle) and radial turbine using R245fa working fluid. *Energy*, vol.41(1), p.514-524.

Klonowicz P., Borsukiewicz-Gozdur A., Hanausek P., Kryllowicz W., and Brüggemann., 2014, Design and performance measurements of an organic vapour turbine. *Applied Thermal Engineering*, vol.63(1), p.297-303.

Macchi E., 1977, Design criteria for turbines operating with fluids having a low speed of sound. Von Karman Instute for Fluid Dynamics. Closed Cycle Gas Turbines, Lecture series 100, May 9-13.

Maraver D., Royo J., Lemort V., and Quoilin S., 2014. Systematic optimization of subcritical and trans-critical organic Rankine cycles (ORCs) constrained by technical parameters in multiple applications. Applied energy, 117, p.11-29.

Pini M., Persico G., Casati E., and Dossena V., 2013, Preliminary Design of a Centrifugal Turbine for Organic Rankine Cycle Applications. J. Eng. Gas Turbines and Power, vol. 135(4):10.1115/1.4023122.

Rinaldi E., Buonocore A., Pecnik R., and Colonna P., 2013, Inviscid stator/rotor interaction of a single stage high expansion ratio ORC turbine. 2nd International Seminar on ORC Power Systems. Rotterdam, The Netherlands, 7-8 October.

Rohlik H., 1972, Radial Inflow Turbines, Chapter 10 in Glassman A. J., Turbine Design and Application: Volume 1-3, NASA, 388 pages.

Uusitalo A, Honkatukia J, Turunen-Saaresti T, Colonna P, Larjola J., 2013, Siloxanes as working fluids for mini ORC turbogenerators based on "high speed technology". *J. Eng. Gas Turbines and Power*, vol.135;042305.

Uusitalo A., Turunen-Saaresti T., Guardone A., and Grönman A., 2014, Design and Modeling of Highly Supersonic Small Scale Radial ORC Turbine Stator with High Molecular Complexity Working Fluids. ASME Turbo Expo 2014,16-20 June 2014, Germany.

van Buijtenen J.P., Larjola J., Turunen-Saaresti T., Honkatukia J., Esa H. and Backman J., 2003, Design and validation of a new high expansion ratio radial turbine for ORC application. 5th European conference on Turbomachinery, Prague, March 17-22.

Verneau A., 1987, Supersonic Turbines for Organic Fluid Rankine Cycles from 3 to 1300 kW: Small High Pressure Ratio Turbines. Von Karman Institute for Fluid Dynamics, Lecture series 7,June 15-18.

EXPERIMENTAL INVESTIGATION OF A RADIAL MICROTURBINE IN ORGANIC RANKINE CYCLE SYSTEM WITH HFE7100 AS WORKING FLUID

Tomasz Z. Kaczmarczyk*, Grzegorz Żywica, Eugeniusz Ihnatowicz

The Szewalski Institute of Fluid-Flow Machinery, Polish Academy of Sciences
Centre of Mechanics of Machines, Department of Turbine Dynamics and Diagnostics
Gen. J. Fiszera 14 st., 80-231 Gdańsk, Poland
tkaczmarczyk@imp.gda.pl, gzywica@imp.gda.pl, gieihn@imp.gda.pl

* Tomasz Z. Kaczmarczyk, e-mail: tkaczmarczyk@imp.gda.pl

ABSTRACT

The paper presents the results of experimental investigation of the ORC system with prototype microturbine. The prototype of biomass boiler has been used as a heat source. The boiler with a power rating of 25 kW_{th} is powered by biomass (wood pellets) using an auger. The biomass boiler heats thermal oil which is directed to the evaporator where the low boiling refrigerant evaporates. The maximum temperature of the thermal oil in the evaporator is about 210 ^{o}C – 215 ^{o}C. The solvent HFE7100 was used as the working fluid in the ORC system. The prototype of four-stage radial microturbine and biomass boiler has been designed and built at the Institute of Fluid-Flow Machinery of the PAS in Gdańsk. The designed electric capacity of microturbine is 2.7 kW_e at maximum speed of 24000 rpm. The isentropic efficiency for this fluid-flow machine is about 70%. The generated electricity is dissipated by an electric heater with a power of 5 kW_e and eleven light bulbs 100 W_e each. Electrical load can be adjusted according to your needs. At the inlet of the microturbine a condensate separator was applied to protect the blades from erosion and to ensure the proper operation of gas bearings. In the initial phase the steam microturbine is supplied with a high degree of superheat in the range from 30 K to 40 K (the warm phase of the microturbine). During normal operation of the microturbine, superheating degree of the low boiling fluid is in the range of 5 K to 10 K. The working fluid after expansion in microturbine is directed to the regenerator and then to the condenser. The heat supplied to the condenser is dissipated by a fan cooler with maximum power of 50 kW_{th}. Depending on the flow rate of the glycol in the condenser the absolute pressure is in the range of 1.2 bar - 3 bar and a temperature of the working fluid in the range from 20 ^{o}C to 65 ^{o}C can be obtained. The paper presents the characteristics of the ORC system and radial microturbine for different variants of flow rates for different working mediums (thermal oil, HFE7100, glycol). During testing of the ORC system with the prototype of radial microturbine and the biomass boiler (fired with wood pellets) the maximum electrical output power was around 1551 W_e.

1. INTRODUCTION

The Directive 2009/28/WE, approved by the European Union, has committed the majority of its Member States to increase the share of renewable energy sources in total energy consumption to 20% by 2020 (15% in Poland). This is not only an active fight against global climate change, but also a key contribution to boosting the development of modern technologies. That is why the scientists continue to search for new energy-saving technologies. One idea is to use new RES systems or modify existing systems by making use of CHP installations. Combined heat and power (CHP) production, e.g. in ORC systems, can be an alternative for traditional power engineering systems. The cogeneration systems are characterized by energy savings and environmental-friendly technologies. The use of micro-CHP system can easily satisfy single-family home demand for heat and electricity, reducing CO_2 emissions to atmosphere. It is estimated that in order to satisfy these demands for one single-family house, one needs to use a CHP system whose electrical power does not exceed 10 kW_e. For multi-family buildings, power capacity of CHP systems should be in the range of 10 – 30 kW_e (Liu et

al., 2011, Onovwiona et al., 2006, Quoilin et al., 2010). In order to meet the EU directives and trends, for systems using RES, a domestic micro power plant (based on the ORC cycle) has been built at the Institute of Fluid-Flow Machinery, in Gdańsk. An expansion device is seen as a key element in any ORC installation which principally decides of the whole system efficiency. That is why many scientists carry out research on ORC cycles with various types of expanders i.e. vane, scroll, piston, screw expanders as well as Stirling engines or turbines. Mayer et al. (2013) investigated into the ORC system with a scroll expander and HFC-M1 as the working fluid. The scroll Air Squared expander had the following rated parameters: expansion coefficient 3.5, nominal rotational speed 3600 rpm, pressure 13.8 bar, displacement 12 cm^3/rev. Purified exhaust gases from the Capstone gas turbine were used as a heat source. The temperature of gas was about 220 ^{o}C and its mass flow was about 0.3 kg/s. The Carnot efficiency was about 10.1% and the thermal efficiency reached 5.7%. Lemort et al. (2009) investigated the ORC system with a prototype of scroll expander and working medium HCFC-123. As an expansion device a modified oil-free scroll compressor was applied. Two hot air flows were used as a heat source. The isentropic expander effectiveness was in the range from 42% to 68% for the pressure ratio of the expander in the range from 2.7 to 5.4. The maximum cycle efficiency was about 7.4%. Quoilin et al. (2010) have proposed different analytical models of components and parameters of the ORC system. Difference between the measured electric power generated by the expander and power value calculated by a numerical model was less than 10%. Declaye et al. (2013) investigated the oil-free scroll expander in an ORC system with R245fa. The scroll expander was obtained by modifying an open-drive scroll compressor to run in reverse. The maximum isentropic efficiency depends on the rotational speed. For an inlet pressure 12 bar, it ranges from 71.3% at 3500 rpm to 75.7% at 2500 rpm. The maximum shaft power is 2.00 kW at 3500 rpm for a pressure ratio of 7.18 and an inlet pressure of 12 bar. The minimum shaft power is 0.21kW at 3000 rpm for a pressure ratio of 2.36 and an inlet pressure of 9 bar. The maximum cycle efficiency is 8.54% at 3000 rpm for a pressure ratio of 7.1 and an inlet pressure of 12 bar. The minimum cycle efficiency is 0.1% at 3000 rpm for a pressure ratio of 2.36 and an inlet pressure of 9 bar. The exergetic efficiency is 48% at 3000 rpm for pressure ratio 4.32 and an inlet pressure of 12 bar. Qiu et al. (2012) tested the ORC system with 50 kW$_{th}$ biomass-pellet boiler and vane-type air motor as an expander. The experimental results show that the CHP system generated about 860 W$_e$ of electricity, efficiency of electricity generation was 1.41% and CHP efficiency was 78.69%. Bahrami et al. (2013) performed thermodynamic analysis of an ORC cycle, in conjunction with a Stirling engine. The following working mediums were tested: FC72, FC87, HFE7000, HFE7100, Novec649, n-pentane, R245fa and toluene. Operating temperatures of ORC was between 80 ^{o}C and 140 ^{o}C. The steam turbine was used as an expansion device. Total power efficiency in the range 34% to 42% was observed for different cases. The ORC cycle efficiency was in the range of 15-19%, depending on the used working medium. They found that the best mediums in this cycle were: toluene, HFE7100 and n-pentane. Smith et al. (2006) carried out research on the ORC cycle with R124 as a working medium. Twin screw compressor was used as an expander. The machine was coupled to a generator, rotating at 1800 rpm, using a vee belt drive. Initial tests showed that the expander generated 22 kW of shaft power with an adiabatic efficiency of 74%. The unit cost is in the range of $1500-2000/kW$_e$ (water cooled) and $2500/kW$_e$ (air cooled). Seher et al. (2012) performed experimental studies and computational simulations of the ORC system equipped with two expanders, turbine and piston machine. The heat source was a 12 l heavy duty engine. The thermal power input to the WHR (waste heat recovery) system was from 100 kW$_{ht}$ to 300 kW$_{th}$. They analyzed several working mediums, including water, toluene, ethanol, R246fa and MM (Hexamethydisiloxane). The piston expander operated as a single-cylinder double acting type and power take-off was at engine speed. Dimensions of the piston machine are: displacement 0.9 l, stroke 81 mm, piston diameter 87 mm. The calculated effective power of the piston machine amounts to 12 kW$_e$ (that is about 5% of the Diesel engine power). The measured mechanical power was around 14 kW (that is about 4.3% of the engine power). The experiment was carried out using water as a working medium. The maximum water pressure reached around 32 bar and the maximum temperature was about 380 ^{o}C. The double-stage constant-pressure turbine was the second expander. The maximum speed of the turbine was 150000 rpm. The numerical simulation of the ORC cycle with water as a working medium gave the following results: maximum turbine output power 10 kW with an efficiency of 66%. The results of the measurements were as follows: maximum power reached around 9 kW at turbine's rotational speed of about 120000 rpm. The most favourable solutions are

either a piston machine using water or ethanol as working fluid and a turbine using ethanol. Kaczmarczyk et al. (2013a), Kaczmarczyk et al. (2013b) investigated the ORC system with an expansion valve (simulating work of a microturbine) and a radial microturbine. The experimental investigation conducted in the regenerative ORC test bench with a gear pump and a radial microturbine gave the following physicochemical parameters of HFE7100 (working medium): temperature 180 ^{o}C, pressure 11.76 bar, working medium flow rate 0.16 kg/s. Reaching the shaft rate of 254 Hz, the microturbine generates electric power of 360 W_e. The Carnot efficiency of the regenerative ORC system with a microturbine was about 32% and the thermal efficiency of the regenerative ORC system with a microturbine was about 5.2%. Liu et al. (2010) used a modified air turbine motor as a turbine in the ORC system. The turbine was connected to a car alternator, which was loaded with resistors and light bulbs. The researchers used two heat sources: electric heater 9 kW_e and a biomass-fired boiler with power 25 kW_{th}. As the working fluid the HFE700 and HFE7100 were used. In the ORC system with electric heater maximum electrical power was 96 W_e, electrical efficiency was 1.06% and the efficiency of the CHP system was over 83%. In the ORC system with biomass boiler electrical efficiency was 1.34%, the efficiency of the CHP system was 88%, and the maximum electric power was about 284 W_e. Li et al. (2011) presented a theoretical and experimental study of heat loss in the radial-axial turbine (with power 3.3 kW_e) in the ORC system. It was a quantitative study on the convection and radiation heat transfer. The results show that the external radiative and convective heat loss coefficient was about 3.2 W/m^2K and 7.0 W/m^2K respectively, when the ORC operated around 100 °C. The total heat loss coefficient in the ORC experimental test was about 16.4 W/m^2K, where its value was estimated at 94.5 W_e. The expander efficiency will be overestimated by about 2.9% if the external heat loss is not taken into consideration. Pei et al. (2011) presented the results of a prototype of radial-axial turbine operating in ORC cycle with R123 as a working fluid. The turbine isentropic efficiency is about 62.5% and ORC efficiency is around 6.8%. The turbine shaft power was about 1 kW.

2. EXPERIMENTAL STAND – ORC INSTALLATION

The ORC installation in the Laboratory of Cogenerative Micro Power Plants is composed of three basic cycles: a heating cycle, cooling cycle and a working fluid cycle. The ORC test bench with a HFE7100 droplet separator is presented in Figure 1.
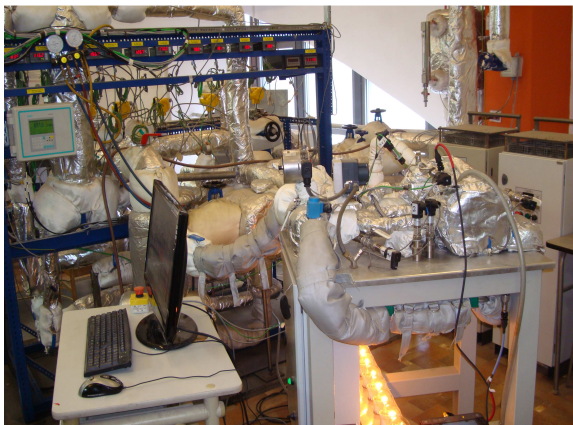

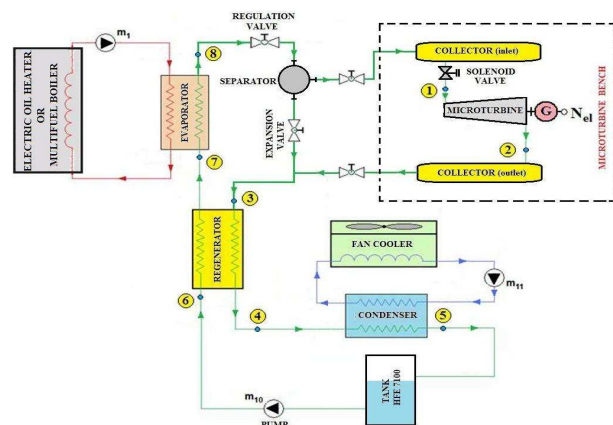**Figure 1:** The ORC system with a microturbine and a set of heaters in the test bench

Figure 2: Measurement scheme of the regenerative ORC with a microturbine

The heating cycle consists of oil gear pumps made by Tapflo (model TG L018) and two independent heat sources: a prototypical multifuel boiler and a set of two prototypical electric thermal oil heaters that can operate independently or in series/in parallel. The regulation of rotational speed of the oil gear pumps was carried out through the frequency converter made by Bonfiglioli Synplus (model SPL200 03 F). The ORC installation can operate using an expansion valve (simulating operation of a microturbine), microturbine or a group of expanders. The gear pump used in the experimental system to feed liquid HFE7100 is supplied by Scherzinger (model 4030). The pump can provide a maximum operating pressure of 14 bar, flow rate of 15.75 l/min and rotation speed of 4000 rpm. The maximum

power output of the pump is 0.75 kW. The output capacity pump can be adjusted from 0-100%, using a frequency inverter made by LS (model iG5A). The measurement scheme of the regenerative ORC system with a microturbine is presented in Figure 2. The characteristic points 1 – 8 for the regenerative cycle have been marked. These points were used to determine the changes in thermodynamic state of the working medium in the ORC installation.

2.1 Microturbine

The ORC system cooperates with a high-speed four-stage radial microturbine whose parameters are as follows: nominal power 2.7 kW$_e$, nominal rotational speed 24000 rpm and isentropic efficiency of about 70%. Figure 3 presents a photograph of the microturbine.

Figure 3: Experimental stand of the microturbine

The turbine shaft is integrated with an electric energy generator and encased in a sealed housing. Given the hermetic construction and the high rotational speed, aerostatic gas bearings powered by a low-boiling medium vapor were used. The microturbine is equipped with a control and measurement system which assures good functioning of the device as well as reception and conditioning of electric energy.

2.2 Heat sources

As it has previously been mentioned, the heating cycle has two heat sources. The first one is a multifuel boiler, alternatively fuelled with biomass, town gas, or gas obtained by gasification of biomass. The other heat source is a prototypical electric flow heater for thermal oil. Both the multifuel boiler (Figure 4) and the electric heater (Figure 5) can operate independently or in series. The prototypical electric flow heater for thermal oil consists of two modules: LKM-25/75-300 and LKM-25/75-301.

Figure 4: Prototype multi-fuel boiler with a solid fuel reservoir (biomass-pellets)

Figure 5: Prototype electric flow heater for thermal oil

Both modules can operate independently or in series and are designed to heat non-conductive fluids (thermal oil) to the temperature of about 250 ^{o}C with low power flow density (below 3 W/cm^2) and the power of 2x24 kW$_e$. The heater is powered from the network with alternative (50 Hz), three-phase voltage of 3x400 VAC. The boiler is equipped with a coil heat exchanger for double exhaust gas circulation which increases its effectiveness. The maximal boiler power during biomass combustion (pellets of about 5 mm diameter) is about 30 kW$_{th}$.

2.3 Cooling system

The third cycle in the ORC installation is the cooling system consisting of fan coolers made by GEA (model TDR 01 06 53-C) with a water spraying system, glycol pump made by LFP (model 25 POeC100 Mega) with inverters, JAD-type and plate heat exchangers and piping. The cooling system of the ORC installation performs two tasks. First, it enables cooling of the thermal oil coming to the evaporator, and thus increases the range of adjustment of oil temperature. Moreover, additional cooling of oil protects the system against the excessive temperature rise or enables quick cooling of thermal oil in case of loss of electricity or a breakdown, which assures higher safety while operating the ORC installation. Oil cooling is performed with the use of a JAD-type heat exchanger, cooling glycol pump and a fan cooler. The other important task of the cooling system is quick cooling of the HFE7100 vapor in the condenser (plate exchanger), in a way to obtain liquid of the temperature of 65 ^{o}C at the inlet of the circulation pump.

2.4 The measuring and data acquisition system

The measuring system is based on the National Instruments (NI) devices. The NI PXIe-8130 controller, with appropriate software, controls the operation of the system. Signals from temperature, pressure, power and flow rate sensors, after adjustment in the SCXI-1102b module, are converted into digital form using the data acquisition (DAQ) boards: PXI-6280 and PXI-6251. The NI SCXI-1102B amplifier module with the SCXI-1303 terminal block, the SCXI-1125 and the SCXI-1313 were applied to generate both analogue and digital control signals. The software for the measurement system was made using the NI LabVIEW graphical programming platform. All temperatures were measured with a type K (model TP-211K-b) thermocouple having a diameter of 0.5 mm and a length of 100 mm, with an accuracy of ±0.1°C (made by Czaki). All pressures were measured with pressure transducers made by Trafag (model NAH 8253), with accuracy of 0.15% over the full scale range (16 bar). Differential pressure were measured with a smart differential pressure transmitters by Aplisens (model APR-2000ALW and APR-2200ALW) with permissible measuring error ±0.1%, accuracy of 0.075% over the full scale range (0.5 bar). The Flow rate of the thermal oil was measured with an ultrasonic flowmeter made by Simens (model Sitrans FUS1010,) with 1% at v≥ 0.3 m/s. The flow rate of the HFE7100 was measured using Coriolis mass flowmeter made by Simens (model Sitrans FC Massflo Mass 2100) with an accuracy of ±0.1%. The flow rate of the glycol was measured using turbine flowmeter made by Hoffer (model HO3/4X3/4-30-B-1) with an accuracy of ±0.25%. The electric power output of the generator was measured using a meter of network parameters made by Lumel (model ND20) with phase current and voltage ± 0.2%; power (active, reactive and apparent) ± 0.5%; tangent φ ± 1%; frequency ± 0.2% of the measured value, active/reactive energy ± 0.5%.

2.5 Measurement process

As a result of heating the working medium (thermal oil, HFE7100 and glycol), the changes in the flow rate take place, being caused by the change of physicochemical parameters (i.e. density, viscosity). The definition of steady state was introduced. Steady state denotes the state in which the flow rate change of the working medium does not exceed 1% of the maximum flow rate for 15 minutes. The acceptable maximal (1%) flow rates are: for the thermal oil 0.004 kg/s, for the HFE7100 0.002 kg/s and for the glycol 0.005 kg/s. Additionally, the change of average pressure in the steady state should not exceed 0.12 bar (i.e. 1% of the maximum pressure value) for 15 minutes, and the changes in temperature values should not exceed ± 1 ^{o}C.

3. EXPERIMENTAL RESULTS OF MICROTURBINE IN THE ORC CYCLE

3.1 Thermal-flow characteristics of the ORC installation

Figure 6 presents the graph of the working medium (HFE7100 and thermal oil) temperature changes in the evaporator (system with an electric flow heater for thermal oil).
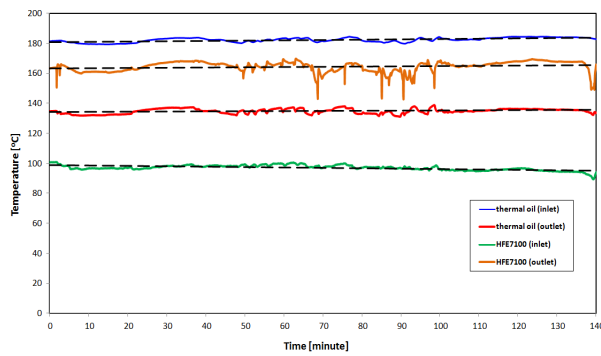
Figure 6: The temperature of HFE7100 and thermal oil in the evaporator vs time
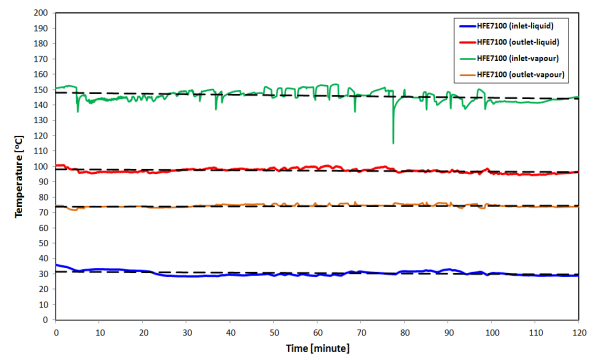

Figure 7: The temperature of HFE7100 in the regenerator vs time

Figure 6 shows that the temperature of thermal oil at the inlet to the evaporator was stable reaching about 182 ^{o}C and was about 138 ^{o}C at the outlet. The temperature of HFE7100 at the inlet to the evaporator was about 100 ^{o}C and reached about 163 ^{o}C at the outlet. The temperaure changes of HFE7100 in the regenerator on the liquid and vapor sides in the steady state are presented in Figure 7. Figure 7 shows that the temperature of HFE7100 at the inlet to the vapour side of the regenerator was about 145 ^{o}C, and about 75 ^{o}C at the outlet, which gives the temperature difference of about 70 ^{o}C. The temperature of HFE7100 at the inlet to the liquid side of the regenerator was about 30 ^{o}C and about 98 ^{o}C at the outlet. Figure 8 presents the temperature changes in the HFE7100 and glycol in the condenser in the steady state.
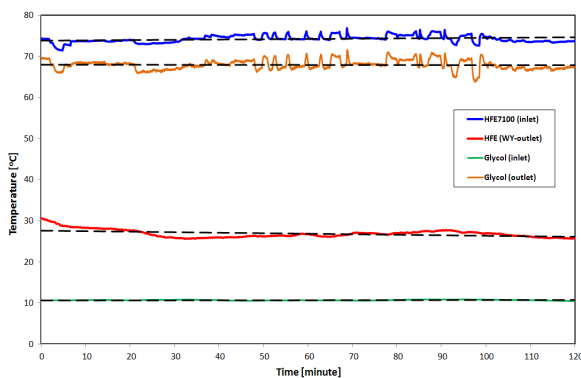
Figure 8: The temperature of HFE7100 and glycol in the condenser vs time
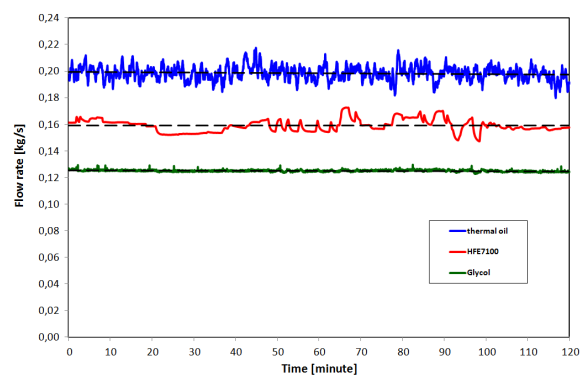
Figure 9: The flow rate of working medium vs time (during microturbine operation)

The temperature of glycol (Figure 8) at the inlet to the condenser was about 10 ^{o}C and 68 ^{o}C at the outlet. The temperature of HFE7100 at the inlet to the condenser reached about 75 ^{o}C and was 28 ^{o}C at the outlet. Figure 9 presents the flow rate waveforms for thermal oil, HFE7100 and glycol measured during microturbine operation. The analysis of the measurement data shows that the average flow rate of the thermal oil was about 0.21 kg/s. Moreover, the average flow rate values for the HFE7100 and glycol were around 0.162 kg/s and 0.125 kg/s, respectively.

3.2 The radial microturbine characteristics

Figure 10 presents the output voltage curve of the radial microturbine recorded during the measurement. Load current diagram of the microturbine generator was shown on Figure 11.
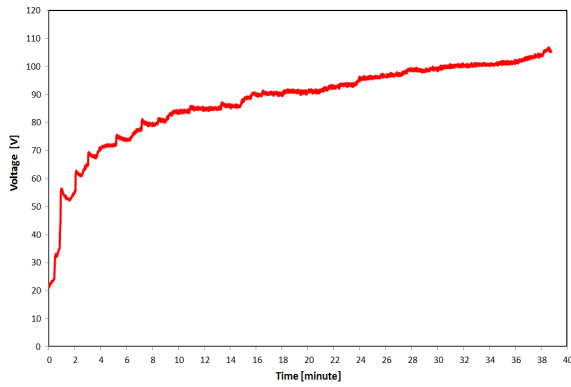
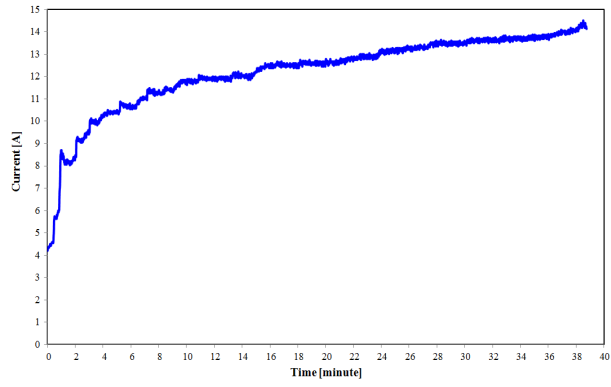**Figure 10:** Voltage generated of the radial microturbine vs time

Figure 11: Load current of the radial microturbine vs time

Maximum voltage generated by the microturbine was around 107 V, while the maximum load current was about 14.5 A. Electrical power curve for the radial microturbine operating in the ORC system was shown in Figure 12. The Figure 13 presents the graph containing the course of microturbine rotational speed in relation to the measurement time.
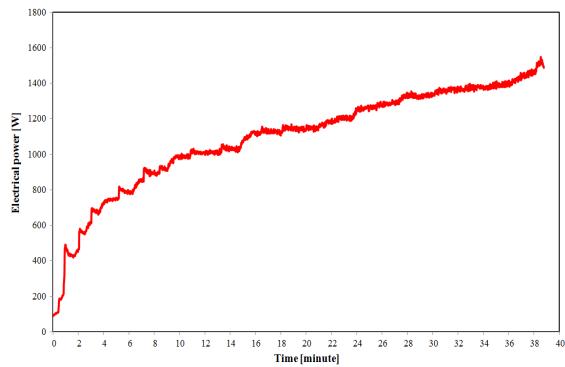

Figure 12: Electric power curve registered during microturbine operation
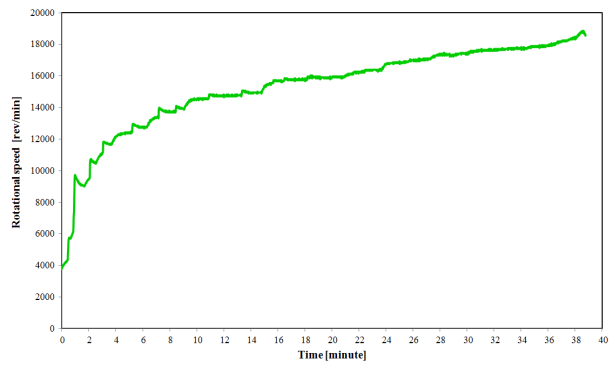
Figure 13: Microturbine rotational speed registered during the measurement

The maximum electric power generated by the microturbine reached the level of 1551 W_e, at the rotational speed of about 18700 rpm. The electric power generated by the microturbine versus rotational speed and pressure drop in the microturbine are shown in Figures 14 and 15 respectively.

y = 3E-06x^2 + 0,0335x - 92,515
R^2 = 0,9989
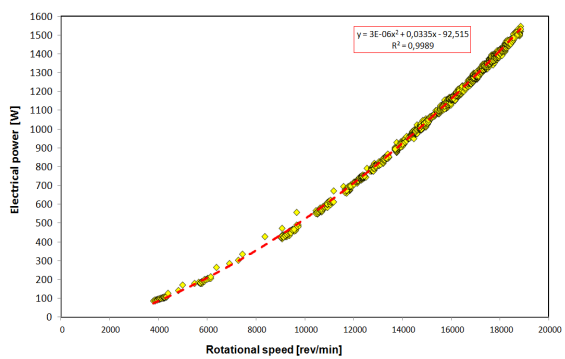
Figure 14: Electric power generated by the microturbine vs rotational speed

y = -3,5421x^3 + 62,773x^2 - 50,898x + 35,024
R^2 = 0,9973
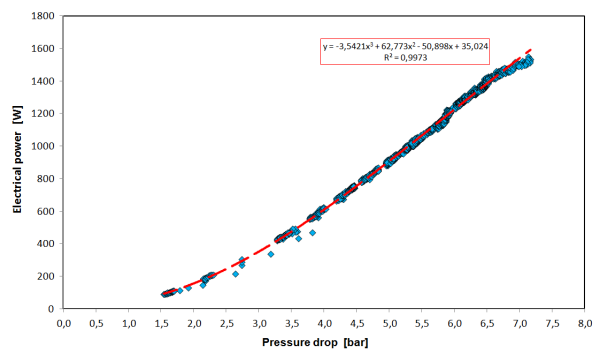
Figure 15: Electric power generated by the microturbine vs pressure drop

On the basis of Figures 14 and 15, knowing the value of rotational speed or pressure drop in the microturbine, electric power of the microturbine can be assessed quickly and easily across the entire power range. These two figures contain red dashed lines representing linear regression, the coefficients of which were calculated by the least squares method. The regression lines are presented

with their corresponding equations and coefficients (R^2). The electric power generated by the microturbine versus pressure ratio and inlet pressure is shown in Figures 16 and 17, respectively.
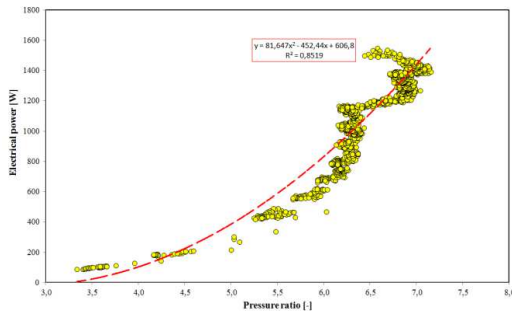

Figure 16: Electric power generated by the microturbine vs pressure ratio
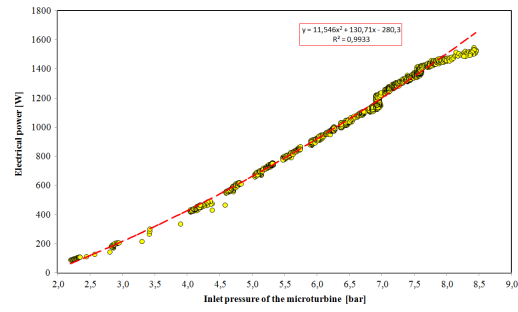

Figure 17: Electric power generated by the microturbine vs inlet pressure

Figure 16 shows that when the pressure ratio is equal to 7, the power generated by the microturbine amounts 1480 W_e. The maximum electric power was generated by the microturbine when the supply pressure was 8.5 bar (Figure 17) and reached about 1550 W_e. The Figures 16 and 17 contain linear regression lines with their corresponding equations and coefficients (R^2). Figures 18 and 19 present the diagram T-s and P-v for the HFE7100 in the ORC system with regeneration, respectively.
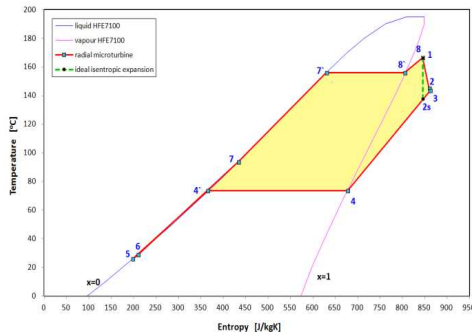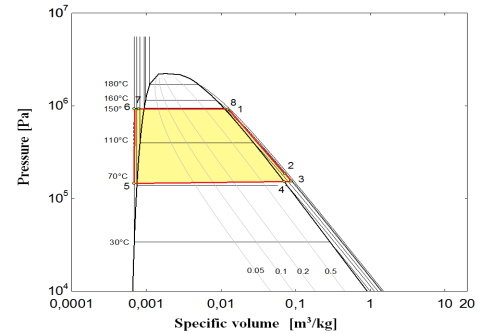

Figure 18: T-s diagram ORC system

Figure 19: P-v diagram ORC system

Figures 18 and 19 shows the temperatures of HE7100 in inlet and outlet of the microturbine were 166.5 $^\circ$C and 145 $^\circ$C respectively. The pressure value at the microturbine inlet was 9.21 bar and outlet 1.86 bar. In this case, efficiency of the radial microturbine amounted to 70.61% and the ORC system efficiency was 5.95%. The calculated Carnot efficiency equalled 31.98% and the exergetic efficiency equalled 18.55%. The equations (1 - 4) on the basis of which the above-mentioned efficiencies were calculated are presented below. The Carnot efficiency was calculated by the relation:

$$\eta_C = 1 - \frac{T_{min}}{T_{max}} \tag{1}$$

where T_{min} and T_{max} – temperature for the upper and lower heat source, respectively.
The isentropic radial microturbine efficiency was calculated from the relation

$$\eta_{s,turb} = \frac{h_1 - h_2}{h_1 - h_{2s}} \tag{2}$$

where h is the refrigerant enthalpy, the subscript numbers indicate the state, and the subscript *s* refers to the isentropic process. The thermal efficiency of the ORC system was calculated by

$$\eta_{ORC} = \frac{(h_1 - h_2) - (h_6 - h_5)}{h_8 - h_6} \tag{3}$$

where h_1, h_2, h_5, h_6 and h_8 are the specific enthalpy of the HFE7100. The exergetic efficiency was calculated from the relation

$$\eta_{exerg} = \frac{\eta_{ORC}}{\eta_C} \tag{4}$$

where η_{ORC} – thermal efficiency of the ORC system, η_C – Carnot efficiency.

Figure 20 presents comparison of the power generated by a rolling-piston expander – Zheng et al. (2013), a scroll expander – Yun et al. (2015) and a radial microturbine – present data, versus pressure ratio. Yun et al. (2015) and Zheng et al. (2013) as the working fluid used a R245fa.
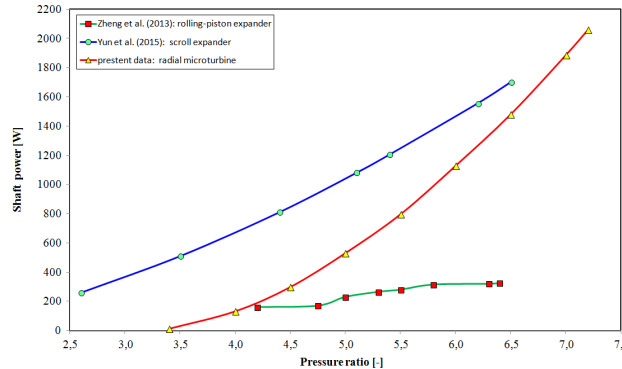

Figure 20: Comparison of the power generated by different expanders and radial microturbine vs pressure ratio

As can be seen in Figure 20, the power curves possess a similar trend. For example, for the pressure ratio 6 the output power of the scroll expander was 1450 W_e, the radial microturbine amounted to 1100 W_e, whereas in the case of the rolling-piston expander it was 300 W_e. The difference between their values manifests itself through the following fact. The values of measured power were obtained using different expansion devices and different working mediums were used.

4. CONCLUSIONS

On the basis of the conducted research on the ORC system with regeneration it was found that the maximum electrical power generated by the radial microturbine reached 1551 W_e. This value was obtained at the rotational speed of 18700 rpm and the HFE7100 supply pressure of 9.21 bar (at the microturbine inlet). The efficiency of the radial microturbine amounted to 70.61%, and the ORC system efficiency was 5.95%. The Carnot efficiency and exergetic efficiency amounted to 31.98% and 18.55%, respectively. The power characteristics contain regression lines along with their corresponding equations in order to facilitate the analyses and comparisons for other researchers.

NOMENCLATURE

h	specific enthalpy	(J/kg)
η	efficiency	(-)
T	temperature	(^{o}C)

Subscript

C	Carnot
e	electrical
exerg	exergy
min	minimum
max	maximum
ORC	organic Rankine cycle

s   isentropic
th   thermal
turb   turbine

REFERENCES

Bahrami, M., Hamidi, A. A., Porkhial, S., 2013, Investigation of the effect of organic working fluids on thermodynamic performance of combined cycle Stirling-ORC. *International Journal of Energy and Environmental Engineering*, 4: p. 1 -9.

Declaye, S., Quoilin, S., Guillaume, L., Lemort, V., 2013, Experimental study on an open-drive scroll expander into an ORC (Organic Rankine Cycle) system with R245fa as working fluid, *Energy*, 55: p. 173-183.

Kaczmarczyk, T. Z., Ihnatowicz, E., Żywica, G., Bykuć, S., Kozanecki, Z., 2013a, Z., Initial experimental investigation of the ORC system in a cogenerative domestic power plant with a microturbine, *8th World Conference on Experimental Heat Transfer, Fluid Mechanics, and Thermodynamics*, Lisbon, Portugal.

Kaczmarczyk, T. Z., Ihnatowicz, E., Bykuć, S., Żywica, G., Kozanecki, Z., 2013b, Experimental investigation of the ORC system in a cogenerative domestic power plant with a microturbine and an expansion valve, *ASME ORC 2nd International Seminar on ORC Power System*, Rotterdam, The Netherlands.

Lemort, V., Quoilin, S., Cuevas, C., Lebrun J., 2009, Testing and modeling a scroll expander integrated into an Organic Rankine Cycle, *Applied Thermal Engineering*, 29: p. 3094-3102.

Li, J., Pei, G., Li, Y., Ji, J., 2011, Evaluation of external of heat loss from a small-scale expander used in organic Rankine cycle, *Applied Thermal Engineering*, 31: p. 2694-2701.

Liu, H., Qiu, G., Shao, Y., Daminabo, F., Riffat, S. B., 2010, Preliminary experimental investigations of a biomass-fired micro-scale CHP with organic Rankine cycle, *International Journal of Low-Carbon Technologies*, 5: p. 81-87.

Liu, H., Shao, Y., Li, J., 2011, A biomass-fired micro-scale CHP system with organic Rankine cycle (ORC) – Thermodynamic modelling studies, *Biomass and Bioenergy*, 35: p. 3985-3994.

Meyer, D., Wong, Ch., Engel, F., Krumdieck, S., 2013, Design and build of 1 kilowatt Organic Rankine Cycle power generator, *35th New Zealand Geothermal Workshop*, Rotorua, New Zealand.

Onovwiona, H. I., Ugursal, V. I., 2006, Residential cogeneration systems: review of the current technology, *Renewable and Sustainable Energy Reviews*, 10: p. 389-431.

Pei, G., Li, J., Li, Y., Wang, D., Ji J., 2011, Construction and dynamic test of a small-scale organic rankine cycle, *Energy*, 36: p 3215-3223.

Qiu, G., Shao, Y., Li, J., Liu, H., Riffat, S. B., 2012, Experimental investigation of a biomass-fired ORC –based micro-CHP for domestic applications, *Fuel*, 96: p. 374 – 382.

Quoilin, S., Lemort, V., Lebrun, J., 2010, Experimental study and modeling of an Organic Rankine Cycle using scroll expander, *Applied Energy*, 87: p. 1260-1268.

Seher, D., Lengenfelder, T., Gerhardt, J., Eisenmenger, N., Hackner, M., Krinn, I., 2012, Waste Heat Recovery for Commercial Vehicles with a Rankine Process, *21st Aachen Colloquium Automobile and Engine Technology*, Aachen, Germany.

Smith, I. K., Stosic, N., Kovacevic, A., Langson, R., 2006, Cost effective small scale ORC for power recovery from low enthalpy geothermal resources. *Proceedings of ASME International Mechanical Engineering Congress and Exposition*, Chicago, Illinois, USA.

Yun, E., Kim, D., Yoon, S. Y., Kim, K. Ch., 2015, Experimental investigation of an organic Rankine cycle with multiple expanders used in parallel, *Applied Energy*, 145: p. 246-254.

Zheng N., Zhao L., Wang X.D., Tan Y.T.: Experimental verification of a rolling-piston expander that applied for low-temperature Organic Rankine Cycle, 2013, *Applied Energy*, 112, p. 1265-1274

ACKNOWLEDGEMENT

OPERATIONAL EXPERIENCE ON ORC USE FOR WASTE HEAT VALORIZATION IN BIOGAS POWER PLANT

Coline Gazet[1], Arthur Leroux[1], Benoit Paillette[1], Antonin Pauchet[1]

[1] ENOGIA SAS,
www.enogia.com
19 Avenue Paul Héroult
13015 Marseilles, France

ABSTRACT

In the overall market of ORC, even though there is a lack of offer in the smaller power ranges (less than 100kW electrical), the potential markets and applications remain very significant. That is why the company ENOGIA was founded in 2009 by four French engineers, which purpose was to develop its own micro-turbine/alternator technology instead of the more classic "modified refrigeration screw or scroll compressor".

The development of the ENOGIA turbo-expander took several years in order to bring an efficient, reliable and affordable expander, as well as the complete ORC system. The development path of these will be presented, as well as the many prototypes built and tested.

The current target market of ENOGIA is biogas power plant efficiency enhancement, and in order to bring efficient and cost efficient solutions for this market, we aim to improve our products with experience from real on-site demonstrators. Different ORC layouts for biogas plants enhancement were identified and will be presented. The two main approaches used are: The hot loop can use water from the biogas engine jacket, which provides low input temperatures, and can be coupled to an exhaust gas exchanger. In order to obtain higher input temperatures, it is possible to design the ORC in "direct evaporation" configuration using directly the exhaust gases. With this layout, higher condensing temperatures can be achieved and heat can therefore be used for customer applications.

In order to show return of experience on the proposed ORC for biogas plant layouts, operational perspectives from significant references of ENOGIA will be presented. Eventually those were positive experiences and ENOGIA is currently developing the product range for future projects.

1. INTRODUCTION

In the overall market of ORC, although there is a lack of commercial offer in the smaller power ranges (less than 100kW electrical), there are very significant potential markets and numerous applications, from waste heat valorization to biomass or geothermal renewable electricity production. This is the reason the company ENOGIA was founded in 2009 by four French engineers. The purpose of ENOGIA was to develop its own micro turbine expander / generator module instead of the more classic approach of "modified refrigeration screw or scroll compressor", because it allows much more design flexibility of the ORC system.

The development of the ENOGIA turbo-expander started in 2009 and took several years in order to bring an efficient, reliable and affordable expander, as well as the complete ORC system. Hereunder is presented the development path of these, as well as the many prototypes built and tested.

2. TURBINE EXPANDER DEVELOPMENT

The first turbine was a small 3kW demonstrator with a very short lifetime of the bearing system. It was meant to be a proof of concept of the high speed close coupled turbine generator, in a hermetic housing. Thanks to this prototype, size of stators and rotors, shape of bladings, were adjusted and tested in both design and off design conditions. Even if this prototype showed significant weaknesses in the bearing system and the sealing system, the main purpose remained showing that the ENOGIA turbine is technically feasible before focusing on its lifetime in order to minimize maintenance costs.
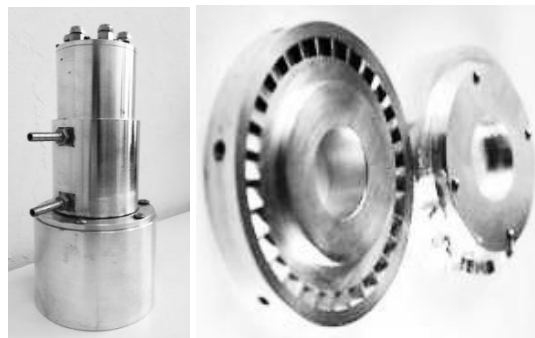

Figure 1: First turbine prototype and bladings

The second version represented the first prototype for a 10kW unit. The expander bearing system was significantly improved with an active oil lubrication system in order to have a better long-term holding. Thanks to adapted components, we succeeded in having a very satisfying fluid-tightness. However this second version met the limitations of the electric generator, which had unsatisfying thermal transfer from the windings to the water cooling system.

Figure 2: Second turbine prototype

A third version used a different permanent magnet generator type, with direct contact between the steel laminations of the stator and the cooling system, and proved to be very reliable and thermally efficient, with reasonable temperature levels in the windings, even at full power or even higher than maximum specified power.
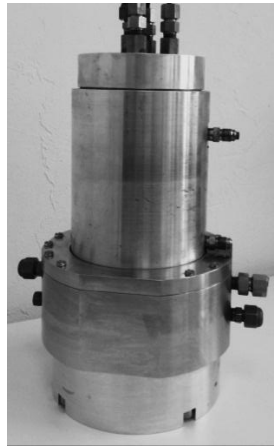
Figure 3: Third turbine prototype

An important difference between the first turbine prototypes and the operational ORC modules for biogas units are the temperatures reached at the evaporator of the ORC unit. Indeed the first tests were made in regenerative cycle with relatively high temperatures, when the biogas genset gives to the ORC warm water at 90°C, sometimes even less. Because of this, ENOGIA had to adapt its technology for biogas applications, especially the working fluid and associated rotors and stators. The company is now able to produce the two products in standardize version: low temperatures without regeneration and medium temperatures with HFE fluid and regenerative cycle.
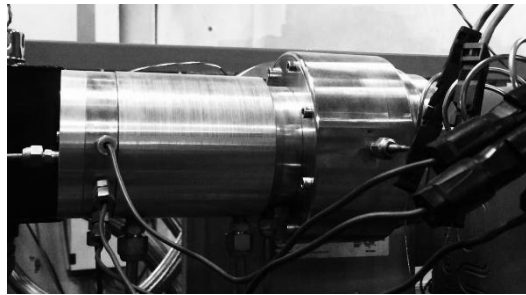

Figure 4: Commercial ENOGIA 10LT-V6 turbine in operation

One of the next steps was the improvement of the fluidic part including some modifications in the overall architecture to minimize pressure losses. The machining was also optimized to obtain the smoothest lines as possible. Moreover, the made-to-measure electric generator and shaft were another required stage to guarantee the turbine performance and reliability. The last changes were related to maintenance, making disassembly easier. ENOGIA is now following an optimization policy concerning mechanical parts in order to reduce production costs.

2. ORC FOR FARM BIOGAS

The current target market of ENOGIA is biogas power plant efficiency enhancement, and in order to bring efficient and cost efficient solutions for this market, the company aims to improve the products with experience from real on-site demonstrators.

3.1 System architecture

Different ORC layouts for biogas were identified and the two main approaches used are:

- The hot loop can use water from the biogas engine jacket, which provides low input temperatures, generally at 90°C. It can be coupled to an exhaust gas exchanger in order to recover a maximum of waste heat. In this configuration, the cold loop temperatures are around 30°C which is often too low and more complicated to reuse than higher temperatures. Sometimes, farmers can use this output heat to dry cereals, to dry straw, to heat greenhouses or to have pre-heat water for cattle. Nevertheless, given the low temperatures, the ORC is usually used only to generate more electricity.
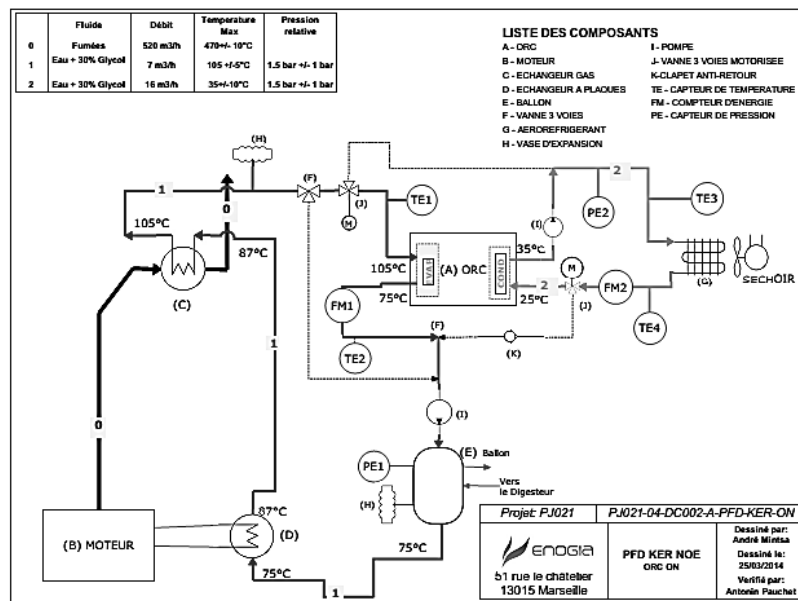

Figure 5: hot water ORC layout (Ker Noé, France)

- In order to obtain higher input temperatures, it is possible to design the ORC in "direct evaporation" configuration using directly the exhaust gases. With this layout, higher condensing temperatures can be achieved and heat can therefore be used for further customer applications especially domestic hot water. The first testing session on this technology with an ENOGIA prototype ORC unit was successfully achieved and the results are really promising.
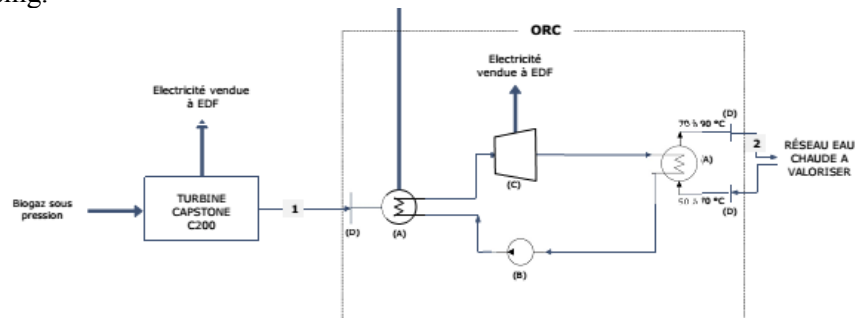

Figure 6: Exhaust gas ORC layout

3.2 Operational experience

In order to show return of experience on the proposed ORC for biogas plant layouts, operational perspectives from significant references of ENOGIA will be presented.

The first reference is the Treviso project in Italy. The ORC is a standard 10 kW unit using low temperatures: 90-70°C for hot loop with a thermal power of about 65kW and cooling ground water around 10-15°C. The main issue was the configuration of the existing plant. The exchanger of the biogas engine was too far from the ORC and piping not enough isolated, resulting in a huge loss of thermal power before the exchanger. The cooling ground water lead to working parameters quite specific (very low condensing pressures) when almost all projects use dry coolers. Thanks to this project, ENOGIA could learn and improve its technology especially concerning pump cavitation, efficiency, lubrication and vibrations besides the biogas engine.

Figure 7: Treviso ORC container with exhaust heat recovery

The second significant reference is the Ker-Noé project in France. It is the same configuration than the unit in Italy, except the cooling loop working with dry coolers. The owner uses the extra heat to dry cereals so that there is a minimum of waste heat in his biogas plant. The main feedback of this project was that theoretical pressure ratios were different from the operational ones so that ENOGIA could redesign the turbo-generator injectors. After almost a year of working, performances of the ORC were analyzed with data from tele-monitoring. The theoretical power production was about 7 kW_e with a thermal power input of 121kW_{th}.

Although the engine thermal power was lower than predicted (about 20kW_{th} less), the ORC produces more than 6kW_e with the best adapted cooling. Finally, the power delivered corresponds to 90% of what ENOGIA expected.

At full load, the isentropic efficiency of the ORC expander reaches 70% no matter the cooling temperatures are, with a generator estimated efficiency of 80%. Except little changes in the regulation law to improve it, the other theoretical parameters were adapted to the existing installation. After these improvements, efficiencies attained 5 to 7 percent range with the very low grade heat available (90/70°C CHP water loop).

Figure 8: Ker Noé ORC unit

As it was said hereinabove, ENOGIA was working on another configuration since 2013, using directly exhaust gases. The issue of "direct evaporation" was to design an adapted gas-fluid exchanger.

This technology was tested for a special non-stationary demand with the help of IFP Energies Nouvelles (also called IFPEN), a major research and innovation center, trusted partner of ENOGIA. The tests made during 2014 and 2015 were very successful and prove the high performance of this technology, which attained approximately 10% gross efficiency.

What makes the ORC unit more efficient is also the regenerative cycle used in conjunction with a novel working fluid, a HFE fluid from 3M; indeed it improves about 30% the overall performance. Another strong point of this technology is the capability to operate with higher condensing temperatures, in the 70°C range, allowing using the ORC unit as a real CHP.

On another side, ENOGIA had been forecast the necessity of security components in the conception phase, knowing what high temperatures imply. During testing, the by-pass on the exhaust gases had been engaged several times. A unit has been recently delivered for an installer of biogas solutions and the hope will be to include an ORC on each of its installation as the technology seems really efficient.
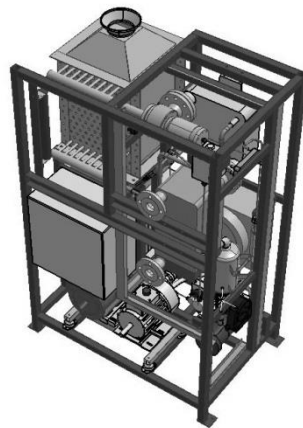

Figure 9: 10kW "Direct Evaporation" ORC unit

3. CONCLUSION

Since 2009, several ORC turbines were engineered and tested for small ORC applications, resulting in a commercial product that is available from ENOGIA, the ENO-10LT 10 kW low temperature ORC module.

This product has been tested at several customer premises in France and in Italy. Eventually those were positive experiences and ENOGIA is currently developing the product range for future projects. The company has developed a wider range of power and has already built 20kW, 40kW and 100kW units, although the last one uses a technology of turbine completely different given the higher power. Current prices go from 1800 to 3000 € per kW, depending on size and features, for ENOGIA's small ORC product range.

ENOGIA R&D team currently develops products with a direct gases evaporator, which will be available for farm biogas, and which first unit will be installed on the exhaust of a Capstone C65 turbine in a farm biogas plant in France. A key advantage of this technology will be that it will also produce hot water, improving the electrical efficiency of the biogas plant, but with very few loss of heating power as well.

ACKNOWLEDGEMENT

OPTIMIZED EFFICIENCY MAPS AND NEW CORRELATION FOR PERFORMANCE PREDICTION OF ORC BASED ON RADIAL TURBINE FOR SMALL-SCALE APPLICATIONS

Kiyarash Rahbar[1]*, Saad Mahmoud[1], Raya K. Al-Dadah[1]

[1] School of Mechanical Engineering,
University of Birmingham, Edgbaston,
Birmingham, UK, B15-2TT
e-mail: kxr965@bham.ac.uk
* Corresponding Author

ABSTRACT

The expander is considered as the most critical component of the ORC. Radial inflow turbine exhibits unique advantages of high efficiency, compact structure and light weight compared to the axial turbine when employed in the small-scale applications such as distributed CHP systems. In most of the ORC studies the turbine efficiency is assumed as a constant input for the optimization of cycle without assuring that the specified turbine efficiency can be achieved by the imposed thermodynamic conditions. In addition, atypical properties of the high-density working fluid and the near-critical operating condition of the ORC requires the turbine design procedure and parameters to be customized for the ORC. This study presents the optimization of a radial ORC turbine for maximum efficiency using mean-line modelling and genetic algorithm (GA). In contrast to the previous studies, real gas equation of state and the most advanced and recent loss models are employed in the code to capture the non-ideal behaviour of the working fluid. The optimized turbine efficiency is achieved by the GA for a wide range of operating conditions and for four organic fluids (R123, R245fa, R1233zd and isobutane). Such results are presented through new generalized maps based on the non-dimensional parameters as the flow and loading coefficients, specific speed and specific diameter. Using regression analysis a new correlation for the turbine efficiency is also presented. These new maps and the correlation are preliminary steps toward improving the previous constant turbine efficacy assumption and have great potential to be integrated with the general optimization methods of the ORC.

1. INTRODUCTION

Recently, ORC technology has received a growing attention due to its competitive performance and flexibility for small to medium scale power generation applications. Majority of studies about the organic Rankine cycle (ORC) are mainly devoted to the methods of selecting appropriate fluid for different applications (Aleksandra and Władysław, 2007, Al-Sulaiman *et al.*, 2011, Dolz *et al.* 2012, Rayegan and Tao, 2011) or to the thermodynamic optimization of the cycle based on a range of performance indexes such as the thermal and exergy efficiencies, net power output or heat exchangers area (Rashidi *et al.* 2011, Hettiarachchi, 2007, Wang *et al.*, 2013). On the other hand, little attention has been paid to the design and performance characteristics of the expander. In all above studies that seek the optimum cycle parameters, fixed values are assigned to the turbine efficiency for a wide range of operating conditions and for various working fluids while ignoring the feasibility that the turbine is capable of achieving these efficiencies in practice. In addition, due to the specific thermodynamic properties of the organic fluids (i.e. large molecular weight and low speed of sound), the turbine can behave differently from those that operate with steam or other gases and needs a special design. Moreover, operating near critical point of organic fluids makes the ideal gas models unsatisfactory and requires the real gas formulation of the turbine expansion. Considering these facets, the use of conventional generalized performance correlation charts such as (Rodgers and Geiser 1987, Balje 1981, Chen and Baines 1994) can become inaccurate when used for performance prediction of turbines operating with organic fluids. In this study a new approach for performance prediction of ORC based

on radial turbine is presented that is suitable for small scale applications such as distributed combined heat and power (CHP) systems with power capacity of up to 50kW. In this novel approach the conventional radial turbine performance maps are updated and optimized based on the real gas properties of organic fluids, genetic algorithm (GA) optimization technique and the most advanced and recent loss models by Aungier (2006). A mean-line model for design, analysis and performance prediction of radial turbines is developed in the engineering equation solver (EES) platform and directly embedded with the ORC system code. Such model allows for replacement of the fixed turbine efficiency by an interactive value that is calculated based on the ORC thermodynamic conditions and working fluids properties and assures that the optimized turbine efficiencies are achievable in practice. Such turbine efficiencies are correlated through new maps against loading and flow coefficients, specific speed and specific diameter for four different organic fluids as R123, R245fa, R1233zd and isobutane. Furthermore, a new correlation for turbine efficiency is presented by employing the regression analysis, though, it is considered to be a preliminary one as it requires to be validated against ORC experimental data which are very limited in the literature and also be extended to other working fluid families such as ethers and siloxanes.

2. NON-DIMENSIONAL PARAMETERS

Turbomachines require a set of non-dimensional parameters that can readily describe the machine's overall performance for assessment, selection and comparison. Following Whitfield and Baines (1990), the basic parameters that influence the behaviour of a turbomachine are collected in the form of a functional relation shown by equation (1).

$$\eta_{ts} = f(\mathrm{ER}_{ts}, \frac{\dot{m}\sqrt{\frac{RT_t}{\gamma}}}{P_t\pi\frac{d^2}{4}}, \frac{\omega d\pi}{60\sqrt{RT_t\gamma}}, \mathrm{Re}, \gamma) \tag{1}$$

With the assumption of single working fluid passes through the turbine and fully developed turbulent flow regime, equation (1) is simplified into a more common form as shown by equations (2) and (3).

$$\eta_{ts} = f(\varphi, \psi, \mathrm{Ma}) \tag{2}$$

$$\eta_{ts} = f(N_s, \mathrm{d}_s, \mathrm{Ma}) \tag{3}$$

Where φ, ψ, N_s, d_s and are the flow and loading coefficients, specific speed and specific diameter and are defined by equations (4) to (7) respectively.

$$\phi = \frac{C_{m5}}{U_4} \tag{4}$$

$$\psi = \frac{\Delta h_{actual}}{U_4^2} \tag{5}$$

$$N_s = \frac{\omega\sqrt{Q_5}}{\Delta h_s^{0.75}} \tag{6}$$

$$d_s = \frac{d_4\Delta h_s^{0.25}}{\sqrt{Q_5}} \tag{7}$$

Since the ORC turbines are often operating at high expansion ratios, the effect of compressibility (Mach number) is quite significant on the expander efficiency and should be included in the final correlation. However, the Mach number is always an outcome of the turbine design procedure and there is no prior knowledge of this parameter unless the detailed turbine design procedure is conducted. Since the aim of this study is to provide a correlation that can estimate the turbine efficiency without performing the turbine design process, which is clearly impractical, and using only non-dimensional parameters, volumetric expansion ratio (*VR*) introduced by Macchi and Perdichizzi (1981) is also included in the analysis to address the effect Mach number. *VR* is the ratio of the turbine stage outlet volumetric flow rate to the turbine stage inlet volumetric flow rate and is defined by equation (8).

$$VR = \frac{Q_5}{Q_1} \tag{8}$$

VR is a more meaningful parameter (in place of expansion ratio or Mach number) that explicitly correlates the degradation of turbine efficiency due to the high Mach numbers (Macchi and Perdichizzi, 1981). In other words, *VR* accounts for the compressibility effect in a more generalized way than other equivalent parameters (expansion ratio and Mach number) and one can estimate its value from the cycle analysis (based on the desired cycle requirements) and without the need for completing the turbine design procedure. Hence, the efficiency of organic turbines (characterized by high Mach numbers) can be more accurately explained in the following functional form:

$$\eta_{ts} = f(\varphi, \psi, VR) \tag{9}$$

In the classical work of Balje (1981) the turbine efficiency is correlated against N_s and d_s in which the best turbine designs lay on the Cordier line. The optimum radial turbine efficiencies are obtained at N_s values in the range of 0.5 to 0.7, however, the selection of an appropriate N_s does not necessarily yield the optimum turbine design. The selection of the optimum N_s can immediately achieve the optimum d_s and eventually the turbine rotor tip diameter, though, no other information is provided regarding to other turbine geometry. Chen and Baines (1994) employed data from a wide range of designs and various applications to correlate the radial turbine efficiencies against the other set of non-dimensional parameters as φ and ψ. They showed that the maximum radial turbine efficiency is obtained at the loading and flow coefficients in the range of 0.9 to 1 and 0.2 to 0.3 respectively. The use of φ-ψ couple is advantageous compared to N_s-d_s as more information about the turbine principal dimensions such as passage areas, inlet and exit blade height and velocity triangles is achieved. The N_s-d_s or φ-ψ performance correlation charts (such as Balje, 1981 and Chen and Baines, 1994) are often dated and may not accurately represent the performance of the modern radial turbines. In addition, atypical characteristics of ORC systems such as high expansion ratios (high Mach number), real gas behavior of working fluids and small turbine dimensions makes the use of these conventional charts questionable. Therefore, it is necessary to update these charts based on real gas properties and advanced loss models while employing an optimization scheme to maximize the radial turbine efficiency.

3. INTEGRATED MODELING AND OPTIMIZAIOTN OF RADIAL TURBINE AND ORC SYSTEM

The methodology for the integrated modeling of the ORC system with the mean-line modeling of radial turbine is followed by the previous works of authors (Rahbar *et al*. 2015a, Rahbar *et al*. 2015b). The ORC system consists of four main components as the evaporator, turbine, condenser and pump. The turbine itself is consists of the volute, nozzle and rotor. Figure 1 shows the schematic of the ORC and radial turbine together with their corresponding temperature-entropy and enthalpy-entropy diagrams respectively. The turbine-ORC model is developed in the EES software to utilize its reliable thermodynamic property functions for real gas modeling of the turbine-ORC system. EES uses the fundamental (Helmholtz free energy) equation of state for determining the thermodynamic properties of the selected organic fluids and details of which can be found in (Lemmon *et al*. 2006). Modelling of the radial turbine is based on a one-dimensional assumption in which there is a mean streamline through the stage that represents the average of passage condition and the thermodynamic properties and flow features (i.e. velocity triangles) are obtained at key stations (shown in Figure 1) across the mean line. With the choice of turbine input variables listed in Table 1 and the initial estimate of the turbine efficiency, the model determines the key geometry parameters for the rotor, nozzle and volute. Using the calculated geometry and the well-established loss correlations the model determines a more accurate estimation of turbine performance. This process is repeated until convergence is achieved for the turbine efficiency. Then with the calculated turbine exit thermodynamic properties (T_5, P_5, h_5, S_5) and the ORC model input variables listed in Table 1, the main cycle parameters such as thermal efficiency, net power output and pump power consumption are determined. However, selection of arbitrary values from the range of input parameters shown in Table 1 does not necessary yields the maximum efficiency for the turbine. Therefore an optimization scheme called genetic algorithm is coupled with the turbine-ORC model to maximize the radial turbine efficiency based on the input variables of Table 1. Moreover, the

optimization algorithm is constrained by some of the critical turbine geometry parameters, flow features and ORC characteristics to assure the feasibility of the optimized turbine dimensions and to achieve high cycle and turbine performances. Figure 2 shows the flow chart of the turbine-ORC model with integrated optimization scheme that details the overall procedure. More information regarding to the detailed modeling, optimization procedure and the imposed constraints can be found in (Rahbar *et al.* 2015a, Rahbar *et al.* 2015b). The turbine loss models employed in this study are expressed as total pressure loss coefficients and include the profile, incidence, blade loading, hub to shroud, tip clearance and distortion losses which are shown by equations (10) to (15) (Aungier, 2006). It should be mentioned that the majority of loss models are developed for the gas turbines with air or flue gases as the working fluids and due to the lack of experimental data in the open literature about the performance of ORC with small-scale organic radial turbines, such loss models should be taken with some care. However, the relative comparison of the performance with different fluids is believed to be primarily correct.
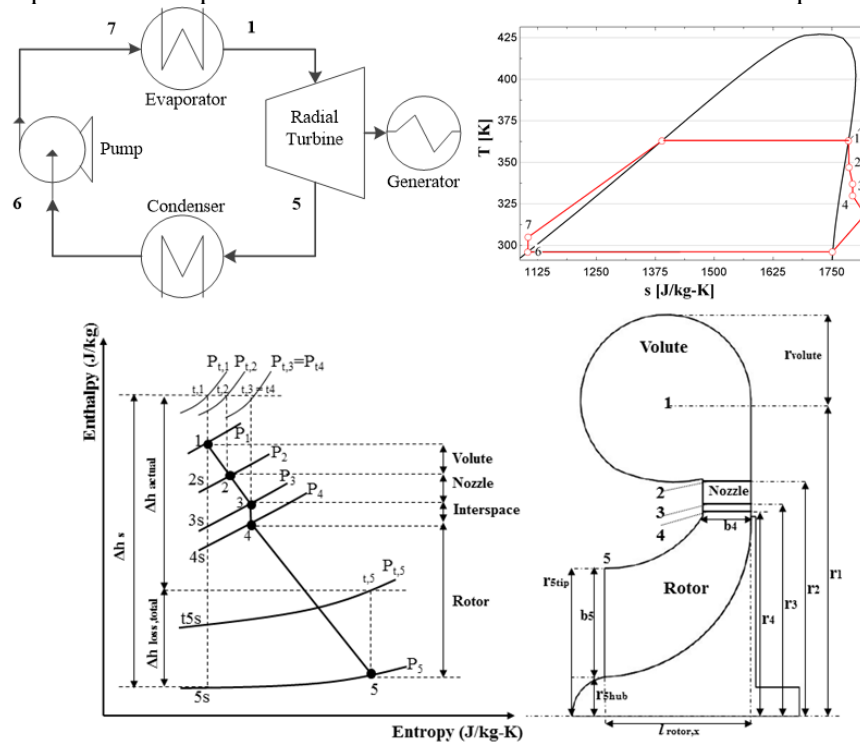

Figure 1: Schematic of the ORC system (top left), ORC temperature-entropy diagram (top right), radial turbine section view (bottom right), radial turbine enthalpy-entropy diagram (bottom left),

Table 1: Input parameters of the turbine-ORC model

Parameter	Unit	Value/Range
Turbine inlet total temperature ($T_{t,1}$)	K	343 - 393
Turbine inlet total pressure ($P_{t,1}$)	kPa	Saturation pressure
Turbine inlet degree of super heating ($T_{superheating}$)	K	1 - 5
Turbine total-to-static expansion ratio (ER_{ts})	-	2 - 8
Turbine rotational speed (ω)	rpm	30000 - 70000
Turbine loading coefficient (ψ)	-	0.7 - 1.4
Turbine flow coefficient (φ)	-	0.15 - 0.5
Turbine rotor exit absolute flow angle (α_5)	deg	-15 - 15
Turbine rotor exit hub to inlet radii ratio (r_{5hub}/r_4)	-	0.2 – 0.3
Turbine nozzle inlet to exit radii ratio (r_2/r_3)	-	1.2 - 1.3
Turbine volute swirl coefficient (SC)	-	0.95
Turbine volute pressure loss coefficient (k_{volute})	-	0.1
ORC mass flow rate of working fluid (m)	kg/s	0. 2 - 1
ORC pump efficiency (η_{pump})	-	0.7
ORC generator efficiency ($\eta_{generator}$)	-	0.96
ORC mechanical efficiency ($\eta_{mechanical}$)	-	0.96

$$Y_{profile} = \frac{2\Theta + \Delta^2}{(1-\Delta)^2} \tag{10}$$

$$Y_{incidence} = \cos^2(\alpha_4 - \arctan(\frac{C_{m4}}{\sigma[U_4 - C_{m4}\tan(\beta_4)]}))(\frac{P_{rel,t,4} - P_4}{P_{rel,t,5} - P_5}) \tag{11}$$

$$Y_{blade,loading} = \frac{1}{24}[\frac{2\pi\frac{|r_5 C_{\theta 5} - r_4 C_{\theta 4}|}{l_{rotor,x}Z_{rotor}}}{W_5}]^2 \tag{12}$$

$$Y_{hub,to,shroud} = \frac{1}{6}[\frac{\kappa b_5 \frac{W_4 + W_5}{2}}{W_5 \cos(\alpha_5)}]^2 \tag{13}$$

$$Y_{tip,clearance} = \frac{0.816\sqrt{2\rho_{average}(P_{rel,t,4} - P_4)}l_{rotor,x}Z_{rotor}\varepsilon}{\dot{m}}(\frac{P_{rel,t,4} - P_4}{P_{rel,t,5} - P_5}) \tag{14}$$

$$Y_{distortion} = (\frac{\frac{r_1 C_1}{r_2} - C_{\theta 2}}{C_2})^2 \tag{15}$$
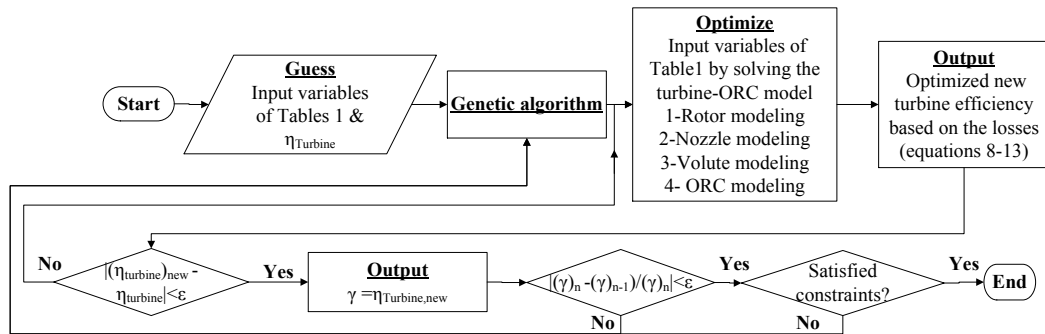

Figure 2: Flow chart for integrated modelling of turbine and ORC system with embedded optimization algorithm

4. RESULTS AND DISCUSSION

In order to conduct the optimization of turbine efficiency it is necessary to determine which parameters have the most significant effects on $\eta_{turbine}$. Following (Rahbar *et al*. 2015a, Rahbar *et al*. 2015b), among the listed parameters in Table 1, $T_{t,1}$, $P_{t,1}$, $T_{superheating}$, ER_{ts}, ω, ψ, φ, α_5 and m have the most significant effects on the $\eta_{turbine}$ and are included in the optimization using genetic algorithm. In order to correlate the variation of the optimized turbine efficiency with non-dimensional parameters and update the conventional φ-ψ and N_s-d_s charts the following specification for the design parameters are set to cover a wide range of designs.

$$T_{t,1} \in (343:393:10)$$
$$\psi \in (0.7:1.4:0.1) \tag{16}$$
$$\varphi \in (0.15:0.5:0.05)$$

Where the first and second terms are the upper and lower boundaries and third term is the step of variation for each parameter. The optimization is conducted for all possible combination of the above design parameters, however, only the optimized updated φ-ψ and N_s-d_s charts for the turbine inlet temperature of 373K are shown for brevity. As presented in Figure 3, the maximum turbine efficiencies are achieved at low flow coefficients with the maximum value of 86% obtained by R1233zd. In the φ-ψ performance charts, the maximum turbine efficiencies vary in the range of 82% to 86% compared to the maximum value of 88% shown by Chen and Baines (1994).This is due to the higher expansion ratios of ORC turbines (about 8) and corresponding supersonic losses compared to the conventional radial gas turbines with the maximum expansion ratios of about 4. In addition, implementation of back swept blading at rotor inlet is advantageous since the turbine efficiency increases at loading coefficients in excess of unity (Rahbar *et al*. 2015b). Comparing the φ-ψ charts shown in Figure 3 with Chen and Baines (1994) reveals that the turbine efficiency increases by a maximum of 3% at loading coefficients greater than unity. In other words the contours of maximum efficiency are slightly shifted to higher loading coefficients. Figure 4 presents the optimized updated N_s-d_s performance charts for the four investigated fluids. Similar to Balje (1981) diagram, the optimum region of N_s-d_s still exists in all charts in which the line of maximum efficiency is equivalent to the theoretical curve that almost gives $N_s d_s$ =2. But in contrast to the conventional radial turbines that the maximum efficiency occurs at the specific speed values of between 0.5 to 0.7, for ORC turbines this optimum value has been shifted to lower specific speed values of between 0.35 to 0.55 as shown in Figure 4.

Although the optimized performance charts shown in Figures 3 and 4 are essential for performance prediction of the ORC turbines, it is more beneficial to present the variation of the optimized turbine efficiency in the form of a mathematical equation. Therefore, linear regression analysis is employed in order to correlate the optimized turbine efficiencies with volumetric expansion ratio, flow and loading coefficients using all the generated design points. Figure 5 shows the linear regression plot for both the turbine inlet temperature of 373K (5a) and also for the complete range of inlet temperature from 343K to 393K (5b). As can be seen in Figure 5 the values of R^2 are quite high and assures that the regression analysis can fairly accurately predict the performance of the ORC radial turbines. Equation 17 shows the first order polynomial obtained based on this regression analysis using all the 417 created design points shown in Figure 5(b) and correlates the turbine efficiency with the volumetric expansion ratio, loading and flow coefficients.

$$\eta_{turbine} = 0.925 - 0.416\phi + 0.0279\psi - 0.00675VR \qquad (17)$$

It should be underlined that the obtained correlation shown by equation 17 is assumed to be a preliminary correlation for performance prediction of ORC radial turbines and is considered as the initial step towards improvement in performance prediction of ORC based on the radial turbines. This is primary due to the fact that the employed loss models are originally developed for gas turbines using air as the working fluid and they should be used with some care. In addition, due to the lack of experimental data for performance of the ORC turbines it is required to validate the developed correlation with real test data upon their availability in open literature. However, it is believed that the proposed methodology is quite novel and has great potential to be further improved and extended for a wider range of organic fluids and broader range of operating conditions.
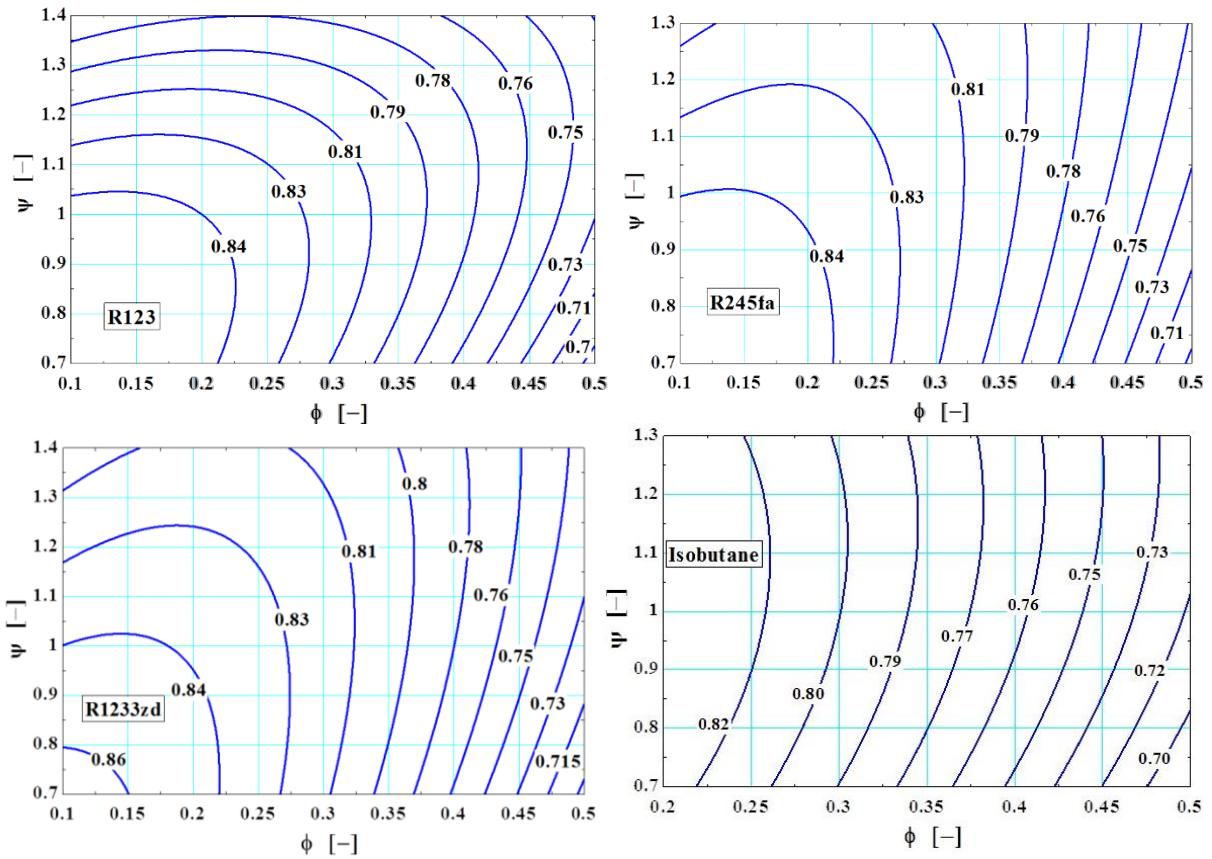
Figure 3: Contours of optimized turbine efficiency based on flow and loading coefficients for four organic fluids as R123, R245fa, R1233zd and isobutane at turbine inlet temperature of 373K
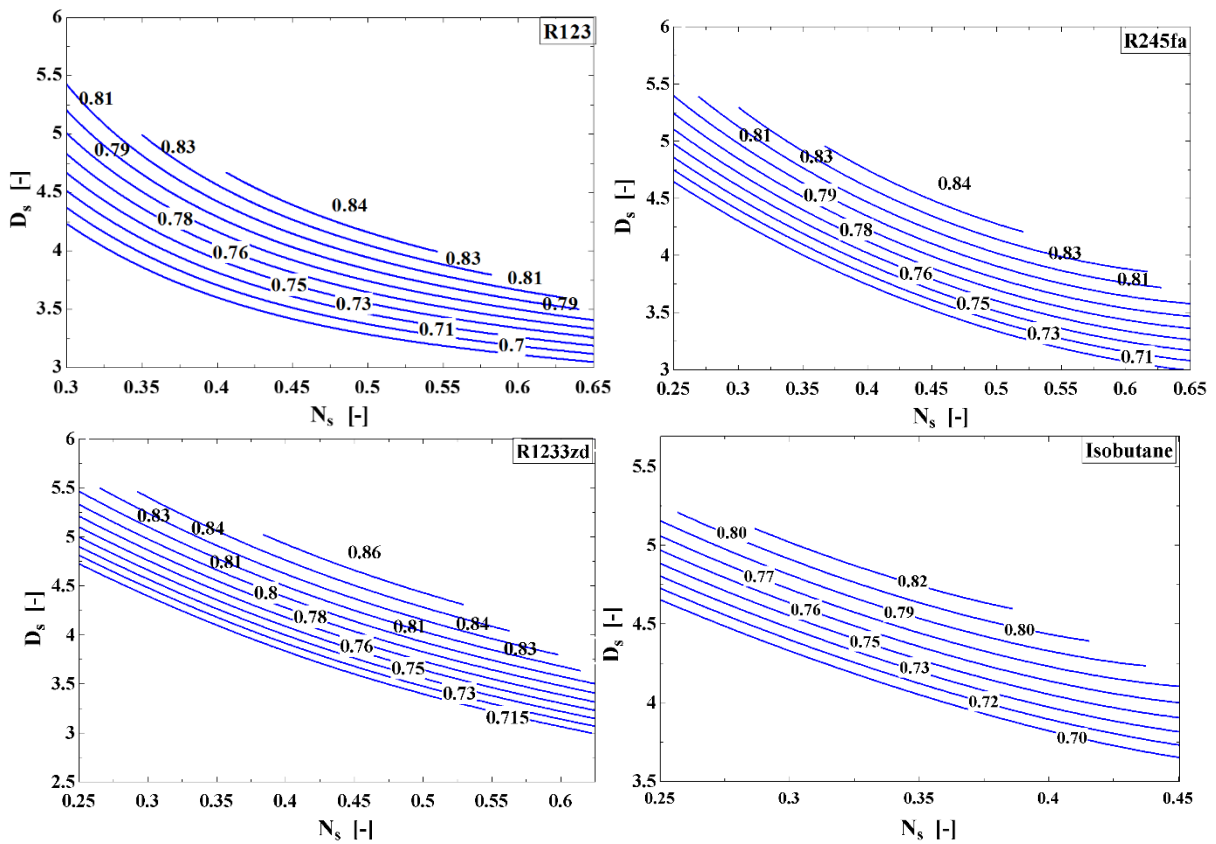

Figure 4: Contours of optimized turbine efficiency based on specific speed and specific diameter for four organic fluids as R123, R245fa, R1233zd and isobutane at turbine inlet temperature of 373K
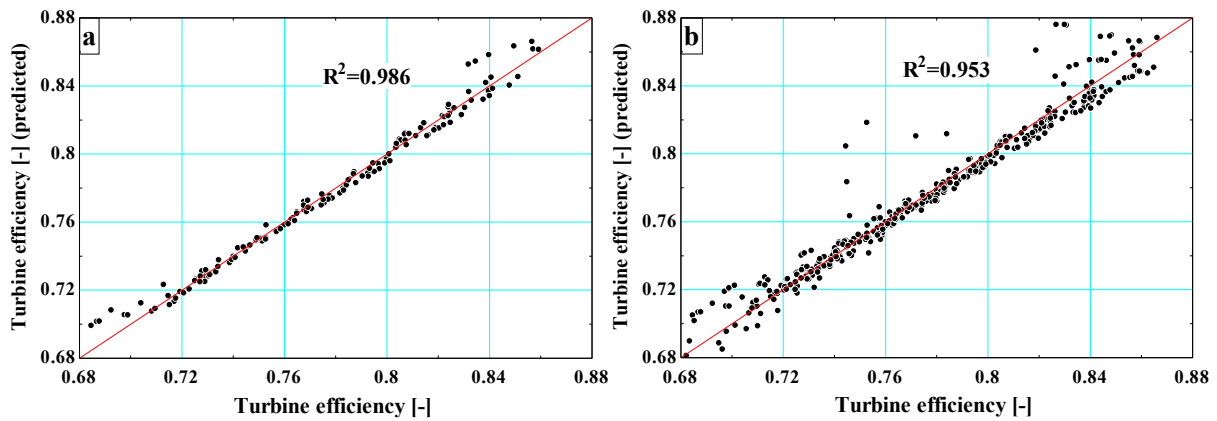
Figure 5: Predicted optimized turbine efficiency as a function of turbine efficiency at turbine inlet temperature of 373K (a) at the full range of turbine inlet temperature from 343K to 393K (b)

5. CONCLUSIONS

This study presents a novel approach that combines the modeling of the ORC system with modeling of radial turbine and allows for optimization of turbine efficiency based on a wide range of input variables. The paper shows that the conventional performance charts are no more sufficient for reliable performance predication of ORC radial turbines. These charts are updated and optimized based on the most advanced loss models and characteristics of organic fluids and ORC system (i.e. real gas behavior and high expansion ratios). The updated performance charts showed that there are considerable variations between them and the conventional ones as the contours of maximum efficiency are shifted to larger loading coefficients and smaller specific speeds respectively. In addition, the optimized charts showed that the maximum efficiency of ORC radial turbines are about 2% lower than the maximum efficiency of radial gas turbines. The R^2 values from the regression analysis showed that the established first order polynomial correlation can fairly accurately predict the performance of ORC turbines, though, it is required to be further modified and validated with the ORC experimental data (which are very scarce in the open literature). These new charts and the correlation could be a useful tool in general optimization procedures of the ORC systems that avoid any arbitrary assumption of turbine efficiency and yield a more accurate estimation of the turbine performance.

NOMENCLATURE

b	blade height	(m)
C	absolute velocity	(m/s)
d	diameter	(m)
d_s	specific diameter	(-)
ER	expansion ratio	(-)
h	enthalpy	(J/kg)
Δh_{actual}	actual specific enthalpy drop	(J/kg)
Δh_s	isentropic specific enthalpy drop	(J/kg)
l	flow path length	(m)
m	mass flow rate	(kg/s)
Ma	Mach number	(-)
N_s	specific speed	(-)
P	pressure	(Pa)
Q	volumetric flow rate	(m³/s)
R	gas constant	(J/kg-K)
r	radius	(m)
Re	Reynolds number	(-)
T	temperature	(K)
U	rotor blade velocity	(m/s)
VR	volumetric expansion ratio	(-)

W	relative velocity	(m/s)
Y	total pressure loss coefficient	(-)
Z_{rotor}	number of rotor blades	(-)
α	absolute flow angle to meridional	(degree)
β	relative flow angle to meridional	(degree)
κ	mean surface curvature	(m^{-1})
σ	slip factor	(-)
γ	specific heat ratio	(-)
ε	rotor casing clearance	(m)
η	efficiency	(-)
φ	flow coefficient	(-)
ψ	loading coefficient	(-)
ω	rotational velocity	(rad/s)
Θ	normalized momentum thickness	(-)
Δ	normalized mass thickness	(-)

Subscript

1-5	stations across the turbine
m	meridional direction
rel	relative value in rotating coordinate system
t	total conditions
ts	total to static
x	axial direction
θ	tangential direction

REFERENCES

Aleksandra, B.G., and Władysław, N.,2007, Maximizing the working fluid flow as a way of increasing power output of geothermal power plant. *Appl Therm Eng* ,27, p. 2074–8.

Al-Sulaiman, F.A., Hamdullahpur, F., and Dincer, I., 2011, Greenhouse gas emission and exergy assessments of an integrated organic Rankine cycle with a biomass combustor for combined cooling, heating and power production. *App Therm Eng*, 31, p. 439–46.

Aungier, R.H., 2006, *Turbine aerodynamics, axial-flow and radial-inflow turbine design and analysis*. ASME Press, New York.

Balje, O.E., 1981, *Turbomachines: a guide to design, selection and theory*. Wiley: New York.

Chen, H., and Baines, N.C., 1994, The aerodynamic loading of radial and mixed flow turbines. *Int. J. Mech Sci*, 36, p. 63-79.

Dolz, V., Novella, R., García, A., and Sánchez, J.H.D., 2012, Diesel engine equipped with a bottoming Rankine cycle as a waste heat recovery system. Part 1: Study and analysis of the waste heat energy. *Appl Therm Eng*, 36, p.269–78.

Hettiarachchi, H.D.M., Golubovic, M., Worek, W.M.,and Ikegami, Y., 2007, Optimum design criteria for an Organic Rankine cycle using low- temperature geothermal heat sources. *Energy*, 32, p.1698–1706.

Lemmon, E.W., Span, R., 2006, Short Fundamental Equations of State for 20 Industrial Fluid. *Chemical & Engineering Data*, 51, p. 785-850

Macchi, E., Perdichizzi, A., 1981, Efficiency prediction for axial flow turbines operating with nonconventional fluids. *J Eng gas turbines power*, 103, p. 718-24.

Rahbar, K., Mahmoud, S., Al-Dadah, R.K., and Moazami, N., 2015, Modeling and optimization of organic Rankine cycle based on a small-scale radial inflow turbine. *Energy Convers and Manag*, 91, p. 186-98.

Rahbar, K., Mahmoud, S., Al-Dadah, R.K., and Moazami, N., 2015, Parametric analysis and optimization of a small-scale radial turbine for organic Rankine cycle. *Energy*, 83, p.696-711.

Rashidi, M.M., Galanis, N., Nazari, F., Basiri Parsa, A., and Shamekhi, L.,2011, Parametric analysis and optimization of regenerative Clausius and organic Rankine cycles with two feed water heaters using artificial bees colony and artificial neural network. *Energy*, 36, p. 5728-40.

Rayegan, R., and Tao, Y.X.,2011, A procedure to select working fluids for solar organic Rankine Cycles (ORCs). *Renewable Energy*, 36(2), p. 659–70.

Wang, J., Yan, Z., Wang, M., Li, M., and Dai, Y., 2013, Multi-objective optimization of an organic

Rankine cycle (ORC) for low grade waste heat recovery using evolutionary algorithm. *Energy Convers and Manag,* 71, p. 146-58.

Rodgers, C., and Geiser, R., 1987, Performance of a high efficiency radial/axial turbine. *Trans ASME J of Turbomachinery*, 109, p. 151-4.

Whitfield, A., and Baines, N.C., 1990, *Design of radial turbomachines*. Longman, New York.

EFFICIENT EVALUATION OF THERMOPHYSICAL PROPERTIES OF WORKING FLUIDS FOR ORGANIC RANKINE CYCLES

Ian Bell

National Institute of Standards and Technology
Boulder, CO
USA

ABSTRACT

The overall topic of this tutorial session is a description of the models that underpin the state-of-the-art thermophysical property libraries, and how these properties can be retrieved in a computationally efficient manner. The emphasis will be placed on the use of the REFPROP property library developed at the National Institute of Standards and Technology (NIST), though other libraries will also be described in some detail.

The first topic of the tutorial session will be a theoretical description of how the models (equations of state, mixture models, transport property formulations, etc.) are constructed. The emphasis of this section will be to describe the theory in a way that is relevant to end-users, such that they can understand the implications of these model formulations on their own code that they write.

Secondly, we will describe the use of the NIST REFPROP library to calculate the parameters of interest, including thermodynamic properties, derivatives of thermophysical properties, mixture phase envelopes, etc. An emphasis will be placed on the different means that can be used to maximize computational efficiency. Furthermore, the various options available for interfacing with REFPROP will be described, including the use of the CoolProp thermophysical property library.

Finally, we will present work that has been recently carried out to use the bicubic tabular interpolation methods of CoolProp to achieve computational speeds for fixed-composition mixtures from REFPROP that are on the order of the computational speed of mixtures that are treated as pseudo-pure fluids. This should be of particular interest to researchers that are carrying out dynamic simulation studies with zeotropic mixtures, as has been proposed in the literature for Organic Rankine Cycles.